NORTHWESTERN UNIVERSITY

Identifying Energy-Structure-Property Relationships in Uranium Metal–Organic Frameworks Through Their Dynamic Crystalline Structural Transformations

A DISSERTATION

SUBMITTED TO THE GRADUATE SCHOOL
IN PARTIAL FULFILLMENT OF THE REQUIREMENTS

for the degree

DOCTOR OF PHILOSOPHY

Field of Chemistry

By

Sylvia Lorraine Hanna

EVANSTON, ILLINOIS

March 2023

ABSTRACT

Identifying Energy-Structure-Property Relationships in Uranium Metal–Organic Frameworks Through Their Dynamic Crystalline Structural Transformations

Sylvia L. Hanna

Uranium is a unique, multifaceted element that possesses rich chemistry and promise for challenging reactions. Pressing demands within nuclear stockpile stewardship and the nuclear energy sector call for development of this relatively understudied element. Uranium metal–organic frameworks (U-MOFs), a class of nanoscale hybrid materials, harness the exceptional attributes of uranium while also further developing its fundamental chemistry. While structure-property relationships in U-MOFs correlate the physical arrangement of atoms in a U-MOF lattice to the resulting material behavior, energy-structure-property relationships allow researchers to *rationalize* these correlations. In this thesis, I identify and investigate energy-structure-property relationships in U-MOFs through the study of their dynamic crystalline structural transformations. Chapters 2-4 illustrate separate aspects of energy-structure-property relationships as individual vignettes (Chapter 2: structure-property relationships, Chapter 3: energy-structure relationships, Chapter 4: energy-property relationships). Finally, Chapter 5 ties energy, structure, and property together to explain *why* structure produces function. This thesis ultimately offers a deeper understanding of U-MOF behavior, discovers novel U-MOF phenomena, and delineates design rules for the budding U-MOF field.

ACKNOWLEDGEMENTS

I am indebted to countless colleagues, collaborators, mentors, friends, and family members for their great impact on my pathway to and journey through my Chemistry Ph.D.

First, I would like to express my sincere gratitude to the teachers who molded and influenced me in my formative years. Mrs. Hibbard – you showed me how interesting math and science were and demonstrated what it looks like to strive for excellence. Mrs. Iles – you erased my stage fright, and I never anticipated how impactful that would be. Thank you to my many music teachers, but especially to Mrs. Neff, Manami, and Elena. The rigorous precision yet elegant finesse you exemplified has carried over into all aspects of my life. Mr. Ham – you still inspire me today to have more faith and live energized.

I have overwhelming gratitude for my mentors at Rowan University and throughout my undergraduate experience who invested undeservedly in my scientific and personal growth and are the real reasons chemistry became my own. I would first like to thank Dr. Bradford Fisher and Dr. Bryan Hamade, who both mentored me with kindness and grace; my short time under your tutelage ingrained in my heart what honest mentorship looks like, and I am eternally thankful for that lesson. I am enormously indebted to Professor Timothy Vaden who simply and straightforwardly taught me chemistry from the book to the bench, and whose research mentorship has had arguably the most notable impact on my scientific training. Thank you to Kyle and Olivia but especially Miranda for introducing me to the way research is done. Professor Gregory Caputo ("co-author") – you are a terrible influence, but a wonderful mentor. Thank you for teaching me about graduate school and encouraging me to go. I am specifically grateful to Professor Nathaniel Nucci whose excitement about science was contagious and who gave me the courage I needed to take a scary step. Professor Kandalam Ramanujachary's ("Chary") passion for inorganic chemistry resonated

with me and helped guide me into the topics of chemistry I think about daily. Thank you to Professor Lark Perez for redeeming organic chemistry. I am very grateful for the investments Professor Haw Yang, Dr. Simon McManus, Professor Joseph Stanzione, Dr. Alexander Bassett, Dr. Silvio Curia, and Professor Jeffrey Hettinger made in my career. These men fostered my development as a scientist by providing me with research opportunities that enabled me to find my way. Kathy Monahan – you were a remarkable asset to my Rowan experience, and I am eternally thankful for your open door, heart, and arms. Jess – I will always be grateful I landed at your table in Biology with Dr. Travis, even if I did arrive atrociously late to our first lab class, as prophesied by Dr. Travis himself. I would like to thank Will and Ian for their friendship and for motivating me to think harder, simpler, and smarter. I have the utmost appreciation for Dr. Lee Talley who greatly influenced my journey to graduate school. Thank you to the Rowan University STEM Symposium, the Rowan University Summer Undergraduate Research Program Symposium, and those who organized and directed it – these were my very first tastes of scientific community and were particularly impactful to my development. To my Rowan University American Sign Language Club executive-board, John Woodruff, Elias, and Stephanie – thank you for supporting my vision and for adding a very meaningful perspective to my life that I will always treasure.

My time at Northwestern University has been life-altering, and I have enormous gratitude for the phenomenal people who have been so critical to both my scientific and personal development. First and foremost, I am immensely indebted to my thesis advisor, Professor Omar K. Farha, and I would like to thank him from the bottom of my heart. Omar's drive and ambition will never cease to inspire me. I am deeply thankful for his guidance in both the scientific and professional aspects of my graduate career and for his reliable and constant support, even in the emergency room of the Northshore hospital. Omar has shown a dedication to my scientific development that I can only

hope to one day repay. Thank you to Dr. Riki Drout ("Richolas") for being my first friend at Northwestern and truly one of the dearest friends I have ever had. You took me under your wing as a very naïve first-year graduate student, and your influence profoundly shaped how I approach scientific research. I have great appreciation for Professor Timur Islamoglu – thank you for always having your door open and for going above-and-beyond to answer my every question thoroughly and with a kind heart; you have been critical to my scientific development. I am very grateful to Dr. Louis Redfern who taught me the methods and value of thoughtful scientific inquiry. I am indebted to Dr. Lee Robison who has spent countless hours mentoring me to write and present scientific stories and who has also shown me incredible friendship. Thank you to Professor Chung-Wei Kung for teaching me about marginal conditions and efficiency. To Dr. Kent Kirlikovali – I am deeply grateful for your mentorship, selflessness, and friendship. You give me a reason to push onwards on difficult days, and you brighten my life with laughter and sincerity. I would like to thank Julia Knapp for all that she has taught me in chemistry and in life. Julia's calming demeanor and reliability have grounded me daily, and I could not choose a better office-mate. Thank you to the ever-fluctuating Actinide Squad, the Ryan 1018 crew, and the Farha group Program Assistants, Abby Rosensweig, Nick Huryk, and Greg Mandell. Thank you to each and every Farhomie I have had the pleasure of working with, including Xingjie, Kaikai, Yufung, Dahee, Courtney, Mike, Madeleine, Yijing, Ahmet, Xuan, Yongwei, Ran, Ken-ichi, Fanrui, Tony, Xinyi, Jiafei, Flo, Kira, Mandy, Rasel, Yongwei, Johannes, Isil, Alyssa, Alejandra, Deb, Sree, Haomiao, Luana, Wei, Chen, Karam, Zoha, Lauren, Seryeong, and Josh. I would be remiss to not mention the Hupp-group members who I have also had the pleasure of interacting with: Subhadip, Jian, Dawn, Boris, Hyun, Cornelius, Rui, Aaron, and many others. Thank you to the Kanatzidis group who graciously accommodated my continuous use of their vacuum sealing line during the last few months of my

Ph.D. I would like to express my thanks to my thesis committee for their investment in my scientific development: Professor Joseph Hupp, Professor Mercouri Kanatzidis, and Professor Kenneth Poeppelmeier.

I am extremely grateful for Northwestern's Integrated Molecular Structure Education and Research Center (IMSERC) where I have spent hundreds of hours over the course of my graduate training. I have a special gratitude for Dr. Christos Malliakas whose tireless mentorship and generosity have been critically important to my scientific growth and to every project I have led in graduate school. Christos exemplified humble brilliance and is a phenomenal role model that I am fortunate to have. Thank you to Dr. Charlotte Stern for her investment in my path through graduate school and for the many conversations over microscopes about life, decision-making, and family.

I would like to thank the various collaborators that I have had the pleasure of working with over the last few years. I am very grateful to Professor Peter Burns for his warmth, overpowering intellect, and intentional support. I must also thank Hrafn Traustason and Sarah Gilson who have both welcomed me into the community of actinide scholars. Professor Laura Gagliardi and her team, specifically Saumil Chheda and Dr. Debmalya Ray, elevated our research findings through their detailed computational efforts, for which I am very grateful. I have particularly benefited from Professor Christopher Hendon who has participated in scientific discussions in a most constructive and engaging manner. I must also thank Professor J. Fraser Stoddart, Professor Diego Gomez-Gualdron, every member of the Actinide Center of Excellence, and the various other collaborators and co-authors who have made such a notable impact on my scientific training.

I would like to acknowledge the generous funding from the Actinide Center of Excellence, Stewardship Science Graduate Fellowship, Ryan Fellowship (Pat and Shirley Ryan), CAS Future

Leaders Program, Innovations in Nuclear Technology R&D Awards, The Graduate School at Northwestern, and NUBonD which enabled me to perform research, travel to a variety of scientific conferences, and develop enriching connections and beautiful memories that I look back on fondly. Conference trips were some of my most enjoyable graduate school experiences, and I am very grateful to have met kindred spirits like Steven Crossley, Dylan Sherman, Robbie Woodward, Sandra Strangeby, and Drew Morrill through them.

In addition to those mentioned above, I am incredibly grateful for the individuals who have made this place my home. Wasson – I am deeply thankful for your camaraderie, dependability, honesty, integrity, empathy, and advice. Your friendship has been the most valuable relationship of my graduate experience. Thank you to Austin who has deeply impacted the way I view science within my broader worldview – your wit, intellect, friendship, and curiosity have brought excitement to even the dullest moments. Kenton, Rodrigo, and Tim – thank you for bringing laughter, warmth, and invaluable companionship to our circle. Ward – your kind and genuine heart is so inviting, and Kaster – thank you for being such a reliable friend. I must express my sincere gratitude to the Covenant Presbyterian Church community, especially to Pastor Aaron Baker, James, Shawn, Brendan, Katie, Alex, Amanda, Julie, and Amy. I would also like to acknowledge the Villa Park Christian Assembly, specifically Heba and Walaa Yakoub and Mike and Audrey Vienot.

It is with great respect that I acknowledge the entire entourage of scientific minds who contributed to the development of the COVID-19 vaccine. I am also very thankful for Dr. Theodore Mazzone and Dr. Charles Chen, both of whom have rigorously cared for my health and wellness over the last several years. I must also acknowledge Laura and Paul from bodypump who contributed to my wellness through fitness.

My hearty gratitude is due to the people at Sandia National Laboratories who mentored and supported me. Most importantly, I thank Dr. Susan Henkelis-Halls for her guidance, strength, and care. Thank you also to Ben, Jess, Matt, Kyle, Yibin, Justin, and Nate for adopting me into your circle. I have great respect for Dr. Matthew Gomez – thank you for your quietness, reliability, support, and commitment to integrity. I must also thank David Rademacher, Benjamin Galloway, Haylie Lobeck, Providence Presbyterian Church, and Pastor Randy Steele for their great influence on my time as a visiting scientist in Albuquerque.

I would like to express my sincere gratitude to Elysse Longiotti for her guidance and impact on my professional development journey. To Sophie Tidd, Dr. Mareena Robinson Snowden, Dr. Andrea Greyson, Dr. Juan Callejas, Dr. Patricia Ansems Bancroft, Dr. Matthew Belowich, Dr. Cory Valente, Dr. Alexia Finotello, Dr. Jon Axtell, Dr. Kyle McDonald, Dr. Karena Smoll, and all of Dow BEST – you each played an integral role in my early career development for which I am deeply thankful.

Thank you to Aphhia, Maryanne, Michelle, Shaunessy, Julie, Sami, Martha, Carmen, and the wonderful people at Colonia Chapel: your support, friendship, and guidance have been invaluable, even from hundreds of miles away.

I cannot fully express my overwhelming gratitude for the remarkable family unit I have been blessed with. Without their consistent involvement in my life and ever-constant love, I would have never earned a single degree or become the person I am today. I am enormously indebted to my Mother and Father; their investment in my education, immense personal and professional sacrifices, and powerful faith have enabled me to live the life I do now. Mom – thank you for your tireless prayers, encouragement, selflessness, and commitment to excellence. Dad – you are my biggest role model, and I strive to embody your wisdom, generosity, kindness, and precision. I am

also profoundly grateful for my Siblings, recently grown in number from three to five; as my closest friends, my Siblings have grounded me through every ordeal and have filled my life with meaning, laughter, and rich memories that I will forever treasure. I am eternally thankful for Lydia's voice-of-reason, grace, honesty, and strength; she is my close confidante and constantly champions me at every step. David – thank you for your candor, humor, drive, and intuition; your steadfastness inspires me, and you have carried me out of dark times. I am deeply grateful for Heather Lily whose sweetness, simplicity, humor, spirit, selflessness, support, and kindness light up my life and constantly inspire me to live better. Andrew – thank you for challenging me and advising me. Bethany – thank you for your constant support and generosity.

Finally, I must thank God for giving me breath every day, for the wins, for the losses, and for the lessons.

TABLE OF CONTENTS

LIST OF TABLES

LIST OF FIGURES

LIST OF SCHEMES

CHAPTER 1. Energy-Structure-Property Relationships in Uranium Metal–Organic Frameworks

1.1 Chapter Summary

Located at the foot of the periodic table, uranium is a relatively underexplored element possessing rich chemistry. In addition to its high relevance to nuclear power, uranium shows promise for small molecule activation and photocatalysis, among many other powerful functions. Researchers have used metal–organic frameworks (MOFs) to harness uranium's properties, and in their quest to do so, have discovered remarkable structures and unique properties unobserved in traditional MOFs. More recently, (*e.g.* the last 8-10 years), energetic analyses have supplemented structure-property studies in uranium MOFs (U-MOFs). This chapter summarizes how these budding energy-structure-property relationships in U-MOFs enable a deeper understanding of chemical phenomena, enlarge chemical space, and elevate the field to targeted, rather than exploratory, discovery. Importantly, this chapter encourages interdisciplinary connection between experimentalists and theorists by demonstrating how these collaborations have elevated the entire U-MOF field.

2.2 Introduction to Uranium in Metal–Organic Frameworks

Among the diverse chemistry that the periodic table offers, uranium stands distinctly apart from *s*-, *p*-, and *d*-block metals, and even from its actinide and lanthanide relatives. With three *f*-electrons and unique electronic structure,[1] uranium's character is complex and multifaceted. Indirect relativistic orbital expansion endows uranium with diverse oxidation states ranging from U(I) to U(VI),[2-6] resulting in impressive redox performance.[7] High coordination numbers and multiple bonding characterize uranium's coordination, and relativistic effects also change the extent of its bonding covalency.[7-9]

Consequently, these fundamental singularities amplify into the striking properties of uranium's molecular species and materials. Perhaps its most notable function, uranium shows promise for challenging reactions relevant in the highly industrialized Haber-Bosch and Fischer-Tropsch

processes.[10-12] Uranium's ability to activate small molecules is not only limited to N_2 and CO, but also extends to other environmentally relevant species including CO_2, NO, and hydrocarbons.[7] Additionally, uranium possesses powerful photoredox abilities,[13-15] impressive single molecule magnetism,[15-17] and burgeoning catalytic capacity.[18-20]

It was not until over a century after its discovery by Martin Klaproth that uranium's radioactive and energetic fission properties were discovered.[9] Use of fissile uranium radioisotopes during the Manhattan Project projected a historically negative image on uranium, with deep scientific and societal implications. This image, paired with actual or perceived fear regarding its safety, is responsible in part for the relatively underdeveloped nature of scientific research on uranium. Currently, pressing demands within nuclear stockpile stewardship[21] and the nuclear energy sector[22] call for development of uranium, made possible primarily through the scientific study of its depleted ^{238}U isotope.[23]

While the combined efforts of various scientific minds have advanced uranium's molecular and material chemistry remarkably, this thesis focuses on the study of uranium's crystal chemistry. Specifically, researchers have harnessed unique attributes of uranium by installing it in nanoscale hybrid materials called metal–organic frameworks (MOFs) which possess directional, mathematically predictable bonding patterns.[24-27] Built from the self-assembly of organic, multitopic linkers and uranium-based single-atom or cluster nodes, uranium MOFs (U-MOFs) are a twist on their classical transition metal-based counterparts. Like traditional transition-metal MOFs, U-MOFs boast crystallinity, higher-order dimensionality, synthetic tunability, and impressive porosity. However, electronic, architectural, and behavioral differences make U-MOFs fundamentally distinctive.[28-30] Importantly, U-MOFs provide valuable insight into the intersection of environmental stewardship and nuclear fuel processes, as their chelation environments mirror

that of the uranium mineral, studtite.[31] Additionally, U-MOFs possess optimal attributes to harness and develop uranium chemistry in a relatively facile manner; spatially separated nodes discourage ever-present disproportionation, and facile hydrothermal/solvothermal MOF syntheses allow researchers to tune the ligand environment without re-developing complex organometallic syntheses. We refer to this broad class of materials as uranium MOFs (U-MOFs) for the remainder of this Perspective, but we note that they are also referred to as uranium–organic frameworks (UOFs) or uranium coordination polymers in the literature.

Most commonly, U-MOFs crystallize as hexavalent uranium polyhedra[32, 33] connected by organic linkers. In its hexavalent state, uranium typically exists as the linear, symmetric uranyl $[UO_2]^{2+}$ dication (Scheme 1.1c) where U(VI) binds to two axial oxygen atoms with short 1.8 Å bonds. The equatorial plane remains available for binding to carboxylate,[29] phosphonate,[34] imidazolate, and other groups, forming bipyramidal polyhedra.[30, 35-40] The hydrolysis of uranium can produce nodes with a plethora of nuclearity, and less-common node motifs comprised of clusters or lower-valent uranium also occur. Advancement of U-MOF underlying design principles has led to a library of impressive hybrid structures and unprecedented arrangements.[30, 41-43] This structural collection boasts emerging properties applied in catalysis, photochemistry, waste capture, electronics, sensing, non-linear optics, and luminescence. Importantly, ties between structure and property have been crucial to the progress of the U-MOF field from exploratory synthesis to more targeted development.[28, 35, 44-52]

A third dimension of exploration remains – that of energy. While structure-property relationships correlate the physical arrangement of atoms in a U-MOF lattice to the resulting material behavior, fundamental energetic investigations allow researchers to *rationalize* these correlations. Energy-structure-property relationships thereby offer a deeper understanding of phenomena, explaining

why structure produces function. This understanding becomes crucial for the rational design of targeted U-MOF materials with specific and enhanced properties that are energetically accessible. Indeed, energy-structure-property relationships ultimately offer a very precise knob to not only fine-tune existing material properties through structure, but to also discover next-generation materials with novel properties.

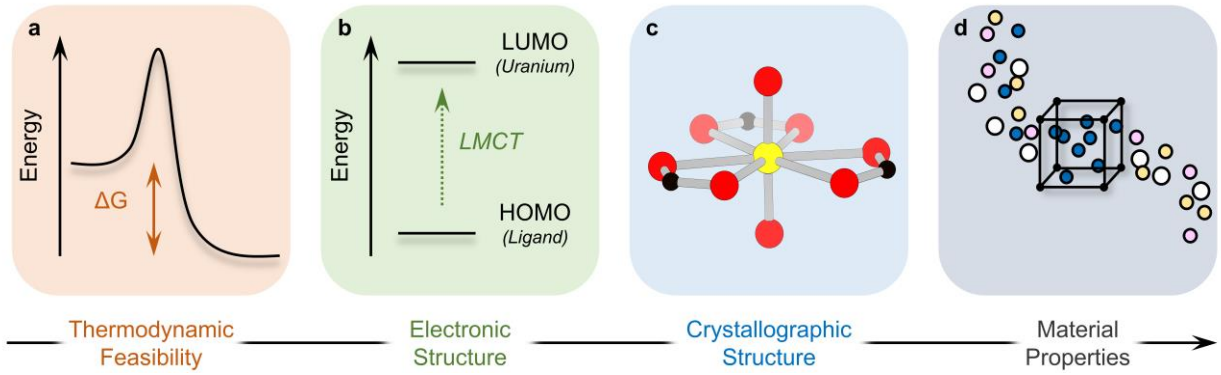

Scheme 1.1 Structure of this chapter, progressing from (a, b) fundamental energetic characterization of U-MOFs to (c) structures and (d) resulting properties.

Over the last 8-10 years, the U-MOF field has begun to investigate energy-structure-property relationships. This chapter serves to highlight the impact and importance of newly established energy-structure-property relationships in the development of U-MOFs. We structure this chapter to progress from the energetic characterization of U-MOFs to the ways in which energy affects structure, and finally to the resulting connections between energy, structure, and property. We begin by examining the energy landscape on which U-MOFs lie (Part I, Scheme 1.1a): are the targeted structures energetically accessible? Next, we discuss the electronic structure and properties of energetically feasible U-MOFs (Part II, Scheme 1.1b). Part III moves from U-MOF electronic structure to crystallographic structure and explains how structural distortions and geometries originate in energetic phenomena (Scheme 1.1c). In Part IV, we consider how energetics inform properties (Scheme 1.1d). Finally, we discuss the future potential of energy-

structure-function maps as a method to harness knowledge as the field ages. As an underlying theme, this chapter emphasizes the interdisciplinary relationship between experiment and calculation and is not designed to alienate either audience, but rather to enhance the connection between the two.

1.3 Energetic Accessibility of U-MOFs

Emergent U-MOF structures and properties depend upon the energetic feasibility of constructing the structure to begin with (Scheme 1.1a). While both thermodynamic and kinetic drivers impact framework formation, the U-MOF field has focused primarily on investigating the former. Calculated free energies of formation thus provide valuable insight into the thermodynamic stability of desired U-MOF products relative to their starting form. This information in turn assists in predicting and explaining our power to synthetically access specific ligand and node motifs or even entire topologies.

For example, Li *et. al.* reported the single-crystal-to-single-crystal transformation of the U-MOF URCP3 to URCP4 and calculated that ligand coordination in the URCP4 isomer favored its relative stability. Both isomers crystallize with a uranyl node, a pseudorotaxane cucurbit[6]uril-based linker, and a sulfate anion (derived from the uranyl sulfate starting material). However, while URCP3 possesses a monodentate linker and bidentate sulfate, URCP4 holds a bidentate linker and monodentate sulfate. The thermodynamic stability of the URCP4 ligand binding motif over that of its isomer explains the irreversible and spontaneous transformation of URCP3 to URCP4 (Fig. 1.1a).[53] Thermodynamics of ligand binding can also be observed in the study of Ejegbavwo *et. al.* to post-synthetically install capping linkers into U_6-Me_2BPDC-8 (Me_2BPDC^{2-} = 2,2′-dimethylbiphenyl-4,4″-dicarboxylate). Theoretical calculations supported observed linker installation in the isostructural Th-based MOF and predicted the energetic feasibility of U_6-

Me_2BPDC-8 transformation to a 10-connected (-308.372 kJ mol^{-1}) or 12-connected (-640.880 kJ mol^{-1}) MOF.[54]

In addition to ligand crystallization, the composition and structure of uranium nodes also depend on their energetic accessibility. The Shustova group demonstrated this concept during their efforts to extend MOF modularity by integrating actinide ions through transmetalation. Interestingly, attempted transmetalation of a Zr_6 cluster UiO-type MOF (Zr_6-Me_2BPDC-8) with actinides proved unsuccessful, while transmetalation of the analogous U_6-Me_2BPDC-8 MOF with Th resulted in $Th_{5.65}U_{0.35}$-Me_2BPDC-8 and marked the first actinide-to-actinide cation exchange in MOFs. Density functional theory (DFT) calculations revealed an unfavorable energy to substitute six Zr node atoms to U (Fig. 1.1b); thus favorable substitution energy for U to Th likely allows for its successful transmetalation.[55] The use of U as a surrogate for Np motivated Saha and Becker to similarly investigate the energetic favorability of Np incorporation into U-MOFs. Computational studies suggested thermodynamically favorable incorporation of Np, even in the face of changing node geometry.[56]

Combining the effects of U-MOF linker and node motifs with framework topology reflects overall lattice stability. In collaboration with the Hendon group, our group used total energy calculations paired with experimental studies to quantify the synthetic feasibility of a metastable U-MOF isomer, NU-1306. Isomers NU-1305 and NU-1306, both comprised of a tetrakis(4-carboxyphenyl)methane linker and mononuclear uranyl node, crystallized in **ctn** and **bor** topologies, respectively. We identified the thermodynamic stability of NU-1305 over NU-1306 (Fig. 1.1c) and demonstrated how these energetic phenomena allowed conversion from metastable NU-1306 to globally stable NU-1305, but not vice-versa.[57]

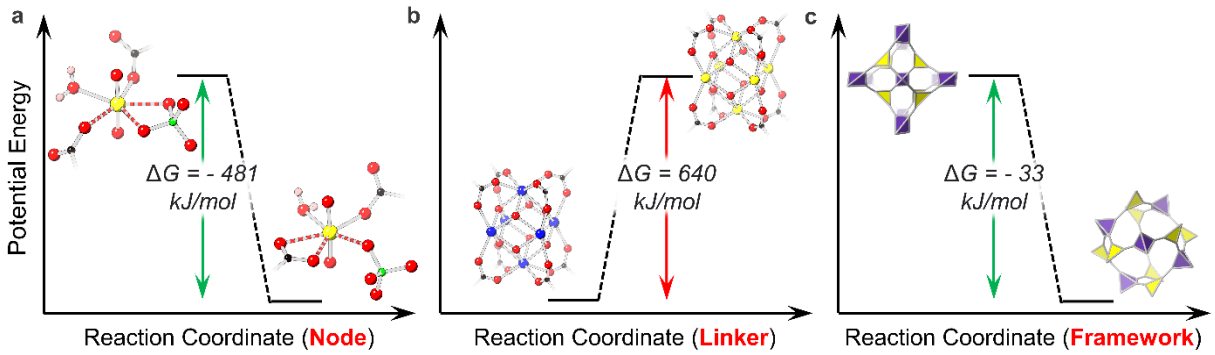

Figure 1.1 Thermodynamic favorability of (a) ligand moti: URCP3 on the left and URCP4 on the right. Bonds of interest are dashed; (b) node motifs: Zr_6 cluster on the left and U_6 cluster on the right; (c) framework topologies in U-MOFs in: NU-1306 on the left and NU-1305 on the right. O is shown in red, U in yellow, C in black, H in pink, S in green, and Zr in blue.

1.4 Effect of U-MOF Electronic Structure on Coordination and Bonding

Once envisioned U-MOF structures become synthetically feasible, researchers resolve their electronic properties by characterizing the energy levels of the frontier molecular orbitals involved in electronic transitions. Simulated DFT calculations compliment absorption, infrared, raman, fluorescence, and photoluminescence spectroscopy to elucidate the fundamental nature of bonding in U-MOFs. Ultimately, these studies demonstrate how *f*- and/or *d*-electrons affect U-MOF material properties.

Frontier molecular orbitals in uranyl-based U-MOFs most often possess a highest occupied molecular orbital (HOMO) with primarily ligand character. Specifically, phenyl- or benzene-based π character[58, 59] and 2p orbitals from carboxylate oxygen atoms[60-63] dominate this energetic regime. The lowest unoccupied molecular orbital (LUMO) is primarily stabilized by uranium and exhibits 5*f* character[58, 60-65] or uranyl *d*-orbital qualities.[59, 66] Ligand to metal charge transfer (LMCT) in these compounds point to electronic promotion from organic linker to uranium center and is often indicated by low energy absorption bands (Scheme 1.1b).[66, 67] Calculated natural charges in electronically active frameworks also reflect LMCT behavior: while the natural charge of the free uranyl cation is expected to be 2.81, bound uranyl cations in MOFs show values in the range of

1.38-1.54.[60, 68-70] Pandey *et. al.* published a detailed study systematically exploring DFT methods to distinguish the contribution from organic and inorganic components to the HOMO-LUMO band gap origin in U-MOFs.[71]

Since relativistic effects strongly influence uranium bond covalency, U-MOF electronic structures closely relate to the ionic vs. covalent nature of linker-to-node bonding. In general, organic linkers predominantly exhibit covalent bonding characteristics while the metallic uranyl node demonstrates ionic bonding characteristics.[61] Bond order and electron density calculations of axial (U-oxo) and equatorial bonds in the uranyl subunit closely link to their specific character. Calculated and experimental bond lengths for uranyl-oxo bonds in U-MOFs exhibit double bond (2.0-2.1)[62, 69, 72, 73] or partial triple bond (2.20-2.37)[63, 67, 74] character. These axial bonds are classified as covalent bonds, justifying their relatively inert behavior compared to U-O equatorial bonds. U-oxo bonding character in MOFs can, however, be influenced by the presence of other interacting ions.[70, 75-77] Equatorial U-O bonds predominantly exhibit smaller bond orders (0.3-0.6) which suggest mostly ionic or weak covalent character.[62, 67, 69, 72-74, 78]

These electronic structure considerations directly affect U-MOF bonding features and coordination behavior. For example, in a variety of uranyl-based MOF systems containing both U-O and U-N equatorial bonds, stronger interactions with uranium originate from oxygen-bound rather than nitrogen-bound ligands.[59, 72, 73] While this behavior corresponds with uranium's well-known oxophilicity, it also reflects the stronger LMCT of carboxylic acid-based linkers over nitrogen-bound linkers like phenanthroline.[69] The Sun group also demonstrated effects of the HOMO-LUMO gap in their uranyl-based MOF system. While pairing the uranyl node with a terpyridine-based metalloligand produced infinite 1D chain structures, addition of the auxiliary 4,4′-biphenyldicarboxylic acid linker resulted in 3D catenated frameworks. Interestingly, increasing

dimensionality from 1D to 3D systems decreased the HOMO-LUMO gap from 4.29 eV to 2.93 eV, suggesting that addition of the auxiliary ligand resulted in more diffuse electronic motion.[68]

1.5 Energetic Origins of Crystallographic U-MOF Configurations

The influence of energetics on U-MOF crystallization impacts resulting material properties dramatically. Because structural distortions, unusual geometries, and unique bonding originate in energetic phenomena or instability, theoretical calculations provide insight into the nature of these crystallographically characterized configurations. Within uranyl-based MOFs (Scheme 1.1c), energetic effects influence axial U-oxo bonds, equatorial node bonds, and overall crystallization preference.

For example, Chen *et. al.* reported a U-MOF containing unusual 173.3° curvature in the typically linear 180° uranyl dication (Fig. 1.2a).[70] The 8-coordinate uranyl unit was bound to two bidentate 1,4-benzenedicarboxylic acid linkers and two monodentate 1-(4-(1*H*-imidazol-1-yl)-2,5-dimethylphenyl)-1*H*-imidazole linkers. DFT investigations revealed that the electronegative heterocyclic imidazole units induced the bent uranyl geometry by generating higher charge populations in the valence U 6*d* shell. Studies by the Cahill group on harnessing terminal oxo chemistry reveal energetic foundations of both non-covalent and covalent oxo interactions in U-MOFs. In one case, 1D chains of the uranyl cation bound to benzoic acid, *m*-chlorobenzoic acid, *m*-bromobenzoic acid, or *m*-iodobenzoic acid non-covalently assembled through hydrogen or halogen-oxo interactions (Fig. 1.2d). Through DFT calculations, the relative strength of these non-covalent halogen-oxo interactions was shown to originate in inductive effects and halogen polarizability.[76] Conversely, covalent oxo-Ag^{+} interactions in a separate U-MOF decreased uranyl bond orders through electron donation from Ag^{+} to U–oxo σ- or π-antibonding orbitals.[77]

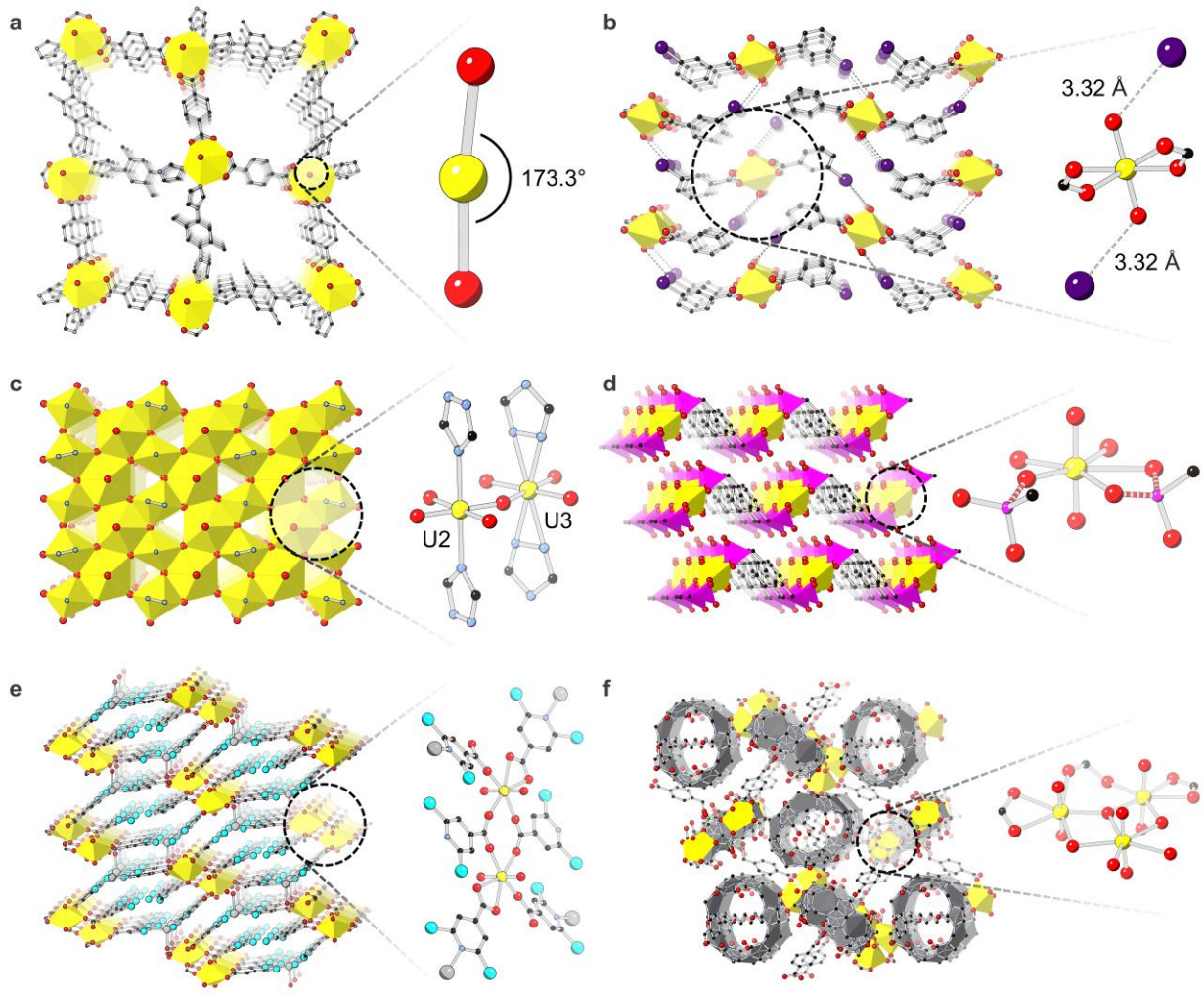

Figure 1.2 Crystal structures demonstrating (a) distortion of axial U-O bonds. Only one of the structure's three interpenetrated lattices is shown for clarity; (b) axial U-O bond interaction with iodine from the *m*-iodobenzoic acid linker; (c) Kagome lattice and equatorial U-O bonding modes; (d) equatorial bonding of phosphonate-based linkers to uranyl in $[NH_4]_2[UO_2(pmb)]$. NH_4 is removed from the structure for clarity, and phosphonate linkers are terminated at carbon atoms. Bonds of interest are dashed; (e) U-Ag-2,6-DCPCA containing Ag-N bonds; (f) *N*,*N*′-bis(4-cyanobenzyl)-1,4-diammoniobutane dinitrate are bound to an asymmetric trinuclear uranyl node and are encapsulated by cucurbit[6]uril shown in grey panels. O is shown in red, U in yellow, C in black, S in green, I in navy, N in light blue, P in pink, Cl in aqua, and Ag in grey. H are hidden for clarity.

Equatorial U-O bonding modes and distortions also originate in energetic roots.[79] In their report of the first *f*-element Kagomé topology coordination complex, Smetana *et. al.* observed disorder between two complementary mutually excluding U positions. Bound monodentately by triazolate-based linkers, U2 occupied 84.6%, and U3, bound in a bidentate fashion, occupied 15.4% (Fig.

1.2b). The nature of this disorder was clarified through DFT studies on triazolate linker interactions; strong repulsions between triazole nitrogen atoms and nearby oxygen atoms prevented bidentate triazole binding in U2 while additional hydrogen-bond stabilization in U3 compensated for N-O repulsions and encouraged bidentate triazole coordination.[80] Theoretical calculation also helped distinguish binding motifs of equatorial groups in uranyl phosphonate compounds. For example, the 1,4-phenylenebis(methylene))bis(phosphonic acid) linker can bind to uranyl through both P-O^- and P=O motifs, driven by electrostatic forces or electron lone pair donation, respectively (Fig. 1.2e). The Wang group confirmed their assignment of these crystallographic binding modes through calculations of bond indices and electron density.[81]

Apart from specific geometries of axial U-oxo or equatorial U-O bonds, effects of energetics have also been observed on U-MOF overall structure. For instance, Mei *et. al.* reported an energy decomposition analysis which identified an Ag-N bond as the driving force for the formation of the U-MOF, U-Ag-2,6-DCPCA (H-2,6-DCPDA = 2,6-dichloroisonicotinic acid) (Fig. 1.2c).[62] Findings by the same group also directly related the unique weaving configuration of their polyrotaxane polythreaded U-MOF to the asymmetric coordination of its trinuclear node through quantum chemical calculations (Fig. 1.2f).[82]

1.6 Energetic Origins of U-MOF Structure-Property Relationships

A strong driver in the exploration of U-MOFs is the potential for discovery of novel properties (Scheme 1.1d). Indeed, the multifaceted character of uranium promises behaviors that transition metal-, lanthanide-, and even other actinide-based MOFs cannot provide. Chemical structures can explain or correlate to emergent properties, but the underlying reasons for their existence lie in energetic processes. The combination of theoretical calculations with experiment thereby describes why certain U-MOF structures produce properties such as spontaneous de-interpenetration,

photochromism, radiation resistance, radioactive waste capture, and catalysis.[83-85] This fundamental understanding of U-MOF behaviors not only explains chemical phenomena but also enhances material properties.

One recent example of novel behaviors in U-MOFs is our group's discovery of spontaneous de-interpenetration–a property unobserved in any network material to date.[86] De-interpenetration transformed NU-1303-*6*, a 6-fold interpenetrated U-MOF with 14.2 Å and 19.8 Å pores, into an open, single-lattice structure with 40.7 Å pores and record-high free void space (96.6%). This generation of porosity in the absence of external stimuli proves valuable for various applications including gas storage, catalysis, and electronics. Energetic investigations into the origins of this phenomena revealed that charged point-point repulsions between anionic uranyl nodes, present across the entire energy landscape, drove structural changes and reversed typical thermodynamic framework favorability (Fig. 1.3a).

U-MOFs also exhibit impressive optoelectronic properties,[87, 88] as seen in the first photochromic actinide-based framework, reported by the Shustova group.[89] Using a photoswitchable spiropyran-based linker paired with a heterometallic Th_5U cluster node, Martin *et. al.* accessed dynamically controlled conductivity and electronic properties. Importantly, electronic structure calculations revealed fundamental differences between photochromic Th_5U MOFs and non-photoresponsive Th_5U MOFs; frontier orbitals of the former involved in electronic transitions originated from U and Th 5*f* orbitals while those of the latter localized on the linker (Fig. 1.3b). In this way, photophysical properties in actinide MOFs were tied to electronic structure for first time.

U-MOFs also show value as adsorbent materials for fission product waste and contamination remediation. For example, the Wang group reported a U-MOF with impressive radiation resistance up to 200 kGy of γ and β irradiation and excellent chemical stability.[90] Additionally, this U-MOF

exhibited selective Cs(I) removal from aqueous solution with a distribution coefficient at the same order of commercial materials. These properties were attributed to the rare U-MOF structure, where 2D graphene-like sheets of $[(CH_3)_2NH_2][UO_2(L2)]\cdot 0.5DMF\cdot 15H_2O$ (L2=3,5-di(4′-carboxylphenyl) benzoic acid) catenate into a 3D framework with geometric distortions in the equatorial uranyl plane. Linear transit calculations further revealed that structural umbellate distortions were rooted in electronic behavior; repulsions from the umbrella-shaped equatorial carboxylate ligands pushed O_4's valence orbitals up in energy, producing a better orbital energy match with uranium's contracted 5*f* valence orbitals (Fig. 1.3c).

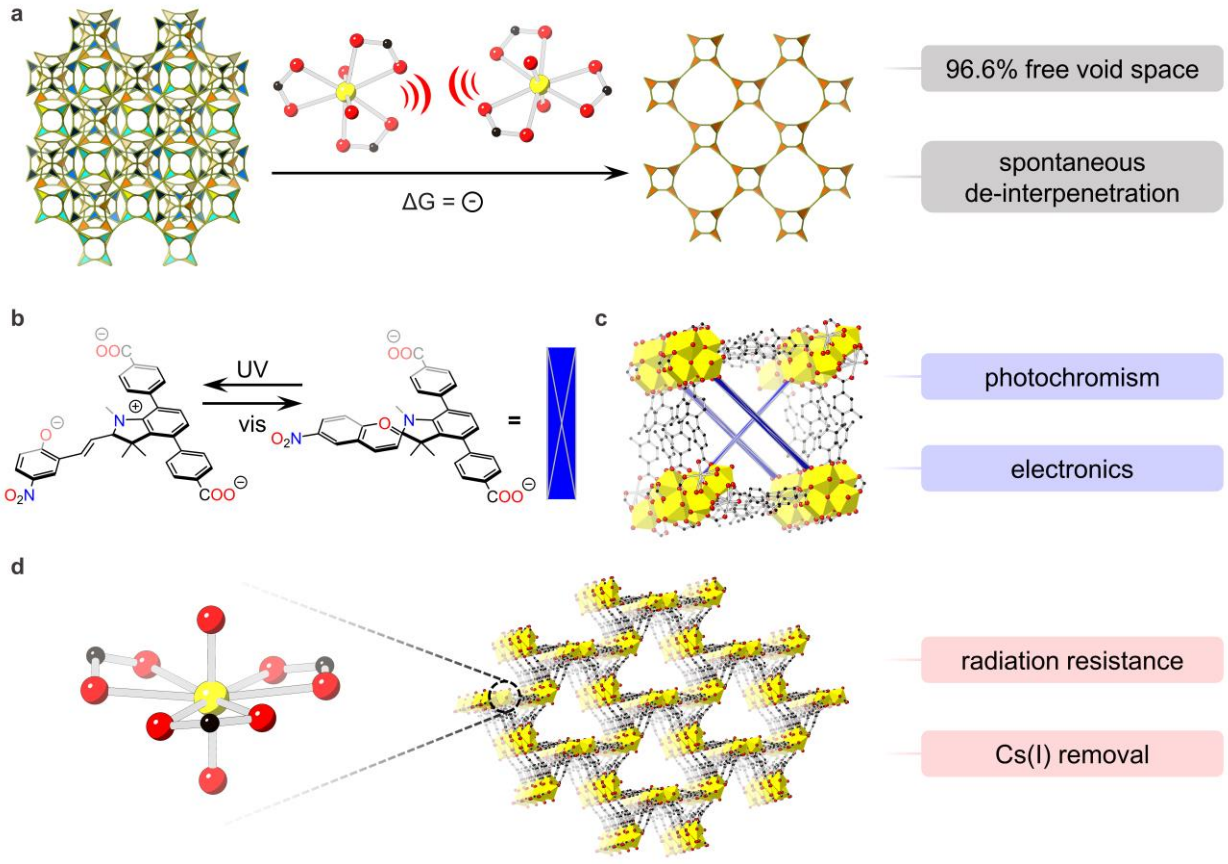

Figure 1.3 Energy-structure-property relationships in (a) the spontaneous de-interpenetration of NU-1303-*6*, (b) photochromic spiropyran linker in (c) actinide-based framework, (d) U-MOF with umbellate distortions. O is shown in red, C in black, H are hidden for clarity. U is shown in yellow in all panels except for (c) where heterometallic nodes are comprised of $Th_{4.77}U_{1.23}$.

2.7 Conclusions and Outlook

Energy-structure-property relationships in U-MOFs enable a deeper understanding of chemical phenomena, enlarge chemical space, and elevate the U-MOF field to targeted, rather than exploratory, discovery. In this Perspective, we have detailed the impacts of energetic studies on U-MOF thermodynamic feasibility, electronic structure, crystallographic structure, and material properties. We believe that energy-structure-property relationships lie at the heart of innovation and progress, and their detailed development will inspire the next generation of U-MOF materials with advanced properties. Importantly, close connections between experiment and calculation are crucial for this type of progress, particularly in the field of U-MOFs where much of uranium's promise remains undiscovered.

As the field of U-MOF ages and the library of energetically characterized materials increase, concrete and organized connections between energy, structure, and properties become vital. Looking forward, we propose the eventual application of energy-structure-function maps in the U-MOF field.[91-96] These maps rely on machine learning to reveal the energetically accessible regions of the system's lattice-energy surface and propose possible structures and properties for the building blocks of choice. Such a tool promises special value for exploring the multifaceted, complex, and unique crystal chemistry of uranium.

CHAPTER 2. Guest-Dependent Single-Crystal-to-Single-Crystal Phase Transitions in a Two-Dimensional Uranyl-Based Metal–Organic Framework

A vignette on structure-property relationships.

Portions of this chapter appear in the following manuscript:

Hanna, S. L.; Zhang, X.; Otake, K.; Drout, R. J.; Li, P.; Islamoglu, T.; Farha, O.K., Guest-Dependent Single-Crystal-to-Single-Crystal Phase Transitions in a Two-Dimensional Uranyl-Based Metal–Organic Framework. *Cryst. Growth. Des.* **2018**, *19*(1), 506-512.

2.1 Chapter Summary

Two-dimensional metal–organic frameworks (2D-MOFs) have shown promise in gas storage and separation applications due to their structural isomerism in response to external stimuli such as temperature, mechanical pressure, and/or guest molecules. Here, we describe the guest-dependent phase transitions of a uranyl-based 2D-MOF, **NU-1302**, observed as single-crystal-to-single-crystal transformations. Different stacking configurations of the same structure were observed in N,N-dimethylformamide (DMF) and ethanol, and after supercritical CO_2 activation. The structural isomerism upon exposure to different solvents and when solvent-free demonstrated the ability of this system to respond to guests by shifting neighboring 2D sheets, resulting in the expansion or contraction of one-dimensional (1D) channels.

2.2 Two-Dimensional Uranyl-Based Metal–Organic Frameworks

A unique class of scientifically intricate, architecturally striking, and artistically exquisite structures, metal–organic frameworks (MOFs) integrate the diversity and tunability of organic molecules and the structural integrity of inorganic compounds into crystalline, porous networks. MOFs are composed of inorganic nodes and organic linkers which self-assemble into chemically diverse structures with typically high surface areas.[26, 27, 97, 98] With applications ranging from gas storage and separation,[99, 100] catalysis,[101-103] and magnetism[104, 105] to carbon dioxide capture[106, 107] and water purification, [108, 109] MOFs display a broad variety of uses. Additionally, these materials can be easily modified post-synthetically to match designed functions.[110, 111] While often encountered as rigid frameworks, MOFs have been observed to move or breath in response to environmental stimuli such as guest molecules,[112-114] temperature,[115, 116] mechanical pressure,[117] or electric fields,[118] demonstrating properties that are beneficial for applications such as gas storage and separations. Among these, two-dimensional MOFs (2D-MOFs) have an inherent advantage and unique capability for structural isomerism due to the supramolecular interactions between

sheets. The structural dynamics of 2D-MOFs [119-123] have engendered properties such as luminescence[124] and magnetism.[125]

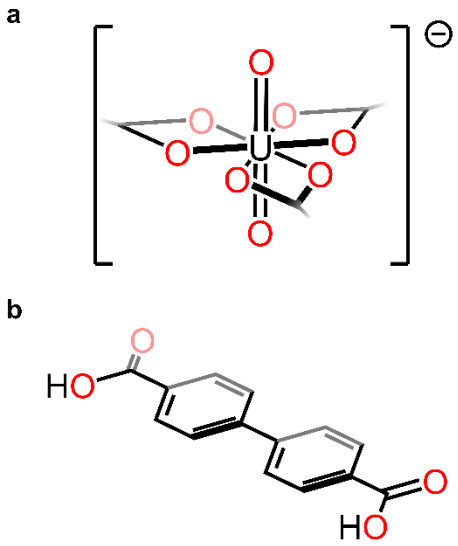

Figure 2.1 Molecular building blocks used in the synthesis of **NU-1302**. (a) Uranyl based node where red oxygen atoms denote linker binding. (b) Biphenyl-4,4'-dicarboxylic acid linker.

A structural building block that often leads to the formation of 2D-MOFs is the uranyl $[UO_2]^{2+}$ ion. The uranyl ion is an approximately linear, doubly charged species consisting of uranium(VI) bound to two axial oxygen atoms.[33] Uranyl species based on U(VI) predominantly make bonds in the equatorial plane given that the oxo bond valence limit is principally saturated.[32, 33] Thus, because the uranyl secondary building unit (SBU) is geometrically planar (Fig 1a), the dimensionality of a uranyl-based MOF is dictated by the torsion of its organic linkers. We have previously exemplified this by coupling the same uranyl SBU to linkers with high intramolecular torsion angles to yield two three-dimensional MOFs (NU-1300[46] and NU-1301[126]), one of which (NU-1301) is the lowest density synthetic material reported. Further, a vast library of uranyl-based nets have been seen in the literature,[29, 41, 126-128] displaying various building blocks,[129-131] unique clusters,[132, 133] and structural identifiers.[134] Many of these have shown applications in selective dye

adsorption[135] and photocatalysis.[136-138] While most reported uranyl-based MOFs are 2D sheets, few reports have demonstrated dynamic systems which respond to external stimuli such as pressure,[139] temperature,[140] or guest molecules.

Herein, we report single-crystal-to-single-crystal phase transitions of the 2D uranium MOF, **NU-1302**, constructed from the planar uranyl node and planar biphenyl-4,4'-dicarboxylic acid linker[141] (Fig 1) which exhibits structural isomerism in response to different solvents and when solvent-free. An initial crystal structure revealed that the 2D sheets were eclipsed and not completely aligned, and given the supramolecular interactions between sheets, we hypothesized that the sheets could further shift. To this end, we chose to interrogate the dynamic abilities of the system using the presence and absence of solvent guest molecules. Single-crystal-to-single-crystal transformations allowed us to observe three structural isomers of **NU-1302** in which the channels contracted as the solvent was exchanged from N,N-dimethylformamide (DMF) to ethanol, and finally removed *via* supercritical CO_2 activation. The corresponding structural isomers are named as **NU-1302-DMF** (referred to in this text as **2-DMF)**, **NU-1302-EtOH** (referred to in this text as **2-EtOH)**, and **NU-1302-SA** (referred to in this text as **2-SA)**, respectively. To the best of our knowledge, this is the first report of a supercritical CO_2 activated, solvent-free, uranium MOF single-crystal structure.

2.3 Crystallographic Evidence for NU-1302 Phase Transitions

Single-crystal X-ray diffraction studies of **2-DMF** revealed that the material crystallized with the uranyl ion coordinated equatorially to six oxygens from three different linker carboxylates. Each linker coordinated to two uranyl centers, resulting in an SBU of hexagonal bipyramidal geometry. **2-DMF** adopted *C2/c* symmetry with unit cell lengths of a = 16.7 Å, b = 47.5 Å, and c = 10.9 Å and formed 2D sheets of the (6,3) honeycomb (**hcb**) topology, resembling hexagonal rings with a

uranyl SBU occupying each vertex. The **hcb** topology is often observed in uranyl carboxylate compounds,[136, 141] as the formation of this topology is highly favored from 3-connected nodes and 2-connected linkers. Of the five edge transitive 2-periodic nets that exist, only **hcb** is composed of 3-connected vertices.[142] Thus, **hcb** is the only viable topology for these building blocks. Upon solvent exchange to ethanol, single crystal X-ray diffraction studies of **2-EtOH** elucidated a stacking structure similar to **2-DMF** with *C2/c* symmetry and **hcb** topology. Along the *b* axis, the unit cell length of **2-EtOH** remained similar to that of **2-DMF**; however, the cell lengths decreased by approximately 6 Å along the *a* axis and increased by approximately 4 Å along the *c* axis. Encouraged by these results which demonstrated the structural dynamism of **NU-1302**, the crystals were dried by employing supercritical CO_2 (sc-CO_2) to obtain **2-SA** which crystalized in the $P\bar{1}$ space group, indicating a more dramatic phase change. **2-SA** retained the same **hcb** topology and node-linker coordination observed in **2-DMF** and **2-EtOH** (Table 2.1).

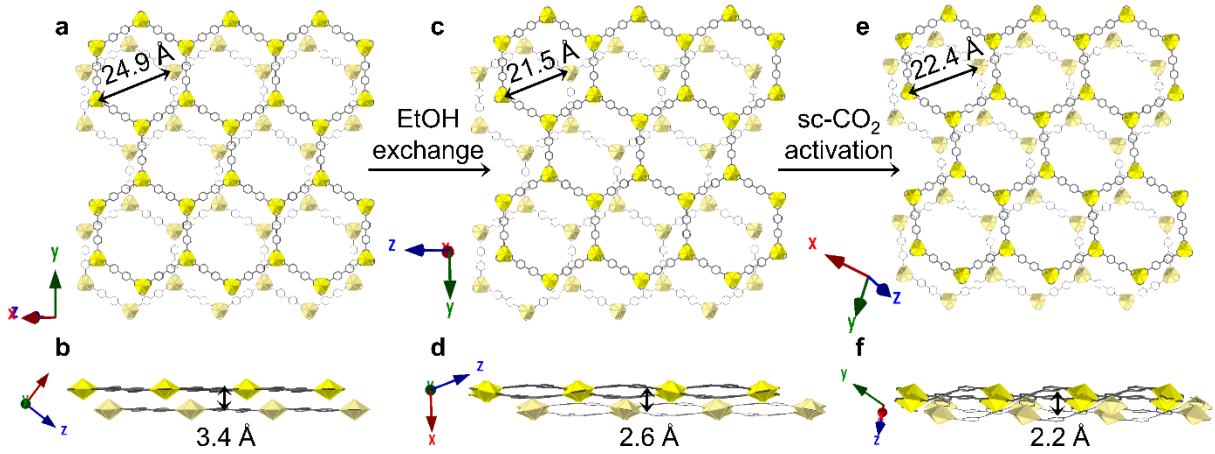

Figure 2.2 Stacking of sheets in **2-DMF** (a, b), **2-EtOH** (c, d), and **2-SA** (e, f). Layers A and B are shown for each stacking mode. More precise distance values can be found in Table S2.

While the node-linker connectivity is identical in all three stacking configurations, the orientation of sheet stacking, inter-layer spacing, and linker flexibility differ between isomers. For example, **2-DMF** exhibits the largest distance between uranium atoms on adjacent sheets (24.9 Å), while

this spacing is decreased by 14% in **2-EtOH** (21.5 Å), resulting in smaller channel openings (Fig 2.2a and c). **2-DMF** also exhibits stacked planar sheets (Fig 2.2b), while the sheets of **2-EtOH** bend in a wave-like fashion (Fig 2.2d). The layers of **2-DMF** orient in an ABCABC stacking pattern along the *b* axis, while the layers of **2-EtOH** exhibit an ABAB stacking pattern along the *b* axis. In **2-DMF** and **2-EtOH**, the distances between the layers are 3.4 Å and 2.6 Å, respectively, and are identical throughout each stacking mode (Fig 2.8a and b). Unlike **2-EtOH**, the sheets of **2-SA** bend dramatically to the degree where docking is observed, a phenomenon which has been previously seen in covalent organic frameworks (COFs).[143] **2-SA** exhibits an ABAB stacking pattern where the sheets align along the axis shown in Figure 2.8c. In this isomer, layer A curves upward while layer B curves downward (Fig 2.2f). Due to this concave/convex pattern of stacking, the distance between layers A and B is 2.2 Å, but the distance between layer B and the following layer A is 1.8 Å; these inter-layer distances continue to alternate throughout the structure. Similarly, the distance measured between uranium atoms on sheets A and B of **2-SA** is 22.4 Å (Fig 2.2e); however, this distance is reduced to 21.9 Å between layer B and the adjacent layer A. This spacing between uranium atoms on adjacent sheets continues to alternate between these two values throughout the structure. Only layers A and B of each stacking mode are shown for clarity in Figure 2.2, but the stacking of multiple layers can be observed in Figure 2.7.

Among these three isomers, **2-DMF** exhibits the most eclipsed and therefore open alignment; **2-EtOH** displays a more staggered and closed arrangement, while **2-SA** features the most contracted orientation. This can be evidenced by the solvent accessible pore volume of each structural isomer which decreases from 63% to 53% to 32% for **2-DMF**, **2-EtOH**, and **2-SA**, respectively. **2-DMF** possesses uniform 1D channels along the (001) plane with diameters of 12 Å. **2-EtOH** features a similar channel along the (101) plane with a diameter of 2.5 Å. Conversely, **2-SA** has 3.5 Å

diameter pores and no observable channels, presumably due to the extensive shifting and docking of sheets. Additionally, the uranium density of each structure (calculated by multiplying the unit cell density by the percent uranium in each formula unit) mirrors the degree of openness: as the stacking modes become more compact, the uranium density increases from 0.367 g cm^{-3}(**2-DMF**) to 0.470 g cm^{-3} (**2-EtOH**) to 0.632 g cm^{-3} (**2-SA**). Moreover, the distances between adjacent sheets corresponding to each stacking mode follow the trend of **2-DMF** >**2-EtOH** >**2-SA** with values of 3.4 Å, 2.6 Å, and 2.2 Å/1.8 Å, respectively (Fig 2.2b, d, and f).

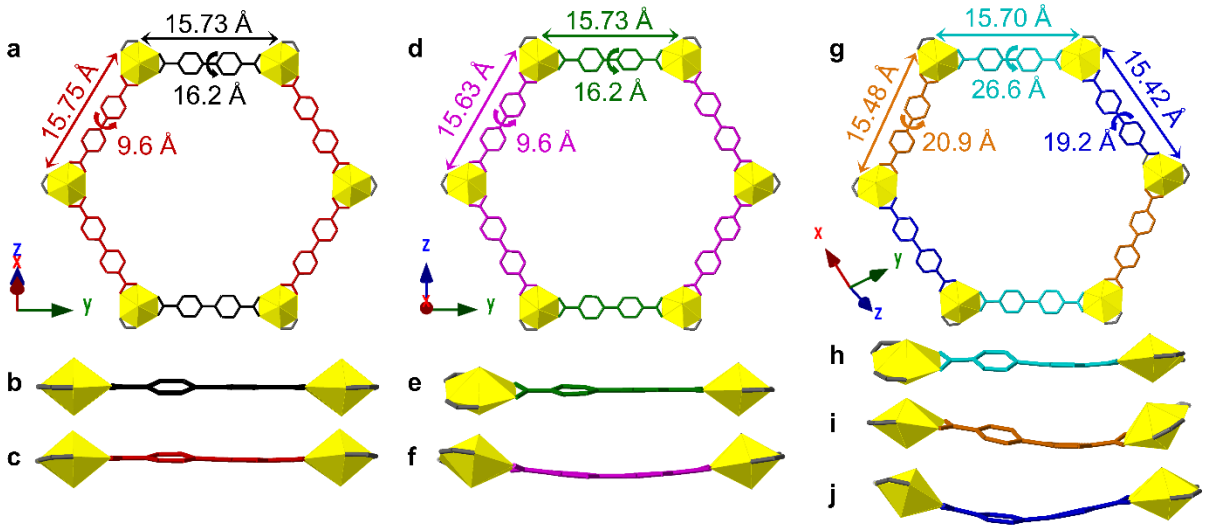

Figure 2.3 Distorted hexagonal rings resulting from linker flexibility. (a) Two linker motifs (black and red) in **2-DMF**. (b) Shorter linker motif in **2-DMF** with greater dihedral angle. (c) Longer linker motif in **2-DMF** with smaller dihedral angle. (d) Two linker motifs (green and pink) in **2-EtOH**. (e) Longer linker motif in **2-EtOH** with greater dihedral angle. (f) Shorter linker motif in **2-EtOH** with smaller dihedral angle. (g) Three linker motifs (orange, aqua, blue) in **2-SA**. (h) Longest linker motif in **2-SA** with greatest dihedral angle. (i) Intermediate linker motif in **2-SA**. (j) Shortest linker motif with smallest dihedral angle. More precise parameter values can be found in Table 2.2.

2.4 NU-1302 Isomers Possess Varying Levels of Distortion

We observed slightly distorted hexagonal rings in all three structures because the biphenyl-4,4'-dicarboxylic acid linker is flexible, resulting in linker bending and a dihedral angle between linker phenyl rings. In **2-DMF**, the linker adopts two unique motifs. In the first motif, the two uranyl

centers bound to a single linker are separated by 15.73 Å, and the linker phenyl rings are related by a dihedral angle of 16.2°, while the second motif features a larger separation between two connected uranyl ions (15.75 Å) and a smaller dihedral angle (9.6°) (Fig 2.3a). Each hexagonal ring possesses two linkers opposite each other which adopt the first motif (Fig 2.3b), while the remaining four adopt the second (Fig 2.3c). **2-DMF** demonstrates the least distortion among the three structural isomers with a difference in uranyl-to-uranyl distance of only 0.02 Å between the two motifs. Two linker motifs are also present in **2-EtOH.** As opposed to the inverse relationship between uranyl-to-uranyl distance and linker dihedral angle seen in **2-DMF**, the linker motif in **2-EtOH** with the shorter uranyl-to-uranyl distance (15.63 Å) exhibits a smaller dihedral angle (8.3°) and the motif with the longer uranyl-to-uranyl distance (15.75 Å) displays a larger dihedral angle (10.5°) (Fig 2.3d). We attribute this observation to the bowed nature of the shorter linker (Fig 2.3f); because of the added bend, the linker is unable to twist further without disrupting the uranyl position. Similar to **2-DMF**, two opposite linkers in the hexagonal ring of **2-EtOH** adopt the first, non-bowed motif (Fig 2.3e), while the rest adopt the second, bowed motif (Fig 2.3f). Of these four bowed linkers, two bow in the positive direction and two bow in the negative direction. In **2-EtOH**, linker bowing causes the isomer to distort slightly more than in **2-DMF** generating a difference between uranyl-to-uranyl distances of 0.12 Å.

The distortion in structure **2-SA**, however, is the most dramatic as revealed by the presence of three structural linker motifs (Fig 2.3g). The first motif exhibits insignificant bowing, a uranyl-to-uranyl distance of 15.70 Å, and a dihedral angle of 26.6° (Fig 2.3h). The second displays partial bowing, a shorter uranyl-to-uranyl distance (15.48 Å), and a smaller dihedral angle (20.9°) (Fig 2.3i). Finally, the third motif demonstrates the most dramatic bowing, the shortest uranyl-to-uranyl distance (15.42 Å), and the smallest dihedral angle (19.2°) (Fig 2.3j). Of the three structures, **2-SA**

exhibits the largest differences in uranyl-to-uranyl distances between the linker motifs (0.28 Å). Similar to **2-EtOH**, the linker motif in **2-SA** with the least bowing displays the largest dihedral angle and longest uranyl-to-uranyl distance, while the linker motif with the most bowing corresponds to the smallest dihedral angle and shortest uranyl-to-uranyl distance. The degree of distortion in structures **2-DMF**, **2-EtOH**, and **2-SA** increases in a trend similar to the extent of structure openness with **2-DMF** being least distorted and most open and **2-SA** being most distorted and most closed. The distortion of these polymorphs can be further clarified by observing the uranium-oxo bond distances (Table 2.3 and Fig 2.9).

2.5 Flexibility in NU-1302

The flexible nature of the sheet stacking modes upon solvent exchange from DMF to ethanol to supercritical activation with CO_2 can also be confirmed in the bulk *via* PXRD (Fig 2.4). All three structural isomers retain their bulk crystallinity following solvent exchange and activation. While the powder pattern of bulk **2-DMF** agrees well with the pattern simulated from the single-crystal data, full conversion from one stacking mode to another after solvent exchange was not attained. Specifically, bulk **2-EtOH** exhibits a peak at a 2θ of 7.5º characteristic of the simulated pattern of **2-DMF**. Incomplete conversion between stacking modes has also been observed in previous reports of single-crystal-to-single-crystal transformations.[119] Furthermore, the reversibility of this crystal transformation between **2-EtOH** and **2-DMF** was observed (Fig 2.10).

The two major diffraction peaks belonging to **2-DMF** which correspond to the (020) plane (Fig 2.4, green highlight) and the (110) plane (Fig 2.4, blue highlight) were compared to the simulated pattern of **2-EtOH** to demonstrate the change in unit cell parameters. Since the unit cell *b* axis measures 47 Å in both **2-DMF** and **2-EtOH**, the position of the (020) plane does not shift between the powder patterns of **2-DMF** and **2-EtOH**. However, due to the 6 Å decrease in the *a* axis from

2-DMF to **2-EtOH**, the position of the peak corresponding to the (110) plane shifts to a higher angle in **2-EtOH**.

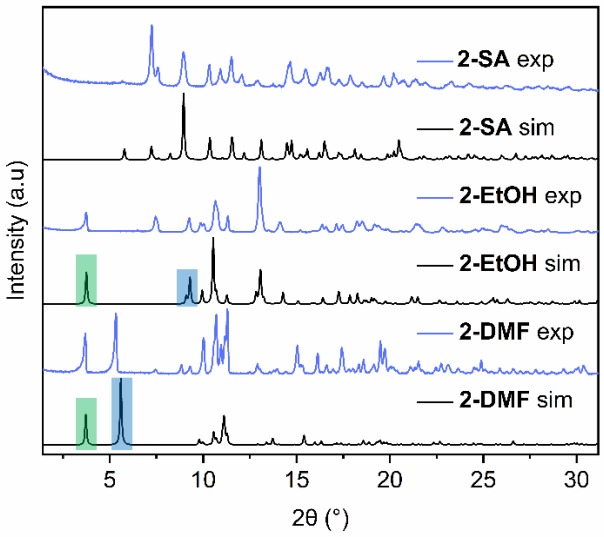

Figure 2.4 Simulated (black) and experimental (blue) PXRD patterns of **2-DMF**, **2-EtOH**, and **2-SA**. Peaks highlighted in green denote the (020) plane, and those highlighted in blue denote the (110) plane.

The structural flexibility of **2-SA** was further probed by CO_2 adsorption-desorption measurements at 195 K because a phase change, from monoclinic (**2-EtOH**) to triclinic (**2-SA**), was observed after supercritical activation.{, #462} An initial type I isotherm, characteristic of a microporous material, with a step at 11 mbar and a total pore volume of 0.19 $cm^3\ g^{-1}$ at 0.99 P/P_0 was observed (Fig 2.5). This step at low pressure followed by a sharp inflexion in uptake, often referred to as gate-opening, is a defining feature of flexible materials that exhibit a conversion from a narrow-pore arrangement to a wider-pore conformation while remaining crystalline throughout the adsorption process.[144-149] We hypothesize that initial CO_2 pressure induces the sheets of **2-SA** to shift from their closed conformation to a more open stacking arrangement.

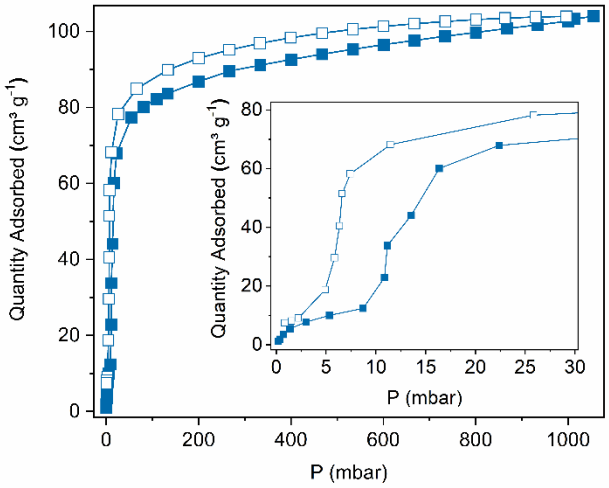

Figure 2.5 CO_2 isotherm of **2-SA** at 195 K displaying a step at 11 mbar. Filled squares denote adsorption, while empty squares denote desorption. The low-pressure region is enlarged in the inset for clarity.

2.6 Conclusions

Single-crystal-to-single-crystal transformations of a 2D uranyl-based MOF, **NU-1302**, have shown a dynamic system in different guest environments. Changes in the orientation of adjacent sheets with respect to one another, interlayer spacing, linker dihedral angle, and linker bowing upon solvent exchange from DMF to ethanol and subsequent activation by supercritical CO_2, demonstrated phase transitions in response to guest molecules, a phenomenon rarely reported among 2D uranyl-based MOFs. **NU-1302** exhibits an open-channel stacking in DMF (**NU-1302-DMF**), a slightly contracted arrangement in ethanol (**NU-1302-EtOH**), and a significantly constricted orientation upon supercritical CO_2 activation (**NU-1302-SA**). Additionally, the phase transitions were monitored with PXRD and gas sorption experiments which demonstrated the flexibility of the activated structure. The ability of this system to alter its channel conformation in response to guest conditions shows promise for the development of materials for applications requiring dynamic systems that can respond to external stimuli.

2.7 Additional Information

2.7.1 Materials

All chemicals were purchased from the supplier and used without further purification, including uranyl nitrate hexa-hydrate (≥ 98%, International Bio-Analytical Industries, Inc.), biphenyl-4,4'-dicarboxylic acid (97%, Sigma-Aldrich), trifluoroacetic acid (99%, Sigma-Aldrich), N,N-dimethylformamide (≥ 99.8%, certified ACS, Fisher Scientific), and anhydrous ethanol (95.27%, histological grade, Fisher Scientific).

Caution! Uranyl nitrate hexahydrate contains depleted uranium; necessary precautions should be adhered to when handling this chemical.

2.7.2 Methods and Instrumentation

2.7.2.1 Powder X-ray Diffraction

Powder X-ray diffraction (PXRD) measurements of all stacking modes were collected on a STOE STADI P diffractometer equipped with a copper Kα1 source and a 1D strip detector. **2-DMF** and **2-EtOH** were prepared for PXRD by drop-casting from DMF and ethanol, respectively, and dried on the benchtop until the bulk solvent evaporated. **2-SA** was prepared for PXRD as a dry powder. CO_2 adsorption-desorption isotherms were collected on a Micromeritics ASAP 2020 at 195 K after **2-SA** was activated under dynamic vacuum on a Micromeritics Smart VacPrep unit for two hours at 60°C.

2.7.2.2 Single-Crystal X-ray Diffraction

Single-crystal X-ray structure analyses were carried out using a Bruker Kappa APEX II CCD detector equipped with a Cu Kα (λ = 1.54178 Å) I μS micro-source with MX optics. The single crystals were mounted on MicroMesh (MiTeGen) with paratone oil. The structures were determined by direct methods (SHELXT 2014/5)[150] and refined by full-matrix least-squares refinement (SHELXL-2017/1)[151] using the Yadokari-XG[152] or Olex2[153] software packages. The

disordered non-coordinated solvents were removed using the PLATON SQUEEZE program.[154] The refinement results are summarized in Table 2.1. It is noted that "ghost" residual electron density was observed close to the heavy uranium atoms (Table 2.1 and Fig 2.7) in **NU-1302-SA.** Crystallographic data for the crystal structures in CIF format have been deposited in the Cambridge Crystallographic Data Centre (CCDC) under deposition numbers CCDC-1871257 (**NU-1302-DMF**), 1876935 (**NU-1302-EtOH**), and 1876934 (**NU-1302-SA**). The data can be obtained free of charge *via* www.ccdc.cam.ac.uk/data_request/cif (or from the Cambridge Crystallographic Data Centre, 12 Union Road, Cambridge CB2 1EZ, U.K.). The spacing between the 2D sheets of **2-DMF**, **2-EtOH**, and **2-SA** was calculated by averaging the uranium positions of each sheet into a single plane and measuring the distance between each plane. Dihedral angles and interatomic distances were calculated in Olex2, and pore and channel diameters were calculated using Diamond.

2.7.2.3 Optical Microscope

Crystal images were obtained using a Nikon SMZ1500 microscope.

2.7.3 Synthesis and Preparation of NU-1302

NU-1302 was synthesized by combining 7 mL of a 20 mM uranium nitrate hexa-hydrate stock solution prepared in DMF (70 mg, 0.14 mmol) with 5.04 mL of a 41.3 mM biphenyl-4,4'-dicarboxylic acid stock solution prepared in DMF (50.4 mg, 0.21 mmol) and trifluoroacetic acid (0.21 mL, 2.74 mmol) in an 8-dram glass vial. The cloudy solution was sonicated for five minutes and heated in a sand bath in a 120 °C oven. After 72 hours, the vial was removed from the oven, and yellow crystals of approximately 50 microns in size (Fig 2.6a) were observed on the bottom and walls of the vial. The yellow supernatant was decanted, and the crystals were immediately washed three times for five minutes with fresh DMF. The crystals were then soaked in fresh DMF for two days, producing **2-DMF**. Following this, the crystals were washed three times in ethanol

for 30 minutes and allowed to soak in fresh ethanol for two days, resulting in **2-EtOH**. Finally, the material was activated with supercritical carbon dioxide (sc-CO_2) using a Tousimis™ Samdri® PVT-3D critical point dryer[155] at a bleed rate of 1.0 cc/min, yielding **2-SA**. After solvent exchange and activation, the 50 micron crystal size was maintained (Fig 2.6b and c).

2.7.4 Distortion Reflected by Uranium-oxo Bond Distances

Of the two crystallographically unique uranium atoms present in **2-DMF**, both oxo bonds to U1 and to U2 are crystallographically equivalent within the respective SBU, with oxo bonds to U2 slightly longer than those to U1. **2-EtOH** follows a similar trend in that both oxo bonds of U1 are equivalent, and those of U2 are also equivalent; however, the U2–oxo bonds are shorter than the U1–oxo bonds. **2-SA** shows similar bond lengths to **2-EtOH**, with the shortest bond belonging to U2. Not surprisingly, due to the triclinic crystal system of **2-SA**, the two U2-oxo bonds measure different lengths. Both **2-EtOH** and **2-SA** exhibit decreased U-oxo bond lengths, which aligns with the increased distortion observed in these structures (Fig 2.9). The relatively large standard uncertainty of the bond length combined with the thermal vibration (data collected at 200K) and the absorption correction on very thin, plate-like crystals prevent us from obtaining more accurate bond lengths.

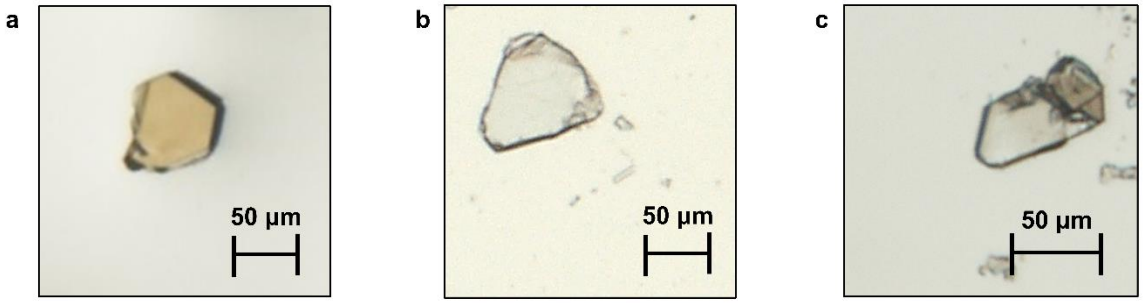

Figure 2.6 Single crystal images of (a) 2-DMF, (b) 2-EtOH, and (c) 2-SA.

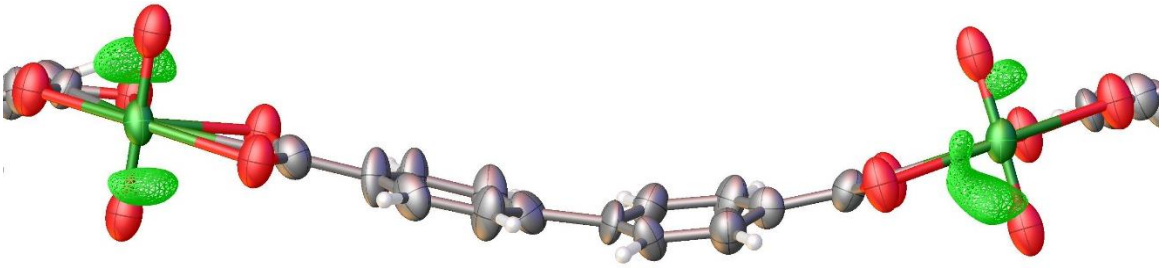

Figure 2.7 Difference electron density map (green mesh at the level of 2.0 eÅ^{-3}) of **2-SA** showing the “ghost” electron density close to the heavy uranium atom.

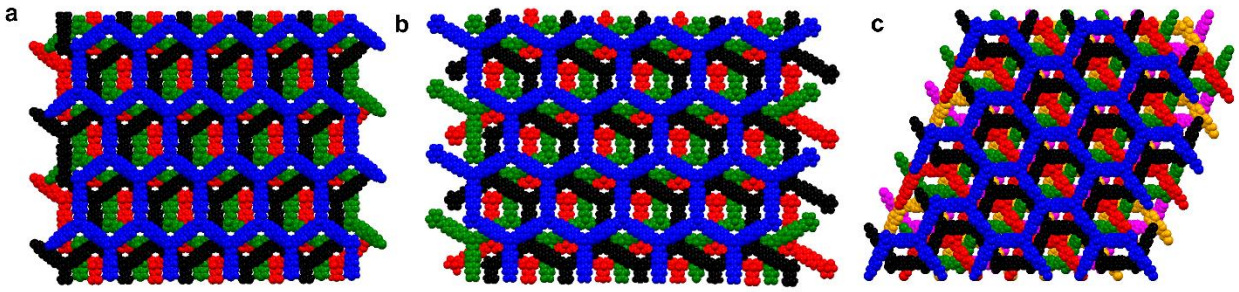

Figure 2.8 Stacking of layers along respective axes where each layer is denoted by a different color. (a) ABCABC stacking of **2-DMF**. (b) ABAB stacking of **2-EtOH**. (c) ABAB stacking of **2-SA**.

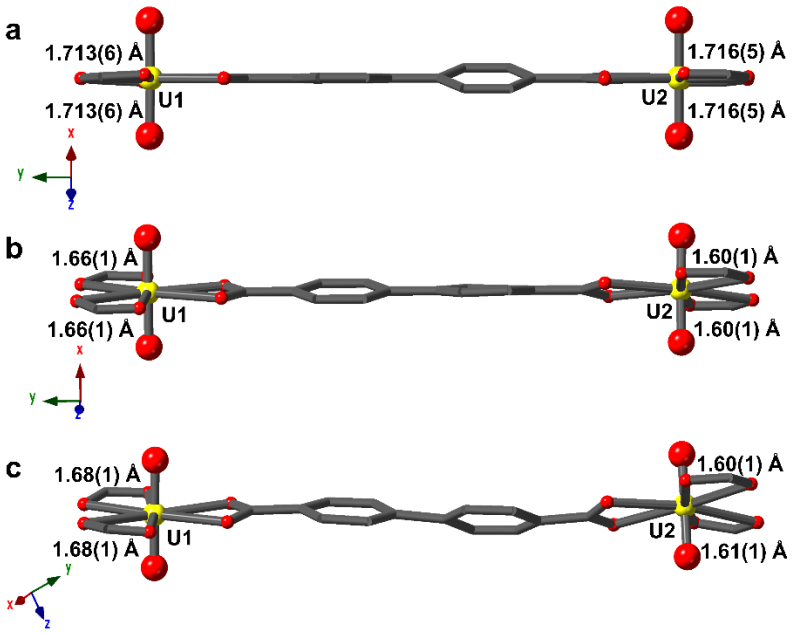

Figure 2.9 Bond lengths of U1–oxo and U2–oxo in (a) **2-DMF**, (b) **2-EtOH**, and (c) **2-SA**. Carbon is represented in grey, uranium in yellow, and oxygen in red.

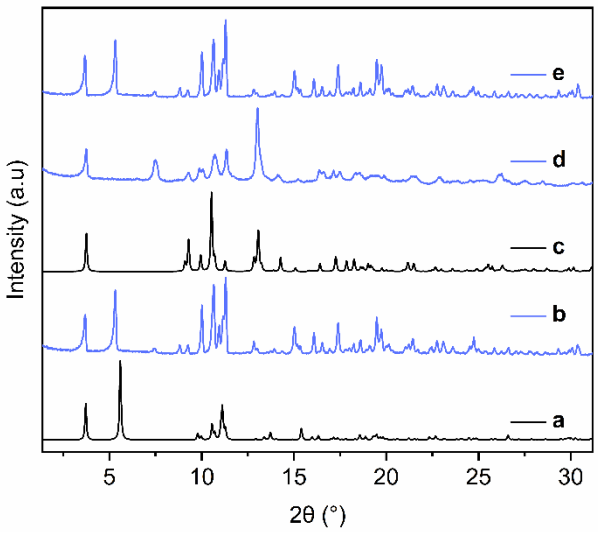

Figure 2.10 PXRD patterns showing reversibility of conversion from **2-EtOH** back to **2-DMF**. (a) Simulated pattern of **2-DMF**. (b) Experimental pattern of **NU-1302** soaked in DMF, producing **2-DMF**. (c) Simulated pattern of **2-EtOH**. (d) Experimental pattern of same sample from b soaked in ethanol for two days, producing **2-EtOH**. (e) Experimental pattern of same sample from b and d soaked in DMF for two days, producing **2-DMF**.

Table 2.1 Crystallographic data for structural isomers **NU-1302-DMF**, **NU-1302-EtOH**, and **NU-1302-SA**.

	NU-1302-DMF	**NU-1302-EtOH**	**NU-1302-SA**
Empirical formula	$C_{21}H_{12}O_8U$	$C_{21}H_{12}O_8U$	$C_{42}H_{24}O_{16}U_2$
Formula weight	630.34	630.34	1260.67
Temperature (K)	200(2)	200(2)	200(2)
Crystal system	monoclinic	monoclinic	triclinic
Space group	C2/c	C2/*c*	$P\bar{1}$
a (Å)	16.7384(8)	10.538(1)	13.453(1)
b (Å)	47.478(2)	47.071(3)	14.409(1)
c (Å)	10.8543(5)	14.379(1)	15.244(1)
α (°)	90	90	103.528(5)
β (°)	91.253(3)	109.610(7)	108.588(5)
γ (°)	90	90	106.757(5)
Volume (Å^3)	8623.8(7)	6718.9(1)	2502.9(3)
Z	8	8	2
ρ_{calc} (g cm^{-3})	0.971	1.246	1.673
μ (mm^{-1})	10.791	13.851	18.591
F(000)	2352.0	2352.0	1176.0
Crystal size (mm^3)	0.030 × 0.030 × 0.020	0.07 × 0.04 × 0.02	0.02 × 0.02 × 0.005
Radiation	CuKα (λ = 1.54178)	CuKα (λ = 1.54178)	CuKα (λ = 1.54178)
2Θ range for data collection (°)	3.722 to 130.874	7.512 to 118.214	6.554 to 110.22
Index ranges	-19 ≤ h ≤ 18, -53 ≤ k ≤ 55, -12 ≤ l ≤ 9	-11 ≤ h ≤ 11, -51 ≤ k ≤ 48, -14 ≤ l ≤ 15	-12 ≤ h ≤ 14, -14 ≤ k ≤ 15, -15 ≤ l ≤ 16
Reflections collected	29126	12291	15957
Independent reflections	7319 [R_{int} = 0.0389, R_{sigma} = 0.0331]	4539 [R_{int} = 0.0588, R_{sigma} = 0.0694]	5837 [R_{int} = 0.0758, R_{sigma} = 0.0886]
Data/restraints/parameters	7319/0/275	4539/0/241	5837/6/475
Goodness-of-fit on F^2	1.023	1.038	1.061
Final R indexes [I>=2σ (I)]	R_1 = 0.0328, wR_2 = 0.0907	R_1 = 0.0552, wR_2 = 0.1492	R_1 = 0.0548, wR_2 = 0.1379
Final R indexes [all data]	R_1 = 0.0404, wR_2 = 0.0988	R_1 = 0.0695, wR_2 = 0.1576	R_1 = 0.0713, wR_2 = 0.1489
Largest diff. peak/hole (e Å^{-3})	1.64/-0.62	1.50/-1.73	3.80/-1.08

Table 2.2 Interatomic distances and torsion angles for structural isomers **NU-1302-DMF**, **NU-1302-EtOH**, and **NU-1302-SA**.

	Distance between U atoms on adjacent sheets (Å)	Torsion angle (°)	Uranyl-to-uranyl distance (Å)
2-DMF	24.945(2)	9.6(3)	15.7483(9)
		16.2(3)	15.731(2)
2-EtOH	21.521(2)	10.5(2)	15.745(2)
		8.3(5)	15.632(1)
2-SA	21.938(2) 22.393(2)	20.9(4)	15.481(2)
		19.2(5)	15.424(1)
		26.6(6)	15.704(1)

Table 2.3 Uranium-oxo bond lengths for U1 and U2 in **2-DMF**, **2-EtOH**, and **2-SA**.

Oxo Bond	2-DMF(Å)	2-EtOH(Å)	2-SA(Å)
U1-oxo	1.713(6)	1.66(1)	1.68(1)
	1.713(6)	1.66(1)	1.68(1)
U2-oxo	1.716(5)	1.60(1)	1.60(1)
	1.716(5)	1.60(1)	1.61(1)

CHAPTER 3. Identification of a Metastable Uranium Metal–Organic Framework Isomer Through Non-Equilibrium Synthesis

A vignette on energy-structure relationships.

Portions of this chapter appear in the following manuscript:

Hanna, S. L.; Debela, T. T.; Mroz, A. M.; Syed, Z. H.; Kirlikovali, K. O.; Hendon, C. H.; Farha, O.K., Identification of a Metastable Uranium Metal–Organic Framework Isomer Through Non-Equilibrium Synthesis. *Chem. Sci.* **2022**, *13*, 13032-130

3.1 Chapter Summary

Since the structure of supramolecular isomers determines their performance, rational synthesis of a specific isomer hinges on understanding the energetic relationships between isomeric possibilities. To this end, we have systematically interrogated a pair of uranium-based metal–organic framework topological isomers both synthetically and through density functional theory (DFT) energetic calculations. Although synthetic and energetic data initially appeared to mismatch, we assigned this phenomenon to the appearance of a metastable isomer, driven by levers defined by Le Châtelier's principle. Identifying the relationship between structure and energetics in this study reveals how non-equilibrium synthetic conditions can be used as a strategy to target metastable MOFs. Additionally, this study demonstrates how defined MOF design rules may enable access to products within the energetic phase space which are more complex than conventional binary (e.g., kinetic vs. thermodynamic) products.

3.2 Energetic Phase Space of Supramolecular Isomers

Supramolecular isomerism occurs when more than one type of network superstructure exists for the same set of molecular building blocks.[156] This phenomenon produces chemically similar materials with divergent properties, an occurrence with widespread implications. For example, protein isoforms and misfolding dramatically affect disease,[157, 158] polymorphism of pharmaceutical cocrystals influences drug development,[159, 160] and isomer selectivity in supramolecular arrays allows for engineered materials with exquisite structure-property control.[161-163] Since isomer structure thus accounts for varying material performance, understanding the chemical processes that select for these structures will aid in the targeted synthesis of specific isomers.

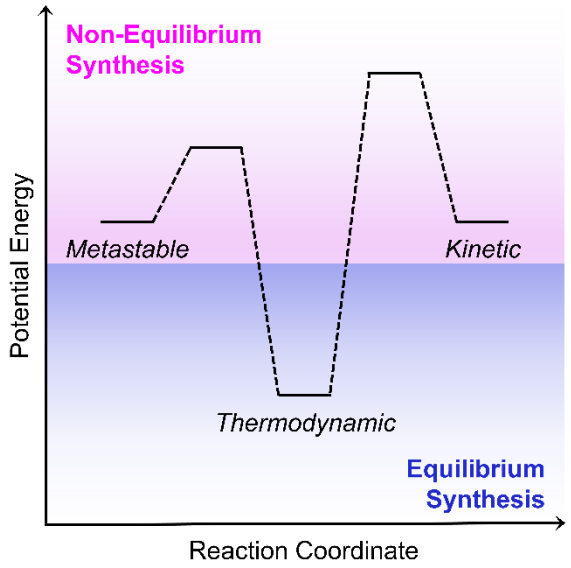

Scheme 3.1 Energy landscape of supramolecular products. Non-equilibrium non-dissipative syntheses produce metastable and kinetic products (top, pink), and equilibrium syntheses produce thermodynamic products (bottom, blue).

Synthetic selectivity between supramolecular isomers is broadly derived from the energetic relationships between them.[164] Ideally, this phase space can be mapped on an energy landscape containing both local and global energy minima (Scheme 3.1). We note that for network superstructures, this phase space becomes complex and often contains more than merely binary energetic minima. For a classical non-dissipative supramolecular organization, the global energy minimum occurs under an equilibrium environment as the thermodynamic product. Conversely, local energy minima (e.g., kinetic or metastable products) arise under non-equilibrium environments and strongly depend on synthetic conditions.[165, 166] For instance, kinetic products are favored by rapid assembly and are accessed through kinetic control by shifting the height of existing activation energy barriers. Metastable products, however, are local energetic minima that become thermodynamically stable under the conditions of growth.[167] Thus, thermodynamic control favors metastable products by shifting chemical equilibria using levers defined by Le Châtelier's principle. As an example, several studies have shown that removal of products during

a reaction shifts the chemical equilibrium towards the product side and generates a metastable material.[167-171]

This interplay between supramolecular structure, properties, and energetics appears in a class of self-organized network assemblies termed metal–organic frameworks (MOFs). MOFs comprise inorganic nodes and organic linkers which self-assemble into porous, crystalline materials with widespread functions.[24, 27, 172] According to graph theory, one set of node and linker building blocks can connect in various arrangements to produce distinct topologies with unique underlying periodic nets.[173, 174] Due to this phenomenon, MOFs exhibit topological isomerism, producing various framework nets–often with unique properties–from the same set of linker and node components.[175, 176] However, energetic analyses of MOF isomer phase space are generally limited to binary thermodynamic and kinetic topological isomers in traditional transition metal-based MOFs.[177-184] Widening the energetic understanding of MOF topological isomers involves: 1) defining what causes a certain topology to be favored, 2) determining how isomer energetics inform synthesis design rules, and 3) implementing thermodynamic control to access less explored metastable phases[185, 186] in non-traditional MOFs.[130, 187]

In this study, we aim to address these three thrusts through an energetic analysis of topological isomerism in an actinide MOF system. Since structure-property relationships in actinide-based MOFs prove to be unlike those of traditional transition metal-based MOFs,[188, 189] we hypothesize that the energetic analysis of actinide MOF isomers will provide unique insight into their synthetic relationship. Here, we select a MOF system with a tetrahedral linker (tetrakis(4-carboxyphenyl)methane or **TCPM**) and a triangular, uranyl-based node (Fig 3.1c). The assembly of these building blocks results in two distinct isomeric topologies: ***ctn*** (Fig 3.1a) and ***bor*** (Fig 3.1d).[173] By systematically varying synthetic parameters, including temperature, modulator ratio,

and reaction concentration, we aimed to selectively isolate one isomer as the thermodynamic product at high modulator amount, high temperature, and low concentration. Instead, we obtained ***bor*** (NU-1306) under high modulator and high temperature conditions, and we isolated ***ctn*** (NU-1305) under low reaction concentration conditions. To understand these conflicting data points, we examined the crystal structures and employed geometric strain analysis as well as density functional theory (DFT) calculations, which indicate that NU-1305 is thermodynamically favored by 8 kcal mol^{-1}. By identifying that the synthesis of NU-1306 is in fact favored by thermodynamically controlled non-equilibrium conditions, we attribute this apparent mismatch between synthetic and energetic parameters to NU-1306 being a metastable phase. Identifying the relationship between structure and energetics in this study reveals how non-equilibrium synthetic conditions can be used as a strategy to target metastable MOFs. More generally, this investigation contributes to a broader understanding of isomeric options within the complex superstructure phase space.

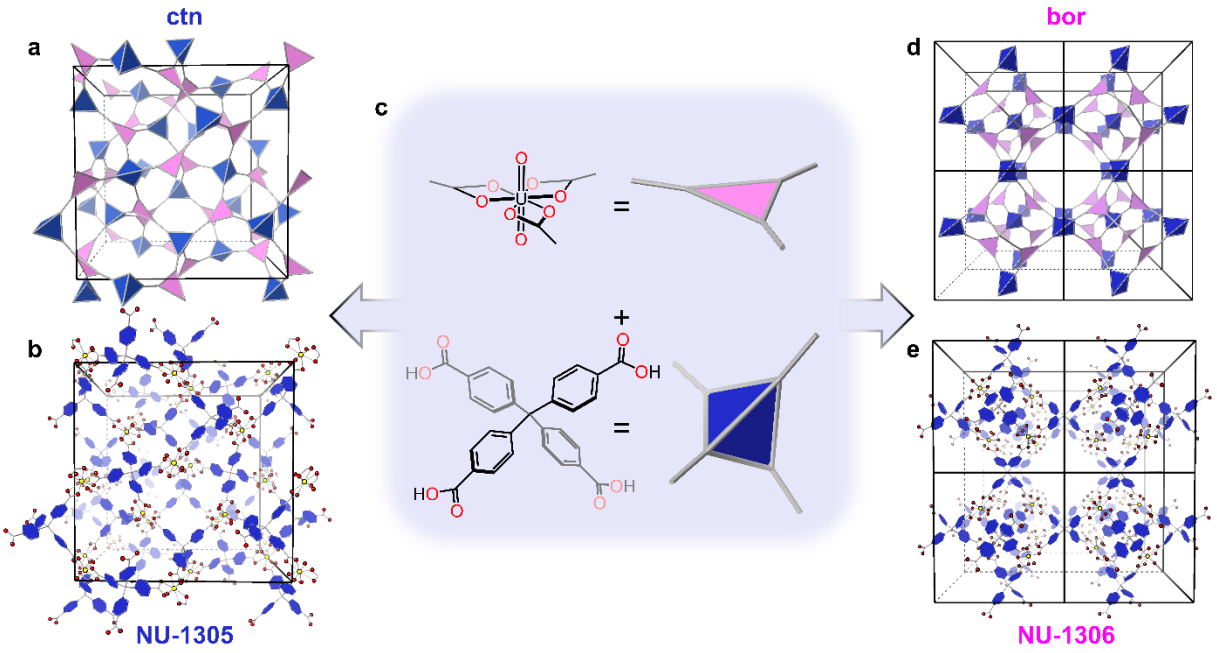

Figure 3.1 Topological isomers NU-1305 and NU-1306. Augmented topological nets for (a) *ctn* and (d) *bor* resulting from the assembly of (c) a triangular node building block and a tetrahedral linker building block. Crystal structures of (b) NU-1305, in the *ctn* topology, and (e) NU-1306, in the *bor* topology. In (b) and (e), uranium is shown in yellow, oxygen in red, and carbon in blue. Hydrogen atoms are omitted for clarity.

3.3 Synthetic Conditions Favor NU-1305 as Energetically Stable Isomer

Following the synthetic procedure detailed in section *3.7.3.1*, self-assembly of the triangular uranyl node and tetrahedral **TCPM** linker produced single crystals of ***ctn*** topology, named NU-1305 (Fig 3.1b, Fig 3.6),[78, 190] and single crystals of ***bor*** topology, named NU-1306 (Fig 3.1e, Fig 3.7). Both MOFs consist of a hexagonal bipyramidal uranyl node coordinated equatorially to three **TCPM** linkers through their carboxylate oxygen atoms (Fig 3.9b). Each MOF is (3,4)-connected with a formula of $H^+[UO_2(\mathbf{TCPM})_{0.75}]^-$ or $H_3O^+[UO_2(\mathbf{TCPM})_{0.75}]^-$ (Figs 3.14-3.16).

NU-1305 exhibits one type of pore, comprised of eight nodes and six linkers. The largest sphere to fit in this pore possesses a radius of 19.5 Å (Fig 3.8), and further crystallographic details for NU-1305 can be found in the report by Hu et al.[78] NU-1306 crystallized in the non-centrosymmetric P-43m space group with a cubic unit cell of $a=b=c=20.9$ Å and a solvent-

accessible pore volume calculated by PLATON of 84%. Octahedral cages of 12.8 Å radii, each comprised of four nodes and six linkers, connect through vertices to form apertures with 22 Å radii (Fig 3.9c-d). Further crystallographic details can be found in Table 3.1.

After confirming the formation of both topological isomers, we then aimed to determine their respective positions within the system's energy landscape. To do so, we examined which isomer required more thermodynamically favored synthetic conditions by systematically varying the modulator ratio, temperature, and reaction concentration. Since coordinating modulator is thought to compete with linkers for binding sites on metal ions, increased amounts of modulator should favor thermodynamic products by slowing down self-assembly kinetics.[191, 192] Published literature also indicates that higher temperatures favor thermodynamic MOF products by providing more energy to surmount higher activation energy barriers.[178, 180] Finally, lower reaction concentrations lead to less frequent reactant collisions, which effectively decrease reaction kinetics and afford thermodynamic MOF products.[192] Thus, we anticipated that these synthetic levers would indicate which topology lies lower on the energy landscape.

Maintaining a 1.6:1 ratio of $UO_2(NO_3)_2$ (node) to **TCPM** (linker) in 0.8 mL *N*,*N*-dimethylformamide (DMF) at 120 °C, we first varied the formic acid (FA) modulator to DMF ratio from 0.03 FA:DMF to 0.15 FA:DMF. Powder X-ray diffraction (PXRD) revealed that samples with a FA:DMF ratio from 0.03 to 0.09 resulted in NU-1305, while samples with a FA:DMF ratio from 0.10 to 0.15 resulted in NU-1306 (Fig 3.2a). Thus, decreased modulator produced NU-1305, while increased modulator produced NU-1306, pointing to NU-1306 as the thermodynamic product. We note that isomer selectivity using modulator may be influenced by the presence of missing linker defects (Fig 3.22, Table 3.4).[193]

Next, we selected the conditions from above with a FA:DMF ratio of 0.09, which favored NU-1305 growth at 120 °C, as a starting point but varied the temperature of the reaction. Under identical synthetic conditions, increasing the temperature to 160 °C afforded a mixture of isomers, and heating at 170 °C favored the formation of pure NU-1306 (Fig 3.2b). Similar to the requirement for increased modulator concentrations for the synthesis of NU-1306, the formation of NU-1306 at higher reaction temperatures implies that it is the thermodynamically favored topological isomer.

Finally, to test the effect of reaction concentration on isomer product, we selected the conditions above that formed NU-1305 (0.09 FA:DMF, 0.8 mL DMF, 120 °C) and diluted the reaction media, expecting to observe a transformation to the more thermodynamically stable NU-1306. Interestingly, we only observed the presence of NU-1305 and did not observe any transformation to NU-1306 by PXRD analysis (Fig 3.11). Instead, diluting the reaction conditions used to produce NU-1306 (0.10 FA:DMF, 0.8 mL DMF, 120 °C) by increasing the amount of DMF from 0.8 mL to 1.8 mL yielded PXRD patterns in which the characteristic peaks for NU-1306 decreased in intensity while those of NU-1305 grew (Fig 3.2c). Contrary to previous systematic testing with modulator and temperature, these data indicate that lower reaction concentrations favor NU-1305, assigning NU-1305 as thermodynamically stable.

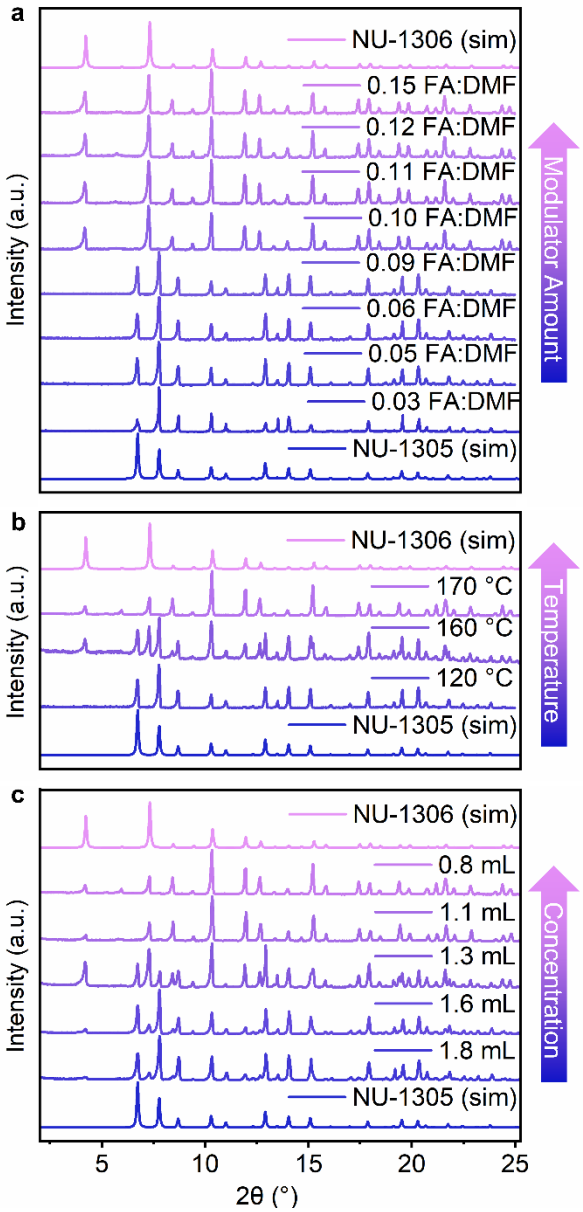

Figure 3.2 Isolated isomers through tuned synthetic conditions. PXRD data of reaction products from systematically (a) increasing modulator amount while holding temperature and reaction concentration constant, (b) increasing reaction temperature while holding modulator amount and reaction concentration constant, or (c) increasing reaction concentration while holding modulator and temperature constant. Diffraction patterns are normalized.

3.4 Energetic Calculations, Geometric Analysis, and Synthetic Conversion Parameters Favor NU-1306 as Energetically Stable Isomer

To gain insight into the phenomena guiding selectivity for one isomer over the other, we calculated the energetic minima of each topology using periodic hybrid Density Functional Theory (DFT)

(Fig 3.19, Table 3.3). We further decomposed the energetic contributions by isolating the configurational differences in energy as a function of ligand and node geometry, respectively. Calculations revealed that NU-1305 is 8 kcal mol^{-1} more stable than NU-1306 (Fig 3.3e). Through disassembly of the MOF, the NU-1305 node and linker conformations were found to be favored over those of NU-1306 by 4.8 and 3.2 kcal mol^{-1}, respectively.

A geometric analysis of building block components and crystal conformation also supports the energetic favorability of NU-1305 over NU-1306. The NU-1306 linker dihedral angles exhibit a higher standard deviation from the mean than those of NU-1305, showing increased distortion of the NU-1306 linker component (Fig 3.3c, Fig 3.18, Table 3.2). The energetically unfavorable co-facial configuration of the linker in NU-1306 in turn destabilizes the node. While the node equatorial plane and the plane of the immediately-bound linker phenyl ring remain flush in NU-1305 (1.25° angle between planes, Fig 3.3b), a 9.57° angle appears between these planes in NU-1306, adding strain on the node (Fig 3.3d, Fig 3.17). Furthermore, the crystal density of NU-1306 lies at 0.470 g cm^{-3} while that of NU-1305 is 0.521 g cm^{-3}, suggesting NU-1305 as the more energetically stable structure.[177, 191]

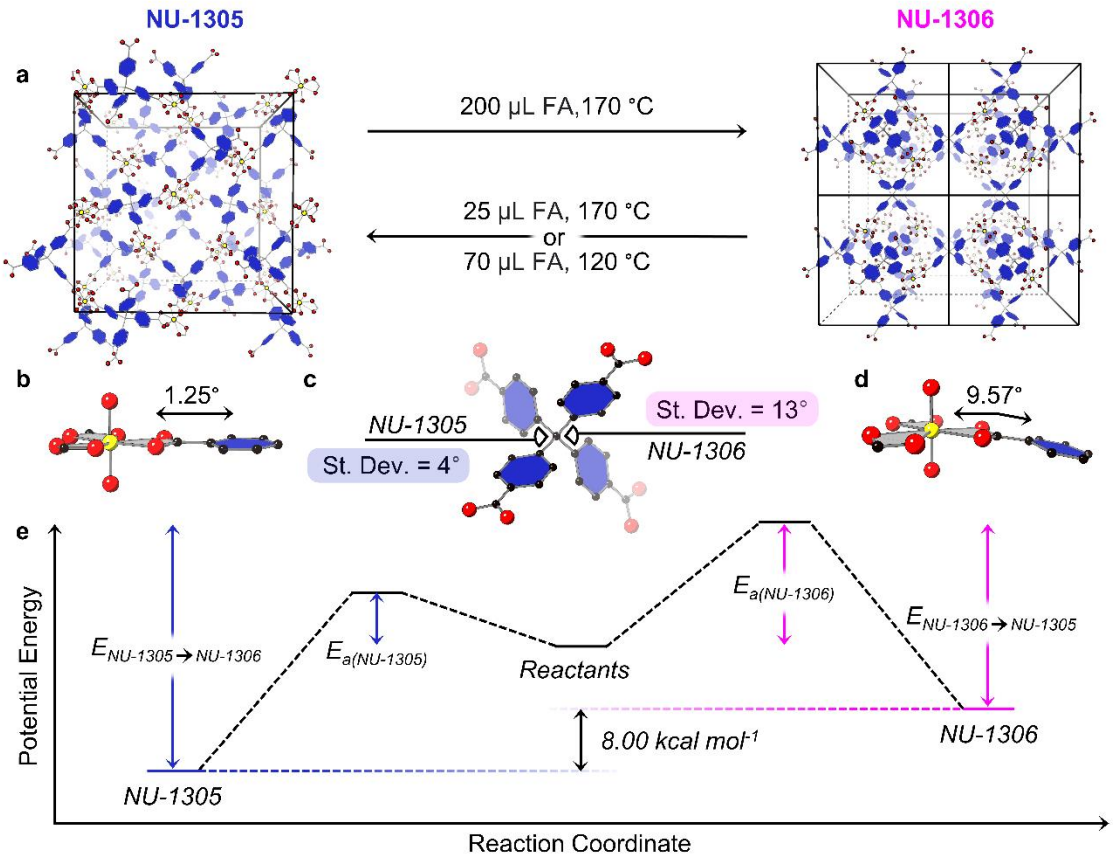

Figure 3.3 Energetic analysis of isomer favorability. (a) Conversion of NU-1305 (left) to NU-1306 (right) and vice versa. Geometric analysis of (b) NU-1305 and (d) NU-1306 nodes. Only the immediately bound phenyl ring of one attached linker is shown for clarity (c) Standard deviation of linker dihedral angles for NU-1305 and NU-1306. In panels b-d, uranium is shown in yellow, oxygen in red, and carbon in black. Hydrogen atoms are omitted for clarity. (e) Reaction coordinate diagram of NU-1305 and NU-1306 isomers. This panel is qualitative.

In addition to the geometric analysis, conversion between topological isomers verified their respective locations within the system's energy landscape. Synthetic conditions involving high temperature and increased modulator suggest a higher activation energy barrier to form NU-1306, while reaction concentration-dependence, DFT calculations, and geometric analysis indicate that NU-1305 lies lower on the energy landscape (Fig 3.3e). If both these deductions are true, then the energy required to convert from NU-1305 to NU-1306 should be higher than the energy needed to convert isomers in the opposite direction (Fig 3.3e). To test this hypothesis, we heated DMF suspensions of individual MOF isomers in the presence of additional modulator and determined

the least harsh conditions (lowest amount of modulator, lowest temperature) needed to observe isomer conversion. We found that NU-1305 converts to NU-1306 by submerging 5 mg of washed NU-1305 in fresh DMF with 200 µL FA at 170 °C (Fig 3.3a, Fig 3.12), while conversion from NU-1306 to NU-1305 requires either 25 µL FA at 170 °C or 70 µL FA at 120 °C (Fig 3.3a, Fig 3.13). From these experiments, it is apparent that converting from NU-1305 to NU-1306 requires harsher conditions (high modulator, high temperature) than converting from NU-1306 to NU-1305 (either low modulator and high temperature or high modulator and low temperature). These data reveal that NU-1305 does indeed lie lower in the energy landscape. Thus, these synthetic conversion parameters, paired with the geometric analysis of both MOF isomers, support the DFT findings of NU-1305 as the thermodynamically favored isomer.

3.5 Non-Equilibrium Synthesis Indicates that NU-1306 is a Metastable Isomer

The question then arises: how can the apparent mismatch between synthetic and energetic parameters in this system be explained? The answer to this question lies in the high temperature synthesis of NU-1306, which occurs with a starting 0.8 mL DMF volume and 0.09 FA:DMF ratio at 170 °C, well above the DMF solvent boiling point (153 °C). Because the reaction vessel used in this synthesis is not pressure-rated, evaporated solvent escapes as the reaction mixture is heated, decreasing the total reaction volume by the end of the reaction (Fig 3.4b). This behavior is not observed for the reaction performed at 120 °C under otherwise analogous conditions, which produces NU-1305 (Fig 3.4a).

Thus, multiple factors may potentially influence the selection of NU-1306 over NU-1305 under these high temperature conditions, including 1) increased effective reaction concentration, 2) energy added to the system from high temperature, and 3) loss of reaction components through evaporation. If loss of material is responsible for NU-1306 growth at high temperature, it would

imply that non-equilibrium conditions affect isomer selectivity, an important consideration for understanding the apparent mismatch between synthetic and energetic parameters in this system. Thus, we set out to deconvolute these three factors and determine which of them encourages NU-1306 growth at 170 °C.

If reaction concentration rather than temperature or material loss promotes the growth of NU-1306 at high temperatures, then the same reaction performed at 120 °C at high concentration should produce NU-1306. We thus performed a control experiment at 0.09 FA:DMF and 120 °C with the same total volume found at the completion of the 170 °C NU-1306 reaction. However, these conditions afford NU-1305 with very minor NU-1306 peaks observed by PXRD analysis, demonstrating that the increased reaction concentration does not account for full NU-1306 growth in this case (Fig 3.11). We note that due to the three-dimensionality of the energy landscape, higher reaction concentrations at 0.10 FA:DMF favor pure NU-1306 (Fig 3.2c), while the same experiments run here at 0.09 FA:DMF do not (Fig 3.11).

Next, to deconvolute the effects of temperature and loss of material, we employed a pressure reaction vessel where solvent cannot escape. If loss of material is important for NU-1306 growth, then we expect the high temperature reaction (0.8 mL DMF, 0.09 FA:DMF, 170 °C) run in a closed pressure vessel to not produce NU-1306. However, if NU-1306 still grows under these conditions, then energy added to the system from high temperature promotes NU-1306 growth. The synthesis performed in a closed system resulted in the formation of an amorphous, black product (Fig 3.10a-b), implying that loss of material is crucial to NU-1306 formation at high temperatures. To emphasize that loss of material promotes NU-1306 growth but has no effect on NU-1305 growth, we demonstrated that the identical 120 °C synthesis of NU-1305 still proceeds when performed in

a closed pressure vessel (Fig 3.10c). Thus, we deduce that loss of material over time is in fact important for the formation of NU-1306.

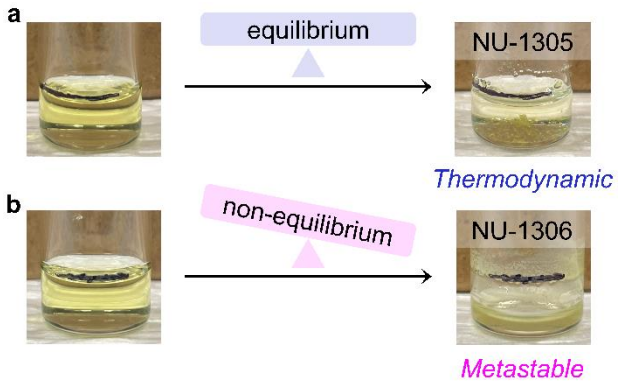

Figure 3.4 Non-equilibrium conditions for NU-1306 synthesis. Photographs of (a) NU-1305 and (b) NU-1306 before (left) and after (right) the reaction. A black horizontal line drawn on the glass vial indicates the initial solvent line before heat was added. Reaction conditions are identical (0.9 FA:DMF, 0.8 mL DMF, 1.6:1 node:linker) except that (a) was heated at 120 °C for 24 hours while (b) was heated at 170 °C for 1 hour.

Analysis of this reaction provides insight into what type of material loss occurs under these conditions. While MOF synthesis is a complex phenomenon, we postulate a simplified reaction for this system in Equation 1, including components directly involved in the reaction. Here, an unquantified molar ratio (*n*) of formic acid decomposes to volatile products (either CO and H_2O in pathway 1 or CO_2 and H_2 in pathway 2). Gas chromatography experiments reveal that both pathways are present for the two isomer MOF syntheses, and that pathway 1 dominates for NU-1306 synthesis while pathway 2 dominates for NU-1305 synthesis (Figs 3.20 and 3.21).

Eq 1. $1.6\ UO_2(NO_3)_2$ + **TCPM** + $1855\ CH_2O_2$ à NU-130X + *n* CO + *n* H_2O *(pathway 1)*

or

$1.6\ UO_2(NO_3)_2$ + **TCPM** + $1855\ CH_2O_2$ à NU-130X + *n* CO_2 + *n* H_2 *(pathway 2)*

where X = 5 or 6

Solvent loss in the NU-1306 synthesis indicates that volatile formic acid byproducts are also removed from the closed reaction system. Importantly, since NU-1306 only forms on the sides of

the vial at the solvent/air interface (Fig 3.4b), MOF product likewise is constantly syphoned out of the reaction media as the volume level decreases. Thus, multiple products leave the NU-1306 reaction as it progresses. We note that NU-1305, which forms as large crystals mostly on the bottom of the vial, still remains available for growth within the reaction media, with minimal solvent loss (Fig 3.4a).

According to Le Châtelier's principle, when products are removed from a reaction, the equilibrium balance becomes tilted in favor of product formation; this can result in non-equilibrium thermodynamic control of a metastable product.[167, 168, 171] Here, we observe a similar occurrence: products are removed from the reaction media, which stabilizes a phase that is not the thermodynamic ground state. Thus, NU-1306 becomes thermodynamically stable under the conditions of growth, even though it is a local energetic minimum. This higher temperature reaction indicates that NU-1306 is a metastable phase, which also reveals why other thermodynamic reaction parameters such as high modulator amount favor this product. Thus, from the energetic analysis of this system, we observe NU-1305 as the topological isomer at the global energy minimum (thermodynamic product) and NU-1306 at a local energy minimum (metastable product).

3.6 Conclusions

In conclusion, we demonstrate how the identification of a metastable phase resolves seemingly contradictory synthetic parameters and energetic calculations within a set of uranium MOF topological isomers. We systematically synthesized two distinct topological isomers ***ctn*** and ***bor***, named NU-1305 and NU-1306, respectively. While NU-1306 appeared to be thermodynamically favored by synthetic trends involving modulator and temperature, reaction concentration trends, DFT calculations, geometric analysis, and isomer conversion identified NU-1305 as the

thermodynamically favored isomer by 8 kcal mol^{-1}. Since the high-temperature synthesis of NU-1306 depends on the removal of products from the reaction media over time, non-equilibrium thermodynamic control is apparent in this system, following Le Châtelier's principle. Thus, we attribute the apparent mismatch between synthetic and energetic parameters to NU-1306 being a metastable phase that becomes thermodynamically stable under the conditions of growth.

The interplay between structure and energetics in this study informs design rules for topological MOF isomers by revealing that even topologies of local energetic minima may be favored thermodynamically under non-equilibrium synthesis conditions. Synthetic trends that traditionally point to the appearance of a thermodynamic MOF product, such as high modulator and high temperature, may not provide sufficient proof for the global thermodynamic product within the entire system. Instead, we encourage the use of a suite of factors for identifying MOF location within the three-dimensional energy landscape, including synthetic parameters, crystal structure examination, geometric strain analysis, and energetic calculations. Additionally, the apparent mismatch observed in this study encourages us to explore phase space outside of conventional binary (e.g., kinetic vs. thermodynamic) product options. Finally, this study also reveals how implementing thermodynamic control can access less explored metastable phases in non-traditional uranium-based MOFs. Targeting non-equilibrium synthetic conditions through Le Châtelier's principle can thus be used as a strategy to access metastable MOFs with unique properties and functions. More generally, investigating the relationship between structure and energetics broadens our understanding of phase space in both actinide materials and supramolecular isomers.

3.7 Additional Information

3.7.1 Materials

All chemicals were purchased from the supplier and used without further purification. Tetraphenylmethane (Sigma-Aldrich), sodium hydroxide (Sigma-Aldrich), bromine (Sigma-Aldrich), ethanol (Fisher Scientific), chloroform (Fisher Scientific), Xantphos (Sigma-Aldrich), *N*-formylsaccharin (TCI America), potassium fluoride (anhydrous, Acros Organics), palladium(II) acetate (trace metal basis, Acros Organics), *N*,*N*-dimethylformamide (DMF, anhydrous, DriSolv, Millipore Sigma), and triethylamine (Fisher Scientific) were used to make the **TCPM** linker. Other chemicals used herein include uranyl nitrate hexahydrate (International Bio-Analytical Industries Inc.), formic acid (Millipore Sigma), DMF (Fisher Scientific), ethanol (Fisher Scientific), acetonitrile (Fisher Scientific), acetone (Fisher Scientific), sulfuric acid-d_2 (Millipore Sigma), dimethyl sulfoxide-d_6 (Millipore Sigma), and dimethylamine solution 40 wt. % in H_2O (Millipore Sigma).

Caution! Uranium salts are radioactive chemicals and contain depleted uranium (^{238}U). Necessary precautions must be adhered to when handling uranium salts.

3.7.2 Methods and Instrumentation

3.7.2.1 Powder X-ray Diffraction (PXRD)

PXRD data were obtained using a Stoe STADI P diffractometer, equipped with a CuKα1 source and a 1D strip detector. Transmission mode was used for all samples. Samples were prepared for PXRD by removing the DMF solvent, washing with fresh ethanol two times, and dropcasting onto the sample holder.

3.7.2.2 Single Crystal X-ray Diffraction (SCXRD)

A NU-1306 single crystal was mounted using paratone oil and a MiTeGen loop onto a Rigaku XtaLAB Synergy diffractometer equipped with a micro-focus sealed X-ray tube PhotonJet (Cu) X-ray source and a Hybrid pixel Array detector (HyPix). The temperature of the crystal, set to 273.15K, was controlled with an Oxford Cryosystems low-temperature device. Data reduction was

performed with the CrysAlisPro software using an empirical absorption correction with spherical harmonics. Using Olex2, the structure was solved with the SHELXT structure solution program using intrinsic phasing. The model was refined with ShelXL using least-squares minimization. Crystallographic data for NU-1306 has been deposited at The Cambridge Crystallographic Data Centre (CCDC) under deposition number 2203723. This data can be obtained free of charge *via* www.ccdc.cam.ac.uk.

3.7.2.3 Optical Microscope

Optical images were acquired with a Nikon SMZ1500 microscope.

3.7.2.4 Nuclear Magnetic Resonance (NMR) Spectroscopy

^{1}H spectra of **TCPM** linker were collected on an A600, Bruker Avance III 600 MHz or an Au400, Bruker Avance III HD Nanobay 400 MHz instrument. ^{1}H spectra of digested MOFs were collected on an A600, Bruker Avance III 600 MHz instrument.

3.7.2.5 Supercritical CO_2 (sc-CO_2) Activation

Activation with sc-CO_2[155] was performed on a Tousimis Samdri PVT-3D critical point dryer, using a bone-dry CO_2 syphon tank. We followed a previously reported procedure.[188]

3.7.2.6 Gas Chromatography-Flame Ionization Detection (GC-FID)

CO and CO_2 separation and analysis were performed using an Agilent 7890A GC equipped with an FID. An aliquot of 0.5 mL sample gas was manually injected directly into an Agilent HP-Plot-Q column (19095P-QO4, Inner Diameter: 0.53 mm, Length: 30 m, Film Thickness: 40 μm) *via* a split/splitless inlet using a Hamilton 1750 SL Gastight syringe equipped with Sample Lock. The detector was equipped with an ARC Jetanizer methanizer jet to allow for the detection of CO and CO_2. A second split/splitless inlet was used to maintain the flow of carrier gas through the HP-Molesieve column. The entire method was isothermal (T=35 °C) and used nitrogen as a carrier gas set to 4 mL. CO and CO_2 gas-phase species were identified using calibration standards with

retention times of 1.88 and 2.93 minutes, respectively. Samples were prepared in Biotage 0.5-2 mL vials and crimped caps equipped with septa.

3.7.2.7 Thermal Activation

Thermal activation was performed under ultrahigh vacuum at 120 °C for 18 hours using a Micromeritics Smart VacPrep (SVP) instrument.

3.7.2.8 Thermogravimetric Analysis (TGA)

TGA experiments were performed using a TGA/DSC 1 LF (Mettler Toledo) instrument with STARe (v16.10) software. Samples were loaded into a 100 μL aluminum pan, heated from 30 °C to 120 °C, held at 120 °C for 1 hour, cooled from 120 °C to 30 °C, and heated from 30 °C to 600 °C. All ramp rates were performed at 5 °C/min in air.

3.7.3 Syntheses

*3.7.3.1 Tetrakis(4-carboxyphenyl)methane (**TCPM**)*

First, tetrakis(4-bromophenyl)methane (Scheme 3.2, **2**) was synthesized. To a 500 mL two-neck round bottom flask, equipped with a magnetic stir bar, we installed an outlet adaptor connected *via* rubber tubing to a pipette that was immersed in a solution of sodium hydroxide (20%, 250 mL). Tetraphenylmethane (10 g, 31.21 mmol) (Scheme 3.2, **1**) was then added to the flask. Next, neat bromine (11.1 mL, 216.64 mmol) was slowly added with continuous stirring at room temperature. The resultant, dark orange slurry was stirred for 25 min. Following this, 200 mL of ethanol, cooled to -78 °C, was added to the flask, and the suspension was sonicated and filtered. Precipitated material was then sonicated in 200 mL of saturated sodium sulfite solution and isolated by filtration. The crude product was then purified *via* recrystallization by solubilizing in 500 mL of a 1:1 mixture of boiling ethanol/chloroform followed by cooling in a freezer for 30 min. The compound was then filtered and dried to afford 13.9 g (70% yield).

TCPM was then synthesized based on a modified procedure from the literature (Scheme 3.2, **3**).[194] To an oven-dried, 200 mL heavy wall pressure vessel from Chemglass in a glovebox under Ar atmosphere, we added Xantphos (468.8 mg, 0.81 mmol) and palladium (II) acetate (121.2 mg, 0.54 mmol), followed by approximately 75 mL of anhydrous *N*,*N*-dimethylformamide (DMF). The Xantphos/Pd mixture was periodically swirled at room temperature while the remaining reagents were measured out. Next, tetrakis(4-bromophenyl)methane (2.21 g, 3.47 mmol) and potassium fluoride (2.62 g, 45.1 mmol) were added to the reaction flask. Lastly, *N*-formylsaccharin (4.75 g, 22.5 mmol) was added, resulting in effervescence. The reaction flask was quickly capped with a back seal solid PTFE bushing, equipped with a viton o-ring, and removed from the glovebox, after which it was vigorously stirred at 80 °C for approximately 3 days. After cooling to room temperature, 21 mL of triethylamine and 20 mL of deionized water were added to the reaction mixture, and it was stirred at room temperature for at least overnight. Following this, the volatiles were removed *in vacuo*. The crude product was then suspended in deionized water *via* sonication and isolated *via* vacuum filtration. After, it was suspended in 1 M NaOH (*aq*), and insoluble, dark solids were removed *via* vacuum filtration. The filtrate was next acidified with HCl to approximately pH = 1, and the precipitated product was collected from the aqueous solution *via* vacuum filtration. This precipitate was then dissolved in 1 M NaOH (*aq*) and passed through a Supor® 100 membrane disc filter (Pall, 0.1 µm – 47 mm, plain), followed by acidification with HCl to approximately pH = 1. It was collected *via* vacuum filtration and dried in a vacuum oven at 85 °C for 1-2 days, affording 1.56 g of a white solid (91% yield) (Fig 3.5).

3.7.3.2 NU-1305 Single Crystals

Single crystals of NU-1305 were synthesized by combining 0.5 mL (9.958 µmol) of a 10 mg mL^{-1} (19.915 mM) uranyl nitrate hexahydrate solution in N,N-dimethylformamide (DMF), 0.306 mL

(6.164 µmol) of a 10 mg mL^{-1} (20.1422 mM) **TCPM** solution in DMF, and 30 µL of formic acid (FA) in a 1.5 dram glass vial. The mixture was sealed in the glass vial, sonicated for 2 minutes, and placed in a 120 °C oven for 24 hours. Large 200 µm tetrahedrally-shaped yellow crystals were observed on the bottom and walls of the vial that were submerged in solvent (Fig 3.6).

3.7.3.3 NU-1306 Single Crystals

Single crystals of NU-1306 were synthesized by combining 0.5 mL (9.958 µmol) of a 10 mg mL^{-1} (19.915 mM) uranyl nitrate hexahydrate solution in N,N-dimethylformamide (DMF), 0.306 mL (6.164 µmol) of a 10 mg mL^{-1} (20.1422 mM) **TCPM** solution in DMF, and 25 µL of formic acid (FA) in a 1.5 dram glass vial. The mixture was sealed in the glass vial, sonicated for 2 minutes, and placed in a sand-bath in a 45 °C oven for 72 h (the resulting solution was still clear). The vial was then left undisturbed at room temperature for 14 weeks. Large tetrahedrally-shaped yellow crystals were observed on the bottom and walls of the vial that were submerged in solvent, similar to those of NU-1305. Additional block-shaped crystals were also observed on the headspace walls of the vial (Fig 3.7). A selected 78 x 100 x 117 µm block crystal diffracted to reveal the structure of NU-1306. Data collection and refinement details are included in Table 3.1. The asymmetric unit, node coordination, and pore sizes can be found in Figure 3.9. PLATON was used to calculate 84% solvent accessible pore volume.

3.7.3.4 Bulk MOF Syntheses Varying Modulator Ratio

NU-1305 and NU-1306 were synthesized by varying the modulator ratio in the following manner. 0.5 mL (9.958 µmol) of a 10 mg mL^{-1} (19.915 mM) uranyl nitrate hexahydrate solution in DMF and 0.306 mL (6.164 µmol) of a 10 mg mL^{-1} (20.1422 mM) **TCPM** solution in DMF were combined in a 1.5 dram glass vial. Either 25, 40, 50, 70, 80, 90, 100, or 120 µL of FA was added to the linker and node mixture. We define each modulator amount by the volumetric ratio of FA to DMF (0.806 mL total) such that samples with 25 µL FA are 0.03 FA:DMF, 40 µL FA are 0.05

FA:DMF, 50 µL FA are 0.06 FA:DMF, 70 µL FA are 0.09 FA:DMF, 80 µL FA are 0.10 FA:DMF, 90 µL FA are 0.11 FA:DMF, 100 µL FA are 0.12 FA:DMF, and 120 µL FA are 0.15 FA:DMF. Each mixture was sealed in its glass vial, sonicated for 2 minutes, and placed in a 120 °C oven. Samples with 0.03 FA:DMF remained in the oven for 24 h, 0.05 and 0.06 FA:DMF for 48 h, 0.09 FA:DMF for 7 days, 0.10, 0.11, and 0.12 FA:DMF for 5 days, and 0.15 FA:DMF for 6 days. All samples with a FA:DMF ratio at or below 0.09 resulted in NU-1305, and all samples with a FA:DMF ratio at or above 0.10 resulted in NU-1306.

3.7.3.5 Bulk MOF Syntheses Varying Temperature

NU-1305 and NU-1305 were synthesized by varying the reaction temperature in the following manner. 0.5 mL (9.958 µmol) of a 10 m gmL^{-1} (19.915 mM) uranyl nitrate hexahydrate solution in DMF, 0.306 mL (6.164 µmol) of a 10 m gmL^{-1} (20.1422 mM) **TCPM** solution in DMF, and 70 µL FA (11.5 DMF:FA) were combined in a 1.5 dram glass vial. The mixture was sealed in the glass vial and sonicated for 2 minutes. Samples were placed in either a 120 °C oven for 24 h, a 160 °C for 6 h, or a 170 °C oven for 1 h. Samples run at 170 °C were wrapped in Teflon tape to slow down solvent loss. Samples at 120 °C resulted in NU-1305, 160 °C in a mixture of both isomers, and 170 °C in NU-1306. When the 170 °C synthesis was performed in a sealed pressure reaction vessel, black product (Fig 3.10a) appearing amorphous by PXRD (Fig 3.10b) was observed. When the 120 °C synthesis was performed in a sealed pressure reaction vessel, NU-1305 was still observed (Fig 3.10c).

3.7.3.6 Bulk MOF Syntheses Varying Reaction Concentration

NU-1305 and NU-1306 were synthesized by varying the reaction concentration in the following manner. 0.5 mL (9.958 µmol) of a 10 mg mL^{-1} (19.915 mM) uranyl nitrate hexahydrate solution in DMF, 0.306 mL (6.164 µmol) of a 10 mg mL^{-1} (20.1422 mM) **TCPM** solution in DMF, and 80 µL FA (0.10 FA:DMF) were combined in a 1.5 dram glass vial. Either 0, 0.25, 0.5, 0.75, or 1 mL

of additional DMF was added to the linker and node mixture. We define each reaction by its total volume. Thus, samples with 0 mL added DMF have a 0.8 mL total volume, 0.25 mL added DMF have a 1.1 mL total volume, 0.5 mL added DMF have a 1.3 mL total volume, 0.75 mL added DMF have a 1.6 mL total volume, and 1 mL added DMF have a 1.8 mL total volume. Each mixture was sealed in its glass vial, sonicated for 2 minutes, and placed in a 120 °C oven for 6 days. Samples with 0.8 and 1.1 mL total volume resulted in NU-1306 while samples with a total volume at or above 1.3 gradually possessed less NU-1306 and more NU-1305.

The same reactions were run with 70 µL FA instead (0.09 FA:DMF) diluted to either 1.8 total mL (48h reaction time) or concentrated to 0.4 total mL (24h reaction time) (Fig 3.11).

3.7.4 MOF Conversion Parameters

3.7.4.1 Conversion of NU-1305 to NU-1306

NU-1305 was converted to NU-1306 by first soaking synthesized NU-1305 in fresh DMF for one hour and repeating this procedure three times. Then, 5 mg of NU-1305, 1 mL fresh DMF, and 200 µL FA were added to a 1.5 dram vial, sealed, and placed in a 170 °C oven for 3.5 h. The resulting solid was identified as NU-1306 by PXRD (Fig 3.12). Attempting conversion at less harsh conditions resulted in no observed conversion to NU-1306.

3.7.4.2 Conversion of NU-1306 to NU-1305

NU-1306 was converted to NU-1305 by first soaking synthesized NU-1306 in fresh DMF for one hour and repeating this procedure three times. Conversion was accomplished using two sets of conditions. The first condition involved combining 5 mg of NU-1306, 1 mL fresh DMF, and 25 µL FA in a 1.5 dram vial. The vial was then sealed and placed in a 170 °C oven for 1 h. The second condition involved combining 5 mg of NU-1306, 1 mL fresh DMF, and 70 µL FA in a 1.5 dram vial. The vial was then sealed and placed in a 120 °C oven for 3 days. The resulting solids from

both sets of conditions were identified as NU-1305 by PXRD (Fig 3.13). Attempting conversion at less harsh conditions resulted in no observed conversion to NU-1305.

3.7.5 Counterion Analysis

Since NU-1305 and NU-1306 are anionic MOFs, we expect that either dimethylammonium (from the degradation of DMF), H^+, or H_3O^+ act as counterbalancing cations. To search for the presence of dimethylammonium, we implemented ^{1}H NMR analysis. NU-1305 and NU-1306 were each prepared by first washing in fresh acetonitrile and exchanging the acetonitrile once every hour for three hours. Samples were then soaked in acetonitrile overnight (~16 hours) and activated *via* sc-CO_2 activation. Approximately 2-3 mg of activated MOF was sonicated in five drops of sulfuric acid-d_2, diluted to approximately 0.5 mL with dimethyl sulfoxide-d_6, and sonicated again. ^{1}H NMR spectra of NU-1305 (Fig 3.14) and NU-1306 (Fig 3.15) was integrated per node (0.75 linkers per node), and doublets at 7.22 and 7.77 ppm are assigned to the **TCPM** linker. We did not observe any peaks for dimethylammonium in either sample. A control experiment of dimethylamine treated under the same digestion conditions shows peaks for dimethylammonium at 2.8 and 2.9 ppm (3:1 integration, respectively). Comparing this spectrum to those of NU-1305 and NU-1306 confirms that dimethylammonium is not present in either sample (Fig 3.16). Thus, we deduce that either H^+ or H_3O^+ act as counterbalancing cations, similar to results we have reported previously. [188]

3.7.6 Geometric Analysis

3.7.6.1 Node Geometry Analysis

The node geometry was measured in Mercury by first calculating the plane which includes a uranium atom and the two oxygen atoms from an equatorially bound linker (plane A). The plane holding the immediately bound linker phenyl ring was also calculated (plane B). We then measured the angle between the two planes for both NU-1305 and NU-1306, which was 1.25° and 9.57°, respectively (Fig 3.17).

3.7.6.2 Linker Geometry Analysis

Linker geometry was analyzed in Mercury by measuring the linker dihedral angles for NU-1305 and NU-1306 (Fig 3.18). There are six total dihedral angles per linker, listed in Table 3.2. While both MOF linkers had similar mean dihedral angle values, the standard deviation of these angles from the mean differed significantly, showing that the angle range and distortion in NU-1306 is larger than that of NU-1305. (Table 3.2).

3.7.6.3 Crystal Density

Crystal density was measured in CrystalMaker. The density of NU-1306 lies at 0.470 g cm^{-3} while that of NU-1305 is 0.521 g cm^{-3}.

3.7.7 Density Functional Theory Calculations

Beginning with the experimentally collected crystallographic positions, the cell parameters of both the **bor** and **ctn** structures were geometrically equilibrated using VASP. The geometries were obtained using a 500 eV planewave cutoff, a 2 x 2 x 2 k-grid, paired with the PBEsol functional. Energy was converged to within 0.005 eV per atom. The computational lattice constants $a=b=c$ were found to be 20.98 Å, and 32.20 Å for **bor** (NU-1306) and **ctn** (NU-1305), respectively. These values were in excellent agreement with the experimental values of 20.90 Å and 32.12 Å for the **bor** (NU-1306) and **ctn** (NU-1305) structures, respectively. The calculated axial and equatorial U-O bond lengths for both polymorphs are similar to the experimental values and can be found in Table 3.3. To obtain higher level electronic structure information (density of states, bond energies, accurate comparison of isomer energies) single point HSE06 calculations were performed on the equilibrium structures.[195] These energies were compared, and the lowest energy isomer was deduced by normalizing for differences in cell size. A background charge was applied to correct the oxidation state of each MOF in order to compensate for the existence of hydronium contained

within the pores. The work functions were obtained using the ΔSCF method. A summary of the computational findings is presented in Figure 3.19.

To compare the energetics of the linkers and nodes, the linker and node geometries were extracted from the equilibrium structures. The linkers were then computed as the tetra-anion without optimization in Gaussian09, using HSE06 and a triple zeta polarized basis. The nodes were computed with passivating formates added. The U-O bond lengths were not allowed to relax, but the C-O and C-H bonds were allowed to reach equilibrium. This approach maintained the local coordination environment of the node within the MOF, while also maintaining the local symmetry around the U-centers.

3.7.8 Gas Chromatography Analysis

We analyzed the byproducts of the NU-1305 and NU-1306 reactions using gas chromatography (GC). Pathway 1 in Equation 1 can be distinguished by the presence of CO, and pathway 2 by the presence of CO_2. Thus, we analyzed the headspace of the NU-1305 and NU-1306 reactions for CO and CO_2 to determine if one or both pathways are operative.

For the 120 °C NU-1305 synthesis at 0.03 FA:DMF, GC measurements were taken at a 7-hour timepoint and after completion of the reaction. Both CO and CO_2 were observed at 7 hours and after reaction completion, suggesting that both pathways 1 and 2 are operative in NU-1305 formation under these conditions (Fig 3.20). By integrating the area under each peak, we observed a CO_2:CO ratio of 10.5:1 at 7 hours and 5.4:1 at reaction completion. This data indicates that pathway 2 dominates for the entirety of the reaction and that formic acid degradation through pathway 1 increases over the course of the reaction (while still not usurping pathway 2).

For the 120 °C NU-1306 synthesis at 0.15 FA:DMF, GC measurements were taken at a 31-hour timepoint and after completion of the reaction. Similar to NU-1305, both CO and CO_2 were

observed at 31 hours and after reaction completion, suggesting that both pathways 1 and 2 are operative in NU-1306 formation under these conditions (Fig 3.21). By integrating the area under each peak, we observed a CO:CO_2 ratio of 1.6:1 at 31 hours and 3.6:1 after reaction completion. This data indicates that pathway 1 dominates for the entirety of the reaction and that formic acid degradation through pathway 2 decreases over the course of the reaction (while still not usurping pathway 1).

Thus, while both pathways are present for the two isomer MOF syntheses, pathway 1 dominates for NU-1306 synthesis while pathway 2 dominates for NU-1305 synthesis.

3.7.9 Missing Linker Analysis

Missing linker was determined using TGA. A blank sample was measured to account for thermal expansion upon heating, and this trace was subtracted from all sample traces. Using $H^+[UO_2(\mathbf{TCPM})_{0.75}]^-$ as the formula of the starting material and U_3O_8 as the material remaining after the TGA measurement, we calculated an expected 56.3% linker for both NU-1305 and NU-1306. TGA data shows a general trend of decreasing linker present with increasing modulator amount (Fig 3.22), revealing an increasing percentage of missing linker with increasing modulator (Table 3.4).

Scheme 3.2 Synthesis of tetrakis(4-carboxyphenyl)methane

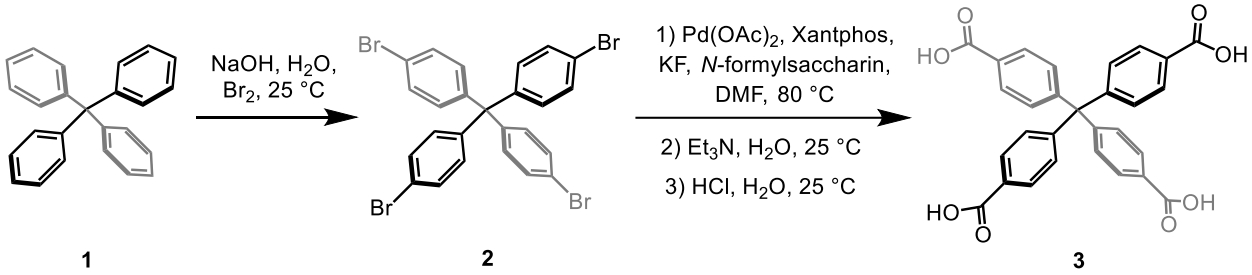

1 **2** **3**

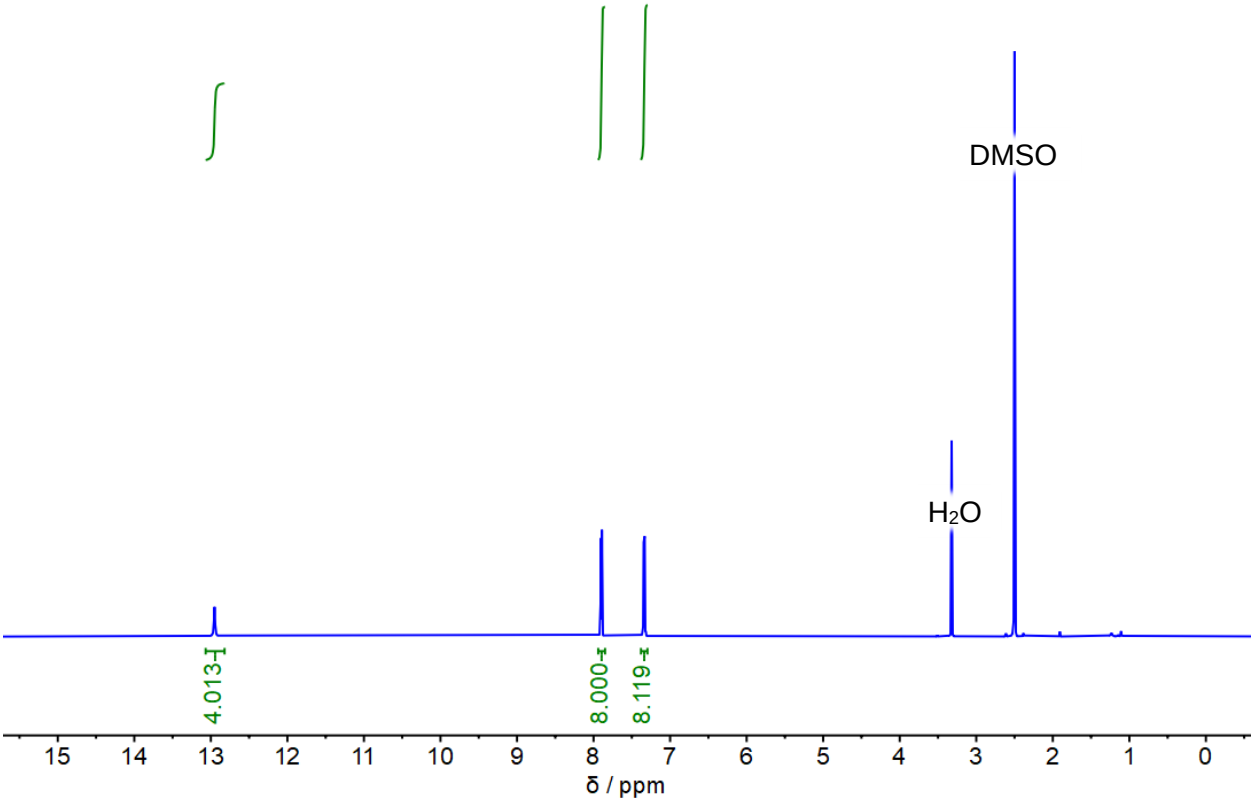

Figure 3.5 ^{1}H NMR spectra of TCPM in dimethyl sulfoxide-d_6 (DMSO).

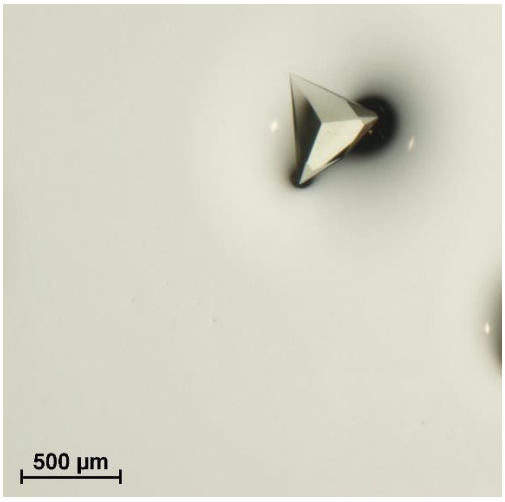

Figure 3.6 Optical image of NU-1305 single crystal.

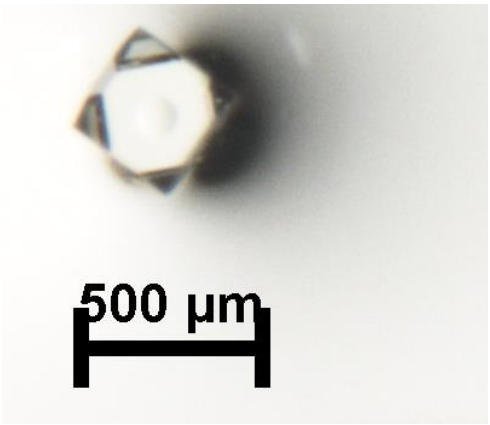

Figure 3.7 Optical image of NU-1306 single crystal.

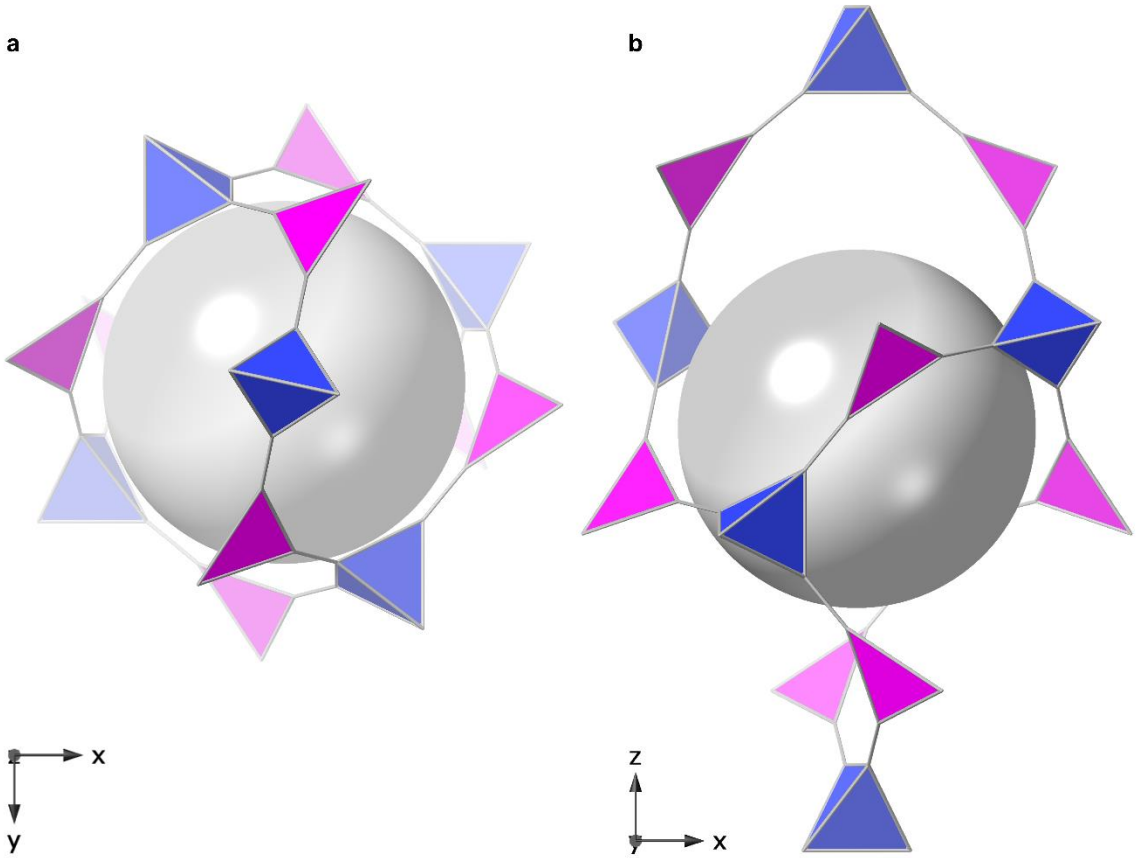

Figure 3.8 Augmented crystal structure and pore size of NU-1305 down the (a) z and (b) y axes.

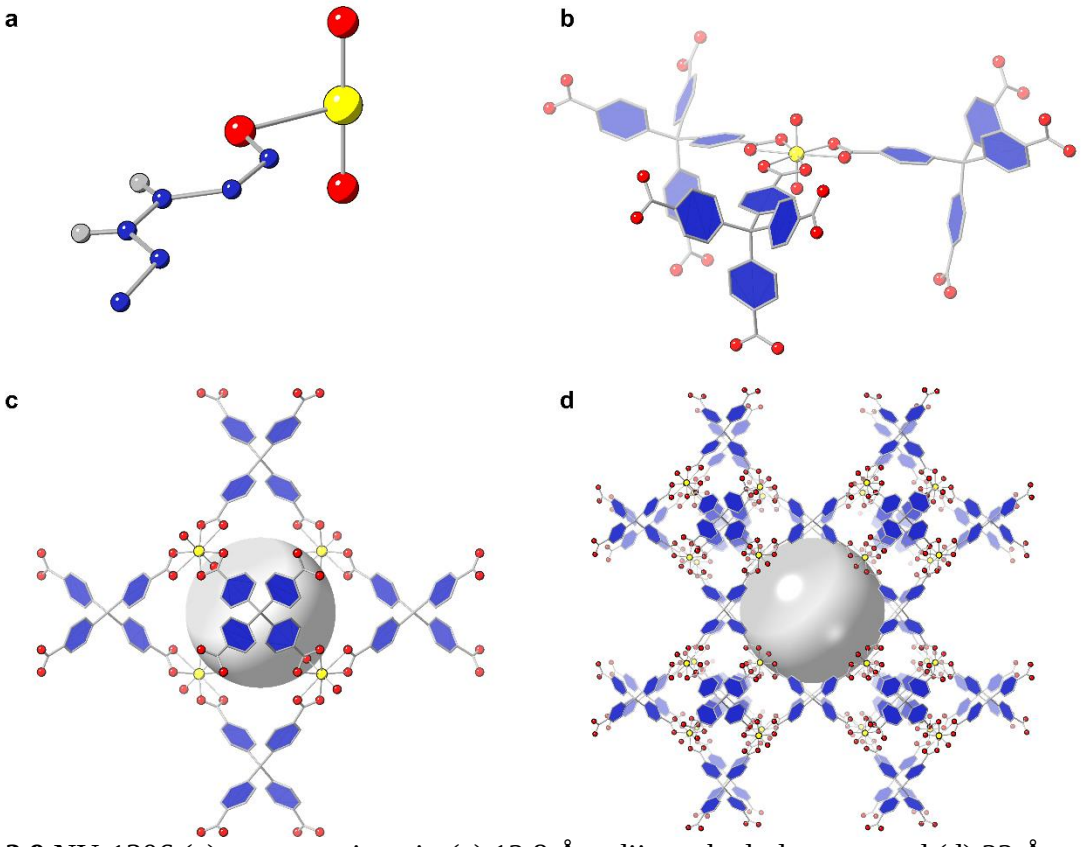

Figure 3.9 NU-1306 (a) asymmetric unit, (c) 12.8 Å radii octahedral cages, and (d) 22 Å radii apertures. (b) Node coordination of both NU-1305 and NU-1306. Uranium is shown in yellow, oxygen in red, and carbon in blue. Hydrogen atoms are omitted in all panels, but they are shown in grey in panel a for clarity.

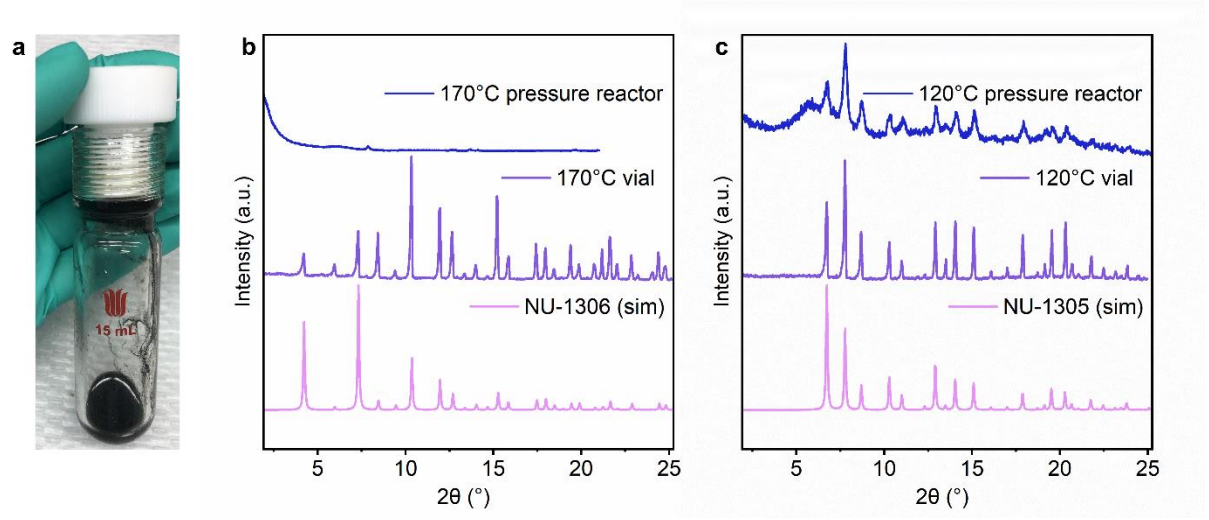

Figure 3.10 (a) Black product from 170 °C reaction in pressure reactor. PXRDs of (b) NU-1306 and (c) NU-1305 syntheses in pressure reactors and glass vials compared to their respective simulated patterns.

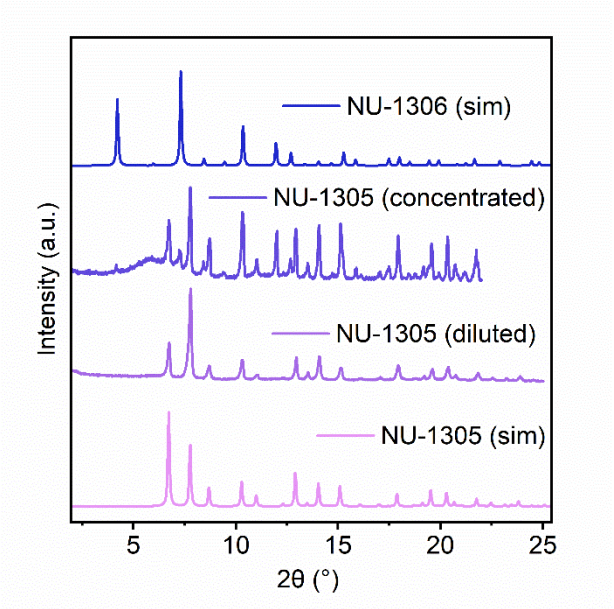

Figure 3.11 Results of diluting (total volume of 1.8 mL) and concentrating (total volume of 0.4 mL) the initial synthesis that formed NU-1305 (0.09 FA:DMF, 0.8 mL DMF, 120 °C).

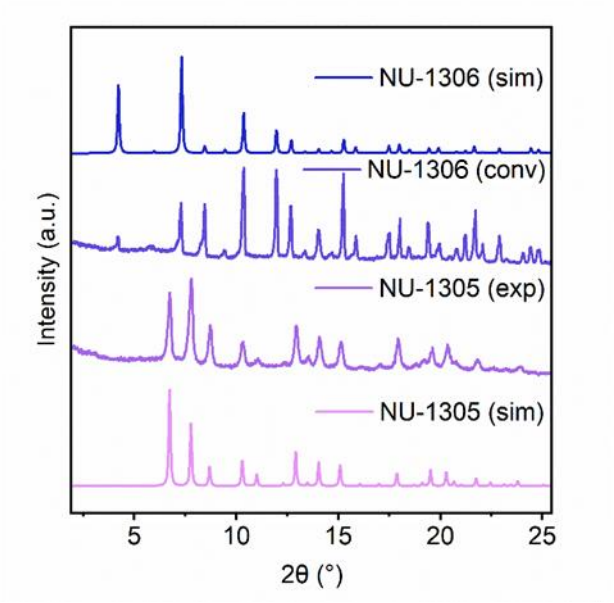

Figure 3.12 PXRD showing conversion of NU-1305 to NU-1306. From bottom to top: simulated NU-1305, experimental NU-1305, experimental NU-1305 converted to NU-1306, and simulated NU-1306.

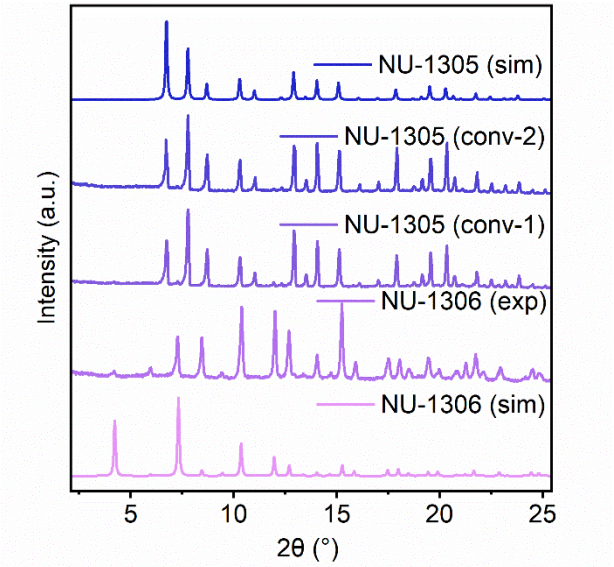

Figure 3.13 PXRD showing conversion of NU-1306 to NU-1305. From bottom to top: simulated NU-1306, experimental NU-1306, experimental NU-1306 converted to NU-1305 under condition one, experimental NU-1306 converted to NU-1305 under condition two, and simulated NU-1305.

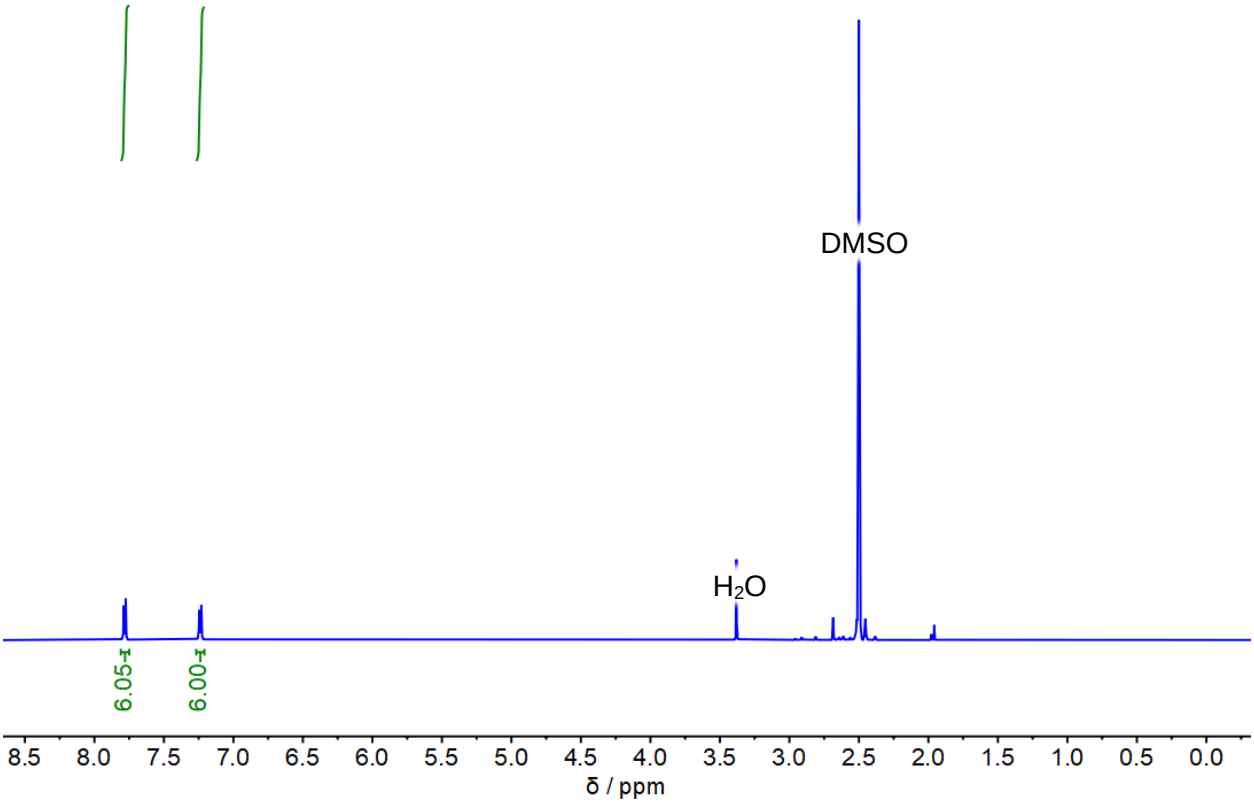

Figure 3.14 ^{1}H NMR spectra of acid-digested NU-1305 in dimethyl sulfoxide-d_6 (DMSO).

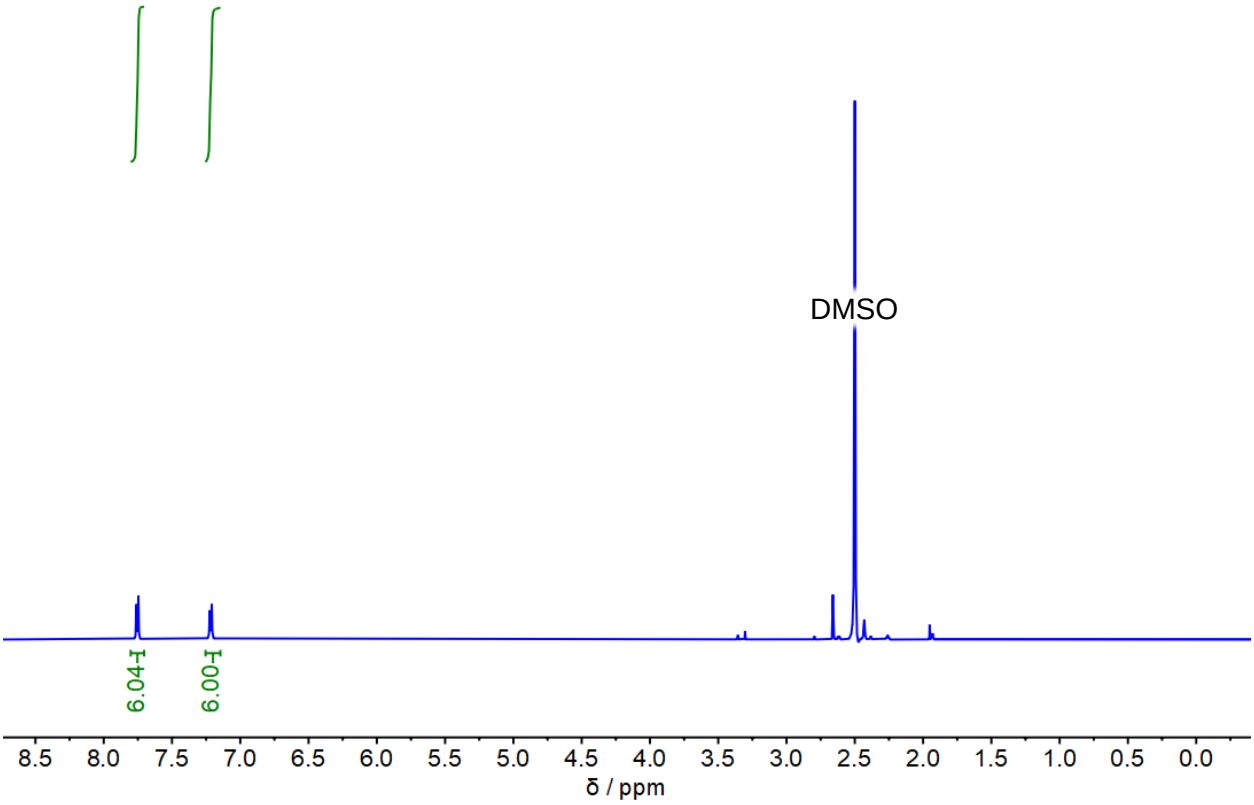

Figure 3.15 ^{1}H NMR spectra of acid-digested NU-1306 in dimethyl sulfoxide-d_6 (DMSO).

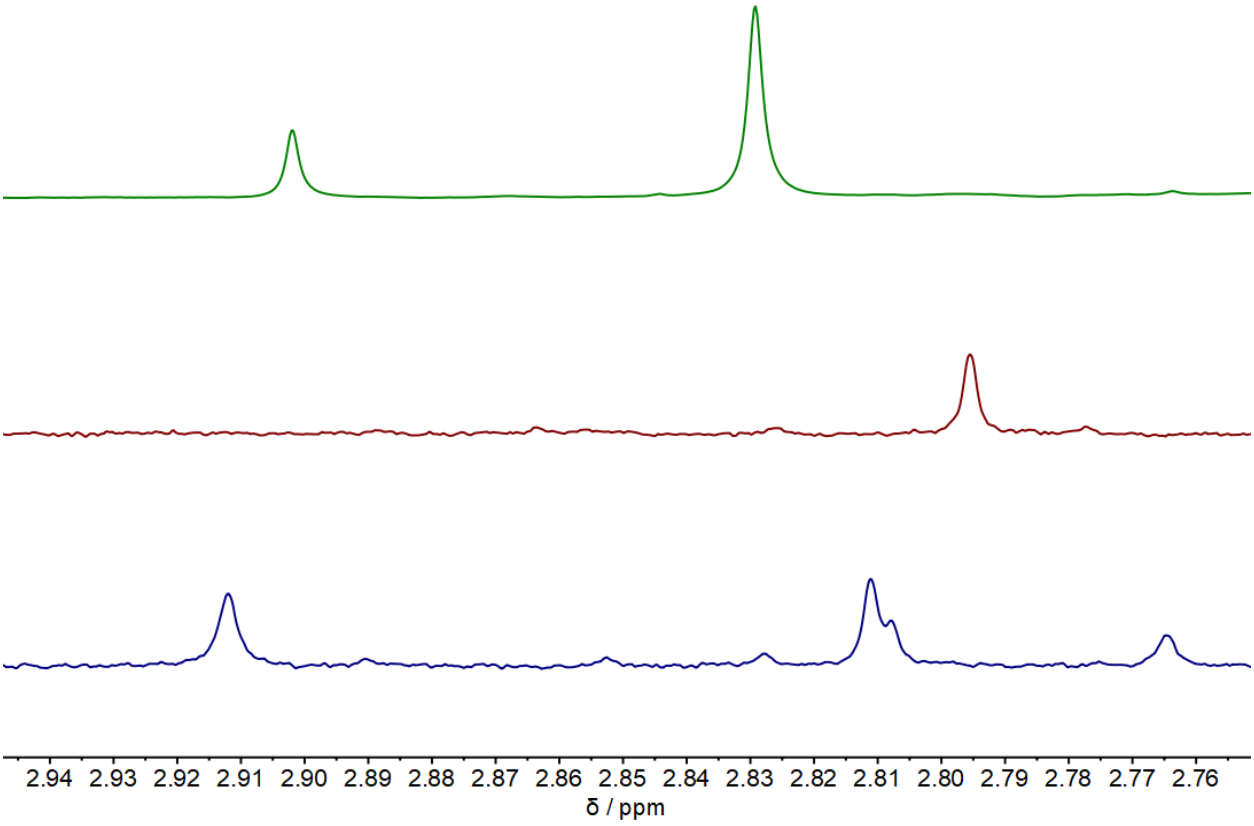

Figure 3.16 ^{1}H NMR spectra of dimethylamine (top) compared to acid-digested NU-1306 (middle) and acid-digested NU-1305 (bottom) in dimethyl sulfoxide-d_6 (DMSO).

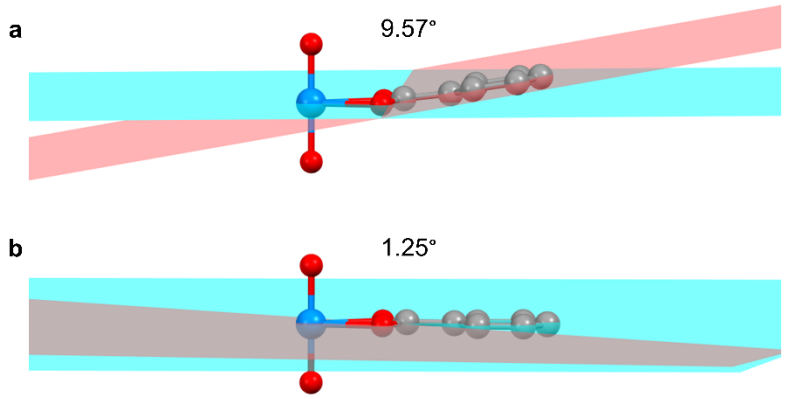

Figure 3.17 Geometric analysis of (a) NU-1306 and (b) NU-1305 nodes. Plane A is shown in aqua, and plane B is shown in red. Uranium is shown in blue, oxygen in red, and carbon in gray. Hydrogen atoms are omitted for clarity.

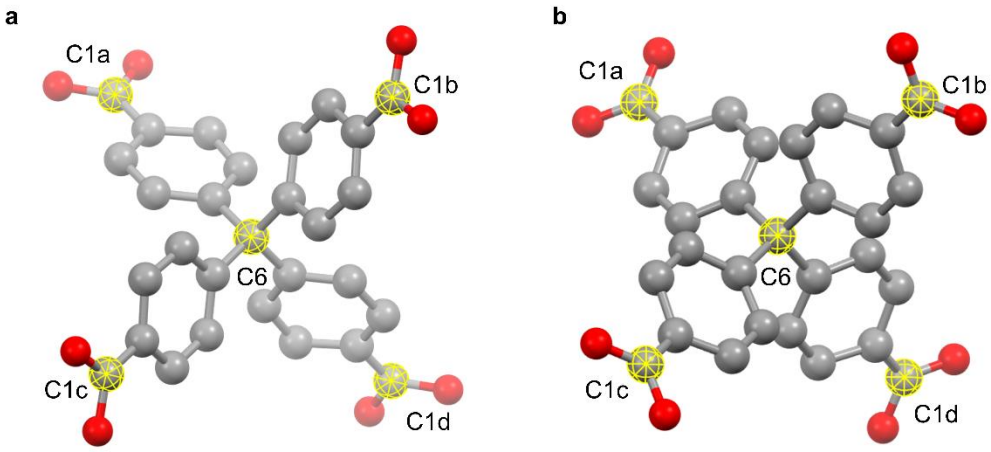

Figure 3.18 Geometric analysis of (a) NU-1306 and (b) NU-1305 linkers. Yellow highlighted carbon atoms were used to measure dihedral angles in Table 3.2. Oxygen is shown in red and carbon in gray. Hydrogen atoms are omitted for clarity.

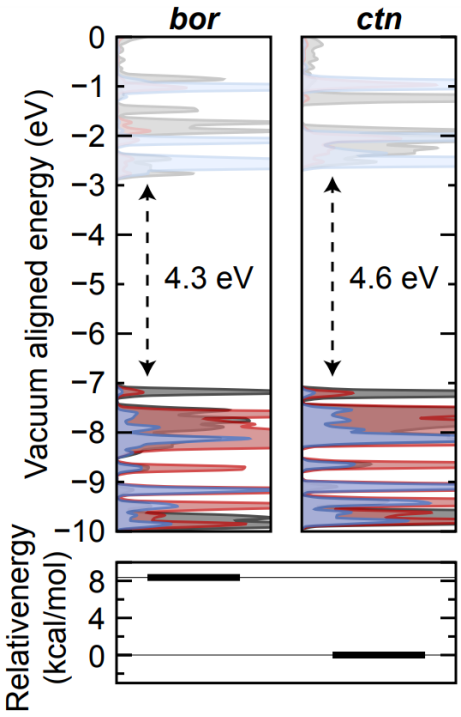

Figure 3.19 Summary of DFT results. The ctn (NU-1305) and bor (NU-1306) structures are predicted to have similar electronic properties (top), but ctn is 8 kcal mol^{-1} more stable than the bor topology (bottom).

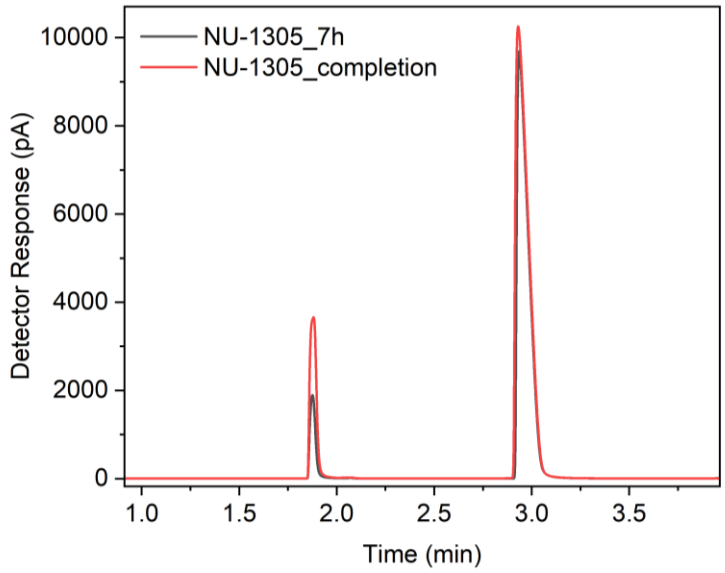

Figure 3.20 GC trace for NU-1305 synthesis. CO is observed at 1.88 minutes retention time and CO_2 at 2.93 minutes retention time.

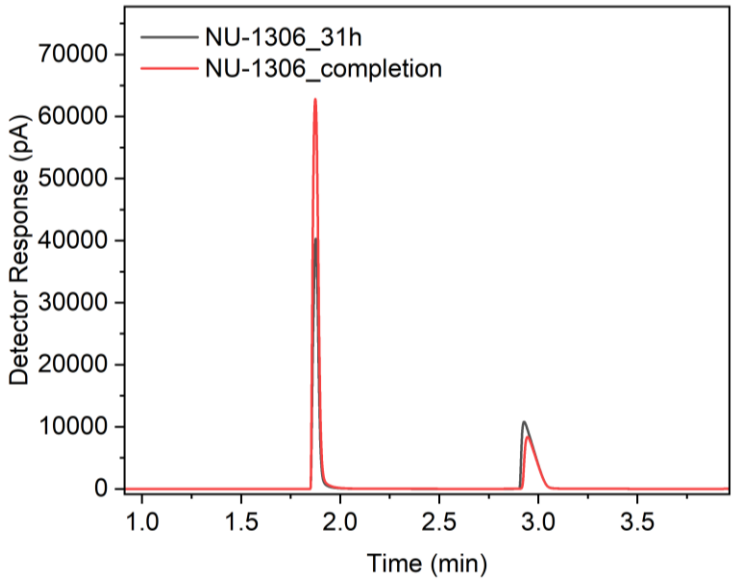

Figure 3.21 GC trace for NU-1306 synthesis. CO is observed at 1.88 minutes retention time and CO_2 at 2.93 minutes retention time.

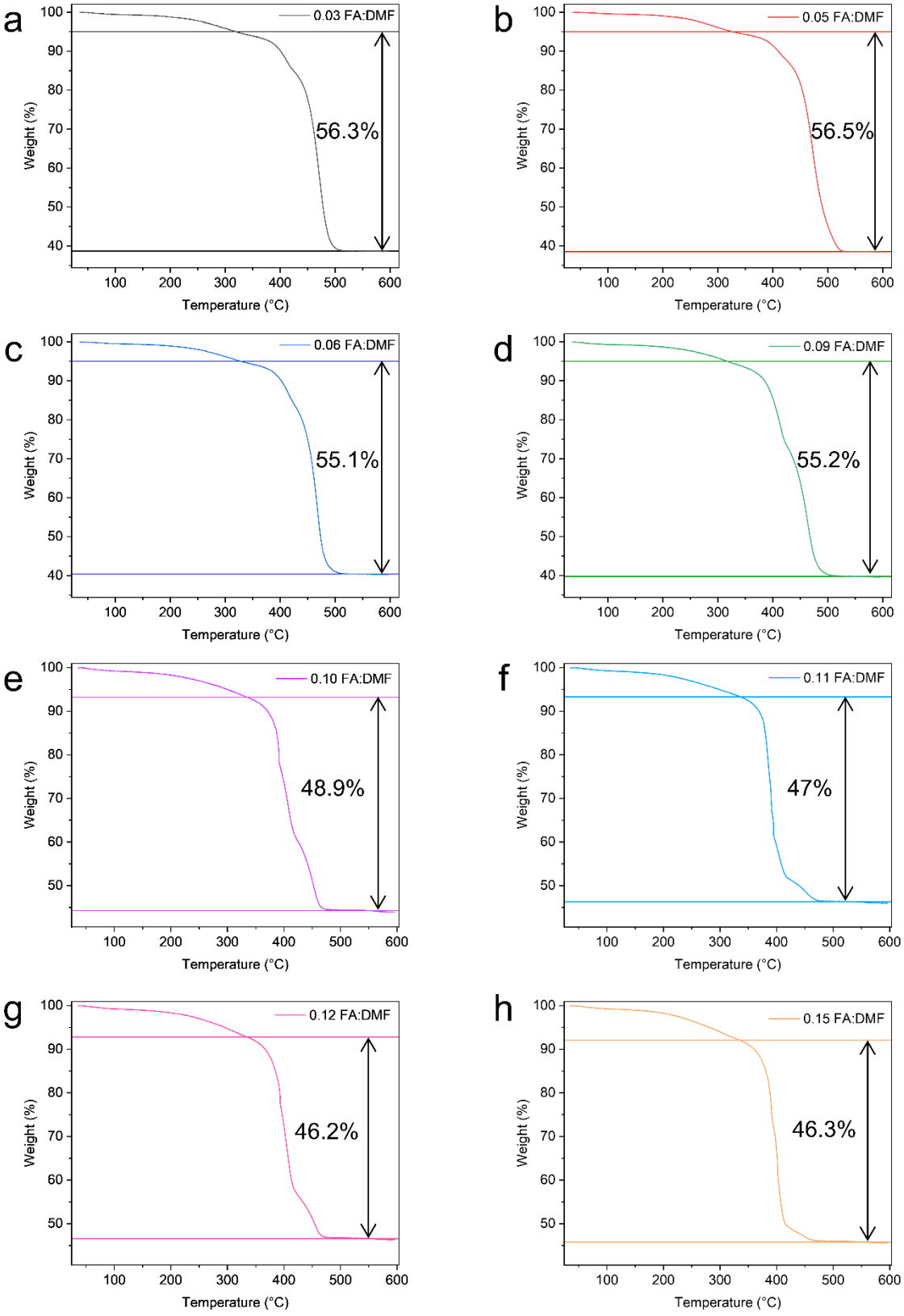
a
0.03 FA:DMF
56.3%
b
0.05 FA:DMF
56.5%
c
0.06 FA:DMF
55.1%
d
0.09 FA:DMF
55.2%
e
0.10 FA:DMF
48.9%
f
0.11 FA:DMF
47%
g
0.12 FA:DMF
46.2%
h
0.15 FA:DMF
46.3%
Weight (%)
Temperature (°C)

Figure 3.22 TGA data of NU-1305 (a-d) and NU-1306 (e-h) synthesized at different FA:DMF ratios.

Table 3.1 Single crystal data and structure refinement details for NU-1306.

	NU-1306
Empirical formula	$C_{87}H_{48}O_{32}U_4$
Formula weight	2557.37
Temperature/K	273.15
Crystal system	cubic
Space group	P-43m
a (Å)	20.90200(10)
b (Å)	20.90200(10)
c (Å)	20.90200(10)
α (°)	90
β (°)	90
γ (°)	90
Volume (Å^3)	9131.95(13)
Z	1
ρ_{calc} (g cm^{-3})	0.465
μ (mm^{-1})	5.098
F(000)	1194.0
Crystal size (mm^3)	0.078 × 0.100 × 0.117
Radiation	CuKα (λ = 1.54178)
2Θ range for data collection (°)	4.228 to 144.008
Index ranges	$-25 \leq h \leq 24$, $-25 \leq k \leq 19$, $-14 \leq l \leq 25$
Reflections collected	33250
Independent reflections	3351 [Rint = 0.0388, Rsigma = 0.0146]
Data/restraints/parameters	3351/2/57
Goodness-of-fit on F2	1.114
Final R indexes [I>=2σ (I)]	R1 = 0.0668, wR2 = 0.1786
Final R indexes [all data]	R1 = 0.0695, wR2 = 0.1825
Largest diff. peak/hole (e Å^{-3})	1.53/-1.73
Flack parameter	0.027(12)

Table 3.2 Linker dihedral angles, measured in degrees. Refer to Figure 3.18 for atom labels.

Angle	NU-1305	NU-1306
C1a-C6-C1b	112.6	118.8
C1a-C6-C1c	112.6	118.8
C1a-C6-C1d	103.3	92.2
C1b-C6-C1c	112.6	92.2
C1c-C6-C1d	112.6	118.8
C1d-C6-C1b	103.3	118.8
Mean	109.5	110.0
St. Dev.	4.4	12.5

Table 3.3 Node bond lengths from experimental and geometry-optimized structures.

MOF	Experimental		Calculated	
	$U\text{-}O_{axial}$ (Å)	$U\text{-}O_{equ}$ (Å)	$U\text{-}O_{axial}$ (Å)	$U\text{-}O_{equ}$ (Å)
NU-1305	1.78	2.42 (50%)* 2.41 (50%)*	1.80	2.47
NU-1306	1.80	2.45	1.80	2.47

*Equatorial bond lengths in the experimental structure of NU-1305 are 2.42 Å 50% of the time and 2.42 Å 50% of the time.

Table 3.4 Percent missing linker for NU-1305 and NU-1306 synthesized at different FA:DMF ratios.

FA:DMF	Missing Linker (%)
0.03	0
0.05	0
0.06	1.2
0.09	1.1
0.10	7.4
0.11	9.3
0.12	10.1
0.15	10

CHAPTER 4. Kinetics and Mechanism of a Metal–Organic Framework Interpenetration Phase Transformation

A vignette on energy-property relationships.

4.1 Chapter Summary

Crystalline materials undergo valuable phase transformations, and the energetic processes that underly these transformations can in part be characterized through in-depth kinetic studies. Here, we report the first kinetic characterization of metal–organic framework interpenetration, specifically in the phase transformation of NU-1200 to its doubly interpenetrated counterpart, STA-26. Using time-resolved *in-situ* X-ray diffraction, we monitored phase transformation reaction profiles and extracted quantitative kinetic information using the Avrami-Erofe'ev model. As a result, we obtained activation energies for the Zr- and Hf-NU-1200 transformation to Zr- and Hf-STA-26, respectively, revealing slower phase change kinetics for MOFs with stronger bonds. Finally, we paired kinetic data with experimental observations to classify the mechanistic model of this phase transformation as partial dissolution. We anticipate that this kinetic and mechanistic understanding will broadly inform further studies on the energetics of crystallization.

4.2 Phase Transformatio

In all fields of chemistry, the energetic principles of thermodynamics and kinetics characterize transformations from one state, phase, or isomer to another.[196, 197] Thermodynamics concerns itself with the relative stabilities of the starting and ending states on a potential energy surface. The free energy difference between these states (ΔG) describes whether the phase transformation is endergonic (uphill) or exergonic (downhill). While equilibrium and its surrounding effects lie at the heart of thermodynamics, kinetics addresses the pathway to reach equilibrium. How much energy does the system require to break bonds of the first phase and form bonds of the second? The activation energy (E_a), which identifies the barrier to reaching the transition state and eventual equilibrium (Scheme 4.1b), answers these kinetic questions.[198] Although thermodynamics and kinetics stand distinctly apart, their implications intimately couple.[177, 196, 199] Pairing the two complimentary concepts unearths the complete picture of the phase transformation occurring and

can lead to deeper mechanistic revelations of how chemical interactions within the system lead to the observed product.

Energetically characterizing phase transformations thus carries profound implications for rational design of chemical structures and control of physicochemical properties in systems ranging from molecules[200, 201] to materials.[202, 203] For example, ligand rearrangements in sodium nitroprusside provide insight into its medicinal usage for hypertension (Scheme 4.1a and c);[204, 205] phase transformations in crystalline solids like perovskites and layered metal oxides affect their performance in optical applications, thermoelectricity, and superconductivity (Scheme 4.1d and e).[199, 206-208]

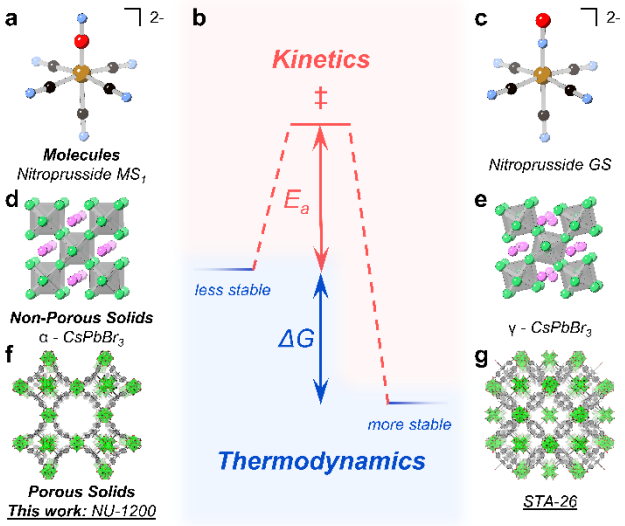

Scheme 4.1 Kinetics and thermodynamics of phase transformations. (b) Exergonic phase transformation from a less stable to a more stable state. (a) Metastable MS_1 isomer of sodium nitroprusside with oxygen-bound ambidentate N-O ligand. (c) Ground state GS isomer of sodium nitroprusside with nitrogen-bound ambidentate N-O ligand. (d) Less stable cubic α phase of perovskite $CsPbBr_3$. (e) More stable orthorhombic γ phase of perovskite $CsPbBr_3$. (f) Less stable MOF NU-1200 and (g) its more stable interpenetrated phase, STA-26.

While less explored than their molecular or classical solid-state counterparts, porous crystalline solids such as metal–organic frameworks (MOFs)[24, 25] also benefit from thermodynamic and kinetic characterization of their phase transformations.[209-211] Comprised of self-assembled metal

nodes and organic linkers, MOFs reticulate into three-dimensional, porous networks. These frameworks, while stable and crystalline, often behave dynamically,[212-214] resulting in phase changes and associated variations in performance. For example, the structural response of MOFs to mechanical stress affects their post-synthetic processing for commercialization,[215, 216] flexibility upon adsorption of carbon dioxide and methane influences gas adsorption and storage,[217-219] and MOF transformations into denser interpenetrated phases impact catalytic activity and gas storage and separations.[220-222]

MOF phase transformations are often thermodynamically characterized:[180, 223, 224] researchers study the relative stabilities of starting and ending phases, develop synthetic methods to traverse the potential energy surface between the two, and quantify their differing performances. However, many questions remain regarding the kinetic processes[225-231] behind these transformations.

In this study, we thoroughly characterize the kinetics of a MOF interpenetration phase change for the first time (Scheme 4.1f and g). Due to its chemical stability,[232] isostructural metal analogs,[233] and tunable interpenetration conditions,[234] we selected the transformation of NU-1200 to its doubly interpenetrated counterpart, STA-26, as our model system.[235, 236] Using *in-situ* time-resolved X-ray diffraction, we monitor phase transformation reaction profiles to extract quantitative kinetic information on interpenetration. Additionally, we confirm that this method of kinetic analysis is sensitive enough to experimentally reveal energetic differences between MOFs with similar metal-oxygen bond dissociation energies ($\Delta Hf_{Zr\text{-}O}$ = 760 kJ mol^{-1}, $\Delta Hf_{Hf\text{-}O}$ = 791 kJ mol^{-1}). Finally, we link kinetic parameters with experimental observations to propose a mechanistic model for this transformation. This report fundamentally investigates the energetics of MOF phase transformations, and provides a deeper understanding of interpenetration, influential in applications including gas adsorption, gas separation, and catalysis.[222] More generally, this study

contributes to the rational design of synthetically plausible nanostructures with desirable and controlled chemical properties.

4.3 NU-1200 to STA-26 Phase Transformation

NU-1200 was first reported in 2016 as a structure consisting of 8-connected $Zr_6(\mu_3\text{-}OH)_4(\mu_3\text{-}O)_4(OH)_4(OH_2)_4$ nodes and 3-connected 4,4′,4″-(2,4,6-trimethylbenzene-1,3,5-triyl)tribenzoic acid (**TMTB**) linkers (Schemes 4.2a and 4.3, Figs. 4.4-4.5).[232, 235] In 2018, reports of its doubly-interpenetrated counterpart, STA-26, surfaced,[236] and in 2021, we demonstrated that the Zr-NU-1200 phase can post synthetically transform to the Zr-STA-26 phase upon the introduction of heat, formic acid, and N,N'-dimethylformamide (DMF) (Scheme 4.2b).[234] Since new linker and node sources are not introduced to the system during the phase transformation, structural components of NU-1200 must contribute to the formation of STA-26 through breaking and forming of chemical bonds. Interpenetration converts the mesoporous Zr-NU-1200 structure with 14 Å sodalite cages and 20 Å channels to the microporous Zr-STA-26 framework comprised of two identical lattices. In STA-26, sodalite cages of the second lattice reside in the channels of the first lattice, introducing $Im\bar{3}m$ centering to the originally $Pm\bar{3}m$ Zr-NU-1200 crystal symmetry. Apart from these structural distinctions, the ***the*** topology persists across both phases, and the cubic unit cell parameters remain very similar (a=b=c=28.33 *Å* in Zr-NU-1200, and a=b=c=28.16 *Å* in Zr-STA-26).

Before analyzing the kinetics of this phase transformation, we characterized the generalizability of NU-1200 analog interpenetration across transition metals and actinides, since Zr-NU-1200 can also crystallize in the analogous Hf- and Th-based structures.[233, 237] As anticipated, pristine Zr-NU-1200 (Figs. 4.8 and 4.20) converts to Zr-STA-26 (Fig. 4.23a) when exposed to interpenetration conditions, and nitrogen physisorption experiments demonstrate how its two large pores disappear over time and microporous STA-26 appears (Fig. 4.1a-c, Table 4.3). We attribute the slight

increase in uptake, surface area, and pore volume at 255 minutes to an increase in Zr-STA-26 crystallinity upon its full formation (see section 4.7.5.5).

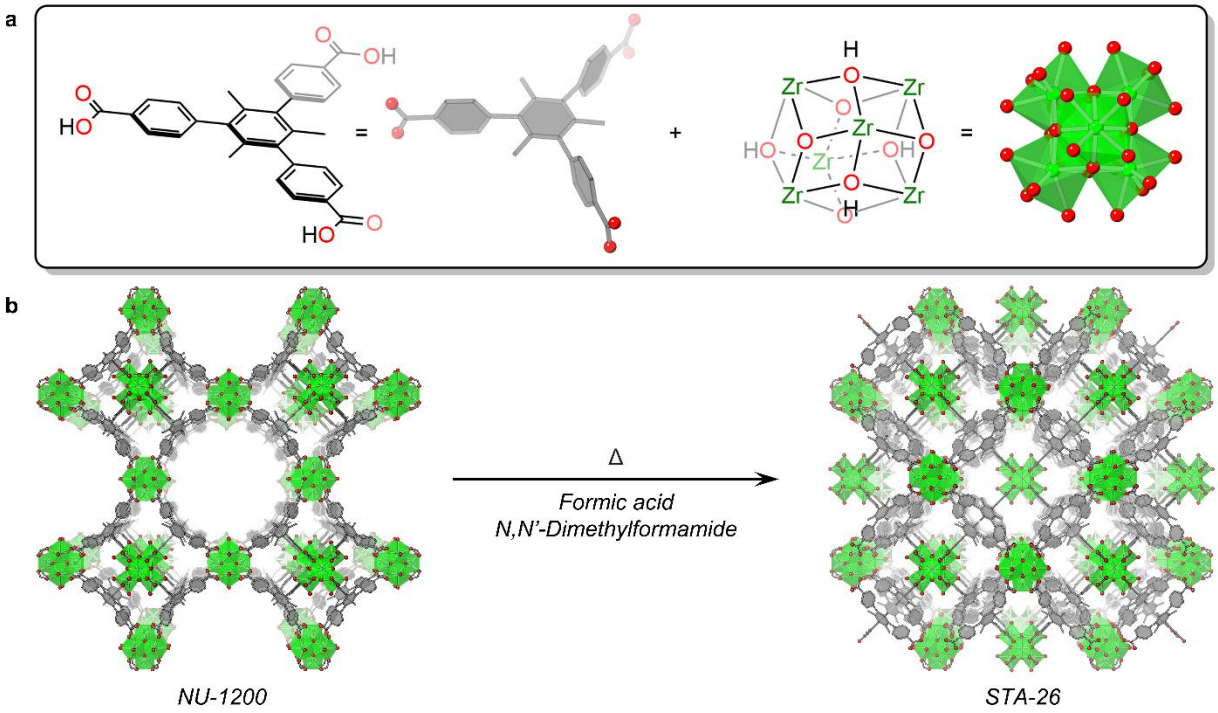

Scheme 4.2 NU-1200 to STA-26 phase transformation. (a) Structures of 4,4′,4″-(2,4,6-trimethylbenzene-1,3,5-triyl)tribenzoic acid (**TMTB**) linker, $Zr_6(\mu_3\text{-}OH)_4(\mu_3\text{-}O)_4(OH)_4(OH_2)_4$ node, and their equivalent visual representations in (b). (b) Transformation of NU-1200 to STA-26.

Pristine Hf-NU-1200 (Figs. 4.8 and 4.20) also experiences conversion to Hf-STA-26 under analogous interpenetration conditions (Fig. 4.23b). Nitrogen isotherms reveal a general trend of decreasing uptake, BET area, pore volume, and pore width over time (Fig. 4.1d-f, Table 4.3). Similar to Zr-STA-26, this trend reverses from 180-360 minutes due to an increase in Hf-STA-26 crystallinity upon its full formation (Fig. 4.25, see section 4.7.5.6). Additionally, we attribute the slight increase in uptake, BET area, and pore volume after 40 minutes to defects introduced to the NU-1200 structure by the interpenetration conditions (Fig. 4.24, see section 4.7.5.6).

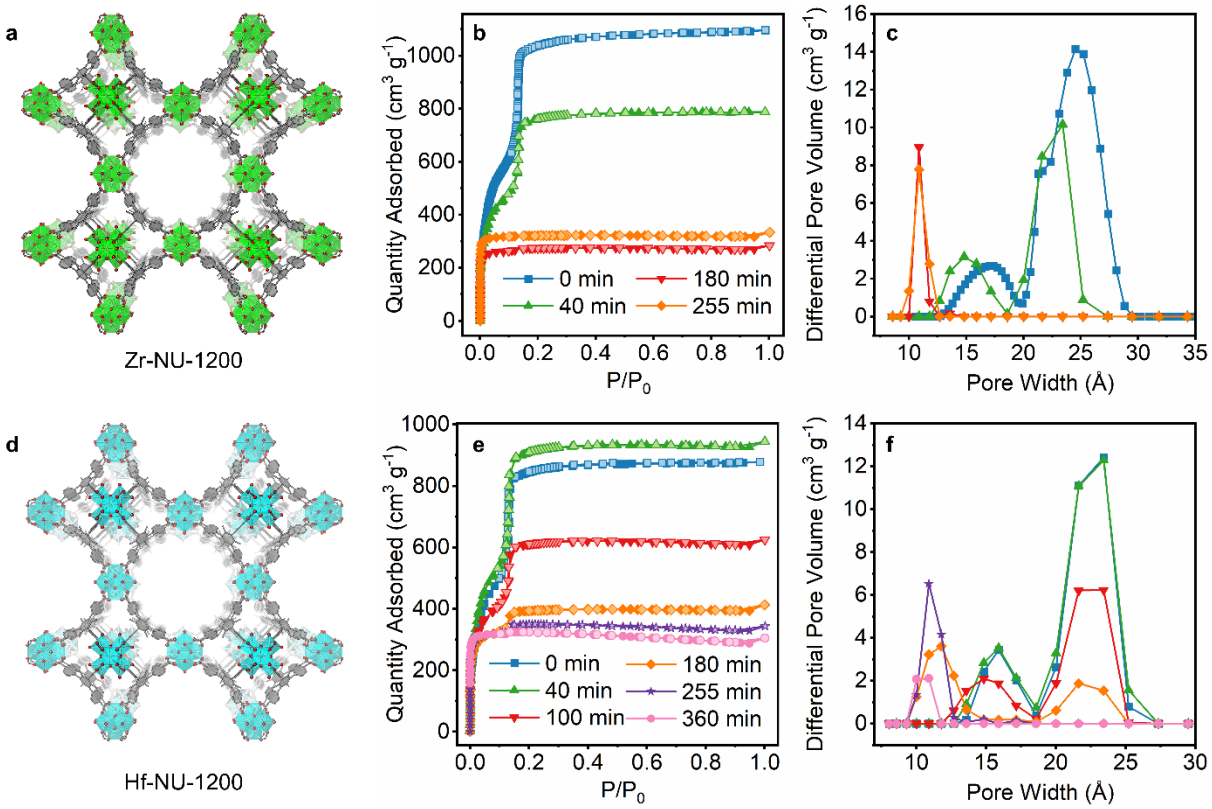

Figure 4.1 Interpenetration of Zr- and Hf-NU-1200. (a) Zr-NU-1200 and (d) Hf-NU-1200 MOF structures. (b) Nitrogen isotherms and (c) pore size distributions monitoring the interpenetration of Zr-NU-1200 to Zr-STA-26. (e) Nitrogen isotherms and (f) pore size distributions monitoring the interpenetration of Hf-NU-1200 to Hf-STA-26.

Unlike its Zr- and Hf- counterparts, Th-NU-1200 refused to interpenetrate under our attempted conditions (Figs. 4.8, 4.15, 4.18, 4.20-4.21, Tables 4.2-4.3). Indeed, treatment of pristine Th-NU-1200 particles under a variety of temperatures, MOF concentrations, acid concentrations, and reaction time scales resulted in etching damage and no observed growth of a second lattice (Fig. 4.22). We hypothesize that this behavior is related to the coordination differences between the Th_6 cluster node and Zr_6 and Hf_6 nodes. While Zr(IV) and Hf(IV) are 8-coordinated metals, Th(IV)'s enlarged coordination sphere allows it to be 9-coordinate. Thus, Th(IV) ions coordinate to six additional water molecules per each Th_6 cluster.[238-240] Considering the likely formation of additional hydrogen bonding interactions at the Th_6 nodes, interpenetration in Th-NU-1200 may be disfavored due to steric hindrance from larger hydrogen-bonded network at node sites.

In an effort to compare actinides NU-1200 interpenetration to that of transition metals, we developed a synthesis for the U-NU-1200 analog (Fig. 4.8, 4.27). Here, we observed U_6 cluster nodes comprised of U(IV). Unfortunately, due to the favorable and rapid oxidation of U(IV) to U(VI), the poor stability of this material proved impractical for studying its interpenetration. However, possible interpenetration of U-NU-1200 can be modeled through studies of Zr-NU-1200 and Hf-NU-1200 since their structures are analogous in charge and coordination.

4.4 Kinetics of NU-1200 to STA-26 Phase Transformation

We next investigated the kinetics of the NU-1200 to STA-26 non-equilibrium transformation. How much energy is required to surmount the activation barrier to reach the high-energy transition state? Does the activation energy required to break and form bonds differ between the Zr and Hf systems which possess similar metal-oxygen bond energies? To answer these questions, we implemented *in-situ* time-resolved X-ray diffraction to monitor reaction profiles as a function of time. By collecting quantitative kinetic information from single Bragg features with changing intensities, rate constants and activation energies of the phase transformation can be extracted.[228, 241, 242]

Due to the inversion symmetry introduced by centering of the new lattice in STA-26, diffraction peak locations remain constant throughout the phase transformation while peak intensities change (Fig. 4.23). Intensity changes can be most clearly observed in the first four primary reflections where the ⟨100⟩ and ⟨111⟩ Bragg features (corresponding to the peaks at 3.00 °2θ and 5.31 °2θ, respectively, in the Zr system and peaks at 3.12 °2θ and 5.43 °2θ, respectively, in the Hf system) decay in intensity while the ⟨110⟩ and ⟨200⟩ Bragg features (corresponding to the peaks at 4.32 °2θ and 6.14 °2θ, respectively, in the Zr system and peaks at 4.44 ° 2θ and 6.27 °2θ, respectively, in the Hf system) grow in intensity. Thus, disappearance of the NU-1200 phase can be monitored by the decay of the ⟨100⟩ and ⟨111⟩ reflection intensities, and emergence of the STA-26 phase can

be monitored by the increase of the ⟨110⟩ and ⟨200⟩ reflection intensities. While the two Bragg features corresponding to a single phase should in principle provide the same kinetic information, we monitored both reflections per phase to ensure internal consistency.

We exposed 2 μm MOF particles to a DMF:FA ratio of 2.5 (Figs. 4.7-4.10, Table 4.1) and tracked the changing reaction profiles of both phases for the Zr and Hf systems at temperatures ranging from 80 °C to 140 °C (Fig. 4.28). Baseline-corrected representative data for the conversion of Zr-NU-1200 to Zr-STA-26 at 90 °C can be found in Figure 4.2b, and its most intense Bragg reflections at ⟨111⟩ and ⟨200⟩ showing NU-1200 decay (Fig. 4.2a) and STA-26 growth (Fig. 4.2c), respectively, are highlighted (Figs. 4.29-4.107, Table 4.5).

To quantify the changes in reaction profiles, we calculated the integrated intensities of the primary Bragg features as a function of time (Fig. 4.107). Next, we plotted the normalized peak intensities (α) against the reduced time ($t-t_0$), defined as the reaction time (t) minus the induction time (t_0), to form crystallization curves (Figs 4.2d, 4.29-4.106). Crystallization curves were then parameterized using the Avrami-Erove'ev equation,[243-245] a widely applied expression to model the kinetics of crystallization in various materials (Eq. 2).[229, 246-253]

$$\alpha = 1 - \exp\{-(k(t-t_0))^n\} \qquad \text{Eq. 2}$$

By modeling the extent of crystallization (α) as a function of the reduced time ($t-t_0$), the rate constant (k) and mechanistic crystallization information (n) can be extracted from the sigmoidal curves.[228, 241] Using a least-squares fit to the Avrami-Erove'ev model we extracted rate constants for NU-1200 disappearance and STA-26 growth in both the Zr and Hf systems (Figs. 4.29-4.104, Table 4.6). Additionally, we verified the Avrami-Erove'ev sigmoidal fits using its linear equivalent, the Sharp-Hancock equation (Eq. 3), where n is derived from the slope of the fit line and $nln(k)$ from the y-intercept (Figs. 4.29-4.104, Table 4.6).[228, 241]

$$\ln[-\ln(1-\alpha)] = n\ln(t-t_0) + n\ln(k) \qquad \text{Eq. 3}$$

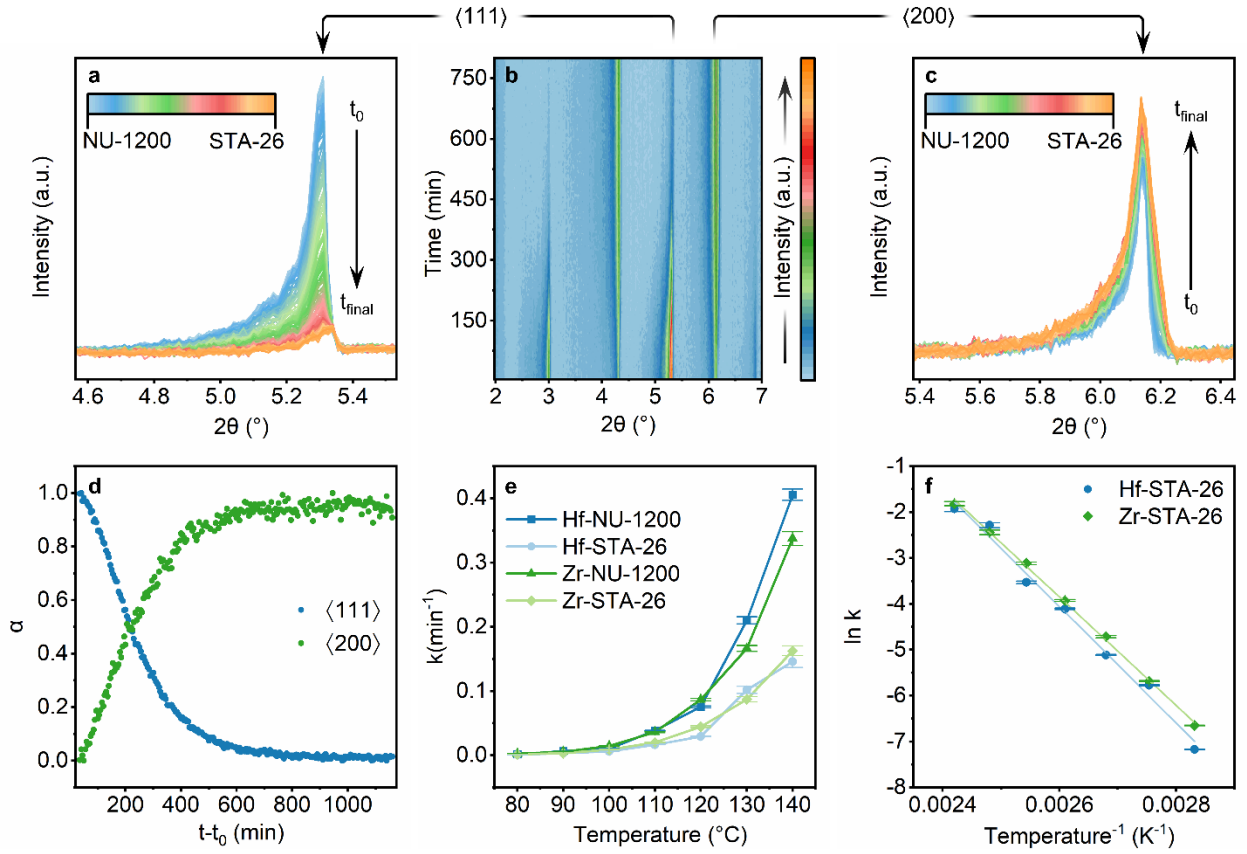

Figure 4.2 Kinetic analysis of time-resolved diffraction data. (b) 3-dimensional contour plot of first four Bragg features in the transformation of Zr-NU-1200 to Zr-STA-26 at 90 °C. (a) Stacked PXRDs enlarged to show the intensity change in the ⟨111⟩ and (c) ⟨200⟩ Bragg features in the transformation of Zr-NU-1200 to Zr-STA-26 at 90 °C over time. (d) Crystallization curve of Zr-NU-1200 converting to Zr-STA-26 at 90 °C. (e) Extracted Avrami-Erofe'ev rate constants as a function of temperature. (f) Arrhenius plots for Zr- and Hf-STA-26 formation.

Both sigmoidal and linear fittings produced comparable results (Table 4.9), but we employ the Avrami-Erove'ev fitting values for further analysis due to their lower error. Since kinetic information for NU-1200 decay extracted from the ⟨100⟩ and ⟨111⟩ Bragg feature crystallization curves also proved similar, further studies were carried out using the ⟨111⟩ Bragg feature crystallization curve because of the higher signal-to-noise ratio and cleaner data. Likewise, the ⟨200⟩ reflection was selected over the ⟨110⟩ for STA-26 growth.

The extracted kinetic information provides correlations between NU-1200 disappearance and STA-26 emergence for both Zr and Hf systems. As temperature levels elevate, the reaction kinetic energy rises, and the rates of transformation of both phases subsequently increase (Fig. 4.2e and 4.108). Although their transformations proceed on concurrent timescales (Fig. 4.2d), STA-26 growth rates consistently lag behind NU-1200 decay rates by an average factor of one-half (Fig. 4.2e, Table 4.6). This implies that STA-26 growth depends on NU-1200 decay. Indeed, since interpenetration occurs in the absence of new linker and node sources (Scheme 4.2b), structural components from the first phase must contribute to the second. Related further discussion can be found in the following section.

With quantitative kinetic information in hand, we calculated activation energies using the Arrhenius equation (Fig. 4.2f). Consistent with their metal-oxygen bond energies ($\Delta Hf_{Zr\text{-}O}$ = 760 kJ mol^{-1}, $\Delta Hf_{Hf\text{-}O}$ = 791 kJ mol^{-1}), Zr- and Hf-STA-26 formation call for 25.2 and 27.9 kcal mol^{-1}, respectively (Table 4.10). The stronger Hf-O bonds require larger amounts of energy to break and reform than their slightly weaker Zr-O counterparts, resulting in slower kinetics of transformation. Thus, although the Hf and Zr MOFs possess similar metal-oxygen bond energies, this kinetic analysis is sensitive enough to experimentally reveal energetic differences between the two systems.

4.5 Mechanistic Model of NU-1200 to STA-26 Phase Transformation

Determining the reaction energy profile can also produce a mechanistic understanding of how chemical interactions within the NU-1200/STA-26 system lead to the observed interpenetrated product. We set out to first characterize the conditions that affect phase transformation and then generate a mechanistic model for conversion.

Regardless of the model of transformation, conversion of the initial NU-1200 particles likely occurs first from the peripheries and then extends to the core. If this is true, particle size should influence the rate of transformation, with larger particles transforming slower than smaller particles. We tested the effects of particle size on conversion rate by comparing the phase transformations of 600 nm, 2 μm, and 4 μm Zr- and Hf-NU-1200 particles using time-resolved *in-situ* PXRD (Figs. 4.6-4.14, 4.16-4.17, 4.169, Tables 4.1-4.3). Extracted Avrami-Erofe'ev rate constants show a decrease in conversion rate at larger particle sizes and support the concept of phase transformation from particle exterior to core (Figs. 4.109 and 4.111, Tables 4.5-4.6).

In order for the transformation to ensue, heat and formic acid must be present. Kinetic differences at increasing temperatures reveal that heat is a source of activation for conversion. If formic acid is also a source of conversion activation, it thus follows that higher concentrations of formic acid should increase the conversion rate. Time-resolved *in-situ* PXRD experiments and extracted Avrami-Erofe'ev rate constants demonstrated that this hypothesized trend held true; we observed a decrease in conversion rate at lower concentrations of formic acid and an increase at higher concentrations (Figs. 4.110-4.111, Tables 4.5-4.6).

To gather deeper insight into the mechanistic model of phase transformation, we investigated the sequential method of conversion. Because interpenetration transpires in the absence of new linker and node sources, it follows that linker and node components from the first NU-1200 phase comprise the structure of the second STA-26 phase. Indeed, as discussed above, correlating conversion rates implies that STA-26 growth depends on NU-1200 decay (Fig. 4.2e). Thus, the phase transformation can occur following one of two simplified models: 1) Complete dissolution of NU-1200 into its linker and node building blocks followed by nucleation and growth of new STA-26 particles. 2) Partial dissolution where portions of the NU-1200 particles dissolve and

produce free linker and node monomers. These monomers then assemble into a second interpenetrated lattice, transforming the NU-1200 particles to STA-26, and nucleation of new particles does not occur (Fig. 4.3a). Since the dissolution and growth stages in model 1 could overlap temporally, correlating NU-1200 decay and STA-26 growth rates from time-resolved *in-situ* PXRD does not provide enough information to distinguish the two models. Instead, we differentiate the conversion models using experimental observations combined with kinetic information.

One major distinction between the two models is the factor of new particle nucleation. If complete dissolution occurs (model 1), the original NU-1200 particles disappear and new particles nucleate; if partial dissolution occurs (model 2), the original NU-1200 particle framework remains largely intact. To differentiate the two conversion models, we grew large Zr-NU-1200 single crystals (Fig. 4.3c) and exposed them to interpenetration conditions. If phase transformation follows model 1, we expect the 20 NU-1200 crystals to transform into STA-26 powder or – in a less likely event – STA-26 single crystals of different morphology or size. Conversely, if phase transformation follows model 2, we expect the NU-1200 crystals to transform into STA-26 crystals of the same morphology and size. After the conversion completed, we observed retained crystal size and morphology, supporting the partial dissolution model (Fig. 4.3d). Bulk PXRD measurements of the same crystal batch before and after exposure to interpenetration conditions confirm that the single crystal phase transformation did in fact occur (Fig. 4.3b).

Complimentary SEM images tracking particle size and morphology during conversion also back the partial dissolution model (Fig. 4.27). While the Zr-NU-1200 particles initiate their interpenetration journey as pristine, cubic crystals (Fig. S23a), they first become damaged by etching (Fig. 4.26b-c) but maintain their cubic morphology until conversion completion (4.26d-e).

This data strengthens the case for partial dissolution since the particle size distribution is maintained, and pristine new nucleated particles are not observed.

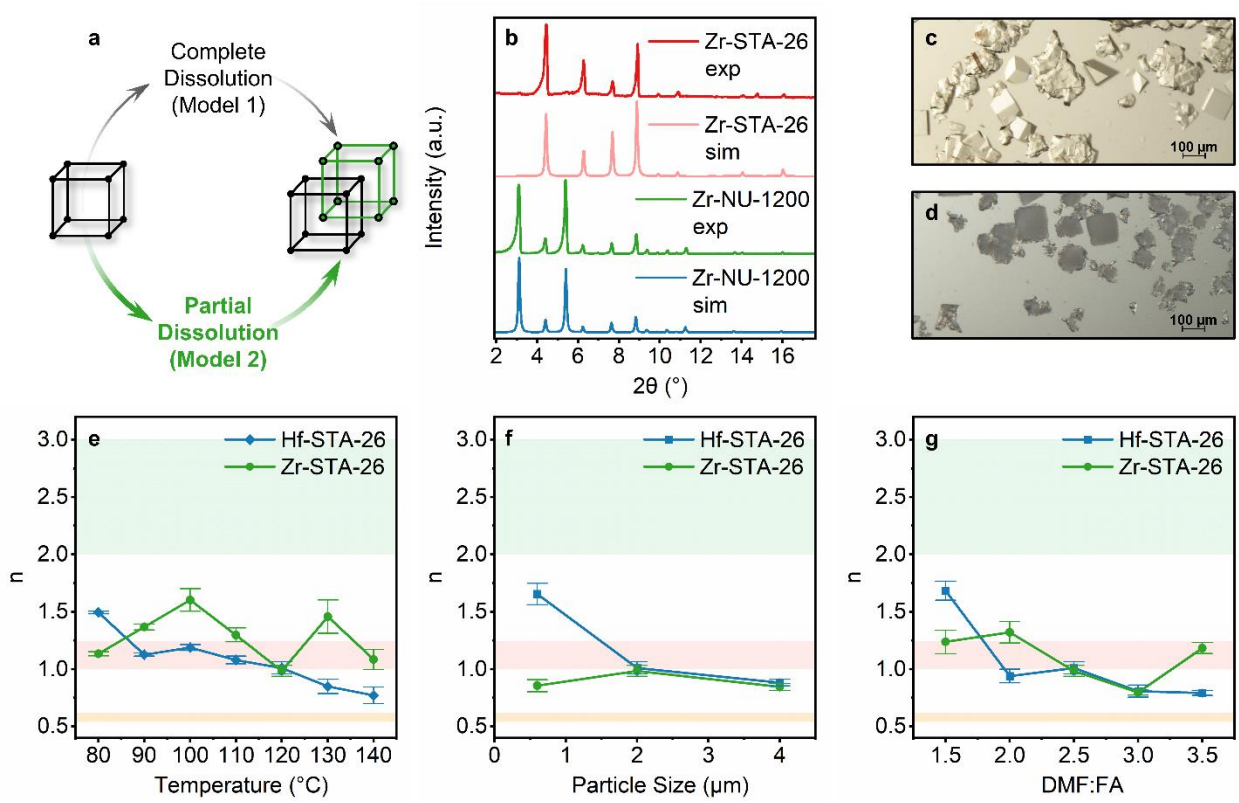

Figure 4.3 Mechanistic model of phase transformation. (a) Two possible models for phase transformation. (b) PXRD of (c) Zr-NU-1200 crystals converting to (d) Zr-STA-26 crystals. (e) Avrami exponent values at different temperatures, (f) particle sizes, and (g) formic acid concentrations. For (e)-(g), orange panels (bottom) indicate the zero-order region, salmon panels (middle) denote the first-order region, and green panels (top) mark higher-order regions.

Finally, we returned to the Avrami-Erofe'ev kinetic model (Eq. 2) to gather information on the sequential method of NU-1200 to STA-26 conversion. As mentioned above, the Avrami exponent, *n*, provides information on the mechanistic nature of crystallization. Values between 0.54-0.62 suggest a zero-order, diffusion-controlled mechanism; a first-order, phase-boundary-controlled mechanism is indicated by values of 1.00–1.24; values between 2.00–3.00 designate a mechanism controlled by nucleation and growth.[228, 241] Thus, in our system of interest, zero-order *n* values support model 1 while first-order *n* values strengthen model 2. We extracted Avrami exponents

from sigmoidal crystallization curves of STA-26 growth at different temperatures (Fig. 4.3e), particle sizes (Fig. 4.3f), and formic acid concentrations (Fig. 4.3g). In all cases, *n* values follow a first-order mechanism and remain similar for both Zr and Hf systems. This data not only suggests that phase-boundary growth dominates but also indicates that the transformation mechanism is not affected by metal identity, temperature, particle size, or acid conditions (Figs. 4.112-4.114, Table 4.6). Taken together, these findings support our proposed model 2 of partial dissolution.

3.6 Conclusions

In conclusion, we report the first kinetic analysis of MOF interpenetration, specifically in the phase transformation of NU-1200 to its doubly interpenetrated counterpart, STA-26. We implement Avrami-Erofe'ev modeling of time-resolved *in-situ* X-ray diffraction to quantify rate constants and activation energies for Zr- and Hf-NU-1200 transformation to Zr- and Hf-STA-26, respectively. Observed differences in the activation energies of this transformation of Zr and Hf systems (25.2 and 27.9 kcal mol^{-1}, respectively) consistent with their metal-oxygen bond energies ($\Delta Hf_{Zr\text{-}O}$ = 760 kJ mol^{-1}, $\Delta Hf_{Hf\text{-}O}$ = 791 kJ mol^{-1}), reveal slower phase change kinetics for MOFs with stronger bonds. Additionally, this kinetic analysis is sensitive enough to experimentally reveal energetic differences between the two systems with similar metal-oxygen bond dissociation energies. Finally, we paired kinetic data with experimental observations to classify the mechanistic model of this phase transformation as partial dissolution. This study provides insight into MOF interpenetration, and the methodology used in this study can easily be applied to other crystalline systems with parallel energetic similarities. More generally, we anticipate that this kinetic and mechanistic understanding will broadly inform further studies on the energetics of crystallization.

4.7 Additional Information

4.7.1. Materials

Caution! Thorium and uranium salts are radioactive chemicals and contain ^{232}Th and ^{238}U, respectively. Necessary precautions must be adhered to when handling these salts.

All chemicals were purchased from the supplier and used without further purification, including 1,3,5-tribromo-2,4,6-trimethylbenzene (TCI America), methyl 4-(4,4,5,5-tetramethyl-1,3,2-dioxaborolan-2-yl)benzoate (Sigma Aldrich), K_3PO_4 (Millipore Sigma), dioxane (Fisher Scientific), $Pd(PPh_3)_4$ (Millipore Sigma), dichloromethane (Fisher Scientific), $MgSO_4$ (Fisher Scientific), celite (Millipore Sigma), hexanes (Fisher Scientific), ethyl acetate (Fisher Scientific), SiO_2 (Millipore Sigma), methanol (Fisher Scientific), tetrahydrofuran (Fisher Scientific), sodium hydroxide (Sigma-Aldrich), hydrochloric acid (Fisher Scientific), dimethyl sulfoxide-d_6 (Millipore Sigma), chloroform-*d* (Millipore Sigma), N,N-dimethylformamide (DMF, Fisher Scientific), zirconyl chloride octahydrate (Millipore Sigma), trifluoroacetic acid (TFA, Millipore Sigma), halfnium chloride (Millipore Sigma), sodium deuteroxide (Cambridge Isotope Laboratories, Inc.), uranium tetrachloride (International Bio-Analytical Industries, Inc.), thorium nitrate (International Bio-Analytical Industries, Inc.), deuterium oxide (Cambridge Isotope Laboratories, Inc.), formic acid (FA, Fisher Scientific), 0.7 mm quartz capillaries (Charles Supper).

4.7.2. Instrumentation

4.7.2.1 Powder X-ray Diffraction (PXRD)

PXRD data collected in flat plate transmission holders were obtained using a Stoe STADI P diffractometer, equipped with a CuKα1 source and a 1D strip detector. Samples were prepared for PXRD by removing the DMF solvent, washing with fresh ethanol three times, and dropcasting onto the sample holder. PXRD data collected in Debye-Scherrer mode were obtained using a Stoe

STADI MP diffractometer, equipped with a CuKα1 source and a 1D strip detector. A Stoe high temperature furnace equipped with a 1 mm wide heating element was attached to the Stoe STADI MP for all high temperature measurements.

4.7.2.2 Scanning Electron Microscopy (SEM)

SEM images were collected using either a Hitachi SU8030 or a JEOL 7900FLV microscope. Before imaging, samples were prepared by drop-casting from acetone onto SEM pin stub specimen mounts and coating with 9 nm of OsO_4 in a Denton Desk III TSC Sputter Coater.

4.7.2.3 Thermal Activation

Thermal activation was performed under ultrahigh vacuum at 120 °C for 18 hours using a Micromeritics Smart VacPrep (SVP) instrument.

4.7.2.4 Nitrogen Physisorption

Nitrogen isotherms were collected at 77 K on a Micromeritics ASAP 2420 and analyzed using the BET theory.[254] The Carbon Black STSA thickness curve model was used to determine the external surface areas using t-plots.[255]

4.7.2.5 Nuclear Magnetic Resonance (NMR) Spectroscopy

^{1}H spectra of digested Thorium MOFs were collected on an A600, Bruker Avance III 600 MHz instrument. All other ^{1}H spectra were collected on an Ag500, Bruker Avance III 500 MHz instrument.

4.7.2.6 Imaging

Optical images were acquired with a Nikon SMZ1500 microscope

4.7.3. Syntheses

*4.7.3. 4,4',4''-(2,4,6-trimethylbenzene-1,3,5-triyl)tribenzoic acid (**TMTB**)*

The synthesis of **TMTB** was adapted from a previous report.[233, 256] A Suzuki-Miyaura cross coupling reaction was performed by adding 1,3,5-tribromo-2,4,6-trimethylbenzene (5.3 g, 15 mmol), methyl 4-(4,4,5,5-tetramethyl-1,3,2-dioxaborolan-2-yl)benzoate (21 g, 75 mmol), K_3PO_4 (22.5 g, 106 mmol), dioxane (600 mL), and water (40 mL) to a 1000 mL two-necked round bottomed Schlenk flask. The mixture was bubbled with argon for 30 minutes before adding $Pd(PPh_3)_4$ (750 mg, 0.32 mmol) and bubbling with argon for 30 more minutes. The flask was equipped with a water condenser and refluxed under argon at 98 °C for 6 days. Next, the majority of solvent was removed using a rotary evaporator, and four extractions of water with DCM were performed. The DCM layers were collected, combined, and dried with $MgSO_4$ before being filtered through celite and concentrated using a rotary evaporator. The mixture was purified by column chromatography (SiO_2, 10:1 ratio of hexanes:ethyl acetate) to produce **A** as a white solid (6.4 g, 76%). ^{1}H NMR (500 MHz, $CDCl_3$) δ 8.15 – 8.07 (m, 6H), 7.33 – 7.27 (m, 6H), 3.94 (s, 9H), 1.66 (s, 9H). (Scheme 4.3, Fig. 4.4).

6.4 g of **A** were then added to a 500 mL round bottom flask along with 192 mL methanol, 192 mL tetrahydrofuran, and 112 mL 10M NaOH (aq) and refluxed at 70 °C for 72 h. The solution was then cooled, and the organic solvent was removed using a rotary evaporator. The remaining aqueous solution was then acidified with 2M HCl (aq), and the product, **TMTB**, was observed as a white precipitate. The final product was washed with water until the pH was neutral, dried at room temperature, and dried in a vacuum oven for 24 h (5.5 g, 93%). ^{1}H NMR (500 MHz, DMSO) δ 13.00 (s, 3H), 8.05 – 7.98 (m, 6H), 7.39 – 7.32 (m, 6H), 1.61 (s, 9H). (Scheme 4.3, Fig. 4.5).

4.7.3.2 600 nm Zr-NU-1200

TMTB (10 mg, 0.02 mmol) and DMF (2 mL) were added to a 1.5 dram glass vial. The mixture was sonicated for 5 minutes, and $ZrOCl_2 \cdot 8H_2O$ (17 mg, 0.073 mmol) was added to the solution.

The mixture was then sonicated for 10 minutes, and 90 μL TFA was added to the solution. Finally, the mixture was sonicated 5 additional minutes, and placed in a 120 °C oven for 24 hours. A white powder was observed as the MOF product (Fig. 4.6a).

4.7.3.3 2 μm Zr-NU-1200

This synthesis was adapted from previous reports.[233, 234] **TMTB** (10 mg, 0.02 mmol) and DMF (2 mL) were added to a 1.5 dram glass vial. The mixture was sonicated for 5 minutes, and $ZrOCl_2 \cdot 8H_2O$ (17 mg, 0.073 mmol) was added to the solution. The mixture was then sonicated for 10 minutes, and 180 μL TFA was added to the solution. Finally, the mixture was sonicated 5 additional minutes, and placed in a 120 °C oven for 24 hours. A white powder was observed as the MOF product (Fig. 4.6b).

4.7.3.4 4 μm Zr-NU-1200

TMTB (10 mg, 0.02 mmol) and DMF (2 mL) were added to a 1.5 dram glass vial. The mixture was sonicated for 5 minutes, and $ZrOCl_2 \cdot 8H_2O$ (17 mg, 0.073 mmol) was added to the solution. The mixture was then sonicated for 10 minutes, and 250 μL TFA was added to the solution. Finally, the mixture was sonicated 5 additional minutes, and placed in a 120 °C oven for 66 hours. A white powder was observed as the MOF product (Fig. 4.6c).

4.7.3.5 Single Crystal Zr-NU-1200

The procedure developed by Wang, X. *et al* was followed to synthesize single crystals of Zr-NU-1200.[233]

4.7.3.6 Zr-NU-1200 Preparation

The following preparation procedure was performed for all above syntheses of Zr-NU-1200 except for the single crystal synthesis. Upon cooling, the MOF powder was collected and centrifuged at 7,500 rpm. The supernatant was removed, replaced with fresh DMF, and allowed to rest for one

hour; this process was repeated three times total. The powder was transferred to a new glass vial and 12 mL DMF and 500 μL 4M HCl were added to the vial. The vial was placed in a 100 °C oven for 24 hours. Upon cooling, the MOF powder was collected and centrifuged at 7,500 rpm. The supernatant was removed, replaced with fresh DMF, and allowed to rest for one hour; this process was repeated three times total. The supernatant was removed, replaced with fresh acetone, and allowed to rest for one hour; this process was repeated three times total, where the final wash rested for 18 hours.

4.7.3.7 600 nm Hf-NU-1200

TMTB (10 mg, 0.02 mmol) and DMF (2 mL) were added to a 1.5 dram glass vial. The mixture was sonicated for 5 minutes, and $HfCl_4$ (17 mg, 0.05 mmol) was added to the solution. The mixture was then sonicated for 10 minutes, and 50 μL TFA was added to the solution. Finally, the mixture was sonicated 5 additional minutes, and placed in a 120 °C oven for 24 hours. An off-white powder was observed as the MOF product (Fig. 4.6d).

4.7.3.8 2 μm Hf-NU-1200

This synthesis was adapted from a previous report.[233] **TMTB** (10 mg, 0.02 mmol) and DMF (2 mL) were added to a 1.5 dram glass vial. The mixture was sonicated for 5 minutes, and $HfCl_4$ (17 mg, 0.05 mmol) was added to the solution. The mixture was then sonicated for 10 minutes, and 90 μL TFA was added to the solution. Finally, the mixture was sonicated 5 additional minutes, and placed in a 120 °C oven for 38 hours. An off-white powder was observed as the MOF product (Fig. 4.6e).

4.7.3.9 4 μm Hf-NU-1200

TMTB (10 mg, 0.02 mmol) and DMF (2 mL) were added to a 1.5 dram glass vial. The mixture was sonicated for 5 minutes, and $HfCl_4$ (17 mg, 0.05 mmol) was added to the solution. The mixture

was then sonicated for 10 minutes, and 150 μL TFA was added to the solution. Finally, the mixture was sonicated 5 additional minutes, and placed in a 120 °C oven for 72 hours. An off-white powder was observed as the MOF product (Fig. 4.6f).

4.7.3.10 Hf-NU-1200 Preparation

The following preparation procedure was performed for all above syntheses of Hf-NU-1200. Upon cooling, the MOF powder was collected and centrifuged at 7,500 rpm. The supernatant was removed, replaced with fresh DMF, and allowed to rest for one hour; this process was repeated three times total. The powder was transferred to a new glass vial and 12 mL DMF and 500 μL 4M HCl were added to the vial. The vial was placed in a 100 °C oven for 24 hours. Upon cooling, the MOF powder was collected and centrifuged at 7,500 rpm. The supernatant was removed, replaced with fresh DMF, and allowed to rest for one hour; this process was repeated three times total. The supernatant was removed, replaced with fresh acetone, and allowed to rest for one hour; this process was repeated three times total, where the final wash rested for 18 hours.

4.7.3.11 Th-NU-1200

This synthesis was adapted from a previous report.[233] Solution A was made from $Th(NO_3)_4$ (1g) and DMF (20 mL). Solution B was made from **TMTB** (150 mg) and DMF (2 mL). Then, 400 μL of Solution A, 400 μL of solution B, 90 μL H_2O, and 25 μL TFA were added to a 1.5 dram glass vial. The mixture was sonicated for 5 minutes and placed in a 120 °C oven for 24 hours. A white powder was observed as the MOF product (Fig. 4.8). Upon cooling, the MOF powder was collected and centrifuged at 7,500 rpm. The supernatant was removed, replaced with fresh DMF, and allowed to rest for one hour; this process was repeated three times total. The supernatant was removed, replaced with fresh acetone, and allowed to rest for one hour; this process was repeated three times total, where the final wash rested for 18 hours.

4.7.3.12 U-NU-1200

TMTB (10 mg, 0.02 mmol) and DMF (2 mL) were added to a 1.5 dram glass vial. The mixture was sonicated for 5 minutes, and UCl_4 (20 mg) and 50 μL TFA were added to the solution. The mixture was then sonicated for 5 minutes and placed in a 120 °C oven for 24 hours. A dark green powder was observed as the MOF product (Fig. 4.8, 4.27).

4.7.4. NU-1200 Characterization

4.7.4.1 Particle Size Distribution

To obtain the average particle size of each Zr-NU-1200 and Hf-NU-1200 synthesis (Fig. 4.6), we measured the particle size of fifty different particles using SEM (Fig. 4.7) and calculated the standard deviation from the mean (Table 4.1). Because the Zr-NU-1200 570 ± 111 nm and the Hf-NU-1200 644 ± 221 nm particles fall within error of each other, we call these particles "600 nm". Because the Zr-NU-1200 1.94 ± 0.53 μm and the Hf-NU-1200 1.96 ± 0.67 μm particles fall within error of each other, we call these particles "2 μm". Because the Zr-NU-1200 4.45 ± 1.29 μm and the Hf-NU-1200 3.68 ± 1.16 μm particles fall within error of each other, we call these particles "4 μm".

4.7.4.2 Phase Identity and Crystallinity

PXRD demonstrates that Zr-, Hf-, Th-, and U-NU-1200 crystalline phase were first synthesized regardless of the particle size (Fig. 4.8).

4.7.4.3 Capping Formates

To quantify the amount of capping formate present per node, we digested the different particle sizes of Zr-, Hf-, and Th-NU-1200 by sonicating ~1mg of thermally activated MOF powder in 5 drops of 0.1M NaOD, sonicating for 10 minutes, diluting the mixture with 0.6 mL D_2O, sonicating for 10 minutes, and removing any non-digested particles using a syringe filter. NMR

measurements of the resulting solutions revealed 2-3 formates present per node (Fig. 4.9-4.15, Table 4.2)

4.7.4.4 Nitrogen Uptake

Nitrogen isotherms were collected for 600 nm, 2 μm, and 4 μm batches of Zr-NU-1200 and Hf-NU-1200 as well as Th-NU-1200 (Figs. 4.16-4.18, Table 4.3). As the particle size increases, the pore volume and BET area also increase. Due to the higher amounts of modulator needed to produce larger particles, we attribute this trend to the increased crystallinity of the batches with larger particle sizes. Using thickness-plots (t-plots), we also calculated the external surface area of each batch. As anticipated, smaller particles possess a larger percentage of external surface area (Fig. 4.19). Finally, isotherms of different metal MOFs at the same 2 μm particle size are graphed both gravimetrically (Fig. 4.20a) and volumetrically (Fig. 4.20b) to demonstrate how differences in apparent uptake between Zr-NU-1200, Hf-NU-1200, and Th-NU-1200 may be attributed to metal molar mass.

4.7.5. Ex-situ Phase Transformation of NU-1200 to STA-26

4.7.5.1 Zr-NU-1200 to Zr-STA-26 Conversion Procedure

10 mg of thermally activated 2 μm Zr-NU-1200 was placed in a 1.5 dram glass vial in a 2 mL solution of DMF:FA=2.5 (2 mL DMF plus 0.8 mL FA). The mixture was sonicated for ~1 minute. Multiple identical vials were similarly arranged and placed in a 120 °C oven at the same in order to monitor the conversion over time. A vial was removed from the oven at certain time points during the conversion, and the entire conversion was complete by ~240 minutes.

4.7.5.2 Hf-NU-1200 to Hf-STA-26 Conversion Procedure

In order to maintain the same molar ratio of MOF to solvent as the Zr-NU-1200 to Zr-STA-26 conversion, 12.5 mg of thermally activated 4 μm Hf-NU-1200 was placed in a 1.5 dram glass vial

in a 2 mL solution of DMF:FA=2.5 (2 mL DMF plus 0.8 mL FA). The mixture was sonicated for ~1 minute. Multiple identical vials were similarly arranged and placed in a 120 °C oven at the same in order to monitor the conversion over time. A vial was removed from the oven at certain time points during the conversion, and the entire conversion was complete by ~360 minutes.

4.7.5.3 Th-NU-1200 Lack of Conversion

Conversion attempts resulted in a retained Th-NU-1200 PXRD pattern (Fig. 4.21) and damaged morphology (Fig. 4.22).

4.7.5.4 Monitoring Phase Transformation by PXRD

The phase transformation was monitored by observing changes in PXRD peak intensity over time (Fig. 4.23). The most intense Zr-NU-1200 peaks (3.12 °2θ, 5.40 °2θ) and Hf-NU-1200 peaks (3.16 °2θ, 5.46 °2θ) decayed in intensity over time while the most intense Zr-STA-26 peaks (4.41 °2θ, 6.24 °2θ) and Hf-STA-26 peaks (4.46 °2θ, 6.31 °2θ) increased in intensity over time.

4.7.5.5 Nitrogen Physisorption of Zr-NU-1200 to Zr-STA-26

Nitrogen isotherms show a general trend of decreasing BET area and pore volume from 0 min to 40 min to 100 min as interpenetration occurs. However, BET area and pore volume increase at 180 min (Fig. 4.1b, Table 4.4). We attribute this change in surface area trend to the STA-26 phase most likely being not fully formed at 100 minutes. As time progresses and the STA-26 phase fully forms at 180 min, the crystallinity of the material increases, as does the uptake.

4.7.5.6 Nitrogen Physisorption of Hf-NU-1200 to Hf-STA-26

Nitrogen isotherms show a general trend of decreasing BET area and pore volume as interpenetration occurs, with several exceptions (Fig. 4.1e, Table 4.4). First, the BET area and pore volume are observed to increase from 0 to 40 minutes. This may be due to the hot DMF removing extra-framework species that may block full uptake. To rule this possibility out, we set up an

analogous reaction of Hf-NU-1200 in hot DMF with no formic acid present for 40 minutes (12.5 mg of thermally activated 4 μm Hf-NU-1200 in 2 mL DMF at 120 °C). The resulting isotherm from this reaction appeared identical to that of the 0-minute time point (Fig. 4.24), suggesting that hot DMF does not wash out extra-framework species that may block nitrogen uptake. Instead, we propose that the introduction of formic acid over 40 minutes may slightly increase the surface area and pore volume by creating defects in the structure.

Similar to the case of Zr-STA-26, while showing a general trend of decreasing BET area and pore volume as interpenetration occurs, the BET area and pore volume begin to increase as the Hf-STA-26 phase fully forms from 180 min to 360 min (Fig. 4.1e, Table 4.4). We attribute this change in surface area trend to the STA-26 phase being not fully formed at 100 minutes. The increase in STA-26 crystallinity from 180 min to 360 min can be seen at low isotherm pressures in Figure 4.25.

4.7.5.7 Monitoring Phase Transformation by SEM

Zr-NU-1200 was monitored by SEM as it transformed to Zr-STA-26 (Fig. S23). To compliment in the *in-situ* measurements described below, conditions similar to the *in-situ* measurements were applied: 100 μL DMF and 40 μL FA (2.5 ratio of DMF:FA) were added to 2 mg of thermally activated Zr-NU-1200 in a 0.5 dram glass vial. Multiple sets of these vials were placed in a 120 °C oven and removed at 0.25, 0.5, 1, and 1.5 hours. Each aliquot was washed three times with fresh DMF and three times with fresh acetone before being prepared for imaging. SEM images show pristine crystals at 0 hours (Fig. 4.26a), etching damage at 0.25 and 0.5 hours (Fig. 4.26b and c, respectively), and less etching damage at 1 and 1.5 hours (Fig. 4.26d and e, respectively). Significant appearance of fresh smaller particles is not observed, suggesting that this

transformation does not proceed by nucleation of new particles. Etching followed by "healing" of the crystals suggests that partial dissolution is operative.

4.7.6. In-situ Conversion of NU-1200 to STA-26

4.7.6.1 Experimental Setup

In-situ PXRD studies were designed to mimic oven growth conditions as closely as possible. However, the concentration of MOF in solvent was increased by four for all *in-situ* growth studies to maintain a good signal-to-noise ratio of diffraction peaks. We note that an increase in MOF concentration does result in a faster phase transformation. Thus, we avoid kinetic comparisons of *in-situ* studies to oven growth studies.

Samples were first prepared by weighing thermally activated MOF (1 mg of 600 nm, 2 μm, or 4 μm Zr-NU-1200; 1.2 mg of 600 nm, 2 μm, or 4 μm Hf-NU-1200) using a 0.1 μg ultramicrobalance into a 0.5 mL glass dram vial. The MOF was then ultrasonically mixed in 70 μL of solvent where the DMF:FA ratio was either 3.5 (54.5 μL DMF and 15.5 μL FA), 3 (52.5 μL DMF and 17.5 μL FA), 2.5 (50 μL DMF and 20 μL FA), 2 (47 μL DMF and 23 μL FA), or 1.5 (42 μL DMF and 28 μL FA). A list of samples details is provided in Table 4.5 and samples are named A-Z; 2 μm samples with DMF:FA=2.5 run at 120 °C were used as the standard conditions unless certain experimental conditions were varied. Samples could be prepared up to 2 days before measurement without affecting reaction kinetics.

A syringe was used to transfer several μL of each MOF solution to a 0.7 mm diameter quartz capillary, such that the total volume added filled 1.5 cm of capillary length. The capillaries were frozen using liquid nitrogen and sealed with a flame torch under vacuum such that the total capillary length was approximately 3 cm with 50% headspace. The quartz capillaries were then inserted into 6-inch-long 0.92 mm diameter Kapton capillaries and situated close to one of the

Kapton capillary openings. Glass wool was packed on either side of the quartz capillary to secure it within the Kapton capillary.

The capillary setup was then placed into the Stoe STADI MP furnace. Since the in-situ measurement was collected without sample spinning (to mimic undisturbed oven growth conditions), the furnace was offset to allow incoming X-rays to directly hit the MOF sample at the bottom of the capillary. As a result, omega was slightly adjusted as well to ensure a low signal-to-noise ratio. Due to this hardware rearrangement, indicative peak locations slightly shifted for Zr-NU-1200 (3.12 to 3 °2θ, 5.40 to 5.31 °2θ), Hf-NU-1200 (3.16 to 3.12 °2θ, 5.46 to 5.43 °2θ), Zr-STA-26 (4.41 to 4.32 °2θ, 6.24 to 6.14 °2θ), and Hf-STA-26 (4.46 to 4.44 °2θ, 6.31 to 6.27 °2θ) (Fig. 4.28 demonstrates this shift for Zr-NU-1200). We also observed a change in the relative intensity of the two strongest Bragg reflections for each phase (mentioned above) when the MOF sample is solvated in a capillary. For example, this intensity difference for Zr-NU-1200 can be observed in Figure 4.28 where we plot PXRD data of the same batch of Zr-NU-1200 sample measured as a dry powder (transmission flat disk) and a solvated sample (Debye-Scherrer mode). This experiment suggests that relative peak intensity differences between these two diffractograms are not due to MOF phase transformation but to solvation and the mode of measurement. Diffraction data was collected with exposure times ranging from 5 min to 35 sec (Table 4.5).

4.7.6.2 Background Subtraction and Integrated Peak Area Calculation

Diffraction data was analyzed utilizing Python 3.9 with the Spyder 5.5.4 user interface. The background signal was subtracted from the data by using the peakutils baseline function, which fits the baseline to a polynomial (degree=10) (Fig. 4.107). Time-resolved *in-situ* PXRD data for all measurements after background subtraction and intensity changes of the two most intense Bragg reflections for each phase after background subtraction are shown in Figure 4.1 and Figures

4.29-4.107. Next, the area was calculated under discrete peaks of interest with the trapz function. This function uses the trapezoidal rule to approximate the area under the curve by defining discrete trapezoids, calculating and then summing their areas. Ranges of integration were manually selected for each peak of interest. For the full code, please refer to the github repository found at: https://github.com/mbar11/insitupxrdareaunderthecurve.

4.7.6.3 Avrami-Erofe'ev Fitting

Integrated peak areas for Bragg reflections of interest (Zr-NU-1200: ⟨100⟩ = 3 °2θ, ⟨111⟩ = 5.31 °2θ; Hf-NU-1200: ⟨100⟩ = 3.12 °2θ, ⟨111⟩ = 5.43 °2θ; Zr-STA-26: ⟨110⟩ = 4.32 °2θ, ⟨200⟩ = 6.14 °2θ; Hf-STA-26: ⟨110⟩ = 4.44 °2θ, ⟨200⟩ = 6.27 °2θ) were normalized and plotted against reduced time ($t-t_0$). Then, OriginPro was used to perform a least-squares fit to the Avrami-Erofe'ev kinetic model and extract *k* and *n* values (Figs. 4.29-4.106, 4.108-4.114, Table 4.6). We fit the data from two peak for each phase to demonstrate analogous fittings and *k* and *n* values within each dataset. However, only the ⟨111⟩ and ⟨200⟩ reflections were tabulated and analyzed, due to their higher peak intensity, superior signal-to-noise, and subsequent improved kinetic fittings.

4.7.6.4 Sharp-Hancock Fitting

The same workflow was followed as in section 6.3, and OriginPro was used to perform a linear fit to the Sharp-Hancock kinetic model and extract *k* and *n* values (Figs. 4.29-4.106, 4.108-4.110, 4.112-4.114, Table 4.6).

4.7.6.5 Activation Energies

By employing the Arrhenius equation, inverse Temperature (in Kelvin) was plotted against ln *k*, and OriginPro was used to perform a linear fit to the data. The negative slope of the line was multiplied by R (universal gas constant, 8.3144598 J mol^{-1} K^{-1}) to calculate the activation energy in J mol^{-1} which was then converted to units of kcal mol^{-1} (Table 4.7).

4.7.7. Supplementary Schemes, Figures, and Tables

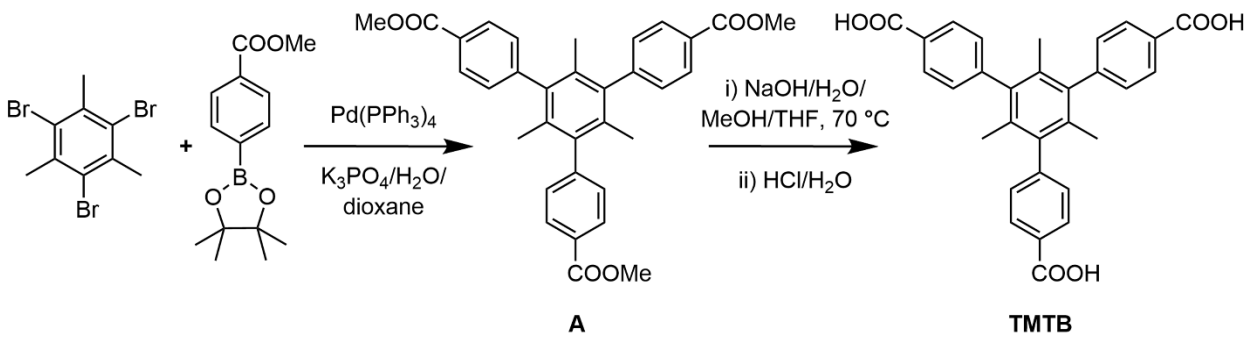

Scheme 4.3 Synthesis of 4,4',4''-(2,4,6-trimethylbenzene-1,3,5-triyl)tribenzoic acid (TMTB)

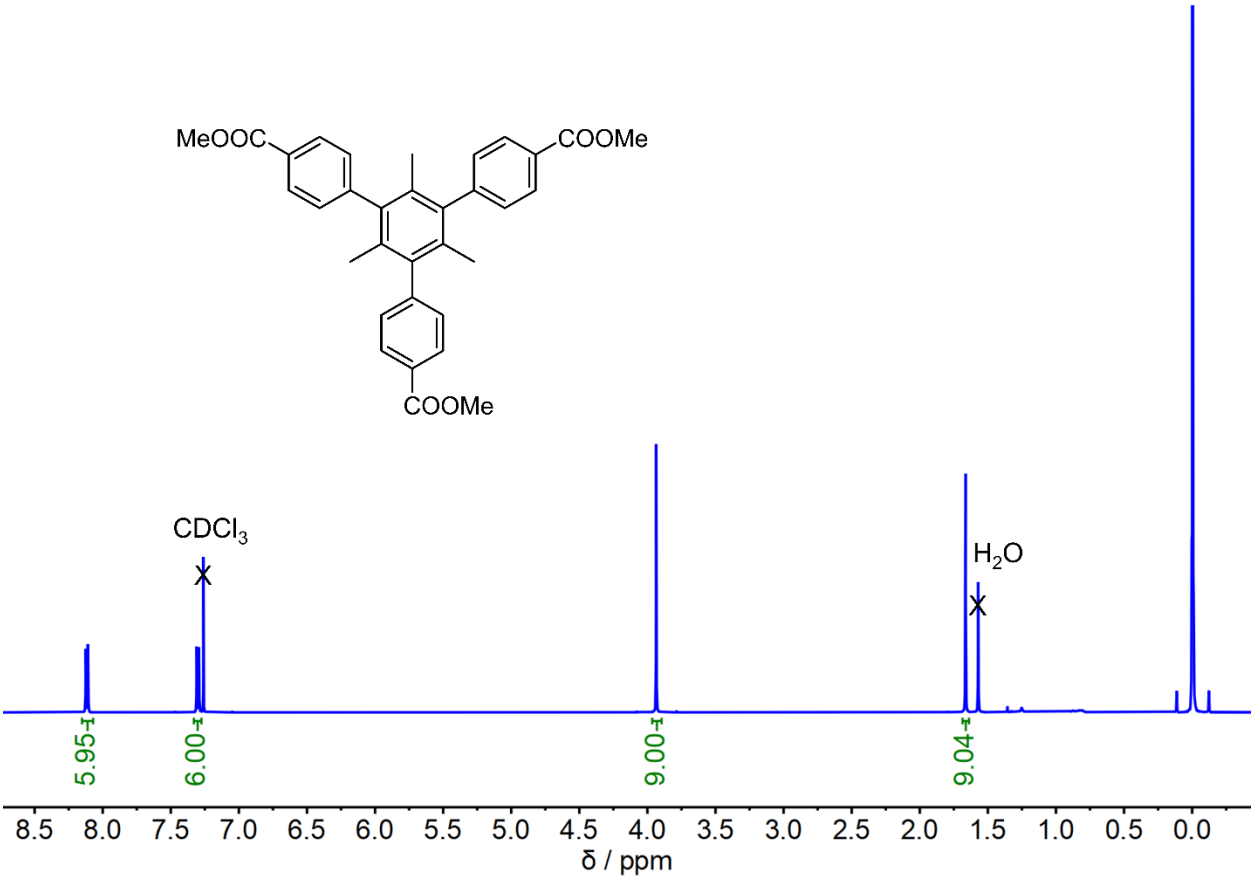

Figure 4.4 ^{1}H NMR spectra of **A** in chlorform-*d*.

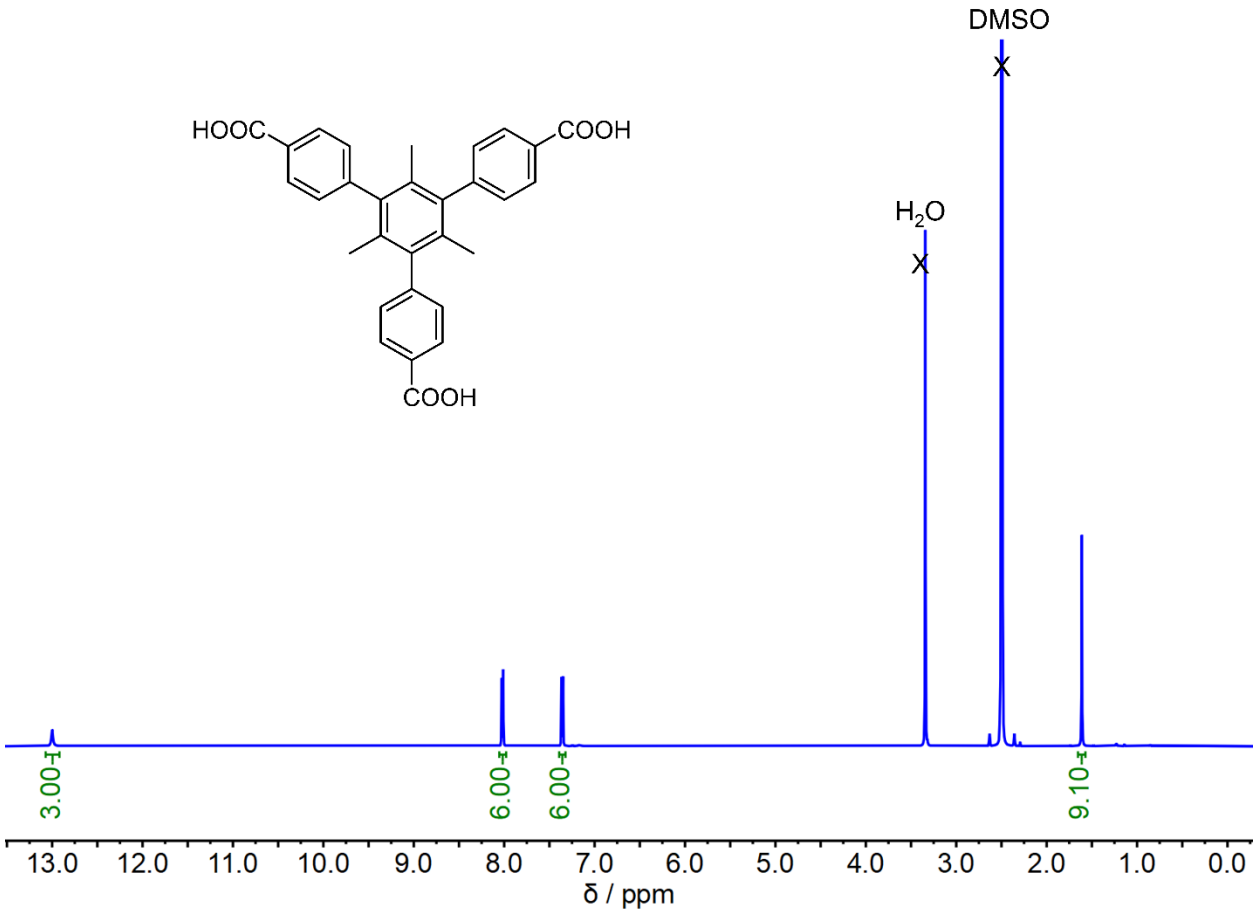

Figure 4.5 ^{1}H NMR spectra of **TMTB** in dimethyl sulfoxide-d_6 (DMSO).

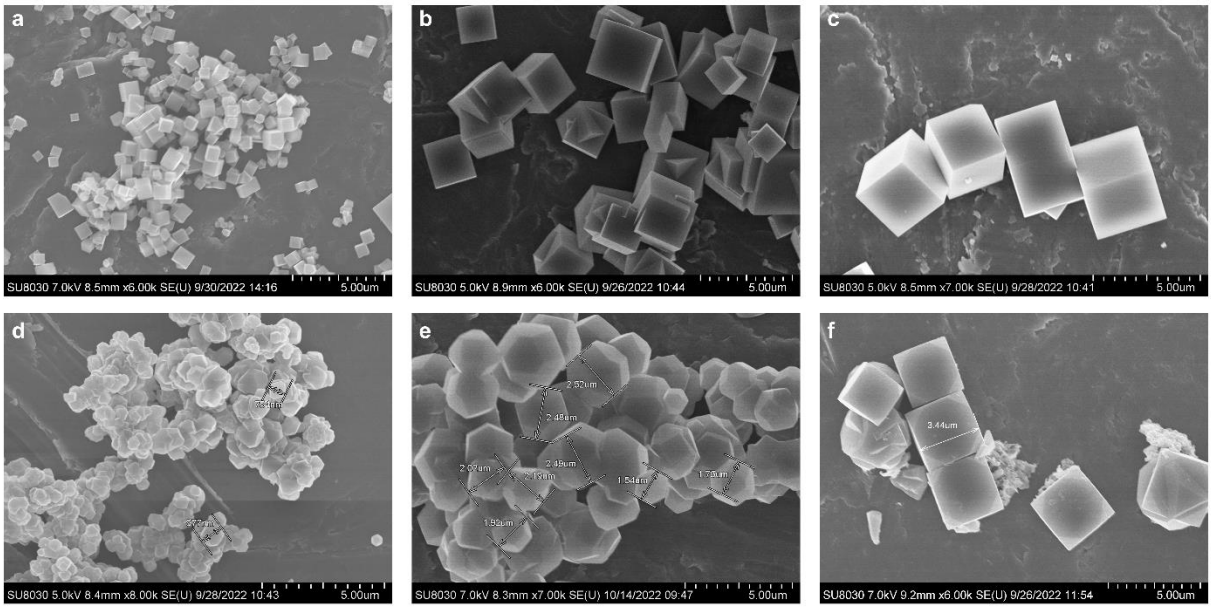

Figure 4.6 SEM of (a) 600 nm, (b) 2 μm, and (c) 4 μm Zr-NU-1200 particles and (d) 600 nm, (e) 2 μm, and (f) 4 μm Hf-NU-1200.

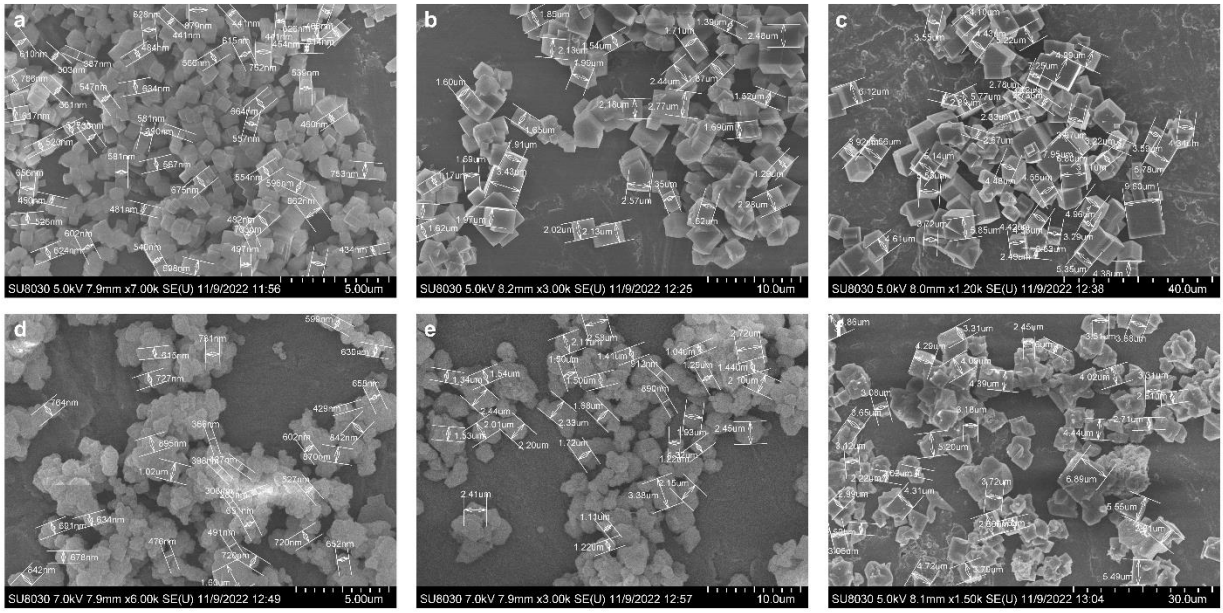

Figure 4.7 Zoomed-out SEM of (a) 600 nm, (b) 2 μm, and (c) 4 μm Zr-NU-1200 particles and (d) 600 nm, (e) 2 μm, and (f) 4 μm Hf-NU-1200 with particle sizes marked.

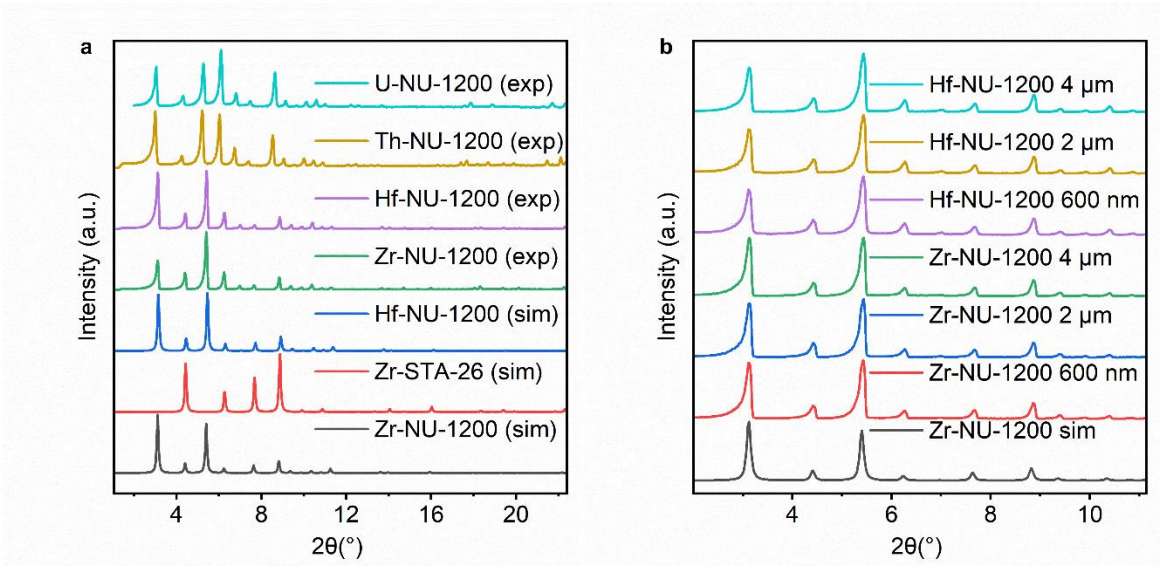

Figure 4.8 PXRD of (a) activated Zr-, Hf-, Th-, and U-NU-1200 analogs and (b) activated Zr- and Hf-NU-1200 at different particle sizes.

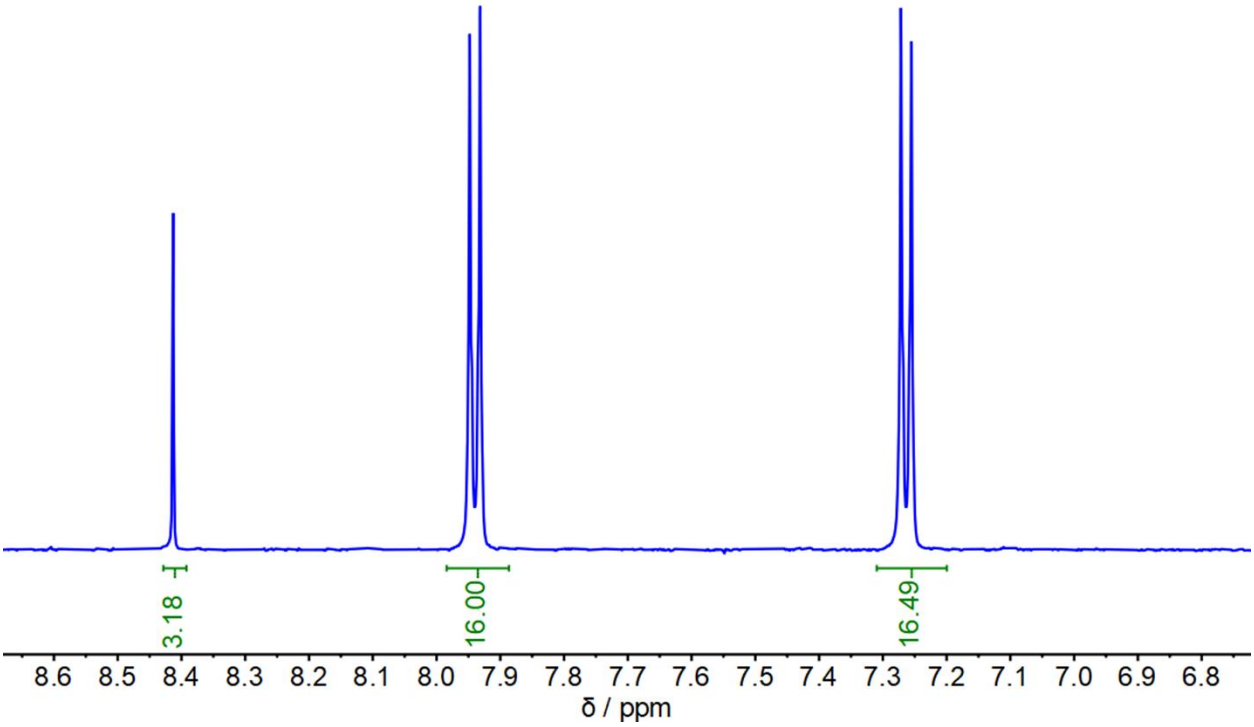

Figure 4.9 ^{1}H NMR spectra of base-digested 600 nm Zr-NU-1200 in D_2O. Signals are integrated as number of protons per node.

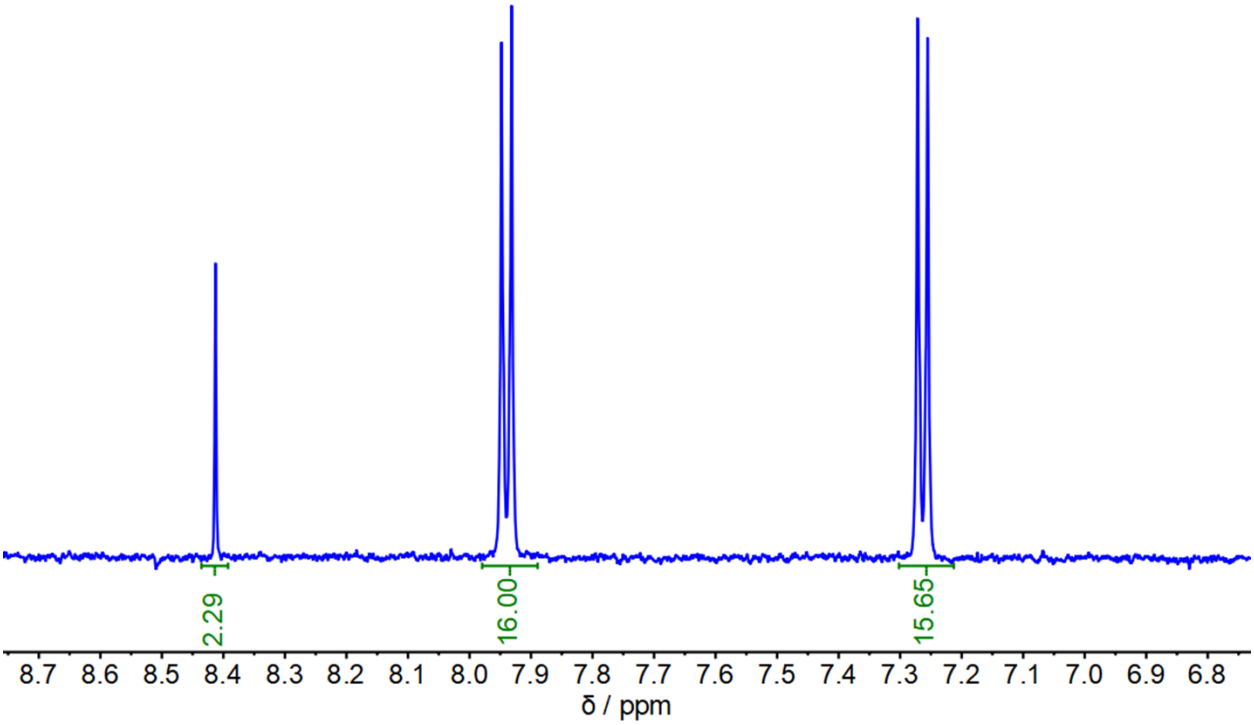

Figure 4.10 ^{1}H NMR spectra of base-digested 2 μm Zr-NU-1200 in D_2O. Signals are integrated as number of protons per node.

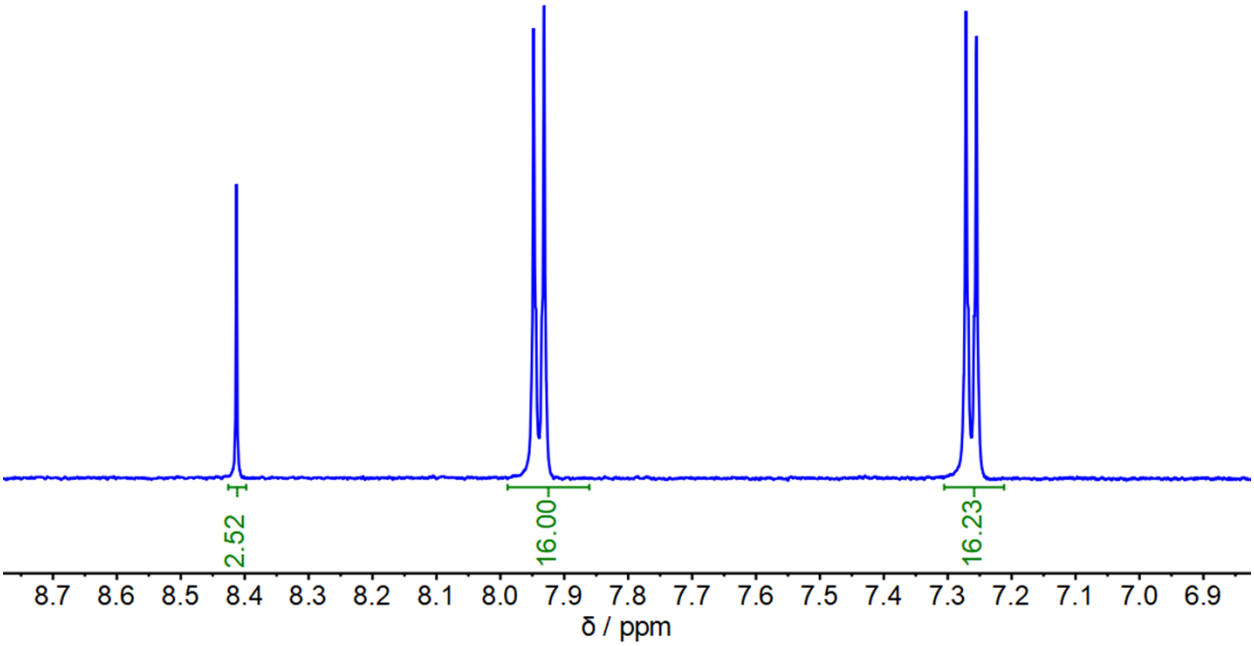

Figure 4.11 ^{1}H NMR spectra of base-digested 4 μm Zr-NU-1200 in D_2O. Signals are integrated as number of protons per node.

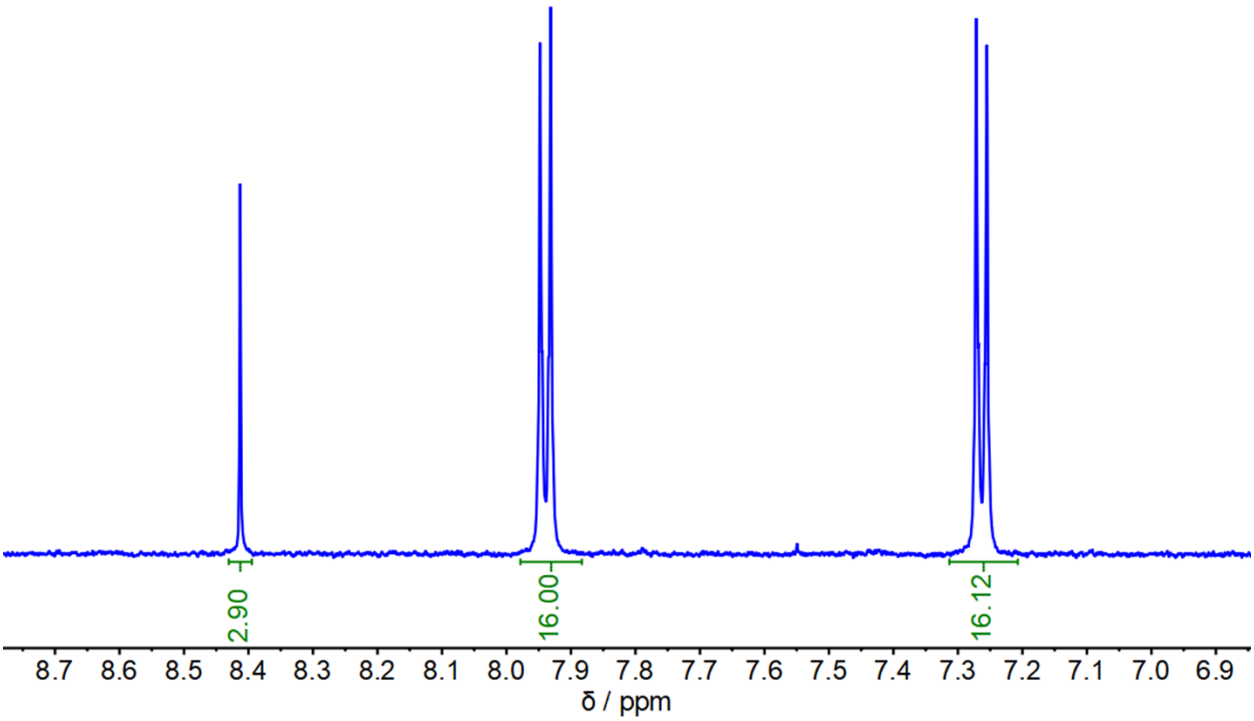

Figure 4.12 ^{1}H NMR spectra of base-digested 600 nm Hf-NU-1200 in D_2O. Signals are integrated as number of protons per node.

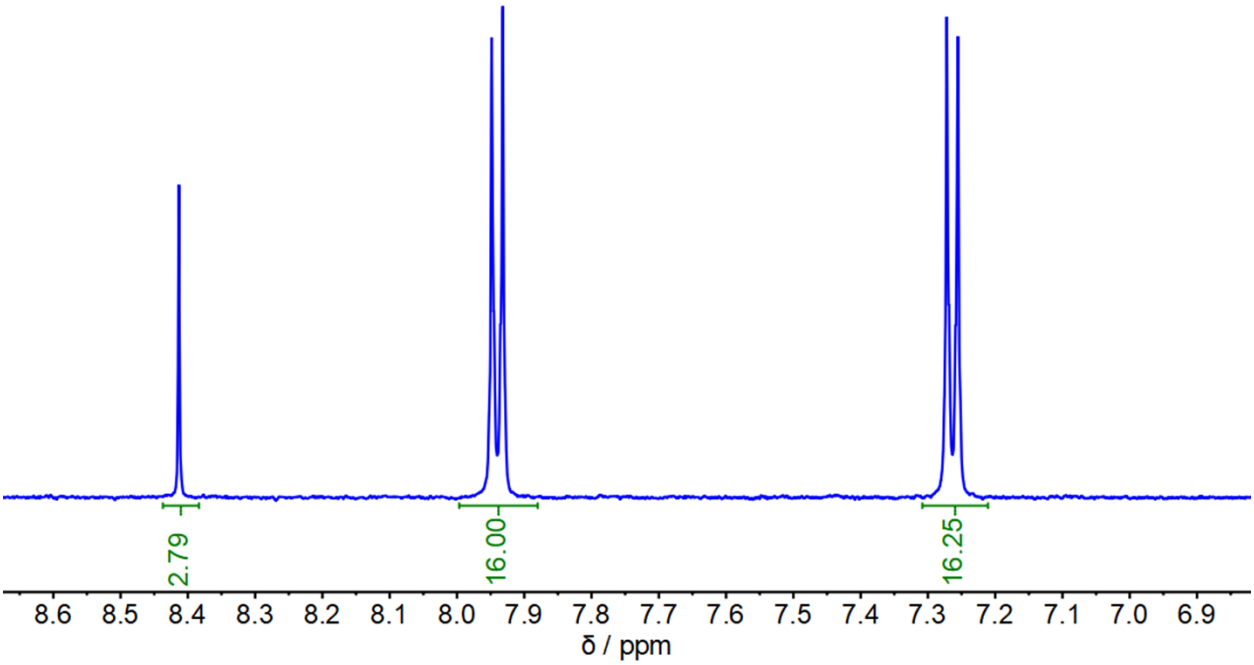

Figure 4.13 ^{1}H NMR spectra of base-digested 2 μm Hf-NU-1200 in D_2O. Signals are integrated as number of protons per node.

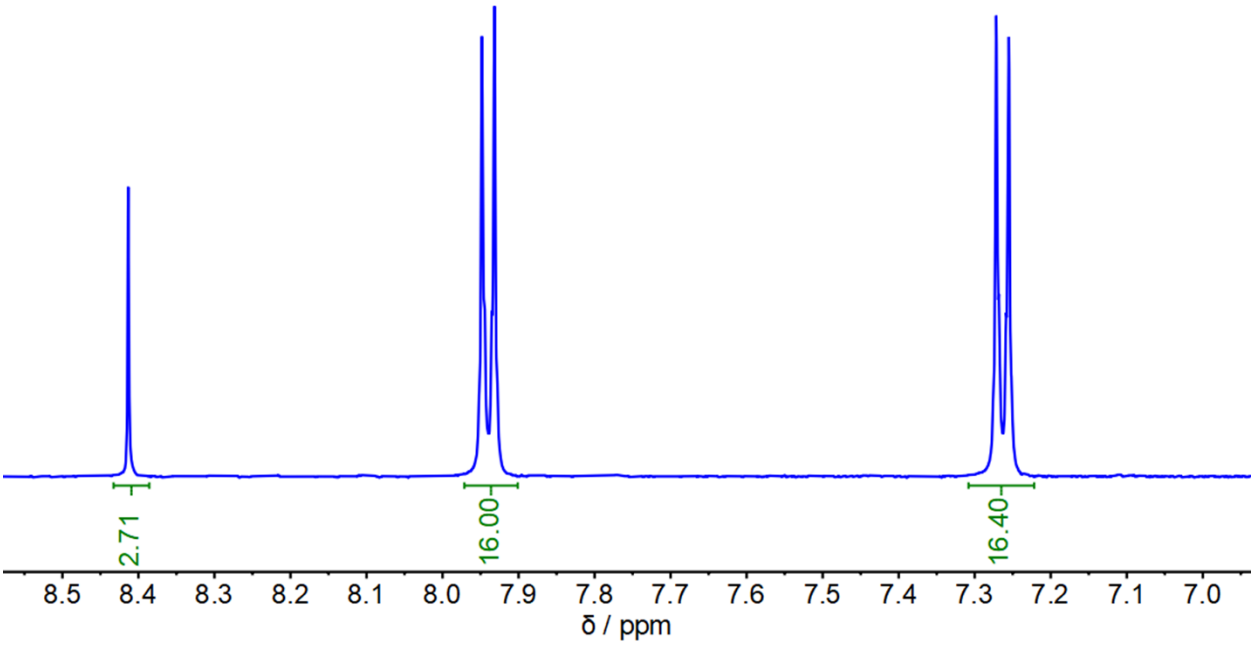

Figure 4.14 ^{1}H NMR spectra of base-digested 4 μm Hf-NU-1200 in D_2O. Signals are integrated as number of protons per node.

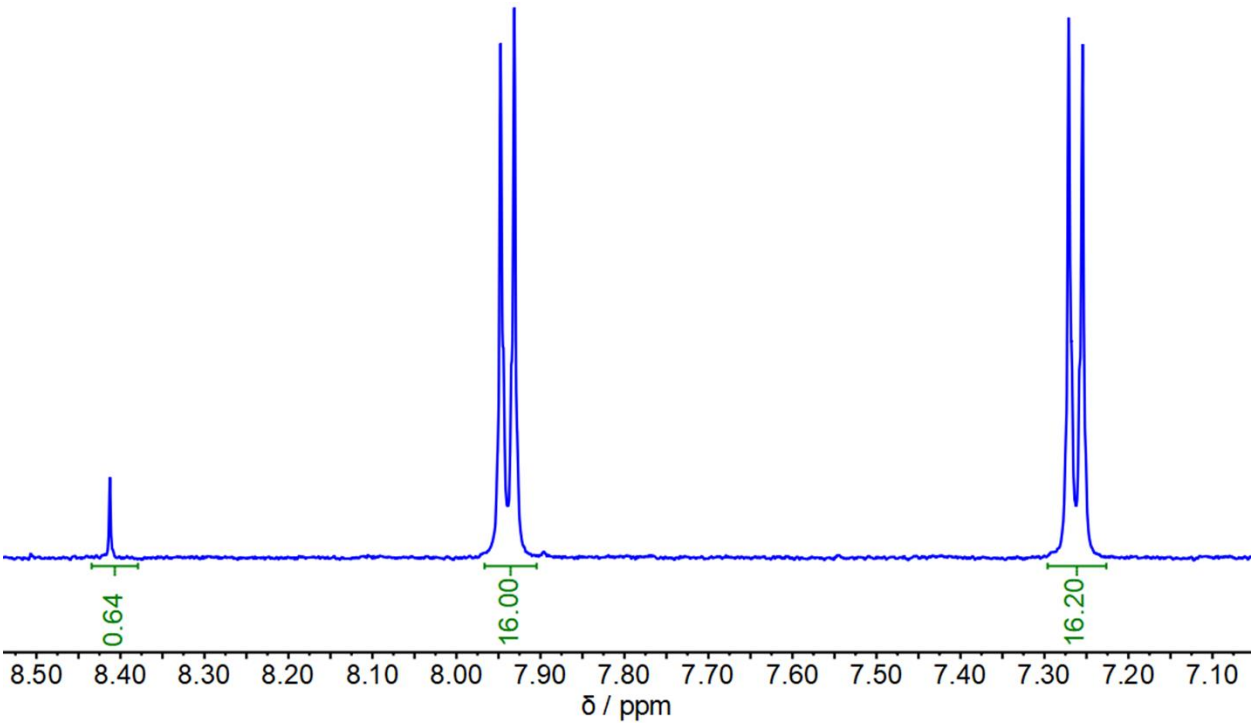

Figure 4.15 ^{1}H NMR spectra of base-digested Th-NU-1200 in D_2O. Signals are integrated as number of protons per node.

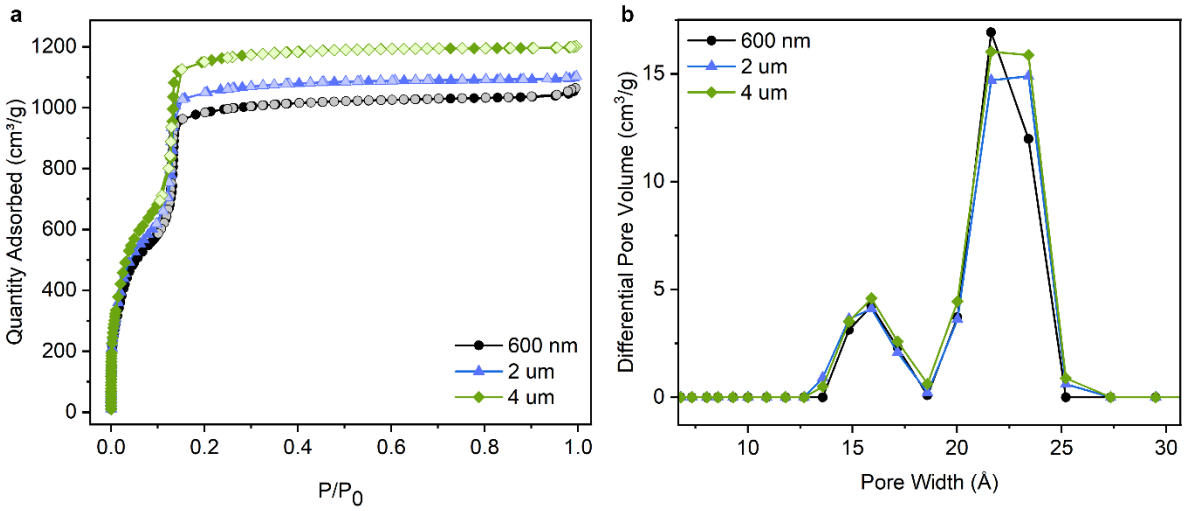

Figure 4.16 (a) Nitrogen physisorption isotherms and (b) pore size distributions of Zr-NU-1200 at different particle sizes.

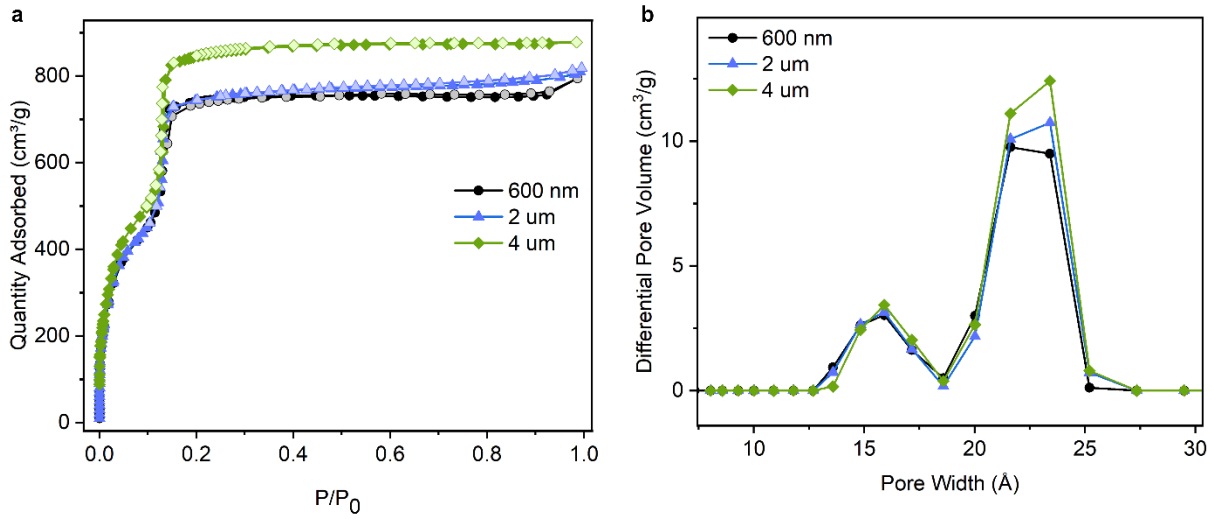

Figure 4.17 (a) Nitrogen physisorption isotherms and (b) pore size distributions of Hf-NU-1200 at different particle sizes.

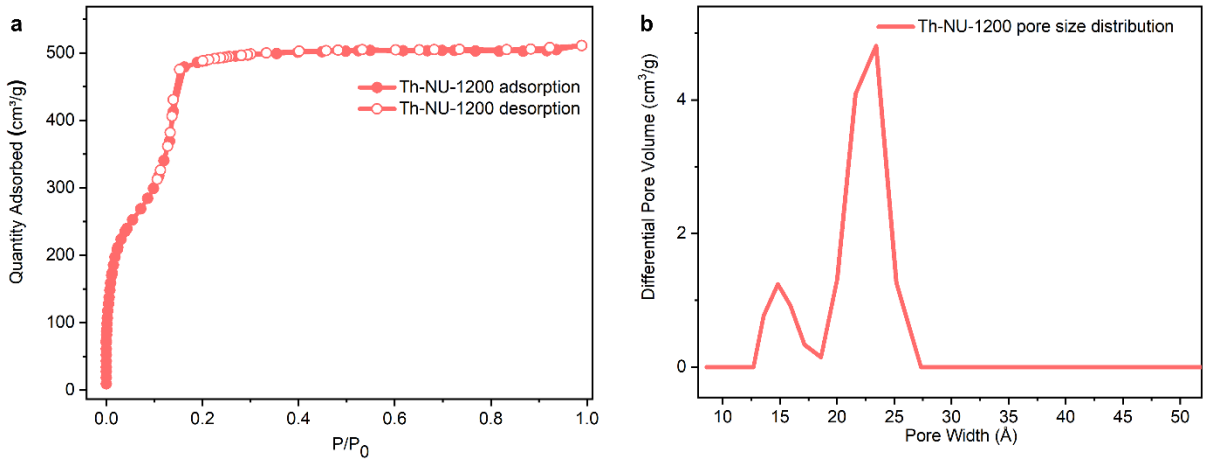

Figure 4.18 (a) Nitrogen physisorption isotherm and (b) pore size distribution of Th-NU-1200.

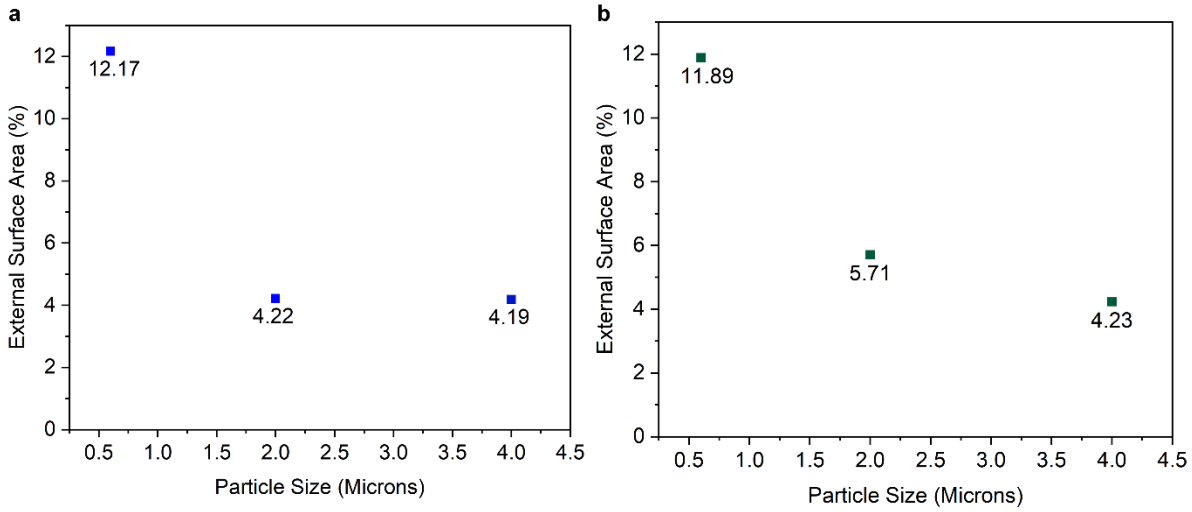

Figure 4.19 Percent external surface area as a function of particle size for (a) Zr-NU-1200 and (b) Hf-NU-1200 samples. Values calculated from t-plots.

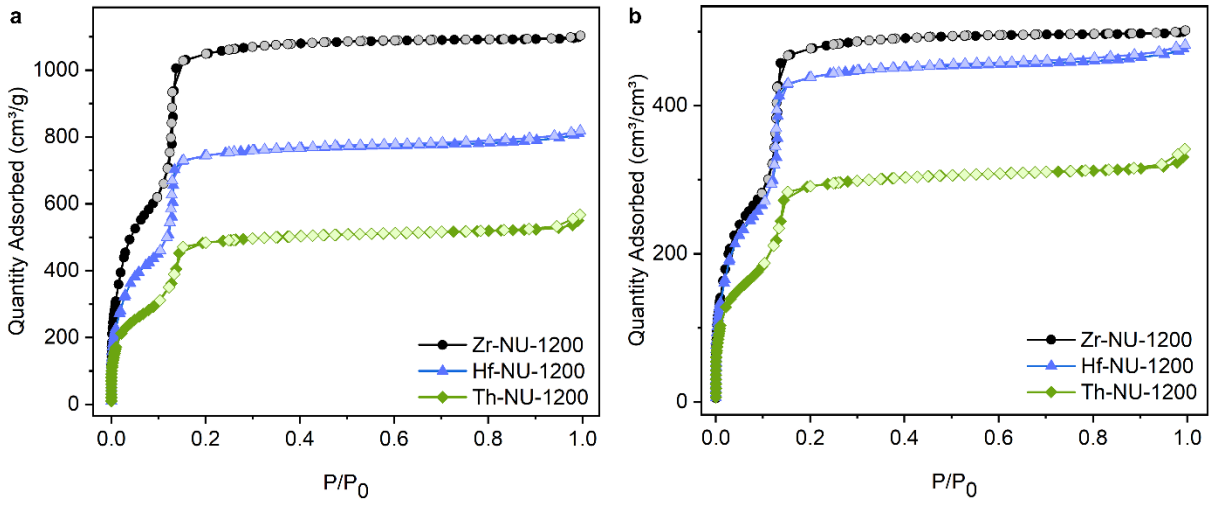

Figure 4.20 (a) Gravimetric and (b) volumetric nitrogen physisorption isotherms of Zr-, Hf-, and Th-NU-1200.

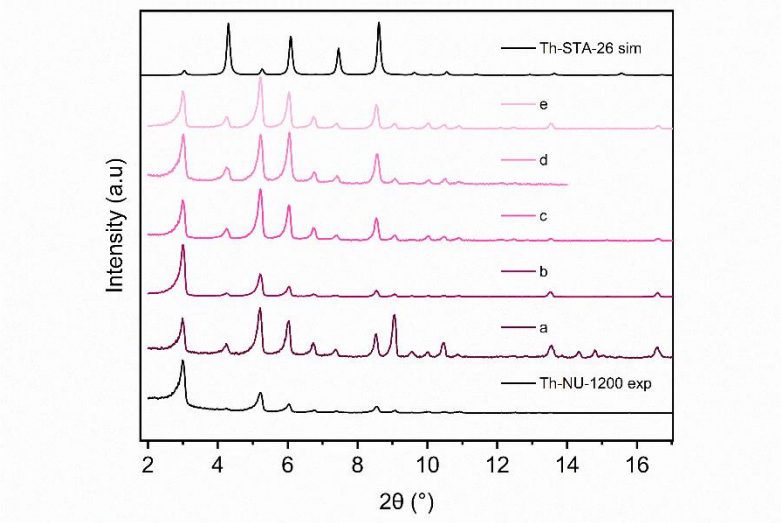

Figure 4.21 Representative sample of PXRD patterns obtained after subjecting Th-NU-1200 to interpenetration conditions. Under conditions a-e, which include a variety of concentrations, temperatures, and reaction times, Th-NU-1200 is still observed.

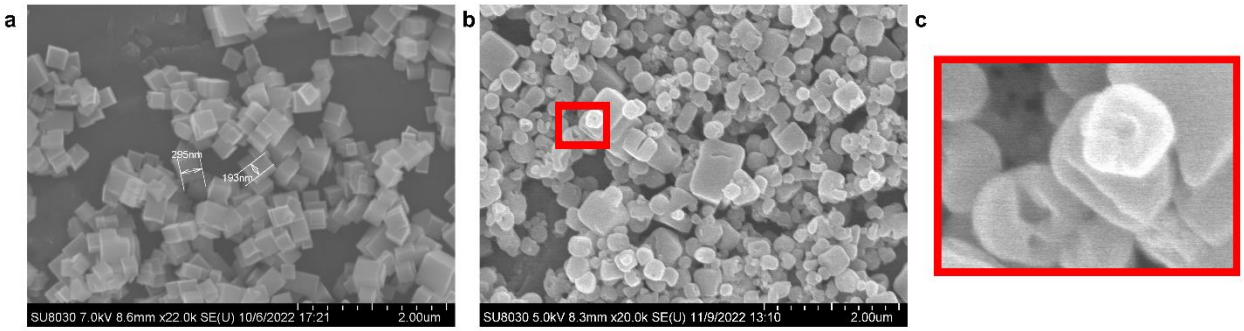

Figure 4.22 SEM of (a) pristine Th-NU-1200, (b) Th-NU-1200 after exposure to interpenetration conditions, and (c) inset of (b) showing etching damage of particles.

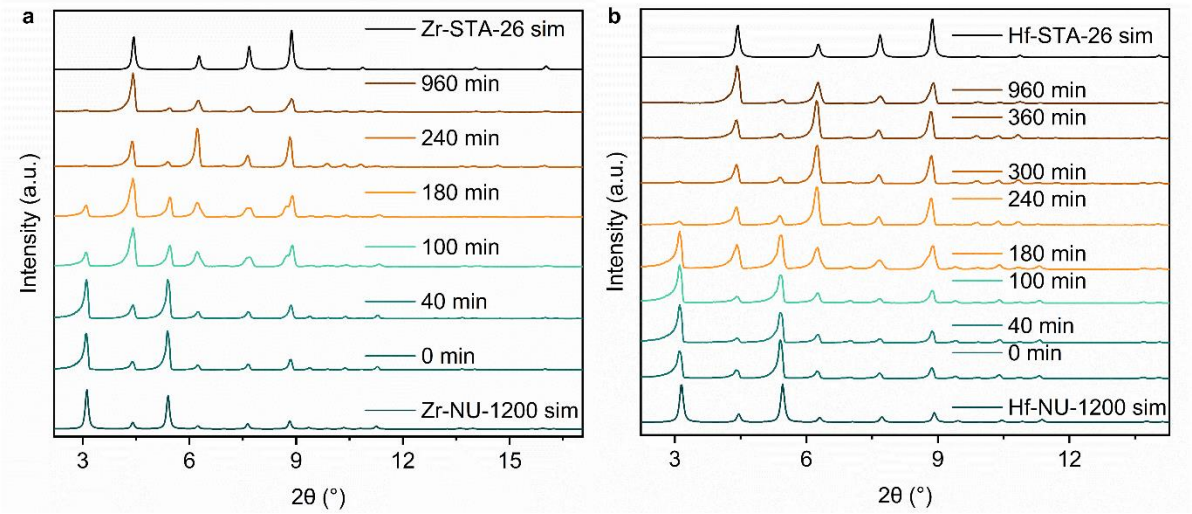

Figure 4.23 *Ex-situ* PXRD of (a) Zr-NU-1200 transformation to Zr-STA-26 and (b) Hf-NU-1200 transformation to Hf-STA-26.

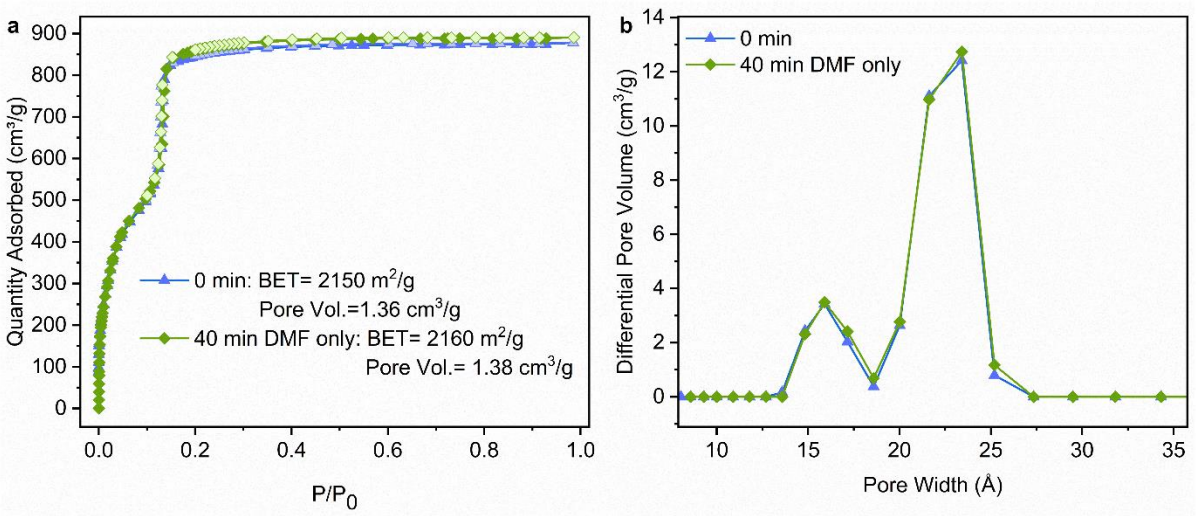

Figure 4.24 (a) Nitrogen physisorption isotherm and (b) pore size distribution of Hf-NU-1200 after exposure to hot DMF wash.

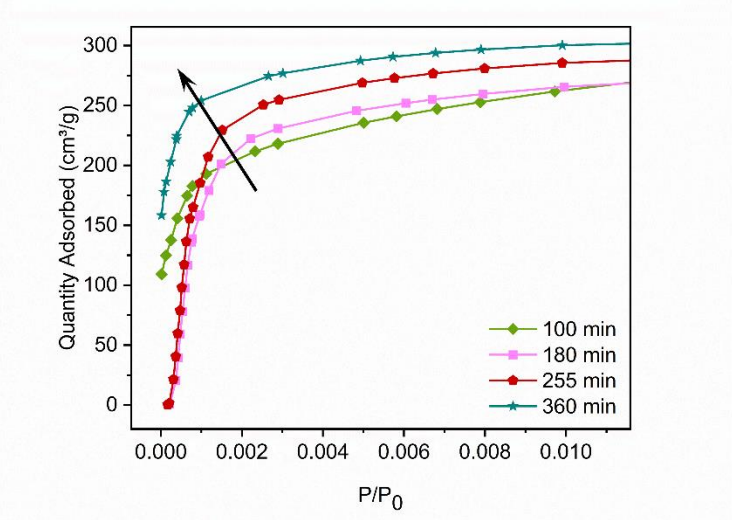

Figure 4.25 Inset of Figure 4.1e.

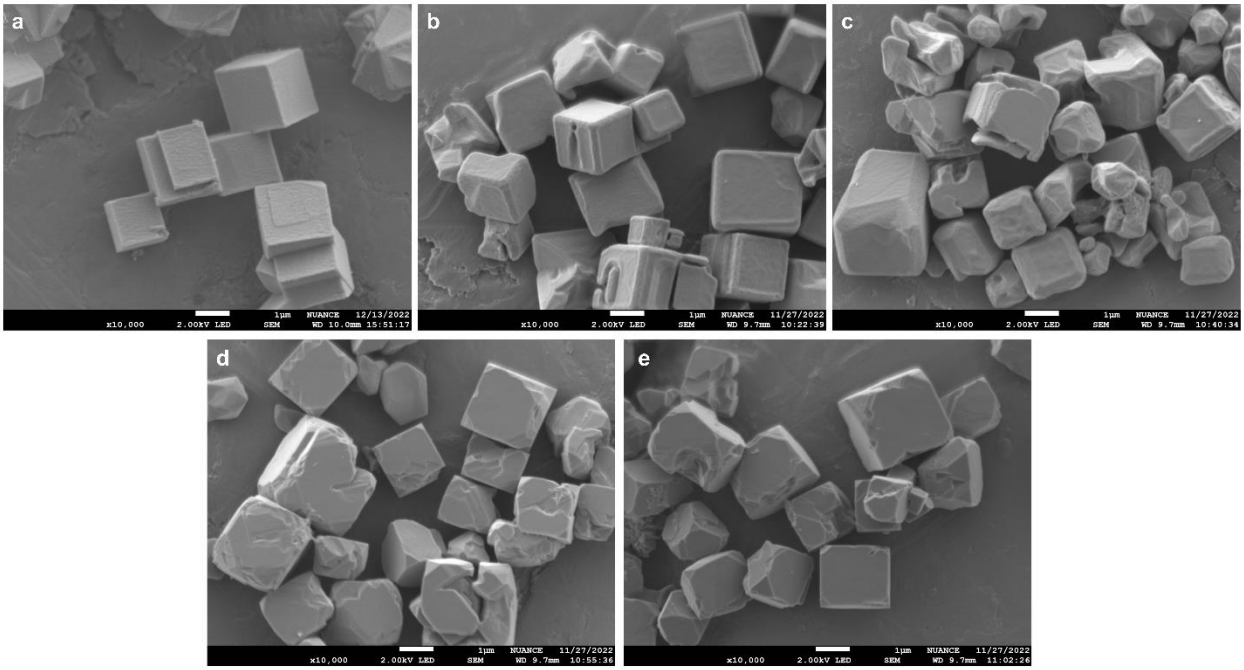

Figure 4.26 SEM of (a) pristine Zr-NU-1200 and Zr-NU-1200 crystals after exposure to in-situ interpenetration conditions for (b) 0.25 h, (c) 0.5 h, (d) 1 h, and (3) 1.5 h.

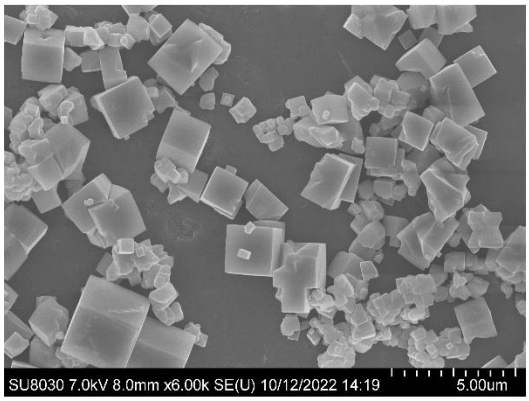

Figure 4.27 SEM of U-NU-1200.

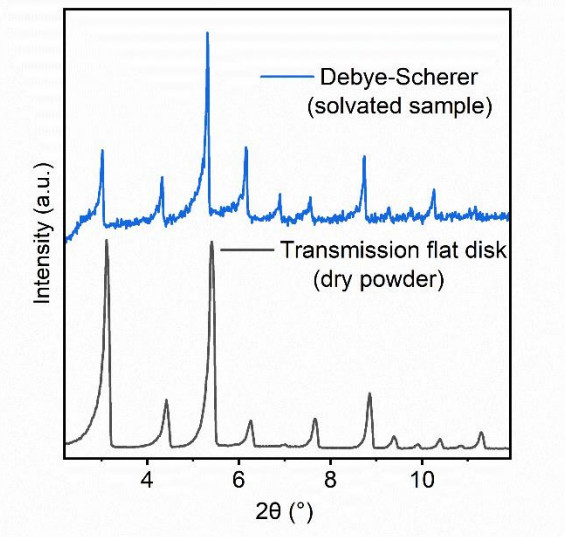

Figure 4.28 PXRD of same Zr-NU-1200 powder in transmission mode (flat disk) and Debye-Scherer mode. Peaks can be seen to slightly shift and change in intensity in Debye-Scherer mode.

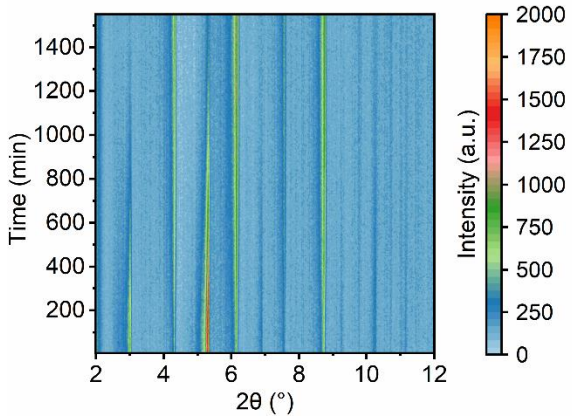

Figure 4.29 Time-resolved *in-situ* PXRD of 2 μm Zr-NU-1200 in DMF:FA=2.5 at 80 °C.

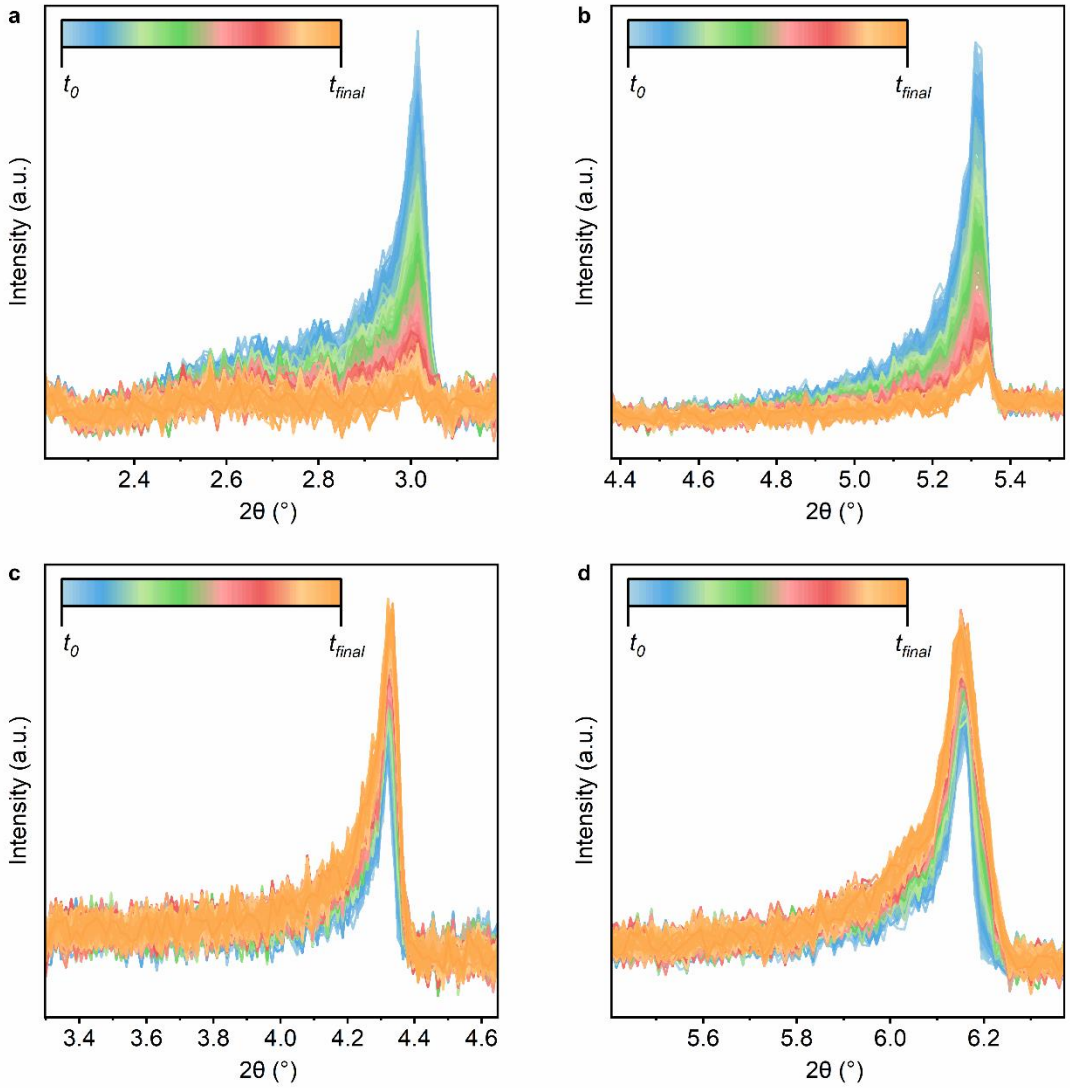

Figure 4.30 Time-resolved *in-situ* PXRD of the (a) ⟨100⟩, (b) ⟨111⟩, (c) ⟨110⟩, and (d) ⟨200⟩ Bragg features of 2 μm Zr-NU-1200 in DMF:FA=2.5 at 80 °C.

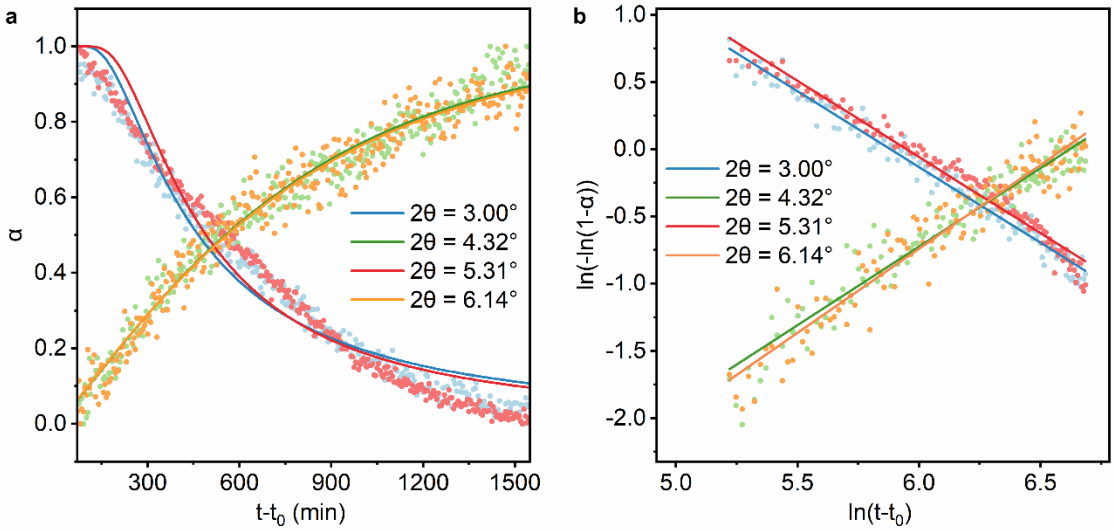

Figure 4.31 (a) Crystallization curve and Avrami fitting and (b) Sharp-Hancock plot and linear fitting for 2 µm Zr-NU-1200 in DMF:FA=2.5 at 80 °C.

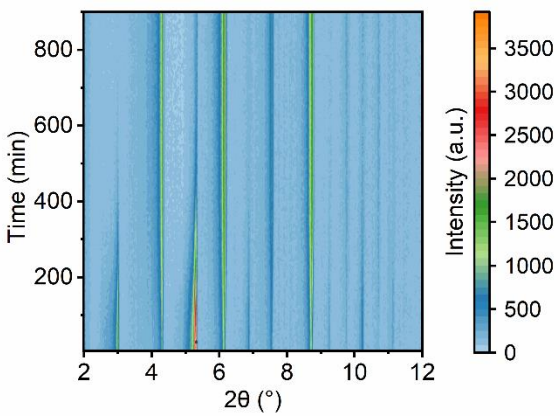

Figure 4.32 Time-resolved *in-situ* PXRD of 2 μm Zr-NU-1200 in DMF:FA=2.5 at 90 °C.

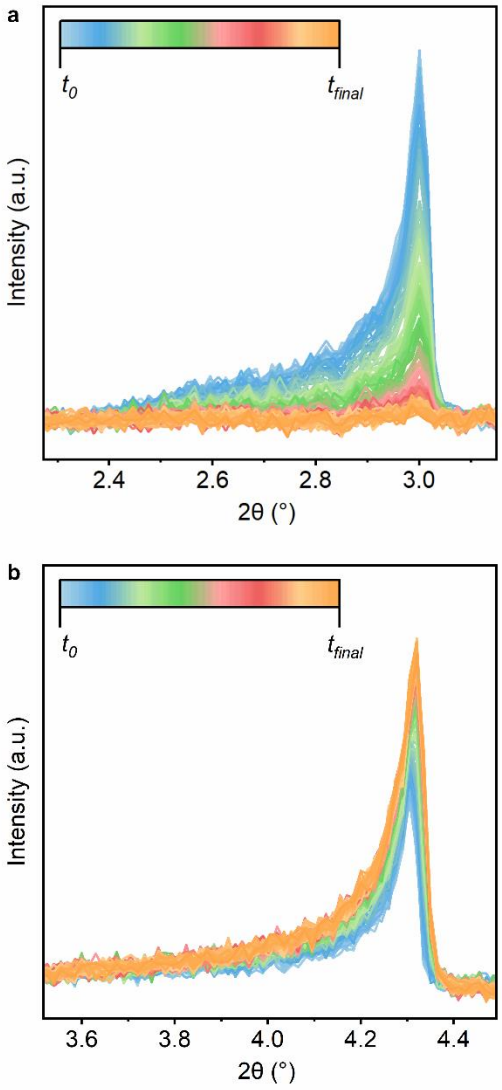

Figure 4.33 Time-resolved *in-situ* PXRD of the (a) ⟨100⟩ and (b) ⟨110⟩ Bragg features of 2 μm Zr-NU-1200 in DMF:FA=2.5 at 90 °C.

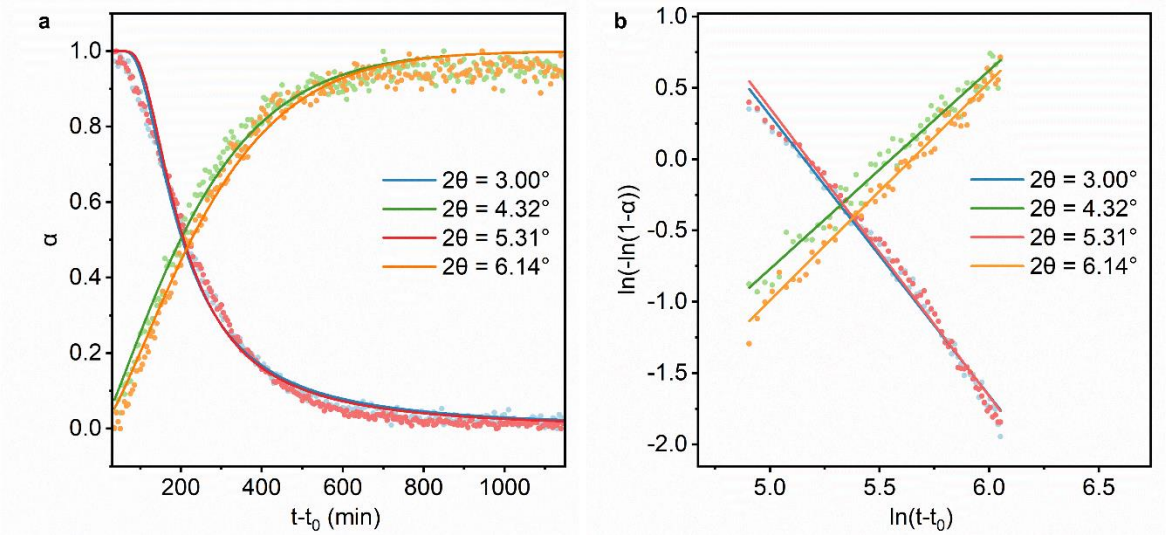

Figure 4.34 (a) Crystallization curve and Avrami fitting and (b) Sharp-Hancock plot and linear fitting for 2 μm Zr-NU-1200 in DMF:FA=2.5 at 90 °C.

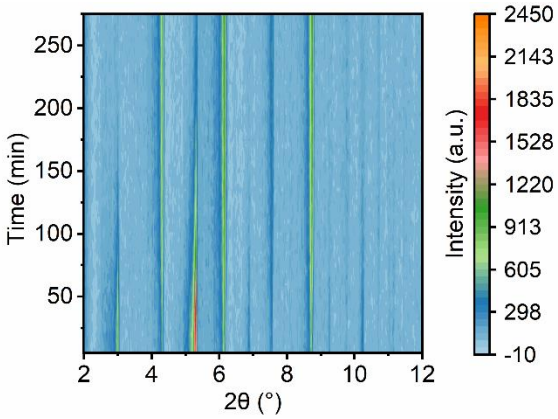

Figure 4.35 Time-resolved *in-situ* PXRD of 2 μm Zr-NU-1200 in DMF:FA=2.5 at 100 °C.

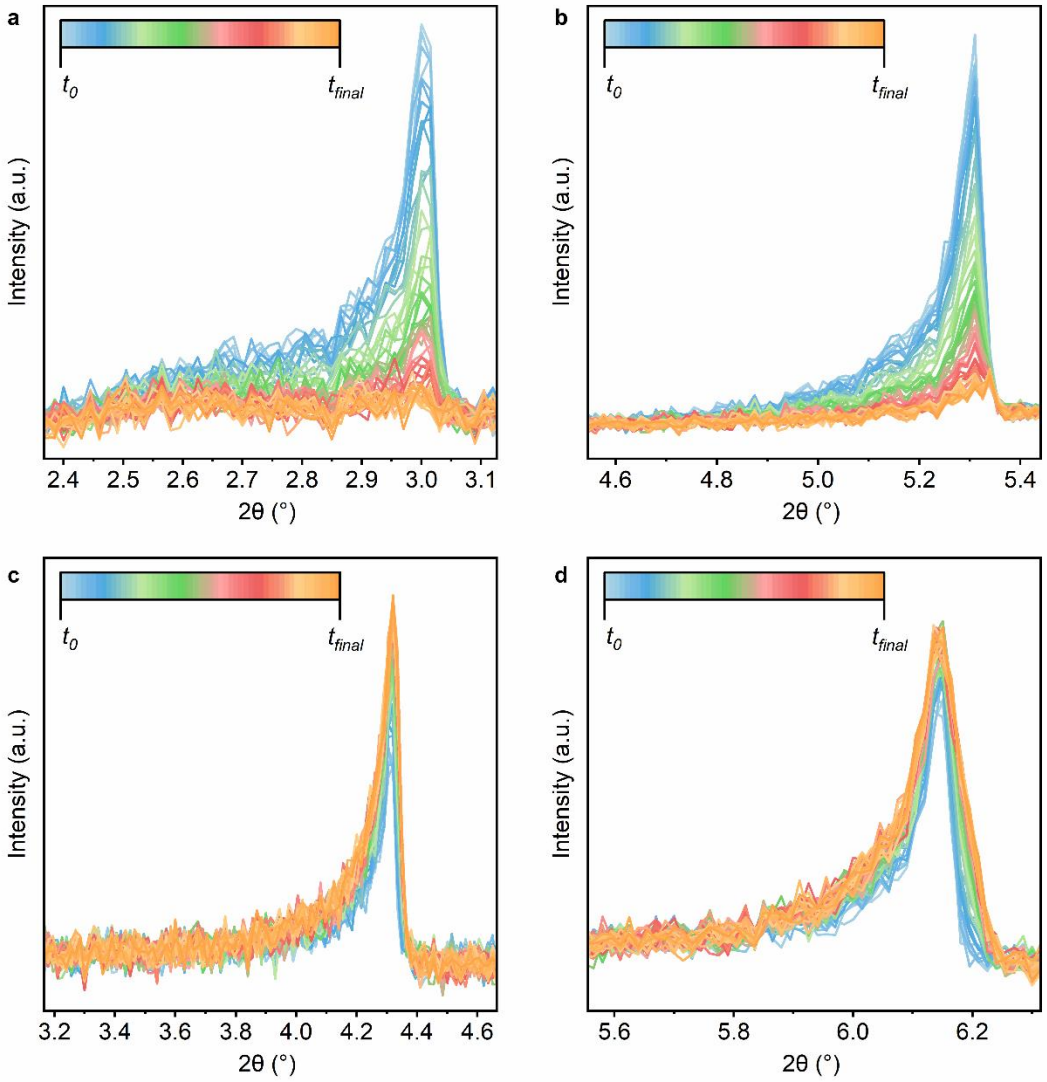

Figure 4.36 Time-resolved *in-situ* PXRD of the (a) ⟨100⟩, (b) ⟨111⟩, (c) ⟨110⟩, and (d) ⟨200⟩ Bragg features of 2 μm Zr-NU-1200 in DMF:FA=2.5 at 100 °C.

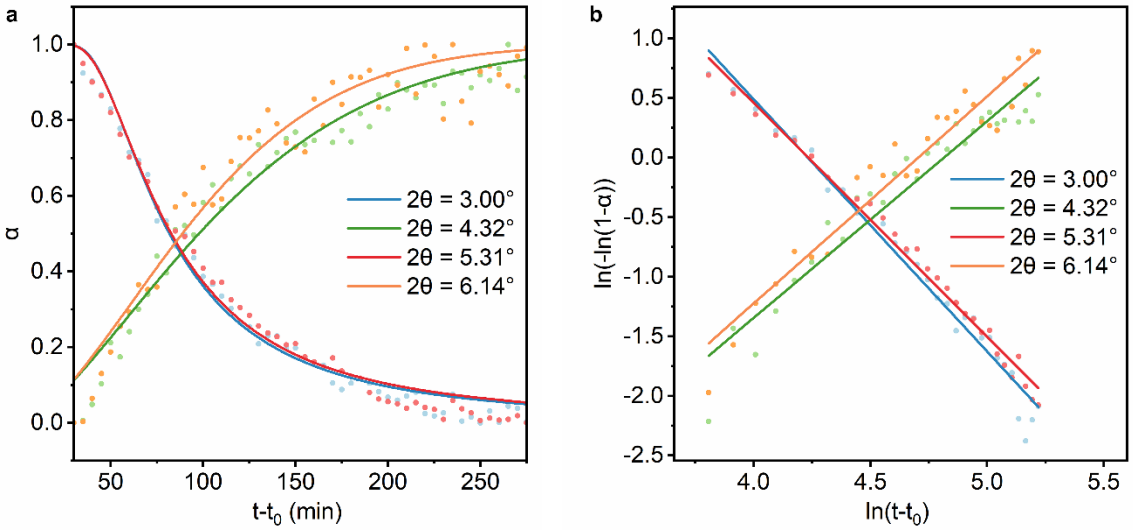

Figure 4.37 (a) Crystallization curve and Avrami fitting and (b) Sharp-Hancock plot and linear fitting for 2 µm Zr-NU-1200 in DMF:FA=2.5 at 100 °C.

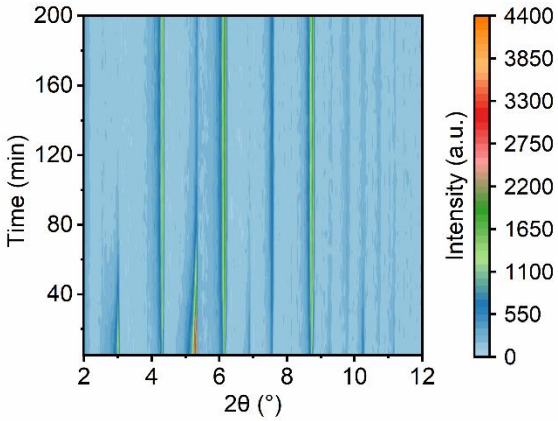

Figure 4.38 Time-resolved *in-situ* PXRD of 2 μm Zr-NU-1200 in DMF:FA=2.5 at 110 °C.

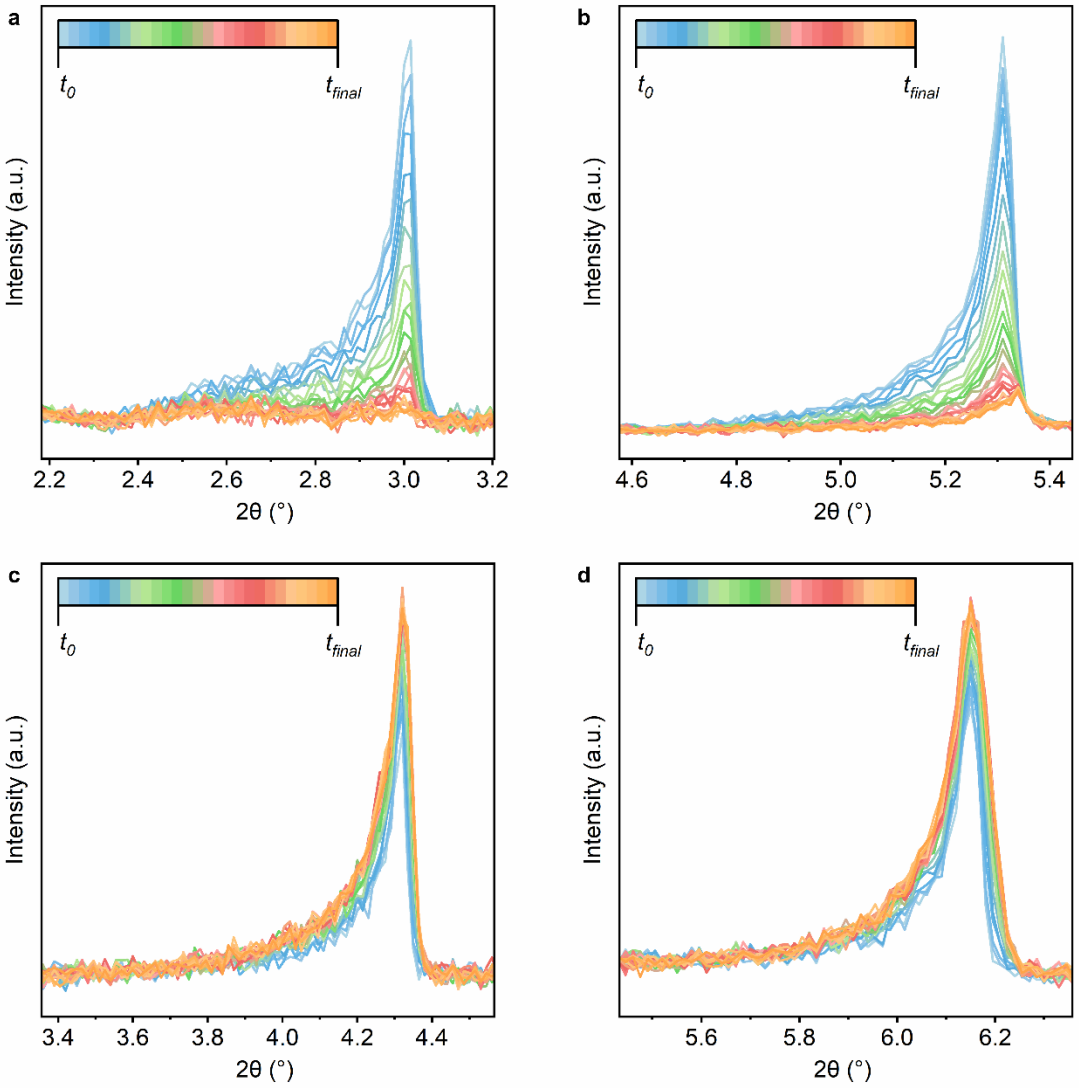

Figure 4.39 Time-resolved *in-situ* PXRD of the (a) ⟨100⟩, (b) ⟨111⟩, (c) ⟨110⟩, and (d) ⟨200⟩ Bragg features of 2 μm Zr-NU-1200 in DMF:FA=2.5 at 110 °C.

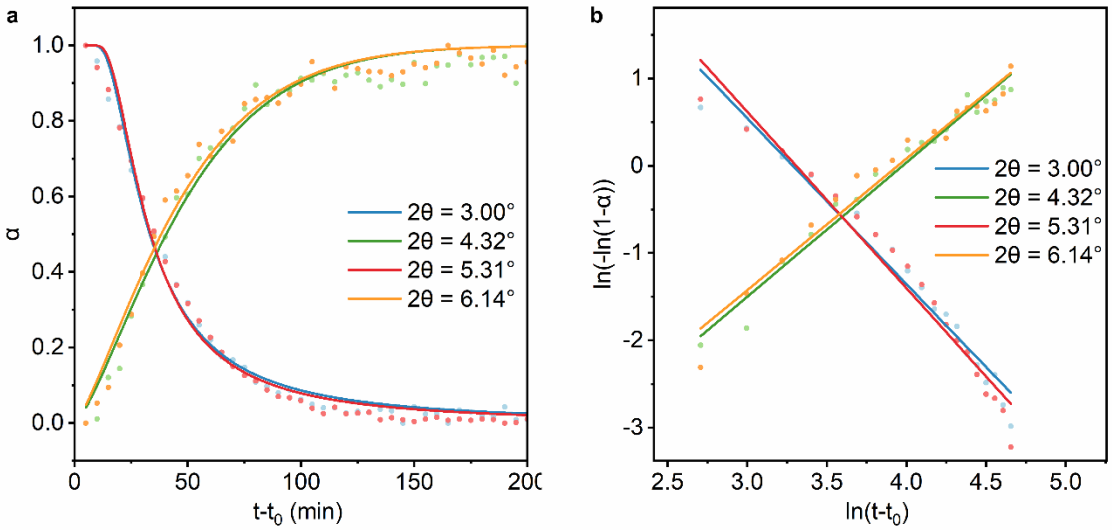

Figure 4.40 (a) Crystallization curve and Avrami fitting and (b) Sharp-Hancock plot and linear fitting for 2 μm Zr-NU-1200 in DMF:FA=2.5 at 110 °C.

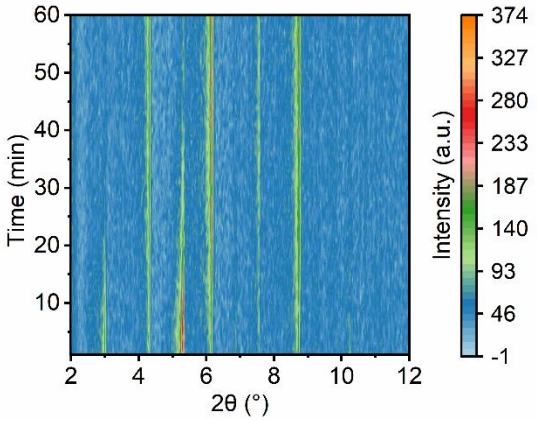

Figure 4.41 Time-resolved *in-situ* PXRD of 2 μm Zr-NU-1200 in DMF:FA=2.5 at 120 °C.

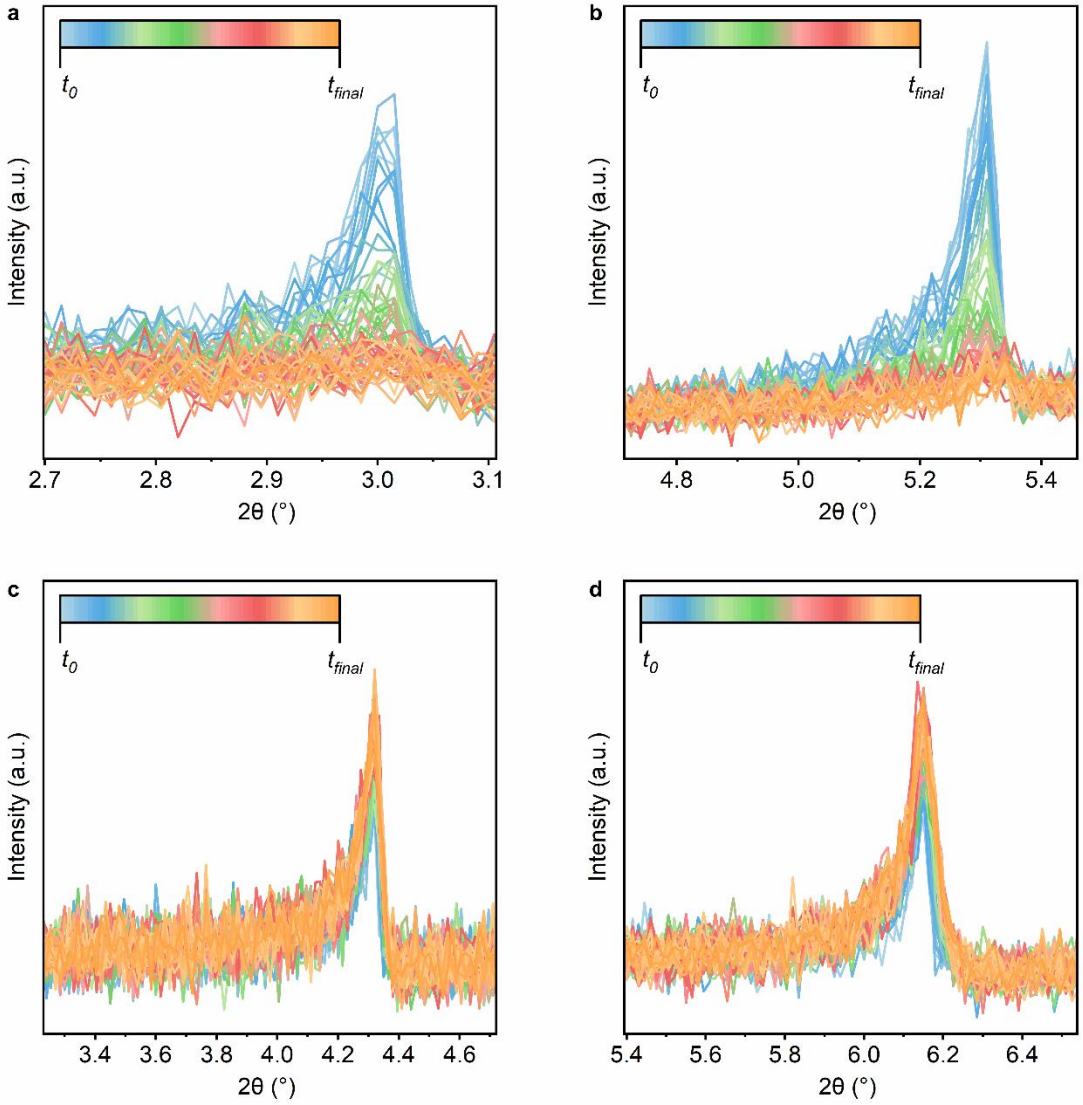

Figure 4.42 Time-resolved *in-situ* PXRD of the (a) ⟨100⟩, (b) ⟨111⟩, (c) ⟨110⟩, and (d) ⟨200⟩ Bragg features of 2 μm Zr-NU-1200 in DMF:FA=2.5 at 120 °C.

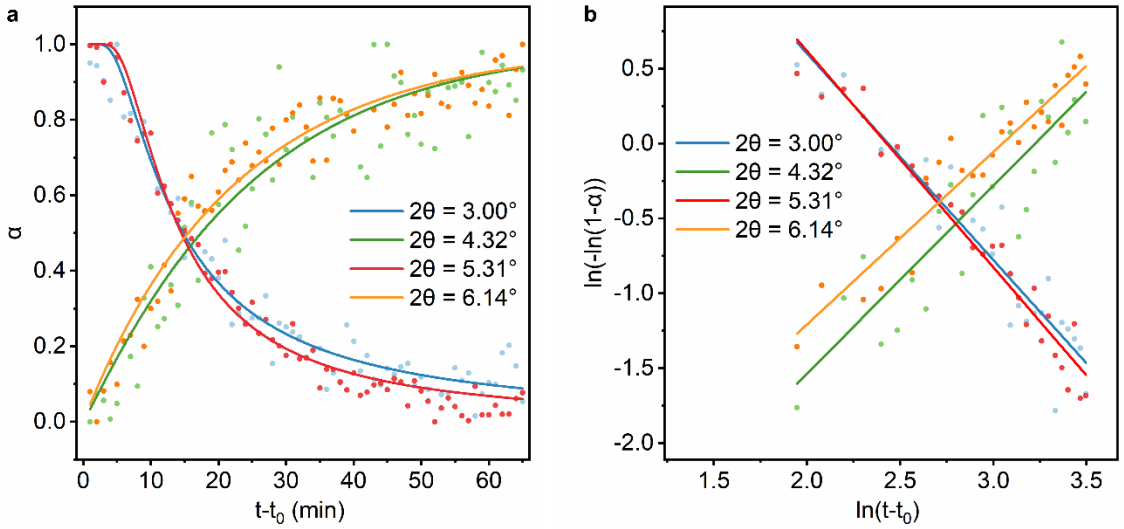

Figure 4.43 (a) Crystallization curve and Avrami fitting and (b) Sharp-Hancock plot and linear fitting for 2 µm Zr-NU-1200 in DMF:FA=2.5 at 120 °C.

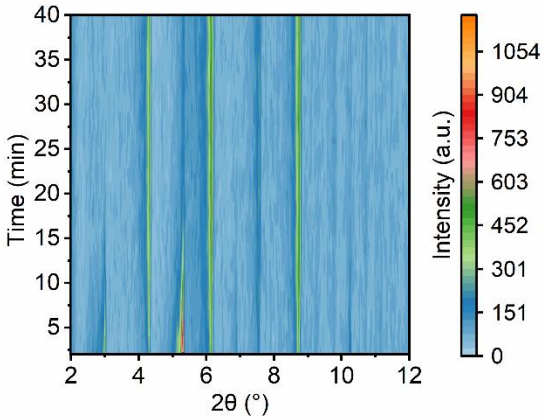

Figure 4.44 Time-resolved *in-situ* PXRD of 2 μm Zr-NU-1200 in DMF:FA=2.5 at 130 °C.

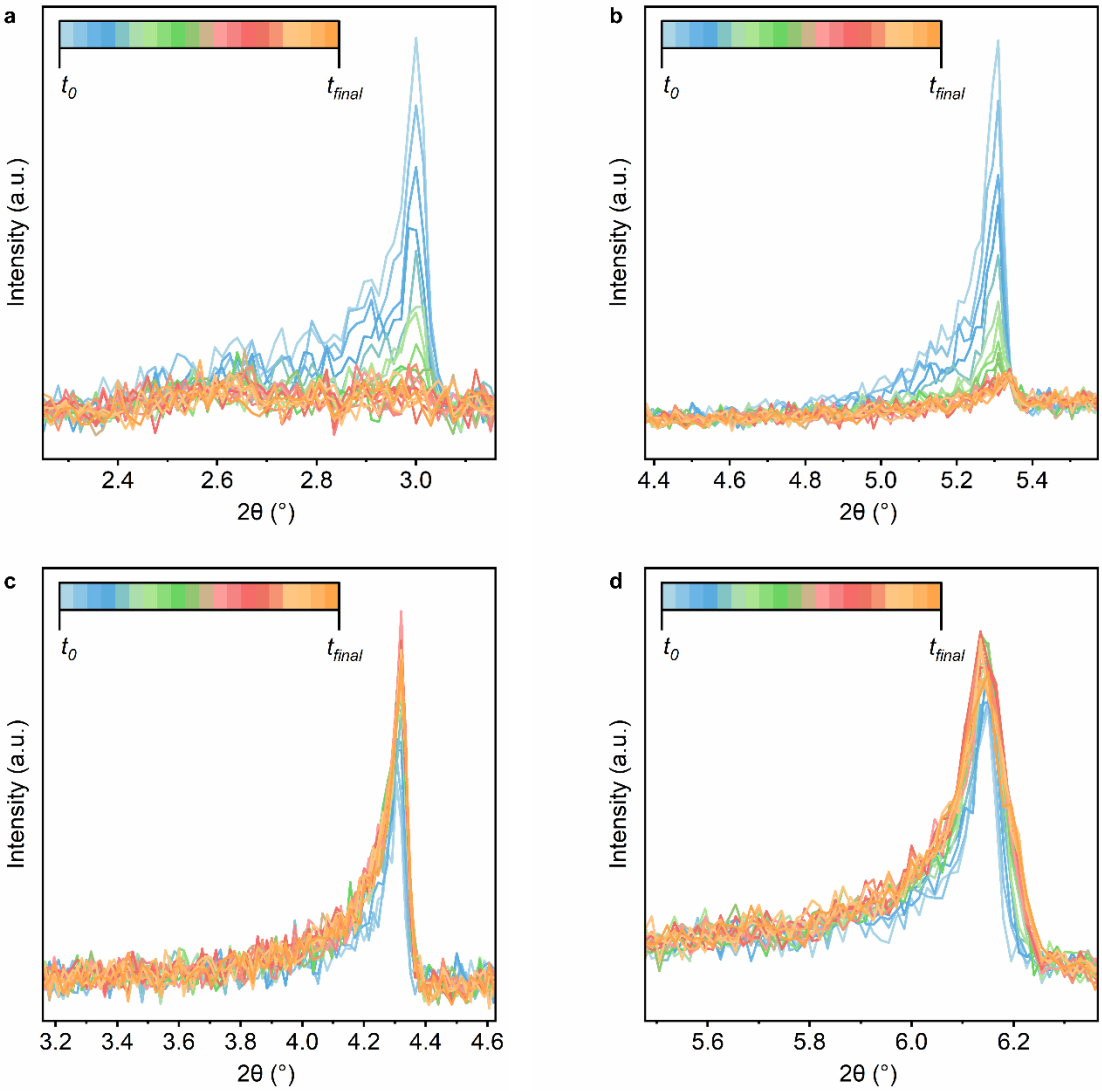

Figure 4.45 Time-resolved *in-situ* PXRD of the (a) ⟨100⟩, (b) ⟨111⟩, (c) ⟨110⟩, and (d) ⟨200⟩ Bragg features of 2 μm Zr-NU-1200 in DMF:FA=2.5 at 130 °C.

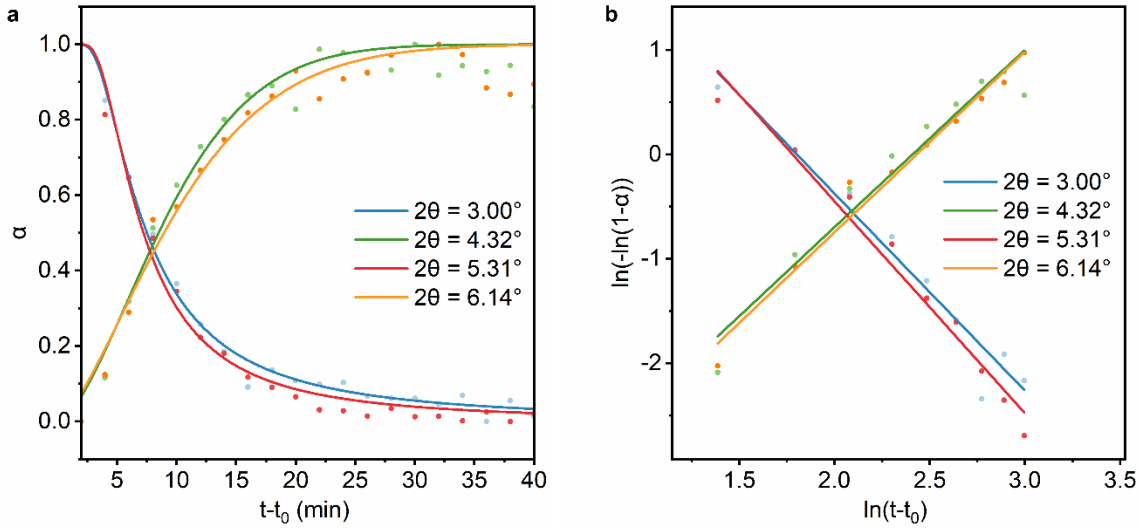

Figure 4.46 (a) Crystallization curve and Avrami fitting and (b) Sharp-Hancock plot and linear fitting for 2 μm Zr-NU-1200 in DMF:FA=2.5 at 130 °C.

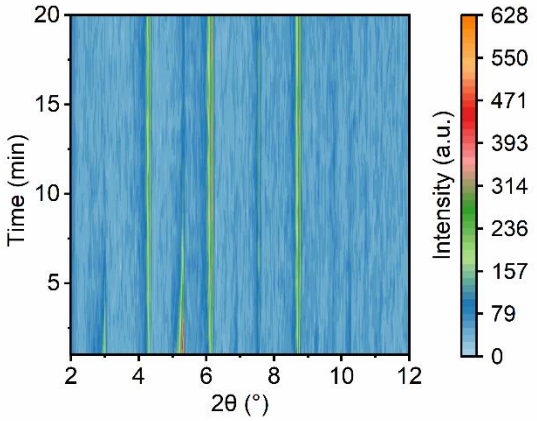

Figure 4.47 Time-resolved *in-situ* PXRD of 2 μm Zr-NU-1200 in DMF:FA=2.5 at 140 °C.

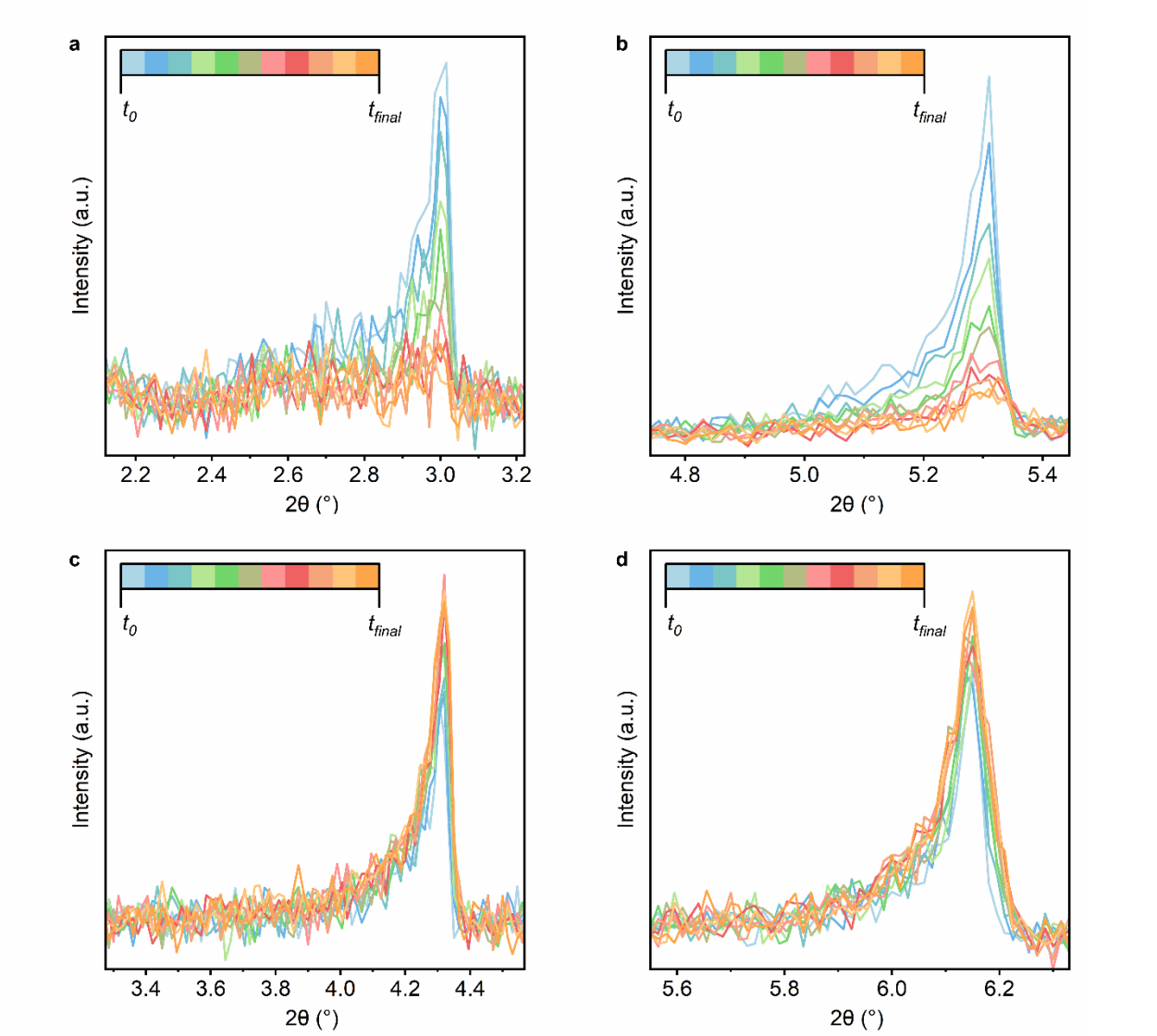

Figure 4.48 Time-resolved *in-situ* PXRD of the (a) ⟨100⟩, (b) ⟨111⟩, (c) ⟨110⟩, and (d) ⟨200⟩ Bragg features of 2 μm Zr-NU-1200 in DMF:FA=2.5 at 140 °C.

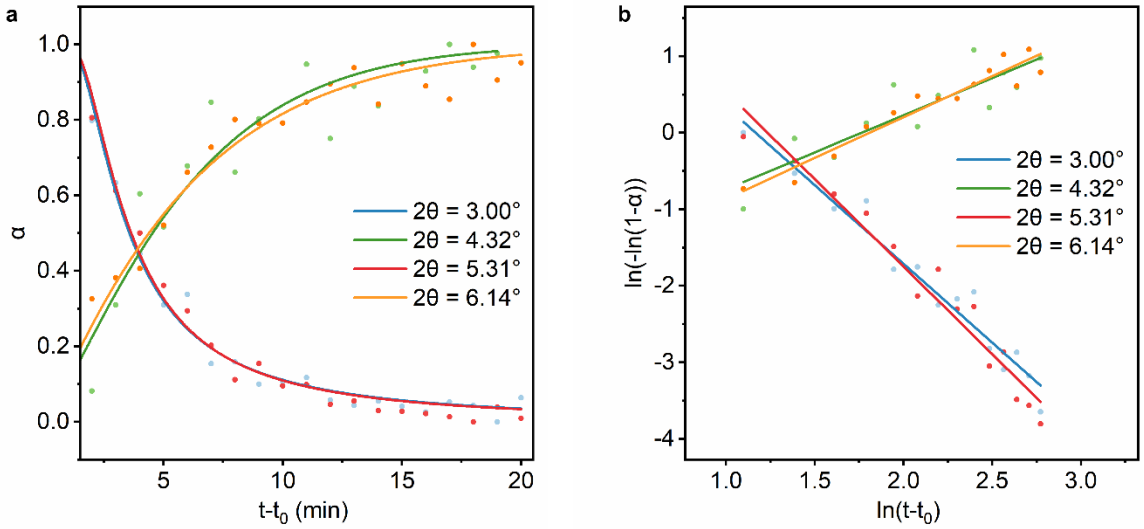

Figure 4.49 (a) Crystallization curve and Avrami fitting and (b) Sharp-Hancock plot and linear fitting for 2 µm Zr-NU-1200 in DMF:FA=2.5 at 140 °C.

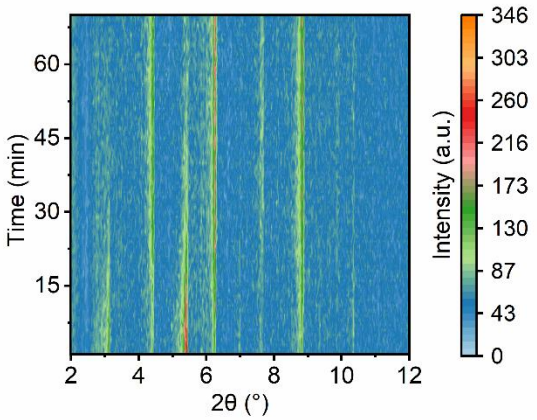

Figure 4.50 Time-resolved *in-situ* PXRD of 600 nm Zr-NU-1200 in DMF:FA=2.5 at 120 °C.

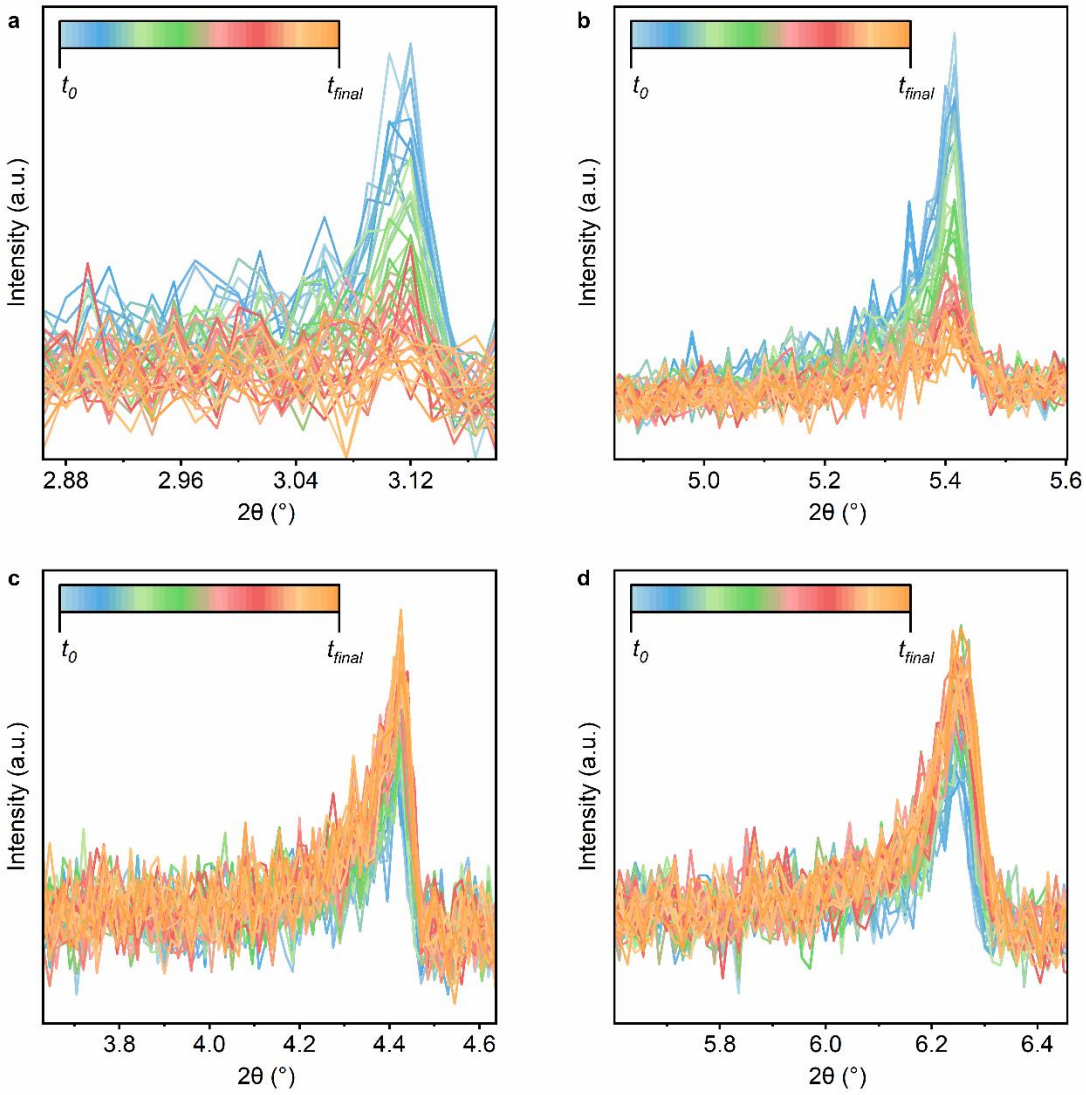

Figure 4.51 Time-resolved *in-situ* PXRD of the (a) ⟨100⟩, (b) ⟨111⟩, (c) ⟨110⟩, and (d) ⟨200⟩ Bragg features of 600 nm Zr-NU-1200 in DMF:FA=2.5 at 120 °C.

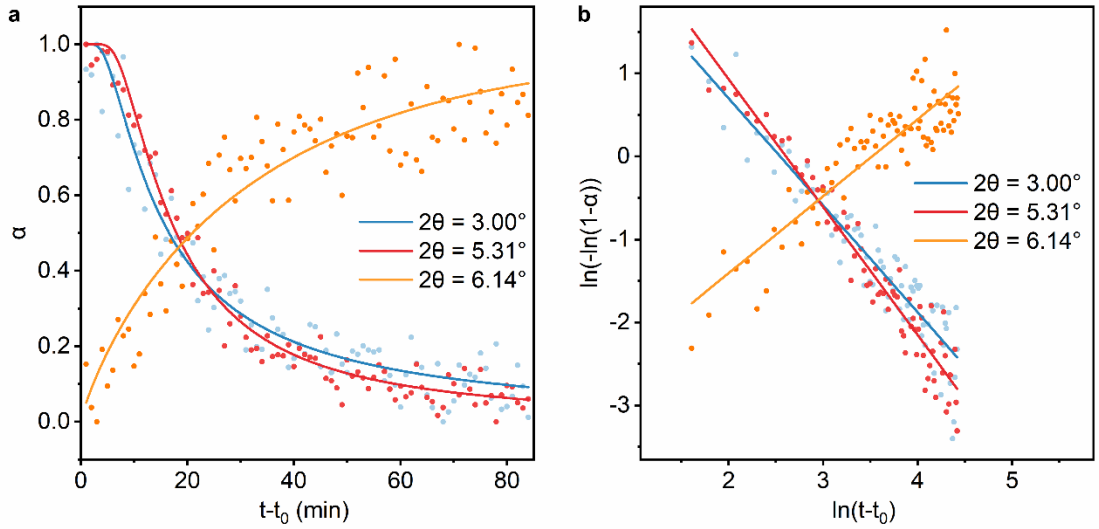

Figure 4.52 (a) Crystallization curve and Avrami fitting and (b) Sharp-Hancock plot and linear fitting for 600 nm Zr-NU-1200 in DMF:FA=2.5 at 120 °C.

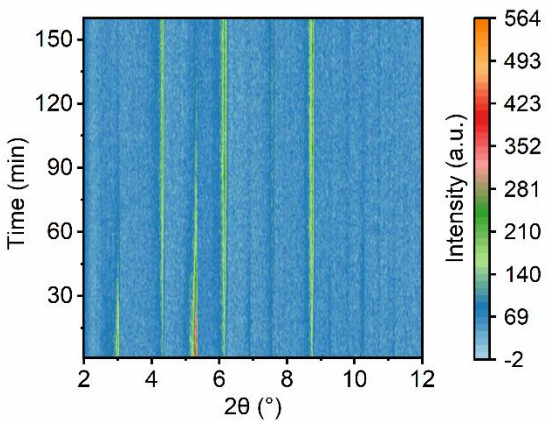

Figure 4.53 Time-resolved *in-situ* PXRD of 4 μm Zr-NU-1200 in DMF:FA=2.5 at 120 °C.

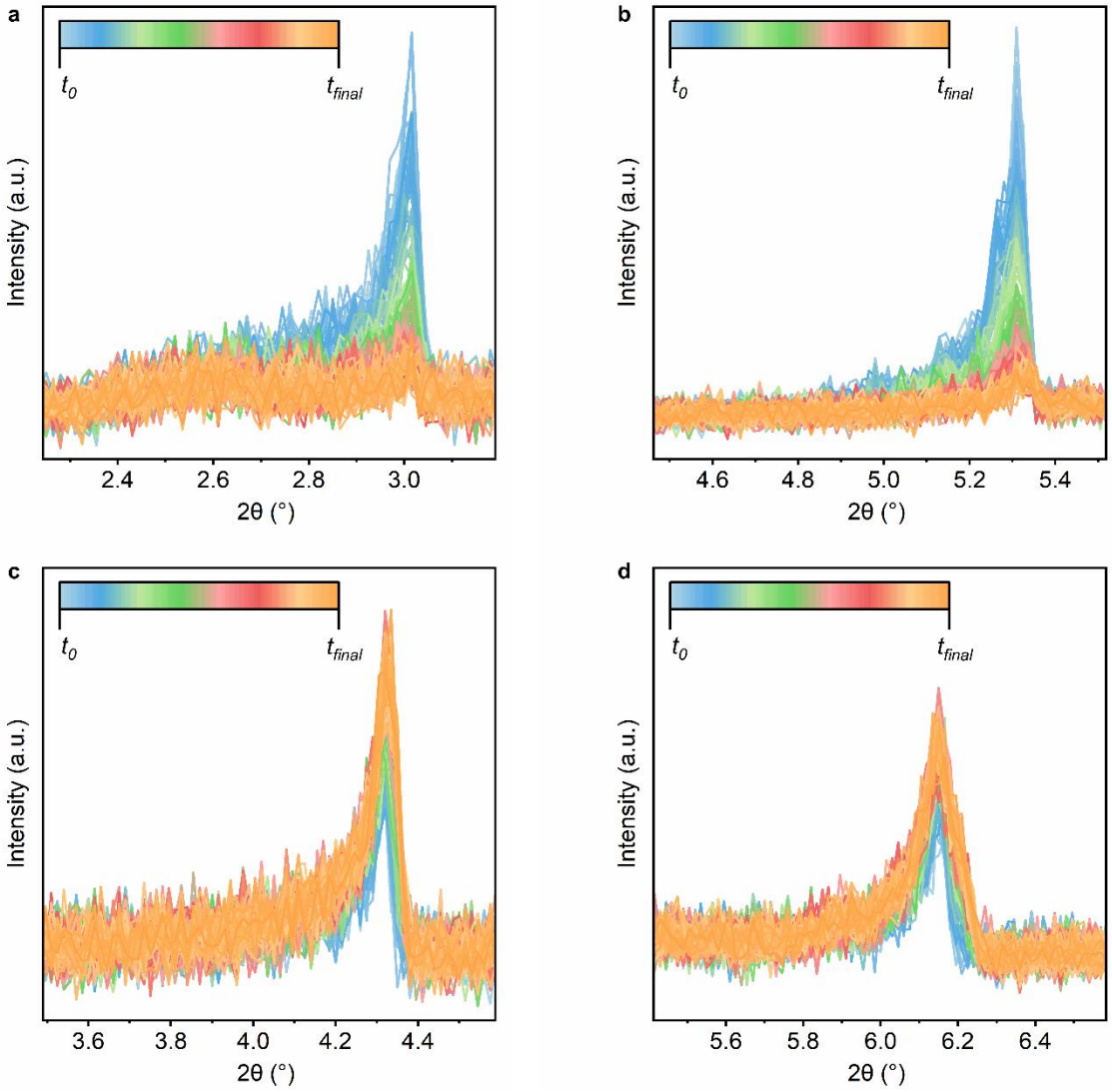

Figure 4.54 Time-resolved *in-situ* PXRD of the (a) ⟨100⟩, (b) ⟨111⟩, (c) ⟨110⟩, and (d) ⟨200⟩ Bragg features of 4 μm Zr-NU-1200 in DMF:FA=2.5 at 120 °C.

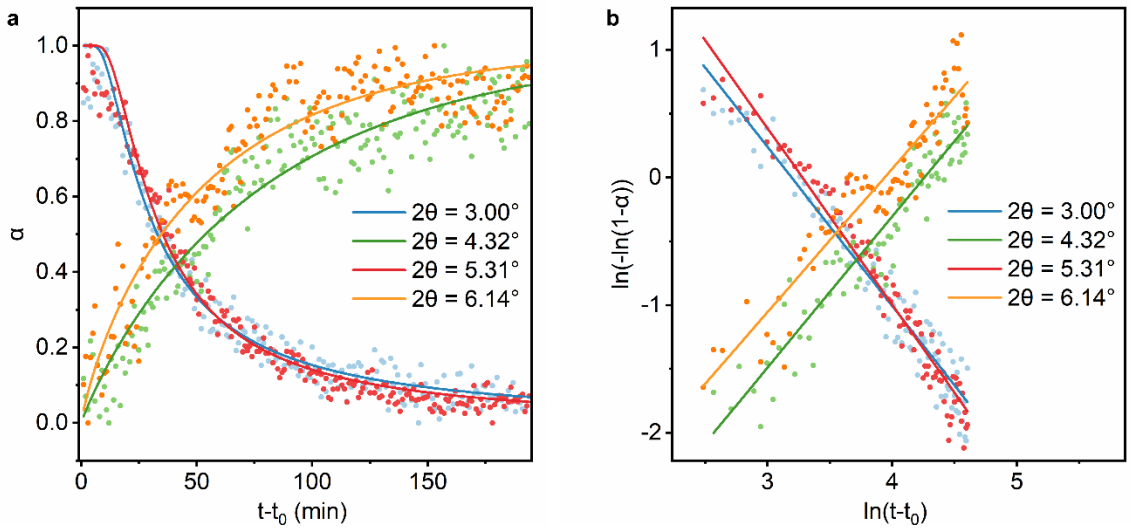

Figure 4.55 (a) Crystallization curve and Avrami fitting and (b) Sharp-Hancock plot and linear fitting for 4 μm Zr-NU-1200 in DMF:FA=2.5 at 120 °C.

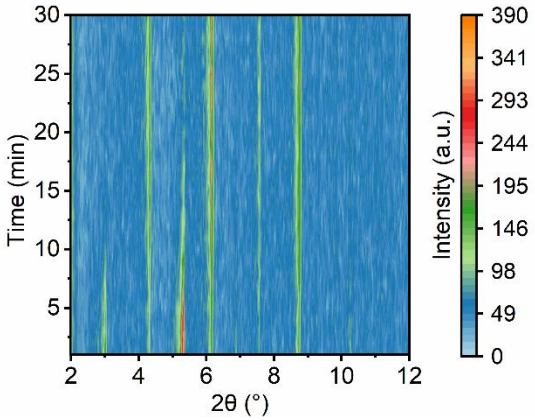

Figure 4.56 Time-resolved *in-situ* PXRD of 2 μm Zr-NU-1200 in DMF:FA=1.5 at 120 °C.

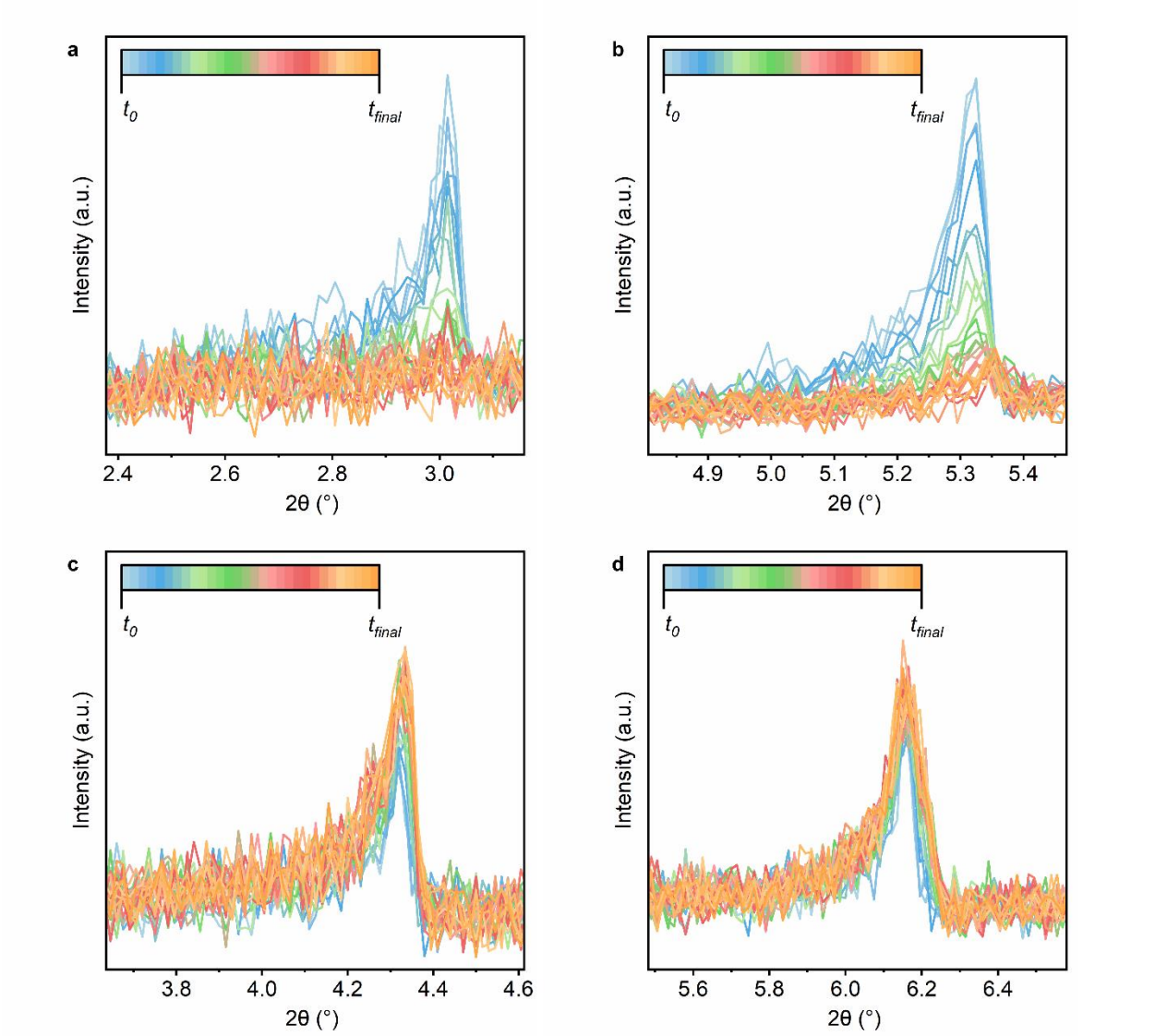

Figure 4.57 Time-resolved *in-situ* PXRD of the (a) ⟨100⟩, (b) ⟨111⟩, (c) ⟨110⟩, and (d) ⟨200⟩ Bragg features of 2 μm Zr-NU-1200 in DMF:FA=1.5 at 120 °C.

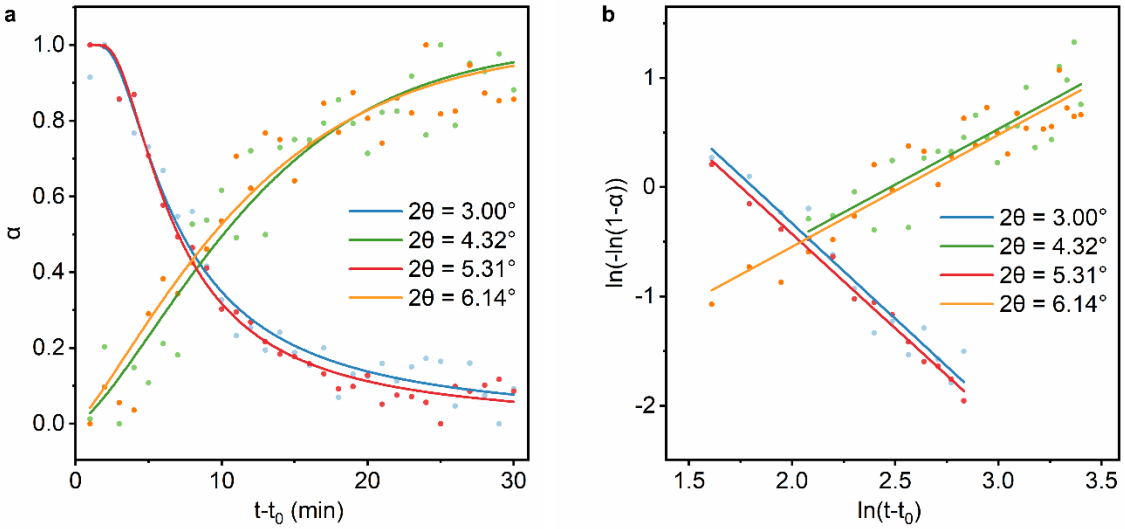

Figure 4.58 (a) Crystallization curve and Avrami fitting and (b) Sharp-Hancock plot and linear fitting for 2 μm Zr-NU-1200 in DMF:FA=1.5 at 120 °C.

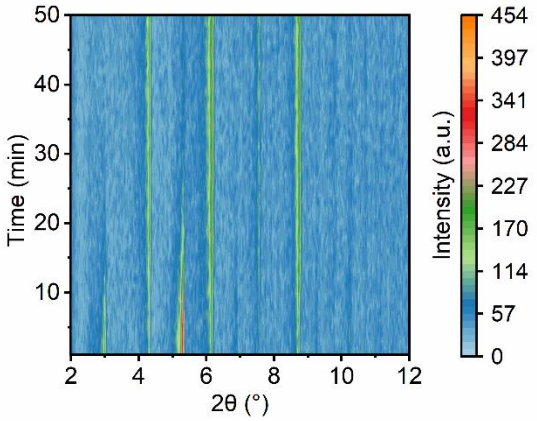

Figure 4.59 Time-resolved *in-situ* PXRD of 2 μm Zr-NU-1200 in DMF:FA=2 at 120 °C.

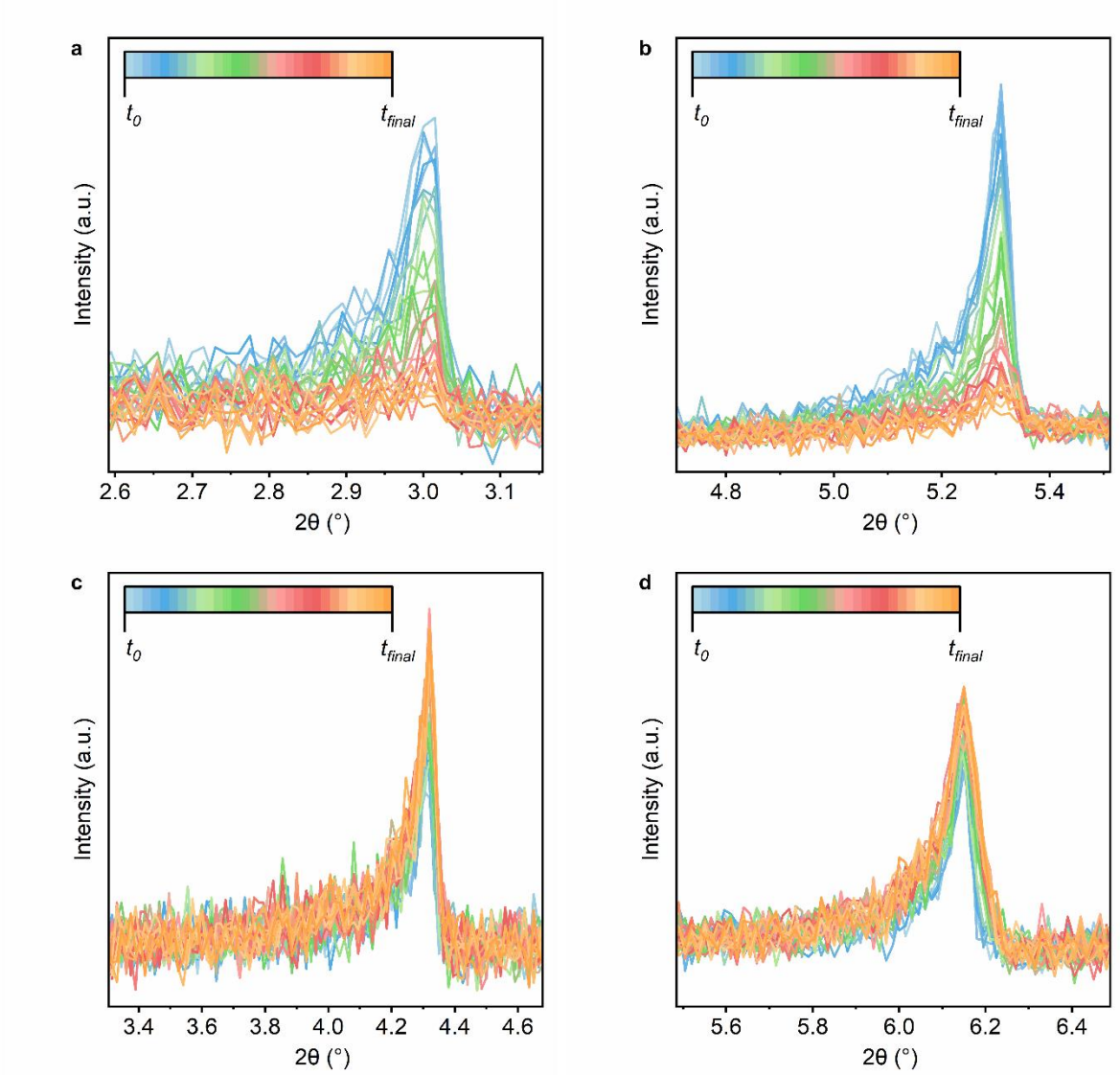

Figure 4.60 Time-resolved *in-situ* PXRD of the (a) ⟨100⟩, (b) ⟨111⟩, (c) ⟨110⟩, and (d) ⟨200⟩ Bragg features of 2 μm Zr-NU-1200 in DMF:FA=2 at 120 °C.

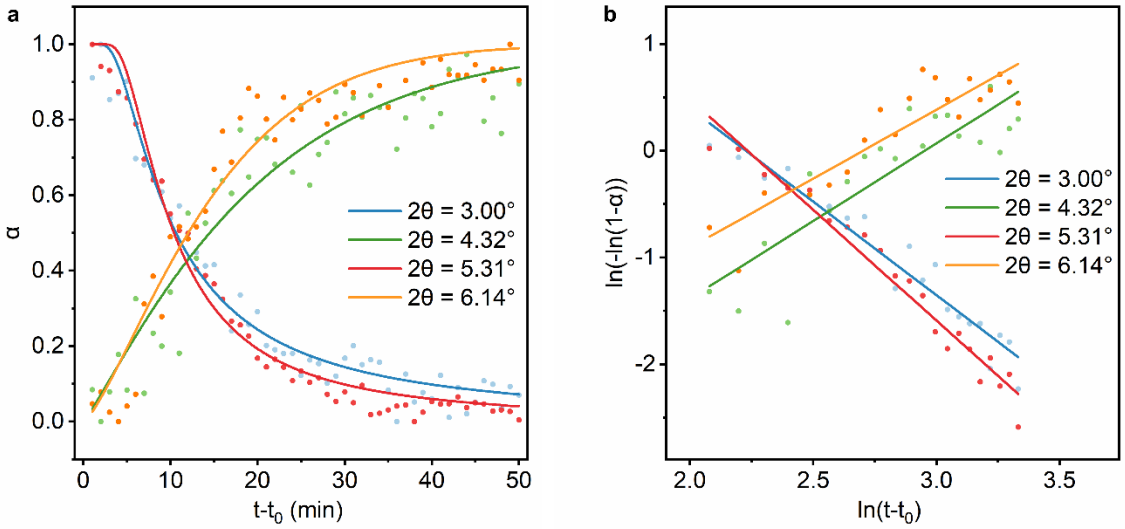

Figure 4.61 (a) Crystallization curve and Avrami fitting and (b) Sharp-Hancock plot and linear fitting for 2 µm Zr-NU-1200 in DMF:FA=2 at 120 °C.

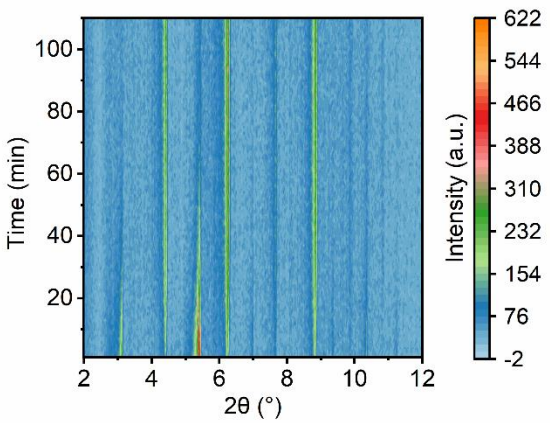

Figure 4.62 Time-resolved *in-situ* PXRD of 2 μm Zr-NU-1200 in DMF:FA=3 at 120 °C.

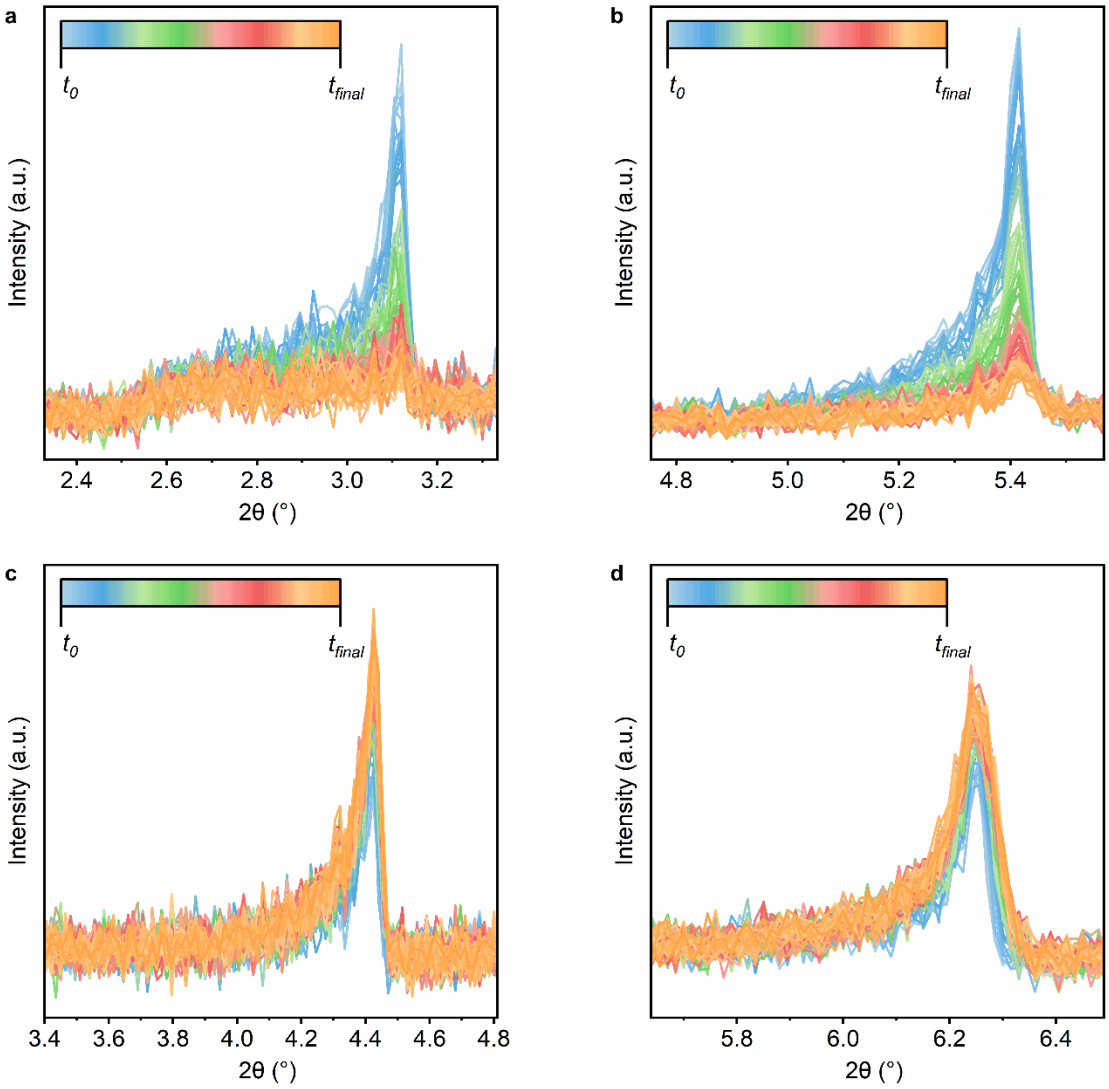

Figure 4.63 Time-resolved *in-situ* PXRD of the (a) ⟨100⟩, (b) ⟨111⟩, (c) ⟨110⟩, and (d) ⟨200⟩ Bragg features of 2 μm Zr-NU-1200 in DMF:FA=3 at 120 °C.

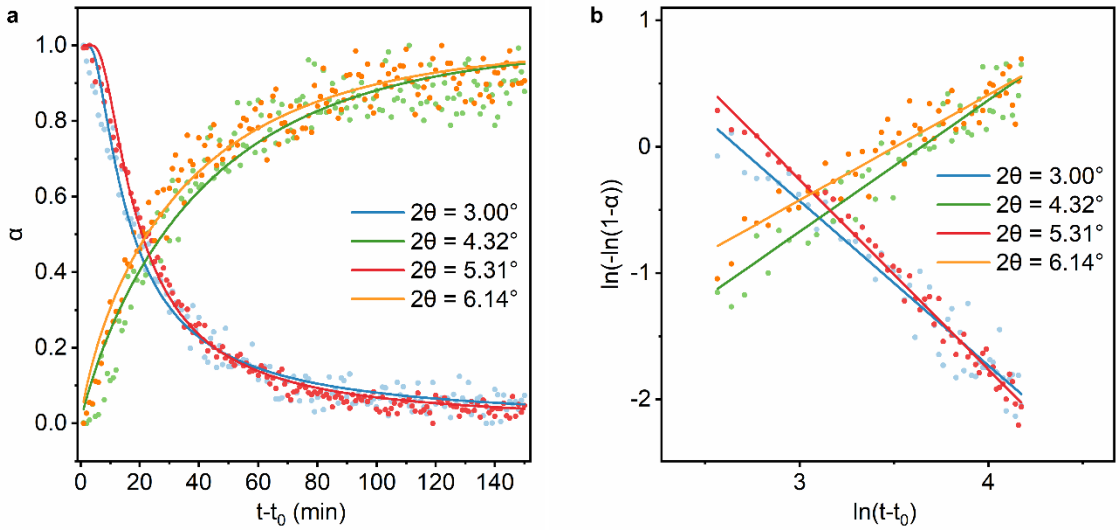

Figure 4.64 (a) Crystallization curve and Avrami fitting and (b) Sharp-Hancock plot and linear fitting for 2 μm Zr-NU-1200 in DMF:FA=3 at 120 °C.

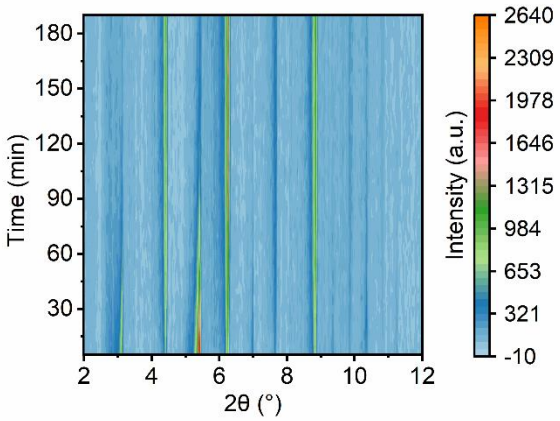

Figure 4.65 Time-resolved *in-situ* PXRD of 2 μm Zr-NU-1200 in DMF:FA=3.5 at 120 °C.

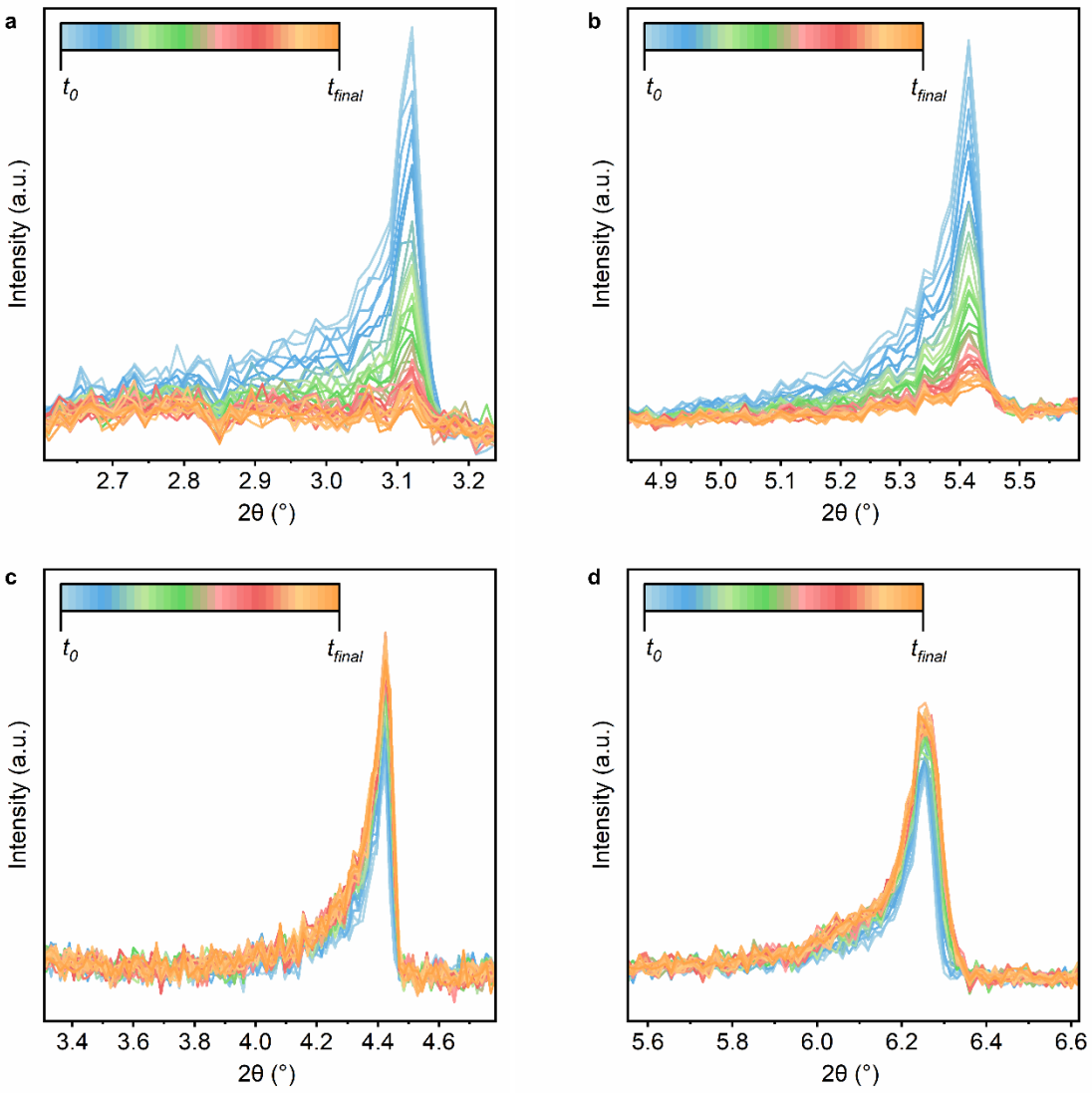

Figure 4.66 Time-resolved *in-situ* PXRD of the (a) ⟨100⟩, (b) ⟨111⟩, (c) ⟨110⟩, and (d) ⟨200⟩ Bragg features of 2 μm Zr-NU-1200 in DMF:FA=3.5 at 120 °C.

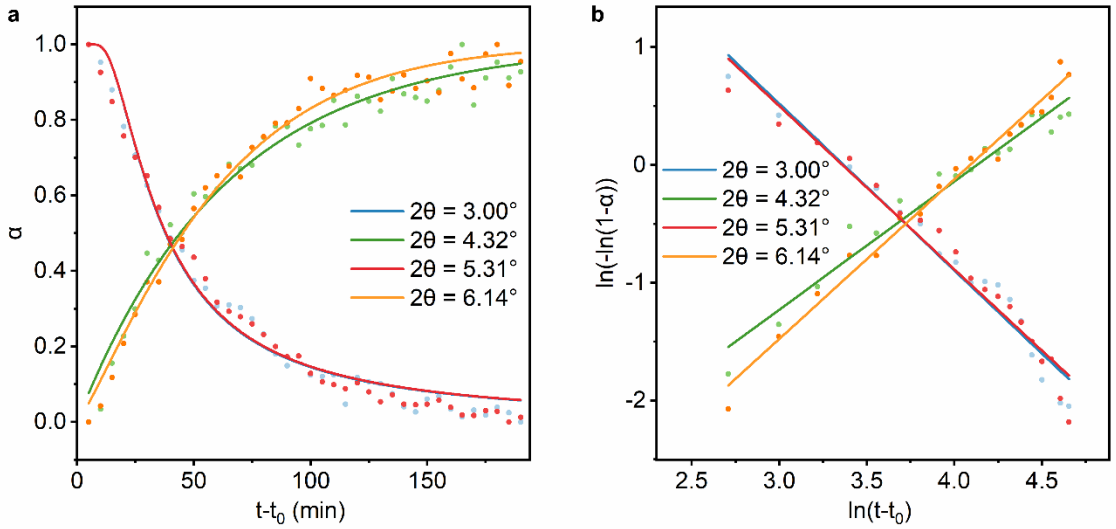

Figure 4.67 (a) Crystallization curve and Avrami fitting and (b) Sharp-Hancock plot and linear fitting for 2 µm Zr-NU-1200 in DMF:FA=3.5 at 120 °C.

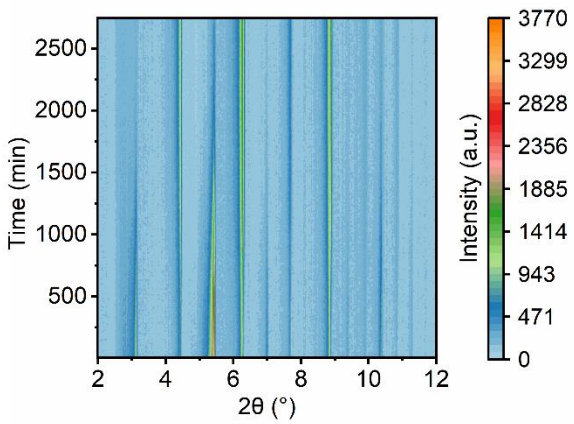

Figure 4.68 Time-resolved *in-situ* PXRD of 2 μm Hf-NU-1200 in DMF:FA=2.5 at 80 °C.

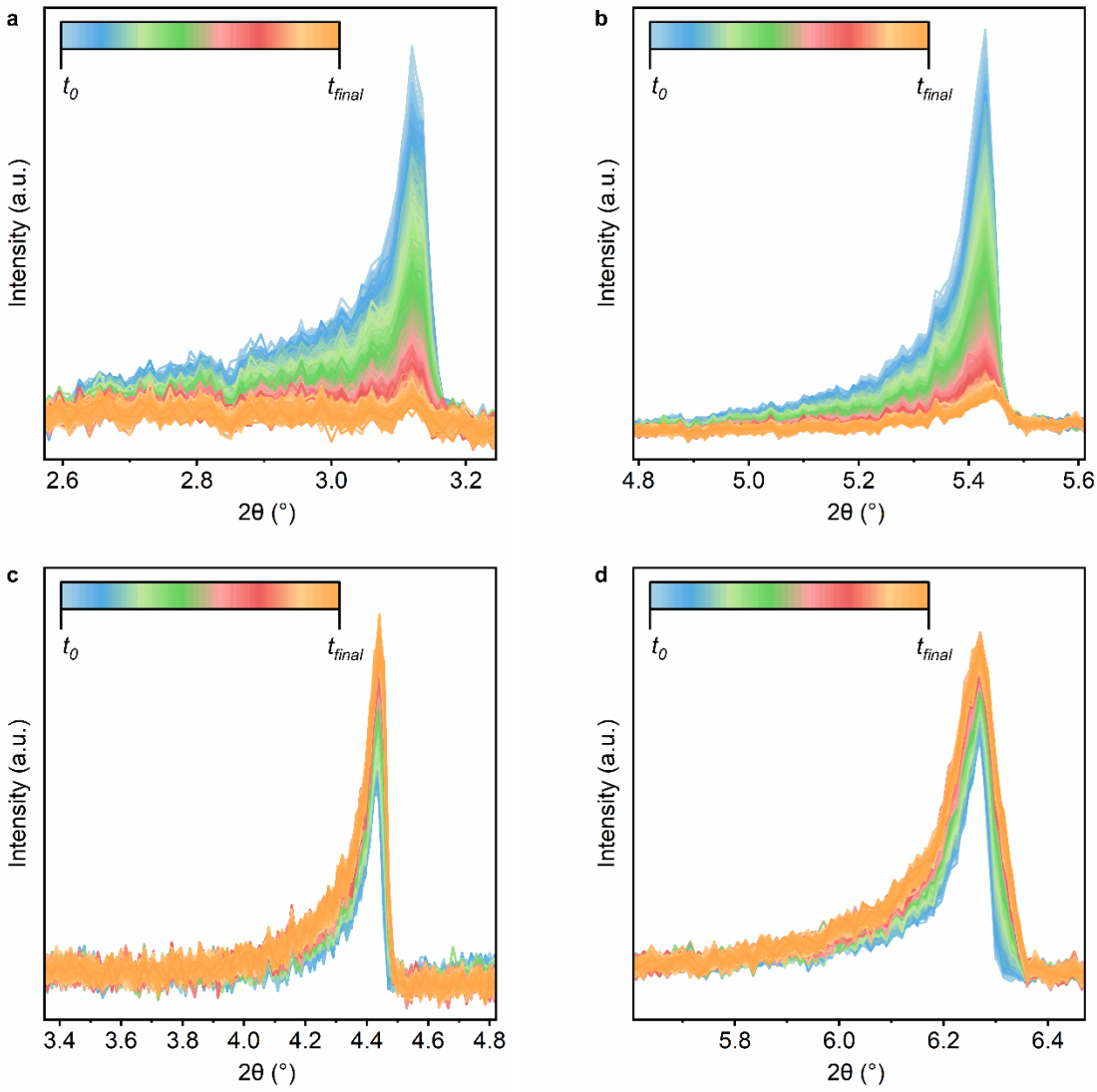

Figure 4.69 Time-resolved *in-situ* PXRD of the (a) ⟨100⟩, (b) ⟨111⟩, (c) ⟨110⟩, and (d) ⟨200⟩ Bragg features of 2 μm Hf -NU-1200 in DMF:FA=2.5 at 80 °C.

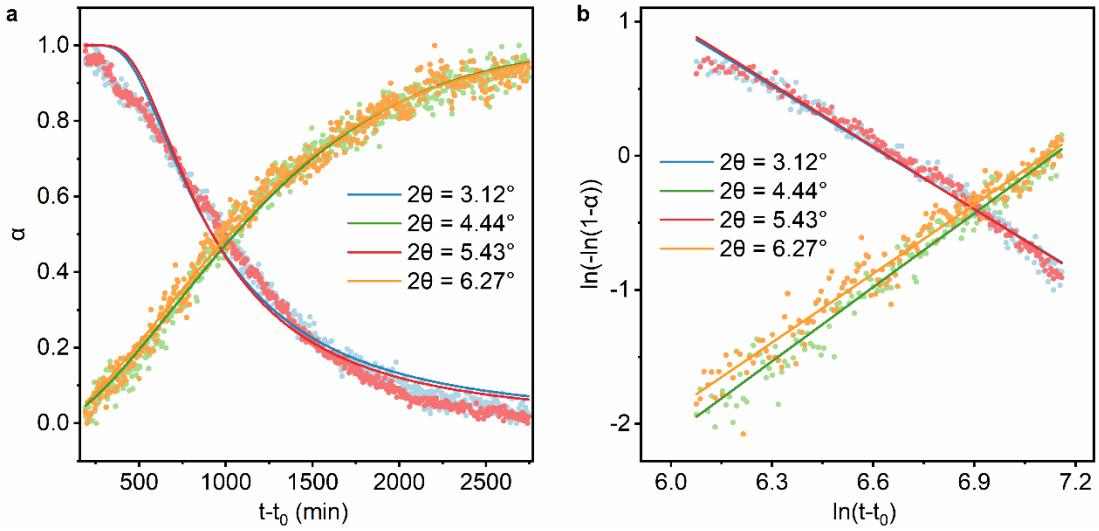

Figure 4.70 (a) Crystallization curve and Avrami fitting and (b) Sharp-Hancock plot and linear fitting for 2 µm Hf -NU-1200 in DMF:FA=2.5 at 80 °C.

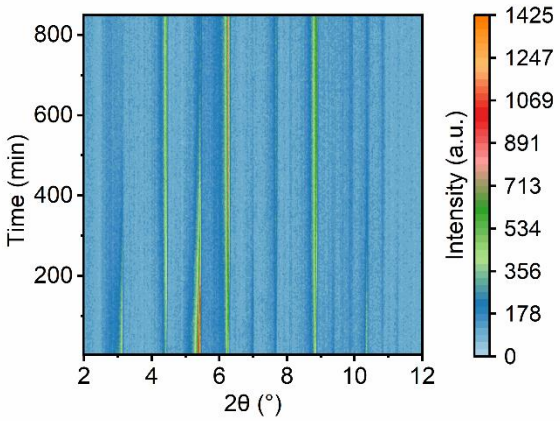

Figure 4.71 Time-resolved *in-situ* PXRD of 2 μm Hf-NU-1200 in DMF:FA=2.5 at 90 °C.

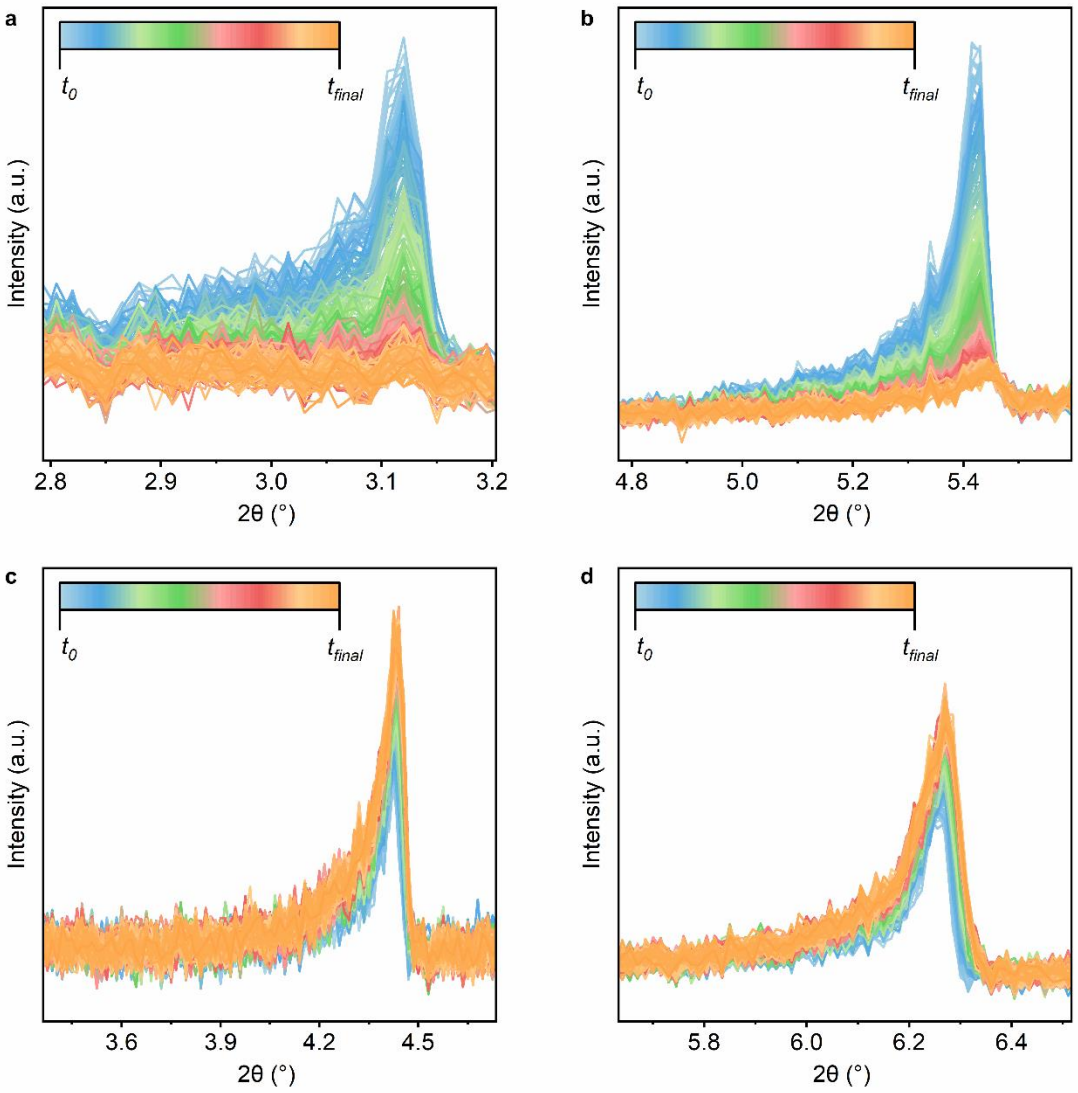

Figure 4.72 Time-resolved *in-situ* PXRD of the (a) ⟨100⟩, (b) ⟨111⟩, (c) ⟨110⟩, and (d) ⟨200⟩ Bragg features of 2 μm Hf-NU-1200 in DMF:FA=2.5 at 90 °C.

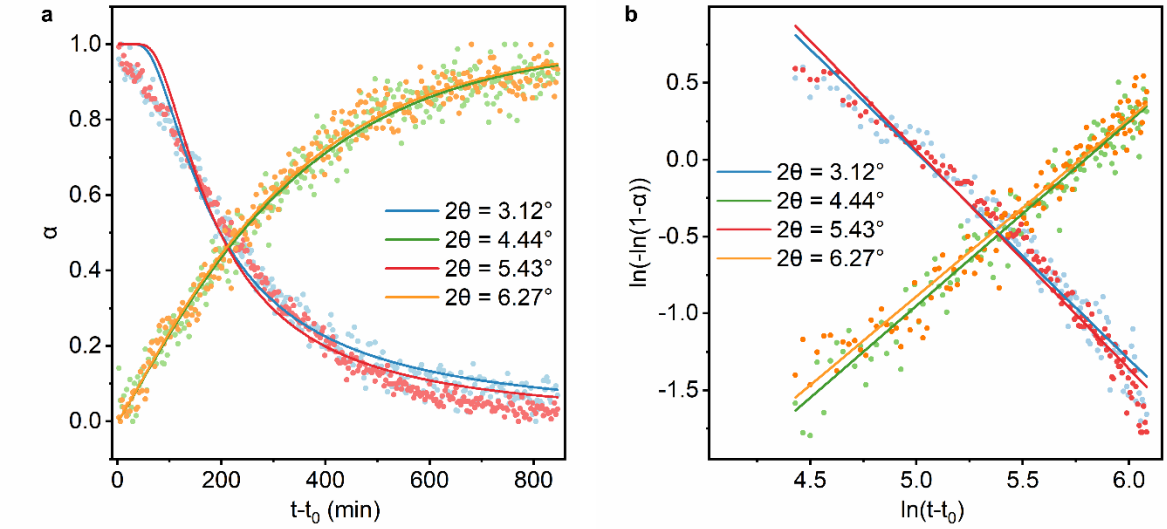

Figure 4.73 (a) Crystallization curve and Avrami fitting and (b) Sharp-Hancock plot and linear fitting for 2 µm Hf-NU-1200 in DMF:FA=2.5 at 90 °C.

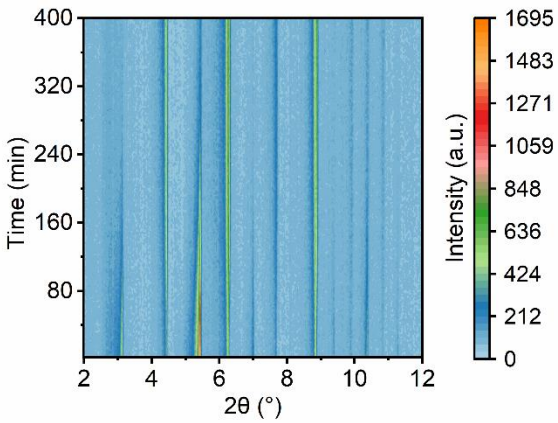

Figure 4.74 Time-resolved *in-situ* PXRD of 2 μm Hf-NU-1200 in DMF:FA=2.5 at 100 °C.

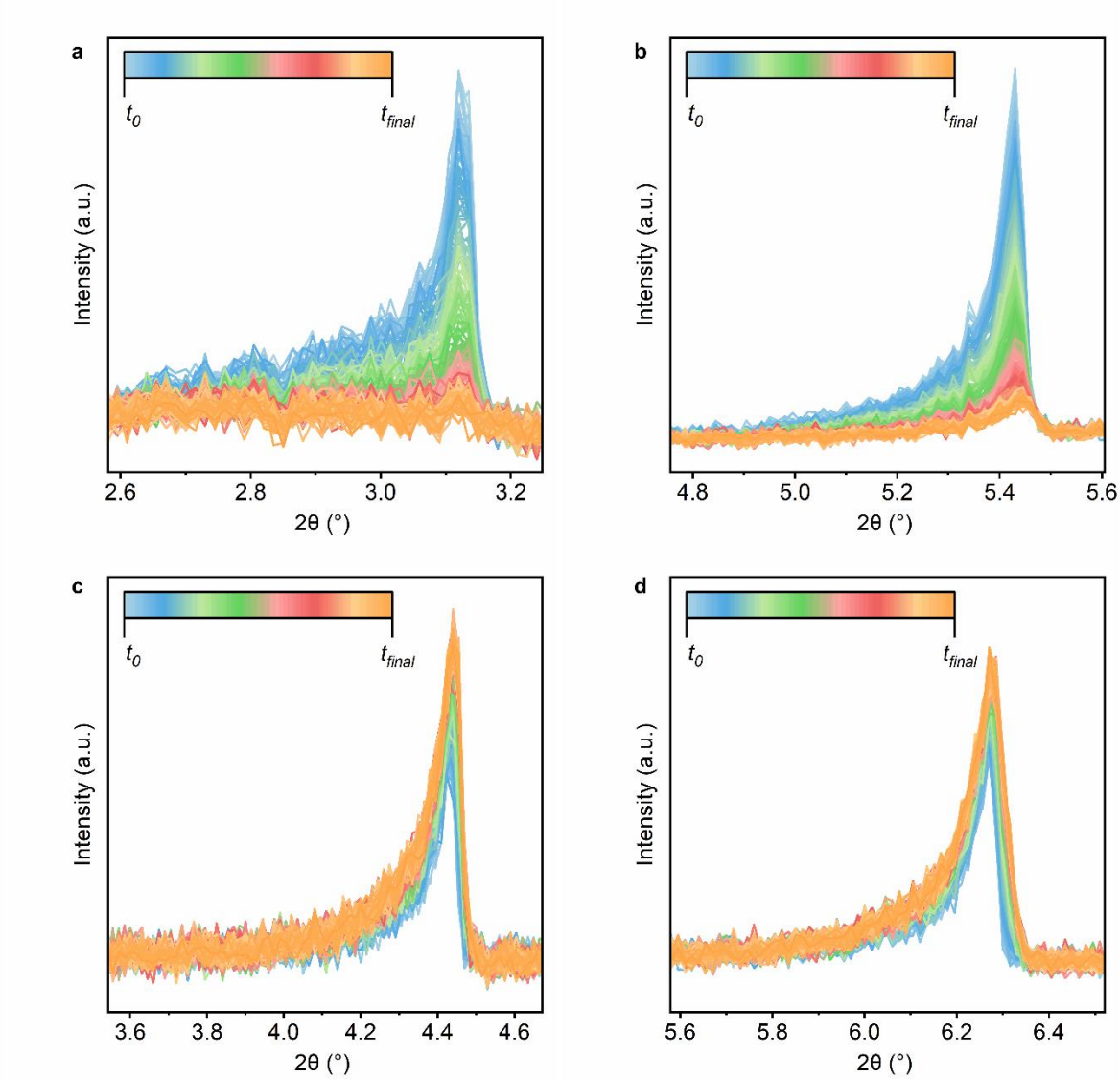

Figure 4.75 Time-resolved *in-situ* PXRD of the (a) ⟨100⟩, (b) ⟨111⟩, (c) ⟨110⟩, and (d) ⟨200⟩ Bragg features of 2 μm Hf-NU-1200 in DMF:FA=2.5 at 100 °C.

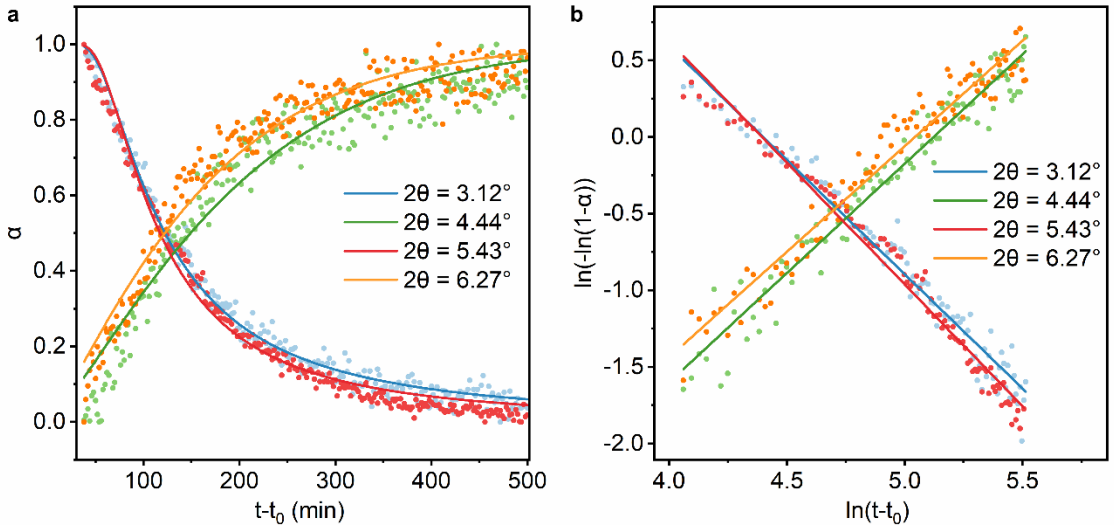

Figure 4.76 (a) Crystallization curve and Avrami fitting and (b) Sharp-Hancock plot and linear fitting for 2 μm Hf-NU-1200 in DMF:FA=2.5 at 100 °C.

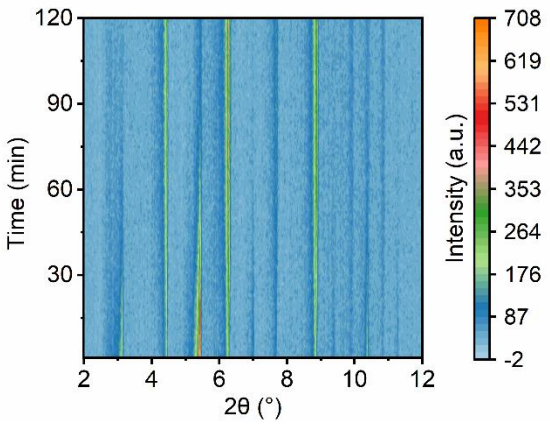

Figure 4.77 Time-resolved *in-situ* PXRD of 2 μm Hf-NU-1200 in DMF:FA=2.5 at 110 °C.

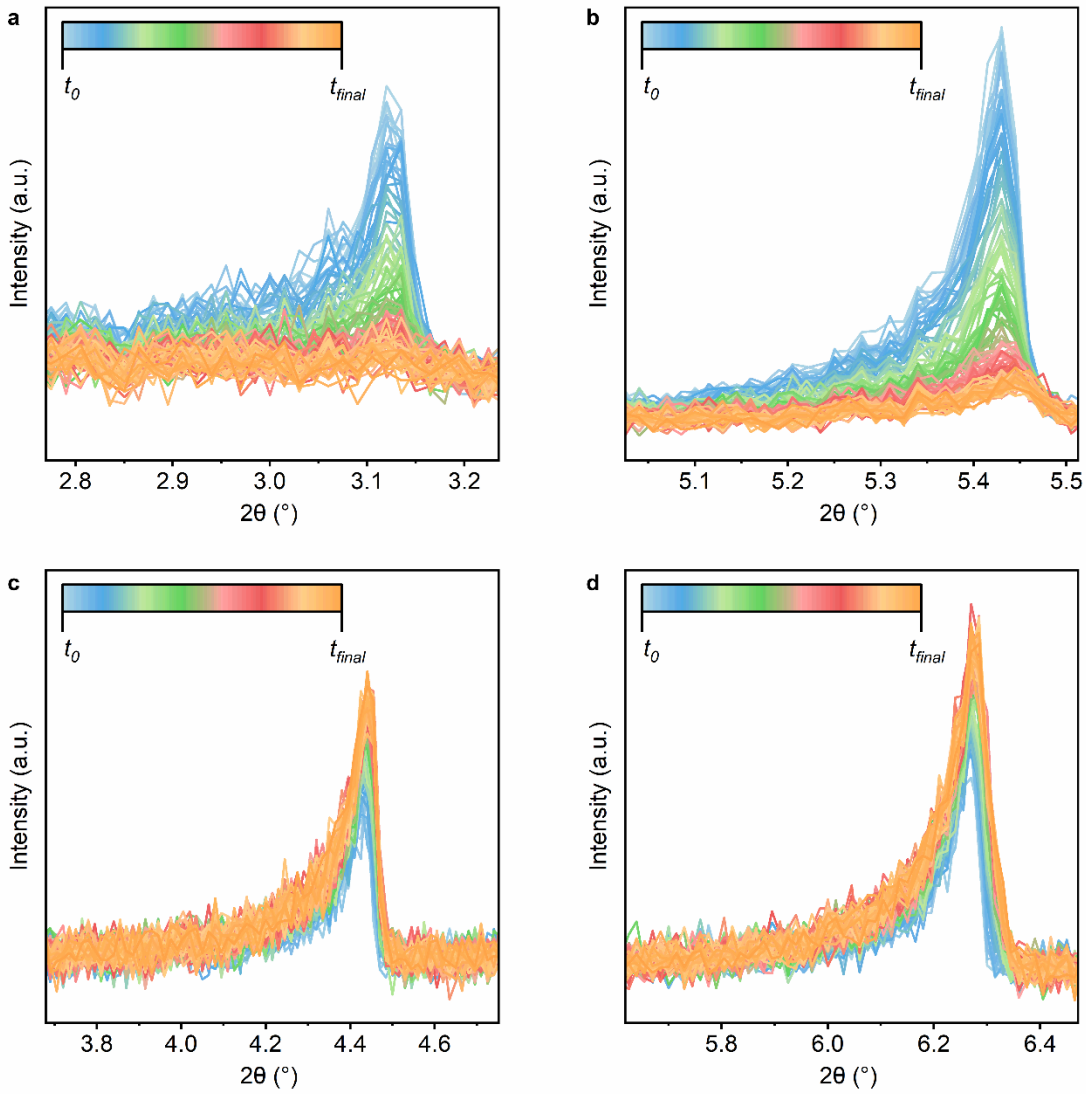

Figure 4.78 Time-resolved *in-situ* PXRD of the (a) ⟨100⟩, (b) ⟨111⟩, (c) ⟨110⟩, and (d) ⟨200⟩ Bragg features of 2 μm Hf-NU-1200 in DMF:FA=2.5 at 110 °C.

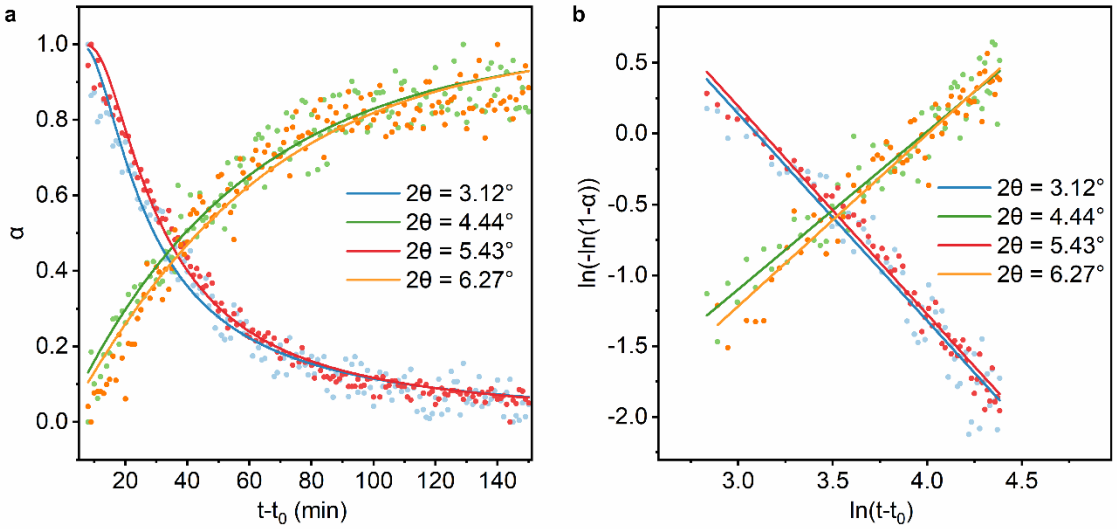

Figure 4.79 (a) Crystallization curve and Avrami fitting and (b) Sharp-Hancock plot and linear fitting for 2 μm Hf-NU-1200 in DMF:FA=2.5 at 110 °C.

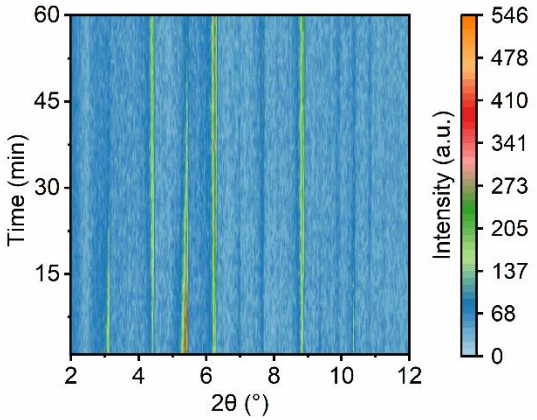

Figure 4.80 Time-resolved *in-situ* PXRD of 2 μm Hf-NU-1200 in DMF:FA=2.5 at 120 °C.

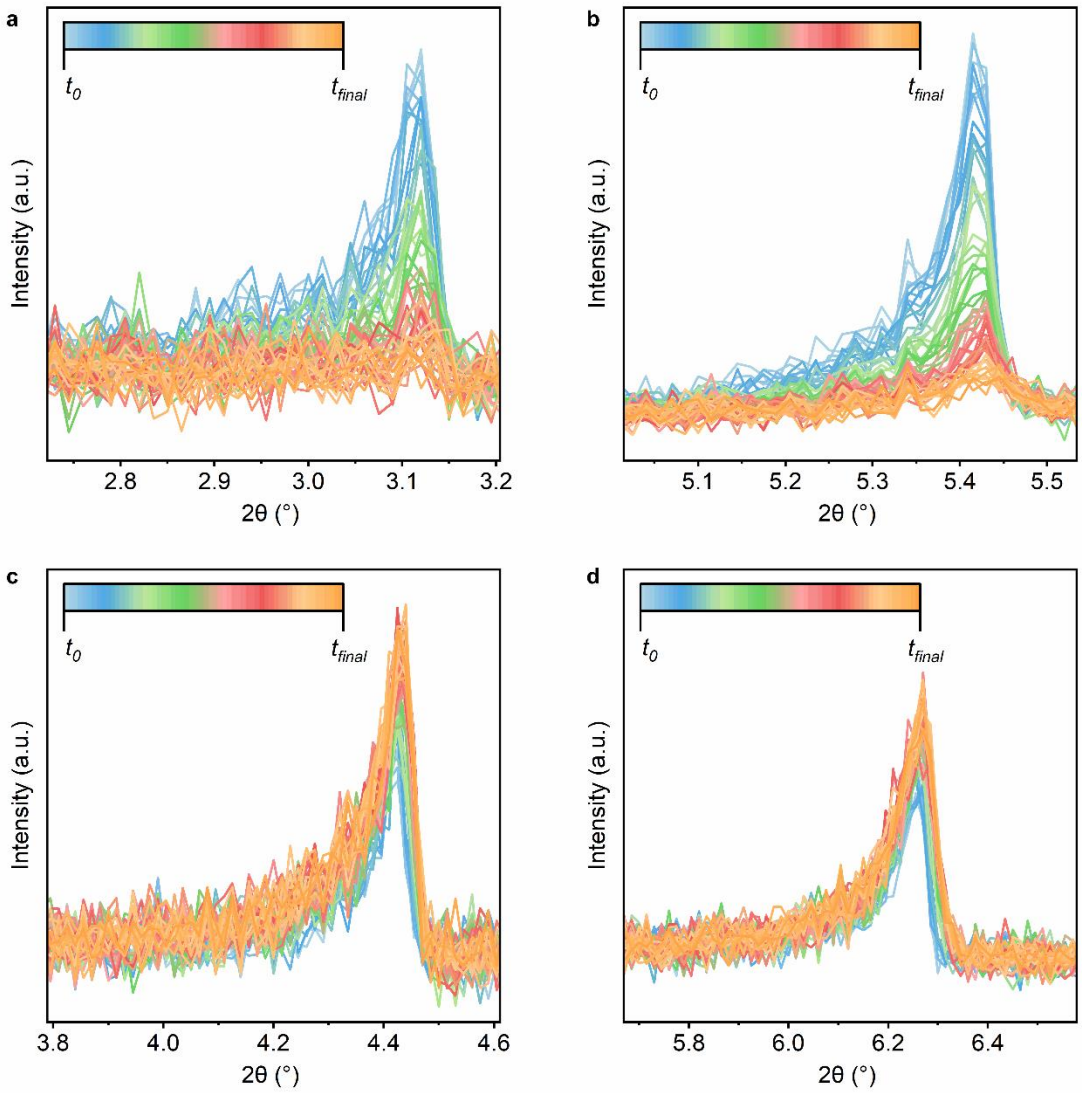

Figure 4.81 Time-resolved *in-situ* PXRD of the (a) ⟨100⟩, (b) ⟨111⟩, (c) ⟨110⟩, and (d) ⟨200⟩ Bragg features of 2 μm Hf-NU-1200 in DMF:FA=2.5 at 120 °C.

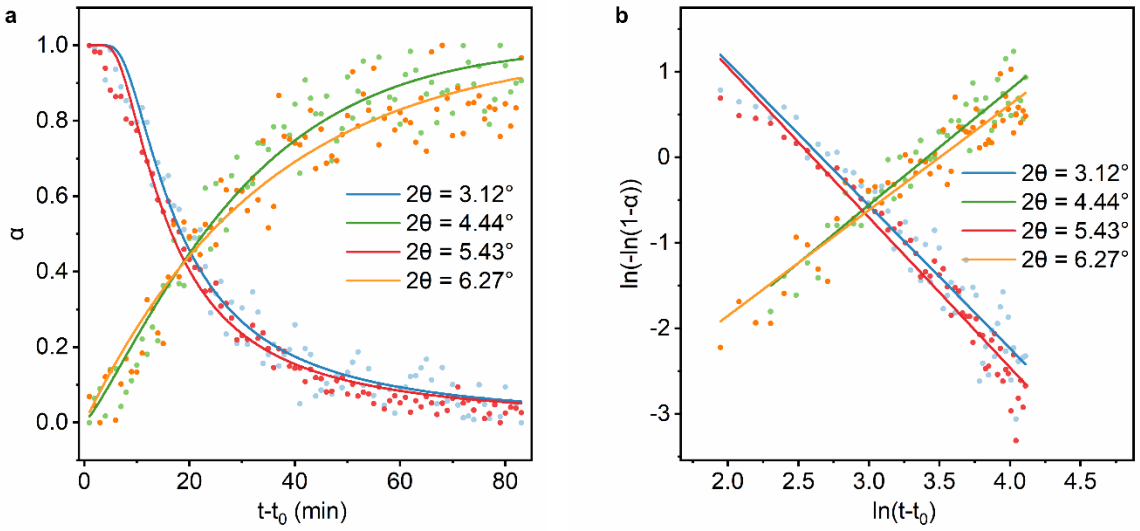

Figure 4.82 (a) Crystallization curve and Avrami fitting and (b) Sharp-Hancock plot and linear fitting for 2 μm Hf-NU-1200 in DMF:FA=2.5 at 120 °C.

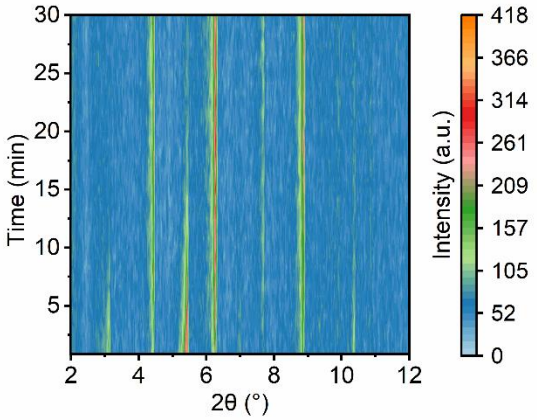

Figure 4.83 Time-resolved *in-situ* PXRD of 2 μm Hf-NU-1200 in DMF:FA=2.5 at 130 °C.

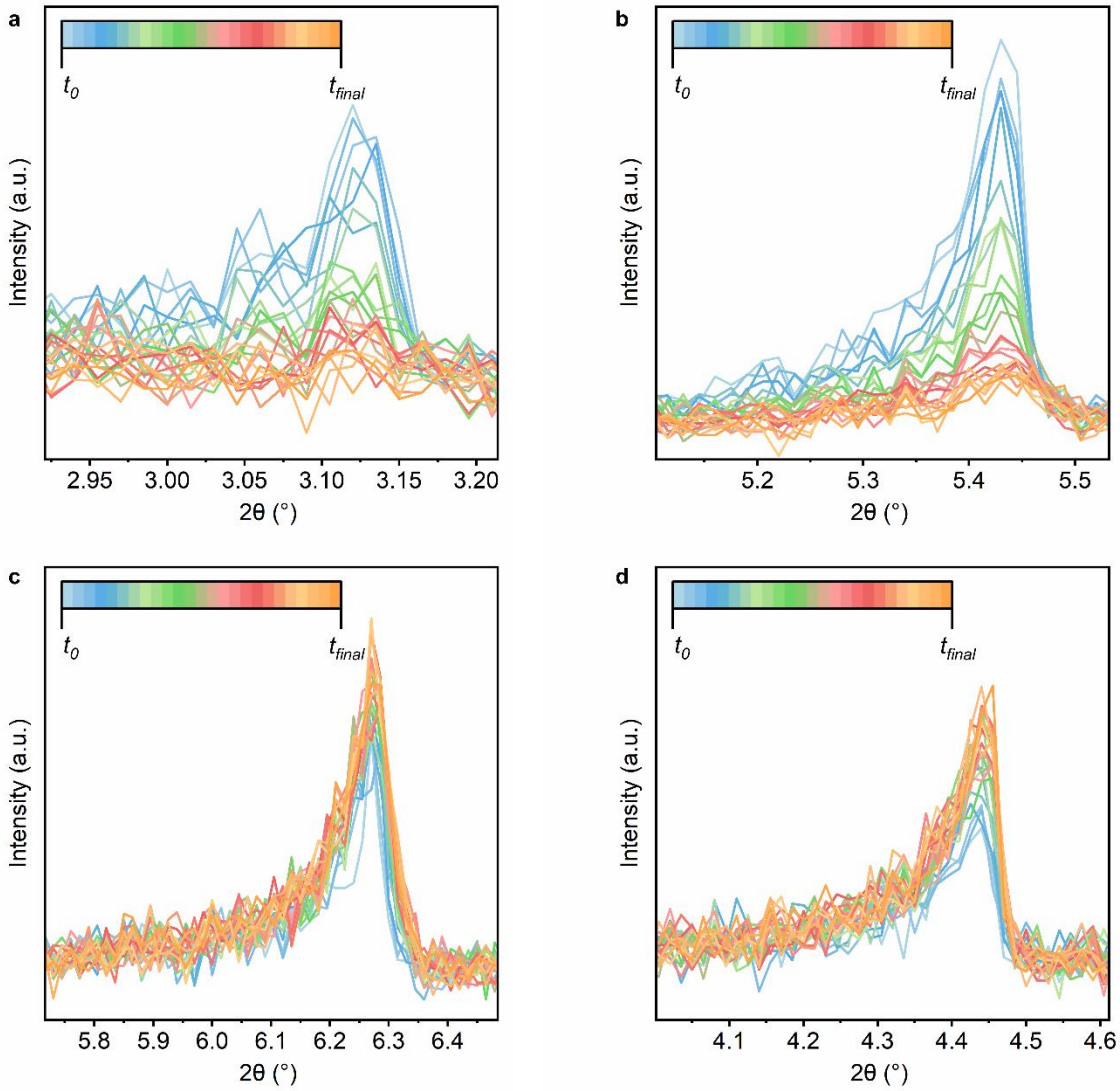

Figure 4.84 Time-resolved *in-situ* PXRD of the (a) ⟨100⟩, (b) ⟨111⟩, (c) ⟨110⟩, and (d) ⟨200⟩ Bragg features of 2 μm Hf-NU-1200 in DMF:FA=2.5 at 130 °C.

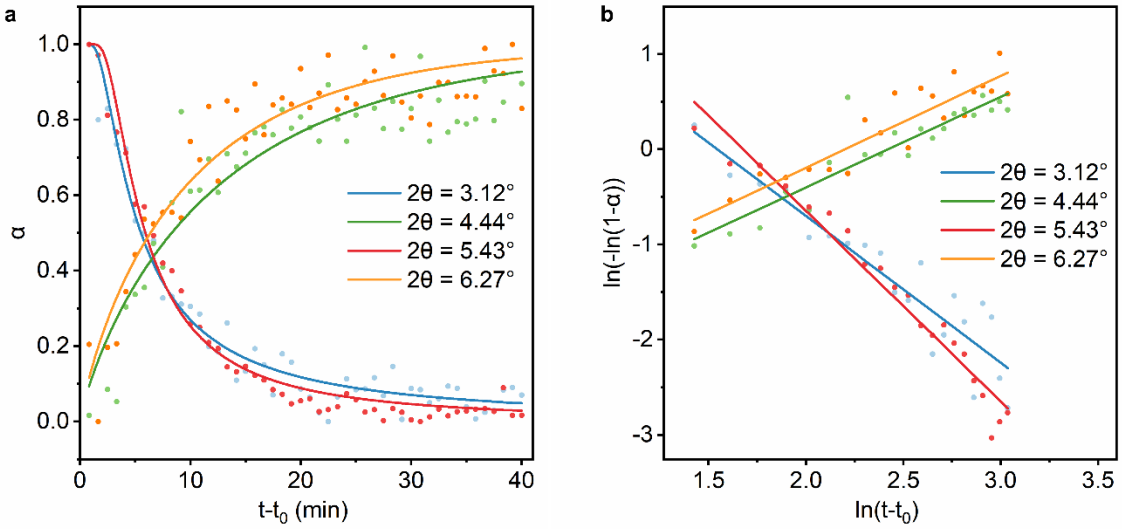

Figure 4.85 (a) Crystallization curve and Avrami fitting and (b) Sharp-Hancock plot and linear fitting for 2 µm Hf-NU-1200 in DMF:FA=2.5 at 130 °C.

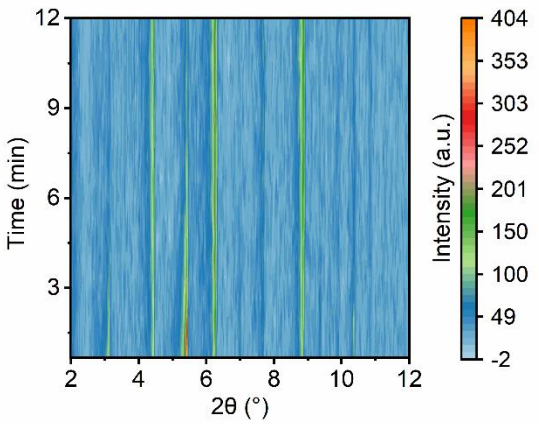

Figure 4.86 Time-resolved *in-situ* PXRD of 2 μm Hf-NU-1200 in DMF:FA=2.5 at 140 °C.

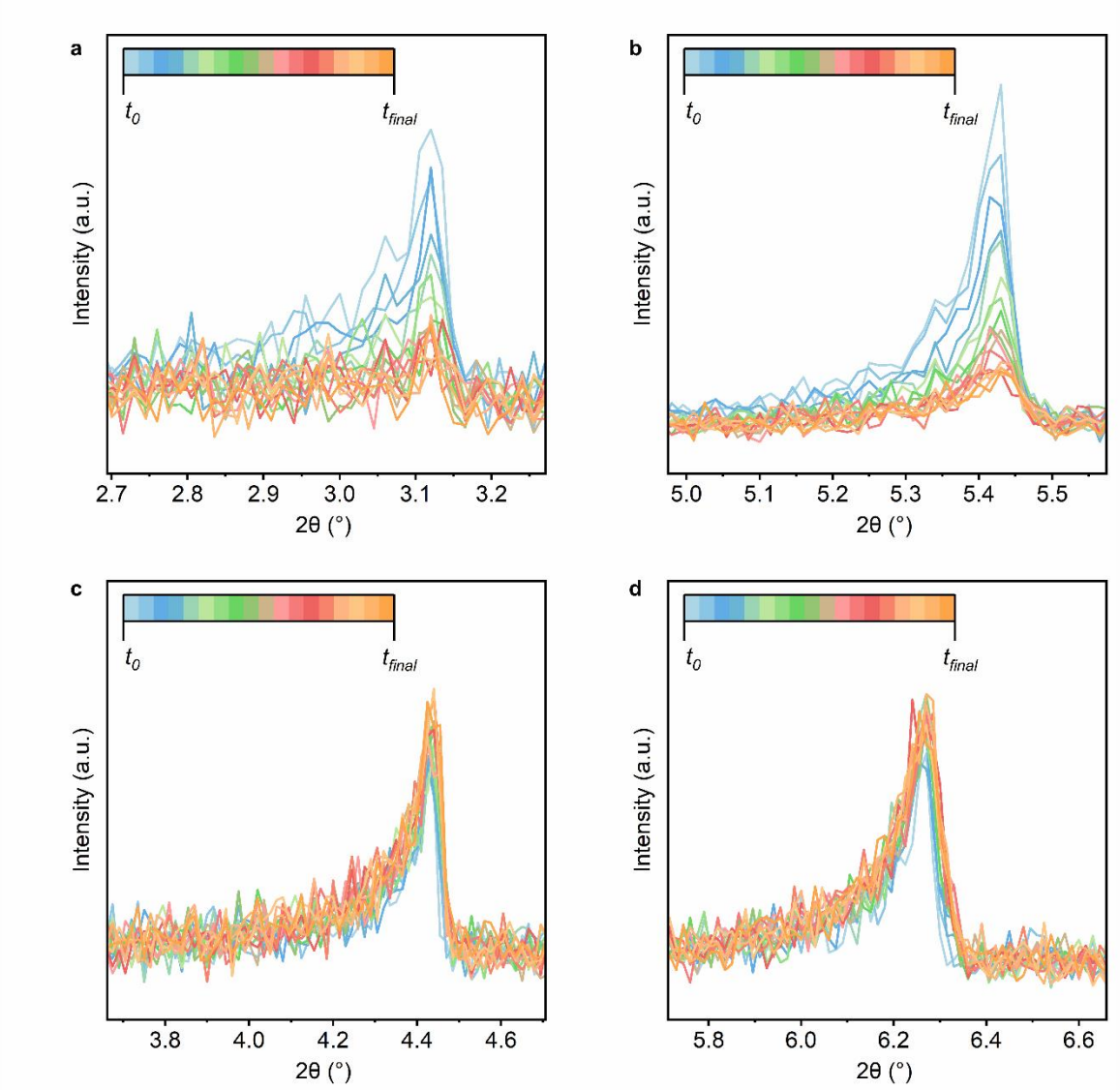

Figure 4.87 Time-resolved *in-situ* PXRD of the (a) ⟨100⟩, (b) ⟨111⟩, (c) ⟨110⟩, and (d) ⟨200⟩ Bragg features of 2 μm Hf-NU-1200 in DMF:FA=2.5 at 140 °C.

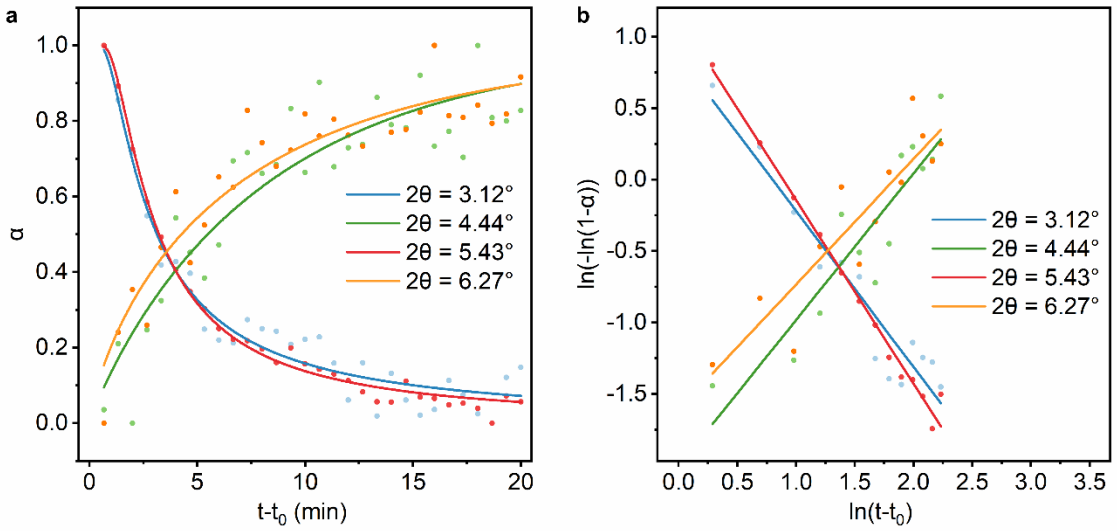

Figure 4.88 (a) Crystallization curve and Avrami fitting and (b) Sharp-Hancock plot and linear fitting for 2 μm Hf-NU-1200 in DMF:FA=2.5 at 140 °C.

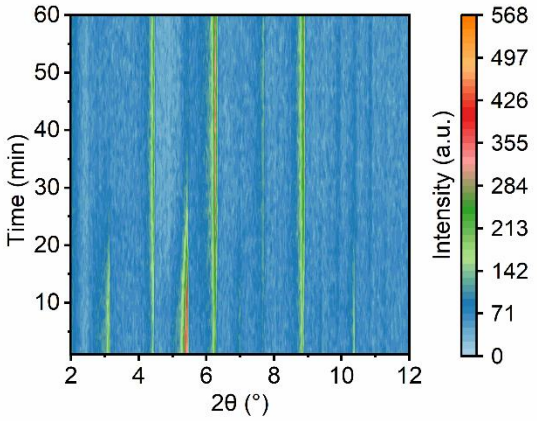

Figure 4.89 Time-resolved *in-situ* PXRD of 600 nm Hf-NU-1200 in DMF:FA=2.5 at 120 °C.

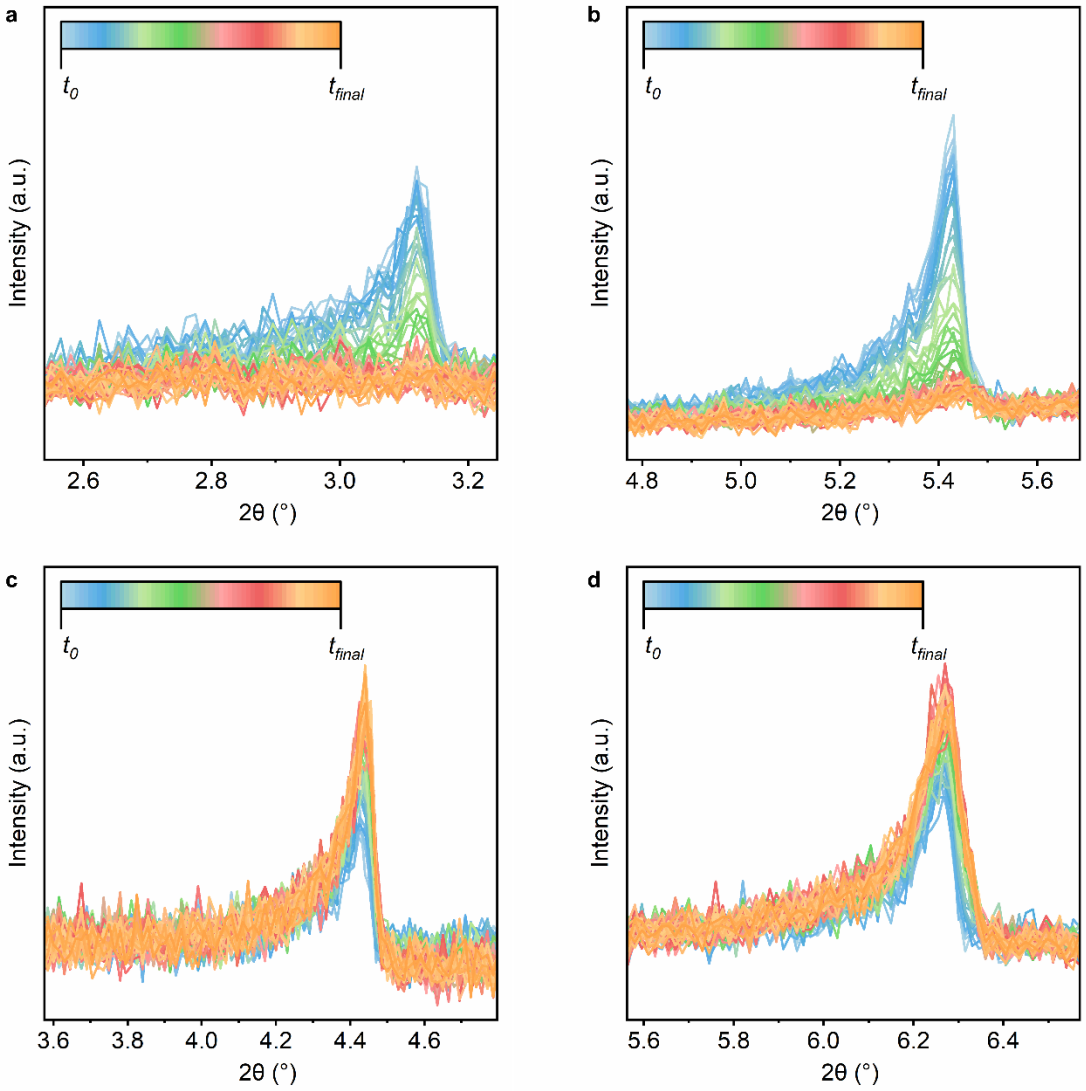

Figure 4.90 Time-resolved *in-situ* PXRD of the (a) ⟨100⟩, (b) ⟨111⟩, (c) ⟨110⟩, and (d) ⟨200⟩ Bragg features of 600 nm Hf-NU-1200 in DMF:FA=2.5 at 120 °C.

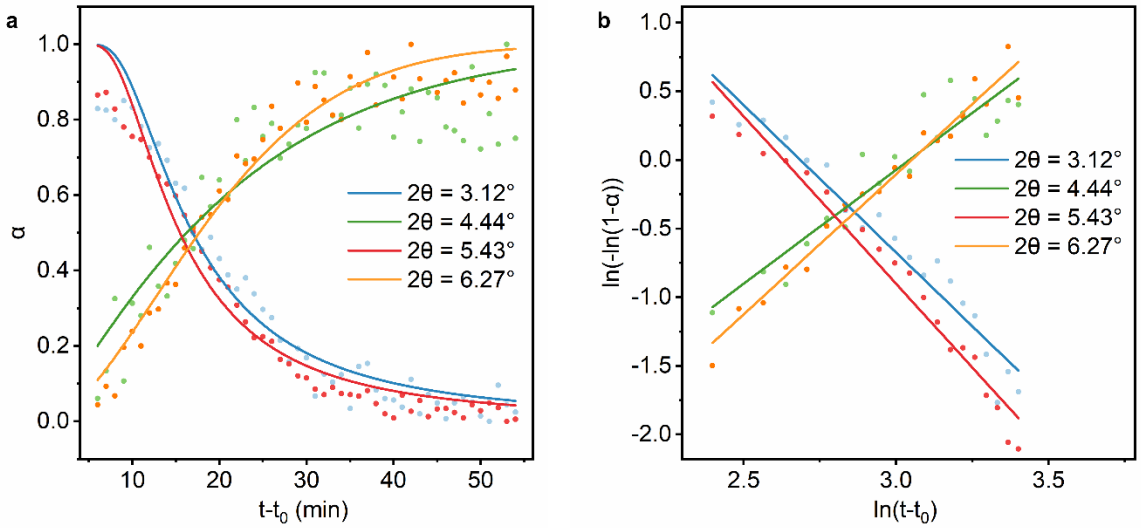

Figure 4.91 (a) Crystallization curve and Avrami fitting and (b) Sharp-Hancock plot and linear fitting for 600 nm Hf-NU-1200 in DMF:FA=2.5 at 120 °C.

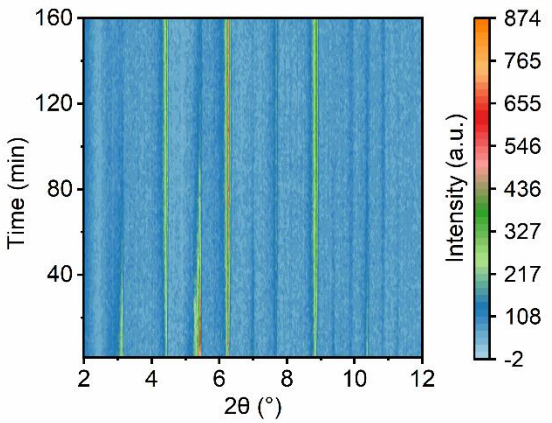

Figure 4.92 Time-resolved *in-situ* PXRD of 4 μm Hf-NU-1200 in DMF:FA=2.5 at 120 °C.

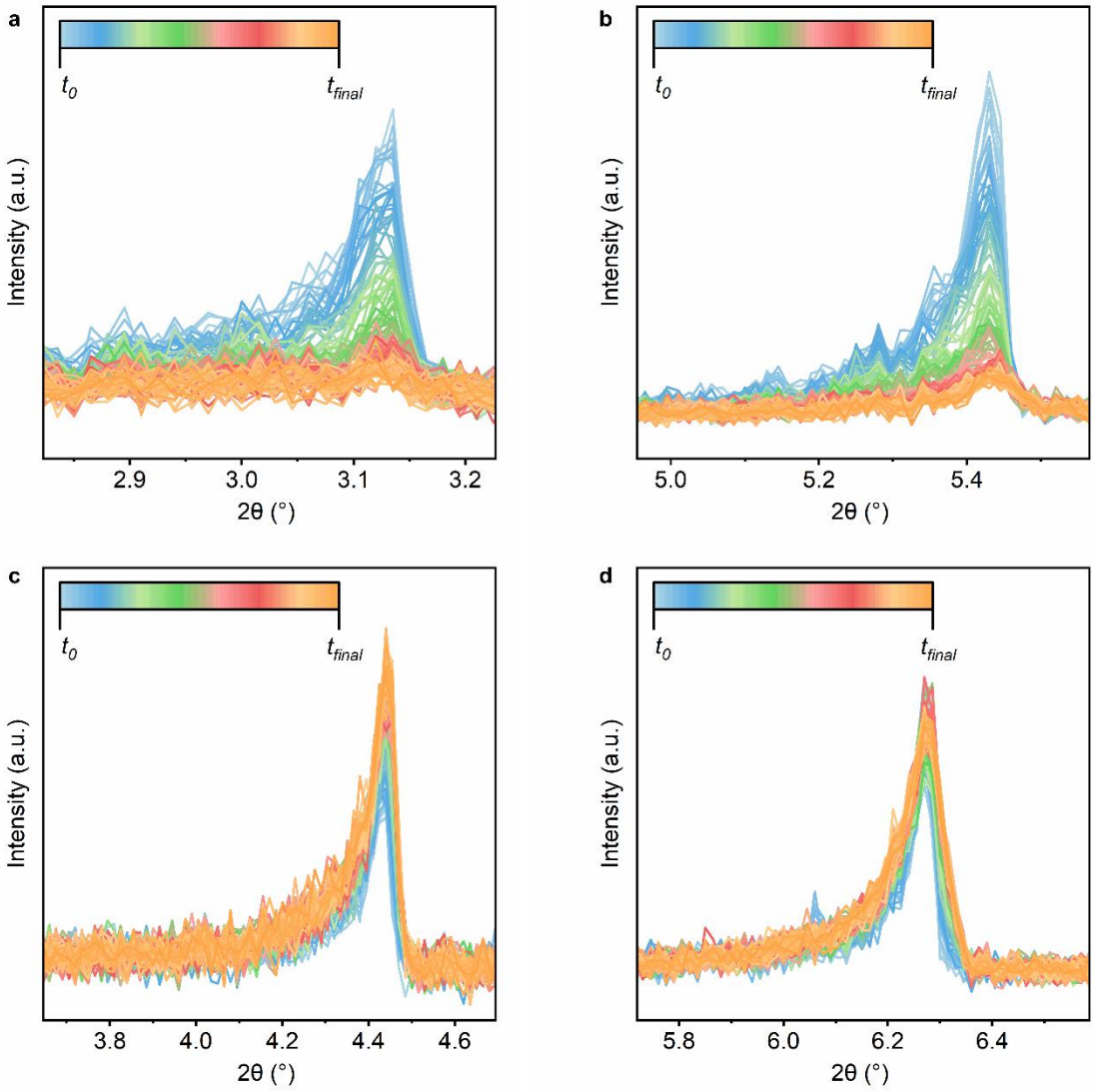

Figure 4.93 Time-resolved *in-situ* PXRD of the (a) ⟨100⟩, (b) ⟨111⟩, (c) ⟨110⟩, and (d) ⟨200⟩ Bragg features of 4 μm Hf-NU-1200 in DMF:FA=2.5 at 120 °C.

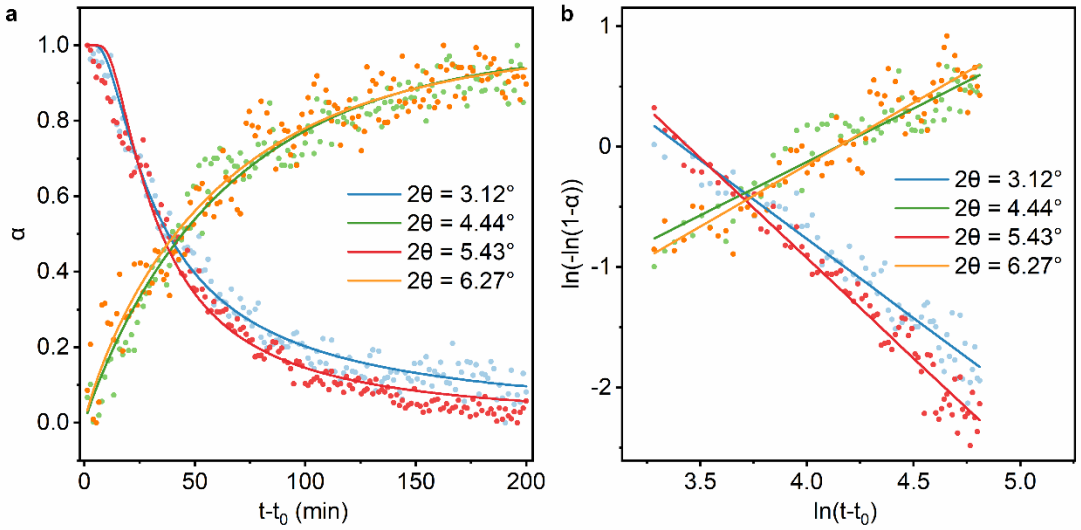

Figure 4.94 (a) Crystallization curve and Avrami fitting and (b) Sharp-Hancock plot and linear fitting for 4 μm Hf-NU-1200 in DMF:FA=2.5 at 120 °C.

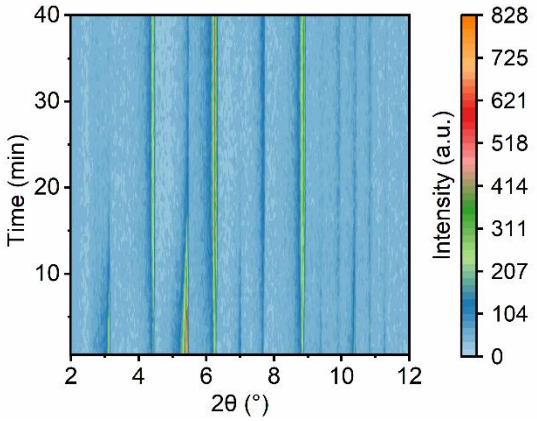

Figure 4.95 Time-resolved *in-situ* PXRD of 2 μm Hf-NU-1200 in DMF:FA=1.5 at 120 °C.

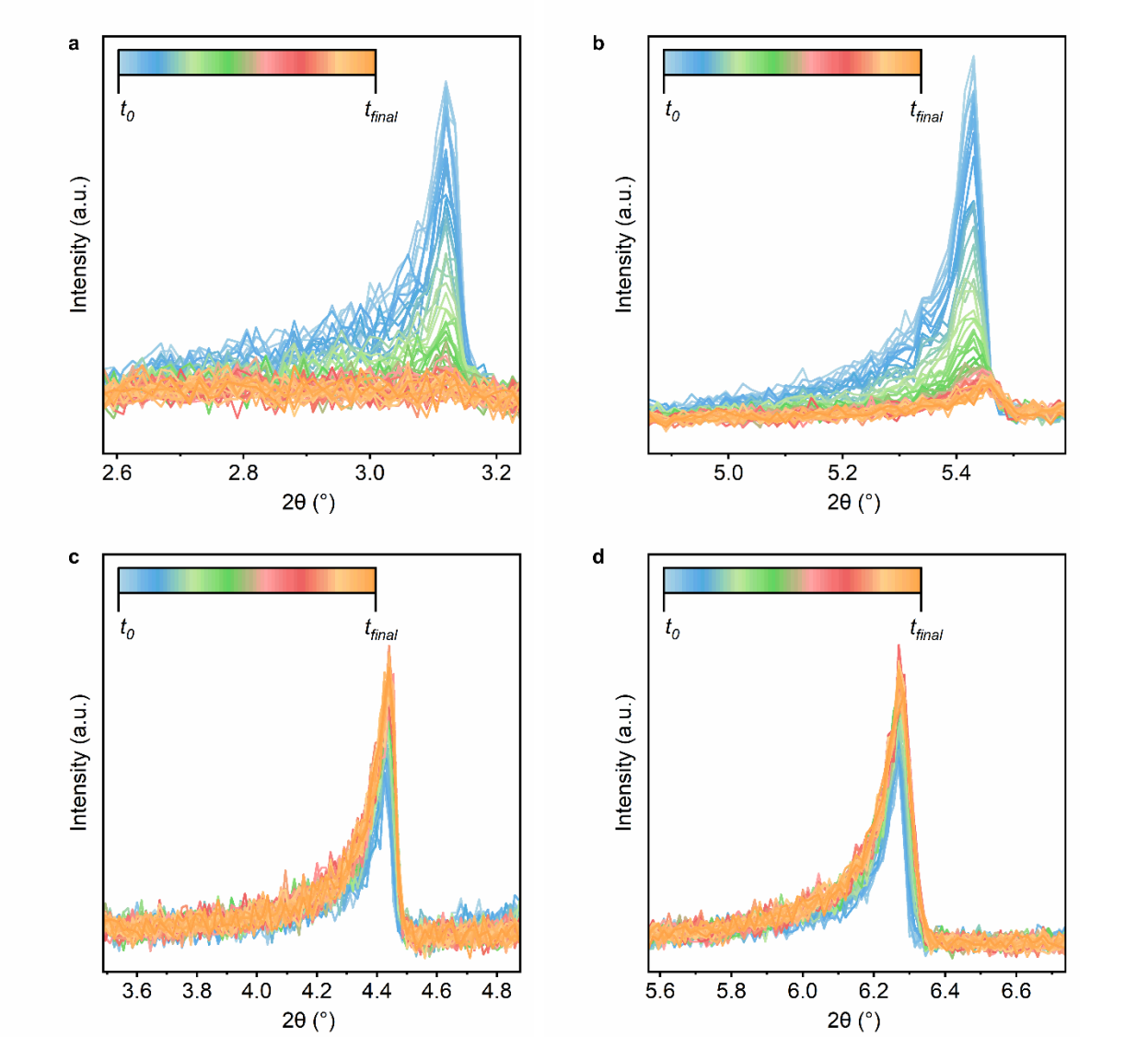

Figure 4.96 Time-resolved *in-situ* PXRD of the (a) ⟨100⟩, (b) ⟨111⟩, (c) ⟨110⟩, and (d) ⟨200⟩ Bragg features of 2 μm Hf-NU-1200 in DMF:FA=1.5 at 120 °C.

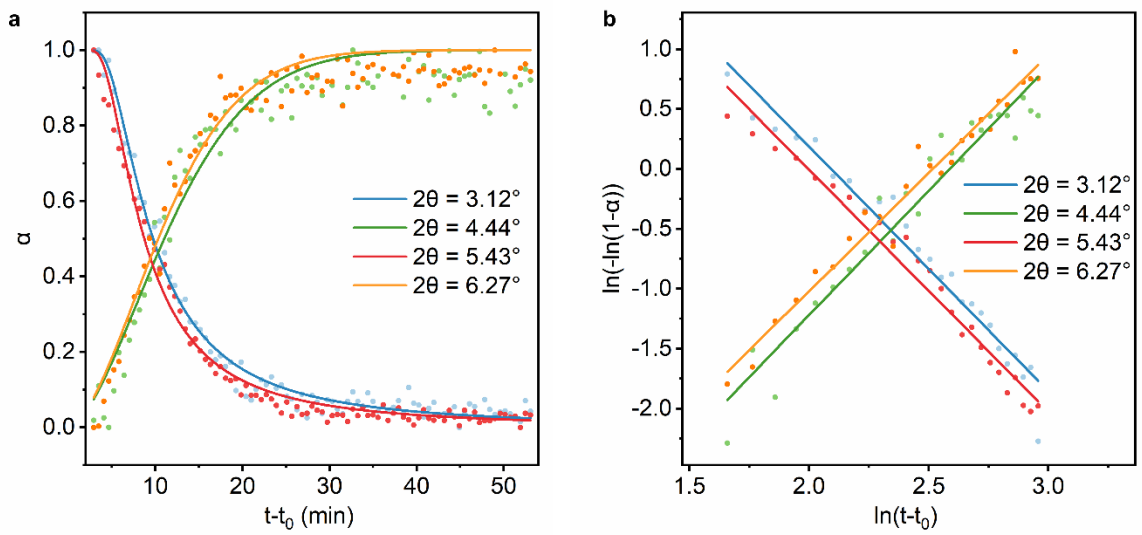

Figure 4.97 (a) Crystallization curve and Avrami fitting and (b) Sharp-Hancock plot and linear fitting for 2 μm Hf-NU-1200 in DMF:FA=1.5 at 120 °C.

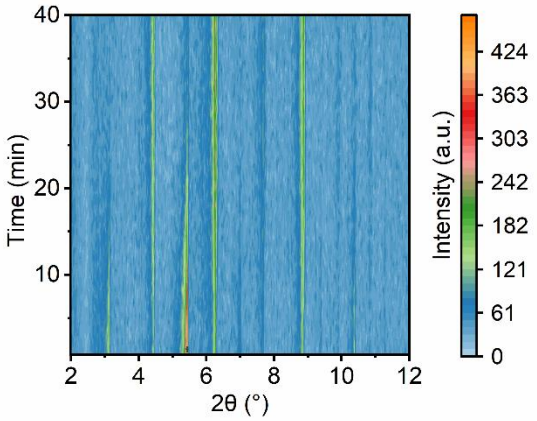

Figure 4.98 Time-resolved *in-situ* PXRD of 2 μm Hf-NU-1200 in DMF:FA=2 at 120 °C.

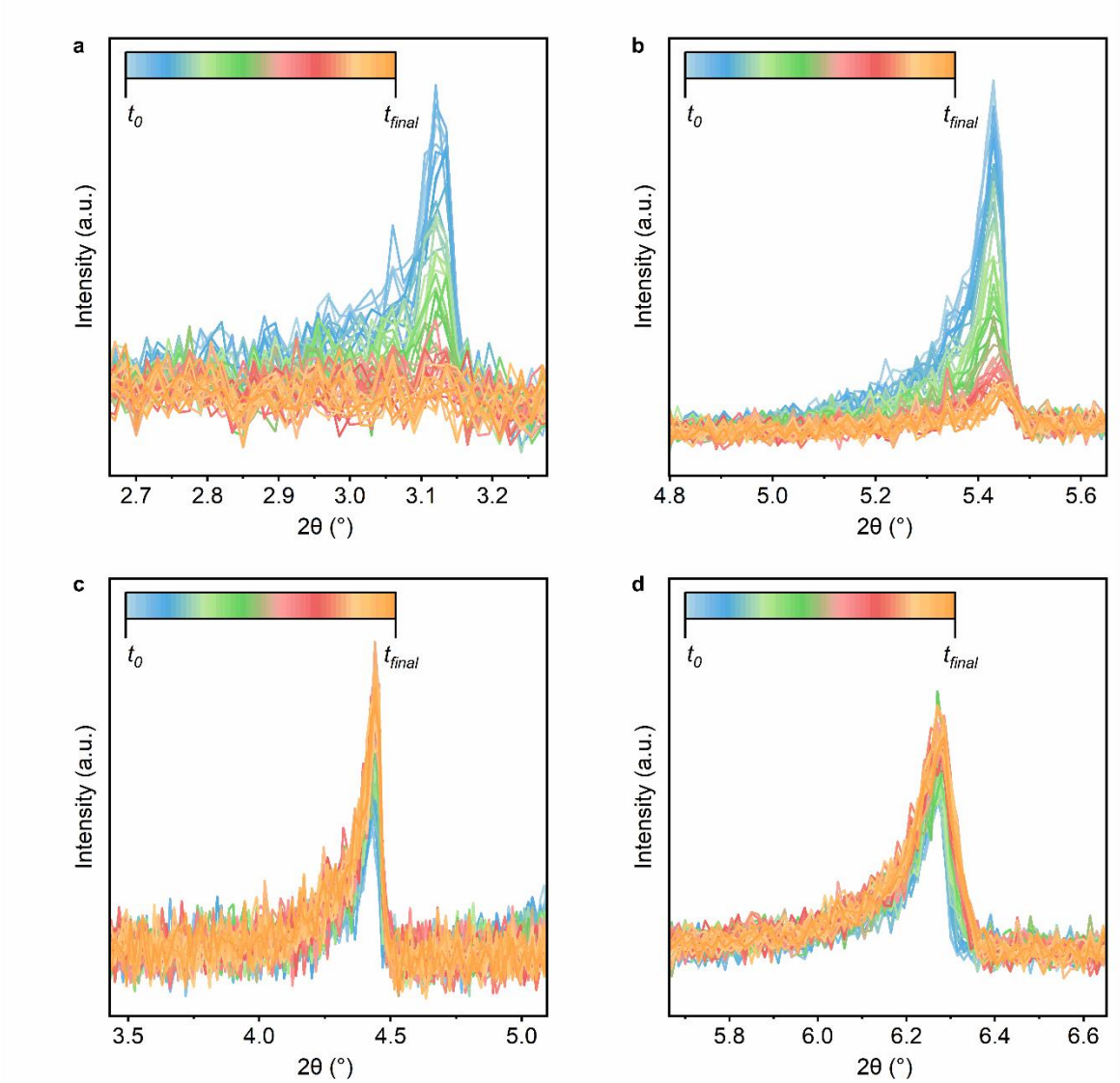

Figure 4.99 Time-resolved *in-situ* PXRD of the (a) ⟨100⟩, (b) ⟨111⟩, (c) ⟨110⟩, and (d) ⟨200⟩ Bragg features of 2 μm Hf-NU-1200 in DMF:FA=2 at 120 °C.

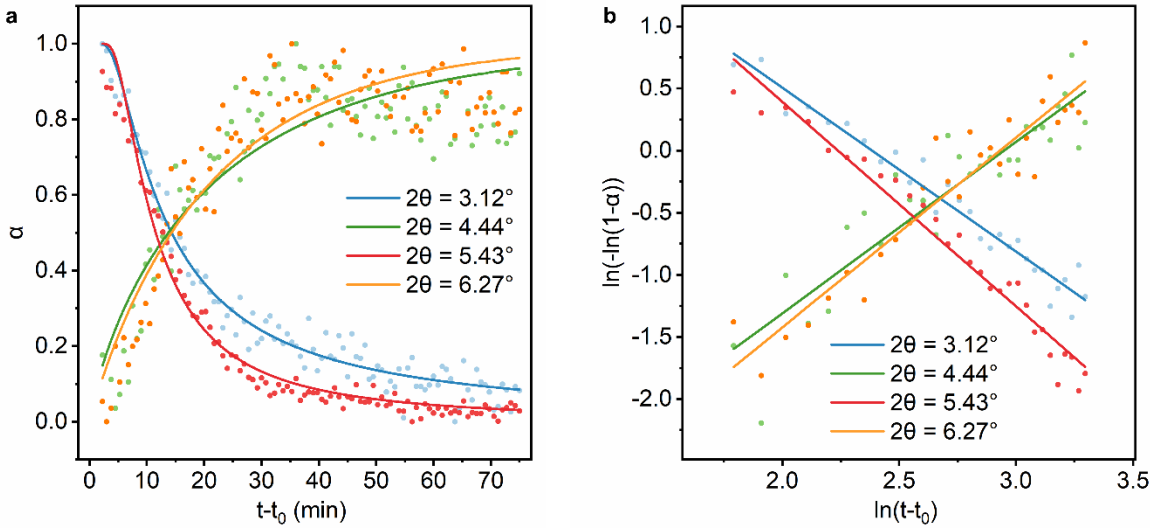

Figure 4.100 (a) Crystallization curve and Avrami fitting and (b) Sharp-Hancock plot and linear fitting for 2 µm Hf-NU-1200 in DMF:FA=2 at 120 °C.

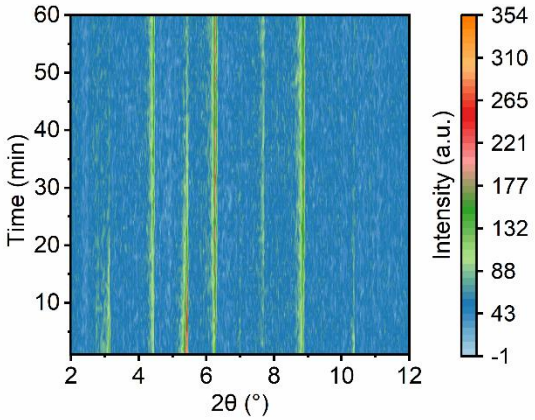

Figure 4.101 Time-resolved *in-situ* PXRD of 2 μm Hf-NU-1200 in DMF:FA=3 at 120 °C.

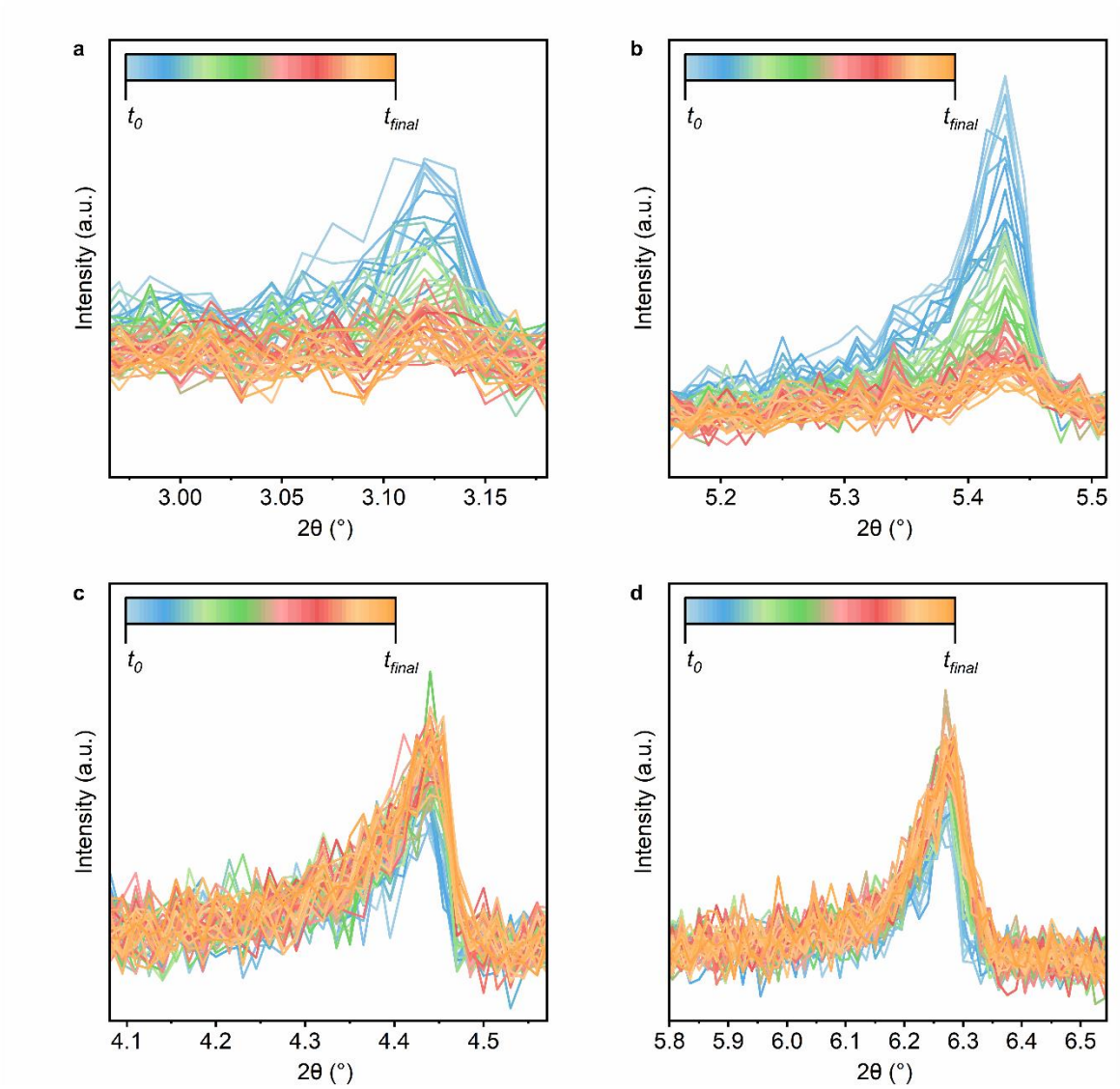

Figure 4.102 Time-resolved *in-situ* PXRD of the (a) ⟨100⟩, (b) ⟨111⟩, (c) ⟨110⟩, and (d) ⟨200⟩ Bragg features of 2 μm Hf-NU-1200 in DMF:FA=3 at 120 °C.

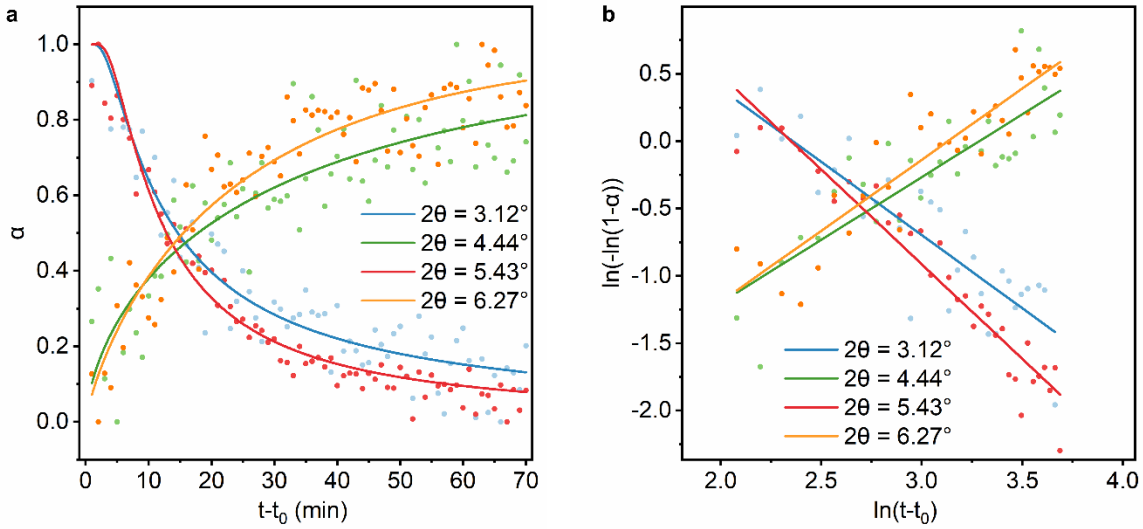

Figure 4.103 (a) Crystallization curve and Avrami fitting and (b) Sharp-Hancock plot and linear fitting for 2 μm Hf-NU-1200 in DMF:FA=3 at 120 °C.

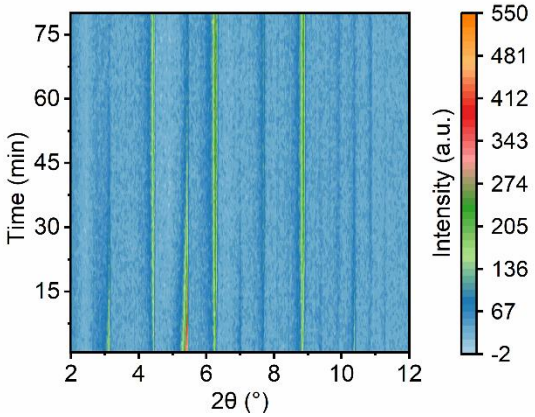

Figure 4.104 Time-resolved *in-situ* PXRD of 2 μm Hf-NU-1200 in DMF:FA=3.5 at 120 °C.

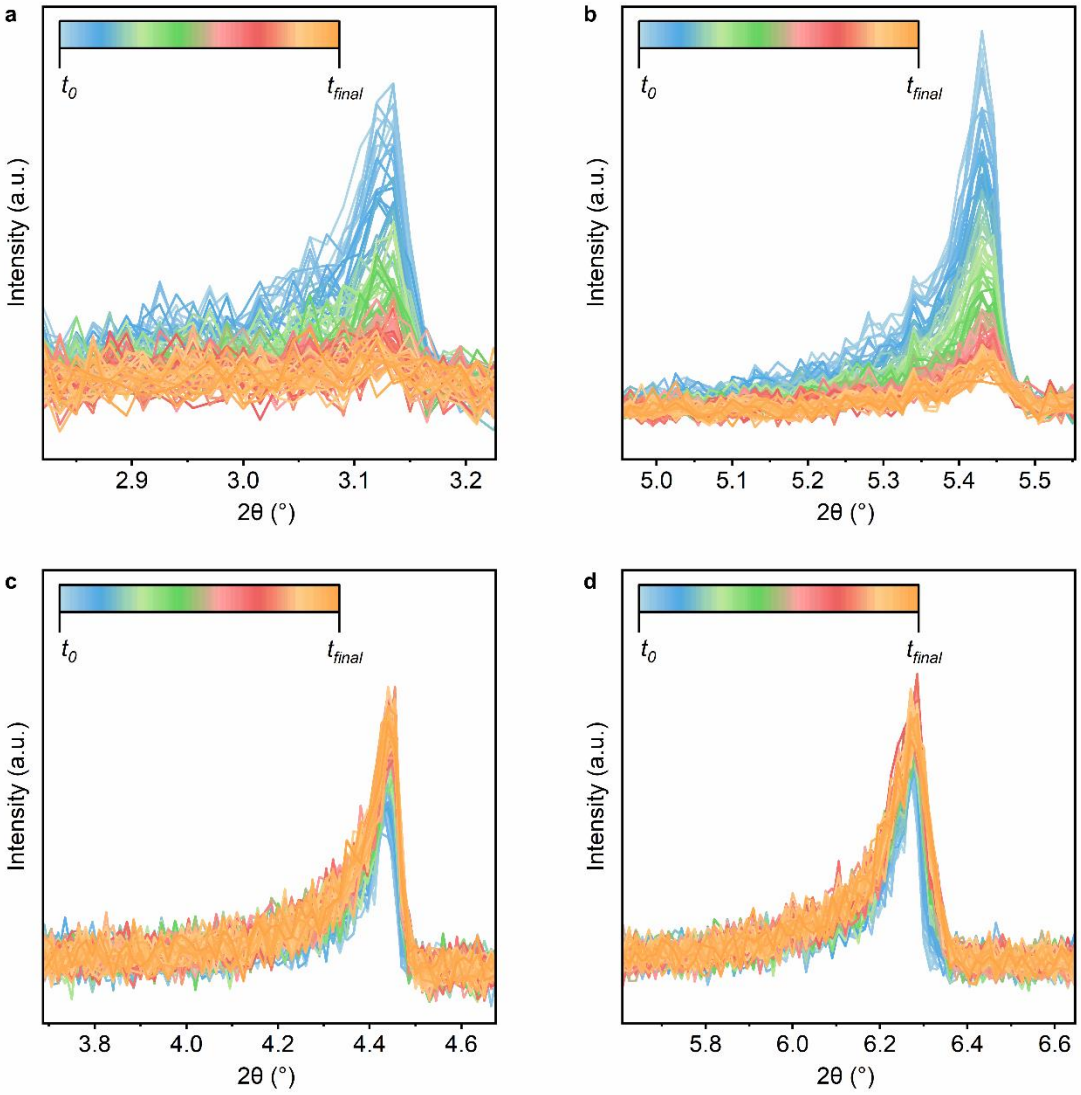

Figure 4.105 Time-resolved *in-situ* PXRD of the (a) ⟨100⟩, (b) ⟨111⟩, (c) ⟨110⟩, and (d) ⟨200⟩ Bragg features of 2 μm Hf-NU-1200 in DMF:FA=3.5 at 120 °C.

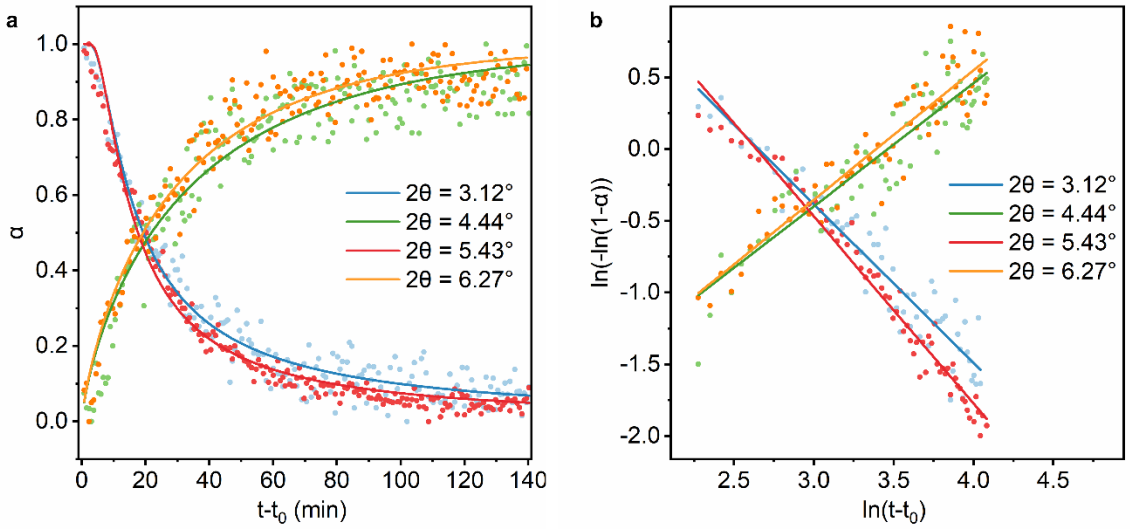

Figure 4.106 (a) Crystallization curve and Avrami fitting and (b) Sharp-Hancock plot and linear fitting for 2 µm Hf-NU-1200 in DMF:FA=3.5 at 120 °C.

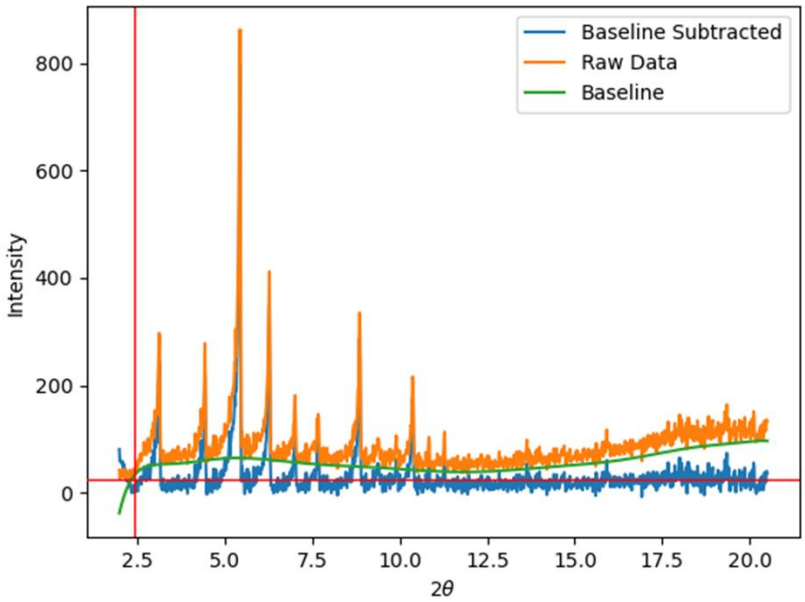

Figure 4.107 Example plot of baseline subtracted PXRD data using the peakutils function in Python.

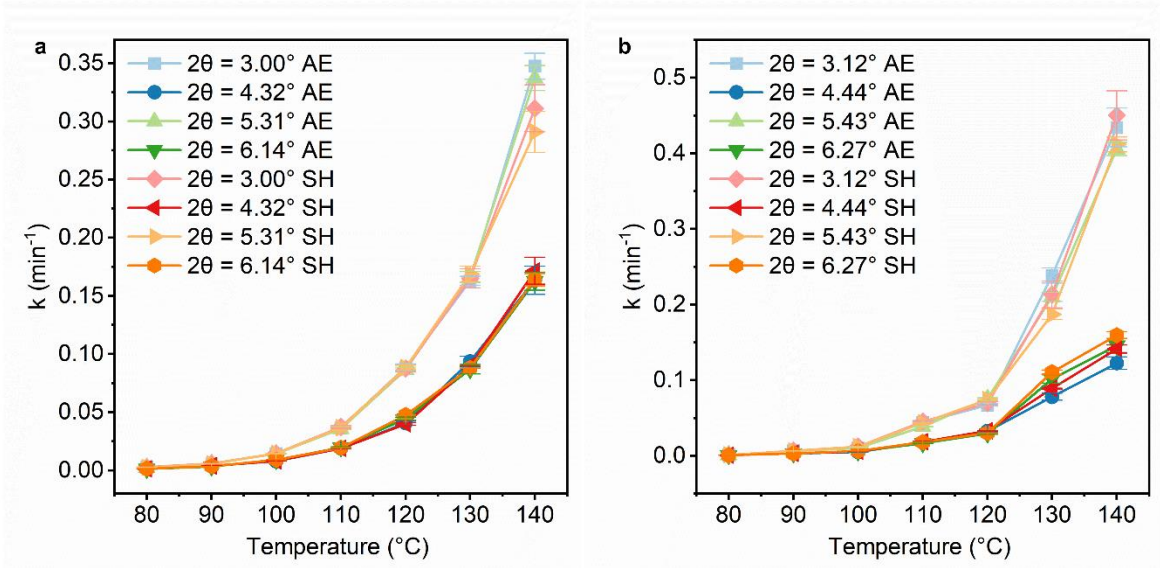

Figure 4.108 Extracted Avrami-Erofe'ev (AE) and Sharp-Hancock (SH) rate constants for ⟨100⟩, ⟨111⟩, ⟨110⟩, and ⟨200⟩ Bragg features plotted as a function of temperature for (a) Zr-NU-1200 and (b) Hf-NU-1200.

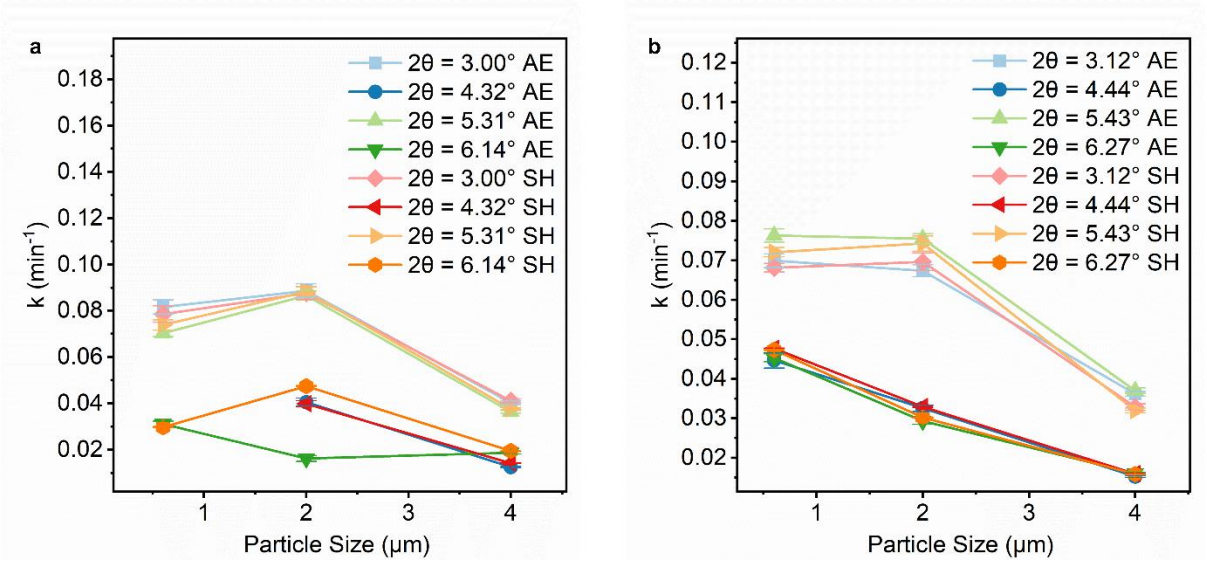

Figure 4.109 Extracted Avrami-Erofe'ev (AE) and Sharp-Hancock (SH) rate constants for ⟨100⟩, ⟨111⟩, ⟨110⟩, and ⟨200⟩ Bragg features plotted as a function of particle size for (a) Zr-NU-1200 and (b) Hf-NU-1200.

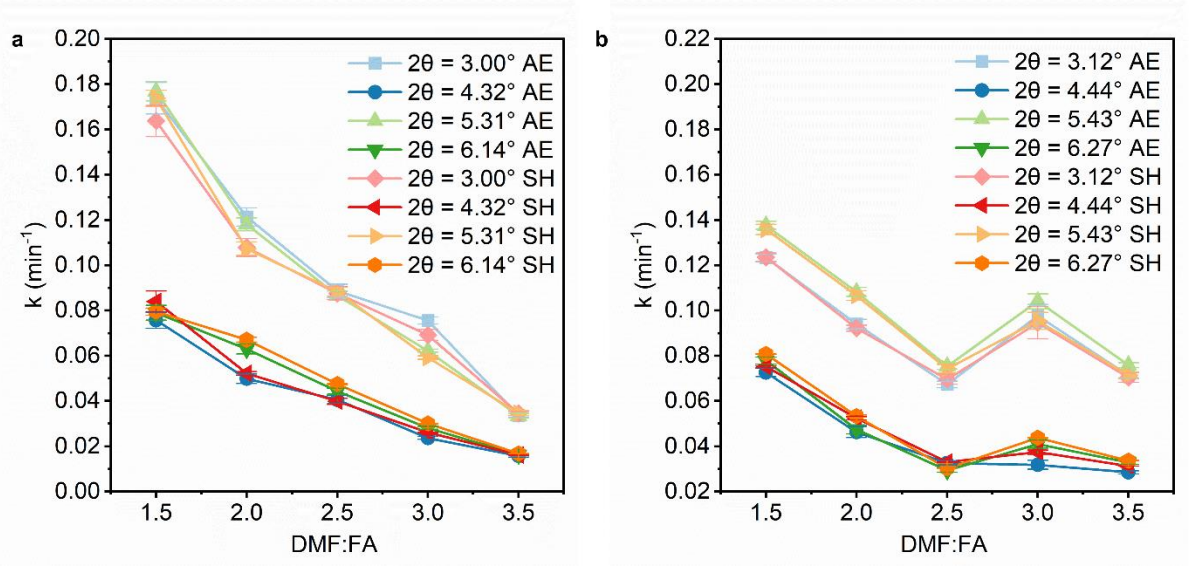

Figure 4.110 Extracted Avrami-Erofe'ev (AE) and Sharp-Hancock (SH) rate constants for ⟨100⟩, ⟨111⟩, ⟨110⟩, and ⟨200⟩ Bragg features plotted as a function of DMF:FA for (a) Zr-NU-1200 and (b) Hf-NU-1200.

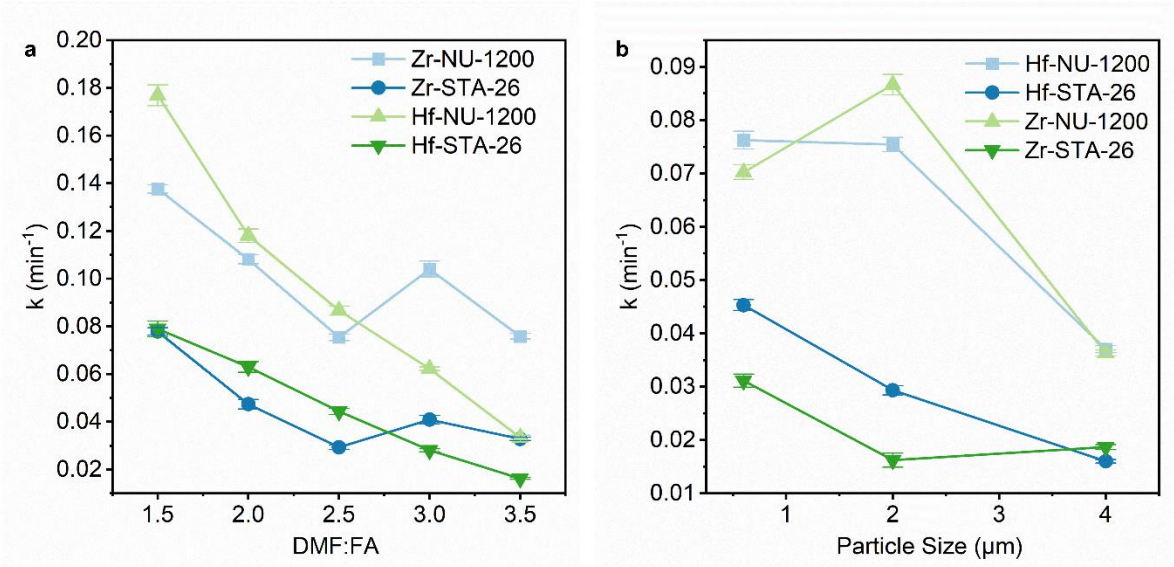

Figure 4.111 Extracted Avrami-Erofe'ev rate constants for ⟨111⟩ and ⟨200⟩ Bragg features plotted as a function of (a) DMF:FA and (b) particle size Zr-NU-1200 and Hf-NU-1200.

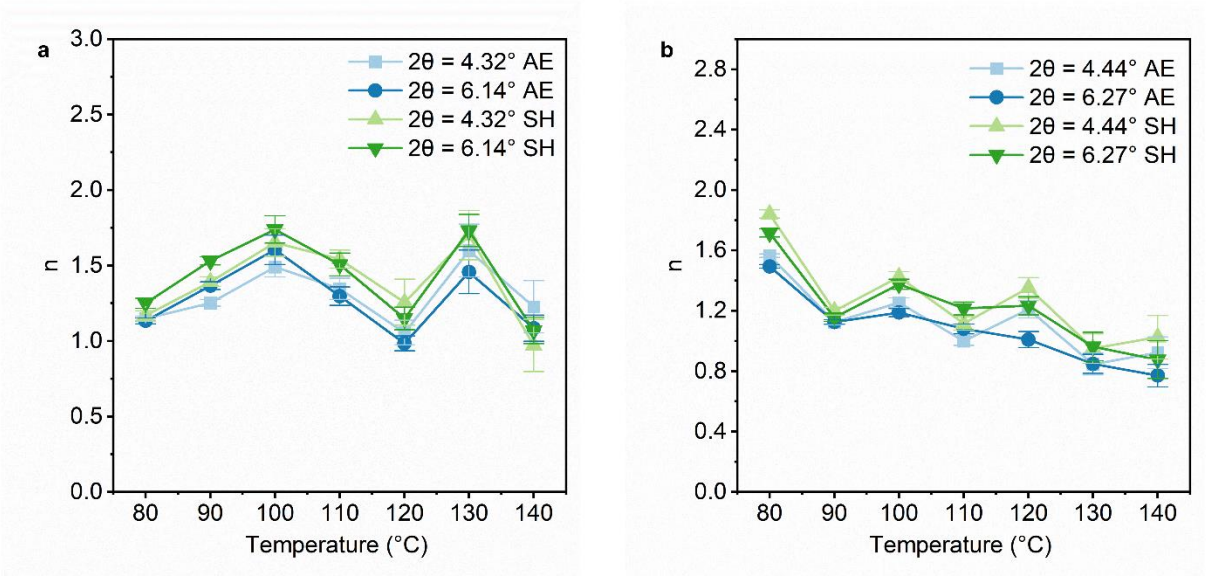

Figure 4.112 Extracted Avrami-Erofe'ev (AE) and Sharp Hancock (SH) *n* values for ⟨110⟩ and ⟨200⟩ Bragg features plotted as a function of temperature for (a) Zr-NU-1200 and (b) Hf-NU-1200.

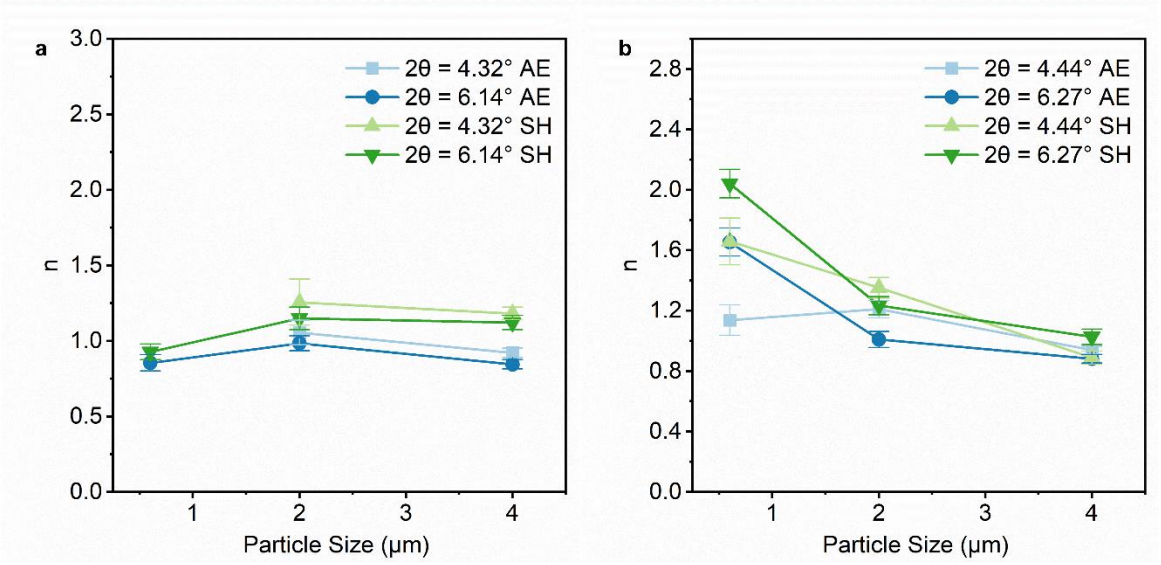

Figure 4.113 Extracted Avrami-Erofe'ev (AE) and Sharp Hancock (SH) *n* values for ⟨110⟩ and ⟨200⟩ Bragg features plotted as a function of particle size for (a) Zr-NU-1200 and (b) Hf-NU-1200.

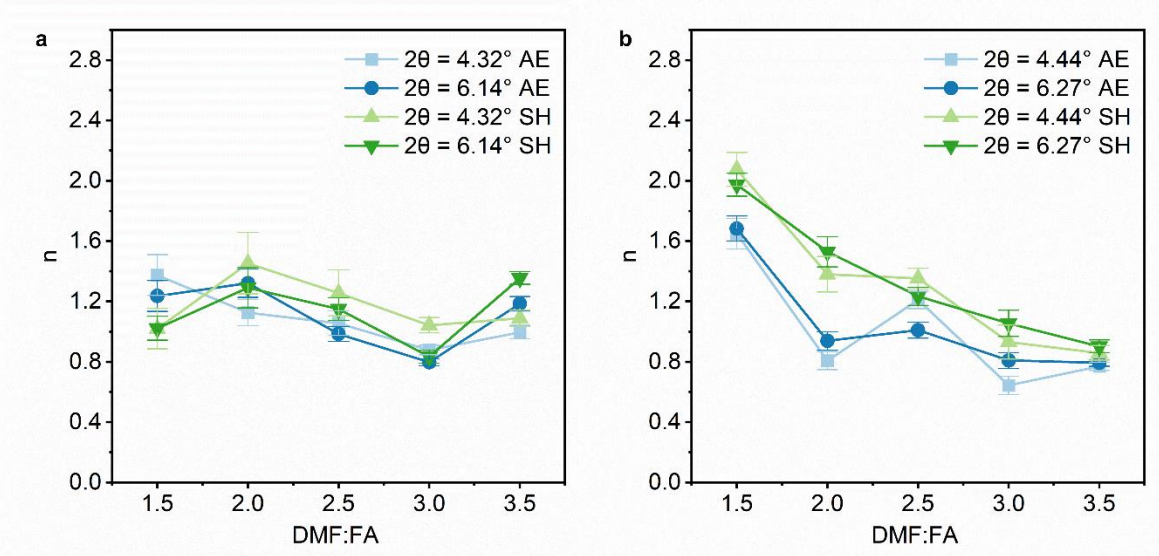

Figure 4.114 Extracted Avrami-Erofe'ev (AE) and Sharp Hancock (SH) *n* values for ⟨110⟩ and ⟨200⟩ Bragg features plotted as a function of DMF:FA for (a) Zr-NU-1200 and (b) Hf-NU-1200.

Table 4.1 Size distributions of Zr-NU-1200 and Hf-NU-1200 particles.

Sample	Average Particle Size	Standard Deviation
“600 nm” Zr-NU-1200	570 nm	110
“2 μm” Zr-NU-1200	1.94 μm	0.53
“4 μm” Zr-NU-1200	4.45 μm	1.29
“600 nm” Hf-NU-1200	644 nm	221
“2 μm” Hf-NU-1200	1.96 μm	0.67
“4 μm” Hf-NU-1200	3.68 μm	1.16

Table 4.2 Capping formates calculated by NMR for Zr-, Hf-, and Th-NU-1200 particles.

MOF	Particle Size	Formate/Node
Zr-NU-1200	600 nm	3.18
	2 μm	2.29
	4 μm	2.52
Hf-NU-1200	600 nm	2.90
	2 nm	2.79
	4 μm	2.71
Th-NU-1200	3.68 μm	0.64

Table 4.3 BET surface area and pore volume values for different sized Zr- and Hf-NU-1200 particles.

Sample	Pore Volume ($cm^3\ g^{-1}$)	BET ($m^2\ g^{-1}$)
600 nm Zr-NU-1200	1.6	2395
2 µm Zr-NU-1200	1.7	2625
4 µm Zr-NU-1200	1.9	2675
600 nm Hf-NU-1200	1.2	1815
2 µm Hf-NU-1200	1.2	1890
4 µm Hf-NU-1200	1.3	2080
Th-NU-1200	0.8	1125

Table 4.4 BET surface area and pore volume values for transformation of Zr- and Hf-NU-1200 to Zr- and Hf-STA-26, respectively.

MOF	Time (min)	Pore Volume ($cm^3\ g^{-1}$)	BET ($m^2\ g^{-1}$)
Zr-NU-1200 to Zr-STA-26	0	1.70	2630
	40	1.22	1990
	100	0.42	1095
	180	0.49	1330
Hf-NU-1200 to Hf-STA-26	0	1.34	2150
	40	1.43	2300
	100	0.94	1680
	180	0.61	1295
	255	0.52	1305
	360	0.47	1320

Table 4.5 Time-resolved *in-situ* PXRD samples and exposure times.

MOF	Sample Name	Particle Size	DMF:FA	Temperature (°C)	Exposure Time (min)
Zr-NU-1200 to Zr-STA-26	A	2 μm	2.5	80	5
	B	2 μm	2.5	90	5
	C	2 μm	2.5	100	5
	D	2 μm	2.5	110	5
	E	2 μm	2.5	120	1
	F	2 μm	2.5	130	2
	G	2 μm	2.5	140	1
	H	600 nm	2.5	120	1
	I	4 μm	2.5	120	1
	J	2 μm	3.5	120	5
	K	2 μm	3	120	1
	L	2 μm	2	120	1
	M	2 μm	1.5	120	1
Hf-NU-1200 to Hf-STA-26	N	2 μm	2.5	80	5
	O	2 μm	2.5	90	5
	P	2 μm	2.5	100	2
	Q	2 μm	2.5	110	1
	R	2 μm	2.5	120	1
	S	2 μm	2.5	130	0.83
	T	2 μm	2.5	140	0.66
	U	600 nm	2.5	120	1
	V	4 μm	2.5	120	1.33
	W	2 μm	3.5	120	0.75
	X	2 μm	3	120	1
	Y	2 μm	2	120	0.75
	Z	2 μm	1.5	120	0.58

Table 4.6 Time-resolved *in-situ* PXRD Avrami-Erofe'ev and Sharp Hancock rate constants and *n* values.

Sample Name	NU-1200		STA-26			
	k **(min^{-1}) Avrami-Erofe'ev**	***k*** **(min^{-1}) Sharp-Hancock**	***k*** **(min^{-1}) Avrami-Erofe'ev**	***k*** **(min^{-1}) Sharp-Hancock**	***n*** **Avrami-Erofe'ev**	***n*** **Sharp-Hancock**
A	0.00253	0.00261	0.00129	0.00137	1.13313	1.25025
B	0.00576	0.00565	0.00340	0.00353	1.36649	1.53053
C	0.01440	0.01449	0.00897	0.00906	1.60338	1.73803
D	0.03588	0.03663	0.01969	0.01934	1.29750	1.50667
E	0.08667	0.08833	0.04440	0.04748	0.98413	1.15031
F	0.16620	0.16872	0.08699	0.08790	1.45710	1.73186
G	0.33729	0.29092	0.16264	0.16392	1.08462	1.06913
H	0.07026	0.07391	0.03113	0.02972	0.85501	0.92775
I	0.03634	0.03769	0.01868	0.01949	0.84546	1.12227
J	0.03343	0.03470	0.01622	0.01675	1.18424	1.35527
K	0.06222	0.05915	0.02811	0.03000	0.79663	0.83488
L	0.11806	0.10726	0.06302	0.06708	1.32089	1.29136
M	0.17689	0.17372	0.07899	0.07956	1.23621	1.02225
N	0.00129	0.00130	0.00077	0.00082	1.49355	1.71628
O	0.00635	0.00646	0.00311	0.00312	1.12685	1.15532
P	0.01039	0.01236	0.00602	0.00645	1.18825	1.37617
Q	0.03855	0.04366	0.01640	0.01827	1.07986	1.21557
R	0.07544	0.07423	0.02934	0.03021	1.01030	1.23418
S	0.21021	0.18713	0.10174	0.11064	0.84909	0.96351
T	0.40570	0.41182	0.14578	0.15961	0.77082	0.87674
U	0.07627	0.07203	0.04532	0.04731	1.65422	2.04123
V	0.03703	0.03194	0.01604	0.01584	0.88185	1.02724
W	0.07586	0.07149	0.03281	0.03369	0.79265	0.90181
X	0.10406	0.09542	0.04097	0.04373	0.80821	1.05477
Y	0.10817	0.10663	0.04743	0.05338	0.93865	1.52892
Z	0.13764	0.13583	0.07788	0.08072	1.68298	1.97366

Table 4.7 Activation energies for Zr- and Hf-STA-26.

Sample	E_a (kcal mol^{-1})	Adjusted R^2
Hf-STA-26	27.86161743	0.97817
Zr-STA-26	24.15509345	0.99907

CHAPTER 5. Discovery of Spontaneous De-Interpenetration Though Charged Point-Point Repulsions

A vignette on energy-structure-property relationships.

Portions of this chapter appear in the following manuscript:

Hanna, S. L.; Chheda, S.; Anderson, R.; Ray, D.; Malliakas, C.D.; Knapp, J. G.; Otake, K.; Li, Peng,; Li, Penghao; Wang, X.; Wasson, M. C.; Zosel, K.; Evans, A. M.; Robison, L.; Islamoglu, T.; Zhang, X.; Dichtel, W. R.; Stoddart, J. F.; Gomez-Gualdron, D. A.; Gagliardi, L.; Farha, O.K., Discovery of Spontaneous De-Interpenetration Through Charged Point-Point Repulsions. *Chem.* **2022**, *8*(1), 225-242.

5.1 Chapter Summary

Energetically driven reduction of porosity through entanglement is ubiquitous in Nature and synthetic systems. This entanglement leads to reduction of valuable internal pore space useful for applications such as catalysis, storage, and sensing. Here, we describe the discovery of spontaneous de-interpenetration in a 6-fold interpenetrated uranium-based metal–organic framework (MOF), NU-1303-*6*. De-interpenetration transforms the small pore (14.2 and 19.8 Å) NU-1303-*6* to its larger pore (40.7 Å) non-interpenetrated counterpart which possesses a record high 96.6% void fraction and 9.2 cm^3g^{-1} pore volume. Density functional theory calculations reveal that this phenomenon originates from charged point-point repulsion between anionic, closely positioned uranium-based nodes in NU-1303-*6*. These repulsions compete with hydrogen-bonded water molecules that bridge together nearby networks, favoring interpenetration. Controlling the interplay between these intermolecular forces enables the reversal of omnipresent energetic equilibria, leading to thermodynamically favored open pore structures. The newly discovered phenomenon of charged point-point repulsion will likely lead to the re-evaluation of non-interpenetrated networks including their design, synthesis, and wide-reaching applications.

5.2 Pervasive Thermodynamic Behaviors of Entangled Molecular Systems

Natural and synthetic entangled molecular systems are invariably considered more stable than their non-interlocked counterparts. This understanding originates from the fact that non-covalent interactions such as hydrogen bonding, π–π stacking, and Van der Waals forces are maximized in tightly packed systems with minimal porosity, thus forming energetically favored thermodynamic products.[257-259] Tightly packed or interlocked structures inherently have less void space compared to their kinetically favored, open counterparts, which reduces the accessible surface for applications of wide-reaching importance such as gas storage,[260, 261] chemical sensing,[262, 263] bio-molecule encapsulation,[264] medical diagnostics,[265] electronics,[266] and catalysis.[267] To maximize the application relevance of porous materials, significant effort has been devoted to synthesizing kinetically preferred and packing-frustrated open-pore materials.[220, 222, 268] Here, we detail the discovery of a phenomenon that we term charged point-point repulsion (CPPR), which

reverses the universal thermodynamics of void space and consequently leads to spontaneous de-interpenetration of interlinked networks.

We demonstrate this phenomenon through the spontaneous de-interpenetration of a 6-fold interpenetrated metal–organic framework (MOF),[24, 26, 269, 270] NU-1303-*6*, to its entirely non-interpenetrated counterpart. NU-1303-*6* initially self-assembles as a densely intercalated periodic system of organic linkers and anionic uranium-based nodes,[43, 44] which are held in close proximity. The short distance between anionic uranyl nodes leads to CPPR-driven spontaneous de-interpenetration, thus reversing the pervasive thermodynamics of porous structures and generating a large-pore open structure (40 Å pore) with record high free void space (96.6%) and pore volume (9.2 cm^3g^{-1}) from an initially nanoporous assembly (<20 Å pores).

Our results reveal how spontaneous de-interpenetration transforms initially crowded systems to thermodynamically favorable products with valuable free internal pore space, often coveted in porous material applications where interpenetration reduces porosity.[271] Additionally, spontaneous de-interpenetration in the absence of external stimuli simplifies the cumbersome process of designing materials that do not interpenetrate, as well as the design of syntheses where metastable products are targeted.[272, 273]

5.3 Discovery of De-Interpenetration

We developed a solvothermal synthesis for NU-1303-*6*, and from single-crystal X-ray diffraction (SCXRD), we found the NU-1303-*6* node consists of the uranyl unit[33]–a single U(VI) atom bound to two axial oxygen atoms–coordinated by six equatorial oxygen atoms (Fig. 5.1a). These equatorial oxygen atoms originate from three separate ditopic, 2,2´-dimethyl-biphenyl-4,4´-dicarboxylic acid (DMBP) linkers (Figs. 5.1b, 5.6-5.7), each of which binds bidentately to the uranyl unit. The uranyl-based node thus holds a –1 formal charge, making the overall framework anionic $(H^+_{0.9}K^+_{0.1}[UO_2(DMBP)_{1.5}]^-$ or $(H_3O^+)_{0.9}K^+_{0.1}[UO_2(DMBP)_{1.5}]^-$, Figs. 5.14-5.16, Table 5.2). The methyl groups located on the biphenylene linkers force rotation around the central carbon-carbon bond, making these building blocks self-assemble into a three-dimensional, **srs**-topology MOF (Fig. 5.12, Table 5.1)[274]. Each **srs** cage is 37.7 Å in diameter (Fig. 5.1c), and a single extended network of NU-1303-*6* is observed in Figure 5.1d. Six of these identical

networks intertwine (Fig. 5.1g) to form NU-1303-*6*, one of the highest-fold interpenetrated uranium MOFs reported to date, featuring 14.4 Å and 19.2 Å cages (Fig. 5.1f). Throughout the extended structure of NU-1303-*6*, there are two reoccurring motifs where anionic nodes on individual networks are separated by close distances. In one motif, the nodes spatially orient in a parallel arrangement, where the closest U–U distance is 9.7 Å (*M1*). In the other motif, the nodes spatially orient in a perpendicular arrangement, where the closest U–U distance is 8.1 Å (*M2*) (Fig. 5.1e). This structural analysis reveals that anionic NU-1303-*6* adopts a crowded, interpenetrated configuration but is based upon an open network topology.

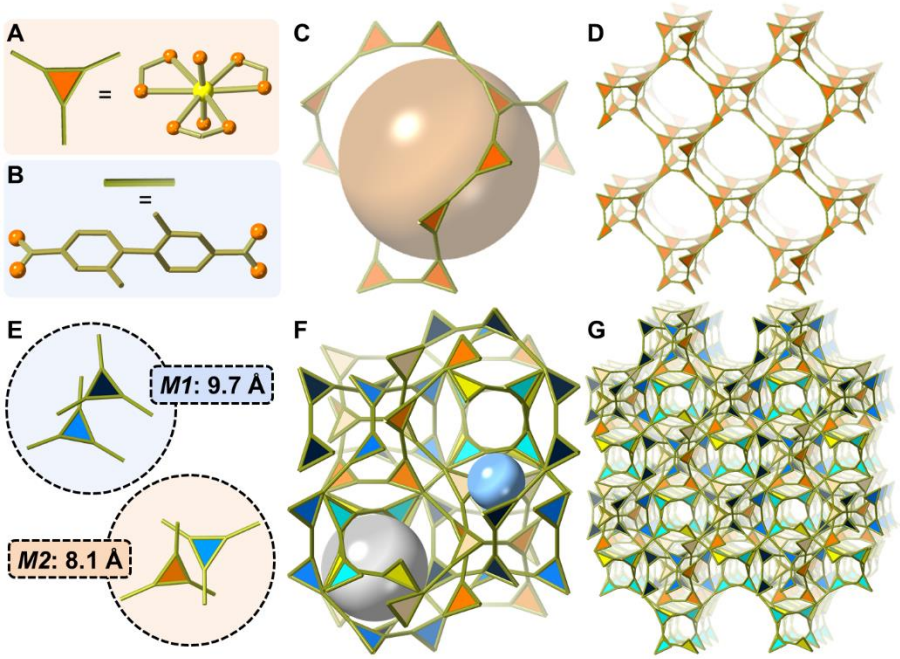

Figure 5.1 NU-1303-*6* interpenetrated structure from SCXRD. Schematic representation of NU-1303-*6* (a) node and (b) biphenylene linker. Atom color scheme: carbon, gold; oxygen, orange; uranium, yellow. H atoms omitted for clarity. (c) One **srs** cage and representative pore size shown by orange sphere. (d) One **srs** network. (e) *M1* and *M2* with close U–U distances. (f) Representative pore sizes of NU-1303-*6* shown by gray and blue spheres. Each network identified by a different color for clarity. (g) Six identical **srs** networks interpenetrate to form NU-1303-*6*.

After soaking NU-1303-*6* in *N*,*N*-dimethylformamide (DMF) for 96 hours, we removed the solvent in the pores by activation using supercritical CO_2[155] followed by thermal activation at 50 °C. We obtained the nitrogen adsorption-desorption isotherm of NU-1303-*6*, and determined its Brunauer-Emmett-Teller (BET) area[254] to be 1735 m^2g^{-1} and its pore volume to be 0.86 cm^3g^{-1}. The nitrogen isotherm (Figs. 5.2d, 5.17,

Table 5.3) possesses steps at relative pressures (P/P_0) of 0.009 and 0.070, corresponding to 14.2 Å and 19.8 Å pores (Figs. 5.2g, 5.18). These align well with the pore sizes determined from the single-crystal structure (Fig. 5.1f). The calculated geometric surface area for NU-1303-*6* reveals a higher expected BET area and pore volume of 2340 m^2g^{-1} and 1.2 cm^3g^{-1}, respectively (Tables 5.4-5.5). We thus activated the material with 74% of the calculated geometric surface area, an occurrence which has also been observed in previous studies[43].

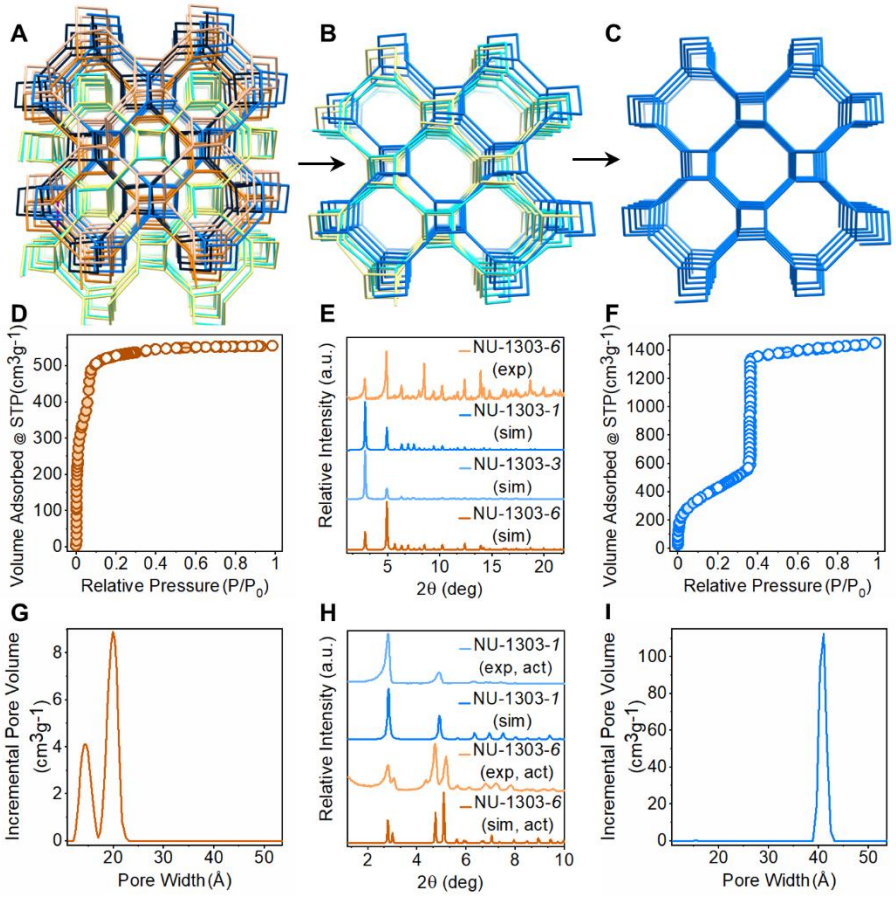

Figure 5.2 De-interpenetration of NU-1303-*6*. (a, b, c) Topological representations of NU-1303-*6*, NU-1303-*3*, and NU-1303-*1*, respectively. (d, f) Nitrogen adsorption-desorption isotherms for NU-1303-*6* and NU-1303-*1*, respectively, at 77 K. Filled circles represent adsorption, and open circles represent desorption. (e) PXRD patterns (top to bottom) of experimental NU-1303-*6* in DMF, simulated NU-1303-*1*, simulated NU-1303-*3*, and simulated NU-1303-*6*. (g, i) Pore-size distributions for NU-1303-*6* and NU-1303-*1*, respectively. (h) PXRD patterns (top to bottom) of experimental activated NU-1303-*1*, simulated NU-1303-*1*, experimental activated NU-1303-*6*, and simulated activated NU-1303-*6*.

We discovered a drastic structural change in NU-1303-*6* after we left the MOF to soak in DMF for 144 days at room temperature. The isotherm obtained after activation no longer indicated two steps at low relative pressure, but instead acquired one large step at P/P_0 = 0.36, an increase in pore volume to 2.25 cm^3g^{-1}, and a decrease in BET area to 1525 m^2g^{-1} (Figs. 5.2f, 5.41, Table 5.3). Additionally, the pore size distribution revealed a much larger 40.7 Å pore (Fig. 5.2i). The significant increase in pore volume and pore size, coupled with the concurrent change in BET area, indicate the removal of framework walls. We hypothesized that this unanticipated phenomenon could be explained by de-interpenetration of 6-fold interpenetrated NU-1303-*6* to its completely non-interpenetrated counterpart (NU-1303-*1*).

In search of more evidence to support this observation, we captured an intermediate three-fold interpenetrated single-crystal structure of NU-1303 (NU-1303-*3*) after soaking the NU-1303-*6* crystals in DMF for 29 days (Figs. 5.2b, 5.33-5.34, Tables 5.1, 5.12). Additionally, single-crystals of NU-1303-*1* were preserved after soaking NU-1303-*6* in DMF for 946 days (Fig. 5.35). Since the low resolution of the NU-1303-*1* SCXRD data only revealed the uranium positions instead of the full structure, we additionally modeled NU-1303-*1* in Materials Studio by removing 5 of the 6 **srs** networks from NU-1303-*6* while retaining the same topology and unit cell parameters (Figs. 5.2c, 5.36). To ensure that this model matched the SCXRD data, we paired the extinction analyses from SCXRD with Le Bail analysis of a NU-1303-*1* powder sample (Fig. 5.37), and we generated lattice parameters for the experimental structure. These experimental parameters matched those from the modeled structure precisely (Table 5.8). In this way, the SCXRD uranium positions of NU-1303-*1* were validated both experimentally through powder refinement and computationally through Materials Studio modeling. The simulated PXRD generated from the single-crystal data also matches well with the simulated PXRD generated from the structural model (Fig. 5.38). Collectively, these findings are consistent with the presence of NU-1303-*1*.

While one might imagine that de-interpenetration etches away at portions of all 6 frameworks rather than removing 5 entire frameworks, this NU-1303-*1* structure confirms that etching is not operative. Additionally, we anticipate that de-interpenetration *via* etching would result in a material with a wide

distribution of multiple continuous pore sizes[275]. However, we observe only one pore size by gas physisorption (40 Å, Fig. 5.2i) which matches well with the structure solution (37.7 Å) and further confirms that complete de-interpenetration from a 6-fold interpenetrated MOF to its non-interpenetrated counterpart occurs.

We obtained further evidence for de-interpenetration from an isotherm of NU-1303-*6* soaked in DMF for an intermediate amount of time (17 days) which showed intermediate (higher than NU-1303-*6*, but lower than NU-1303-*1*) pore volume and pore-size distributions (Figs. 5.30-5.32, Table 5.3). Additionally, evidence for de-interpenetration was also observed through the appearance of uranium in the DMF soaking solution, detected *via* inductively coupled plasma-mass spectrometry and ultraviolet-visible spectroscopy (Fig. 5.29).

Because simulated powder X-ray diffraction (PXRD) patterns of NU-1303-*6*, NU-1303-*3*, and NU-1303-*1* all display similar peak positions (Fig. 5.2e), distinguishing interpenetration levels using PXRD peak positions is not feasible. Additionally, peak intensity provides little structural information, as the 150–200 μm crystallite size (Fig. 5.11) introduces preferred orientation. Instead, we analyzed peak splitting to distinguish interpenetration level by PXRD. While the experimental NU-1303-*6* PXRD peak positions prior to activation match the simulated patterns (Fig. 5.2e), after activation, the first two major PXRD peaks split (Fig. 5.2h). In contrast, NU-1303-*1* exhibited no peak splitting after activation and matched well with the simulated NU-1301-*1* pattern (Fig. 5.2h). Thus, peak splitting after activation is an indicator of NU-1303-*6*, while the absence of peak splitting following activation suggests the presence of NU-1303-*1*. These findings are consistent with the interpenetration levels observed from nitrogen physisorption. This evidence supports de-interpenetration (Fig. 5.2a-c) in the absence of external stimuli. To identify the structural changes which cause peak splitting in NU-1303-*6* after activation, we generated PXRD patterns and structural models that matched the experimental patterns of NU-1303-*6* after activation (Fig. 5.20). This was performed by varying the lattice parameters of the simulated unit cells to maximize peak overlap between the experimental and simulated patterns. The lattice constants obtained from this analysis were

verified by Le Bail fitting (Table 5.8). Analysis of the simulated unit cells revealed that, following activation, NU-1303-*6* transitions to a lower symmetry crystal system, which results in peak splitting.

The final de-interpenetrated NU-1303-*1* boasts remarkable porosity. Calculated nitrogen uptake values for NU-1303-*1* reveal a higher expected geometric surface area of 5700 m^2g^{-1} and a record high calculated 96.6% free volume and 9.2 cm^3g^{-1} pore volume ($H^+_{0.9}K^+_{0.1}$ cation) of any MOF reported to date (Tables 5.4-5.5)[276]. While only 27% of the BET area and 24% of the free volume is accessed experimentally, we attribute this to partial pore collapse[43]. Calculated geometric surface areas and pore volumes for NU-1303-*6* compared to NU-1303-*1* reveal that both values increase after de-interpenetration (Tables 5.4-5.5), which is consistent with the literature[277]. We experimentally demonstrate the differences in pore volume between NU-1303-*6* and NU-1303-*1* through thermogravimetric analysis (Fig. 5.19, Table 5.6).

5.4 Charged Point-Point Repulsion Drives Spontaneous De-Interpenetration

Since no external stimuli propel de-interpenetration, we reasoned that an interaction inherent to the system itself must drive de-interpenetration. Because NU-1303-*6* is 6-fold interpenetrated, it has a high density of closely spaced uranium nodes (Fig. 5.1e); the closest U–U distance is 8.1 Å (*M2*), and equatorial O atoms in *M2* are only separated by 3.7 Å (Fig. 5.50). Additionally, each node holds a –1 formal charge, and uranium atoms possess relatively diffuse electron clouds. Thus, we hypothesized that energetically unfavored charged point-point repulsion (CPPR) between closely positioned anionic nodes on different networks drives NU-1303-*6* de-interpenetration.

To investigate this hypothesis, we performed a density functional theory (DFT) energy decomposition analysis (EDA) using the Amsterdam Density Functional software (ADF 16.0)[278] on *M1* and *M2* (Fig. 5.26). We developed *M1* and *M2* cluster models (Fig. 5.22), where each motif is composed of a pair of fragments, with each fragment comprising a uranyl node and three attached linkers capped with protons ($[UO_2(H–DMBP)_3]^{1–}$). We then determined the interaction energy (ΔE_{int}) between fragments in *M1* and *M2* at varying U–U distance in the gas phase, using the M06-2X density functional[279].

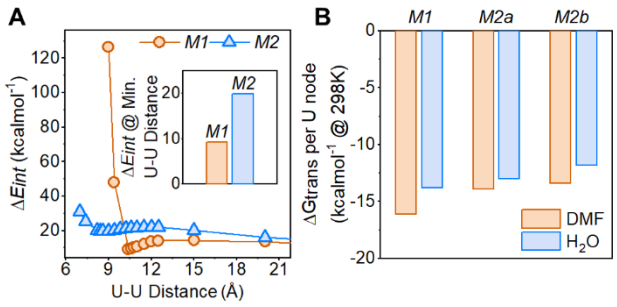

Figure 5.3 DFT computation reveals CPPR and spontaneous nature of de-interpenetration in NU-1303-*6*. (a) Total energy decomposition into ΔE_{int} using M06-2X functional at varying U–U distance. Inset shows energy values at the calculated minimum energy U–U distance for each motif in kcalmol^{-1}. (b) Free energy of transformation calculations of *M1*, *M2a*, and *M2b* in implicit solvent models for DMF (orange) and water (blue), in the presence of H^+ cations.

ΔE_{int} is positive for both motifs over the range of investigated U–U distances (Fig. 5.3a), corroborating our hypothesis that node–node interactions are repulsive and energetically unfavored. For *M1*, ΔE_{int} is positive at close U–U distance and reaches a local minimum energy that is still positive (repulsive) at 10.4 Å. This compares well to the experimental 9.7 Å U–U distance. ΔE_{int} for *M2* is also positive at close U–U distance, with a positive local minimum energy at 8.6 Å, well within reasonable error of the experimental 8.1 Å U–U distance. ΔE_{int} for both *M1* and *M2* then moves towards zero at U–U distances reaching 50 Å (Fig. 5.26a), indicating no interaction between fragments. At the predicted 10.4 Å local minimum for *M1*, the total bonding energy is 9.3 kcalmol^{-1}, while it is 19.9 kcalmol^{-1} for *M2* at 8.2 Å (Fig. 5.3a, inset). These positive ΔE_{int} values at local minimum energy U–U distances highlight that neither motif is energetically favored, and U–U repulsions dominate the electronic energy landscape in NU-1303-*6*. Since *M2* exhibits a more positive ΔE_{int} at its local minimum, we conclude that in gas phase, *M2* is the less energetically favored motif. This is due to the closer distance between *M2* nodes and resulting steric hindrance (Fig. 5.26c).

The positive ΔE_{int} values for both motifs also suggest the formation of NU-1303-*1* is energetically favored. Further DFT-computed free energies for the transformation of NU-1303-*6* to NU-1303-*1* establish that NU-1303-*1* is thermodynamically favored, and that de-interpenetration occurs spontaneously. We calculated free energies of transformation by modeling de-interpenetration of the fragment pairs in the *M1* and *M2*

cluster models into their independent fragments (Fig. 5.27). To account for potential shielding of anionic nodes by counter-cations, we included either H^+, H_3O^+, or K^+ cations in our *M1* and *M2* cluster models, as well as a model with no cations (Eq. 4, Figs 5.22-5.25).

$$(X[UO_2(H-DMBP)_3])_2 \rightarrow 2(X[UO_2(H-DMBP)_3]) \quad \text{Eq. 4}$$

X = H^+, H_3O^+, K^+, or no cation

Because of different possible cation positions around the uranyl nodes, we report two stable configurations for *M2*: *M2a* and *M2b*. Using Eq. 5, we obtained free energies of transformation per uranium for *M1*, *M2a,* and *M2b*.

$$\Delta G\ per\ U = \frac{2*G_{NU-1303-1}-G_{NU-1303-6}}{2} \quad \text{Eq. 5}$$

These calculations were performed in the presence of DMF, using the implicit Solvent Model based on Density (SMD)[280] and the M06-2X functional. For *M1*, *M2a,* and *M2b* in the presence of H^+ (Fig. 5.3b: orange bars), H_3O^+, K^+, or no cation (Fig. 5.28), the free energy is negative, indicating that the transformation of NU-1303-*6* to NU-1303-*1* is thermodynamically favorable and spontaneous. This can be attributed to unfavorable CPPR between anionic uranyl nodes. We note that CPPR is not observed to fully dissolve all six networks of NU-1303-*6*, since bulk NU-1303-*1* is still observed after 752 days of soaking in DMF (Fig. 5.39), and single-crystals of NU-1303-*1* are observed after 946 days of soaking in DMF.

5.5 Charged Point-Point Repulsion *vs.* Bridging Hydrogen-Bonded Water

We observed that under humid conditions, the NU-1303-*6* de-interpenetration timeframe slows. We also noted that the 3.7 Å distance between equatorial oxygen atoms from different nodes in *M2* (Fig. 5.50) forms the optimally-sized pocket to house a water molecule. Coupling these two observations, we reasoned that water from humid atmospheric conditions may interact with neighboring nodes in *M2* to stabilize NU-1303-*6* against de-interpenetration. Upon close inspection of the NU-1303-*6* single-crystal structure, we detected a water molecule hydrogen-bonded between the equatorial oxygen atoms of the two nodes in *M2* (Fig.

5.4a). We did not observe similar behavior in *M1*. Hydrogen-bonding between two interpenetrated networks *via* a single water molecule likely occurs in *M2* because of the closer distance between uranium nodes. Conversely, the separation of nodes is 1.6 Å greater in *M1*, preventing a water molecule from hydrogen-bonding to two distinct networks.

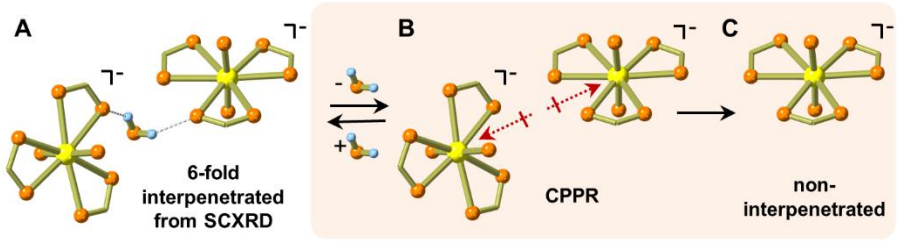

Figure 5.4 Hydrogen-bonded water bridges networks together and hinders CPPR-driven de-interpenetration. (a) SCXRD structure of two uranium nodes in *M2* bridged together by a hydrogen-bonded water molecule. (b) Removing water in *M2* allows for CPPR between the anionic nodes to dominate. (c) CPPR causes de-interpenetration, resulting in one remaining anionic network.

To corroborate the stabilizing effect of hydrogen-bonded water molecules on de-interpenetration, we calculated free energies of transformation per uranium for *M1*, *M2a*, and *M2b* in the presence of water and different cations, using the implicit SMD solvent model for water. As expected, replacing implicit DMF solvent with water results in less-negative free-energies of de-interpenetration (Fig. 5.3b: blue bars). Similar trends were also observed in *M1*, *M2a*, and *M2b* models with other cations and with no cations (Fig. 5.28, Table S10). Hydrogen-bonded water thereby interacts with NU-1303-*6* nodes to stabilize against de-interpenetration.

Thus, two competing interactions are at play in this system: CPPR *vs.* bridging hydrogen-bonded water (Fig. 5.4). In NU-1303-*6*, we experimentally observe a water molecule in *M2* bridging anionic uranium nodes on two different networks, creating favorable hydrogen-bonding interactions, and holding the interpenetrated frameworks together (Fig. 5.4a). However, CPPR favors de-interpenetration, and in the absence of water, (Fig. 5.4b) it drives the interpenetrated lattices apart (Fig. 5.4c). To further support this hypothesis, we soaked NU-1303-*6* in anhydrous solvent and activated it under anhydrous conditions to

prevent water molecules from bridging neighboring networks and thus prevent NU-1303-*6* from interpenetrating. Consistent with our hypothesis, under anhydrous conditions, nitrogen isotherms show that NU-1303-*6* fully de-interpenetrates in four days (Fig. 5.42-5.44, Table 5.3), much faster than the original 144-day de-interpenetration. This observation demonstrates that CPPR drives the spontaneous de-interpenetration of NU-1303-*6*, making a material with more void space thermodynamically favored, while hydrogen-bonded water hinders de-interpenetration.

5.6 Experimental Control for Charged Point-Point Repulsion

To further validate the roles of CPPR and bridging water in de-interpenetration, we synthesized a new MOF, named NU-1304. NU-1304 consists of the same anionic, uranyl-based node as NU-1303-*6* (Fig. 5.1a) and a slightly modified linker: 2,2´,6,6´-tetramethyl-biphenyl-4,4´-dicarboxylic acid (TMBP) (Figs. 5.5a, 5.46). A combination of SCXRD and modeling with Topologically-Based Crystal Constructor (ToBaCCo)[281, 282] revealed the structure of NU-1304 to be the same **srs** topology and anionic, 6-fold interpenetrated framework as NU-1303-*6* ($H^{+}_{0.9}K^{+}_{0.1}[UO_2(TMBP)_{1.5}]^{-}$ or $(H_3O^{+})_{0.9}K^{+}_{0.1}[UO_2(TMBP)_{1.5}]^{-}$, Figs 5.46-5.48, S46-S48, Table 5.2). Analogous to NU-1303-*6*, NU-1304 also has two reoccurring motifs (*M3* and *M4*). *M3* spatially orients in a parallel arrangement, similar to *M1*, and *M4* in a perpendicular arrangement, similar to *M2* (Fig. 5.48). NU-1304 shows an analogous isotherm shape as NU-1303-*6*, with steps at P/P_0 = 0.0071 and 0.0601 (Fig. 5.5b, orange circles); these steps correspond to cages of 12.6 Å and 18.7 Å (Fig. 5.5c, orange trace) and match well with the NU-1304 structure (Fig. 5.48b). NU-1304 exhibits a BET area of 1570 m^2g^{-1} and a pore volume of 0.77 cm^3g^{-1} (Fig. 5.54, Table 5.3). In line with NU-1303-*6*, although the experimental PXRD of NU-1304 before activation matches well with the simulated PXRD from the NU-1304 structural model, it exhibits peak splitting after activation (Fig. 5.5d). As described above, post-activation peak splitting in this system indicates interpenetration. Similar to the case of NU-1303-*6*, we generated PXRD patterns and structural models which matched the experimental PXRD patterns of NU-1304 after activation (Figs. 5.5d, 5.59). These revealed that peak splitting signaled a

transition to lower crystal symmetry, and we verified the obtained lattice constants through Le Bail fitting (Table 5.13). Taken together, this data shows NU-1304 to be an interpenetrated MOF.

While NU-1303-*6* and NU-1304 are isoreticular MOFs, the added methyl substituents in NU-1304 create greater steric hindrance between networks. As a result, the nodes in *M3* and *M4* separate by a greater distance than in *M1* and *M2*, such that the U–U distance in *M3* is 10.2 Å, and in *M4* it is 9.6 Å (Fig. 5.48c-d). We note that even the closest U–U distance present in NU-1304 (*M4*) remains 1.5 Å larger than that of NU-1303-*6* (*M2*, Figs. 5.5a, 5.50). Since NU-1304 is isoreticular to NU-1303-*6*, with the one distinction being the distance between closest anionic nodes, NU-1304 is a valuable control material to study the role of CPPR in de-interpenetration.

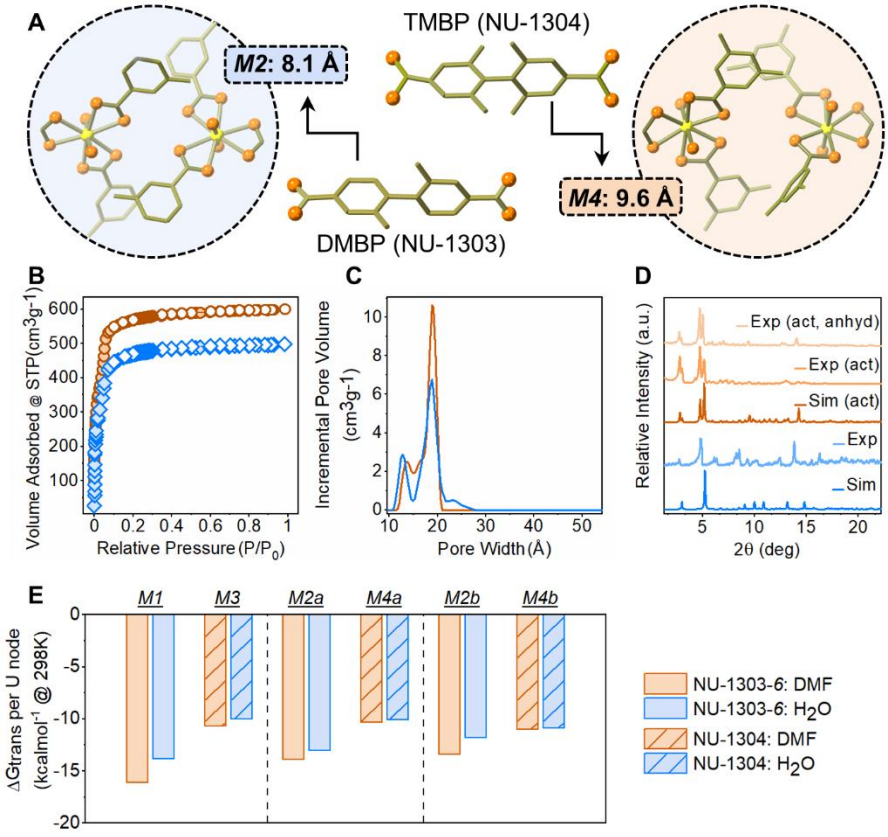

Figure 5.5 De-interpenetration not observed in NU-1304. (a) Biphenylene linkers and structures of *M2* (NU-1303-*6*) and *M4* (NU-1304). Portions of linkers are omitted and/or truncated for clarity. Crystallographically identified water molecule in *M2* and all H atoms are hidden for clarity. Atom color scheme: carbon, gold; oxygen, orange; uranium, yellow. (b) NU-1304 nitrogen adsorption-desorption isotherms after activation (orange circles) and after anhydrous activation (blue diamonds). Filled circles represent adsorption, and open circles represent desorption. (c) Pore-size distributions for NU-1304 after activation (orange) and after anhydrous activation (blue). (d) PXRD patterns (bottom to top) of simulated NU-1304, experimental NU-1304 in DMF, simulated activated NU-1304, experimental activated NU-1304, experimental activated NU-1304 (anhydrous conditions). (e) Free energy of de-interpenetration DFT calculations of *M1*, *M3*, *M2a*, *M4a*, *M2b*, and *M4b* in implicit solvent models for DMF (orange) and water (blue). This data is shown in the presence of H^+ cations, using the M06-2X functional.

Because the closest distance between anionic nodes on neighboring networks in NU-1304 is 1.5 Å larger than that of NU-1303-*6* (Figs. 5.5a, 5.50), less-effective CPPR between nodes is expected. Since CPPR is the driving force for spontaneous de-interpenetration, we thus anticipated that NU-1304 would not exhibit de-interpenetration to the extent of NU-1303-*6*. Indeed, even after 1057 days of soaking in hydrous DMF (913 days longer than NU-1303-*6*) and 10 days of soaking in anhydrous DMF to account for any potential hydrogen-bonded water molecules bridging networks together and favoring interpenetration (6 days and 2.5 times longer than NU-1303-6, Figs. 5.5b-c, 5.55-5.57, Table 5.3), nitrogen isotherms still reveal that NU-1304 remains interpenetrated. Additionally, the PXRD of NU-1304 shows splitting of the first two major peaks following activation (Figs. 5.5d, 5.58-5.59). Similar to NU-1303-*6*, peak splitting after activation indicates the presence of interpenetration, and the absence of splitting suggests that fewer networks are present (Table 5.13). As such, we find that NU-1304 remains interpenetrated under the same conditions that lead to de-interpenetration in the structurally analogous NU-1303-*6*.

While researchers commonly add bulky functional groups to organic linkers to prevent interpenetration[271], we observe the opposite trend with NU-1304. We attribute this exceptional behavior to less-effective CPPR, which is consistent with the NU-1304 de-interpenetration free energy calculations in the presence of implicit solvent. Free energy calculations were performed in the presence of no cations and in the presence of H^+, H_3O^+, and K^+ cations (Figs. 5.5e, 5.60-5.61, Table 5.14). Much like NU-1303-*6*, the different possible cation positions around the uranyl nodes resulted in two stable configurations for *M4*: *M4a* and *M4b*

(analogous to *M2a* and *M2b*). In contrast to *M1*, *M2a*, and *M2b* in NU-1303-*6* (Fig. 5.5e: solid bars), *M3*, *M4a* and *M4b* in NU-1304 possess more positive free-energy values (Fig. 5.5e: striped bars). Indeed, the added stabilization energies for *M3*, *M4a* and *M4b* are 5.4, 3.6, and 2.4 (implicit DMF), and 3.8, 2.9, and 0.9 (implicit water) kcalmol^{-1}, respectively. Similar results were also observed in the presence of H_3O^+, K^+, and no cations (Fig. 5.62). These findings indicate that NU-1304 is more stabilized against de-interpenetration than NU-1303-*6* due to less effective CPPR. Taken together, the exceptional spontaneous de-interpenetration behavior of NU-1303-*6* is attributed to CPPR between closely spaced anionic nodes.

5.7 Conclusions

In conclusion, we have discovered spontaneous de-interpenetration driven by charged point-point repulsion (CPPR), which reverses the universal thermodynamics of stability arising from reduction of porosity and enables the thermodynamic synthesis of highly porous materials. We demonstrate this phenomenon within an anionic, 6-fold interpenetrated MOF, NU-1303-*6*, with closely positioned, charged uranyl nodes, using crystallography, gas physisorption, and DFT calculations. As a result of CPPR, non-interpenetrated NU-1303-*1* with a record high void fraction (96.6%) and pore volume (9.2 cm^{3}g^{-1}) spontaneously forms as the thermodynamic product from the deintercalation of NU-1303-*6*.

Electrostatic interactions are an important fundamental behavior observed throughout multiple scientific disciplines and processes. By incorporating these fundamental interactions into synthetic materials and utilizing them as a functional tool to perform work, energetically demanding phenomena can be readily realized. In this report, we have demonstrated how repulsions of anionic points spontaneously generates useful void space through de-interpenetration. However, in principle, design considerations could be made to employ either anionic or cationic electrostatic interactions in any type of framework, where not only the node, but even the linker, counterion, or other charged groups embedded into the network material drive de-interpenetration. Thus, we expect that the detailed energetic understanding of CPPR and the de-interpenetration phenomenon developed here could be widely generalized for the direct and systematic production of non-interpenetrated structures which self-generate an abundance of valuable pore space. For

instance, recent reports have shown how uranium catalyzes nitrogen fixation[10, 11], which could likely be enhanced in a highly porous material. More fundamentally, this discovery compels a re-evaluation of the thermodynamics of porosity and will inspire an exploration of highly porous molecular systems.

5.8 Additional Information

5.8.1 Materials

Caution! Uranium salts are radioactive chemicals and contains depleted uranium (^{238}U). Necessary precautions must be adhered to when handling uranium salts.

All chemicals were purchased from the supplier and used without further purification, including methyl 3-methyl-4-(4,4,5,5-tetramethyl-1,3,2-dioxaborolan-2-yl)benzoate (Combi blocks, 98%), methyl 4-bromo-3-methylbenzoate (Sigma-Aldrich, 95%), potassium carbonate (Fisher Scientific), tripotassium phosphate (Sigma-Aldrich), tetrakis(triphenylphosphine)palladium(0) ($Pd(PPh_3)_4$) (Sigma-Aldrich), Pd SPhos Gen III catalyst (MilliporeSigma), dioxane (Sigma-Aldrich), dichloromethane (MilliporeSigma), chloroform (Fisher Scientific), dimethylamine (MilliporeSigma), tetraethylammonium chloride (Millipore Sigma), sulfuric acid-d_2 (MilliporeSigma), dimethyl sulfoxide-d_6 (MilliporeSigma), crystal violet (MilliporeSigma), magnesium sulfate (Fisher Scientific), hexanes (Fisher Scientific), ethyl acetate (Fisher Scientific), methanol (Fisher Scientific), tetrahydrofuran (Fisher Scientific), sodium hydroxide (Sigma-Aldrich), hydrochloric acid (MilliporeSigma), uranyl nitrate hexahydrate (International Bio-Analytical Industries Inc.), potassium hydroxide (stored in a desiccator) (Sigma-Aldrich), *N*,*N*-diethylformamide (Fisher Scientific), *N*,*N*-dimethylformamide (Fisher Scientific), N,N-dimethylformamide, anhydrous (MilliporeSigma, sure-seal bottle), ethanol (Fisher Scientific), ethanol, anhydrous (MilliporeSigma, sure-seal bottle), acetonitrile (Fisher Scientific), acetonitrile, anhydrous (MilliporeSigma, sure-seal bottle), concentrated trace nitric acid (> 69%, Thermo

Fisher Scientific, Waltham, MA, USA), 100 µgmL^{-1} U elemental standard (Inorganic Ventures, Christiansburg, VA, USA), 1000 ugmL^{-1} K elemental standard (Inorganic Ventures, Christiansburg, VA, USA).

5.8.2 Methods and Instrumentation

5.8.2.1 NU-1303-6 Single-Crystal X-ray Diffraction (SCXRD)

A single-crystal was mounted directly from the mother liquor onto a MiTeGen loop on a Bruker Kappa diffractometer equipped with a micro-focus CuKα source (MX optics) and an APEX CCD area detector at 200 K. The temperature of the crystal was controlled with an Oxford Cryosystems low-temperature device. Data reduction was performed with the SAINT and APEX software using a multi-scan absorption correction. The structure was solved with the SHELXS[283] structure solution program using direct methods and by using Olex2[153] as the graphical interface. The model was refined with SHELXL[151] using least squares minimization. NU-1303-*6* X-ray crystallographic data has been deposited at the Cambridge Crystallographic Data Centre (CCDC), under deposition number CCDC 2050153. This data can be obtained free of charge from the CCDC *via* www.ccdc.cam.ac.uk.

5.8.2.2 NU-1303-3 SCXRD

A single-crystal was mounted directly from the mother liquor onto a MiTeGen loop on a Bruker Kappa diffractometer equipped with a micro-focus CuKα source (MX optics) and an APEX CCD area detector at 250 K. The temperature of the crystal was controlled with an Oxford Cryosystems low-temperature device. Data reduction was performed with the CrysAlisPro software using an empirical absorption correction with spherical harmonics. Using Olex2, the structure was solved with the SHELXT[150] structure solution program using Intrinsic Phasing and refined with the SHELXL refinement package using Least Squares minimization. NU-1303-*3* X-ray crystallographic data has been deposited at the Cambridge Crystallographic Data Centre (CCDC), under deposition number CCDC 2050154. This data can be obtained free of charge from the CCDC *via* www.ccdc.cam.ac.uk.

5.8.2.3 NU-1303-1 SCXRD

Intensity data of a cubic single-crystal was collected at 200 K. The crystal was mounted on a MiTeGen loop with paratone oil on an XtaLAB Synergy diffractometer equipped with a micro-focus sealed X-ray tube PhotonJet (Cu) X-ray source and a Hybrid Pixel Array Detector (HyPix). The temperature of the crystal was controlled with an Oxford Cryosystems low-temperature device. Data reduction was performed with the CrysAlisPro software using an empirical absorption correction. The structure was solved with the ShelXS structure solution program using the direct methods solution method and by using Olex2 as the graphical interface. The model was refined with ShelXL using least squares minimization.

5.8.2.4 NU-1304 SCXRD

A single-crystal was mounted on MicroMesh (MiTeGen) in paratone oil and transferred to the cold gas stream (100 K) of a Bruker APEX II CCD area detector equipped with a MoKα I μS micro-source with MX optics. Data integration and reduction were performed using the Bruker SAINT program in APEX2. Absorption correction was performed by multi-scan methods using SADABS[284]. The uranium atom positions were determined by *ab initio* methods (SHELXD[285]) and refined by full-matrix least-squares refinement on F^2 (SHELXL) using the Yadokari-XG software package[152].

5.8.2.5 Optical Images

Optical images were acquired with a Nikon SMZ1500 microscope.

5.8.2.6 Powder X-Ray Diffraction (PXRD)

PXRD data was obtained using a Stoe STADI P and a Stoe STADI MP diffractometer, both of which were equipped with a CuKα1 source and a 1D strip detector. Transmission mode was used for all samples measured after activation, and Debye-Scherrer mode was used for all capillary samples measured in solvents. Samples measured in Debye-Scherrer mode were prepared in 1 mm borosilicate glass capillaries (Charles Supper) in their respective solvents. A 0.7 mm borosilicate glass capillary was placed in the 1 mm glass capillary once the sample was loaded and secured with wax to prevent the packed sample from being

displaced during the measurement. Samples measured in Debye-Scherrer mode for Le Bail fitting were prepared in 0.8mm Kapton capillaries in their respective solvents.

5.8.2.7 PXRD Matching Procedure

Simulated PXRD patterns were matched to their corresponding experimental PXRD patterns by varying the lattice parameters of the simulated unit cells to maximize peak overlap between the two patterns. First, the background was removed from the experimental patterns by modeling each peak with a Gaussian function of the correct height and a standard deviation of 0.05. Peaks were identified in the experimental patterns using the *signal.find_peaks* algorithm from the *SciPy Python* package, and only peaks with a minimum width of 5 points and a prominence of 0.05 (intensity units) were considered. We checked manually that all visually discernable peaks were successfully identified using this scheme. Next, the simulated PXRD pattern was matched to its corresponding experimental pattern by maximizing the overlap between the two patterns as a function of the simulated lattice parameters. The optimization was performed using differential evolution as implemented in the *scipy.optimize Python* package. Pattern overlap was determined by the city block distance between the simulated and experimental patterns. A population size of 20 with a recombination rate of 0.80 and a "randtobest1bin" strategy were used during differential evolution. All other differential evolution parameters corresponded to the defaults of the *scipy.optimize.differential_evolution* function. Each simulated pattern was generated using the *pymatgen.analysis.diffraction.xrd Python* package, and each peak was modeled with a Gaussian function of the simulated height and a standard deviation of 0.05. Patterns with split first peaks were matched under the constraints $a = b$ and $\alpha = \beta = \gamma = 90°$. Patterns with single first peaks were matched under the constraints $a = b = c$ and $\alpha = \beta = \gamma = 90°$. The code used for PXRD pattern matching is available at https://github.com/rytheranderson/XRD_matching, and the code versions used are given in Table 5.7.

5.8.2.8 Le Bail Fitting

Le Bail fittings were performed with GSAS-II (version 4917). Background (up to 10 parameters) and cell constants were freely refined. Most profile parameters were fixed based on the values obtained by fitting LaB6 (NIST 660c) except for the Gaussian *U* and Lorentzian *Y* parameters of each sample.

5.8.2.9 Topologically Based Crystal Constructor (ToBaCCo) NU-1304 Modeling Procedure

Our model of NU-1304 was constructed using the Topologically Based Crystal Constructor *(ToBaCCo)*[281, 282]. The NU-1304 linkers were added while maintaining the experimentally determined uranium node positions. The linker atom positions were then optimized according to the DFT linker optimization and the CIF generation procedure described below.

5.8.2.10 Density Functional Theory (DFT) Linker Optimization and CIF Generation

Energy-minima linker geometries for the NU-1303-*6* and NU-1304 structures, under the geometry constraints imposed by the lattice parameters determined by the PXRD matching procedure outlined above, were determined according to the following procedure. First, for each MOF, all linkers of unique length and position relative to the two connected metal nodes were identified and extracted, including the two uranium nodes, where the two additional linker sites on each uranium node were capped with formate, according to the DFT optimized geometry of the node with all formate caps. Next, each of these extracted clusters was optimized using DFT (Gaussian16[286])with all linker atoms allowed to move and the metal/formate cap atom positions kept fixed. The B3LYP/6-31G* functional/basis set[287, 288] was used for all non-metal atoms. The B3LYP /SDD functional/basis set with the SDD ECP was used for uranium atoms. Keeping the nodes fixed in this manner ensured that the relative linker/node orientations were maintained. The DFT optimized linkers were then added back into their original position in each MOF.

5.8.2.11 Supercritical CO_2 (sc-CO_2) Activation

sc-CO_2 activation[155] was performed on a Tousimis Samdri PVT-3D critical point dryer, using either a CO_2 syphon or bone-dry CO_2 syphon tank. A previously reported procedure was followed[260] with several modifications. Before activation, the sc-CO_2 unit chamber was rinsed with the same solvent used for the

most recent MOF soak. The sample was quickly transferred from its sealed tube to a Tousimis "small particle holder" and into the sc-CO_2 unit. Since Tousimis "small particle holders" with 2μm mesh sizes were used to contain the sample, 3 mL of the MOF soaking solution was placed into the unit along with the MOF sample in order to keep the MOF covered in solvent at all times. The unit was cooled slowly (~2° C/minute) and filled with CO_2 *(l)* once 10° C was reached. An initial 20-minute purge was performed. Then, four cycles of a 2-hour soak/3-minute purge were performed. Finally, the unit was heated to ~40° C and set to bleed overnight at 0.5 ccg^{-1}.

5.8.2.12 Thermal Activation

Thermal activation was performed under ultrahigh vacuum using a Micromeritics Smart VacPrep (SVP) instrument.

5.8.2.13 Nitrogen Physisorption

Nitrogen isotherms were collected at 77 K on a Micromeritics Tristar II 3020 and analyzed using the Brunauer–Emmett–Teller (BET) theory[254]. The nonlocal density functional theory (NLDFT)[289] model for pillared clay was used to determine pore size distributions.

5.8.2.14 Nuclear Magnetic Resonance (NMR)

^{1}H spectra of DMBP-OEt, DMBP and $^{13}C\{^{1}H\}$ spectra of TMBP-OEt were collected on an Ag500, Bruker Avance III 500 MHz instrument. ^{1}H spectra of TMBP, TMBP-OEt, and digested NU-1303-*6* and NU-1304 were collected on an A600, Bruker Avance III 600 MHz instrument.

5.8.2.15 Microwave Reactor

Linker synthesis and acid digestions for inductively coupled plasma-optical emission spectrometry experiments were performed on a Biotage Initiator+ microwave reactor (software version 2.3, build 6250).

5.8.2.16 Inductively Coupled Plasma-Optical Emission Spectrometry (ICP-OES)

Quantification of U and K was accomplished using ICP-OES of acid digested samples. Specifically, 2-4 mg of solid samples were digested in 2.5 mL concentrated trace nitric acid and microwaved at 200 °C for

15 minutes. Ultra-pure H_2O (18.2 MΩ·cm) was added to produce a final solution of 3.0% nitric acid (v/v) in a total sample volume of 10 mL. Quantitative standards were made using a 100 $\mu g mL^{-1}$ U elemental standard and a 1000 $\mu g mL^{-1}$ K elemental standard which were used to create a 20 $\mu g g^{-1}$ U calibration standard and a 5 $\mu g g^{-1}$ K calibration standard in 3.0% nitric acid (v/v). ICP-OES was performed on a computer-controlled (QTEGRA software) Thermo iCap7600 ICP-OES (Thermo Fisher Scientific, Waltham, MA, USA) operating in axial view and equipped with an ESI SC-2DX PrepFAST autosampler (Omaha, NE, USA). Online dilution was also carried out by the PrepFAST system and used to generate calibration curves consisting of 20, 10, 5, 1 and 0.5 $\mu g g^{-1}$ U and 5, 2.5, 1 and 0.5 $\mu g g^{-1}$ K. Each sample was acquired using 5 second visible exposure time and 15 second UV exposure time, running 3 replicates. The spectral lines selected for analysis were as follows: U (367.01, 385.96, 263.55 and 409.01 nm) and K (766.49 and 769.90 nm).

5.8.2.17 Inductively Coupled Plasma-Mass Spectrometry (ICP-MS)

Quantification of uranium (U) was accomplished using ICP-MS. Specifically, 50 µL aliquots were isolated from a soaking solution of NU-1303-*6* in DMF. Ultra-pure H_2O (18.2 MΩ·cm) and nitric acid were added to produce a final solution of 3.0% nitric acid in a total sample volume of 10 mL. A quantitative standard was made using a 100 $\mu g mL^{-1}$ U elemental standard which was used to create a 200 $ng g^{-1}$ U standard in 3.0% nitric acid (v/v) in a total sample volume of 50 mL. A solution of 3.0% nitric acid was used as the calibration blank.

ICP-MS was performed on a computer-controlled (QTEGRA software) Thermo iCapQ ICP-MS (Thermo Fisher Scientific, Waltham, MA, USA) operating in STD mode and equipped with a ESI SC-2DX PrepFAST autosampler (Omaha, NE, USA). Internal standard was added inline using the prepFAST system and consisted of 1 $ng mL^{-1}$ of a mixed element solution containing Bi, In, ^{6}Li, Sc, Tb, Y (IV-ICPMS-71D from Inorganic Ventures). Online dilution was also carried out by the prepFAST system and used to generate a calibration curve consisting of 200, 100, 50, 10, and 2 ppb U. Each sample was acquired using 1 survey run (10 sweeps) and 3 main (peak jumping) runs (40 sweeps). The isotopes selected for analysis

were ^{238}U and ^{89}Y, ^{115}In, ^{159}Tb (chosen as internal standards for data interpolation and machine stability). Instrument performance is optimized daily through autotuning followed by verification *via* a performance report (passing manufacturer specifications).

5.8.2.18 Ultraviolet-Visible Spectroscopy (UV-Vis)

Approximately 5 mg of NU-1303-*6* was soaked in 1 mL DMF and left in a capped quart cuvette, which was sealed well with parafilm to prevent solvent loss. Since the MOF particles settled at the bottom of the cuvette, UV-Vis spectra was collected of the DMF solution at different time points. An initial baseline collection was performed with pure DMF solution which was subtracted from the following measurements. Diffuse reflectance UV-Vis spectra of the DMF solution was then recorded with a Shimadzu UV-2600 with a Harrick Praying Mantis diffuse reflectance accessory. We implemented a scan range from 200-800 nm with a data interval of 1.0 nm.

5.8.2.19 Thermogravimetric Analysis (TGA)

TGA experiments were performed using a TGA/DSC 1 LF (Mettler Toledo) instrument with STARe (v16.10) software. Samples were heated from 30 to 600 °C at 10 °C/min under N_2 in a 100 uL aluminum pan.

5.8.2.20 Pore Size Distribution (PSD), Geometric Surface Area, and Void Fraction Calculations

These calculations were performed using RASPA 2.0[290] with framework non-metal atom radii according to the Dreiding forcefield[290] and uranium atom radii according to the Universal Force Field[290]. The geometric surface area for NU-1303-6 was calculated using RASPA (Monte Carlo code) with a N_2 sized probe (Table 5.4), and the void fraction was calculated using RASPA (Monte Carlo code) with a He sized probe (Table 5.5). The calculated pore volume was obtained by multiplying the void fraction by the cell volume.

5.8.2.21 Periodic Density Functional Theory (DFT) Optimization

Periodic DFT calculations were performed using the Vienna Ab initio Simulation Package (VASP 5.3.5)[291] Perdew–Burke-Ernzerhof (PBE) functional along with Grimme's D3 dispersion correction with Becke-

Johnson damping which was used for structural optimization. A planewave energy cutoff of 400 eV, energy convergence criteria of 10^{-5} eV, and force convergence criteria of 0.05 eV/Å were used for all the calculations. The Brillouin zone was sampled using a Γ only *k*-point grid.

5.8.2.22 Energy Decomposition Analysis (EDA)

The EDA of the total interaction energy (ΔE_{int}) for *M1* and *M2* was performed in Amsterdam Density Functional (ADF) 2016 software[278]. Cluster models were extracted from the CIF of NU-1303-*6* and truncated using a capping proton to form -COOH groups (Fig. 5.6). Minnesota's M06-2X density functional[279] was employed for the fragment analysis along with the scalar relativistic zeroth order regular approximation (ZORA) with all electron slater type basis sets of TZP quality. A Voronoi integration scheme with 6.0 significant digits was used for the numerical integrations. The 'Good' quality 'Zlm Fit' density fitting with radial spline functions and real spherical harmonics was employed. No symmetry was imposed in the ADF calculations.

5.8.2.23 Free Energy Cluster DFT Calculations

Free energy of transformation density functional theory (DFT) calculations for NU-1303-*6* were performed on both cation-capped and uncapped cluster models extracted from the respective CIFs in Gaussian 16 software[286] using Minnesota's M06-2X functional[279]. Three capping cations (H^+, H_3O^+, and K^+) were studied. For geometry optimization and frequency calculations, the uranyl node, capping cations, and carboxylate groups of the linkers coordinating equatorially to the node were relaxed while the positions of all other linker atoms were held fixed (Figs. 5.22-5.25, 5.61). A def2TZVP basis set for the relaxed atoms excluding uranium, the Stuttgart-Dresden SDD/SDD basis set/pseudopotential for uranium, and a def2SVP basis set for all other frozen atoms of the linkers were employed. Each linker in the cluster model was truncated using a proton to form a -COOH group to retain its interaction with the methyl group of the other linker. An ultrafine grid was employed for performing the numerical integrations. Vibrational frequencies were computed at the optimized geometries for calculating the free energies and for determining the nature

of the stationary point. The optimized structures had all real vibrational frequencies. Vibrational frequencies below 50 cm^{-1} were corrected to 50 cm^{-1} while computing thermal corrections to free energies. The effect of the implicit solvent was studied by using the implicit SMD solvation model[280] for DMF (N,N-dimethylformamide) and water respectively. The uranium atom has a +6 oxidation state, and hence, all calculations were performed in the singlet state with one negative charge per node+linker motif.

5.8.3 Linker Synthesis

*5.8.3.1 Dimethyl 2,2′-dimethyl-biphenyl-4,4′-dicarboxylate (**DMBP-OMe**) Synthesis*

DMBP-OMe synthesis was adapted from a previous report[292]. A Suzuki-Miyaura cross coupling reaction was performed *via* microwave synthesis by adding 0.66 g methyl 4-bromo-3-methylbenzoate (2.9 mmol), 0.71 g methyl 3-methyl-4-(4,4,5,5-tetramethyl-1,3,2-dioxaborolan-2-yl)benzoate (2.6 mmol), 1.16 g potassium carbonate (8.4 mmol), and 0.155 g tetrakis(triphenylphosphine)palladium(0) (0.13 mmol) to a 20 mL Biotage microwave vial (Scheme 5.1). Three cycles of N_2 purge (5 minutes) and evacuation (5 minutes) were performed on a Schlenk line. 18 mL of dioxane and 2.6 mL water were added with a syringe, and the mixture was bubbled with N_2 for 15 minutes before being heated in the microwave reactor at 150 °C for 6 hours while stirring. This synthesis was repeated twelve additional times for a total of thirteen aliquots. Following the microwave synthesis, all thirteen aliquots were combined and concentrated under reduced pressure. The remaining material was dissolved in a mixture of dichloromethane (DCM) and water and filtered through celite. Following this, four extractions of water with DCM were performed. The DCM layers were collected, combined, and dried with $MgSO_4$ before being filtered and concentrated under reduced pressure until a pink solid was observed. The solid was purified by chromatography (SiO_2, 19:1 ratio of hexanes:ethyl acetate) to produce a light pink solid. The solid was then dissolved in chloroform and refluxed with activated carbon at 70 °C for 2.5 hours. The mixture was then filtered through celite and concentrated to give **DMBP-OMe** as

a white solid (7.3 g, 71%). ^{1}H NMR (500 MHz, $(CD_3)_2SO$), δ = 7.95 (d, *J* = 1.8 Hz, 2H, Ar-H), 7.86 (dd, *J* = 7.9, 1.7 Hz, 2H, Ar-H), 7.26 (d, *J* = 7.8 Hz, 2H, Ar-H), 3.88 (s, 6H, Ar-CH_3), 2.06 (s, 6H, OCH_3) (Scheme 5.1, Fig. 5.6).

*5.8.3.2 2,2′-dimethyl-biphenyl-4,4′-dicarboxylic acid (**DMBP**) Synthesis*

DMBP synthesis was adapted from a previous report[292]. **DMBP-OMe** was first added to a 500 mL round bottom flask along with 65 mL methanol, 65 mL tetrahydrofuran, and 55 mL 2M NaOH (aq), and refluxed at 85 °C, stirring overnight. The solution was then cooled, and the organic solvent was removed under reduced pressure. The remaining aqueous solution was then acidified with ~150 mL 1M HCl (aq), and the product, **DMBP**, was observed as a white precipitate. The final product was washed with water until the pH was neutral, washed with DCM, and dried in a vacuum oven overnight (18 h) (6 g, 86%). ^{1}H NMR (500 MHz, $(CD_3)_2SO$), δ = 7.91 (s, 2H, Ar-H), 7.83 (dd, *J* = 7.8, 1.7 Hz, 2H, Ar-H), 7.22 (d, *J* = 7.8 Hz, 2H, Ar-H), 2.05 (s, 6H, CH_3) (Scheme 5.1, Fig. 5.7).

*5.8.3.3 Diethyl 2,2′,6,6′-tetramethyl-biphenyl-4,4′-dicarboxylate (**TMBP-OEt**) Synthesis*

Following Scheme 5.2, compounds **S1**-**2**[293] and Pd SPhos Gen III catalyst were synthesized according to known literature procedures. **S1** (1.43 g, 5.56 mmol), **S2** (1.69 g, 5.56 mmol), Pd SPhos Gen III catalyst (0.174 g, 0.222 mmol), and THF (10 mL) were added to a 20 mL Biotage microwave reaction vial equipped with a magnetic stir bar. The mixture was degassed by bubbling N_2 for 30 min, at which point degassed aqueous K_3PO_4 solution (2 M, 10 mL) was added. The reaction was heated in the microwave reactor at 100 ˚C for 1 h. After cooling to room temperature, the aqueous layer was removed by a pipette. THF was removed under reduced pressure and the residue was dissolved in CH_2Cl_2 (50 mL). The solution was washed with saturated brine solution (50 mL) and dried (Mg_2SO_4). After removing the solvent, the crude solid was purified by

chromatography (SiO_2, 0% to 75% CH_2Cl_2 in hexanes) to give **TMBP-OEt** as a colorless solid film (0.79 g, 40%). ^{1}H NMR (600 MHz, $CDCl_3$), δ = 7.82 (s, 4H, Ar-H), 4.39 (q, *J* = 7.1 Hz, 4H, OCH_2), 1.92 (s, 12H, Ar-CH_3), 1.41 (t, *J* = 7.1 Hz, 6H, CH_3). ^{13}C NMR (125 MHz, $CDCl_3$), δ = 167.0, 144.3, 135.7, 129.6, 128.9, 31.1, 19.8, 14.5 (Scheme 5.2, Figs. 5.8, 5.9).

*5.8.3.4 2,2′,6,6′-tetramethyl-biphenyl-4,4′-dicarboxylic acid (**TMBP**) Synthesis*

TMBP-OEt (0.76 g, 2.14 mmol) was dissolved in THF (10 mL) in a 20 mL Biotage microwave reaction vial equipped with a magnetic stir bar. Aqueous NaOH solution (1 M, 10 mL) was added, and the resulting mixture was heated in the microwave reactor at 100 ˚C for 2 h. Upon cooling to room temperature, THF was removed under reduced pressure and the remaining aqueous solution was acidified (pH = 1) with aqueous HCl solution (2 M). The resulting white precipitate was collected by filtration, washed with H_2O (20 mL) and dried under high vacuum to give **TMBP** as a white solid (0.57 g, 90%). ^{1}H NMR (600 MHz, $(CD_3)_2SO$), δ = 12.87 (bs, 2H, COOH), 7.77 (s, 4H, Ar-H), 1.86 (s, 12H, Ar-CH_3) (Scheme 5.2, Fig. 5.10). This characterization agrees with the reported literature[294].

5.8.4 NU-1303-6 Supplemental Experimental Procedures

5.8.4.1 Synthesis

Single crystal synthesis of NU-1303-*6* was performed by adding 0.404 mL of a 10 mgmL^{-1} **DMBP** stock in DMF (14.95 μmol) and KOH to a 1.5-dram glass vial. Under high humidity conditions (≥45% humidity), 6.5 μL of 2.08 M KOH (aq) (13.5 μmol) was used, and under low humidity conditions, (<45% humidity), 13 μL of 1M KOH (aq) (13.0 μmol) was used. The sealed vial was sonicated for 5 minutes, and 0.5 mL of a 10 mgmL^{-1} uranyl nitrate hexahydrate stock in *N*,*N*-dimethylformamide (DMF) (9.96 μmol) was subsequently added. The sealed vial was then shaken vigorously by hand for ~5 seconds and sonicated for 30 minutes. The sealed vial was then transferred to a sand bath in a 120° C oven and left overnight (~18 h). Large yellow crystals 150-200 μm in size were observed to grow on the sides and bottom of the vial (Fig. 5.11). Once taken

out of the oven, the vial of MOF made for SCXRD analysis was set aside, and solvent was not exchanged. The synthesis resulted in 72% yield.

This synthetic procedure was scaled up for all other non-SCXRD measurements in the following manner. 2.424 mL of a 10 $mgmL^{-1}$ DMBP stock in DMF (89.7 μmol), and KOH were added to a 2-5 mL Biotage microwave vial and sealed. Under high humidity conditions (≥45% humidity), 15.6 μL of 5M KOH (aq) (78 μmol) was used, and under low humidity conditions (<45% humidity), 78 μL of 1M KOH (aq) (78.0 μmol) was used. The sealed vial was sonicated for 5 minutes, and 3 mL of a 10 $mgmL^{-1}$ uranyl nitrate hexahydrate stock in DMF (59.76 μmol) was subsequently added. The sealed vial was then shaken vigorously by hand for ~5 seconds and sonicated for 30 minutes. The sealed vial was then transferred to a sand bath in a 120° C oven and left overnight (~18 h). Large yellow crystals 150-200 μm in size were observed to grow on the sides and bottom of the vial. Once taken out of the oven, the MOF was immediately washed three times with fresh DMF, making sure to keep the MOF solvated at all times during solvent exchange. Crystals were scraped off the sides and bottom of the vial using a spatula, and if multiple vials of MOF were synthesized at once, MOF from all vials was combined into one batch. The synthesis resulted in 67 % yield.

Note that the NU-1303-*6* synthesis is very sensitive to the molar amount and concentration of KOH added to the synthesis, and a gel will form under improper conditions.

5.8.4.2 SCXRD

NU-1303-*6* single crystal data was collected immediately following synthesis. Data collection and refinement details are included in the Methods section and in Table 5.1. We did not observe the hydrogen-bonding interaction experimentally in *M1 via* SCXRD.

5.8.4.3 Structural Analysis

NU-1303-*6* crystallizes in the $I4_132$ space group with a 44.1 Å cubic unit cell containing 72 **DMBP** linkers and 48 uranyl nodes. The asymmetric unit is shown in Figure 5.12. We used *PLATON*[295] to calculate the solvent-accessible pore volume for the structure (74.7%). Each **srs** cage accommodates 14 uranyl nodes connected by 15 **DMBP** linkers with one type of vertex and one type of edge (Fig. 5.1c). The methyl groups located on the biphenylene linkers force rotation around the central carbon-carbon bond, so that the torsion angle between the two phenylene rings is 76.1° for one third of the linkers and 88.5° for other two thirds (Fig. 5.12). The six networks arrange spatially with respect to each other in three sets of pairs. These three network pairs can be visualized in Figure 5.13 by viewing the structure down the *a*, *b*, and *c* directions. Within each single pair, the closest distance between uranium atoms on different networks is 9.7 Å, denoted as *Motif 1* (*M1*) (Fig. 5.1e). The closest distance between uranium atoms on different sets of network pairs is 8.1 Å, denoted as *Motif 2* (*M2*) (Fig. 5.1e). NU-1303-*6* has 0.34 gcm^{-3} nodes per unit cell (54.4% nodes w/w).

5.8.4.4 Cation Identification

Potential cations from the synthesis of NU-1303-*6* are K^+, UO_2^{2+}, dimethylammonium (from DMF degradation), H^+, or H_3O^+.

To identify if either K^+ or UO_2^{2+} existed as charge-balancing cations in NU-1303-*6*, we implemented ICP-OES analysis. NU-1303-*6* samples were prepared by first washing the MOF in fresh DMF and exchanging the DMF every hour for 3 hours. Three 1-hour ethanol (EtOH) washes were then performed. The sample was then placed in an 80° C vacuum oven for 18 hours and subsequently heated under ultrahigh vacuum on a Smart VacPrep (SVP) instrument (see Methods) at 120° C for 24 hours. A microbalance was used to accurately weigh the sample, which was then prepared for ICP-OES analysis as described in the Methods section. ICP-OES analysis for U and

K revealed 0.1 potassium cations present per uranium; thus, 0.1 K^+ is present per anionic node. Based on the sample mass, the expected U content with UO_2^{2+} as a counterion was calculated. However, ICP-OES analysis revealed a much lower U content, which thus demonstrates that UO_2^{2+} is not present as a counter-cation (Table 5.2).

To determine if dimethylammonium existed as a charge-balancing cation in NU-1303-*6*, we implemented ^{1}H NMR analysis. NU-1303-*6* was prepared for NMR analysis by first washing in fresh DMF and exchanging the DMF every hour for 3 hours. The sample was then placed in a 120° C oven for 18 hours and subsequently heated under ultrahigh vacuum on an SVP instrument at 150° C for 24 hours. NU-1303-*6* was then digested by sonicating ~2 mg of NU-1303-*6* in 5-6 drops of 0.1M NaOD for one hour. Then, 0.5 mL D_2O was added, and the solution was sonicated for 1 hour. After base digestion, dimethylammonium cations should be observed *via* ^{1}H NMR as dimethylamine. However, dimethylamine peaks were not observed from the ^{1}H NMR analysis. Rather, 0.13 DMF were observed per node (Fig. 5.14), attributed to leftover DMF from the soaking and washing steps. To ensure that the ^{1}H NMR signal was correctly assigned to DMF and not dimethylamine, one drop of dimethylamine was added to the same NMR tube, and the sample was remeasured. The peaks assigned as DMF (7.93, 3.01, 2.86 ppm) did not change in intensity, but two new peaks (3.06, 2.90 ppm) were observed which correspond to dimethylamine (Fig. 5.15). This control experiment verified that dimethylammonium is not a charge-balancing cation in NU-1303-*6*.

Thus, we assign the cation as 0.1 K^+ and 0.9 H^+ or H_3O^+ per anionic node, such that the formula for NU-1303-*6* is either $H^+_{0.9}K^+_{0.1}[UO_2(DMBP)_{1.5}]^-$ or $(H_3O^+)_{0.9}K^+_{0.1}[UO_2(DMBP)_{1.5}]^-$.

To further demonstrate that NU-1303-*6* does indeed hold a -1 charge on each uranyl-based node, we performed a cation exchange with tetraethylammonium chloride (TEACl). Approximately 20

mg of NU-1303-*6* was first washed in fresh DMF, and the DMF was then exchanged every hour for 3 hours. The solvent was then exchanged to a solution of TEACl dissolved in DMF (18 $mgmL^{-1}$) and left to soak for 12 hours. Five 1-hour, one 12-hour, five 1-hour, and one 48-hour soaks of the MOF in TEACl solution were then performed at 50 °C (oil bath). Three subsequent 1-hour DMF washes were performed before the sample was then placed in a 120 °C oven for 18 hours and then heated under ultrahigh vacuum on an SVP instrument at 150 °C for 24 hours. NU-1303-*6* was then digested by sonicating ~2 mg of NU-1303-*6* in 5-6 drops of deuterated sulfuric acid for 15 minutes. Then, 0.5 mL deuterated dimethyl sulfoxide ($(CD_3)_2SO$) was added, and the solution was sonicated for 15 minutes. ^1H NMR analysis revealed 0.95 tetraethylammonium (TEA^+) cations per charged node (Fig. 5.16, peaks at 3.07 and 1.03 ppm), indicating close to full cation exchange ($TEA^+[UO_2(DMBP)_{1.5}]^-$).

5.8.4.5 NU-1303-6 Activation and Gas Physisorption

NU-1303-*6* was synthesized following methods discussed above and washed with fresh DMF three times once removed from the oven. 30 mg of NU-1303-*6* was placed in a 15 mL centrifuge tube and soaked in 7 mL of fresh DMF for 96 hours. The solvent was then exchanged to 7 mL of EtOH and allowed to soak for 2 hours. The EtOH solvent exchange was repeated two additional times, ending with a final EtOH exchange and overnight soak. We made sure to keep the MOF solvated at all times during solvent exchange. An additional EtOH exchange was performed immediately before supercritical CO_2 (sc-CO_2) activation (CO_2 syphon tank used). After sc-CO_2 activation, the sample was removed from the unit and immediately prepared for further analysis in a fume hood. Thermal activation at 50° C under ultrahigh vacuum for 24 hours was completed on an SVP, and subsequent N_2 adsorption-desorption studies followed on a Tristar II 3020. The BET analysis summary can be seen in Table 5.3, and the BET surface area plot can be seen in Figure 5.17.

5.8.4.6 Calculated Pore Size Distribution (PSD), Geometric Surface Area, and Void Fraction

The NU-1303-*6* simulated PSD is shown in Figure 5.18. It was calculated using RASPA 2.0[290] with framework non-metal atom radii according to the Dreiding forcefield[290] and uranium atom radii according to the Universal Force Field[290]. Calculated values are 1-2 Å smaller than experimentally determined values, which is within reasonable error. The geometric surface area for NU-1303-*6* was calculated using RASPA (Monte Carlo code) with a N_2 sized probe (a 3.32 Å diameter spherical probe) (Table 5.4), and the void fraction was calculated using RASPA (Monte Carlo code) with a He sized probe (Table 5.5). The calculated pore volume was obtained by multiplying the void fraction by the cell volume.

5.8.4.7 Thermogravimetric Analysis (TGA)

To experimentally demonstrate the difference in pore volume between NU-1303-*6* and NU-1303-*1*, we implemented TGA following the details in the Methods section. Both samples were prepared by drop-casting crystals from DMF onto weigh paper, transferring the semi-dried crystals to a TGA pan, and starting the TGA measurement. Each step was equally timed for NU-1303-*6* and NU-1303-*1* to ensure that both samples lost the same amount of solvent to air. Figure 5.19 shows the normalized TGA traces for NU-1303-*6* and NU-1303-*1*. The first step is attributed to DMF loss from the MOF pores. The significant experimental difference in DMF lost reflects the considerable calculated pore volume difference between NU-1303-*6* and NU-1303-*1* (Table 5.5). In fact, the estimated experimental void fractions from TGA are similar to the calculated void fractions (Table 5.6). We attribute the slightly lower estimated experimental void fractions to solvent loss of DMF from the MOF pores after drop-casting. More importantly, the differences in void fractions between NU-1303-*6* and NU-1303-*1* are almost identical when comparing the calculated to the estimated experimental values. This data then demonstrates the high pore volume of NU-1303-*1* and the differences in pore volume between NU-1303-*6* and NU-1303-*1*.

5.8.4.8 PXRD Matching

The solvent exchange and activation procedure of NU-1303-*6* was monitored using PXRD. As can be seen in Figure 5.20, splitting of the first two major peaks at 2.7° and 4.9° was observed to a small extent after EtOH exchange, and to a much greater extent after activation (Figs. 5.20, 5.21). To understand the structural transformation associated with this splitting, we modeled simulated PXRD patterns which matched the experimental patterns for NU-1303-*6* after EtOH exchange (NU-1303-*6*_EtOH), and after activation (NU-1303-*6*_Act) (Fig. 5.20, Table 5.7). These simulated patterns were matched to experimental patterns using the procedure described in the methods section. We found that peak splitting in the activated experimental pattern could be reproduced in the simulated pattern by breaking the symmetry $a = b = c$. Specifically, $a = b = 41.3$ Å and $c = 48.6$ Å in NU-1303-*6*_Act compared to $a = b = c = 45.3$ Å in NU-1303-*6*_EtOH (Table 5.8). Note that the splitting of the second peak in the experimental NU-1303-*6*_EtOH PXRD pattern was not reproduced in the simulated pattern. However, the splitting of the first two peaks in the simulated patterns become more pronounced as difference between the *a*/*b* and *c* parameters increases in magnitude. Consequently, we expect that the lattice parameters are much nearer the symmetry $a = b = c$ in NU-1303-*6*_EtOH than in NU-1303-*6*_Act.

5.8.4.9 Le Bail Refinement

In order to validate the calculated lattice parameters for NU-1303-*6*_EtOH and NU-1303-*6*_Act, we performed Le Bail refinement on collected powders, following the procedures found in the Methods section. As can be seen in Table 5.8, the models developed *in silico* are reasonably close to what is observed experimentally. The agreement factors are also within reasonable error (Table 5.9).

5.8.4.10 DFT CIF Generation

We then generated CIFs from the optimized unit cells corresponding to the NU-1303-*6* structural conformations adopted over the course of solvent exchange and activation (NU-1303-*6*_EtOH and NU-1303-*6*_Act, respectively. See Supplemental Data). Unit cell expansion or contraction of these highly interpenetrated MOFs can be modeled in two ways: (1) the individual lattices can be moved closer together or farther apart *without changing the shapes of the individual lattices* or (2) the coordinates of all atoms can be changed to account for the contraction/expansion (*i.e.* the fractional coordinates are maintained while the unit cell parameters are altered). *This changes the lattice-lattice distances as well as the shapes of the individual lattices*. Here, we modeled expansion/contraction with method 2. The peak splitting observed in NU-1303-*6*_Act is likely only possible with changes in the linker conformations and lattice-lattice interactions not modeled here, given the pronounced compression of the *a*/*b* dimensions.

5.8.4.11 Periodic DFT Optimization

The primitive unit cells of NU-1303-*6* (constructed based on the experimental unit cell) and NU-1303-*1* were optimized using periodic DFT. A primitive unit cell of NU-1303-*6* has 24 uranyl nodes, while that of NU-1303-*1* consists of 4 uranyl nodes. The computed electronic energy per uranyl node in NU-1303-*6* is 5.8 kcalmol^{-1} higher than in NU-1303-*1* (Eq. 6), which suggests that NU-1303-*6* is less stable than NU-1303-*1* and that de-interpenetration is favored.

$$\Delta E\ per\ U = \frac{6 * E_{NU-1303-1} - E_{NU-1303-6}}{24} = -5.8\ kcal/mol \qquad \text{Eq. 6}$$

The nearest U–U distance in *M1* and *M2* in the optimized unit cell of NU-1303-*6* is 10.6 Å and 8.0 Å, respectively, in good agreement with the experimental U–U distances of 9.7 Å and 8.1 Å, respectively.

The periodic calculations incorporate long-range non-covalent interactions. Even in the presence of these potential interactions, the lower stability of NU-1303-*6* relative to NU-1303-*1* suggests

that de-interpenetration is favored thermodynamically due to electrostatic interactions. Therefore, because de-interpenetration is favored even in the presence of potential non-covalent interactions, and because the prohibitively large unit cell of NU-1303-*6* (1224 atoms) makes it challenging to compute free energies efficiently, we continued our computational study using cluster models (Figs. 5.22-5.25). These cluster models are described below.

5.8.4.12 Energy Decomposition Analysis (EDA)

The cluster models used for EDA can be found in Figure 5.22, and their Cartesian coordinates are included as Supplemental Data.

The EDA in ADF defines the total interaction energy between cluster fragments, ΔE_{int}, as containing contributions from the orbital interaction energy, ΔE_{oi}, and the total steric interactions between the fragments, ΔE_{steric} (Eq. 7):

$$\Delta E_{int} = \Delta E_{oi} + \Delta E_{steric} \quad \text{Eq. 7}$$

In an attempt to determine whether steric interactions or orbital interactions govern the interaction energy of each motif, we analyzed the individual contributions of ΔE_{steric} and ΔE_{oi} to ΔE_{int} of each motif at varying U–U distances using the M06-2X functional, in gas phase. The local minimum energy U–U distance in *M1* is 10.4 Å and in *M2 is* 8.6 Å using the M06-2X functional. The total interaction energy, total orbital interaction energy, and total steric interaction energy along the full range of U–U distance up to 50 Å can be seen in Figure 5.26.

Figure 5.26b shows the computed contribution of the orbital interactions (ΔE_{oi}) (M06-2X) to the total energy for *M1* and *M2*. It accounts for the charge transfer between unoccupied and occupied orbitals. At the predicted 10.4 Å minimum energy U–U distance for *M1*, the total orbital interaction is –13.6 kcalmol^{-1}, while at the predicted 8.6 Å minimum energy U–U distance for *M2*, the total orbital interaction is –8.2 kcalmol^{-1} (Fig. S26b, inset). Thus, for both motifs, there is a significantly favorable charge transfer between the occupied and unoccupied orbitals at smaller U–U distances; this interaction decreases upon increasing

U–U distance until it becomes negligible. The favorable orbital interactions are more dominant for *M1* than for *M2*.

The contribution of the unfavorable steric interactions (ΔE_{steric}), which include the electrostatic interactions and the Pauli repulsion between fragments, to the total bonding energy in *M1* and *M2* is shown in Figure 5.26c (M06-2X). At the predicted 10.4 Å minimum energy U–U distance for *M1*, the total steric interaction is 22.9 kcalmol^{-1}, while at the predicted 8.6 Å minimum energy U–U distance for *M2*, the total steric interaction is 28.0 kcalmol^{-1} (Fig. 5.21c, inset). The positive ΔE_{steric} values between *M2* fragments are greater than those between *M1* fragments, likely because the *M2* minimum U–U distance is smaller, producing a larger steric repulsion between fragments.

Since the free energy calculations below showed similar results and trends for cluster models both with and without cations present, the EDA values should also be similar both with and without cations present. Thus, EDA was performed using cluster models without cations present.

5.8.4.13 Free Energy Cluster DFT Calculations

The cluster models used for free energy calculations can be found in Figures 5.22-5.27, and their Cartesian coordinates are included as Supplemental Data. To account for potential shielding of anionic nodes by counter-cations, we included either H^+ (Fig. 5.23), H_3O^+ (Fig. 5.24), or K^+ (Fig. 5.25) cations in our *M1* and *M2* cluster models. We also performed free energy calculations on an uncapped model (no cation) for comparison (Fig. 5.22).

Because of different possible cation positions around the uranyl nodes, we report two stable configurations for *M2*: *M2a* and *M2b*. The most stable positions of the H^+ cations in *M1*, *M2a*, and *M2b* are shown in Figure 5.23. Each H^+ cation binds preferentially to a linker carboxylate O of each framework (0.97 Å). The most stable positions of the H_3O^+ cations in *M1*, *M2a*, and *M2b* are shown in Figure 5.24. In *M1*, *M2a*, and one cation of *M2b*, one proton from H_3O^+ binds to a carboxylate O of the framework (1.02 Å-1.05 Å) while the remaining water molecule from H_3O^+

interacts through hydrogen-bonds with this proton (1.43 Å- 1.50 Å) and the remaining carboxylate groups of the framework (1.88 Å-1.91 Å). With the second cation of *M2b*, H_3O^+ sits in the pocket between the two uranium nodes and interacts simultaneously through three hydrogen-bonding interactions with the carboxylate O atoms of the two frameworks (1.37 Å-1.78 Å). The equilibrium positions of K^+ cations in in *M1*, *M2a*, and *M2b* are shown in Figure 5.25. The K^+ cations simultaneously interact with two equatorial carboxylate O atoms (2.56 Å-2.62 Å) and one uranyl O (2.90 Å-3.56 Å) in *M1* and *M2a*. This contrasts with the H^+ cations which do not interact with the uranyl O and remain in the equatorial plane of the uranyl group. In *M2b*, one K^+ cation interacts in a similar manner as in *M1* and *M2a*. However, the second K^+ cation interacts simultaneously with two equatorial carboxylate O atoms of each framework (2.54 Å-2.61 Å), thereby, bridging the two frameworks through its four interactions. Similar positions for these cations were obtained in the presence of DMF and water (SMD).

We obtained relative energies (ΔE), enthalpies (ΔH) and free energies (ΔG) of transformation (Eq. 4, Eq. 8, Fig. 5.27) of NU-1303-*6* to NU-1303-*1* by modeling the transformation of interpenetrated cluster models for *M1*, *M2a*, and *M2b* to non-interpenetrated fragments. Each interpenetrated cluster model is made up of a pair of fragments $(X[UO_2(H-DMBP)_3])_2$ where X = H^+, H_3O^+, K^+, or no cation) and each non-interpenetrated fragment is made up of a uranyl node and three attached linkers capped with protons ($2(X[UO_2(H-DMBP)_3]$) where X = H^+, H_3O^+, K^+, or no cation) (Fig. 5.32). We performed these calculations in implicit solvent models for DMF and water (Tables 5.10-5.11).

$$\Delta X \; per \; U = \frac{2 * X_{NU-1303-1} - X_{NU-1303-6}}{2} \qquad \text{Eq. 8}$$

$$(X = E, H, G)$$

The free energies of the uncapped cluster model (Fig. 5.28c, Table 5.11) and the cluster models with cations included (Figs. 5.3B, 5.28a-b, Table 5.10) all predict lower stability of the interpenetrated motifs relative to their non-interpenetrated fragments, similar to what was predicted from periodic calculations. While H_3O^+, and K^+ cations are seen to slightly shield de-interpenetration in *M2b*, they do not prevent de-interpenetration, as evidenced by the negative free energy values in the presence of these cations. The tabulated electronic energies and the corresponding free energies of transformation (Table 5.10-5.11) generally reinstate that de-interpenetration is favored both energetically and entropically (more negative free energies as compared to electronic energies for de-interpenetration). Lastly, the reported energies, enthalpies, and free energies for de-interpenetration of the uncapped model show a similar trend in the stability of the interpenetrated motif relative to the non-interpenetrated motif in the presence of implicit solvent models for both DMF and water (Table 5.11).

Furthermore, the increase in free energies of transformation (less negative free energies) with the change in solvent from DMF to water suggests that water stabilizes the interpenetrated motifs of NU-1303-*6* relative to the non-interpenetrated fragments in NU-1303-*1*, thereby impeding its transformation to NU-1303-*1*. These trends are observed in the presence of cations H^+, H_3O^+, and K^+ (Figs. 5.3B, 5.28a-b, Table 5.10) and no cations (Fig. 5.28c, Table 5.11), except for *M2b* in the presence of H_3O^+ and K^+ (Fig. 5.28a-b). For *M2b* in the presence of H_3O^+, the free energy values in DMF and water are both -9.8 $kcalmol^{-1}$ (Fig. S28a), and for *M2b* in the presence of K^+, the free energy value in water is only 0.3 $kcalmol^{-1}$ more negative than in DMF. While these differences are small and likely insignificant, we attribute them to the multiple interactions that H_3O^+, and K^+ make with the framework atoms in the *M2b* pocket.

5.8.4.14 De-Interpenetration Tracking

We show that dissolved material from the de-interpenetrated frameworks is present in the supernatant of the soaking DMF solvent. Inductively coupled plasma-mass spectrometry (ICP-MS) analysis reveals an increase in uranium concentration over time in the DMF soaking solution (Fig. 5.29a). UV-Vis experiments also show an increase in uranyl signal intensity over time (430, 445, 458, and 578 nm signals), thus corroborating the ICP-MS data (Fig. 5.29b).

5.8.5 NU-1303-3 Supplemental Experimental Procedures

5.8.5.1 SCXRD

NU-1303-*3* single crystal data was collected 29 days after synthesis. Data collection and refinement details are included in the Methods section and in Table 5.1. The single crystals were small and did not diffract very well. The best resolution obtained with a Cu source was 1.35 Å. The 3-dimensional structure also contains a large amount of void space (87.6% of the unit cell volume, from PLATON). Due to the low resolution and disorder, some of the methyl groups on the **DMBP** linkers were not directly observed from the difference electron density map. For similar reasons, some of the hydrogen atoms on the methyl groups were not added due to poor refinement convergence. As a result, they were added by using SHELX restraints such as DFIX, SIMU, DELU and FLAT.

5.8.5.2 Structural Analysis

From SCXRD, NU-1303-*3* has the same node (Fig. 5.1a), linker (Fig. 5.1b), node/linker connectivity, and **srs** topology as NU-1303-*6*. The uranyl-based node is thus a hexagonal bipyramid with a –1 formal charge, and the overall framework is anionic. NU-1303-*3* crystallizes in the *I2* space group with a monoclinic unit cell where a = 38.3 Å, b = 62.2 Å, c = 38.4 Å, $\alpha = \gamma = 90°$, and $\beta = 109.8°$. The unit cell contains 16.5 **DMBP** linkers and 12 uranyl nodes. The methyl groups located on the biphenylene linkers force rotation around the central carbon-carbon bond, so that the torsion angle between the two phenylene rings ranges from 61.79° to 87.04°

(specifically, 61.79°, 69.99°, 71.89°. 76.90°, 79.31°, 76.75°, 81.70°, 82.04°, 83.96°, 87.04° torsion angles were observed). Each **srs** cage accommodates 14 uranyl nodes connected by 15 **DMBP** linkers (Fig. 5.1c). Three of these identical networks intertwine to form NU-1303-*3* (Fig. 5.33). Throughout the extended structure of NU-1303-*3*, there are three reoccurring motifs where anionic nodes on the three individual networks are separated by close distances, named *Motif 5* (*M5*), *Motif 6* (*M6*), and *Motif 7* (*M7*). These three motifs can be observed in Figure 5.34, and the U–U distances for each motif are reported in Table 5.12.

5.8.5.3 Intermediate Interpenetration in NU-1303 Activation and Gas Physisorption

NU-1303-*6* was synthesized following previously discussed methods and washed with fresh DMF three times once removed from the oven. 30 mg of NU-1303-*6* was placed in a 15 mL centrifuge tube and soaked in 7 mL of fresh DMF for 17 days. The solvent was then exchanged to 7 mL of EtOH and allowed to soak for 2 hours. The EtOH exchange was repeated two additional times, ending with a final EtOH exchange and overnight soak. We made sure to keep the MOF solvated at all times during solvent exchange. We then performed sc-CO_2 activation (CO_2 syphon tank used). After sc-CO_2 activation, the sample was removed from the unit and immediately prepared for further analysis in a fume hood. Thermal activation at 50 °C under ultrahigh vacuum for 24 hours was completed on an SVP, and subsequent N_2 adsorption-desorption studies followed on a Tristar II 3020. Analysis of the N_2 isotherm shows a Brunauer-Emmett-Teller (BET) area of 1650 m^2g^{-1} and a pore volume of 1.67 cm^3g^{-1} (Fig. 5.30a). The BET area and pore volume are intermediate values between that of NU-1303-*6* and NU-1303-*1*. Additionally, the pore size distribution shows a mixture of the 15.2 and 20.5 Å pores (expected from NU-1303-*6*), and the 40.7 Å pore (expected from NU-1303-*1*) (Fig. 5.30b). This data thus suggests that a mixture of NU-1303-*6* and NU-1303-*1* are present in this captured intermediate as NU-1303-*6* undergoes de-

interpenetration. The entire activation procedure was monitored at each step by PXRD (Fig. 5.31). Partial splitting of the second major peak at 4.8° (as compared to full splitting of this peak in NU-1303-*6*, Fig 5.2h) also supports the premise of intermediate interpenetration. The BET analysis summary can be seen in Table 5.3, and the BET surface area plot can be seen in Figure 5.32.

5.8.6 NU-1303-1 Supplemental Experimental Procedures

5.8.6.1 Structure

We obtained a SCXRD dataset of the NU-1303-*1* uranium positions. To prepare the SCXRD sample, NU-1303-*6* crystals were first soaked in hydrous DMF for 946 days. Since the NU-1303-*1* crystal quality was poor following the prolonged DMF soak, we performed a cation exchange to crystal violet dye by soaking in a solution of crystal violet dissolved in *N*,*N*-diethylformamide (DEF) for 24 hours. After dye exchange and subsequent washing with fresh DEF solvent, the crystals became a dark purple color, indicating that they had adsorbed the dye (Fig. 5.35). We hypothesize that this method improves the diffraction resolution by replacing disordered solvent from the pores with larger molecules. With this improvement in resolution (the best resolution obtained with a Cu source was 1.60 Å), we obtained the uranium positions of NU-1303-*1 via* SCXRD (Supplemental Data).

Since weak diffraction prevented us from obtaining the positions of light elements (C, O), NU-1301-*1* was modeled by changing the space group of NU-1303-*6* to *P1* in Materials Studio and deleting 5 **srs** networks while maintaining the same topology and unit cell of NU-1303-*6* (Figs. 5.2c, 5.36).

To ensure that this model matched the SCXRD data, we implemented Le Bail analysis of a NU-1303-*1* powder sample (Fig. 5.37). As observed with the single crystal of NU-1303-*1*, the MOF powder did not diffract well at high resolution, which prevented us from obtaining a more precise model using Rietveld refinement. However, pairing the extinction analyses from SCXRD with Le

Bail analysis (see Methods) of the NU-1303-*1* powder sample, we generated lattice parameters for the experimental structure which matched the modeled structure precisely (Table 5.8). Additionally, the simulated PXRD generated from the single crystal data also matches well with the simulated PXRD generated from the structural model (Fig. 5.38). In this way, the SCXRD uranium positions of NU-1303-*1* were validated both experimentally through powder refinement and computationally through Materials Studio modeling.

These findings also reveal that NU-1303-*1* remains present even after 946 days of soaking in DMF (over 2.5 years). We show that this fully de-interpenetrated single crystal also reflects the bulk powder by performing nitrogen physisorption on a sample soaked in hydrous DMF for 752 days (2 years and 22 days). The results show loss of total uptake but reveal full de-interpenetration (Fig. 5.39).

5.8.6.2 NU-1303-1 Activation and Gas Physisorption (752-day DMF soak)

NU-1303-*6* was synthesized following previously discussed methods and washed with fresh DMF three times once removed from the oven. 20 mg of NU-1303-*6* was placed in a 15 mL centrifuge tube and soaked in 7 mL of fresh DMF for 752 days. The MOF was then placed in a 2-5 mL Biotage microwave vial, and the vial was capped. The solvent was then exchanged to 7 mL of anhydrous acetonitrile (MeCN) through the microwave cap septum, using a syringe, and allowed to soak for 1 hour. The MeCN exchange was repeated two additional times through the microwave tube septum using a syringe, ending with a final MeCN exchange and overnight soak. We made sure to keep the MOF solvated at all times during solvent exchange. We then performed sc-CO_2 on a day with low humidity (≤45% humidity), using CO_2 from a CO_2 syphon tank. After sc-CO_2 activation, the sample was quickly removed from the unit and the entire sample holder was transferred directly to a small plastic container which fit snugly. The container was wrapped in

parafilm, and the sample was transferred to an Argon glovebox. The sample was prepared for physisorption studies by sealing it in a sorption tube in the glovebox. Thermal activation at 50 °C under ultrahigh vacuum for 24 hours was completed on an SVP, and subsequent N_2 adsorption-desorption studies followed on a Tristar II 3020 (Fig. 5.39)

5.8.6.3 NU-1303-1 Activation and Gas Physisorption (144-day DMF soak)

NU-1303-*6* was synthesized following previously discussed methods and washed with fresh DMF three times once removed from the oven. 30 mg of NU-1303-*6* was placed in a 15 mL centrifuge tube and soaked in 7 mL of fresh DMF for 144 days. The solvent was then exchanged to 7 mL of EtOH and allowed to soak for 2 hours. The EtOH exchange was repeated two additional times, ending with a final EtOH exchange and overnight soak. We made sure to keep the MOF solvated at all times during solvent exchange. We then performed sc-CO_2 on a day with low humidity (≤45% humidity range), using CO_2 from a CO_2 syphon tank. After sc-CO_2 activation, the sample was removed from the unit and immediately prepared for further analysis in a fume hood. Thermal activation at 50 °C under ultrahigh vacuum for 24 hours was completed on an SVP, and subsequent N_2 adsorption-desorption studies followed on a Tristar II 3020 (Fig. 5.2f, 5.2i). The entire activation procedure was monitored at each step by PXRD (Fig. 5.40). The BET analysis summary can be seen in Table 5.3, and the BET surface area plot can be seen in Figure 5.41. Based on the change in pore size distribution from NU-1303-*6* (Fig. 5.2g) to NU-1303-*1*(Fig. 5.2i), the de-interpenetration yield of a NU-1303-*6* sample soaked in DMF for 144 days is 97%.

5.8.6.4 NU-1303-1 Activation and Gas Physisorption (Anhydrous Conditions)

NU-1303-*6* was synthesized following previously discussed methods and washed with fresh anhydrous DMF three times once removed from the oven. 30 mg of NU-1303-*6* in anhydrous DMF was placed in a 2-5 mL Biotage microwave vial, and the vial was capped. The solvent was then exchanged three times to 7 mL anhydrous DMF through the microwave cap septum, using a

syringe. The vial was then purged with N_2 for one hour, and the MOF was left to soak in anhydrous DMF for 96 hours. The solvent was then exchanged to 7 mL of anhydrous MeCN through the microwave tube septum using a syringe and allowed to soak for 2 hours. This MeCN solvent exchange was repeated two additional times, ending with a final anhydrous MeCN exchange and overnight soak. We made sure to keep the MOF solvated at all times during solvent exchange. We then performed sc-CO_2 activation (bone-dry CO_2 syphon tank used). After sc-CO_2 activation, the sample was quickly removed from the unit and the entire sample holder was transferred directly to a small plastic container which fit snugly. The container was wrapped in parafilm, and the sample was transferred to an Argon glovebox. The sample was prepared for physisorption studies by sealing it in a sorption tube in the glovebox. PXRD samples were also prepared and sealed in the glovebox. Thermal activation at 50 °C under ultrahigh vacuum for 24 hours was completed on an SVP, and subsequent N_2 adsorption-desorption studies followed on a Tristar II 3020. Analysis of the N_2 isotherm shows a BET area of 1515 m^2g^{-1}, a pore volume of 2.34 cm^3g^{-1}, and a pore size distribution of 40.8 Å (Fig. 5.42). The entire activation procedure of NU-1303-*1* was monitored at each step by PXRD (Fig. 5.43). No splitting of the major PXRD peaks after activation was observed. As discussed above and in the manuscript, this demonstrates the presence of fewer networks, rather than multiple networks. The BET analysis summary can be seen in Table 5.3, and the BET surface area plot can be seen in Figure 5.44.

5.8.6.5 Calculated Geometric Surface Area and Void Fraction

The geometric surface area for NU-1303-*1* was calculated using RASPA (Monte Carlo code) with a N_2 sized probe (a 3.32 Å diameter spherical probe) (Table 5.4), and the void fraction was calculated using RASPA (Monte Carlo code) with a He sized probe. The calculated pore volume

was obtained by multiplying the void fraction with the cell volume (Table 5.5). A comparison to the calculated values for NU-1303-*6* is discussed above in section 4.

5.8.6.6 Thermogravimetric Analysis (TGA)

To experimentally demonstrate the difference in pore volume between NU-1303-*6* and NU-1303-*1*, we implemented TGA following the details in the Methods section. A thorough discussion of the procedure and results can be found above in section 4.

5.8.7 NU-1304 Supplemental Experimental Procedures

5.8.7.1 Synthesis

NU-1304 was synthesized by adding 0.5 mL of a 10 $mgmL^{-1}$ uranyl nitrate hexahydrate stock in DMF (9.96 μmol), 0.45 mL of a 10 $mgmL^{-1}$ **TMBP** stock in DMF (15.08 μmol), and 10 μL of 1 M KOH (aq) (10 μmol) to a 1.5 dram glass vial that was then sealed. The vial was shaken vigorously by hand for ~5 seconds and sonicated for 5 hours, shaking vigorously by hand for ~5 seconds every hour. The vial was then transferred to a sand bath, preheated in a 120 °C oven, and left in the oven overnight (~18 h). Large yellow, cubic crystals ~150 μm in size (Fig. 5.45) were observed to grow on the sides and bottom of the vial. The same synthesis procedure was used for SCXRD and all other analysis. Once taken out of the oven, vials of MOF made for SCXRD analysis were set aside, and solvent was not exchanged. The MOF sample made for all other analysis was immediately washed three times with fresh DMF, making sure to keep the MOF solvated at all times. Crystals were scraped off the sides and bottom of the vials using a spatula, and multiple vials from the same batch were combined.12-15 vials were combined to make a batch large enough for physisorption analysis. The synthesis resulted in 57 % yield.

5.8.7.2 Structure

NU-1304 single crystal data was collected 3 days after synthesis. Due to the low resolution of the diffraction data, locations of light-atom (C and O) positions could not be determined. The uranium

positions determined from SCXRD (Supplemental Data) were used to construct the initial structure of NU-1304 for the ToBaCCo structural model and further DFT optimization. Once the linkers were added, we found the experimental/simulated XRD patterns to match better with a slight expansion of the cubic unit cell from 43.4 Å to 44.8 Å (see below for the PXRD matching procedure used).

Given that SCXRD data provided only the uranium node positions, linkers were added to the NU-1304 structure using ToBaCCo while maintaining the experimentally determined node positions (Supplemental Data, NU-1304_ToBaCCo). Linker positions were assessed by calculating the pairwise distances between uranium atoms and adding linkers between all pairs of uranium atoms that could realistically fit a linker. This resulted in a 6-fold interpenetrated MOF which was isoreticular to NU-1303-*6*. ToBaCCo only considers geometry when placing linkers (the centroid of the linker is added to the point equidistant between the two nodes, and the linker is rotated onto the line connecting the two nodes). This means that individual linkers may not be in optimal arrangements with respect to their attached nodes or with respect to the other linkers. Typically, this is addressed by optimizing the atom positions and unit cell parameters using molecular mechanics with a flexible, classical forcefield. However, optimization using UFF4MOF (the only MOF-specific forcefield with parameters for uranium[296]) resulted in distorted uranium nodes. This was unsurprising given that UFF/UFF4MOF only models either 90° or 109.47° angles around uranium atoms, and we expect O–U–O angles of 51.5°, 69.1°, 90.0°, 119.0°, and 172° in the uranium node from DFT calculations. Furthermore, we wanted to maintain symmetry in the simulated structure for further DFT analysis, and molecular mechanics optimizations typically reduce the space group to *P1*. Therefore, we optimized the node/linker geometries individually using DFT according to the procedure described above for NU-1303-*6*. This procedure is expected

to give a realistic geometry for each node-linker-node cluster but does not take into account the interactions between clusters.

5.8.7.3 NU-1304 Structural Analysis

The NU-1304 node consists of the uranyl unit–a single U(VI) atom bound to two axial oxygen atoms–coordinated by six equatorial oxygen atoms (Fig. 5.46a). These equatorial oxygen atoms originate from three separate ditopic, **TMBP** linkers (Fig. 5.46b), each of which binds to the uranyl unit in a bidentate fashion. The uranyl-based node is thus a hexagonal bipyramid with a –1 formal charge and therefore the overall framework is anionic. The asymmetric unit is shown in Figure 5.46c. The methyl groups located on the linker phenyl rings force rotation around the central linker carbon-carbon bond, so that the torsion angle between the biphenylene rings is 67.7° for one third of the linkers and 76.6° for other two thirds (Fig. 5.46b). Due to the rotation around the central linker carbon-carbon bond, these building blocks self-assemble into a three-dimensional, **srs**-topology MOF. Each **srs** cage is 34.8 Å in diameter and accommodates 14 uranyl nodes connected by 15 **TMBP** linkers (Fig. 5.47a-b) with one type of vertex and one type of edge. A single network of NU-1304 can be observed in Figures 4.47c-d. Six of these identical networks interpenetrate (Fig. 5.48a) to form NU-1304. NU-1304 crystallizes in the $I4_132$ space group with a 44.8 Å cubic unit cell containing 72 **TMBP** linkers and 48 uranyl nodes. We used *PLATON* to calculate the solvent accessible pore volume for the structure (71.1%), which also features 12.2 Å and 18.2 Å cages (Fig. 5.48b).

The six networks arrange spatially with respect to each other in three sets of pairs. The three pairs of interpenetrated networks can be observed by viewing the structure down the *a*, *b*, and *c* directions (Fig. 5.49). Within each single pair, the closest distance between uranium atoms on different networks is 10.2 Å, denoted as *Motif 3* (*M3*) (Fig. 5.48c). However, the closest distance

between uranium atoms on different sets of network pairs is 9.6 Å, denoted as *Motif 4* (*M4*) (Fig. 5.48d). Compared to NU-1303-*6* (*M2*), the closest U–U distance present in NU-1304 (*M4*) remains 1.5 Å larger than that of NU-1303-*6* (Fig. 5.50).

5.8.7.4 Cation Identification

Similar to NU-1303-*6*, potential cations from the synthesis of NU-1304 are K^+, UO_2^{2+}, dimethylammonium (from DMF degradation), H^+, or H_3O^+.

To identify if either K^+ or UO_2^{2+} existed as charge-balancing cations in NU-1304, we implemented ICP-OES analysis. NU-1304 samples were prepared in the same manner as NU-1303-*6* (see section 4). ICP-OES analysis for U and K revealed 0.1 potassium cations present per uranium; thus, 0.1 K^+ is present per anionic node. Based on the sample mass, the expected U content with UO_2^{2+} as a counterion was calculated. However, ICP-OES analysis revealed a much lower U content, which thus demonstrates that UO_2^{2+} is not present as a counter-cation (Table 5.2).

To determine if dimethylammonium existed as a charge-balancing cation in NU-1304, we implemented ^{1}H NMR analysis. NU-1304 samples were prepared in the same manner as NU-1303-*6* (see section 4). Dimethylamine peaks were not observed from the ^{1}H NMR analysis. Rather, 0.09 DMF were observed per node (Fig. 5.51), attributed to leftover DMF from the soaking and washing steps. To ensure that the NMR signal was correctly assigned to DMF and not dimethylamine, one drop of dimethylamine was added to the same NMR tube, and the sample was remeasured. The peaks assigned as DMF (7.93, 3.01, 2.86 ppm) did not change in intensity, but two new peaks (3.06, 2.90 ppm) were observed which correspond to dimethylamine (Fig. 5.52). This control experiment verified that dimethylammonium is not a charge-balancing cation in NU-1304.

Thus, we assign the cation as 0.1 K^+ and 0.9 H^+ or H_3O^+ per anionic node, such that the formula for NU-1304 is either $H^+_{0.9}K^+_{0.1}[UO_2(TMBP)_{1.5}]^-$ or $(H_3O^+)_{0.9}K^+_{0.1}[UO_2(TMBP)_{1.5}]^-$.

To further demonstrate that NU-1304 does indeed hold a -1 charge on each uranyl-based node, we performed a cation exchange with tetraethylammonium chloride (TEACl). NU-1304 samples were prepared in the same manner as NU-1303-*6* (see section 4). However, after the 12-hour TEACl soak, only five 1-hour soaks of NU-1304 in TEACl solution were performed at 50 °C (oil bath). NMR analysis revealed 1 tetraethylammonium (TEA^+) cation per charged node (Fig. 5.53, peaks at 3.07 and 1.03 ppm), indicating full cation exchange ($TEA^+[UO_2(DMBP)_{1.5}]^-$).

5.8.7.5 NU-1304 Activation and Gas Physisorption (0-day DMF soak)

NU-1304 was synthesized following previously discussed methods and washed with fresh DMF three times once removed from the oven. 30 mg of NU-1304 was placed in a 15 mL centrifuge tube and the solvent was exchanged to 7 mL EtOH and allowed to soak for 2 hours. This EtOH exchange was repeated two additional times, ending with a final EtOH exchange and overnight soak. We made sure to keep the MOF solvated at all times during solvent exchange. We then performed sc-CO_2 activation (CO_2 syphon tank used). After sc-CO_2 activation, the sample was removed from the unit and immediately prepared for further analysis in a fume hood. Thermal activation at 100 °C under ultrahigh vacuum for 24 hours was completed on an SVP, and subsequent N_2 adsorption-desorption studies followed on a Tristar II 3020 (Fig. 5.5B). The BET analysis summary can be seen in Table 5.3, and the BET surface area plot can be seen in Figure 5.54.

5.8.7.6 NU-1304 Activation and Gas Physisorption (10-day and 1057-day DMF soak)

NU-1304 was synthesized following previously discussed methods and washed with fresh DMF three times once removed from the oven. The sample was then allowed to soak in hydrous DMF for 10 days. The NU-1304 sample was then placed in a 15 mL centrifuge tube and the solvent was

exchanged to 7 mL EtOH and allowed to soak for 1 hour. This EtOH exchange was repeated two additional times, ending with a final EtOH exchange and overnight soak. We made sure to keep the MOF solvated at all times during solvent exchange. We then performed sc-CO_2 activation (CO_2 syphon tank used). After sc-CO_2 activation, the sample was quickly removed from the unit and the entire sample holder was transferred directly to a small plastic container which fit snugly. The container was wrapped in parafilm, and the sample was transferred to a N_2 glovebox. The sample was prepared for physisorption studies by sealing it in a sorption tube in the glovebox. Thermal activation at 50 °C under ultrahigh vacuum for 24 hours was completed on an SVP, and subsequent N_2 adsorption-desorption studies followed on a Tristar II 3020. The same procedure was performed on a batch of NU-1304 soaked in DMF for 1057 days.

The nitrogen isotherm of NU-1304 activated after a 10-day hydrous DMF soak shows steps at identical relative pressures (0.007, 0.0601), and similar pore size distributions (13.5 Å and 18.9 Å) to that of NU-1304 activated with a 0-day DMF soak (Fig. 5.55). The pore volume and BET area are 0.73 cm^3g^{-1} and 1210 m^2g^{-1}, respectively. The BET analysis summary can be seen in Table 5.3, and the BET surface area plot can be seen in Figure 5.56. A similar isotherm and pore size distribution was also observed for NU-1304 soaked in DMF for 1057 days.

5.8.7.7 NU-1304 Activation and Gas Physisorption (Anhydrous Conditions)

NU-1304 was synthesized following previously discussed methods and washed with fresh anhydrous DMF three times once removed from the oven. 30 mg of NU-1304 in anhydrous DMF was placed in a 2-5 mL Biotage microwave vial, and the vial was capped. The solvent was then exchanged three times to 7 mL anhydrous DMF through the microwave cap septum, using a syringe. The MOF was then left to soak in anhydrous DMF for 10 days. The solvent was then exchanged to 7 mL of anhydrous MeCN through the microwave tube septum using a syringe and

allowed to soak for 2 hours. This solvent exchange process was repeated two additional times, ending with a final anhydrous MeCN exchange and overnight soak. We made sure to keep the MOF solvated at all times during solvent exchange. We then performed sc-CO_2 activation (bone-dry CO_2 syphon tank used). After sc-CO_2 activation, the sample was quickly removed from the unit and the entire sample holder was transferred directly to a small plastic container which fit snugly. The container was wrapped in parafilm, and the sample was transferred to a N_2 glovebox. The sample was prepared for physisorption studies by sealing it in a sorption tube in the glovebox. PXRD samples were also prepared and sealed in the glovebox. Thermal activation at 50 °C under ultrahigh vacuum for 24 hours was completed on an SVP, and subsequent N_2 adsorption-desorption studies followed on a Tristar II 3020. The BET analysis summary can be seen in Table 5.3, and the BET surface area plots can be seen in Figure 5.57. The entire activation procedure was monitored at each step by PXRD (Fig. 5.58).

The nitrogen isotherms of NU-1304 and NU-1304 activated under anhydrous conditions are shown in Figure 5.5b. Both isotherms show steps at identical relative pressures (0.007, 0.0601), and similar pore size distributions (13.5 Å and 18.9 Å) (Fig. 5.5c). The pore volume and BET area of NU-1304 are 0.77 cm^3g^{-1} and 1570 m^2g^{-1}, respectively. The pore volume and BET area of NU-1304 activated under anhydrous conditions are 0.93 cm^3g^{-1} and 1805 m^2g^{-1}, respectively. We attribute the increased pore volume and BET area after activation under anhydrous conditions to improved activation.

5.8.7.8 PXRD Matching

Solvent exchange and activation procedures of NU-1304 were monitored using PXRD (Figs. 5.58, 5.59). In both cases, splitting of the first two major peaks at 2.8° and 4.9° was observed after solvent exchange and after sc-CO_2 activation. To understand the structural transformation

associated with this splitting, we modeled simulated PXRD patterns which matched the experimental patterns for NU-1304 after EtOH exchange (NU-1304_EtOH, Supplemental Data), and after subsequent activation (NU-1304_Act, Supplemental Data) (Fig. 5.59). The PXRD patterns were matched in the same way as NU-1303-*6*, by maximizing the overlap between experimental and simulated patterns as a function of the simulated structure unit cell parameters (Table 5.13). Thus, each matching provides the simulated unit cell parameters that result in the closest agreement between simulated and experimental PXRD patterns. This procedure is described in detail in section 4.

5.8.7.9 Le Bail Refinement

In order to validate the calculated lattice parameters for NU-1303_EtOH and NU-1304_Act, we performed Le Bail refinement on collected powders (Fig. 5.59) following the procedures found in the Methods section. As can be seen in Table 5.13, the models developed *in silico* are reasonably close to what is observed experimentally. The agreement factors are also within reasonable error (Table 5.9).

5.8.7.10 DFT CIF Generation

We then generated CIFs from the optimized unit cells corresponding to the NU-1304 structural conformations adopted over the course of solvent exchange and activation (NU-1304_EtOH and NU-1304_Act, respectively. See Supplemental Data). As per the detailed discussion above for NU-1303-*6* (section 4), unit cell expansion/contraction was modeled. The significant compression of the *a* and *b* dimensions of NU-1304_Act result in linker compression in the simulated structure with DFT optimized linkers. In this system, peak splitting upon solvent exchange and activation is an indicator of interpenetration.

5.8.7.11 Free Energy Cluster DFT Calculations

To account for potential shielding of anionic nodes by counter-cations, we included either H^+, H_3O^+, or K^+ cations in our *M3* and *M4* cluster models. We also performed free energy calculations on uncapped models (no cations) for comparison. Because of different possible cation positions around the uranyl nodes, we report two stable configurations for *M4*: *M4a* and *M4b*.

Similar positions of the H^+, H_3O^+, and K^+ cations were observed in *M3* and *M4a* as in the previous study of *M1* and *M2a*. Figure 5.60 shows the positions of the H^+, H_3O^+, and K^+ cations in *M4b*. The H^+ cations bind to a carboxylate O of each framework (0.97 Å). The optimized positions of H_3O^+ shows that one of the hydronium ions forms two hydrogen-bonds with the carboxylate O atoms of the framework (1.43 Å-1.49 Å). The second hydronium ion in the pocket of *M4b* optimizes as an H^+ cation bound to the carboxylate O (1.05 Å) while forming a hydrogen-bond with the remaining water molecule from H_3O^+ in the pocket (1.56 Å). This water molecule further forms a hydrogen-bond with a carboxylate O of the second framework in the pocket (2.18 Å). The optimized positions of K^+ reveal that one K^+ cation exhibits two interactions with a carboxylate O of the framework (2.58 Å) and is positioned 3.58 Å away from the uranyl O. The second K^+ cation in the pocket, however, interacts with two carboxylate O atoms of the same framework (2.69 Å-2.73 Å). This K^+ cation also weakly interacts with the carboxylate O atoms of the second framework in the pocket (3.24 Å-3.36 Å). Similar positions for these cations were obtained in the presence of DMF and water (SMD).

These calculations are described in detail above for NU-1303-*6* and were also performed on NU-1304. The relative energies (ΔE), enthalpies (ΔH), and free energies (ΔG) of transformation (Eq. 4, Eq. 8, Fig. 5.61) of the interpenetrated motifs *M3* and *M4* of NU-1304 to their respective non-interpenetrated fragments in the presence of implicit solvent models for DMF and water using the M06-2X density functional are tabulated in Table 5.14. The free energies of the uncapped cluster

model and the cluster models with cations included (Figs. 5.5e, 5.62, Table 5.14) predict less negative free energies of de-interpenetration of NU-1304 as compared to NU-1303-*6*. This trend holds true for all calculated values except for *M4b* in the presence of H_3O^+ and K^+ (Fig. 5.62). We attribute this to the fact that the *M4b* pocket is larger than the *M2b* pocket; thus, even though H_3O^+ and K^+ make multiple interactions with various framework atoms in the *M4b* pocket, they still do not bridge the two frameworks in *M4b* together to the extent that they do in *M2b*. Generally, these results suggest that the interpenetrated motifs in NU-1304 are more stable than the interpenetrated motifs in NU-1303-*6*. This is attributed to the lower amount of CPPR between the networks in NU-1304 owing to the increased U–U distance and linker–linker distance in NU-1304, due to the bulkier **TMBP** linker.

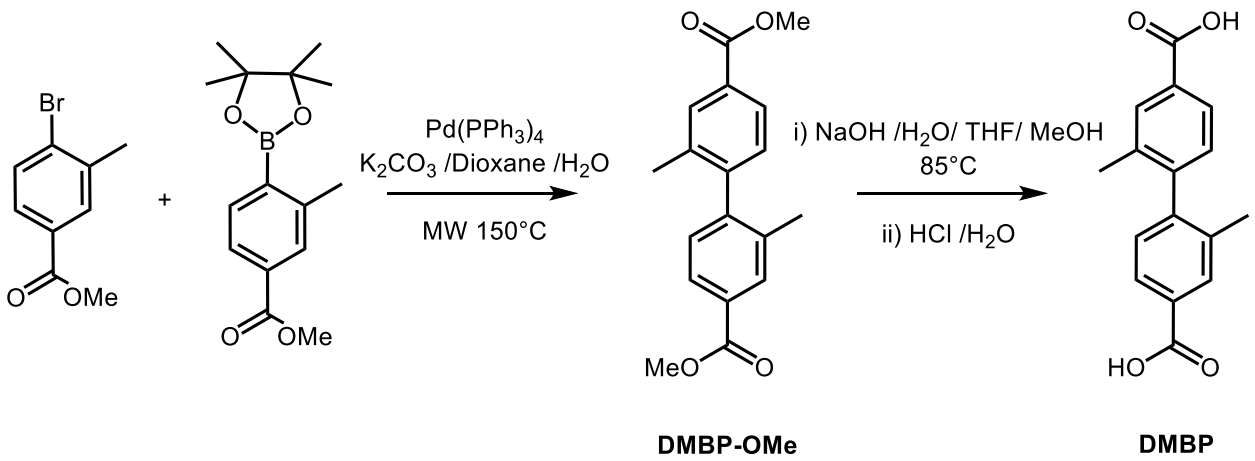

Scheme 5.1 Synthesis of 2,2′-dimethyl-biphenyl-4,4′-dicarboxylic acid (**DMBP**).

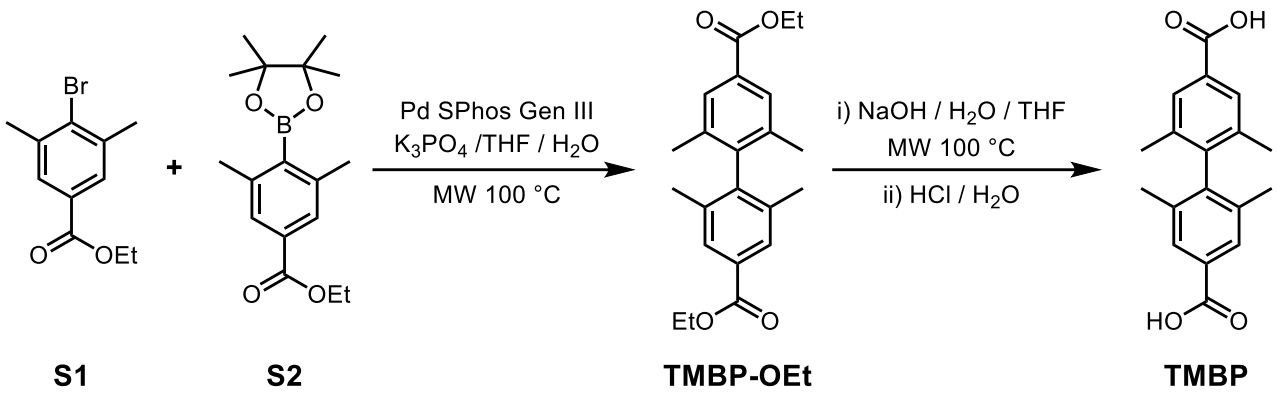

Scheme 5.2 Synthesis of 2,2′,6,6′-tetramethyl-biphenyl-4,4 ′-dicarboxylic acid **(TMBP)**.

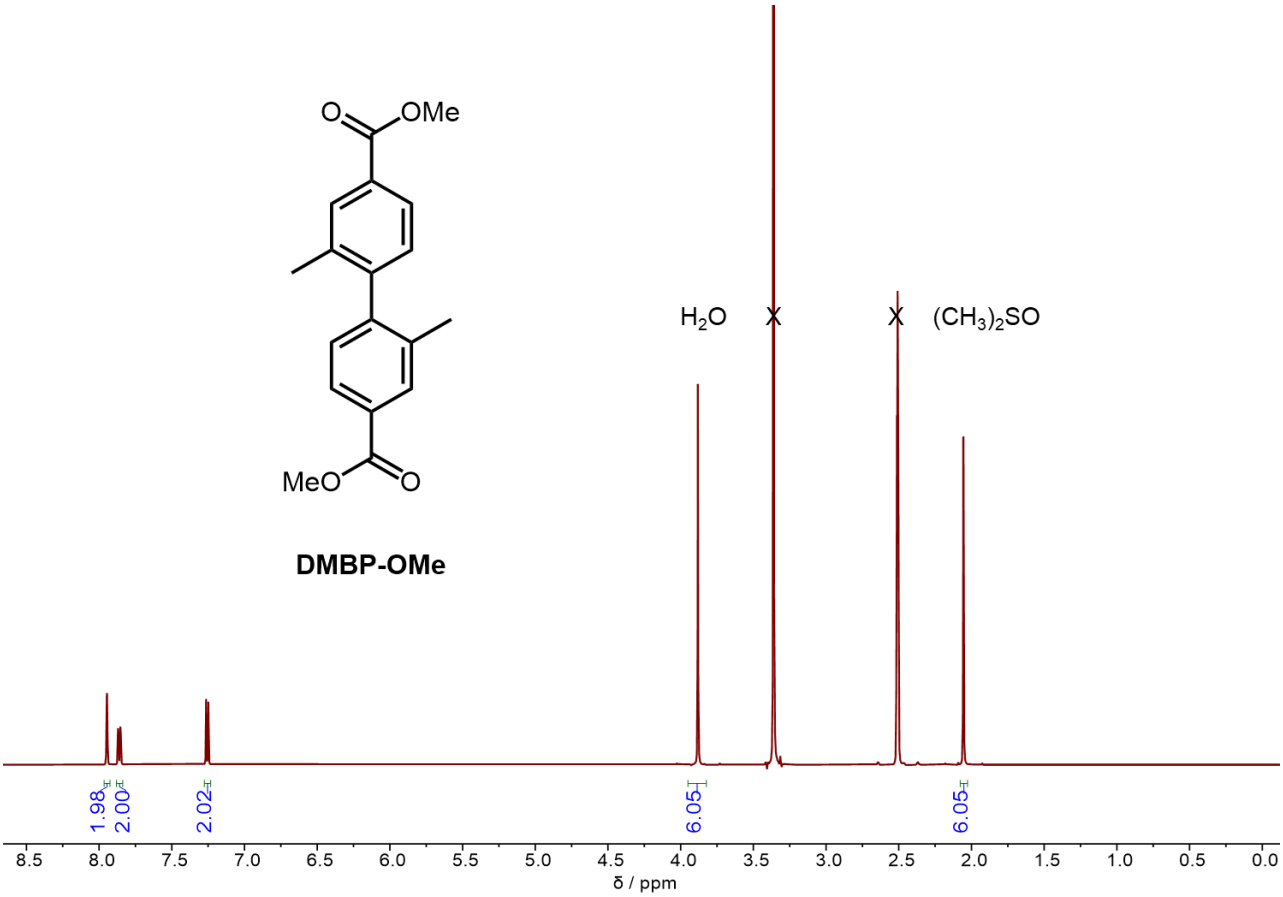

Figure. 5.6 ^{1}H NMR spectrum (500 MHz, $(CD_3)_2SO$, 298 K) of **DMBP-OMe.**

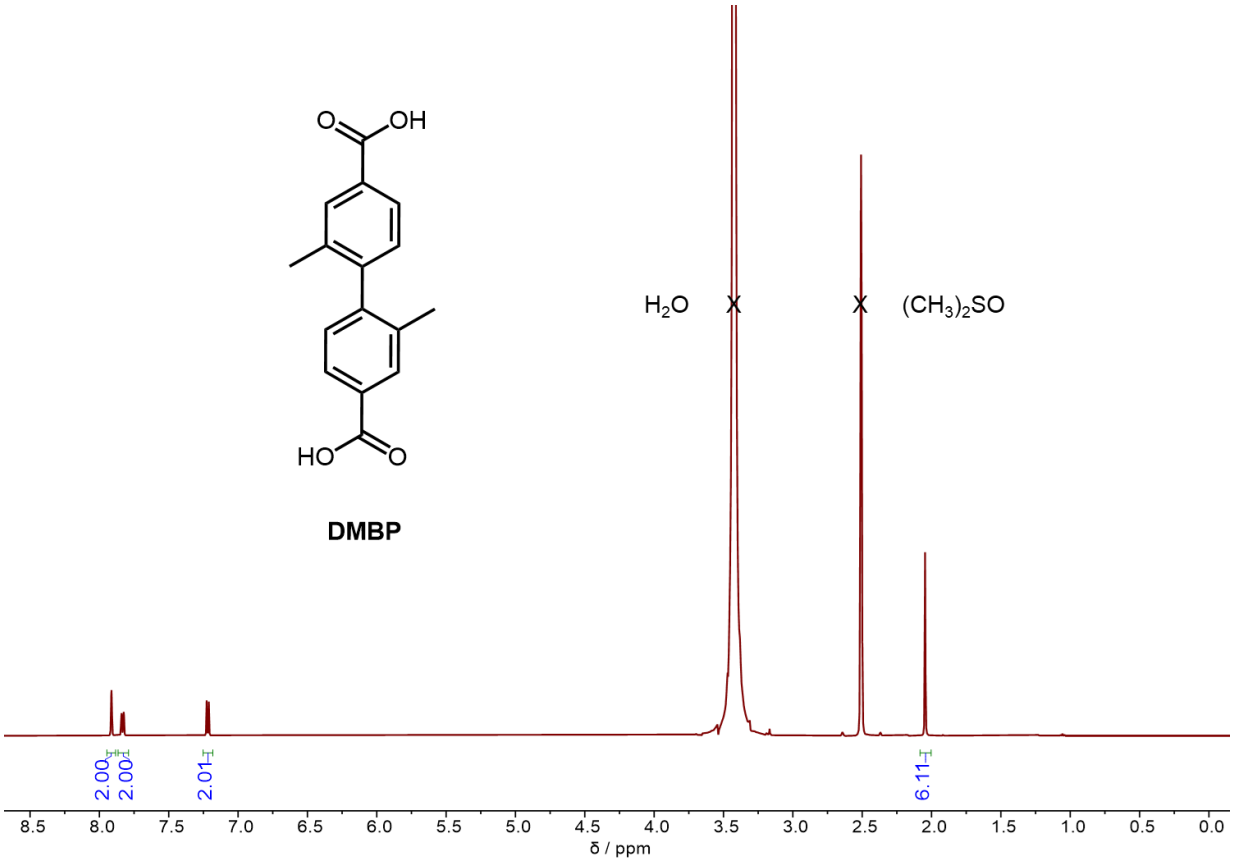

Figure. 5.7 ^{1}H NMR spectrum (500 MHz, $(CD_3)_2SO$, 298 K) of **DMBP**.

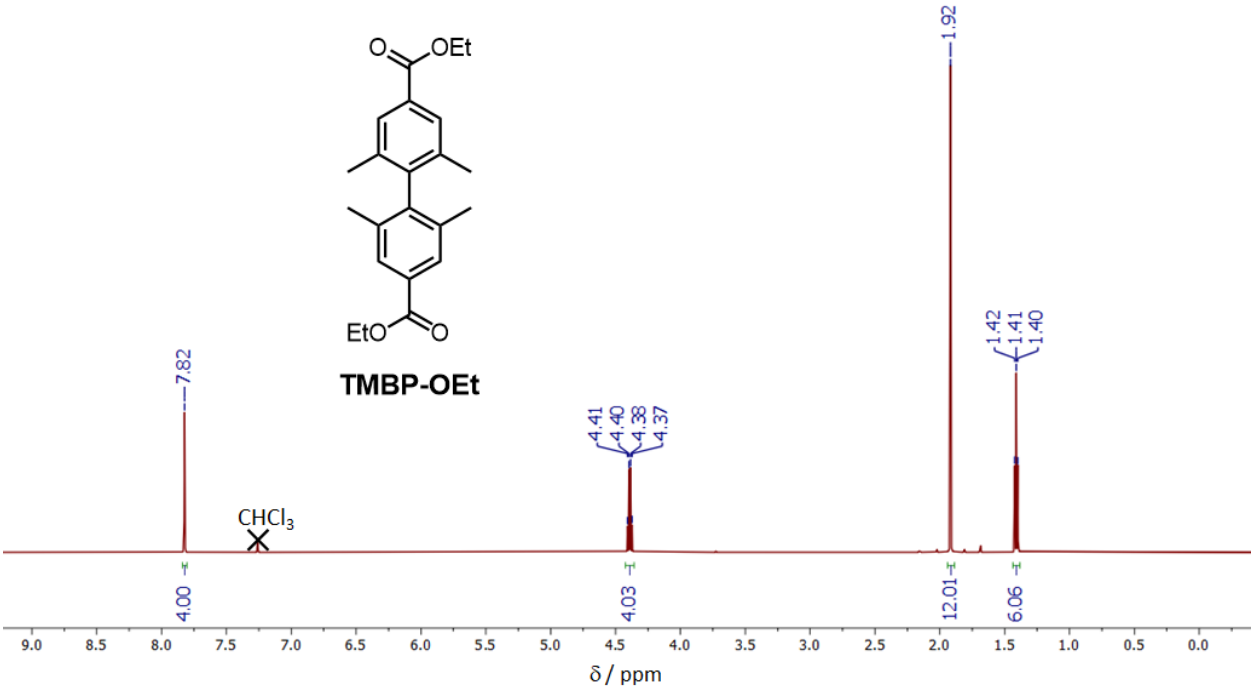

Figure. 5.8 ^{1}H NMR spectrum (600 MHz, $CDCl_3$, 298 K) of **TMBP-OEt**.

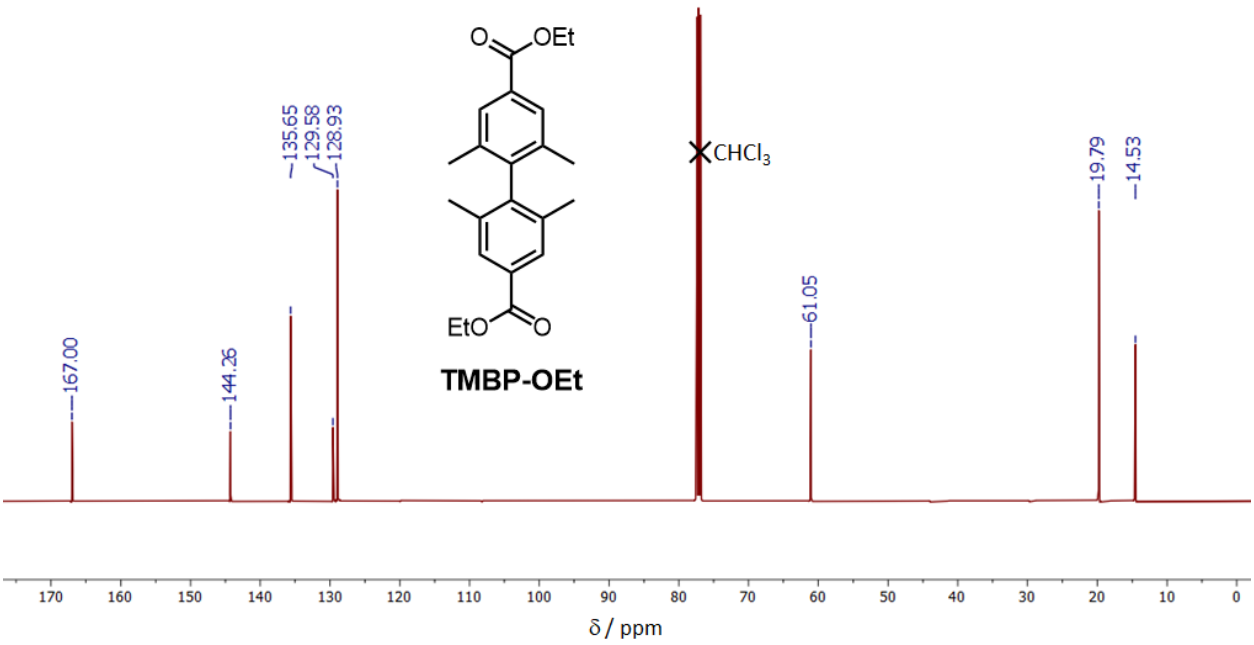

Figure. 5.9 $^{13}C\{^{1}H\}$ NMR spectrum (125 MHz, $CDCl_3$, 298 K) of **TMBP-OEt**.

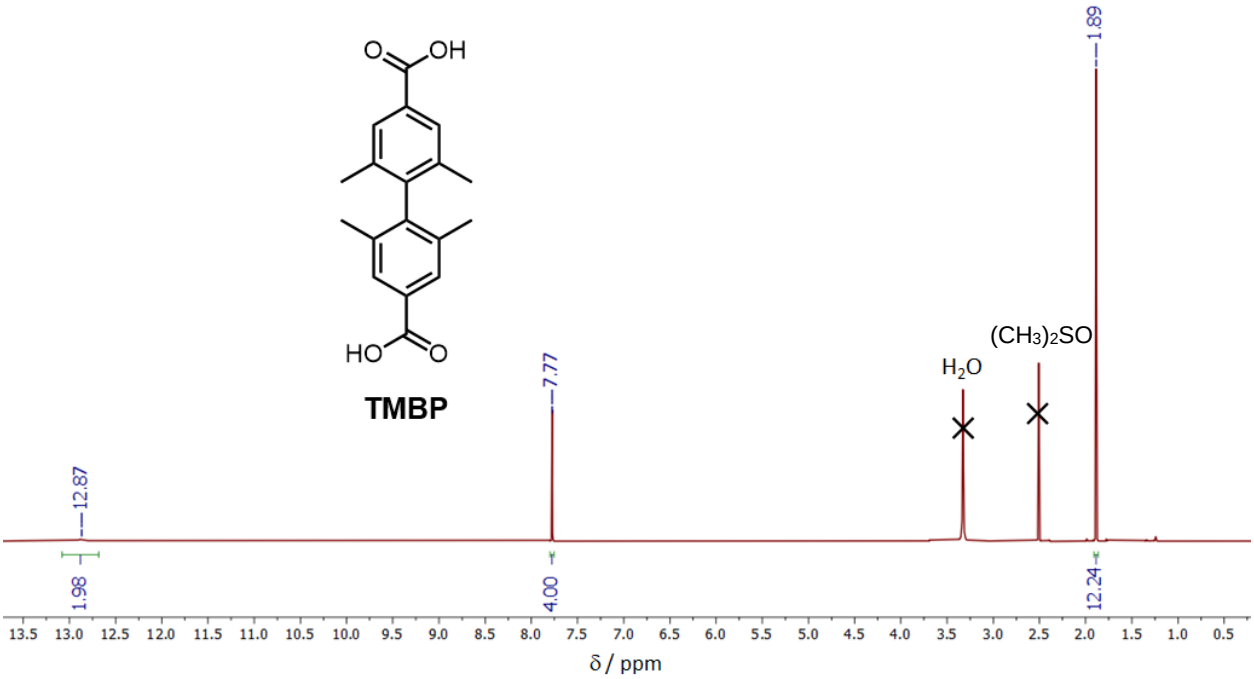

Figure. 5.10 ^{1}H NMR spectrum (600 MHz, $(CD_3)_2SO$, 298 K) of **TMBP**.

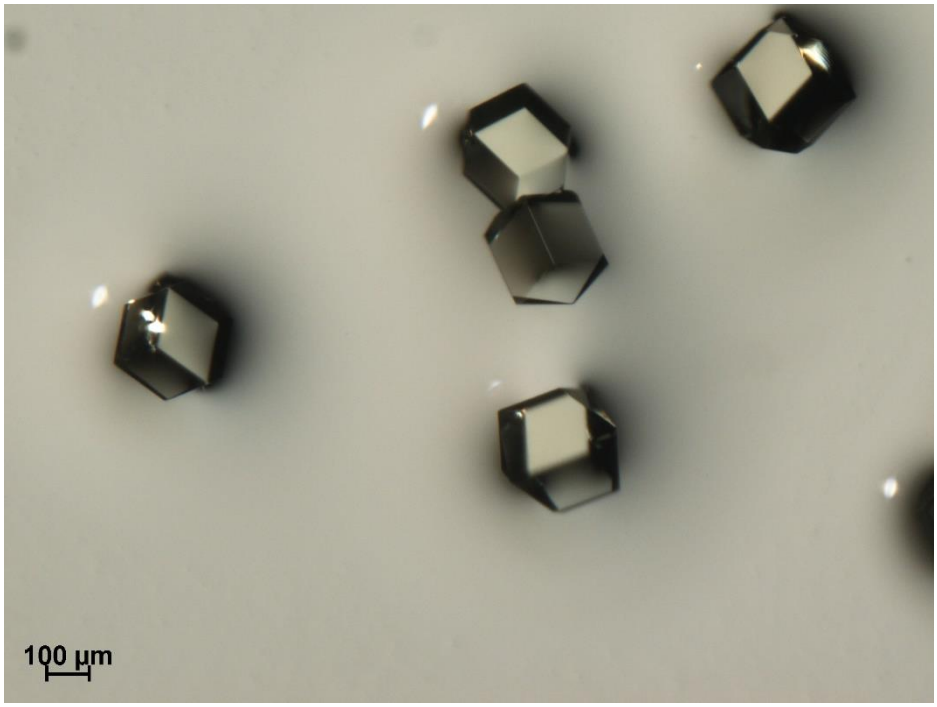

Figure. 5.11 Optical image of NU-1303-*6* single crystals.

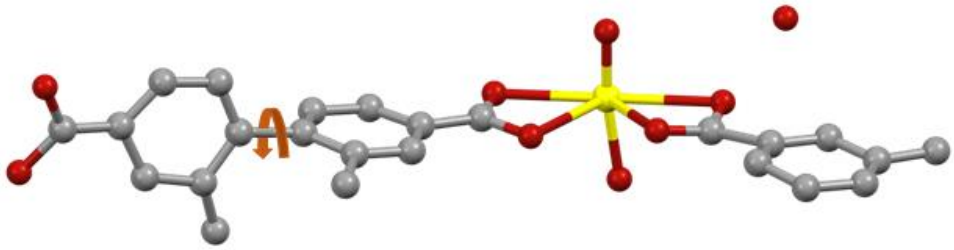

Figure. 5.12 Asymmetric unit of NU-1303-6, showing DMBP linker with torsion between biphenylene rings of 76.1° for one third of the linkers and 88.5° for the other two thirds. Atom color scheme: carbon, gray; oxygen, red; uranium, yellow. H atoms are omitted for clarity.

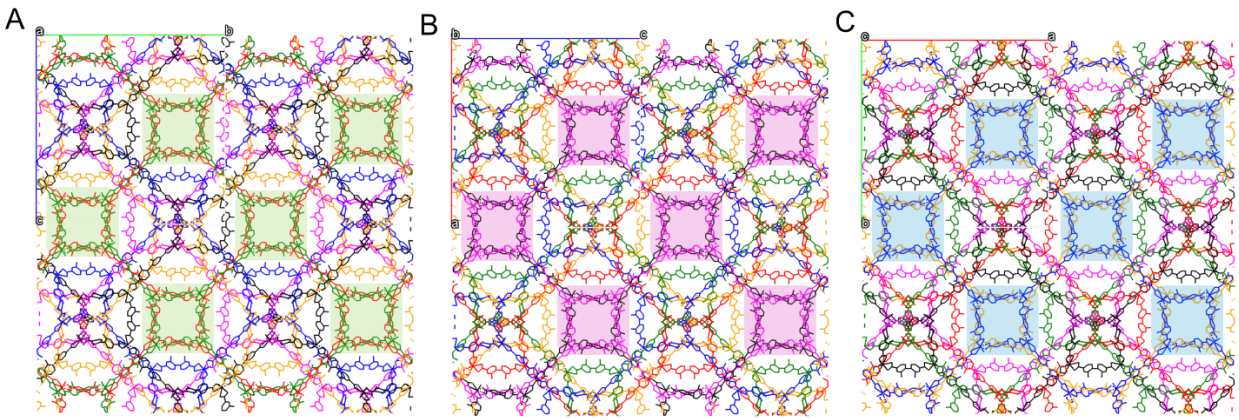

Figure. 5.13 NU-1303-*6*, where each network is represented by a different color. (a) Down the *a* direction, two networks, shown in green and red arrange in a pair. Locations where the pair can be most clearly seen are highlighted by green boxes for ease of viewing. (b) Down the *b* direction, two networks, shown in pink and black arrange in a pair. Locations where the pair can be most clearly seen are highlighted by pink boxes for ease of viewing. (c) Down the *c* direction, two networks, shown in orange and blue arrange in a pair. Locations where the pair can be most clearly seen are highlighted by blue boxes for ease of viewing. H atoms omitted for clarity.

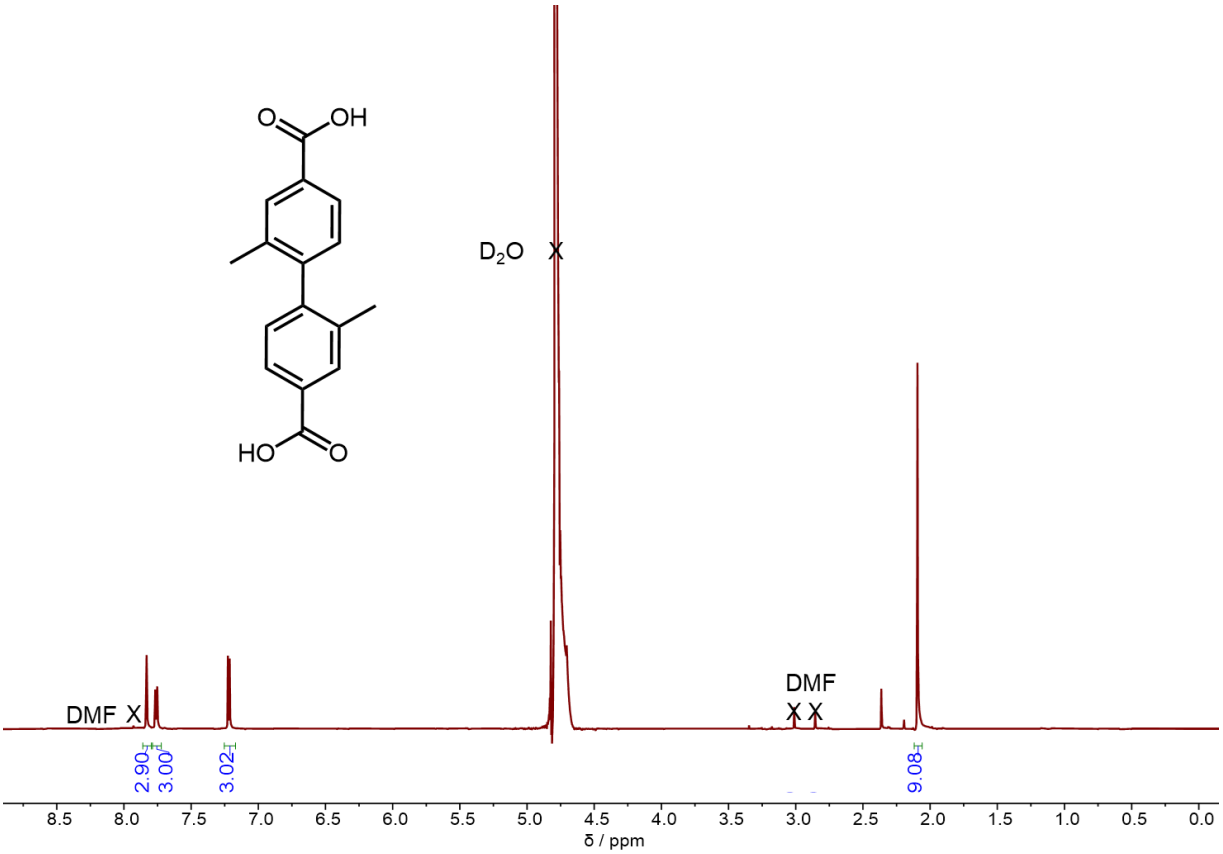

Figure. 5.14 ^{1}H NMR spectrum (600 MHz, D2O, 298 K) of base-digested NU-1303-6. Peak integration is relative to one node (1.5 linkers per node).

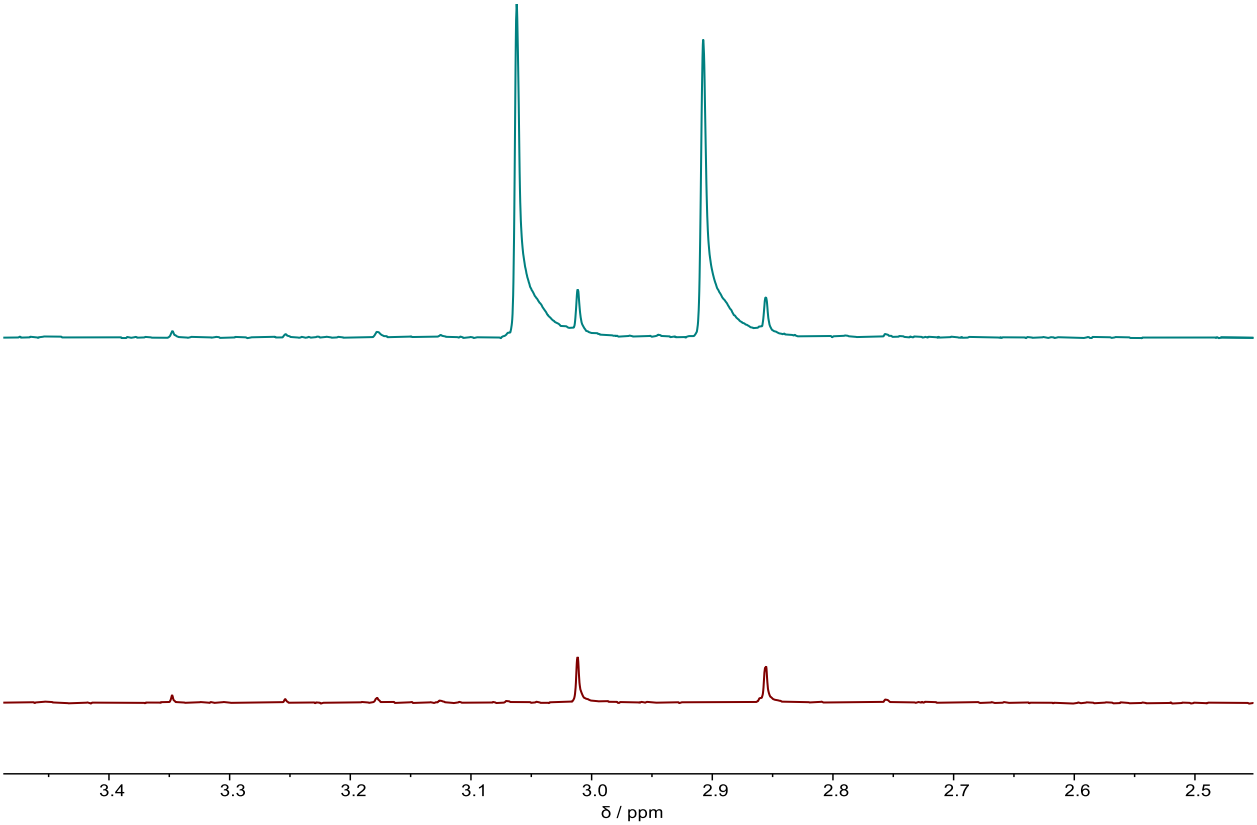

Figure. 5.15 ^{1}H NMR spectrum (600 MHz, D2O, 298 K) of base-digested NU-1303-6 before (bottom) and after (top) addition of dimethylamine.

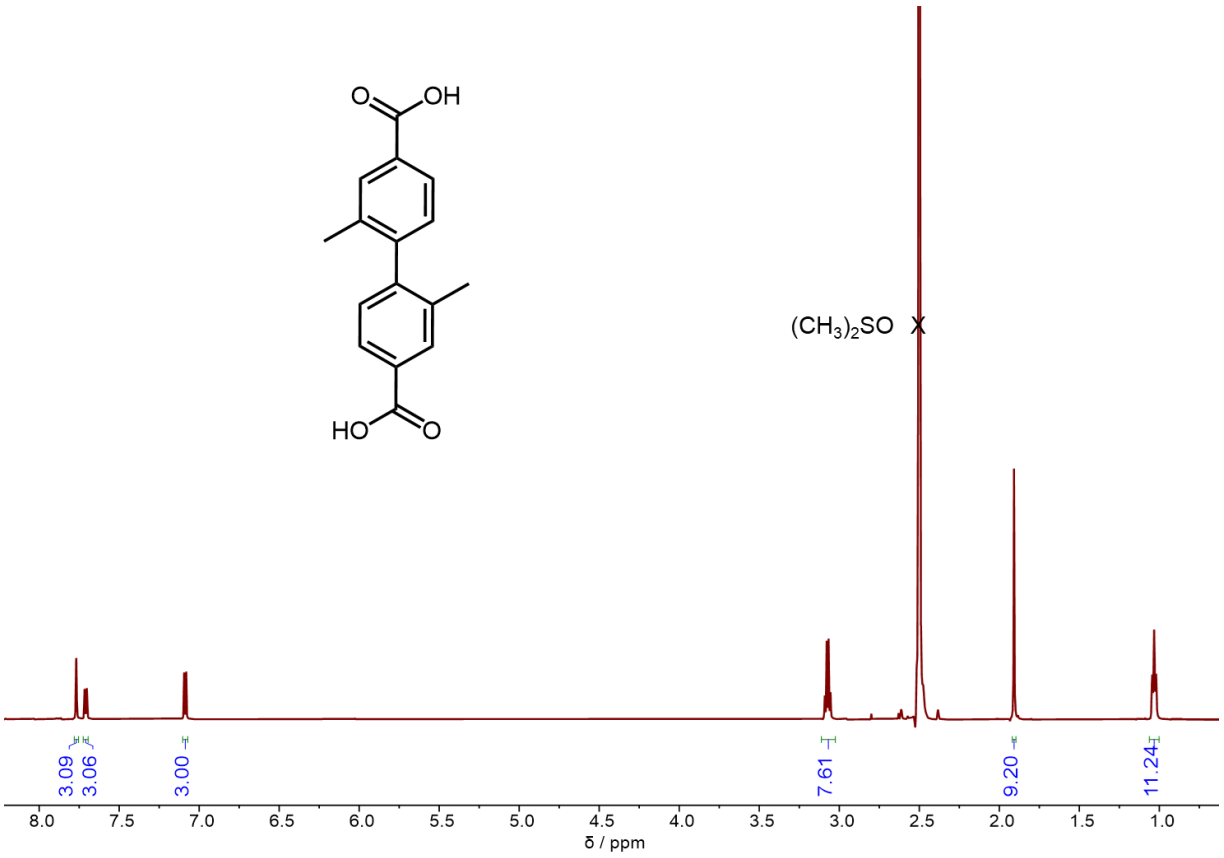

Figure. 5.16 ^{1}H NMR spectrum (600 MHz, D_2O, 298 K) of acid-digested NU-1303-*6* after cation exchange with TEACl. Peak integration is relative to one node (1.5 linkers per node).

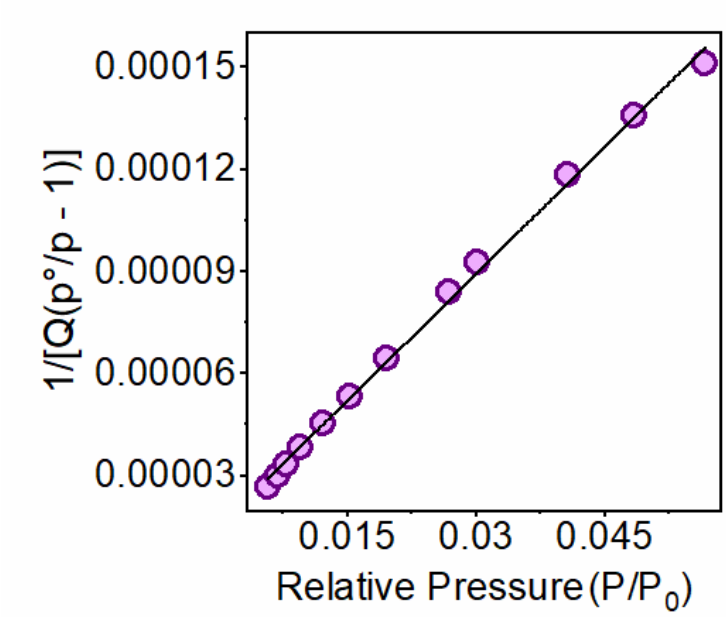

Figure. 5.17 BET surface area plot for NU-1303-*6* with linear fitting. R^2=0.99.

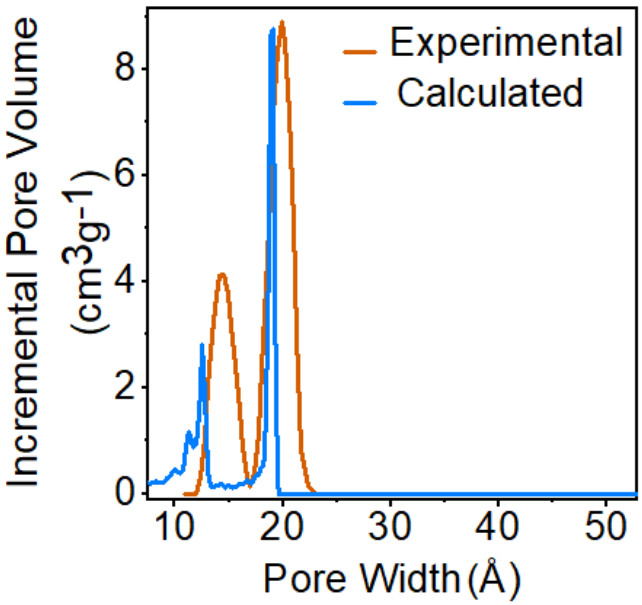

Figure. 5.18 Experimental and calculated pore size distribution of NU-1303-*6*.

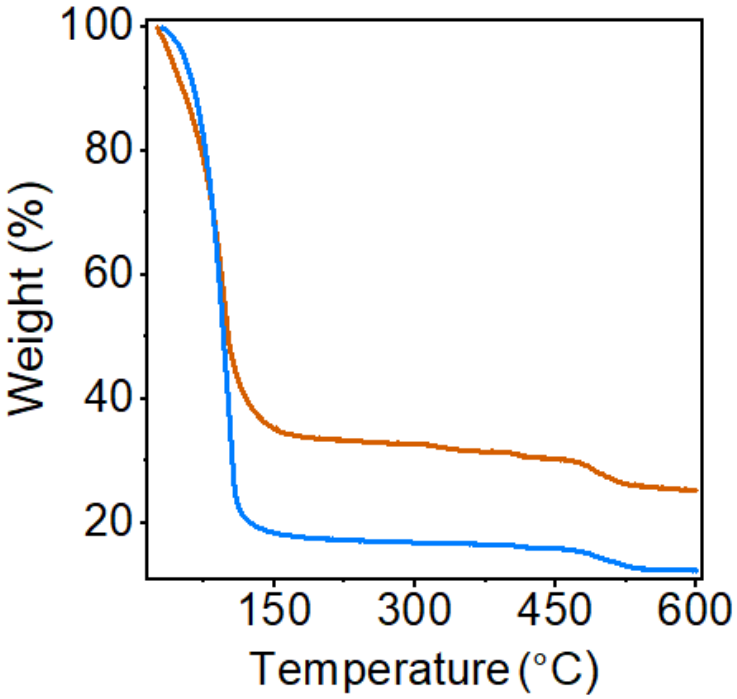

Figure. 5.19 TGA of NU-1303-*6* (orange, top trace) and NU-1303-*1* (blue, bottom trace).

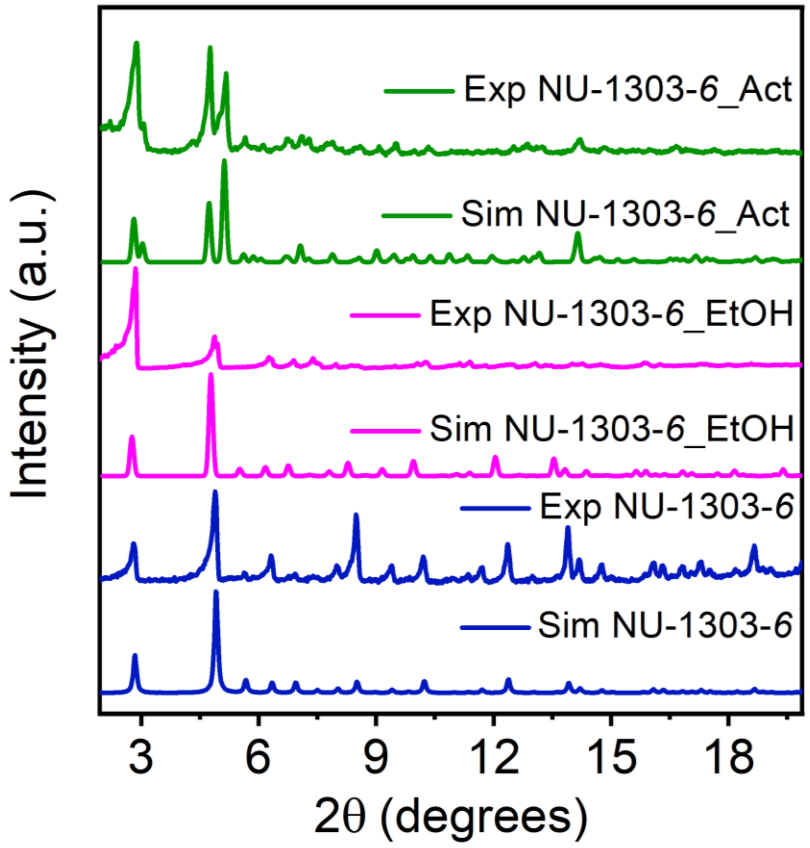

Figure. 5.20 Simulated PXRD matching of NU-1303-*6* after solvent exchange and activation. From bottom to top: Simulated NU-1303-*6* from SCXRD; Experimental NU-1303-*6* in DMF, capillary measurement; Simulated NU-1303-*6*_EtOH; Experimental NU-1303-*6*_EtOH, capillary measurement; Simulated NU-1303-*6*_Act; Experimental NU-1303-*6*_Act.

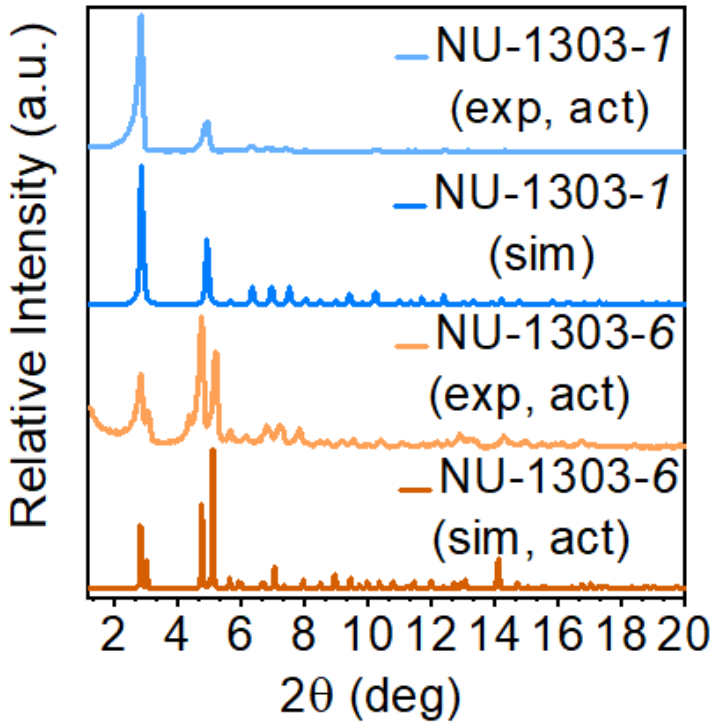

Figure. 5.21 Full range of PXRD patterns (top to bottom) of experimental activated NU-1303-*1*, simulated NU-1303-*1*, experimental activated NU-1303-*6*, and simulated activated NU-1303-*6*.

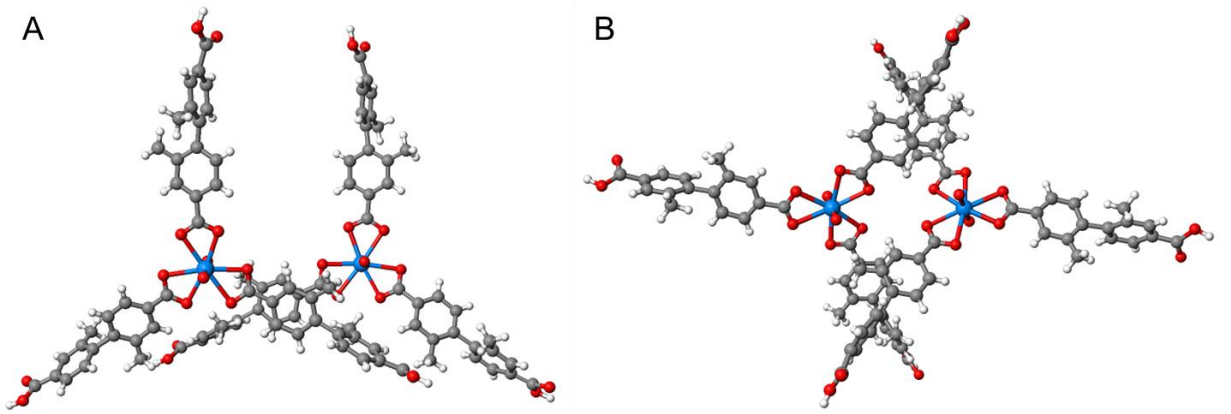

Figure. 5.22 Uncapped cluster models for (a) *M1*, and (b) *M2*, of NU-1303-*6* used for free energy of transformation calculations. The uranyl atoms along with the equatorially coordinating carboxylate groups were relaxed for geometry optimizations and frequency calculations. Atom color scheme: uranium, pink; oxygen, red; carbon, gray; hydrogen, white.

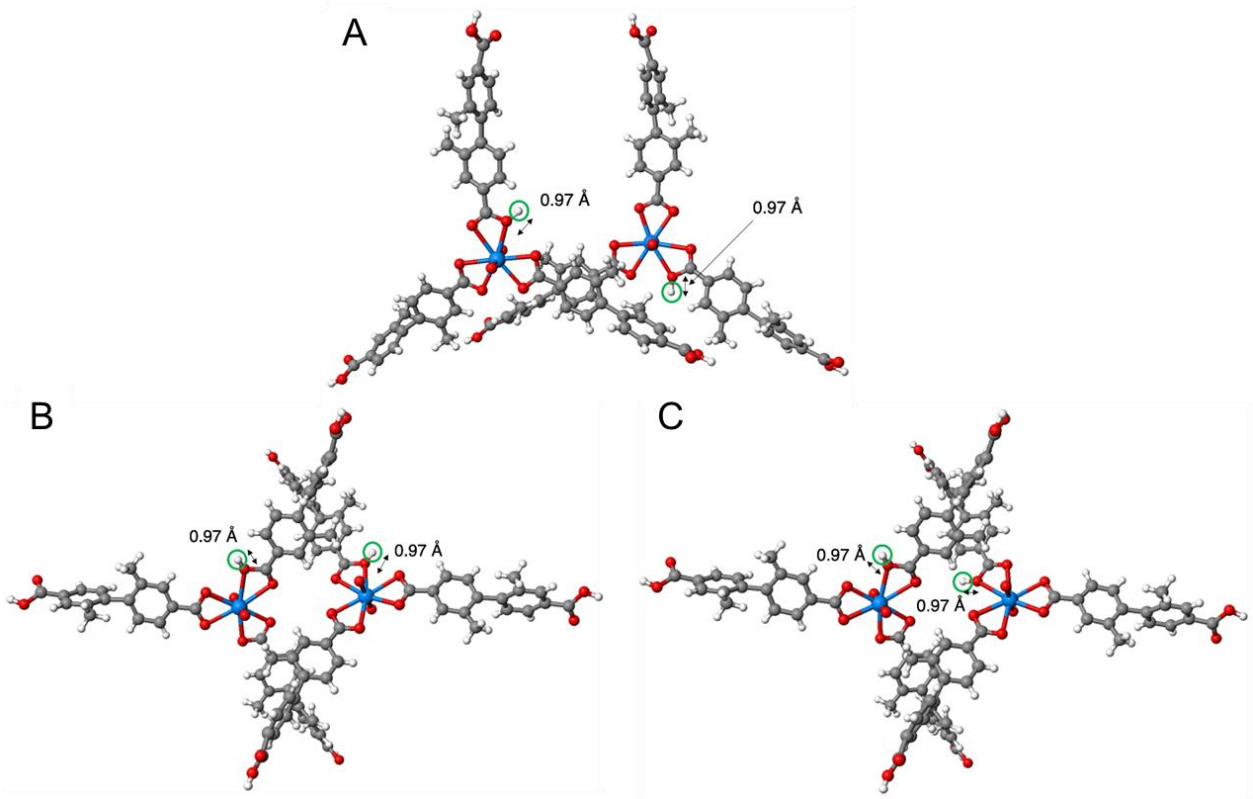

Figure 5.23 NU-1303-*6* cluster models for (a) *M1*, (b) *M2a*, and (c) *M2b* in the implicit solvent model for DMF with the equilibrium positions of H^+ cations circled in green. Atom color scheme: uranium, blue; oxygen, red; carbon, gray; hydrogen, white.

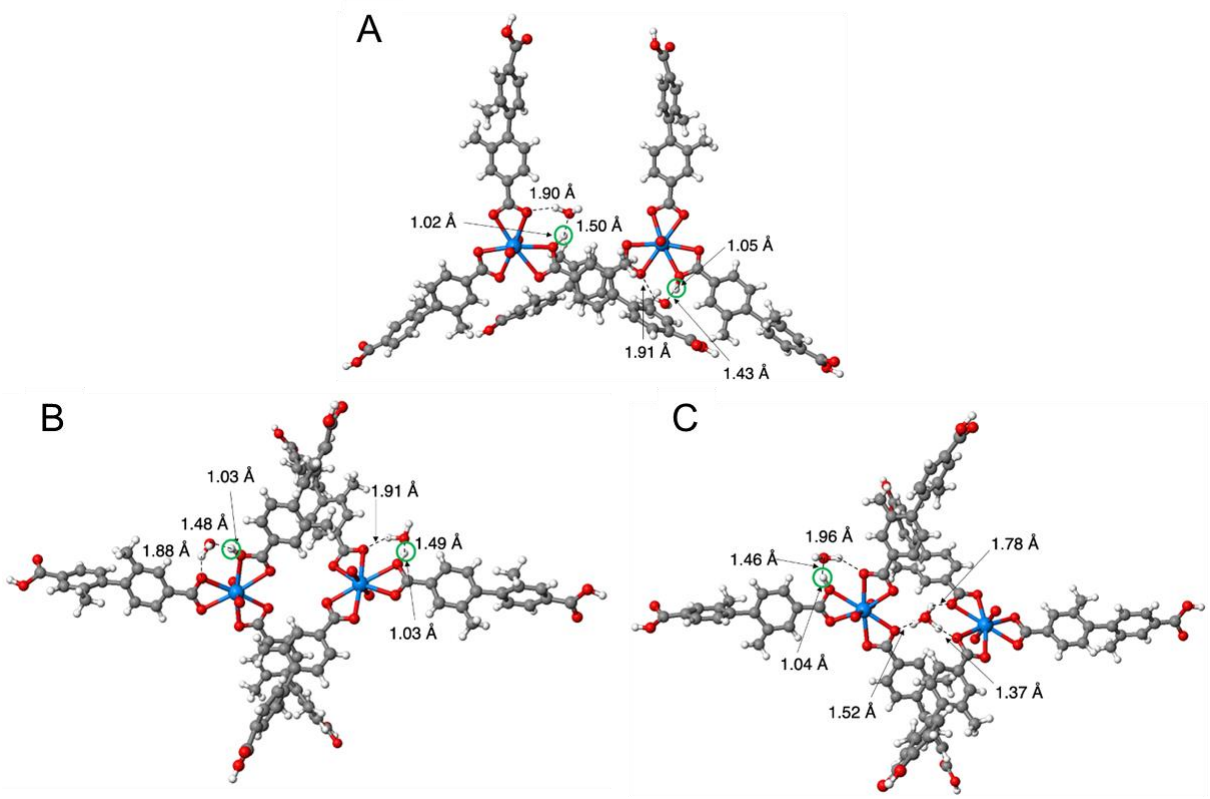

Figure 5.24 NU-1303-*6* cluster models for (a) *M1*, (b) *M2a*, and (c) *M2b* in the implicit solvent model for DMF. Equilibrium positions of H_3O^+ cations are shown, and the closest-binding protons from the H_3O^+ cations are circled in green. Atom color scheme: uranium, blue; oxygen, red; carbon, gray; hydrogen, white.

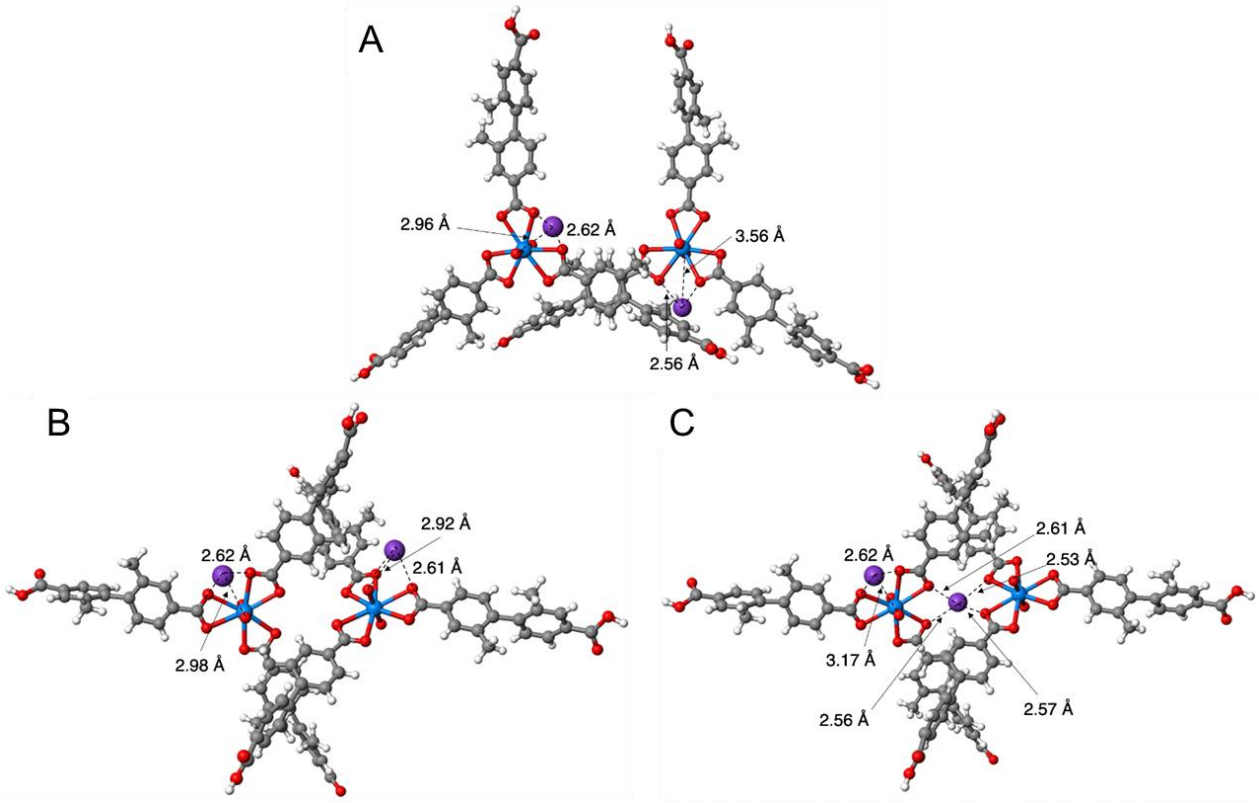

Figure 5.25 NU-1303-*6* cluster models for (a) *M1*, (b) *M2a*, and (c) *M2b* in the implicit solvent model for DMF with the equilibrium positions of K^+ cations shown. Atom color scheme: uranium, blue; potassium, purple; oxygen, red; carbon, gray; hydrogen, white.

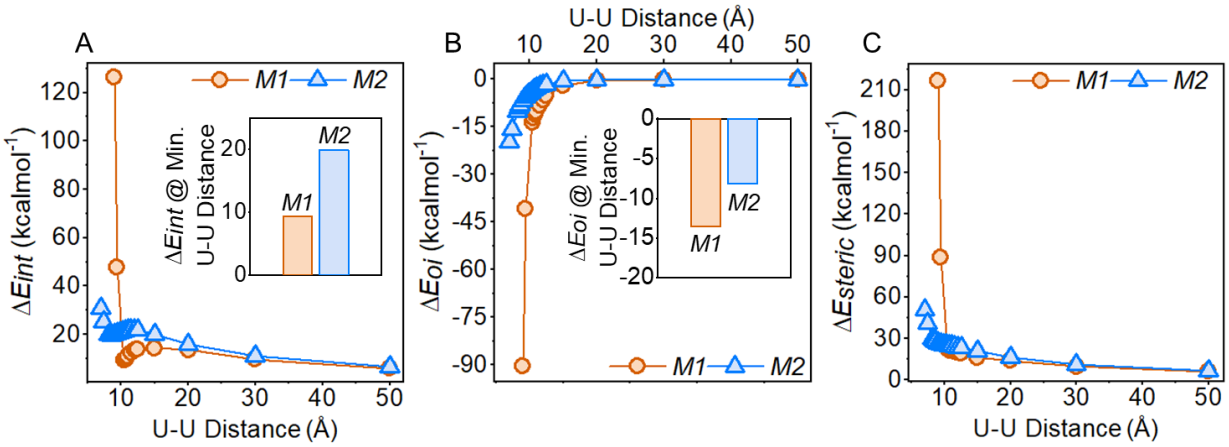

Figure 5.26 NU-1303-*6* total energy decomposition into (a) $\Delta \boldsymbol{E_{int}}$, (b) $\Delta \boldsymbol{E_{oi}}$, and (c) $\Delta \boldsymbol{E_{steric}}$ using the M06-2X functional at varying U–U distance. Full range up to 50 Å shown. Inset shows respective energy values at the calculated minimum energy U–U distance in kcalmol^{-1}.

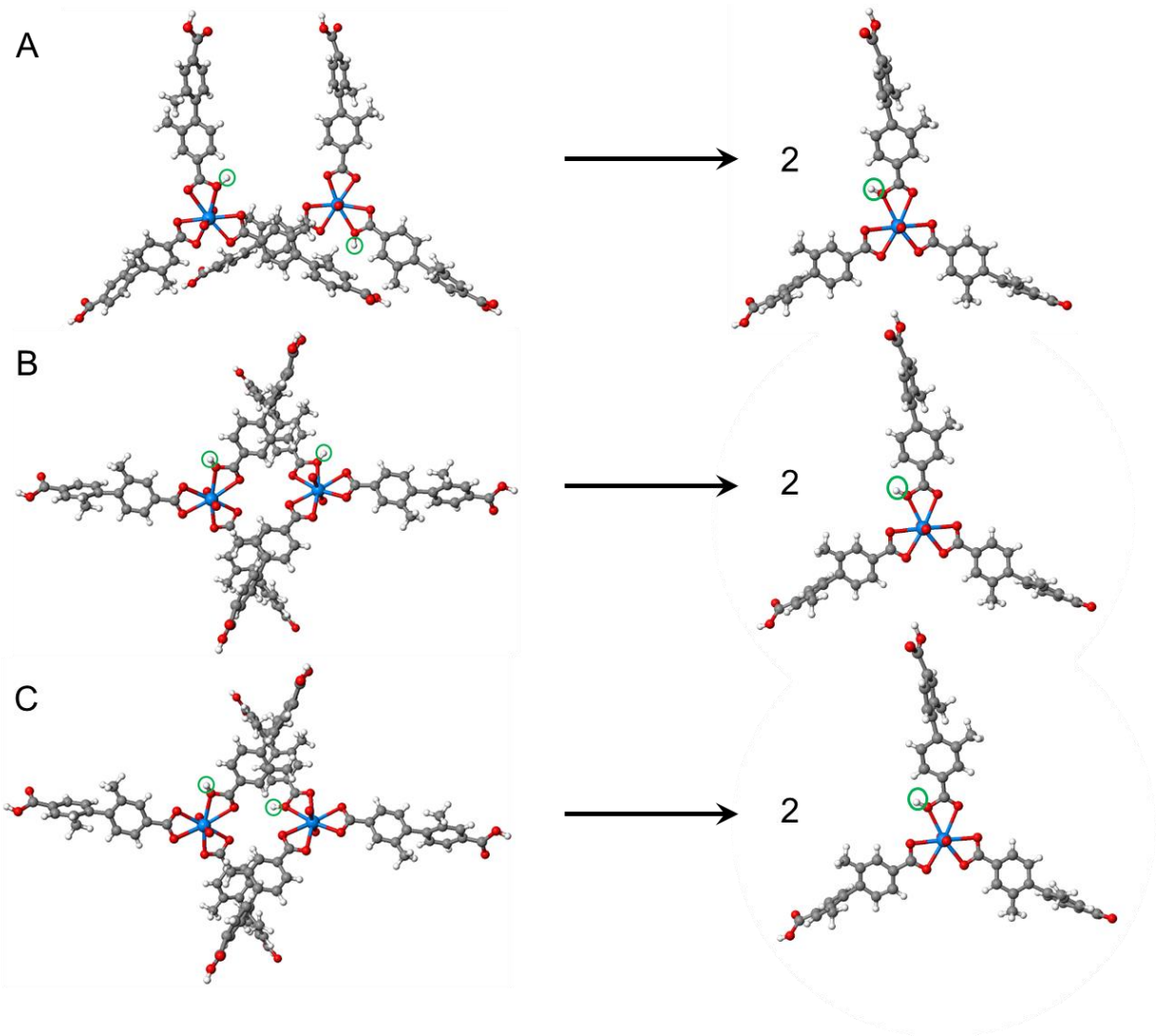

Figure 5.27 Modeling the transformation of (a) *M1*, (b) *M2a*, and (c) *M2b* in NU-1303-*6* to their respective NU-1303-*1* fragments for free energy of transformation calculations. Atom color scheme: uranium, blue; oxygen, red; carbon, gray; hydrogen, white. This model is shown with H^+ cations (circled in green). It is representative for de-interpenetration with uncapped models and models with H_3O^+ and K+ cations.

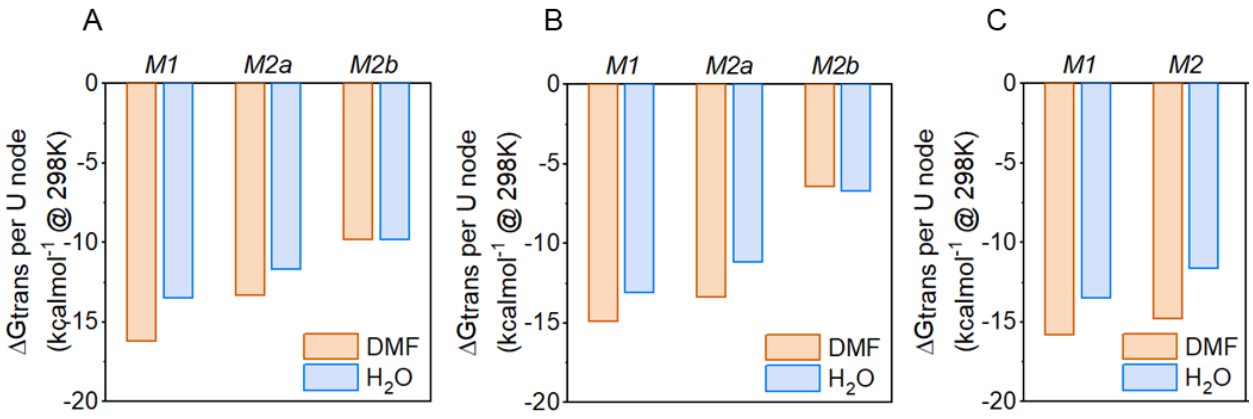

Figure 5.28 Free energy of transformation calculations of *M1*, *M2a*, and *M2b* in implicit solvent models for DMF (orange) and water (blue). Free energy values were calculated in the presence of (a) H_3O^+ cations, (b) K^+ cations, or (c) no cation.

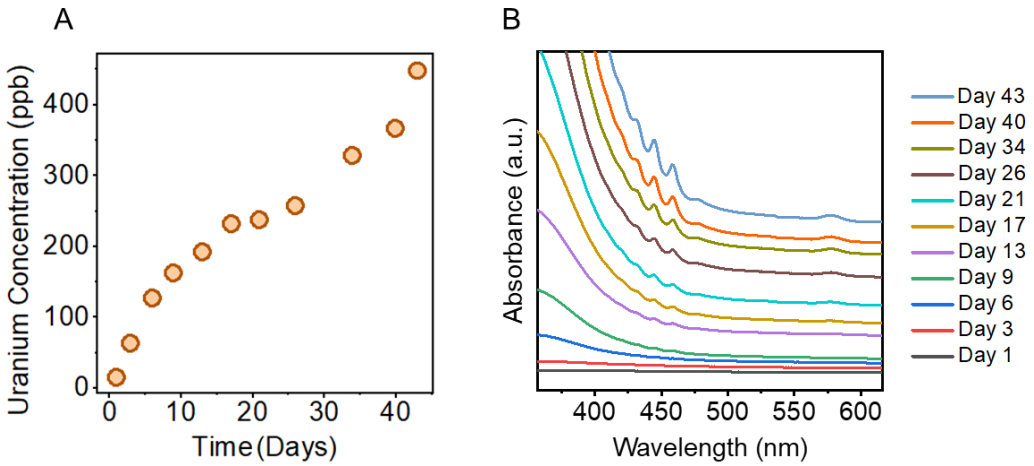

Figure 5.29 (a) ICP-MS of uranium concentration in DMF soaking solution over time, and (b) UV-Vis spectra of DMF soaking solution over time. Spectra are intentionally offset along the y-axis to show the increase in uranyl signals at 430, 445, 458, and 578 nm over time.

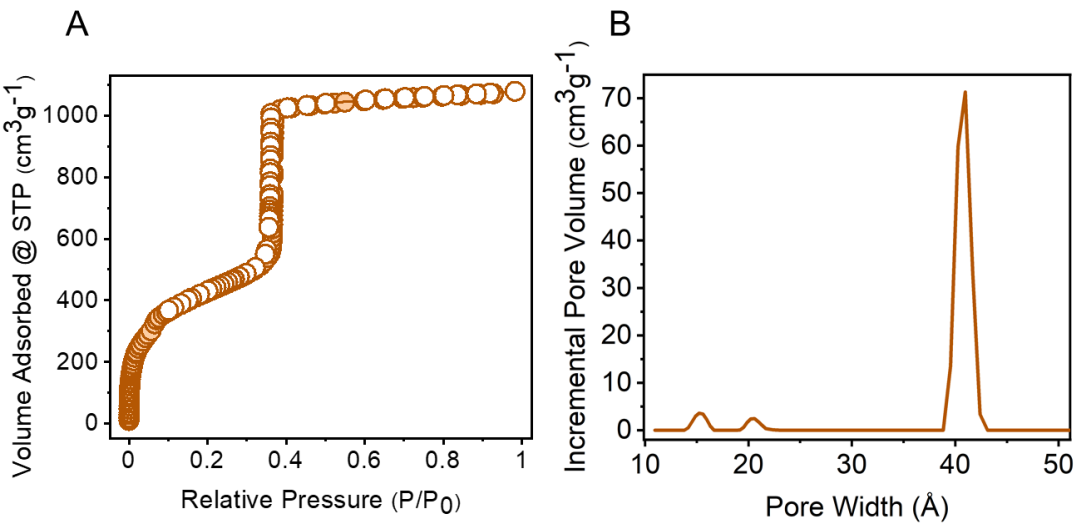

Figure 5.30 (a) Nitrogen isotherm of intermediate interpenetration in NU-1303. Filled circles represent adsorption, and open circles represent desorption. (b) PSD of intermediate interpenetration in NU-1303.

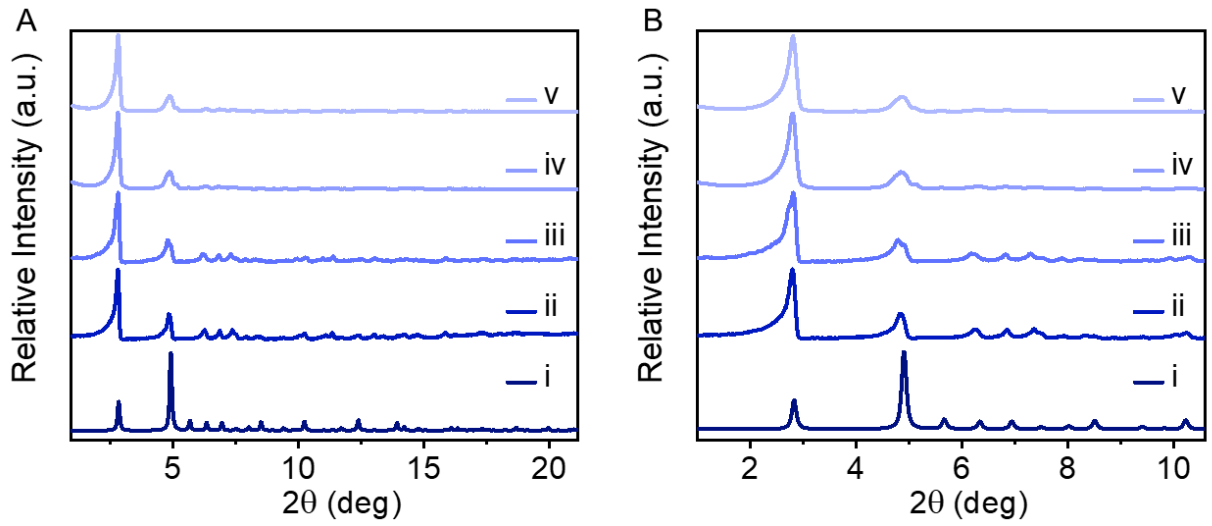

Figure 5.31 (a) PXRD tracking of intermediate interpenetration in NU-1303, and (b) PXRD tracking enlarged at low angle peaks for improved visibility. (i) simulated NU-1303-*6* simulated, experimental NU-1303-6 after (ii) 17-day DMF soak, capillary measurement, (iii) final overnight EtOH soak, capillary measurement, (iv) sc-CO_2 activation, (v) thermal activation at 50° C.

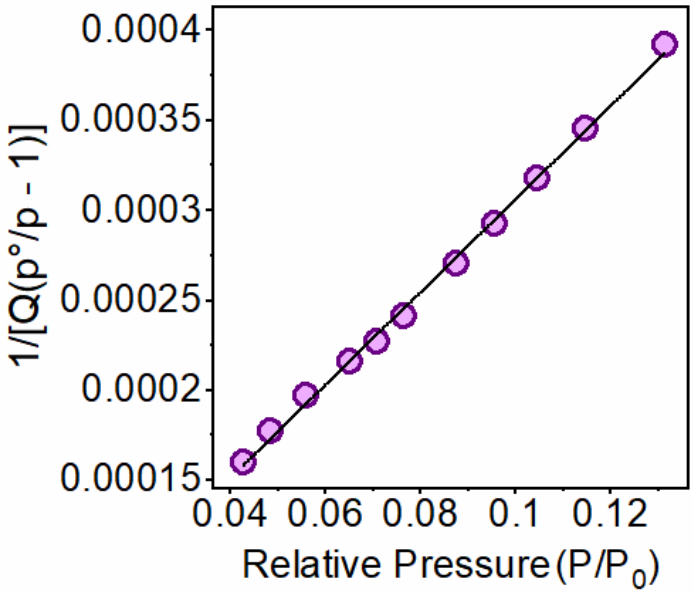

Figure 5.32 BET surface area plot for intermediate interpenetration in NU-1303-*6* with linear fitting. R^2=1.

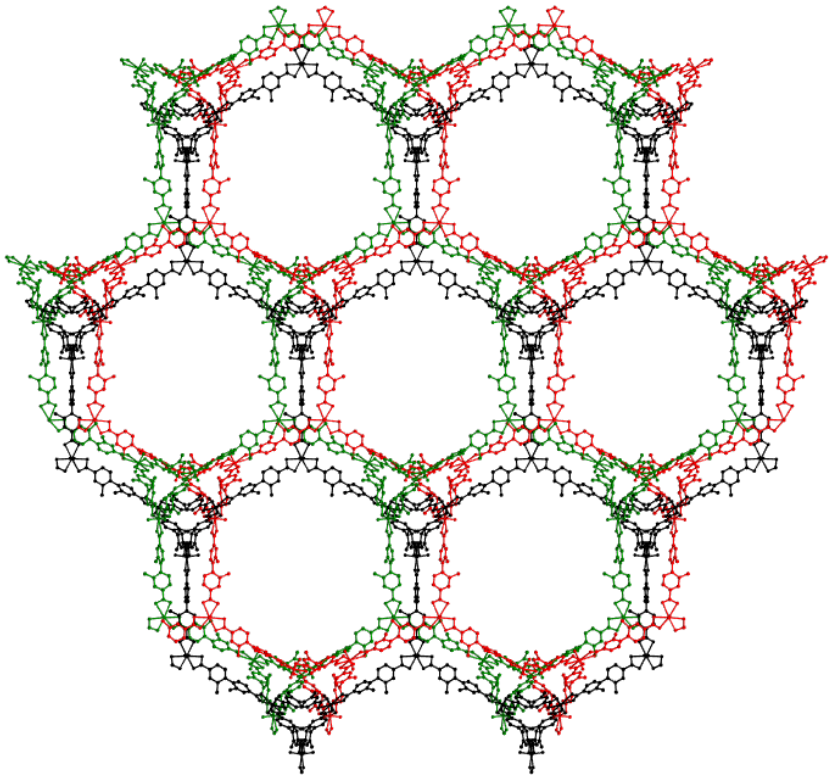

Figure 5.33 NU-1303-*3* seen down the *a* axis, with network 1 in black, network 2 in green, and network 3 in red.

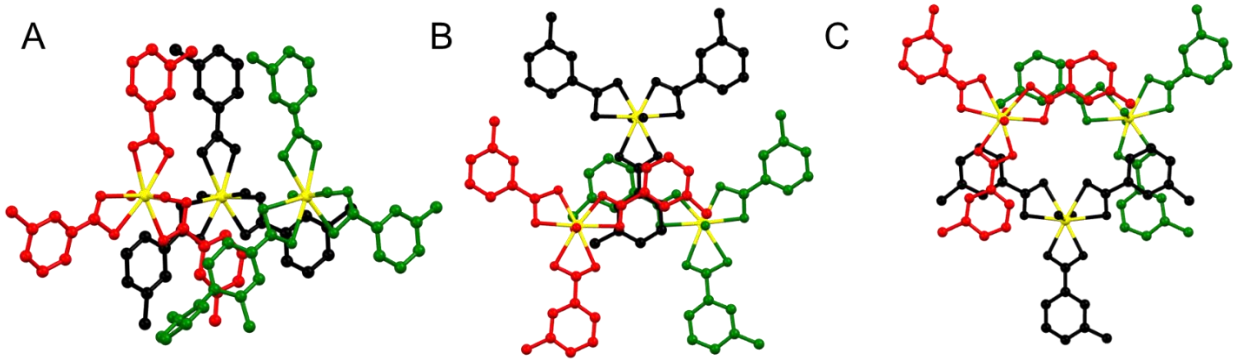

Figure 5.34 NU-1303-*3* node motifs. (a) *M5* shown down the *b* axis. (b) *M6* shown down the *a* axis. (c). *M7* shown down the *c* axis. Network 1 is shown in black, network 2 in green, and network 3 in red. Uranium atoms are shown in yellow.

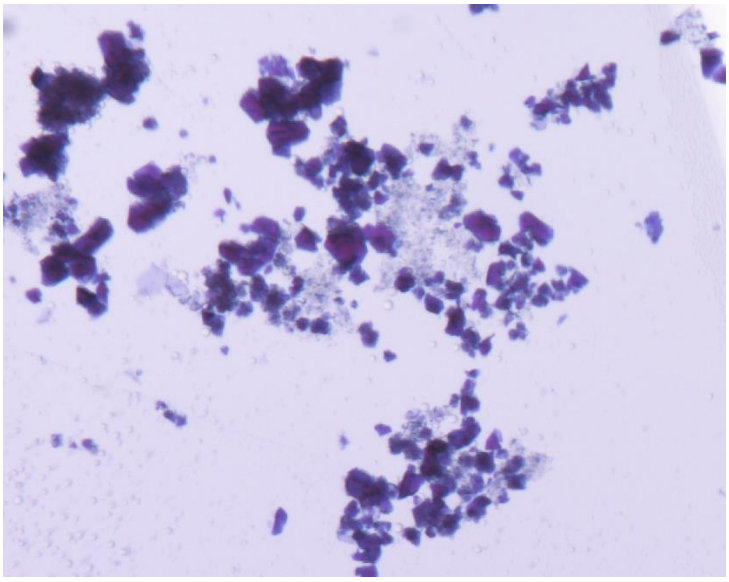

Figure 5.35 Image taken with an optical microscope of NU-1303-*1* crystals after soaking in crystal violet dye.

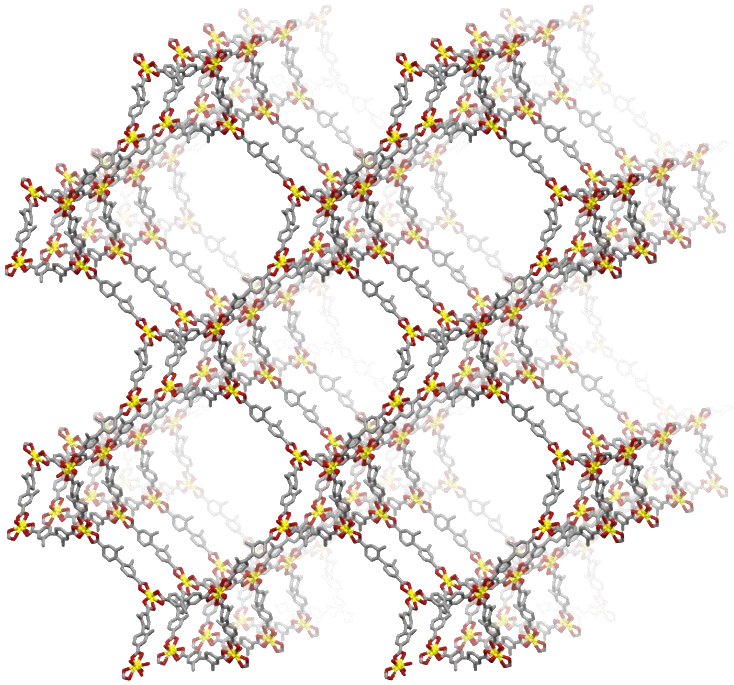

Figure 5.36 Structure of NU-1303-*1*. Atom color scheme: carbon, gray; oxygen, red; uranium, yellow. H atoms are omitted for clarity.

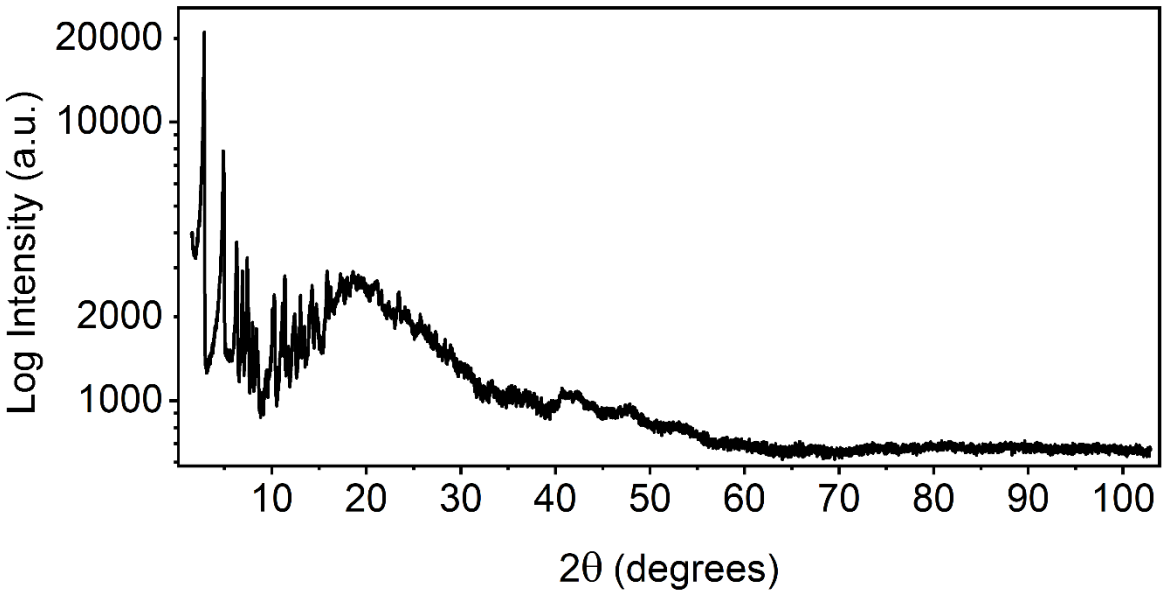

Figure 5.37 PXRD of NU-1303-*1* in log scale.

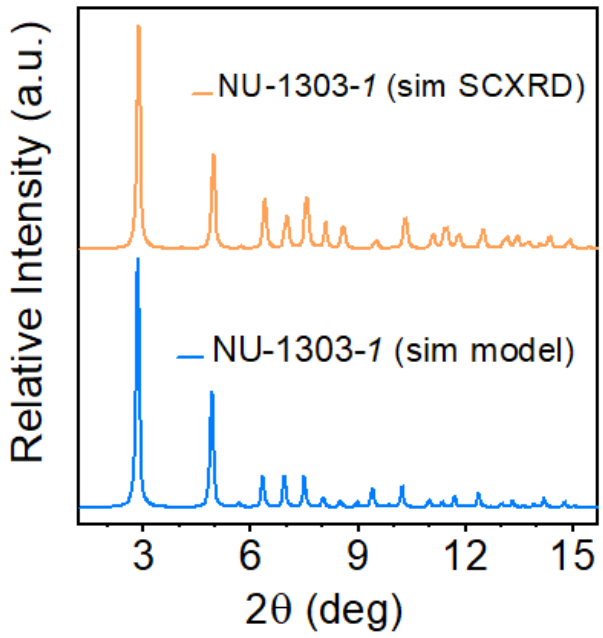

Figure 5.38 PXRD of NU-1303-*1* simulated from SCXRD (top) and from the Materials Studio model (bottom).

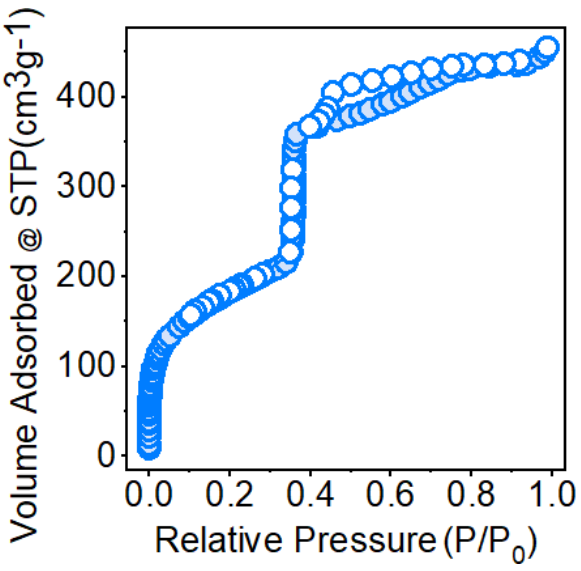

Figure 5.39 Nitrogen isotherm of NU-1303-*1*, after 752-day DMF soak. Filled circles represent adsorption, and open circles represent desorption.

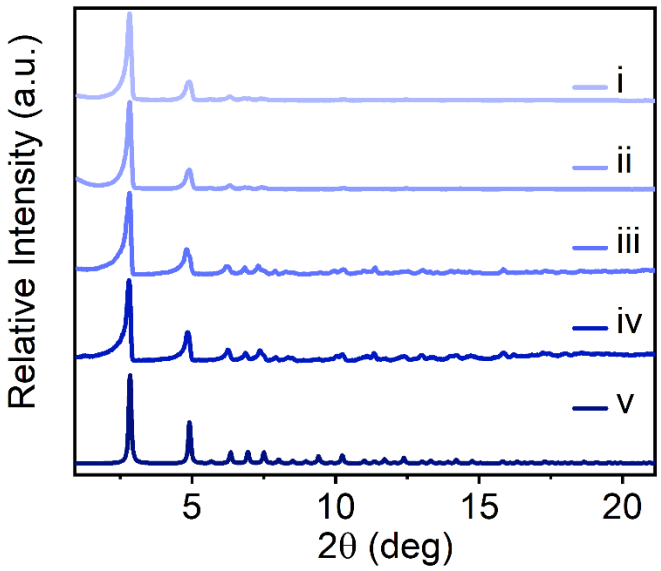

Figure 5.40 PXRD of NU-1303-*1* during solvent exchange and activation. (i) simulated NU-1303-*1*, (ii) NU-1303-*1* in DMF, capillary measurement, (iii) NU-1303-*1* after final overnight EtOH soak, capillary measurement, (iv) NU-1303-*1* after sc-CO_2 activation, (v) NU-1303-*1* after thermal activation at 50° C.

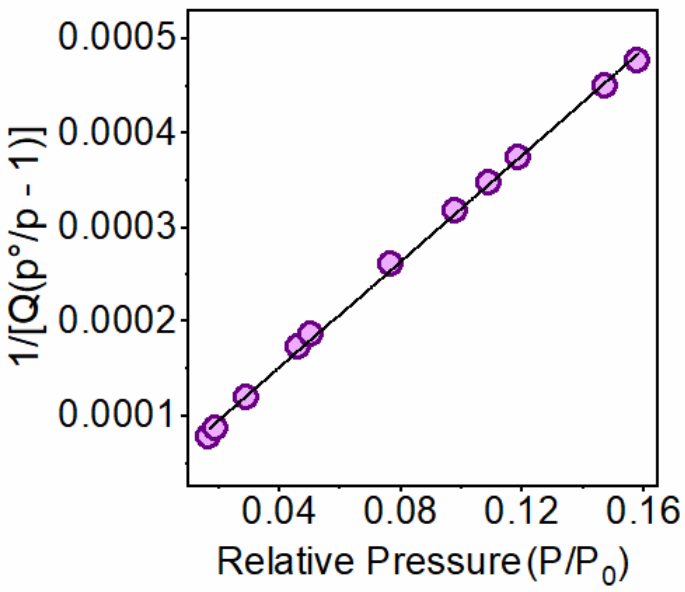

Figure 5.41 BET surface area plot for NU-1303-1 with linear fitting. R2=1.

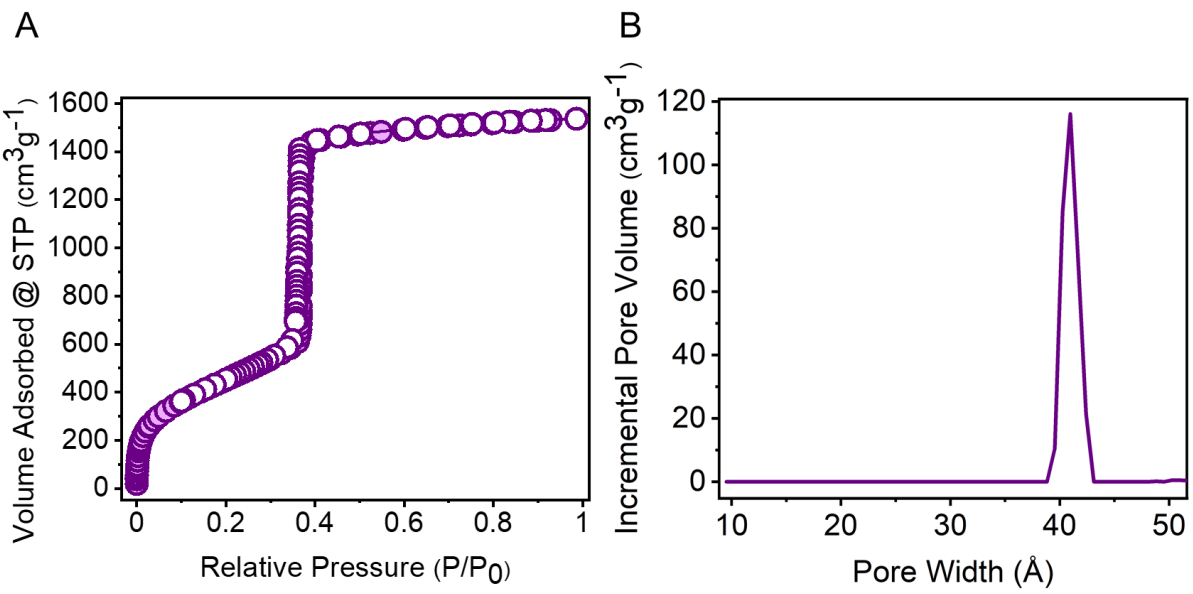

Figure 5.42 (a) Nitrogen isotherm and (b) PSD of NU-1303-*1*, after anhydrous activation. Filled circles represent adsorption, and open circles represent desorption.

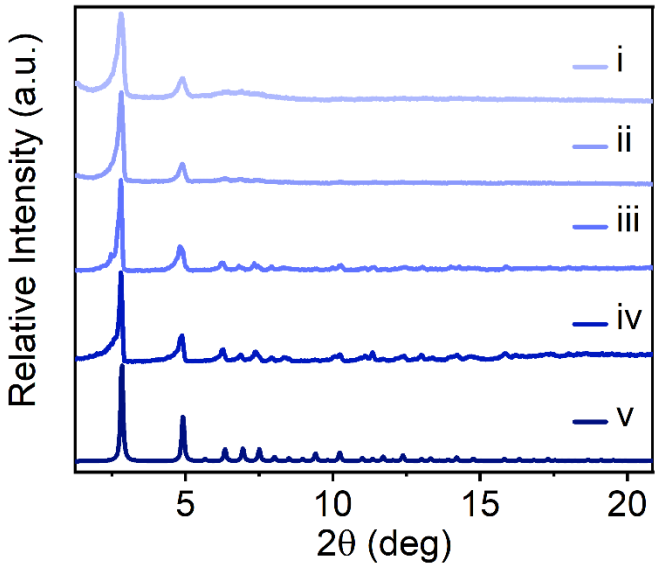

Figure 5.43 PXRD of NU-1303-*1* over the course of anhydrous solvent exchange and activation. (i) simulated NU-1303-*1*, (ii) NU-1303-*1* in anhydrous DMF, capillary measurement, (iii) NU-1303-*1* after final overnight anhydrous MeCN soak, capillary measurement, (iv) NU-1303-*1* after sc-CO_2 activation, (v) NU-1303-*1* after thermal activation at 50° C.

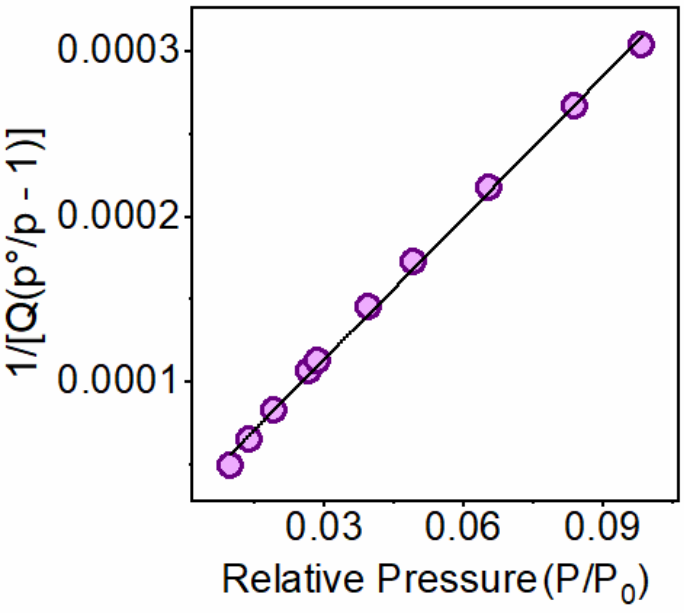

Figure 5.44 BET surface area plot for NU-1303-*1* (anhydrous activation) with linear fitting. R^2=1.

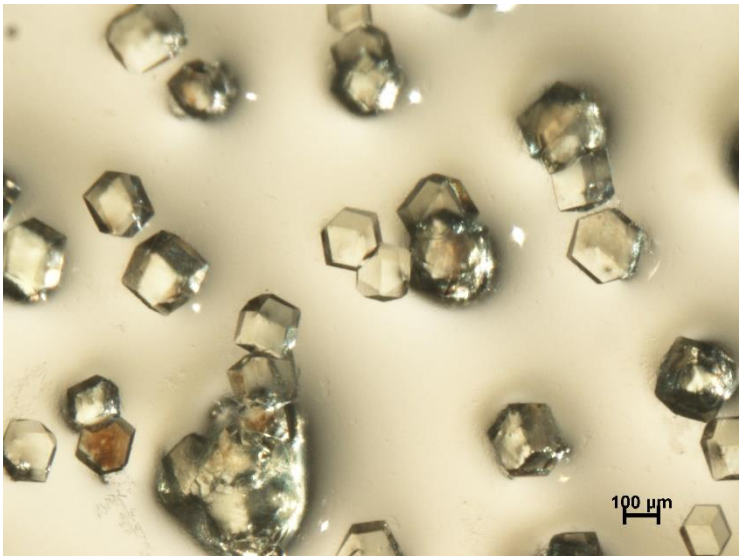

Figure 5.45 Optical image of NU-1304 single crystals.

.

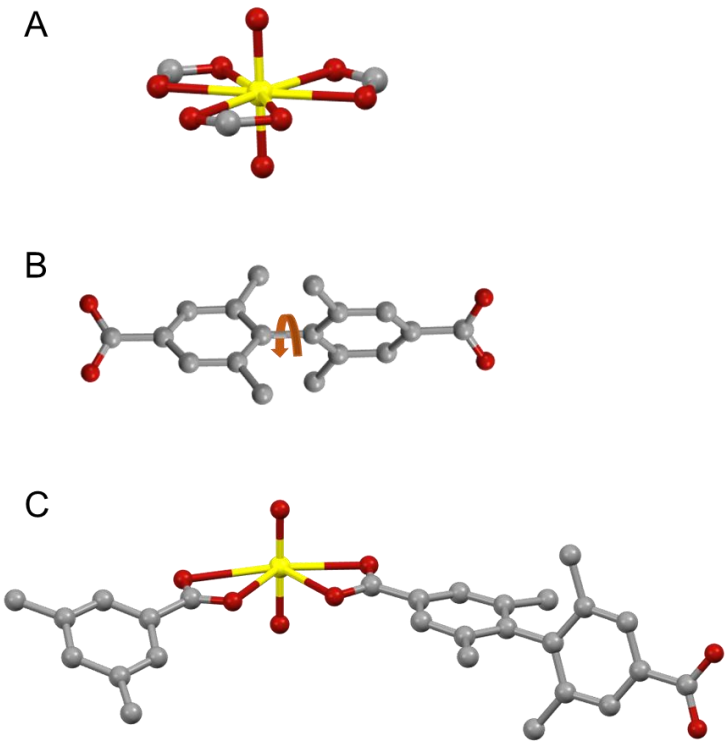

Figure 5.46 NU-1304 (**a**) uranyl node, (**b**) TMBP linker with torsion between biphenylene rings of 67.7° for one third of the linkers and 76.6° for other two thirds, and (**c**) asymmetric unit. Atom color scheme: carbon, gray; oxygen, red; uranium, yellow. H atoms are omitted for clarity.

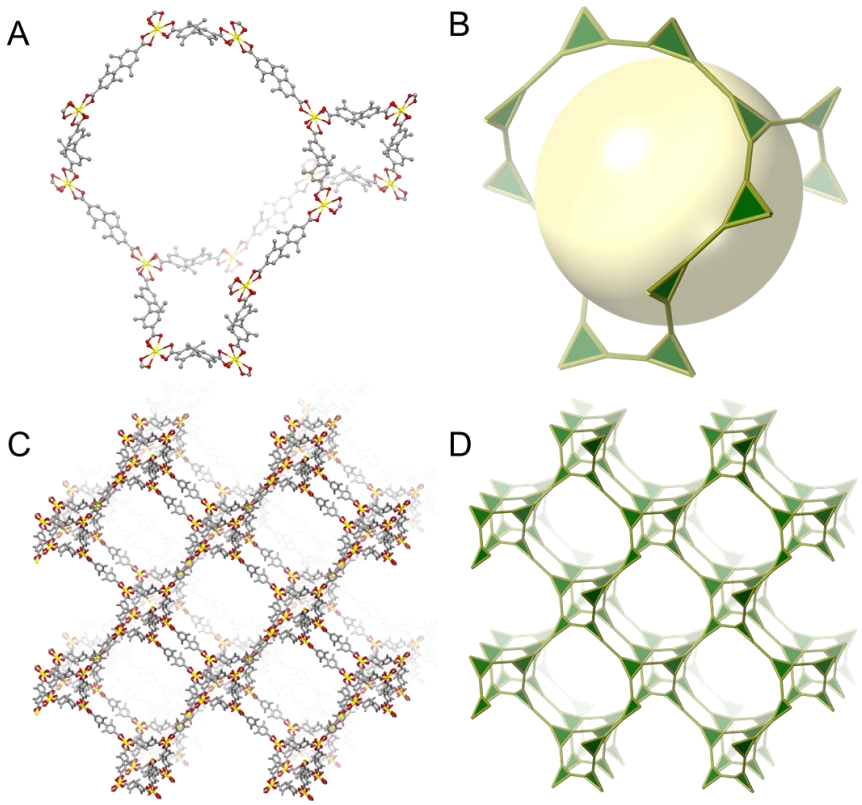

Figure 5.47 One **srs** NU-1304 cage (a) shown in ball and stick form, and (b) shown in the augmented form with a yellow sphere for the representative pore size. (c) One **srs** network of NU-1304 shown in ball and stick form, and (d) shown in augmented form. Atom color scheme: carbon, gray; oxygen, red; uranium, yellow. H atoms are omitted for clarity

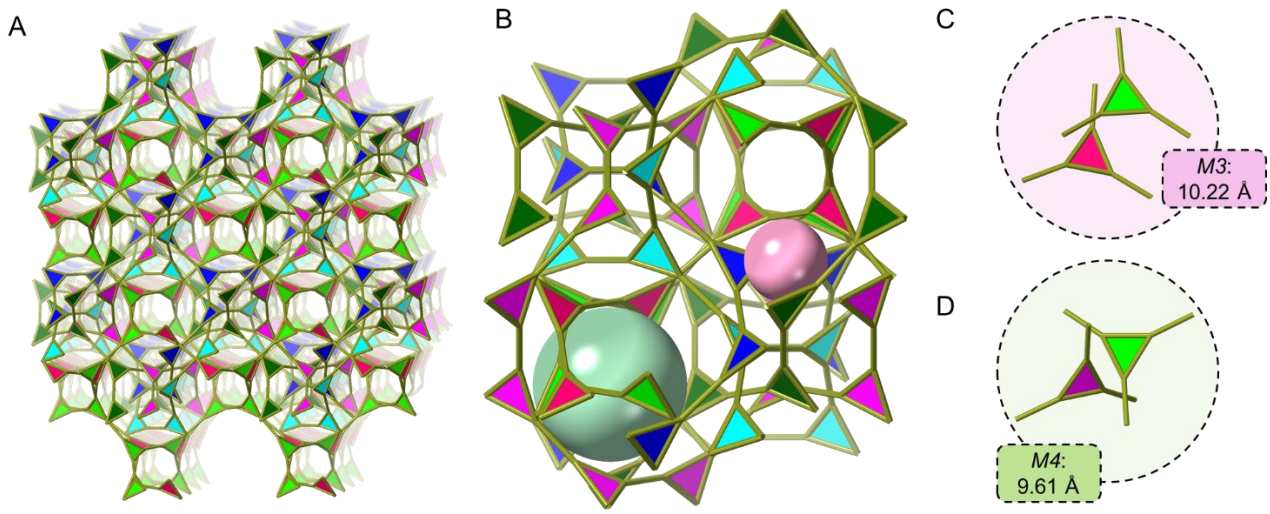

Figure 5.48 (a) Six identical srs networks interpenetrated to form NU-1304. Each network is identified by a different color for clarity. (b) Representative pore size of NU-1304. Green sphere represents 18.2 Å pore, and pink sphere represents 12.2 Å pore. (c) Two NU-1304 nodes in *M3* with a U–U distance of 10.22 Å. (d) Two NU-1304 nodes in *M4* with a U–U distance of 9.61 Å.

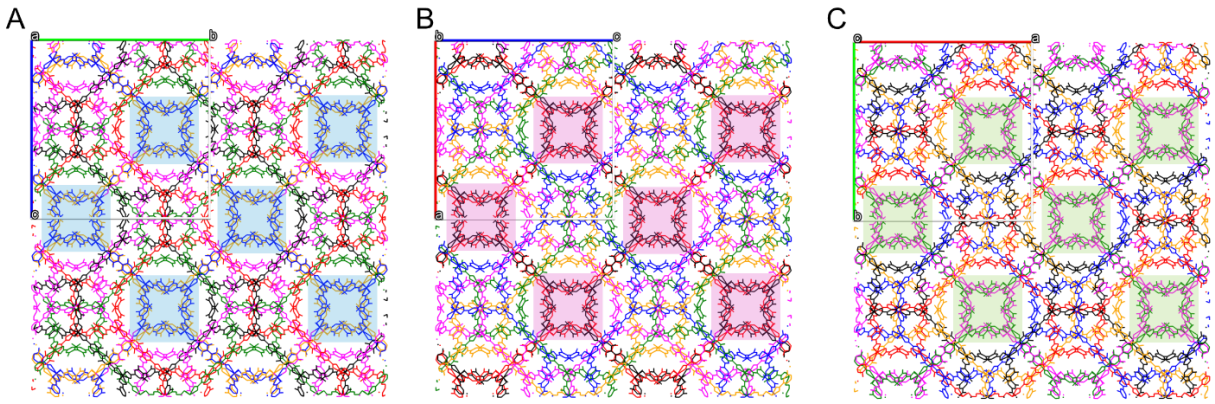

Figure 5.49 NU-1304, where each network is represented by a different color. (a) Down the *a* direction, two networks, shown in blue and orange arrange in a pair. Locations where the pair can be most clearly seen are highlighted by blue boxes for ease of viewing. (b) Down the *b* direction, two networks, shown in red and black arrange in a pair. Locations where the pair can be most clearly seen are highlighted by pink boxes for ease of viewing. (c) Down the *c* direction, two networks, shown in pink and green arrange in a pair. Locations where the pair can be most clearly seen are highlighted by green boxes for ease of viewing. H atoms omitted for clarity.

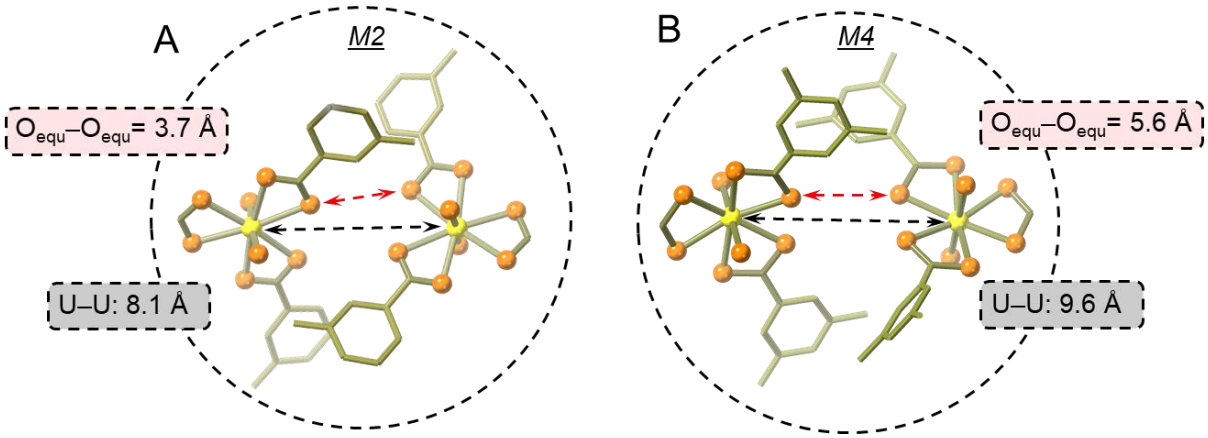

Figure 5.50 Comparison of U–U distances and closest equatorial O–O distances (O_{equ}–O_{equ}) in (a) *M2* (NU-1303) and (b) *M4* (NU-1304). Red arrows demonstrate O_{equ}–O_{equ} distances, and black arrows demonstrate U–U distances.

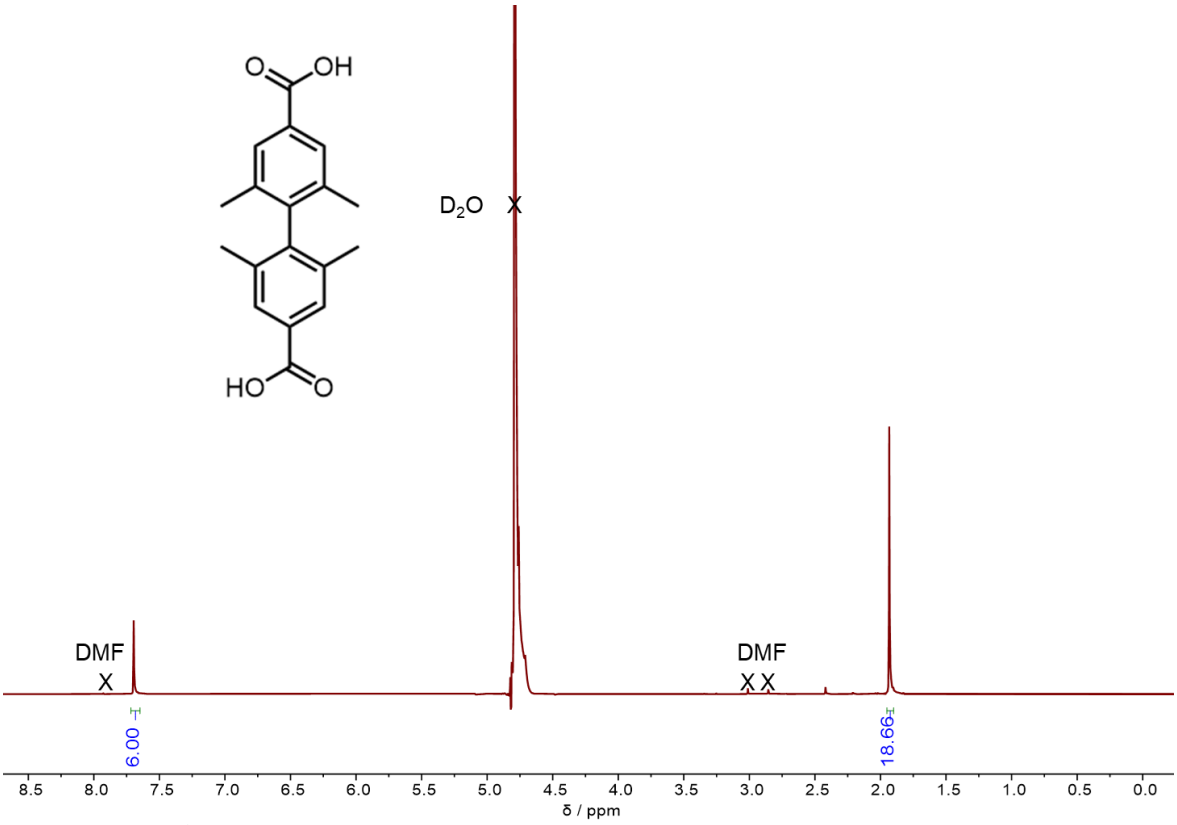

Figure 5.51 ^{1}H NMR spectrum (600 MHz, D_2O, 298 K) of base-digested NU-1304. Peak integration is relative to one node (1.5 linkers per node).

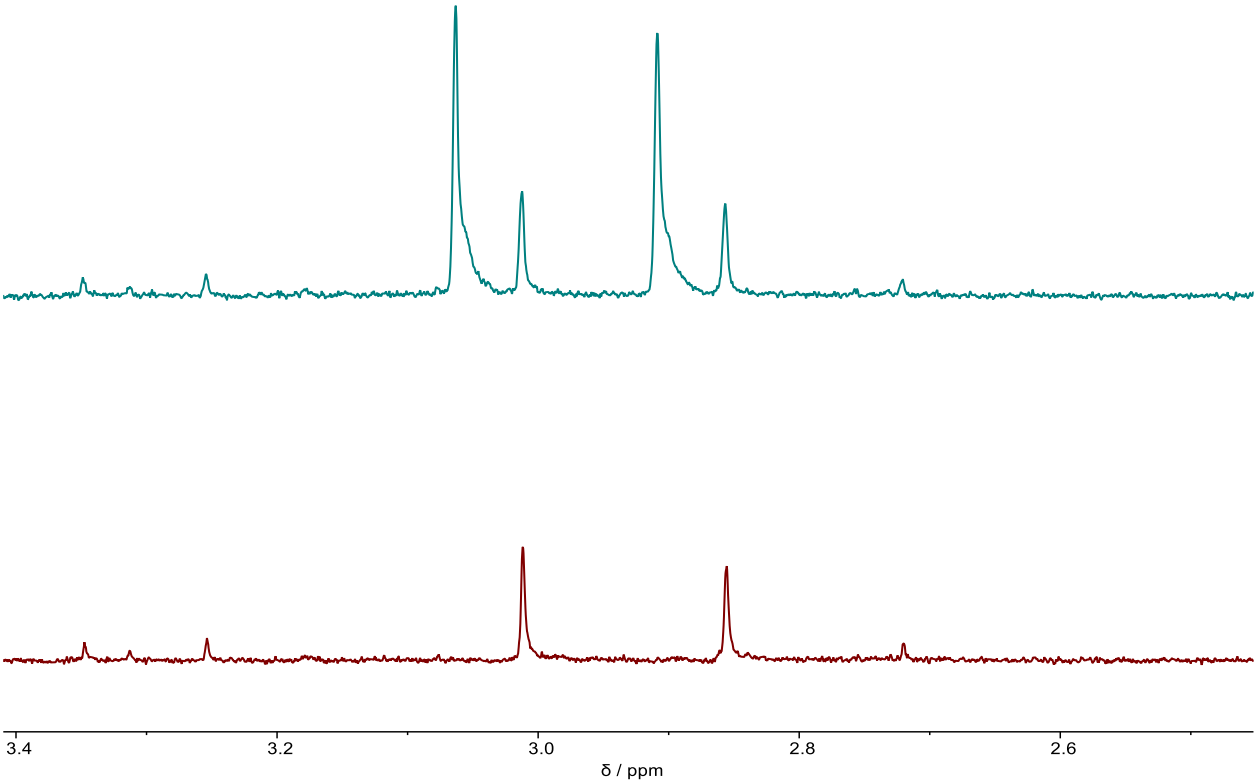

Figure 5.52 ^{1}H NMR spectrum (600 MHz, D2O, 298 K) of base-digested NU-1304 before (bottom) and after (top) addition of dimethylamine.

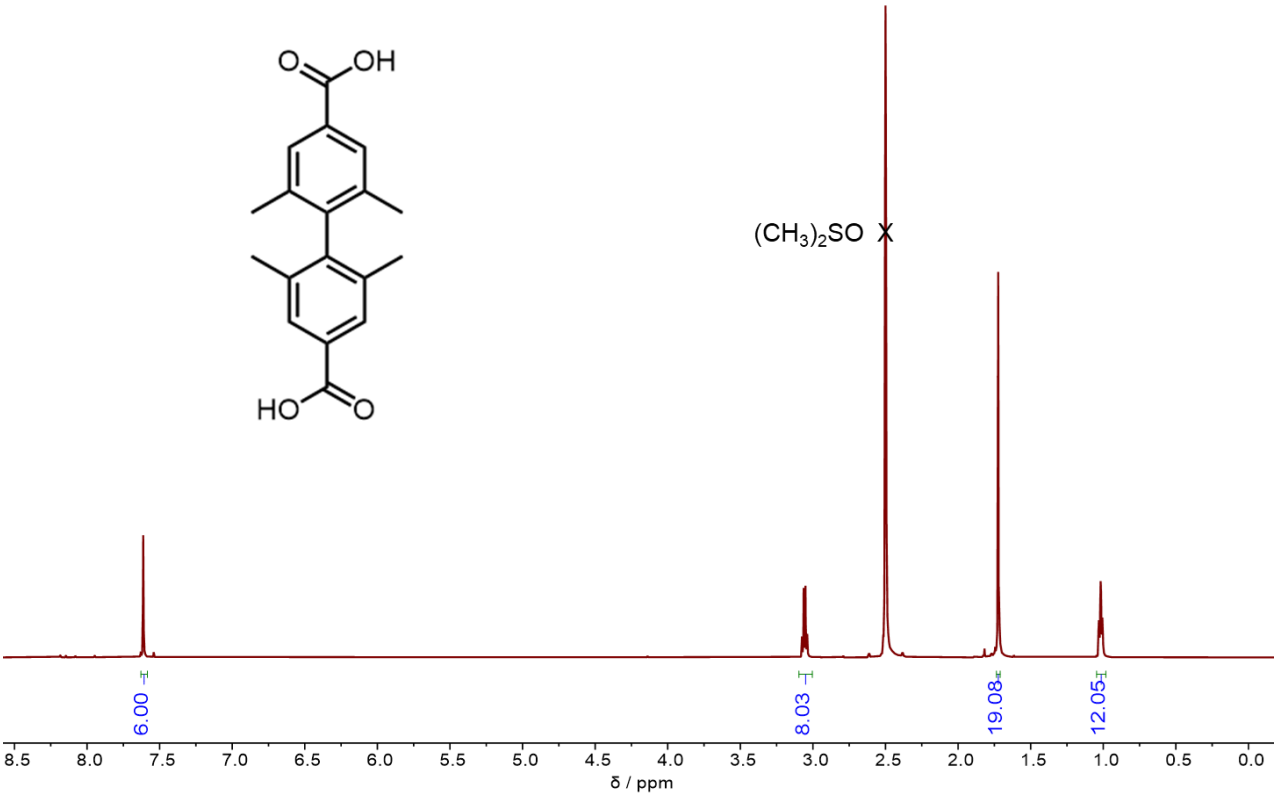

Figure 5.53 ^{1}H NMR spectrum (600 MHz, D_2O, 298 K) of acid-digested NU-1304 after cation exchange with TEACl. Peak integration is relative to one node (1.5 linkers per node).

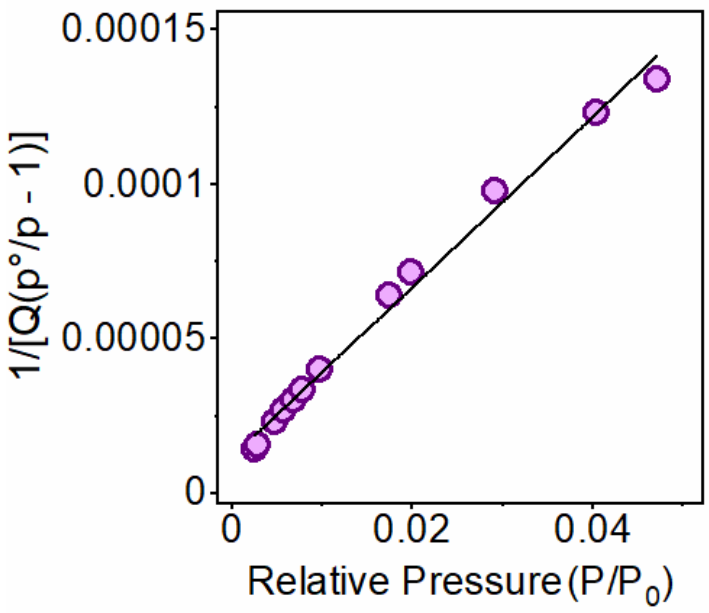

Figure 5.54 BET surface area plot for NU-1304 with linear fitting. R^2=0.99.

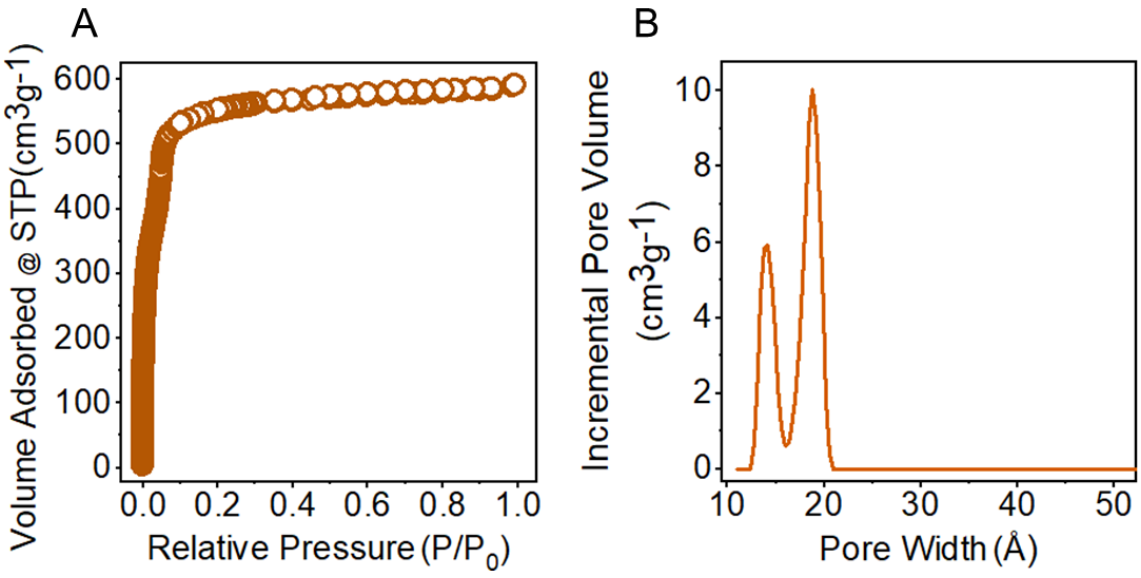

Figure 5.55 (a) Nitrogen isotherm and (b) PSD of NU-1304, after 10-day DMF soak activation. Filled circles represent adsorption, and open circles represent desorption. A similar isotherm was obtained after a 1057-day DMF soak.

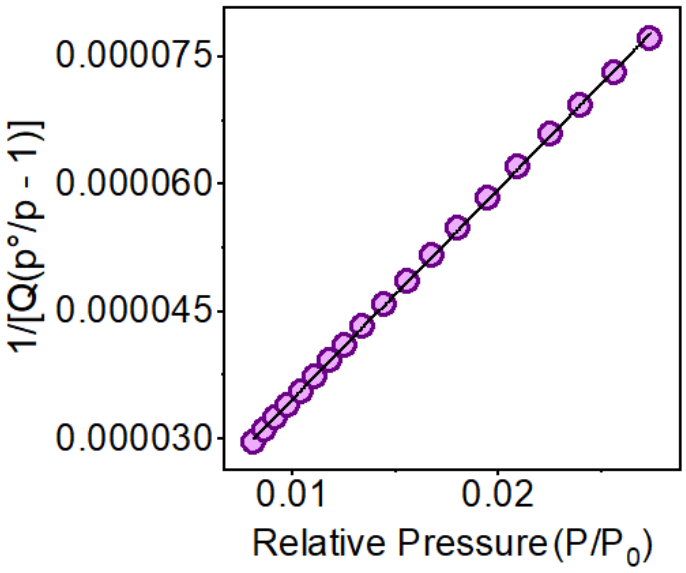

Figure 5.56 BET surface area plot for NU-1304 after 10-day DMF soak with linear fitting. R^2=1.

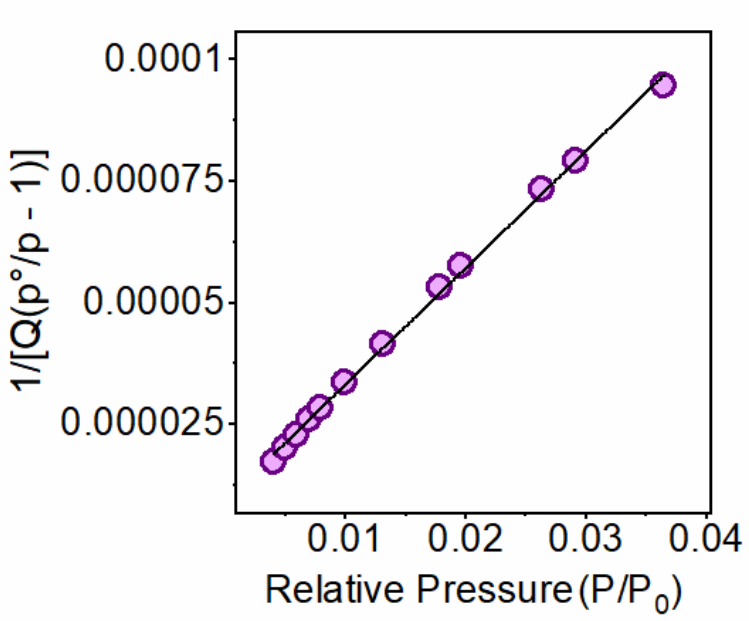

Figure 5.57 BET surface area plot for NU-1304 (anhydrous activation) with linear fitting. R^2=1.

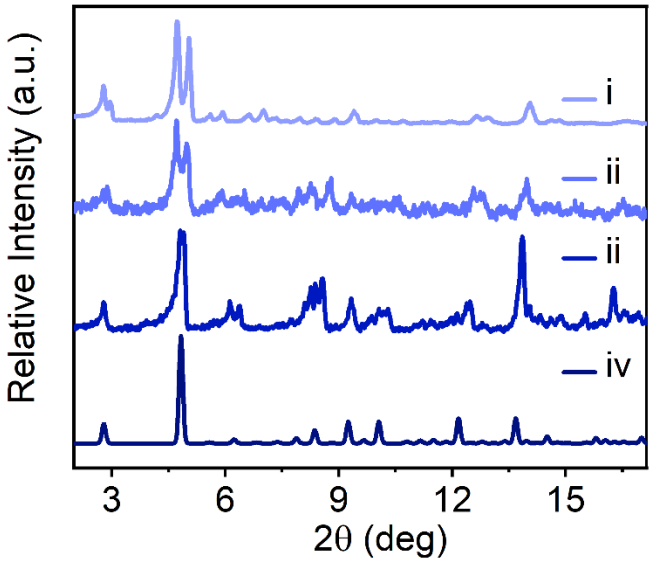

Figure 5.58 PXRD of NU-1304 during anhydrous solvent exchange and activation. (i) simulated NU-1304, (ii) NU-1304 in anhydrous DMF, capillary measurement, (iii) NU-1304 after final overnight anhydrous MeCN soak, capillary measurement, (iv) NU-1304 after activation.

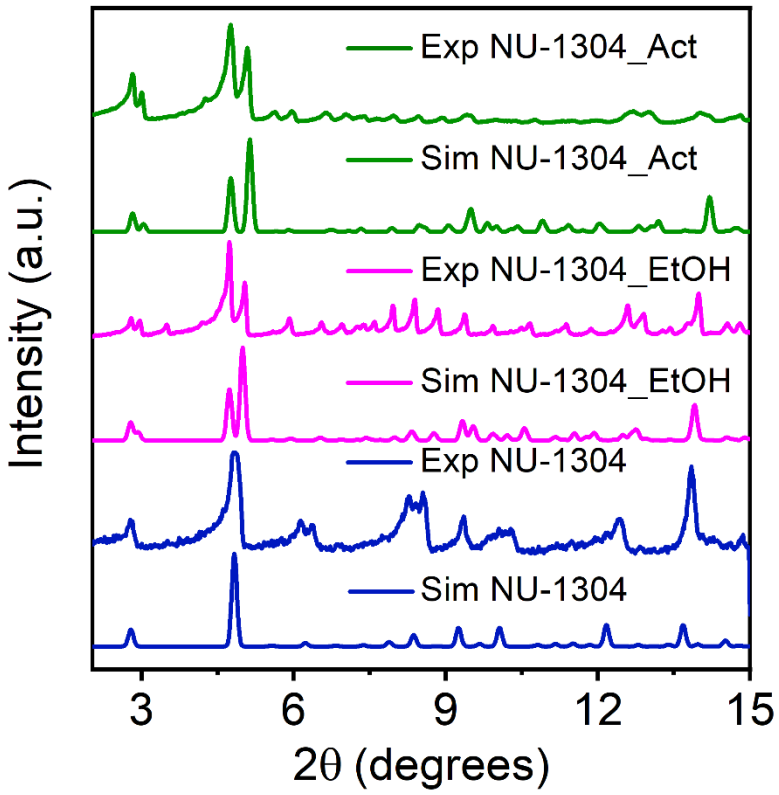

Figure 5.59 Simulated PXRD matching of NU-1304 during solvent exchange and activation. From bottom to top: Simulated NU-1304; Experimental NU-1304 in DMF, capillary measurement; Simulated NU-1304_EtOH; Experimental NU-1304_EtOH, capillary measurement; Simulated NU-1304_Act; Experimental NU-1304_Act.

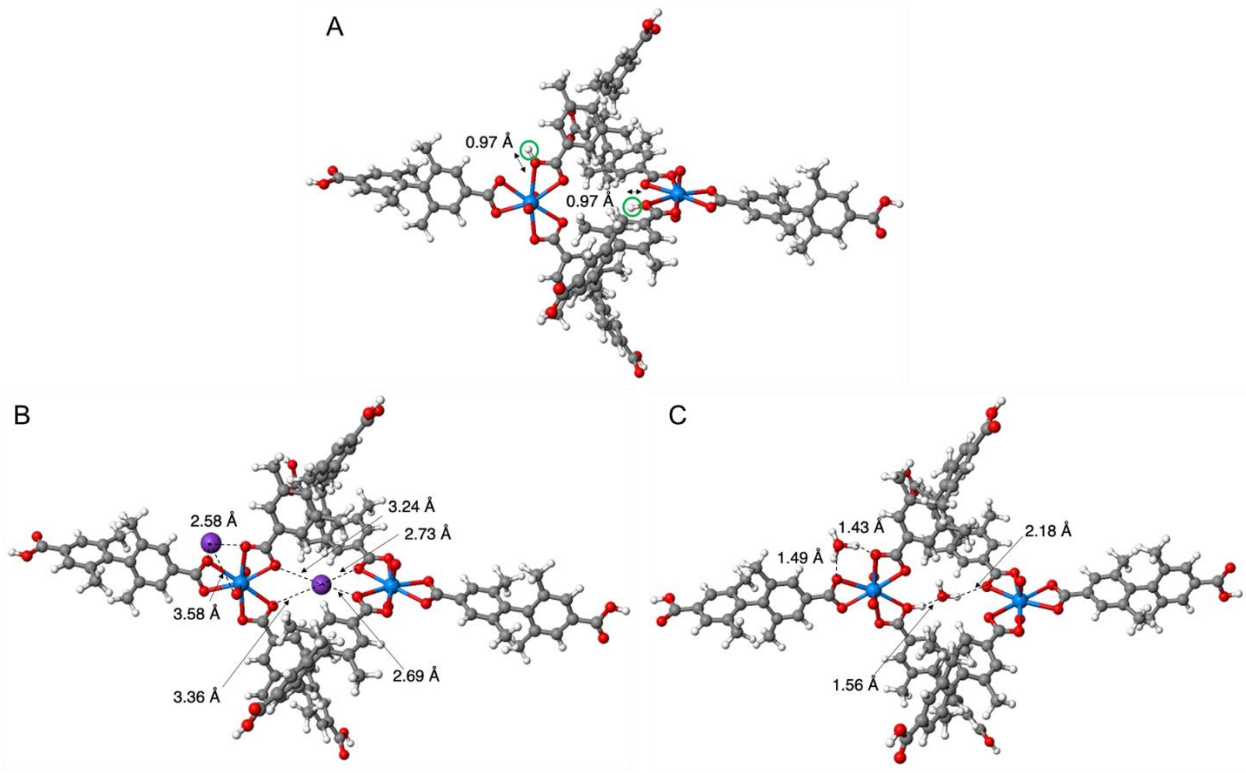

Figure 5.60 NU-1304 cluster models for *M4b* in the presence of (a) H^+ cations (circled in green), (b) K^+ cations, and (c) H_3O^+. Equilibrium positions of all cations are shown in the implicit solvent model for DMF. Atom color scheme: uranium, blue; potassium, purple; oxygen, red; carbon, gray; hydrogen, white.

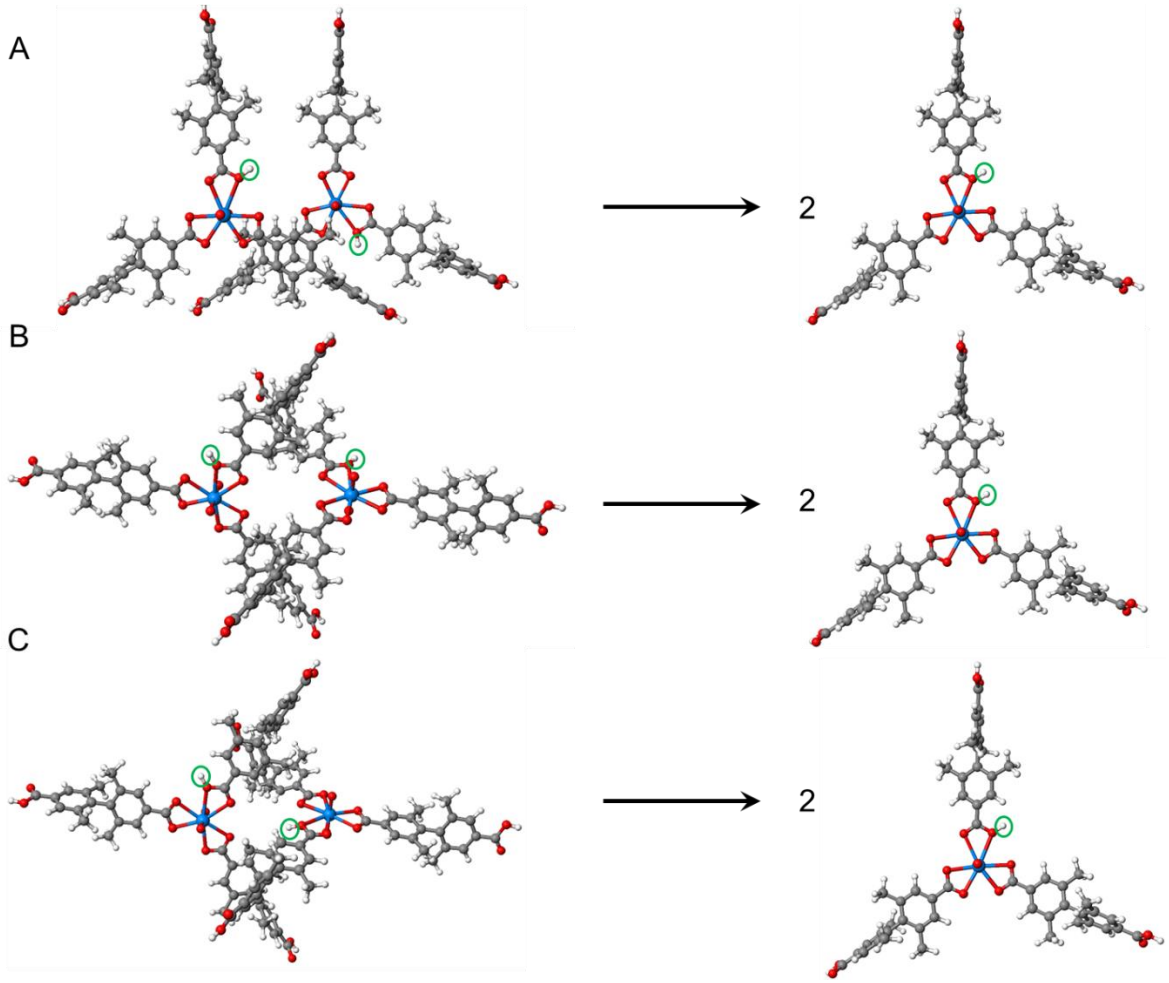

Figure 5.61 Modeling the transformation of (a) *M3*, (b) *M4a*, and (c) *M4b* in NU-1304 to their respective de-interpenetrated fragments for free energy of transformation calculations. Atom color scheme: uranium, blue; oxygen, red; carbon, gray; hydrogen, white. This model is shown with H^+ cations (circled in green). It is representative for de-interpenetration with uncapped models and models with H_3O^+ and K+ cations.

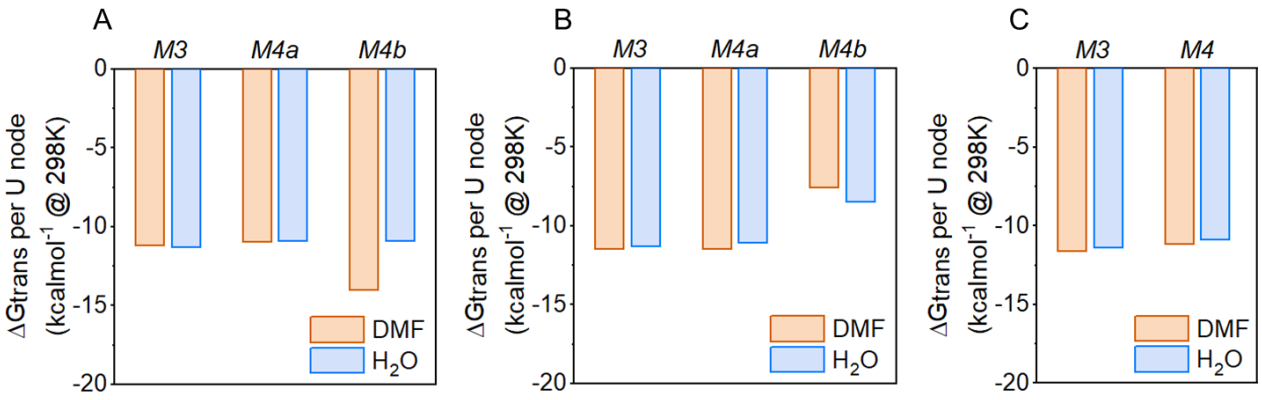

Figure 5.62 Free energy of transformation calculations of *M3*, *M4a*, and *M4b* in implicit solvent models for DMF (orange) and water (blue). Free energy values were calculated in the presence of (A) H_3O^+ cations, (B) K^+ cations, or (C) no cation.

Table 5.1 Crystal data and structure refinement details for NU-1303-*6* and NU-1303-*3*.

Angle	NU-1303-*6*	NU-1303-*3*
Formula	$C_{96}H_{76}O_{33}U_4$	$C_{285}H_{542.13}K_{0.40}N_{63.33}O_{107.27}U_4$
Formula weight	2709.68	7540.61
Temperature/K	200	250
Crystal system	cubic	monoclinic
Space group	$I4_132$	I2
a/Å	44.055(3)	38.3195(9)
b/Å	44.055(3)	62.1514(9)
c/Å	44.055(3)	38.4697(8)
α/°	90	90
β/°	90	109.826(3)
γ/°	90	90
Volume/Å^3	85504(20)	86189(3)
Z	24	2
ρ_{calc}g/cm^3	0.631	0.872
μ/mm^{-1}	6.550	3.629
F(000)	15048.0	23575.0
Crystal size/mm^3	0.306 × 0.246 × 0.174	0.15 × 0.13 × 0.07
Radiation	CuKα (λ = 1.54184)	Cu Kα (λ = 1.54184)
2Θ range for data collection/°	2.836 to 101.052	4 to 69.648
Index ranges	$-38 \le h \le 44$, $-38 \le k \le 44$, $-43 \le l \le 36$	$-28 \le h \le 28$, $-46 \le k \le 43$, $-28 \le l \le 28$
Reflections collected	118738	74798
Independent reflections	7519 [R_{int} = 0.1010, R_{sigma} = 0.0502]	35564 [R_{int} = 0.0615, R_{sigma} = 0.0692]
Data/restraints/parameters	7519/198/278	35564/2652/1620
Goodness-of-fit on F^2	1.071	0.971
Final R indexes [I>=2σ (I)]	R_1 = 0.0738, wR_2 = 0.2246	R_1 = 0.0593, wR_2 = 0.1521
Final R indexes [all data]	R_1 = 0.0975, wR_2 = 0.2483	R_1 = 0.0763, wR_2 = 0.1611
Largest diff. peak/hole / e Å^{-3}	1.23/-0.39	0.35/-0.45

Table 5.2 ICP-OES analysis of expected vs. observed U content in NU-1303-*6* and NU-1304.

Angle	NU-1303-*6* (ppm U)	NU-1304 (ppm U)
Expected (with UO_2^{2+} cation)	18.2	24.1
Observed	12.5	15.8

Table 5.3 BET analysis summary

	NU-1303-*6*	NU-1303 intermediate inter-penetration	NU-1303-*1* (144-day DMF soak)	NU-1303-*1* (anhydrous)	NU-1304 (0-day DMF soak)	NU-1304 (10-day DMF soak)	NU-1304 (anhydrous)
BET surface area (m^2g^{-1})	1,737.8255 ± 27.8871	1,652.7009 ± 25.5642	1,526.2862 ± 18.0803	1,514.5375 ± 23.6980	1,570.9136 ± 47.3212	1,752.1082 ± 6.3617	1,805.3016 ± 23.3989
Slope (gcm^{-3} STP)	0.002490 ± 0.000040	0.002586 ± 0.000041	0.002812 ± 0.000034	0.002845 ± 0.000045	0.002759 ± 0.000083	0.002474 ± 0.000009	0.002402 ± 0.000031
Y-intercept (gcm^{-3} STP)	0.000015 ± 0.000001	0.000048 ± 0.000003	0.000039 ± 0.000003	0.000029 ± 0.000002	0.000012 ± 0.000002	0.000010 ± 0.000000	0.000009 ± 0.000001
C	170.767526	55.159625	72.661048	100.650632	239.607452	249.072039	263.340556
Qm (cm^3g^{-1} STP)	399.2635	379.7062	350.6625	347.9633	360.9157	402.5449	414.7660
Correlation coefficient	0.9987008	0.9988931	0.9993569	0.9990051	0.9954581	0.9998871	0.9991550
Molecular cross-sectional area (nm^2)	0.1620	0.1620	0.1620	0.1620	0.1620	0.1620	0.1620

Table 5.4 Experimental BET areas (nitrogen physisorption) and calculated geometric surface areas (RASPA) for NU-1303-*6* and NU-1303-*1*.

	Experimental BET Area (m^2g^{-1})	**Calculated Geometric Surface Area (m^2g^{-1})**
NU-1303-*6*	1735	2340
NU-1303-*1*	1525	5700

Table 5.5 Experimental (nitrogen physisorption) and calculated (RASPA) void fractions and pore volumes for NU-1303-*6* and NU-1303-*1*, in the presence of different possible cations.

	Experimental Void Fraction (%)	Experimental Pore Volume (cm^3g^{-1})	Calculated Void Fraction (%)	Calculated Pore Volume (cm^3g^{-1})
NU-1303-*6* $(H^+_{0.9}K^+_{0.1}[UO_2(DMBP)_{1.5}])$	54.6	0.86	77.5	1.2
NU-1303-*6* $((H_3O^+)_{0.9}K^+_{0.1}[UO_2(DMBP)_{1.5}]^-)$	55.9	0.86	77.5	1.2
NU-1303-*1* $(H^+_{0.9}K^+_{0.1}[UO_2(DMBP)_{1.5}])$	23.7	2.25	96.6	9.2
NU-1303-*1* $((H_3O^+)_{0.9}K^+_{0.1}[UO_2(DMBP)_{1.5}]^-)$	24.2	2.25	96.6	9.0

Table 5.6 Estimated experimental (TGA) and calculated void fractions for NU-1303-*6* and NU-1303-*1*.

	Calculated Void Fraction (%)	Estimated Experimental (TGA) Void Fraction (%)
NU-1303-*6*	77.5	67
NU-1303-*1*	96.6	83
Difference (%)	19	16

Table 5.7 Code versions used during the PXRD matching procedure

Code	Version
Python	3.7.4
SciPy	1.3.1
pymatgen	2019.12.22

Table 5.8 Calculated (calc.) vs. experimental (expt.) lattice parameters for NU-1303-*6*, NU-1303-*6*_EtOH, NU-1303-*6*_Act, and NU-1303-*1*.

	NU-1303-*6*		**NU-1303-*6*_EtOH**		**NU-1303-*6*_Act**		**NU-1303-*1***	
	Calc.	**Expt. (SCXRD)**	**Calc.**	**Expt. (Le Bail)**	**Calc.**	**Expt. (Le Bail)**	**Calc.**	**Expt. (Le Bail)**
***a* (Å)**	-	44.05(5)	45.3	43.91(1)	41.3	40.75(2)	44.0	44.04(1)
***b* (Å)**	-	44.05(5)	45.3	43. 91(1)	41.3	40.75(2)	44.0	44.04(1)
***c* (Å)**	-	44.05(5)	45.3	43. 91(1)	48.6	48.30(3)	44.0	44.04(1)
***α* (°)**	-	90	90	90	90	90	90	90
***β* (°)**	-	90	90	90	90	90	90	90
***γ* (°)**	-	90	90	90	90	90	90	90

Table 5.9 Agreement factors for Le Bail fitting analysis.

	NU-1303-*6*_EtOH	**NU-1303-*6*_Act**	**NU-1303-*1***	**NU-1304_EtOH**	**NU-1304_Act**
wR	11.6	12.6	11.6	14.0	9.3

Table 5.10 Comparison of cluster DFT-computed absolute (top) and relative (bottom) electronic energies, enthalpies, and free energies of interpenetrated *M1*, *M2a*, and *M2b* (NU-1303-*6*) relative to their NU-1303-*1* fragments, in the presence of different cations. These were performed in implicit solvent models for DMF and water at 298 K using M06-2X; expressed in electronic energies per uranyl node in kcalmol^{-1}.

Motif	Solvent	E	H	G
		Hartree	Hartree	Hartree
Proton				
NU-1303-*1*	DMF	-3380.176713	-3380.062040	-3380.129831
	Water	-3380.189149	-3380.075066	-3380.143170
M1	DMF	-6760.339310	-6760.113853	-6760.208299
	Water	-6760.373091	-6760.148159	-6760.242323
M2a	DMF	-6760.344858	-6760.119470	-6760.215249
	Water	-6760.375249	-6760.150639	-6760.245058
M2b	DMF	-6760.347358	-6760.121896	-6760.217085
	Water	-6760.377531	-6760.152923	-6760.248610
Hydronium				
NU-1303-*1*	DMF	-3456.632824	-3456.491666	-3456.564317
	Water	-3456.645575	-3456.505271	-3456.578097
M1	DMF	-6913.250832	-6912.972583	-6913.077008
	Water	-6913.286727	-6913.009936	-6913.113272
M2a	DMF	-6913.259776	-6912.981089	-6913.086162
	Water	-6913.290918	-6913.014926	-6913.118960
M2b	DMF	-6913.272197	-6912.994861	-6913.097515
	Water	-6913.299945	-6913.023353	-6913.124952
Potassium				
NU-1303-*1*	DMF	-3979.618326	-3979.512995	-3979.585155
	Water	-3979.627469	-3979.522830	-3979.595228
M1	DMF	-7959.226530	-7959.019491	-7959.122813
	Water	-7959.251811	-7959.045547	-7959.148712
M2a	DMF	-7959.231344	-7959.024471	-7959.127685
	Water	-7959.257794	-7959.052073	-7959.154832
M2b	DMF	-7959.254419	-7959.047228	-7959.149963
	Water	-7959.273504	-7959.067406	-7959.169190

Motif	Solvent	ΔE per U node	ΔH per U node	ΔG per U node
		kcalmol^{-1}	kcalmol^{-1}	kcalmol^{-1}
Proton				
NU-1303-*1*	DMF	-	-	-
	Water	-	-	-
M1	DMF	-4.4	-3.2	-16.1
	Water	-1.6	-0.6	-13.8
M2a	DMF	-2.7	-1.4	-13.9
	Water	-1.0	+0.2	-13.0
M2b	DMF	-1.9	-0.7	-13.4
	Water	-0.2	+0.9	-11.8
Hydronium				
NU-1303-*1*	DMF	-	-	-
	Water	-	-	-
M1	DMF	-4.6	-3.4	-16.2
	Water	-1.4	-0.2	-13.5
M2a	DMF	-1.8	-0.7	-13.3
	Water	-0.1	+1.4	-11.7
M2b	DMF	+2.1	+3.6	-9.8
	Water	+2.8	+4.0	-9.8
Potassium				
NU-1303-*1*	DMF	-	-	-
	Water	-	-	-
M1	DMF	-3.2	-2.0	-14.9
	Water	-1.0	-0.04	-13.1
M2a	DMF	-1.7	-0.5	-13.4
	Water	+0.9	+2.0	-11.2
M2b	DMF	+5.6	+6.7	-6.4
	Water	+5.8	+6.8	-6.7

Table 5.11 Comparison of cluster DFT-computed absolute (top) and relative (bottom) electronic energies, enthalpies, and free energies of interpenetrated uncapped *M1* and *M2* (NU-1303-*6*) relative to their NU-1303-*1* fragments. These were performed in implicit solvent models for DMF and water at 298 K using the M06-2X functional; expressed in electronic energies per uranyl node in $kcalmol^{-1}$.

Motif	Solvent	E	H	G
		Hartree	Hartree	Hartree
NU-1303-*1*	DMF	-3379.751518	-3379.649049	-3379.716342
	Water	-3379.764390	-3379.662765	-3379.730091
M1	DMF	-6759.489930	-6759.288746	-6759.382378
	Water	-6759.523907	-6759.323949	-6759.417246
M2	DMF	-6759.492907	-6759.291699	-6759.385460
	Water	-6759.527484	-6759.328176	-6759.423271

Motif	Solvent	ΔE per U node	ΔH per U node	ΔG per U node
		$kcalmol^{-1}$	$kcalmol^{-1}$	$kcalmol^{-1}$
NU-1303-*1*	DMF	-	-	-
	Water	-	-	-
M1	DMF	-4.1	-2.9	-15.8
	Water	-1.5	-0.5	-13.5
M2	DMF	-3.2	-2.0	-14.8
	Water	-0.4	0.8	-11.6

Table 5.12 Distances between networks in *M5*, *M6*, and *M7* of NU-1303-*3*.

	M5	***M6***	***M7***
network 1-network 2 (*Å*)	7.0	8.0	7.9
network 1-network 3 (*Å*)	8.0	8.0	7.9
network 2-network 3 (*Å*)	8.0	10.7	10.1

Table 5.13 Calculated (calc.) vs. experimental (expt.) lattice parameters for NU-1304_EtOH and NU-1304_Act.

	NU-1304_EtOH		NU-1304_Act	
	Calc.	**Expt.**	**Calc.**	**Expt.**
***a* (Å)**	42.6	42.64(1)	*a* (Å)	42.6
***b* (Å)**	42.6	42.64(1)	*b* (Å)	42.6
***c* (Å)**	47.6	47.39(2)	*c* (Å)	47.6
***α* (°)**	90	90	*α* (°)	90
***β* (°)**	90	90	*β* (°)	90
***γ* (°)**	90	90	*γ* (°)	90

Table 5.14 Comparison of cluster DFT-computed absolute (top) and relative (bottom) electronic energies, enthalpies, and free energies of interpenetrated *M3*, *M4a*, and *M4b* (NU-1304) relative to their non-interpenetrated fragments, in the presence of different cations. These were performed in implicit solvent models for DMF and water at 298 K using M06-2X; expressed in electronic energies per uranyl node in kcalmol^{-1}.

Motif	Solvent	E	H	G
		Hartree	Hartree	Hartree
		Proton		
NU-1304 fragments	DMF	-3616.803926	-3616.689699	-3616.758285
	Water	-3616.804906	-3616.690836	-3616.759222
M3	DMF	-7233.610074	-7233.385356	-7233.482621
	Water	-7233.612675	-7233.388796	-7233.486520
M4a	DMF	-7233.611236	-7233.386511	-7233.483800
	Water	-7233.613360	-7233.389194	-7233.486209
M4b	DMF	-7233.608951	-7233.384347	-7233.481446
	Water	-7233.610770	-7233.386443	-7233.483546
		Hydronium		
NU-1304 fragments	DMF	-3693.258276	-3693.117423	-3693.191065
	Water	-3693.258230	-3693.118665	-3693.192221
M3	DMF	-7386.517364	-7386.239429	-7386.346479
	Water	-7386.517158	-7386.241913	-7386.34848
M4a	DMF	-7386.518368	-7386.240390	-7386.347111
	Water	-7386.519175	-7386.243504	-7386.349610
M4b	DMF	-7386.507586	-7386.231317	-7386.337538
	Water	-7386.520490	-7386.244258	-7386.349766
		Potassium		
NU-1304 fragments	DMF	-4216.241266	-4216.136426	-4216.209053
	Water	-4216.239348	-4216.135144	-4216.208518
M3	DMF	-8432.485430	-8432.279262	-8432.384485
	Water	-8432.479687	-8432.275030	-8432.380893
M4a	DMF	-8432.482053	-8432.276910	-8432.381546
	Water	-8432.482052	-8432.276910	-8432.381546
M4b	DMF	-8432.494771	-8432.288742	-8432.39378
	Water	-8432.488954	-8432.283936	-8432.389819

Motif	Solvent	ΔE per U node	ΔH per U node	ΔG per U node
		kcalmol^{-1}	kcalmol^{-1}	kcalmol^{-1}
		Proton		
NU-1304 fragments	DMF	-	-	-
	Water	-	-	-
M3	DMF	+0.7	+1.9	-10.7
	Water	+0.9	+2.2	-10.0
M4a	DMF	+1.1	+2.2	-10.3
	Water	+1.1	+2.4	-10.1
M4b	DMF	+0.3	+1.6	-11.0
	Water	+0.3	+1.5	-10.9
		Hydronium		
NU-1304 fragments	DMF	-	-	-
	Water	-	-	-
M3	DMF	+0.3	+1.4	-11.2
	Water	+0.2	+1.4	-11.3
M4a	DMF	+0.6	+1.7	-11.0
	Water	+0.9	+1.9	-10.9
M4b	DMF	-2.8	-1.1	-14.0
	Water	+1.3	+2.2	-10.9
		Potassium		
NU-1304 fragments	DMF	-	-	-
	Water	-	-	-
M3	DMF	+0.9	+2.0	-10.5
	Water	+0.3	+1.5	-11.3
M4a	DMF	-0.2	+1.3	-11.5
	Water	+1.1	+2.1	-11.1
M4b	DMF	+3.8	+5.0	-7.6
	Water	+3.2	+4.3	-8.5

APPENDIX A. Structural Features of Zirconium-Based Metal–Organic Frameworks Affecting Radiolytic Stability

Portions of this chapter appear in the following manuscript:

Hanna, S. L.; Rademacher, D. X.; Hanson, D. J.; Islamoglu, T.; Olszewski, A. K.; Nenoff, T. M.; Farha, O.K., Structural Features of Zirconium-Based Metal–Organic Frameworks Affecting Radiolytic Stability. *Ind. Eng. Chem. Res.* **2020**, *16*, 7520-7526A

A.1 Appendix Summary

Metal–organic frameworks (MOFs) NU-1000 and UiO-66 are herein exposed to two different gamma irradiation doses and dose rates and analyzed to determine the structural features which affect their stability in these environments. MOFs have shown promise for the capture and sensing of off-gases at civilian nuclear energy reprocessing sites, nuclear waste repositories, and nuclear accident locations. However, little is understood about the structural features of MOFs which contribute to their stability levels under the ionizing radiation conditions present at such sites. This study is the first of its kind to explore the structural features of MOFs which contribute to their radiolytic stability. Both NU-1000 and UiO-66 are MOFs that contain Zr metal-centers with the same metal absorption cross section. However, the two MOFs exhibit different linker connectivity, linker aromaticity, node density, node connectivity, and inter-ligand separations. In this study, NU-1000 and UiO-66 were exposed to high (423.3 Gy min^{-1}, 23 min and 37 sec) and low (0.78 Gy min^{-1}, 4320 min) dose rates of ^{60}Co gamma irradiation. NU-1000 displayed insignificant radiation damage under both dose rates, due to its high linker connectivity, low node density, and low node connectivity. However, low radiation dose rates caused considerable damage to UiO-66, a framework with lower aromaticity and smaller inter-ligand separation. Results suggest that chronic, low radiation environments are more detrimental to Zr MOF stability than acute, high radiation conditions.

A.2 Radiation Resistance of Metal–Organic Frameworks

Late in the year 1959, a series of papers was published, outlining crystal structures of copper(I) nitrate complexes extending in repeating units.[297-299] From the self-assembly of those building units to the current state of the field,[300-303] the landscape of materials chemistry has been significantly altered by the emergence of metal–organic frameworks (MOFs). MOFs are a class of

crystalline materials which self-assemble from inorganic nodes and organic linkers into three-dimensional, nanoporous frameworks.[26, 27, 97, 98] MOFs boast high porosities,[276, 304] facile tunability,[110, 111] and use in multiple applications including catalysis,[305-308] water purification,[309, 310] and gas storage and separation.[311-316] MOFs also show promise in the field of nuclear waste cleanup as scintillators,[317-319] radioactive gas sensors,[320, 321] and selective adsorbents for radionuclides in nuclear reprocessing facilities or at nuclear repository waste sites.[85, 322-328] However, in order to be viable scintillators, sensors, and gas capturing agents under radioactive conditions, MOFs must remain stable under the ionizing radiation present at these sites, such as gamma rays.[329]

The resistance of a solid to gamma irradiation is based on the photon energy, the metal absorption cross section, and the density of the material.[330] Thus, when MOFs are exposed to gamma irradiation, their damage resistance is highly dependent on the node identity, as metals with higher *Z* numbers have larger absorption cross sections. MOF nodes have been suggested to act as "radiation antennae" since they are shown to absorb gamma radiation and transfer the energy to the linker.[317] This leads to multiple radiolysis mechanisms of the linker which result in its subsequent degradation into organic radicals.

Only a small subset of MOFs has been interrogated for stability under gamma irradiation.[49, 90, 250, 324, 327, 330-334] Most commonly, MOFs exhibit increasing damage and declining surface area with increasing radiation dose.[49, 330] However, increasing gamma irradiation doses have also been observed to improve the surface area of some MOFs due to removal of trapped species within the pores,[330] and other MOFs have even shown a complete lack of radiation damage.[90, 324, 332, 333 335] Most of these studies have been performed at different irradiation doses, making comparisons across these investigations difficult to evaluate. While the effect of metal absorption cross section

on MOF stability under gamma irradiation has been demonstrated,[330] no studies assess the role that MOF structural features play in damage resistance. Furthermore, no studies have focused on the effect of gamma irradiation dose rates on MOF degradation and stability.

Herein is a study of the effect of gamma irradiation dose rates on the radiolytic stability of a set of MOFs with the same node and an assumed same metal absorption cross section: NU-1000 and UiO-66. These Zr MOFs are both highly stable, well characterized, and already show promise for radiological gas capture from nuclear waste.[336, 337] Both MOFs contain the same Zr_6O_8 node, but they differ in their node connectivity and organic ligands: NU-1000 is made up of the 8-connected ($Zr_6(\mu_3\text{-}OH)_4(\mu_3\text{-}O)_4$) node and the tetratopic 1,3,6,8-tetrakis(benzoic acid)pyrene (H_4TBAPy) linker (Fig. A.1a); UiO-66 is composed of the 12-connected ($Zr_6(\mu_3\text{-}OH)_4(\mu_3\text{-}O)_4(OH)_4(OH_2)_4$) node and the ditopic 1,4-benzenedicarboxylic acid (BDC) linker (Fig. A.1b). Thus, this study employs MOFs with the same node, yet different linker connectivity, linker aromaticity, node connectivity, node density, and inter-ligand separation. This allows for the direct evaluation of Zr MOF stability versus irradiation dose and dose rate. Furthermore, the resulting stability is then correlated with the unique Zr MOF structural factors present in NU-1000 and UiO-66.

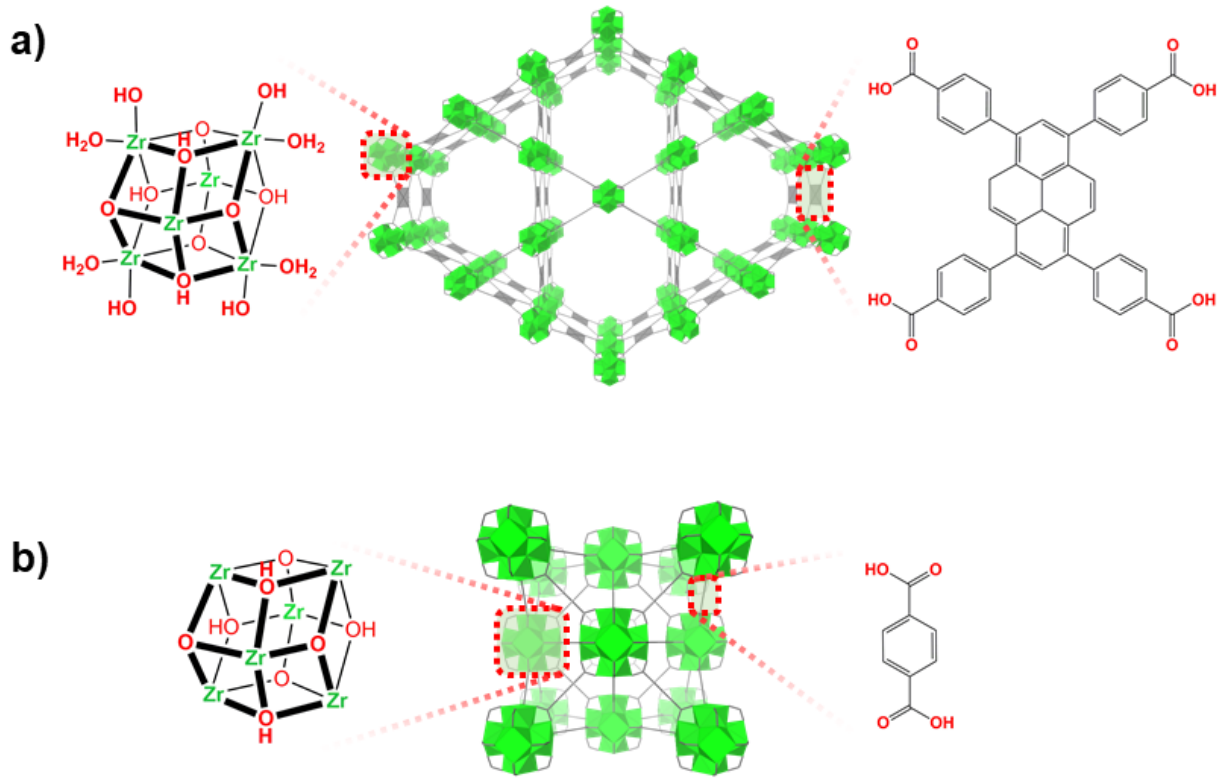

Figure A.1 Assembly of Zr-based MOFs used in this study. (a) NU-1000 with 8-connected Zr_6O_8 node and higher aromaticity, tetratopic H4TBAPy linker. (b) UiO-66 with 12-connected Zr_6O_8 node and lower aromaticity, ditopic BDC linker.

A.3 UiO-66 and NU-1000 Response to Gamma Irradiation

Structural analysis reveals unique radiation dose and dose rate responses of the two Zr MOFs. PXRD demonstrates that NU-1000 shows no apparent response to gamma irradiation dose rates and retains peak intensity without broadening or loss of peaks under both low and high dose rates (Fig. A.2a). Additionally, SEM studies show uniformity in crystal size, regardless of the radiation dose rate, and demonstrate that the morphology of NU-1000 is generally unchanged after these gamma irradiation dose rates (Fig. A.3a-c). The surface area of NU-1000 before gamma irradiation, obtained from nitrogen physisorption measurements, lies at 2160 $m^2 g^{-1}$. This value decreases by 7% (2005 $m^2 g^{-1}$) and 5% (2050 $m^2 g^{-1}$) after low and high gamma irradiation exposure dose rates, respectively (Fig. A.4a). The density functional theory-calculated pore size distribution

for NU-1000 (Fig. A.7) demonstrates retained porosity before and after radiation dose rates. NMR spectra of base-digested NU-1000 demonstrates that the linker has not lost its chemical structure after gamma irradiation dose rates (Fig. A.5). Integration of these signals remains similar before and after both high and low radiation dose rates.

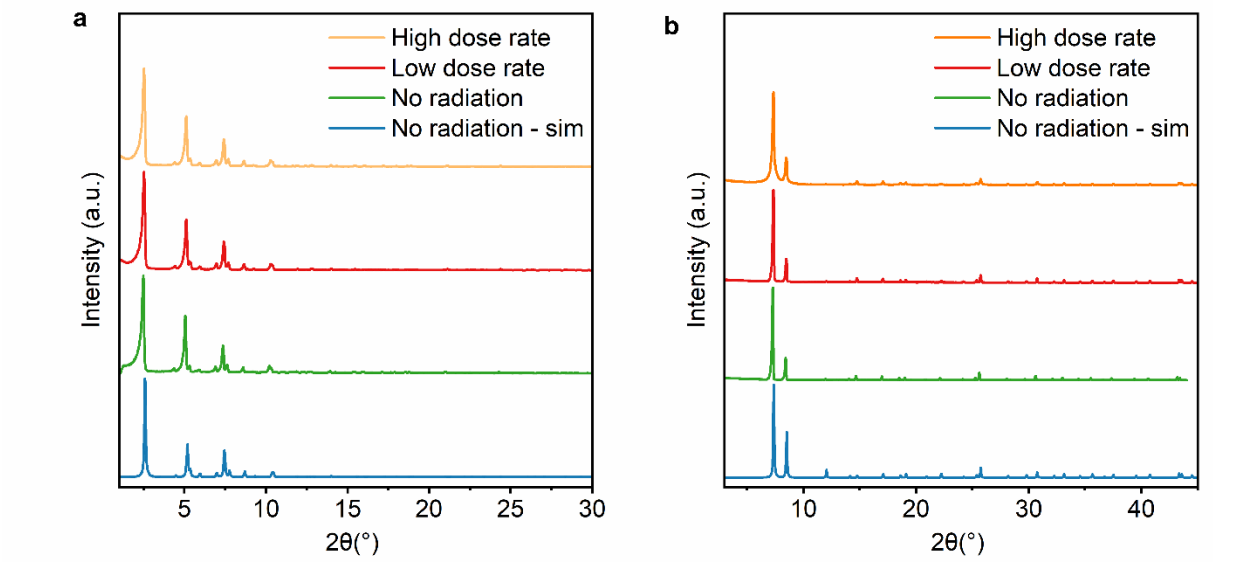

Figure A.2 MOF crystallinity before and after irradiation. PXRD of (a) NU-1000 and (b) UiO-66 demonstrates that NU-1000 retains its crystallinity before and after both high and low gamma irradiation dose rates, while the peak intensity of UiO-66 decreases only after the low dose rate. The black trace identifies the simulated MOF PXRD pattern. NU-1000 PXRD patterns are normalized to the peak at 2.5° 2θ, and UiO-66 PXRD patterns are normalized to the peak at 8.5° 2θ.

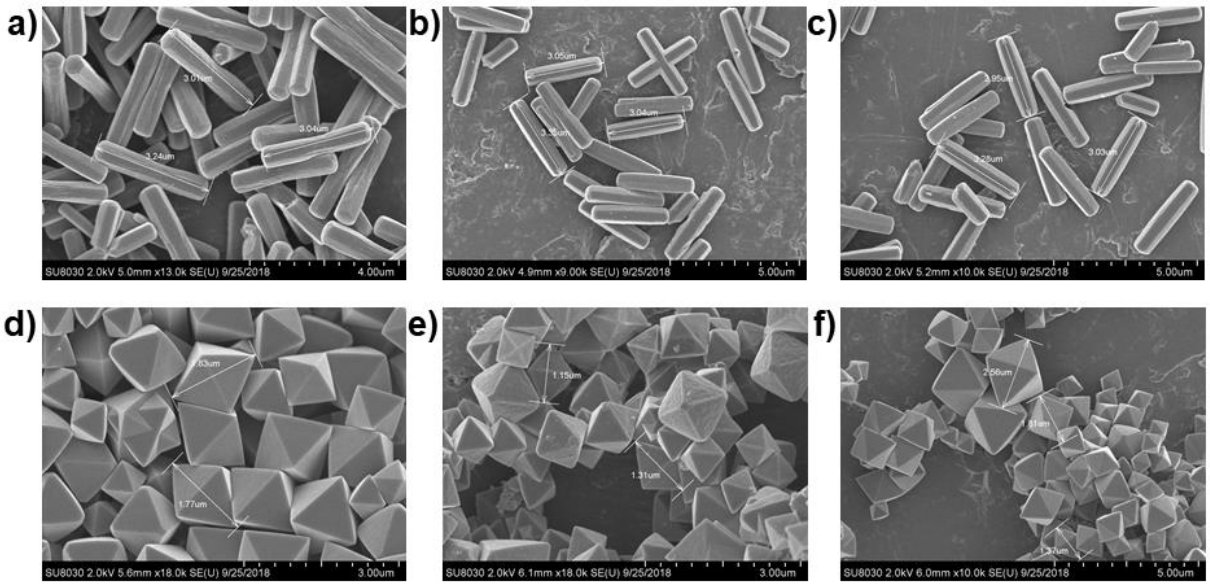

Figure A.3 MOF morphology before and after irradiation. SEM micrographs of NU-1000 and UiO-66 before gamma irradiation (a, d), after the low, chronic dose rate (b, e), and after the high, acute dose rate (c, f), respectively.

UiO-66 also maintains its structural integrity after exposure to the acute irradiation dose rate, as observed by PXRD. However, exposure to the chronic irradiation dose rate appears to adversely affect UiO-66; post-irradiation PXRD shows a loss of peak intensity, specifically, the peak at 12° 2θ (Fig. A.2b) as well as broadening of the first two major peaks (7.2° 2θ and 8.5° 2θ). SEM studies also demonstrate a roughening of crystallite exterior after the low dose rate (Fig. A.3e), as compared to those exposed to no radiation or the high irradiation dose rate (Fig. A.3d, A.3f). Crystal size and morphology remain uniform under both high and low dose rates. While the three NU-1000 surface area values differ to a negligible degree, UiO-66 physisorption measurements result in an interesting finding (Fig. A.4b): a considerable 27% drop in surface area from before radiation (1320 $m^2 g^{-1}$) to after the chronic irradiation dose rate (960 $m^2 g^{-1}$) occurs. However, UiO-66 decreases by only 7% in surface area after the acute irradiation dose rate (1230 $m^2 g^{-1}$). The density functional theory-calculated pore size distribution for UiO-66 (Fig. A.7) demonstrates retained porosity before and after radiation dose rates. NMR spectra of base-digested UiO-66 demonstrates

that the linker has not lost its chemical structure after gamma irradiation dose rates (Fig. A.6). Integration of these signals remains similar before and after both high and low radiation dose rates.

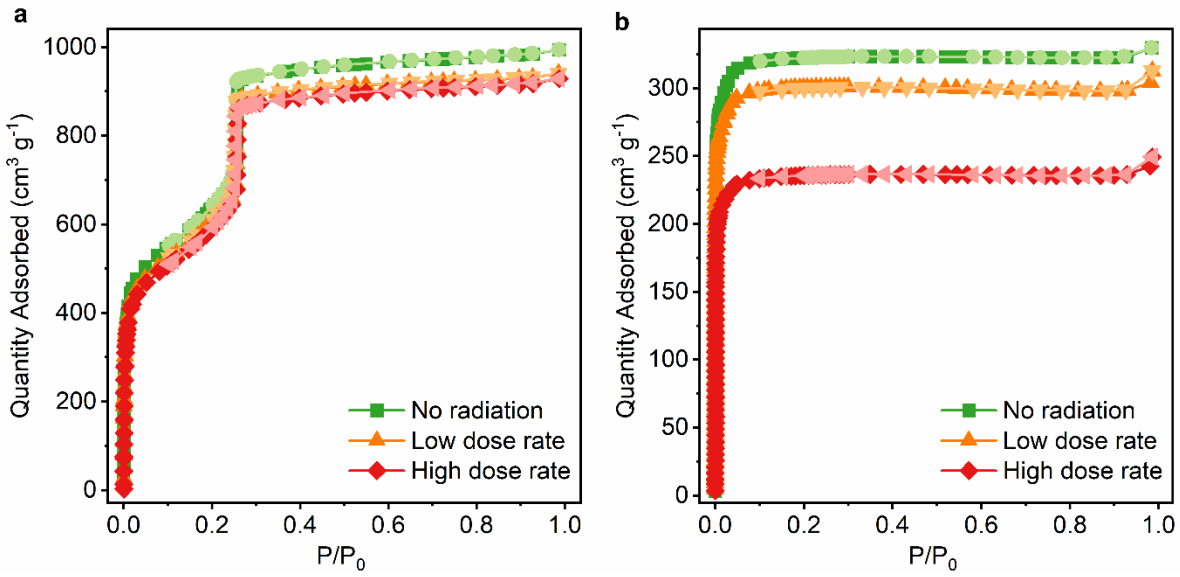

Figure A.4 MOF adsorption before and after irradiation. Nitrogen physisorption isotherms of (a) NU-1000 and (b) UiO-66 before and after their exposure to both high and low gamma irradiation dose rates.

A.4 NU-1000 and UiO-66 Radiolytic Stability Related to Structural Features

The resulting stability or damage of NU-1000 and UiO-66 is related to their varying structural features (see Table A.1). First, UiO-66 is comprised of the ditopic BDC linkers, which are based on one benzene ring. However, NU-1000 is composed of the highly aromatic, tetratopic H_4TBAPy linkers, which are made up of four fused benzene rings. Second, the crystallographically defined lengths of BDC and H_4TBAPy are 5.77 Å and 12.08 Å (length) x 12.04 Å (width), respectively (Fig. A.8). Since BDC is much shorter than the H_4TBAPy linker, the metal nodes in UiO-66 are substantially closer to each other than in NU-1000. Thus, the node density of UiO-66 (0.60 g cm^{-3}) is much higher than that of NU-1000 (0.15 g cm^{-3}). Third, the node connectivity differs between UiO-66 and NU-1000; UiO-66 has a fully 12-connected node with no dangling -OH or H_2O groups, while NU-1000 possesses an 8-connected node with dangling -OH and H_2O groups (Fig.

A.1), easily susceptible to radiolysis. Finally, the shortest crystallographic inter-ligand spacing (the distance between the closest H atoms on two different linkers bound in the same MOF, Fig. A.9) is 4.21 Å in UiO-66 and 3.79 Å in NU-1000 (Table A.1, columns 1-3).

Structural Features	NU-1000	UiO-66	Contribute to Stability
Linker aromaticity	High	Low	---
Linker connectivity	*4	2	High
Node density	*0.15 g cm^{-3}	0.60 g cm^{-3}	Low
Node Connectivity	*8	12	Low
Inter-ligand separation	3.79 Å	4.21 Å	---

Table A.1 Varying structural features of NU-1000 and UiO-66. Those which contribute to MOF stability under gamma irradiation are highlighed in purple (linker connectivity, node density, and node connectivity). * indicates specific structural features which promote the stability of NU-1000.

UiO-66 is stable under acute gamma irradiation dose rates. However, it exhibits structural damage under chronic irradiation dose rates. This is evidenced by the significant decrease in PXRD peak intensity, PXRD peak broadening, 27% drop in surface area, and rough crystallite exterior. An explanation for this behavior is that chronic irradiation dose rates may be more damaging to UiO-66 than acute radiation dose rates, up until a certain final dosage threshold. Here, the lower and more damaging dose (3369.6 Gy) has a low dose rate (0.78 Gy min^{-1}) and lasts for a duration of 4320 minutes (three days), while the higher and less damaging dose (9996.9 Gy) has a high dose rate (423.3 Gy min^{-1}) and only lasts for under thirty minutes. Additionally, similar low dosage radiation studies on UiO-66 that lasted seven hours, rather than three days, resulted in less generated damage.[334] This then demonstrates that irradiation doses with chronic dose rates cause more damage to UiO-66 than acute dose rates, under a certain threshold.

In this investigation, NU-1000 exhibits insignificant radiation damage under both high and low irradiation dose rates. The stability of NU-1000 is confirmed by the PXRD data in which no changes to the crystal powder pattern are apparent before and after irradiation. Furthermore, no changes to the nanopore structure and connectivity are evident as witnessed by the N_2 physisorption isotherms, and SEM displayed no roughening of the crystallite exterior. It is evident that chronic radiation does not affect NU-1000 in the same manner as UiO-66. This can be attributed to three likely causes. First, the higher linker connectivity of NU-1000 makes it more stable towards cleavage of the carboxylate oxygen-zirconium bonds than UiO-66.[318] Second, since the gamma rays are absorbed by the metal and transferred to the linker,[317] the lower density of Zr_6O_8 nodes in NU-1000 allows it to absorb less radiation and thus remain more robust. Third, the low node connectivity causes radiation absorbed by the node to propagate to the dangling -OH and H_2O groups rather than spreading damage solely to the linkers.

These results identify that the factors which contribute to NU-1000 stability under gamma irradiation include the linker connectivity, node density, and node connectivity. These components outweigh other structural elements such as the lower aromaticity and larger inter-ligand separation inherent to UiO-66 (Table A.1, column 4). This indicates that small scale variations at the structural level result in bulk radiation stability and durability differences between similar MOFs.

A.5 Conclusions

Gamma irradiation of Zr MOFs NU-1000 and UiO-66 reveals that NU-1000 remains stable under both high (423.3 Gy min^{-1}) and low (0.78 Gy min^{-1}) dose rates. Interestingly, UiO-66 shows a significant drop in stability when exposed to chronic (long, low) doses rates but remains considerably undamaged under acute (short, high) dose rates. The enhanced stability of NU-1000 is due to its higher linker connectivity, lower node density (0.15 g cm^{-3}), and lower node

connectivity which have a greater effect on Zr MOF damage resistance under gamma irradiation dose rates than the larger inter-ligand separation (4.21 Å) and lower linker aromaticity of UiO-66. The difference in structural stability between related MOFs such as NU-1000 and UiO-66 indicates that MOFs can be designed and tuned for specific radiological applications. For example, NU-1000 may be viable for use as a scintillator, sensor, and capturing agent at nuclear waste sites and other sites with ionizing radiation, while UiO-66 may be more suitable for specific radiation doses and conditions.

This study is the first of its kind to explore which features of MOFs, other than their metal absorption cross section, contribute to their stability under gamma irradiation. Moreover, we investigate the effects of gamma irradiation dose rate, rather than dose, on Zr MOF stability. Additional studies of other Zr_6O_8 cluster-based MOFs are underway to identify which attributes of MOFs most affect Zr MOF stability under varying irradiation conditions. Durability studies under alpha radiation, beta radiation, and X-ray conditions will also be evaluated as well as irradiation in aqueous solutions to better reflect MOF damage for applications such as radionuclide adsorption. Additionally, the effect of air on MOF degradation under irradiation will be investigated, as it may play a role in radiolysis.

A.6 Additional Information

A.6.1 Materials

All reagents were purchased from the supplier and employed without further purification. Zirconyl chloride octahydrate, trifluoroacetic acid (TFA), terephthalic acid, triethylamine (TEA), and sodium deuteroxide (NaOD) were purchased from Millipore Sigma. Benzoic acid, N,N-dimethylformamide (DMF), hydrochloric acid (HCl), and acetone were obtained from Fisher Scientific. Zirconium chloride was acquired from Strem Chemicals, and deuterium oxide was

purchased from Cambridge Isotope Laboratories. H_4TBAPy was synthesized following the published procedure.[338]

A.6.2 Methods and Instrumentation

A.6.2.1 Nitrogen Physisorption

Nitrogen adsorption-desorption isotherms were collected at 77K on a Micromeritics Tristar II 3020 and analyzed using Brunauer-Emmett-Teller (BET) theory.[254]

A.6.2.2 Powder X-ray diffraction (PXRD)

Powder X-ray diffraction (PXRD) of the activated MOFs was performed using a STOE STADI P diffractometer equipped with a copper Kα1 source and a 1D strip detector.

A.6.2.3 Scanning Electron Microscopy (SEM)

To determine particle size and morphology, scanning electron microscope (SEM) micrographs were taken on a Hitachi SU8030. Before imaging, samples were drop-casted from acetone onto SEM pin stub specimen mounts and coated with 9 nm of OsO_4 in a Denton Desk III TSC Sputter Coater.

A.6.2.4 Nuclear Magnetic Resonance (NMR) Spectroscopy

Proton nuclear magnetic resonance (NMR) spectra was collected on a Bruker Advance III 500 MHz system equipped with a DCH CryoProbe (Figs. A.5 and A.6). Samples were prepared for NMR spectroscopy by ultrasonically dissolving 2-3 mg of MOF in 6 drops of 0.01 M NaOD for 10 minutes. 0.5 mL of D_2O was then added to the solution which was sonicated for an additional 10 minutes.

A.6.3 Synthesis of NU-1000 and UiO-66

NU-1000 was synthesized and activated following reported methods,[339] and low-defect UiO-66 was synthesized by modifying reported methods,[340] as follows. Terephthalic acid (900 mg, 5.42 mmol), TEA (140 µL, 1.0 mmol), acetic acid (128.8 mL, 17.5 mmol), and DMF (1260 mL) were

added to a 2-L glass jar and ultrasonically dissolved (Solution A). The clear solution was then incubated in a pre-heated 100 ºC oven for 15 minutes and cooled completely. Meanwhile, $ZrCl_4$ (1260 mg, 5.41 mmol) was dissolved in DMF (90mL) by sonication (Solution B). Solution B was then added to Solution A and incubated in a pre-heated 100 ºC oven for 18 hours. After cooling down to room temperature, the supernatant was decanted, and the white powder settled at the bottom of the jar was collected by centrifugation (7500 rpm, 5 minutes) into six 50-mL centrifuge tubes. The powder was soaked three times in approximately 300 mL of DMF for 20 minutes each time, and then collected by centrifuging between soaks (7500 rpm, 5 minutes, 900 mL DMF total). Three acetone washes were subsequently performed in the same manner, and a final overnight acetone wash was completed before the material was centrifuged down (7500 rpm, 5 minutes) and collected into one 50 mL centrifuge tube. The material was then dried in an 80 ºC vacuum oven overnight and activated at 120 °C for 24 hours under ultrahigh vacuum on a Micromeritics Smart VacPrep instrument. This procedure was repeated five additional times, so that a total of six batches was synthesized. Since separate characterization for each batch indicated similar results, the six batches were combined and characterized using the methods described below.

A.6.4 Gamma Irradiation Studies

Activated NU-1000 and UiO-66 were placed into 20 ml glass vials and irradiated at the Sandia National Laboratories' Gamma Irradiation Facility (GIF) using a ^{60}Co-γ source. 1g-sized samples from the same batch were exposed to either high or low gamma irradiation doses. The high dose rate was 423.3 Gy min^{-1} for 23 minutes and 37 seconds (9996.9 Gy dose), and the low dose rate was 0.78 Gy min^{-1} for 4320 minutes (3 days, 3369.6 Gy dose). The high dose rate is referred to as *acute* since it lasts for a short time at a high rate, and the low dose rate is referred to as *chronic* since it lasts for a longer time at a lower rate. The dose rates were calculated based on time and

distance from the source; dose was calculated from the dose rates and confirmed by dosimetry. The MOFs were then characterized post-irradiation using nitrogen adsorption-desorption isotherms, PXRD, SEM, and NMR.

A.6.4 Node Density Calculations

Node density calculations were performed by multiplying the MOF density by the mass percent of the node, as displayed below:

NU-1000: $0.486\ gcm^{-3} \times 31.4\% = 0.15\ gcm^{-3}$

UiO-66: $1.443\ gcm^{-3} \times 41.8\% = 0.60\ gcm^{-3}$

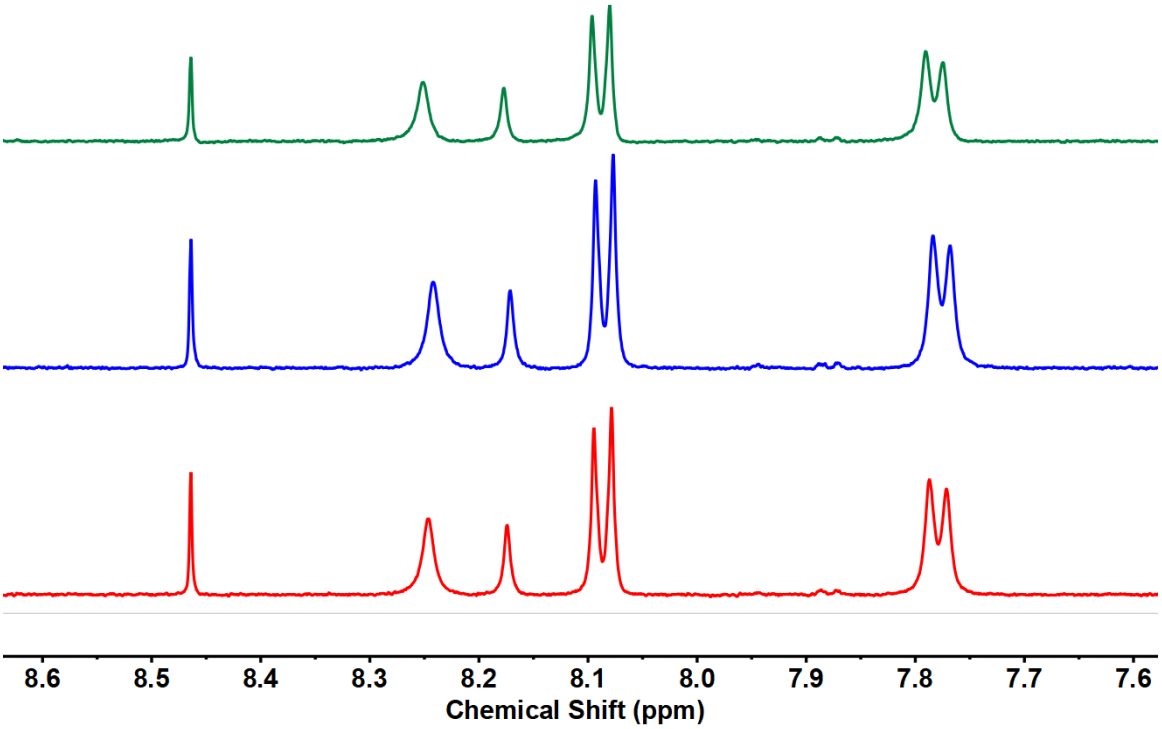

Figure A.5 Proton NMR spectra of NU-1000 before gamma irradiation (top, green), after the low dose rate (middle, blue), and after the high dose rate (bottom, red).

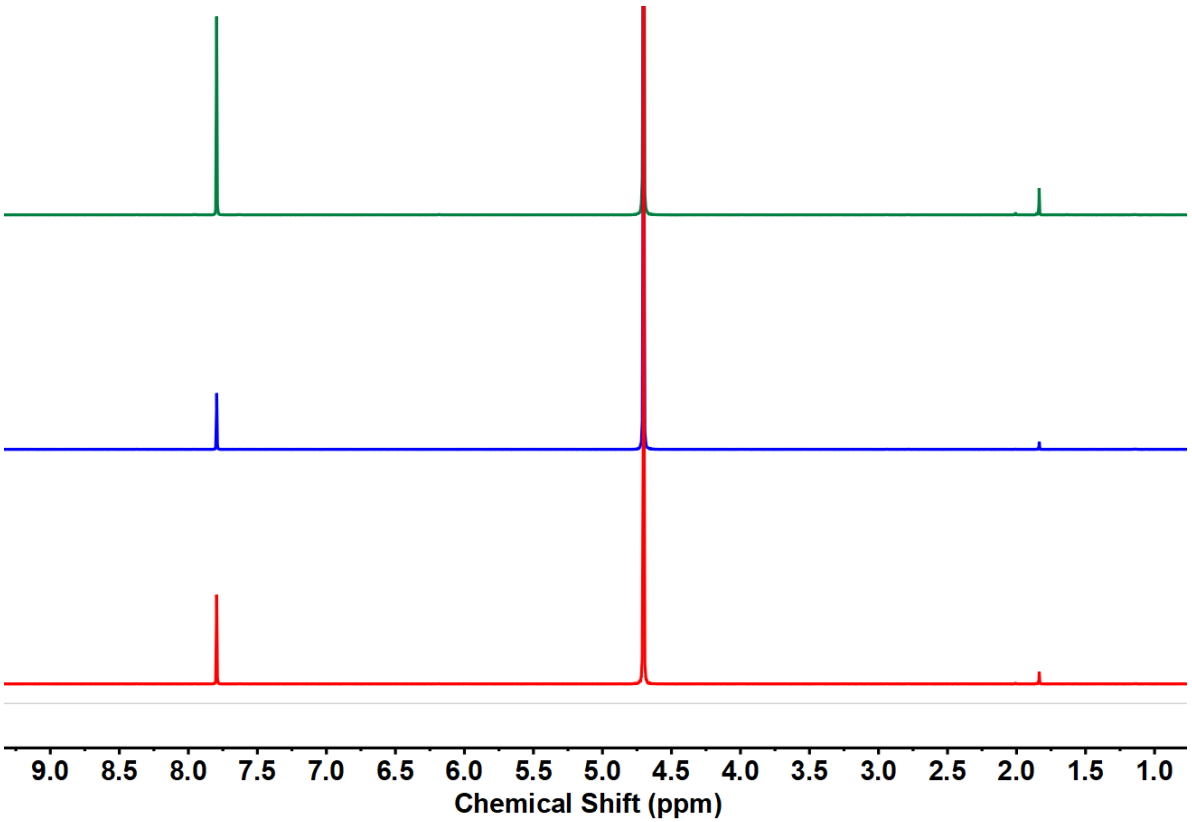

Figure A.6 Proton NMR spectra of UiO-66 before gamma irradiation (top, green), after the low dose rate (middle, blue), and after the high dose rate (bottom, red).

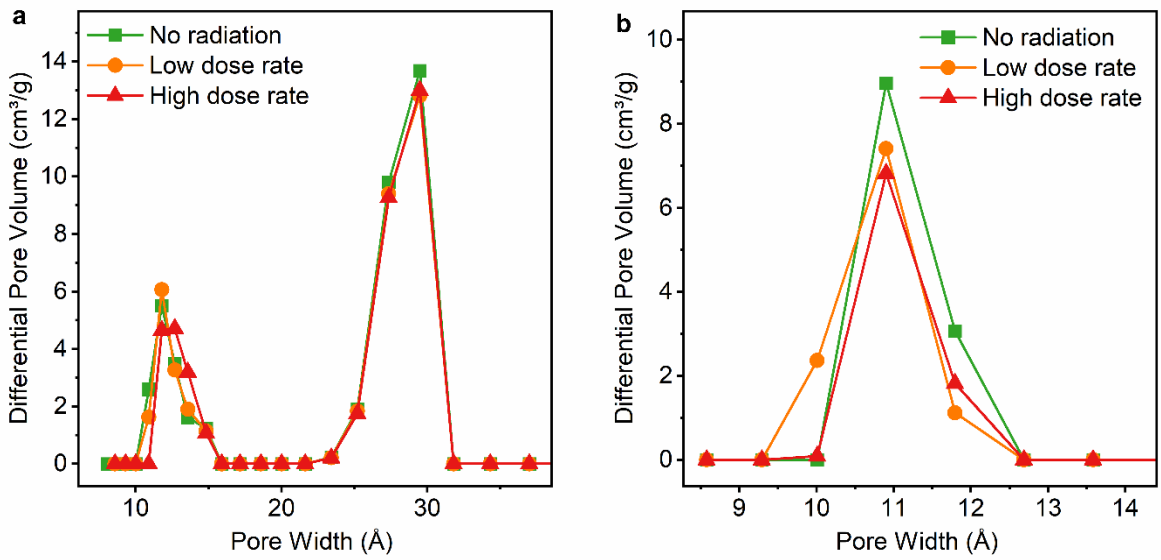

Figure A.7 Pore size distribution based on density functional theory (DFT) calculations of a) NU-1000 and b) UiO-66.

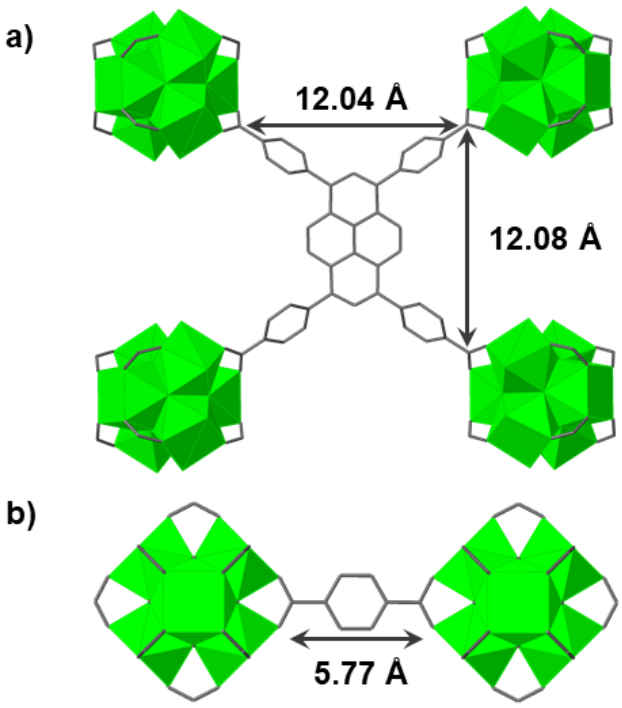

Figure A.8 Dimensions of a) H_4TBAPy linker in NU-1000 and b) BDC linker in UiO-66 with lengths measured from the carbonyl carbons. Carbon is shown in grey, zirconium in green, and hydrogen atoms are omitted for clarity. Figure sizes are not to scale.

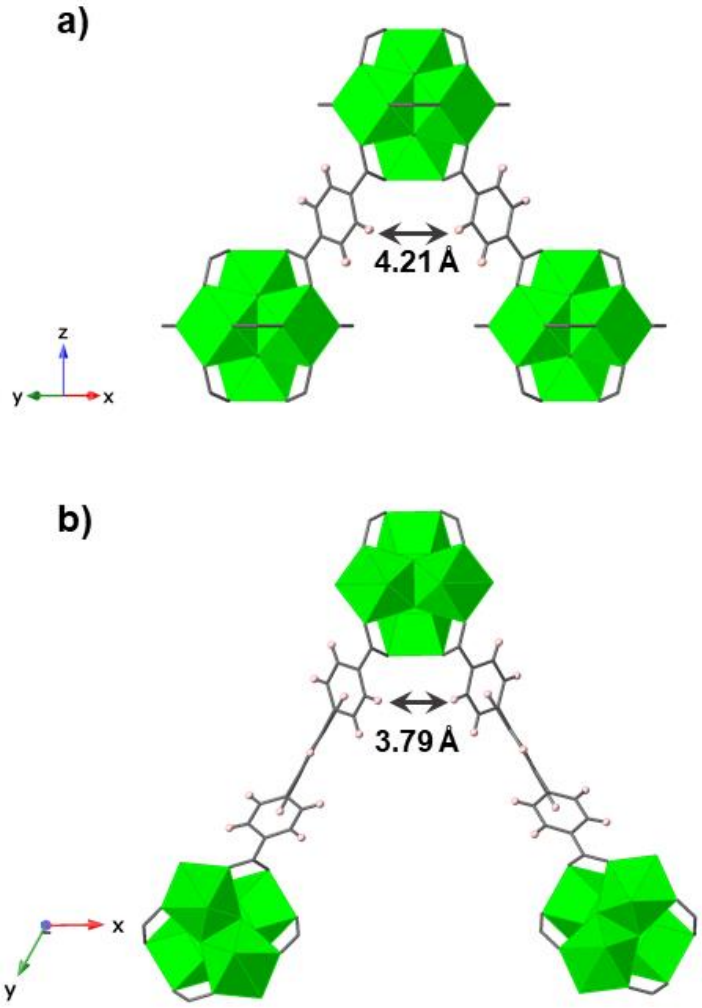

Figure A.9 The distance between the closest H atoms on two different linkers bound to the same MOF, defined as *inter-ligand separation*, for a) UiO-66 looking down the [110] plane and b) NU-1000 looking down the *c* axis. Carbon is shown in grey, zirconium in green, and hydrogen in pink. Figure sizes are not to scale.

REFERENCES

1. Denning, R. G., Electronic structure and bonding in actinyl ions. In *Complexes, Clusters and Crystal Chemistry*, Springer Berlin Heidelberg: Berlin, Heidelberg, 1992; pp 215-276.
2. Barluzzi, L.; Giblin, S. R.; Mansikkamäki, A.; Layfield, R. A., Identification of Oxidation State +1 in a Molecular Uranium Complex. *J. Am. Chem. Soc.* **2022,** *144* (40), 18229-18233.
3. Guo, F.-S.; Tsoureas, N.; Huang, G.-Z.; Tong, M.-L.; Mansikkamäki, A.; Layfield, R. A., Isolation of a Perfectly Linear Uranium(II) Metallocene. *Angew. Chem. Int. Ed.* **2020,** *59* (6), 2299-2303.
4. Castro-Rodriguez, I.; Olsen, K.; Gantzel, P.; Meyer, K., Uranium Tris-aryloxide Derivatives Supported by Triazacyclononane: Engendering a Reactive Uranium(III) Center with a Single Pocket for Reactivity. *J. Am. Chem. Soc.* **2003,** *125* (15), 4565-4571.
5. Maynadié, J.; Berthet, J.-C.; Thuéry, P.; Ephritikhine, M., An Unprecedented Type of Linear Metallocene with an f-Element. *J. Am. Chem. Soc.* **2006,** *128* (4), 1082-1083.
6. Hayton, T. W.; Boncella, J. M.; Scott, B. L.; Batista, E. R.; Hay, P. J., Synthesis and Reactivity of the Imido Analogues of the Uranyl Ion. *J. Am. Chem. Soc.* **2006,** *128* (32), 10549-10559.
7. Liddle, S. T., The Renaissance of Non-Aqueous Uranium Chemistry. *Angew. Chem. Int. Ed.* **2015,** *54* (30), 8604-8641.
8. Bart, S. C.; Meyer, K., Highlights in Uranium Coordination Chemistry. In *Organometallic and Coordination Chemistry of the Actinides*, Albrecht-Schmitt, T. E., Ed. Springer Berlin Heidelberg: Berlin, Heidelberg, 2008; pp 119-176.
9. Grenthe, I.; Drożdżyński, J.; Fujino, T.; Buck, E. C.; Albrecht-Schmitt, T. E.; Wolf, S. F., Uranium. In *The Chemistry of the Actinide and Transactinide Elements*, Morss, L. R.; Edelstein, N. M.; Fuger, J., Eds. Springer Netherlands: Dordrecht, 2006; pp 253-698.
10. Falcone, M.; Chatelain, L.; Scopelliti, R.; Živković, I.; Mazzanti, M., Nitrogen reduction and functionalization by a multimetallic uranium nitride complex. *Nature* **2017,** *547*, 332-335.
11. Falcone, M.; Barluzzi, L.; Andrez, J.; Fadaei Tirani, F.; Zivkovic, I.; Fabrizio, A.; Corminboeuf, C.; Severin, K.; Mazzanti, M., The role of bridging ligands in dinitrogen reduction and functionalization by uranium multimetallic complexes. *Nat. Chem.* **2019,** *11* (2), 154-160.
12. Summerscales, O. T.; Cloke, F. G. N.; Hitchcock, P. B.; Green, J. C.; Hazari, N., Reductive Cyclotrimerization of Carbon Monoxide to the Deltate Dianion by an Organometallic Uranium Complex. *Science* **2006,** *311* (5762), 829-831.
13. Jørgensen, C. K.; Reisfeld, R. In *Uranyl photophysics*, Topics in Inorganic and Physical Chemistry, Berlin, Heidelberg, 1982//; Springer Berlin Heidelberg: Berlin, Heidelberg, 1982; pp 121-171.
14. Natrajan, L. S., Developments in the photophysics and photochemistry of actinide ions and their coordination compounds. *Coord. Chem. Rev.* **2012,** *256* (15), 1583-1603.
15. Hu, D.; Jiang, X., Perspectives for Uranyl Photoredox Catalysis. *Synlett* **2021,** *32* (13), 1330-1342.
16. Moro, F.; Mills, D. P.; Liddle, S. T.; van Slageren, J., The Inherent Single-Molecule Magnet Character of Trivalent Uranium. *Angew. Chem. Int. Ed.* **2013,** *52* (12), 3430-3433.
17. Liddle, S. T.; van Slageren, J., Improving f-element single molecule magnets. *Chem. Soc. Rev.* **2015,** *44* (19), 6655-6669.
18. Fox, A. R.; Bart, S. C.; Meyer, K.; Cummins, C. C., Towards uranium catalysts. *Nature* **2008,** *455* (7211), 341-349.
19. Andrea, T.; Eisen, M. S., Recent advances in organothorium and organouranium catalysis. *Chem. Soc. Rev.* **2008,** *37* (3), 550-567.

20. Hartline, D. R.; Meyer, K., From Chemical Curiosities and Trophy Molecules to Uranium-Based Catalysis: Developments for Uranium Catalysis as a New Facet in Molecular Uranium Chemistry. *JACS Au* **2021,** *1* (6), 698-709.
21. Nacht, M.; Frank, M.; Prussin, S., The Second Nuclear Age (1992–Present). In *Nuclear Security: The Nexus Among Science, Technology and Policy*, Nacht, M.; Frank, M.; Prussin, S., Eds. Springer International Publishing: Cham, 2021; pp 213-263.
22. Was, G. S.; Petti, D.; Ukai, S.; Zinkle, S., Materials for future nuclear energy systems. *J. Nucl. Mater.* **2019,** *527*, 151837.
23. Craft, E. S.; Abu-Qare, A. W.; Flaherty, M. M.; Garofolo, M. C.; Rincavage, H. L.; Abou-Donia, M. B., DEPLETED AND NATURAL URANIUM: CHEMISTRY AND TOXICOLOGICAL EFFECTS. *J Toxicol Env Heal B* **2004,** *7* (4), 297-317.
24. Evans, J. D.; Bon, V.; Senkovska, I.; Lee, H.-C.; Kaskel, S., Four-dimensional metal-organic frameworks. *Nat. Commun.* **2020,** *11* (1), 2690-2700.
25. Kalmutzki, M. J.; Hanikel, N.; Yaghi, O. M., Secondary building units as the turning point in the development of the reticular chemistry of MOFs. *Sci. Adv.* **2018,** *4* (10), eaat9180.
26. Kitagawa, S.; Kitaura, R.; Noro, S.-i., Functional porous coordination polymers. *Angew. Chem. Int. Ed.* **2004,** *43* (18), 2334-2375.
27. Zhou, H. C.; Long, J. R.; Yaghi, O. M., Introduction to metal-organic frameworks. *Chem Rev* **2012,** *112* (2), 673-4.
28. Martin, C. R.; Leith, G. A.; Shustova, N. B., Beyond structural motifs: the frontier of actinide-containing metal–organic frameworks. *Chem. Sci.* **2021,** *12* (21), 7214-7230.
29. Loiseau, T.; Mihalcea, I.; Henry, N.; Volkringer, C., The crystal chemistry of uranium carboxylates. *Coord. Chem. Rev.* **2014,** *266*, 69-109.
30. Andrews, M. B.; Cahill, C. L., Uranyl Bearing Hybrid Materials: Synthesis, Speciation, and Solid-State Structures. *Chem. Rev.* **2013,** *113* (2), 1121-1136.
31. Baker, R. J., Uranium minerals and their relevance to long term storage of nuclear fuels. *Coord. Chem. Rev.* **2014,** *266-267*, 123-136.
32. Burns, P. C.; Ewing, R. C.; Hawthorne, F. C., The crystal chemistry of hexavalent uranium: Polyhedron geometries, bond-valence parameters, and polymerization of polyhedra. *Can. Mineral.* **1997,** *35*, 1551-1570.
33. Burns, P. C., U6+ minerals and inorganic compounds: insights into an expanded structural hierarchy of crystal structures. *Can. Mineral.* **2005,** *43*, 1839-1894.
34. Yang, W.; Parker, T. G.; Sun, Z.-M., Structural chemistry of uranium phosphonates. *Coord. Chem. Rev.* **2015,** *303*, 86-109.
35. Cahill, C. L.; de Lill, D. T.; Frisch, M., Homo- and heterometallic coordination polymers from the f elements. *CrystEngComm* **2007,** *9* (1), 15-26.
36. Cahill, C. L.; Borkowski, L. A., U(VI)-containing metal-organic frameworks and coordination polymers. In *Structural Chemistry of Inorganic Actinide Compounds*, 2007; pp 409-442.
37. Su, J.; Chen, J., MOFs of Uranium and the Actinides. *Struct. Bonding (Berlin, Ger.)* **2015,** *163* (Lanthanide Metal-Organic Frameworks), 265-295.
38. Hu, Y.; Shen, Z.; Li, B.; Tan, X.; Han, B.; Ji, Z.; Wang, J.; Zhao, G.; Wang, X., State-of-the-art progress for the selective crystallization of actinides, synthesis of actinide compounds and their functionalization. *J. Hazard. Mater.* **2022,** *426*, 127838.

39. Hanna, S. L.; Zhang, X.; Otake, K.-i.; Drout, R. J.; Li, P.; Islamoglu, T.; Farha, O. K., Guest-Dependent Single-Crystal-to-Single-Crystal Phase Transitions in a Two-Dimensional Uranyl-Based Metal–Organic Framework. *Cryst. Growth Des.* **2019,** *19* (1), 506-512.
40. Volkringer, C.; Henry, N.; Grandjean, S.; Loiseau, T., Uranyl and/or Rare-Earth Mellitates in Extended Organic–Inorganic Networks: A Unique Case of Heterometallic Cation–Cation Interaction with UVI═O–LnIII Bonding (Ln = Ce, Nd). *J. Am. Chem. Soc.* **2012,** *134* (2), 1275-1283.
41. Wang, K.-X.; Chen, J.-S., Extended Structures and Physicochemical Properties of Uranyl–Organic Compounds. *Acc. Chem. Res.* **2011,** *44* (7), 531-540.
42. Chen, Z.; Li, P.; Zhang, X.; Mian, M. R.; Wang, X.; Li, P.; Liu, Z.; O'Keeffe, M.; Stoddart, J. F.; Farha, O. K., Reticular exploration of uranium-based metal—organic frameworks with hexacarboxylate building units. *Nano Research* **2021,** *14* (2), 376-380.
43. Li, P.; Vermeulen, N. A.; Malliakas, C. D.; Gomez-Gualdron, D. A.; Howarth, A. J.; Mehdi, B. L.; Dohnalkova, A.; Browning, N. D.; O'Keeffe, M.; Farha, O. K., Bottom-up construction of a superstructure in a porous uranium-organic crystal. *Science* **2017,** *356* (6338), 624-627.
44. Dolgopolova, E. A.; Rice, A. M.; Shustova, N. B., Actinide-based MOFs: a middle ground in solution and solid-state structural motifs. *Chem. Commun.* **2018,** *54* (50), 6472-6483.
45. Lv, K.; Fichter, S.; Gu, M.; März, J.; Schmidt, M., An updated status and trends in actinide metal-organic frameworks (An-MOFs): From synthesis to application. *Coord. Chem. Rev.* **2021,** *446*, 214011.
46. Li, P.; Vermeulen, N. A.; Gong, X.; Malliakas, C. D.; Stoddart, J. F.; Hupp, J. T.; Farha, O. K., Design and Synthesis of a Water-Stable Anionic Uranium-Based Metal-Organic Framework (MOF) with Ultra Large Pores. *Angew. Chem., Int. Ed.* **2016,** *55* (35), 10358-10362.
47. Zhang, X.; Li, P.; Krzyaniak, M.; Knapp, J.; Wasielewski, M. R.; Farha, O. K., Stabilization of Photocatalytically Active Uranyl Species in a Uranyl–Organic Framework for Heterogeneous Alkane Fluorination Driven by Visible Light. *Inorg. Chem.* **2020,** *59* (23), 16795-16798.
48. Wang, Y.; Yin, X.; Liu, W.; Xie, J.; Silver, M. A.; Sheng, D.; Chen, L.; Diwu, J.; Chai, Z.; Wang, S.; Wang, Y.; Liu, N.; Chen, J.; Albrecht-Schmitt, T. E., Emergence of Uranium as a Distinct Metal Center for Building Intrinsic X-ray Scintillators. *Angew. Chem. Int. Ed. Engl.* **2018**.
49. Xie, J.; Wang, Y.; Liu, W.; Yin, X.; Chen, L.; Zou, Y.; Diwu, J.; Chai, Z.; Albrecht-Schmitt, T. E.; Liu, G.; Wang, S., Highly Sensitive Detection of Ionizing Radiations by a Photoluminescent Uranyl Organic Framework. *Angew. Chem., Int. Ed.* **2017,** *56* (26), 7500-7504.
50. Halter, D. P.; Klein, R. A.; Boreen, M. A.; Trump, B. A.; Brown, C. M.; Long, J. R., Self-adjusting binding pockets enhance H2 and CH4 adsorption in a uranium-based metal–organic framework. *Chem. Sci.* **2020,** *11* (26), 6709-6716.
51. Wang, S.; Alekseev, E. V.; Ling, J.; Liu, G.; Depmeier, W.; Albrecht-Schmitt, T. E., Polarity and Chirality in Uranyl Borates: Insights into Understanding the Vitrification of Nuclear Waste and the Development of Nonlinear Optical Materials. *Chem. Mater.* **2010,** *22* (6), 2155-2163.
52. Shvareva, T. Y.; Skanthakumar, S.; Soderholm, L.; Clearfield, A.; Albrecht-Schmitt, T. E., Cs+-Selective Ion Exchange and Magnetic Ordering in a Three-Dimensional Framework Uranyl Vanadium(IV) Phosphate. *Chem. Mater.* **2007,** *19* (2), 132-134.

53. Li, F.-z.; Mei, L.; Hu, K.-q.; An, S.-w.; Wu, S.; Liu, N.; Chai, Z.-f.; Shi, W.-q., Uranyl Compounds Involving a Weakly Bonded Pseudorotaxane Linker: Combined Effect of pH and Competing Ligands on Uranyl Coordination and Speciation. *Inorg. Chem.* **2019,** *58* (5), 3271-3282.
54. Ejegbavwo, O. A.; Martin, C. R.; Olorunfemi, O. A.; Leith, G. A.; Ly, R. T.; Rice, A. M.; Dolgopolova, E. A.; Smith, M. D.; Karakalos, S. G.; Birkner, N.; Powell, B. A.; Pandey, S.; Koch, R. J.; Misture, S. T.; Loye, H.-C. z.; Phillpot, S. R.; Brinkman, K. S.; Shustova, N. B., Thermodynamics and Electronic Properties of Heterometallic Multinuclear Actinide-Containing Metal–Organic Frameworks with "Structural Memory". *J. Am. Chem. Soc.* **2019,** *141* (29), 11628-11640.
55. Dolgopolova, E. A.; Ejegbavwo, O. A.; Martin, C. R.; Smith, M. D.; Setyawan, W.; Karakalos, S. G.; Henager, C. H.; zur Loye, H.-C.; Shustova, N. B., Multifaceted Modularity: A Key for Stepwise Building of Hierarchical Complexity in Actinide Metal–Organic Frameworks. *J. Am. Chem. Soc.* **2017,** *139* (46), 16852-16861.
56. Saha, S.; Becker, U., A first principles study of energetics and electronic structural responses of uranium-based coordination polymers to Np incorporation. *Radiochim. Acta* **2018,** *106* (1), 1-13.
57. Hanna, S. L.; Debela, T. T.; Mroz, A. M.; Syed, Z. H.; Kirlikovali, K. O.; Hendon, C. H.; Farha, O. K., Identification of a metastable uranium metal–organic framework isomer through non-equilibrium synthesis. *Chem. Sci.* **2022,** *13* (44), 13032-13039.
58. Liu, C.; Chen, F.-Y.; Tian, H.-R.; Ai, J.; Yang, W.; Pan, Q.-J.; Sun, Z.-M., Interpenetrated Uranyl–Organic Frameworks with bor and pts Topology: Structure, Spectroscopy, and Computation. *Inorg. Chem.* **2017,** *56* (22), 14147-14156.
59. Xu, W.; Si, Z.-X.; Xie, M.; Zhou, L.-X.; Zheng, Y.-Q., Experimental and Theoretical Approaches to Three Uranyl Coordination Polymers Constructed by Phthalic Acid and N,N′-Donor Bridging Ligands: Crystal Structures, Luminescence, and Photocatalytic Degradation of Tetracycline Hydrochloride. *Cryst. Growth Des.* **2017,** *17* (4), 2147-2157.
60. Mei, L.; Wang, C.-z.; Zhu, L.-z.; Gao, Z.-q.; Chai, Z.-f.; Gibson, J. K.; Shi, W.-q., Exploring New Assembly Modes of Uranyl Terephthalate: Templated Syntheses and Structural Regulation of a Series of Rare 2D → 3D Polycatenated Frameworks. *Inorg. Chem.* **2017,** *56* (14), 7694-7706.
61. Saha, S.; Becker, U., The effect of the aliphatic carboxylate linkers on the electronic structures, chemical bonding and optical properties of the uranium-based metal–organic frameworks. *RSC Adv.* **2015,** *5* (34), 26735-26748.
62. Mei, L.; Wu, Q.-y.; An, S.-w.; Gao, Z.-q.; Chai, Z.-f.; Shi, W.-q., Silver Ion-Mediated Heterometallic Three-Fold Interpenetrating Uranyl–Organic Framework. *Inorg. Chem.* **2015,** *54* (22), 10934-10945.
63. Wang, J.-y.; Wu, Q.-y.; Wang, S.; Huang, Z.-w.; Hu, K.-q.; Yu, J.-p.; Mei, L.; Zhang, M.; Chai, Z.-f.; Shi, W.-q., Coordination-driven assembly of actinide-organic polyrotaxanes involving crown ether macrocycles. *Org. Chem. Front.* **2021,** *8* (14), 3686-3694.
64. Liu, C.; Yang, X.-X.; Niu, S.; Yi, X.-Y.; Pan, Q.-J., Occurrence of polyoxouranium motifs in uranyl organic networks constructed by using silicon-centered carboxylate linkers: structures, spectroscopy and computation. *Dalton Trans.* **2020,** *49* (13), 4155-4163.
65. Nelson, A.-G. D.; Rak, Z.; Albrecht-Schmitt, T. E.; Becker, U.; Ewing, R. C., Three New Silver Uranyl Diphosphonates: Structures and Properties. *Inorg. Chem.* **2014,** *53* (6), 2787-2796.

66. Wang, L.; Xu, W.; Li, W.-Y.; Xie, M.; Zheng, Y.-Q., A Water-Stable Uranyl Organic Framework as a Highly Selective and Sensitive Bifunctional Luminescent Probe for Fe3+ and Tetracycline Hydrochloride. *Chem. Asian J.* **2019,** *14* (23), 4246-4254.
67. Liu, C.; Gao, C.-Y.; Yang, W.; Chen, F.-Y.; Pan, Q.-J.; Li, J.; Sun, Z.-M., Entangled Uranyl Organic Frameworks with (10,3)-b Topology and Polythreading Network: Structure, Luminescence, and Computational Investigation. *Inorg. Chem.* **2016,** *55* (11), 5540-5548.
68. Kong, X.; Hu, K.; Mei, L.; Wu, Q.; Huang, Z.; Liu, K.; Chai, Z.; Nie, C.; Shi, W., Construction of Hybrid Bimetallic Uranyl Compounds Based on a Preassembled Terpyridine Metalloligand. *Chem. Eur. J.* **2021,** *27* (6), 2124-2130.
69. Hu, K. Q.; Zhu, L. Z.; Wang, C. Z.; Mei, L.; Liu, Y. H.; Gao, Z. Q.; Chai, Z. F.; Shi, W. Q., Novel Uranyl Coordination Polymers Based on Quinoline-Containing Dicarboxylate by Altering Auxiliary Ligands: From 1D Chain to 3D Framework. *Cryst. Growth Des.* **2016,** *16* (9), 4886-4896.
70. Chen, F.; Wang, C.-z.; Li, Z.-j.; Lan, J.-h.; Ji, Y.-q.; Chai, Z.-f., New Three-Fold Interpenetrated Uranyl Organic Framework Constructed by Terephthalic Acid and Imidazole Derivative. *Inorg. Chem.* **2015,** *54* (8), 3829-3834.
71. Pandey, S.; Demaske, B.; Ejegbavwo, O. A.; Berseneva, A. A.; Setyawan, W.; Shustova, N.; Phillpot, S. R., Electronic structures and magnetism of Zr-, Th-, and U-based metal-organic frameworks (MOFs) by density functional theory. *Comput. Mater. Sci.* **2020,** *184*, 109903.
72. Zhu, L.-Z.; Wang, C.-Z.; Mei, L.; Wang, L.; Liu, Y.-H.; Zhu, Z.-T.; Zhao, Y.-L.; Chai, Z.-F.; Shi, W.-Q., Two novel uranyl complexes of a semi-rigid aromatic tetracarboxylic acid supported by an organic base as an auxiliary ligand or a templating agent: an experimental and theoretical exploration. *CrystEngComm* **2015,** *17* (15), 3031-3040.
73. Kong, X.-H.; Hu, K.-Q.; Wu, Q.-Y.; Mei, L.; Yu, J.-P.; Chai, Z.-F.; Nie, C.-M.; Shi, W.-Q., In situ nitroso formation induced structural diversity of uranyl coordination polymers. *Inorg. Chem. Front.* **2019,** *6* (3), 775-785.
74. Liu, C.; Yang, W.; Qu, N.; Li, L.-J.; Pan, Q.-J.; Sun, Z.-M., Construction of Uranyl Organic Hybrids by Phosphonate and in Situ Generated Carboxyphosphonate Ligands. *Inorg. Chem.* **2017,** *56* (3), 1669-1678.
75. Brager, D. M.; Nicholas, A. D.; Schofield, M. H.; Cahill, C. L., Pb–Oxo Interactions in Uranyl Hybrid Materials: A Combined Experimental and Computational Analysis of Bonding and Spectroscopic Properties. *Inorg. Chem.* **2021,** *60* (22), 17186-17200.
76. Carter, K. P.; Kalaj, M.; Kerridge, A.; Cahill, C. L., Probing hydrogen and halogen-oxo interactions in uranyl coordination polymers: a combined crystallographic and computational study. *CrystEngComm* **2018,** *20* (34), 4916-4925.
77. Carter, K. P.; Kalaj, M.; McNeil, S.; Kerridge, A.; Schofield, M. H.; Ridenour, J. A.; Cahill, C. L., Structural, spectroscopic, and computational evaluations of cation–cation and halogen bonding interactions in heterometallic uranyl hybrid materials. *Inorg. Chem. Front.* **2021,** *8* (5), 1128-1141.
78. Hu, K.-Q.; Jiang, X.; Wang, C.-Z.; Mei, L.; Xie, Z.-N.; Tao, W.-Q.; Zhang, X.-L.; Chai, Z.-F.; Shi, W.-Q., Solvent-Dependent Synthesis of Porous Anionic Uranyl–Organic Frameworks Featuring a Highly Symmetrical (3,4)-Connected ctn or bor Topology for Selective Dye Adsorption. *Chem. Eur. J.* **2017,** *23* (3), 529-532.
79. Mei, L.; Wang, C.-z.; Wang, L.; Zhao, Y.-l.; Chai, Z.-f.; Shi, W.-q., Halogen Bonded Three-Dimensional Uranyl–Organic Compounds with Unprecedented Halogen–Halogen

Interactions and Structure Diversity upon Variation of Halogen Substitution. *Cryst. Growth Des.* **2015,** *15* (3), 1395-1406.
80. Smetana, V.; Kelley, S. P.; Pei, H.; Mudring, A.-V.; Rogers, R. D., Sandwiched Kagomé Lattices in a Coordination Polymer Based on Mixed-Valent Uranium. *Cryst. Growth Des.* **2021,** *21* (3), 1727-1733.
81. Zheng, T.; Wu, Q.-Y.; Gao, Y.; Gui, D.; Qiu, S.; Chen, L.; Sheng, D.; Diwu, J.; Shi, W.-Q.; Chai, Z.; Albrecht-Schmitt, T. E.; Wang, S., Probing the Influence of Phosphonate Bonding Modes to Uranium(VI) on Structural Topology and Stability: A Complementary Experimental and Computational Investigation. *Inorg. Chem.* **2015,** *54* (8), 3864-3874.
82. Mei, L.; Wu, Q.-y.; Yuan, L.-y.; Wang, L.; An, S.-w.; Xie, Z.-n.; Hu, K.-q.; Chai, Z.-f.; Burns, P. C.; Shi, W.-q., An Unprecedented Two-Fold Nested Super-Polyrotaxane: Sulfate-Directed Hierarchical Polythreading Assembly of Uranyl Polyrotaxane Moieties. *Chem. Eur. J.* **2016,** *22* (32), 11329-11338.
83. Kong, X.-H.; Hu, K.-Q.; Mei, L.; Li, A.; Liu, K.; Zeng, L.-W.; Wu, Q.-Y.; Chai, Z.-F.; Nie, C.-M.; Shi, W.-Q., Double-Layer Nitrogen-Rich Two-Dimensional Anionic Uranyl–Organic Framework for Cation Dye Capture and Catalytic Fixation of Carbon Dioxide. *Inorg. Chem.* **2021,** *60* (15), 11485-11495.
84. Xu, W.; Ren, Y.-N.; Xie, M.; Zhou, L.-X.; Zheng, Y.-Q., Six uranyl-organic frameworks with naphthalene-dicarboxylic acid and bipyridyl-based spacers: syntheses, structures, and properties. *Dalton Trans.* **2018,** *47* (12), 4236-4250.
85. Pandey, S.; Jia, Z.; Demaske, B.; Ejegbavwo, O. A.; Setyawan, W.; Henager, C. H.; Shustova, N.; Phillpot, S. R., Sequestration of Radionuclides in Metal–Organic Frameworks from Density Functional Theory Calculations. *J. Phys. Chem. C* **2019,** *123* (44), 26842-26855.
86. Hanna, S. L.; Chheda, S.; Anderson, R.; Ray, D.; Malliakas, C. D.; Knapp, J. G.; Otake, K.-i.; Li, P.; Li, P.; Wang, X.; Wasson, M. C.; Zosel, K.; Evans, A. M.; Robison, L.; Islamoglu, T.; Zhang, X.; Dichtel, W. R.; Stoddart, J. F.; Gomez-Gualdron, D. A.; Gagliardi, L.; Farha, O. K., Discovery of spontaneous de-interpenetration through charged point-point repulsions. *Chem* **2021**.
87. Wang, X.; Wang, Y.; Dai, X.; Silver, M. A.; Liu, W.; Li, Y.; Bai, Z.; Gui, D.; Chen, L.; Diwu, J.; Zhou, R.; Chai, Z.; Wang, S., Phase transition triggered aggregation-induced emission in a photoluminescent uranyl–organic framework. *Chem. Commun.* **2018,** *54* (6), 627-630.
88. Yin, M.; Xiong, X.; Zhang, L.; Gong, L.; Zhao, D.; Luo, F., Luminescence modulation by twisting the branches of organic building blocks in uranyl-organic frameworks. *Cell Rep. Phys. Sci.* **2022,** *3* (6), 100913.
89. Martin, C. R.; Leith, G. A.; Kittikhunnatham, P.; Park, K. C.; Ejegbavwo, O. A.; Mathur, A.; Callahan, C. R.; Desmond, S. L.; Keener, M. R.; Ahmed, F.; Pandey, S.; Smith, M. D.; Phillpot, S. R.; Greytak, A. B.; Shustova, N. B., Heterometallic Actinide-Containing Photoresponsive Metal-Organic Frameworks: Dynamic and Static Tuning of Electronic Properties. *Angew. Chem. Int. Ed.* **2021,** *60* (15), 8072-8080.
90. Wang, Y.; Liu, Z.; Li, Y.; Bai, Z.; Liu, W.; Wang, Y.; Xu, X.; Xiao, C.; Sheng, D.; Diwu, J.; Su, J.; Chai, Z.; Albrecht-Schmitt, T. E.; Wang, S., Umbellate distortions of the uranyl coordination environment result in a stable and porous polycatenated framework that can effectively remove cesium from aqueous solutions. *J. Am. Chem. Soc.* **2015,** *137* (19), 6144-6147.
91. Campbell, J. E.; Yang, J.; Day, G. M., Predicted energy–structure–function maps for the evaluation of small molecule organic semiconductors. *J. Mater. Chem. C* **2017,** *5* (30), 7574-7584.

92. Day, G. M.; Cooper, A. I., Energy–Structure–Function Maps: Cartography for Materials Discovery. *Adv. Mater.* **2018,** *30* (37), 1704944.
93. Musil, F.; De, S.; Yang, J.; Campbell, J. E.; Day, G. M.; Ceriotti, M., Machine learning for the structure–energy–property landscapes of molecular crystals. *Chem. Sci.* **2018,** *9* (5), 1289-1300.
94. Pulido, A.; Chen, L.; Kaczorowski, T.; Holden, D.; Little, M. A.; Chong, S. Y.; Slater, B. J.; McMahon, D. P.; Bonillo, B.; Stackhouse, C. J.; Stephenson, A.; Kane, C. M.; Clowes, R.; Hasell, T.; Cooper, A. I.; Day, G. M., Functional materials discovery using energy–structure–function maps. *Nature* **2017,** *543* (7647), 657-664.
95. Yang, J., Mapping temperature-dependent energy–structure–property relationships for solid solutions of inorganic halide perovskites. *J. Mater. Chem. C* **2020,** *8* (47), 16815-16825.
96. Zhao, C.; Chen, L.; Che, Y.; Pang, Z.; Wu, X.; Lu, Y.; Liu, H.; Day, G. M.; Cooper, A. I., Digital navigation of energy–structure–function maps for hydrogen-bonded porous molecular crystals. *Nat. Commun.* **2021,** *12* (1), 817.
97. Li, H.; Eddaoudi, M.; O'Keeffe, M.; Yaghi, O. M., Design and synthesis of an exceptionally stable and highly porous metal-organic framework. *Nature* **1999,** *402* (6759), 276-279.
98. Yaghi, O. M.; O'Keeffe, M.; Ockwig, N. W.; Chae, H. K.; Eddaoudi, M.; Kim, J., Reticular synthesis and the design of new materials. *Nature* **2003,** *423* (6941), 705-714.
99. Yang, X.; Xu, Q., Bimetallic Metal–Organic Frameworks for Gas Storage and Separation. *Cryst. Growth Des.* **2017,** *17* (4), 1450-1455.
100. Li, B.; Chen, B., Porous Lanthanide Metal–Organic Frameworks for Gas Storage and Separation. In *Lanthanide Metal-Organic Frameworks*, Cheng, P., Ed. Springer Berlin Heidelberg: Berlin, Heidelberg, 2015; pp 75-107.
101. Lee, J.; Farha, O. K.; Roberts, J.; Scheidt, K. A.; Nguyen, S. T.; Hupp, J. T., Metal-organic framework materials as catalysts. *Chem. Soc. Rev.* **2009,** *38* (5), 1450-1459.
102. Zhu, L.; Liu, X.-Q.; Jiang, H.-L.; Sun, L.-B., Metal–Organic Frameworks for Heterogeneous Basic Catalysis. *Chem. Rev.* **2017,** *117* (12), 8129-8176.
103. Shultz, A. M.; Farha, O. K.; Adhikari, D.; Sarjeant, A. A.; Hupp, J. T.; Nguyen, S. T., Selective Surface and Near-Surface Modification of a Noncatenated, Catalytically Active Metal-Organic Framework Material Based on Mn(salen) Struts. *Inorg. Chem.* **2011,** *50* (8), 3174-3176.
104. Zhang, X.; Saber, M. R.; Prosvirin, A. P.; Reibenspies, J. H.; Sun, L.; Ballesteros-Rivas, M.; Zhao, H.; Dunbar, K. R., Magnetic ordering in TCNQ-based metal–organic frameworks with host–guest interactions. *Inorg. Chem. Front.* **2015,** *2* (10), 904-911.
105. Mon, M.; Pascual-Álvarez, A.; Grancha, T.; Cano, J.; Ferrando-Soria, J.; Lloret, F.; Gascon, J.; Pasán, J.; Armentano, D.; Pardo, E., Solid-State Molecular Nanomagnet Inclusion into a Magnetic Metal–Organic Framework: Interplay of the Magnetic Properties. *Chem. Eur. J.* **2015,** *22* (2), 539-545.
106. Sumida, K.; Herm, Z. R.; McDonald, T.; Bloch, E. D.; Mason, J.; Choi, H. J.; Long, J. R., Carbon dioxide capture in metal-organic frameworks. *Chemical Reviews* **2011,** *242*.
107. Shekhah, O.; Belmabkhout, Y.; Chen, Z.; Guillerm, V.; Cairns, A.; Adil, K.; Eddaoudi, M., Made-to-order metal-organic frameworks for trace carbon dioxide removal and air capture. *Nat. Commun.* **2014,** *5*, 4228.
108. Feng, M.; Zhang, P.; Zhou, H. C.; Sharma, V. K., Water-stable metal-organic frameworks for aqueous removal of heavy metals and radionuclides: A review. *Chemosphere* **2018,** *209*, 783-800.

109. Wen, J.; Fang, Y.; Zeng, G., Progress and prospect of adsorptive removal of heavy metal ions from aqueous solution using metal–organic frameworks: A review of studies from the last decade. *Chemosphere* **2018,** *201*, 627-643.
110. Cohen, S. M., Postsynthetic Methods for the Functionalization of Metal–Organic Frameworks. *Chem. Rev.* **2012,** *112* (2), 970-1000.
111. Islamoglu, T.; Goswami, S.; Li, Z.; Howarth, A. J.; Farha, O. K.; Hupp, J. T., Postsynthetic Tuning of Metal–Organic Frameworks for Targeted Applications. *Acc. Chem. Res.* **2017,** *50* (4), 805-813.
112. Zhang, J.-P.; Zhou, H.-L.; Zhou, D.-D.; Liao, P.-Q.; Chen, X.-M., Controlling flexibility of metal–organic frameworks. *Natl. Sci. Rev.* **2017**, nwx127-nwx127.
113. Sakata, Y.; Furukawa, S.; Kondo, M.; Hirai, K.; Horike, N.; Takashima, Y.; Uehara, H.; Louvain, N.; Meilikhov, M.; Tsuruoka, T.; Isoda, S.; Kosaka, W.; Sakata, O.; Kitagawa, S., Shape-Memory Nanopores Induced in Coordination Frameworks by Crystal Downsizing. *Science* **2013,** *339* (6116), 193.
114. Zhang, Y. Y.; Zhang, X.; Lyu, J. F.; Otake, K.; Wang, X. J.; Redfern, L. R.; Malliakas, C. D.; Li, Z. Y.; Islamoglu, T.; Wang, B.; Farha, O. K., A Flexible Metal-Organic Framework with 4-Connected Zr-6 Nodes. *Journal of the American Chemical Society* **2018,** *140* (36), 11179-11183.
115. Zhang, J. P.; Chen, X. M., Exceptional framework flexibility and sorption behavior of a multifunctional porous cuprous triazolate framework. *Journal of the American Chemical Society* **2008,** *130* (18), 6010-6017.
116. Ma, S. Q.; Sun, D. F.; Wang, X. S.; Zhou, H. C., A mesh-adjustable molecular sieve for general use in gas separation. *Angew. Chem. Int. Ed.* **2007,** *46* (14), 2458-2462.
117. Mason, J. A.; Oktawiec, J.; Taylor, M. K.; Hudson, M. R.; Rodriguez, J.; Bachman, J. E.; Gonzalez, M. I.; Cervellino, A.; Guagliardi, A.; Brown, C. M.; Llewellyn, P. L.; Masciocchi, N.; Long, J. R., Methane storage in flexible metal-organic frameworks with intrinsic thermal management. *Nature* **2015,** *527* (7578), 357-+.
118. Ghoufi, A.; Benhamed, K.; Boukli-Hacene, L.; Maurin, G., Electrically Induced Breathing of the MIL-53(Cr) Metal-Organic Framework. *ACS Cent. Sci.* **2017,** *3* (5), 394-398.
119. Biradha, K.; Hongo, Y.; Fujita, M., Crystal-to-Crystal Sliding of 2D Coordination Layers Triggered by Guest Exchange. *Angew. Chem. Int. Ed.* **2002,** *41* (18), 3395-3398.
120. Suh, M. P.; Moon, H. R.; Lee, E. Y.; Jang, S. Y., A redox-active two-dimensional coordination polymer: preparation of silver and gold nanoparticles and crystal dynamics on guest removal. *J. Am. Chem. Soc.* **2006,** *128* (14), 4710-8.
121. Chorazy, S.; Arczynski, M.; Nakabayashi, K.; Sieklucka, B.; Ohkoshi, S., Visible to Near-Infrared Emission from Ln(III)(Bis-oxazoline)-[Mo(V)(CN)8] (Ln = Ce-Yb) Magnetic Coordination Polymers Showing Unusual Lanthanide-Dependent Sliding of Cyanido-Bridged Layers. *Inorg. Chem.* **2015,** *54* (10), 4724-36.
122. Agarwal, R. A.; Mukherjee, S., Two-dimensional flexible Ni(II)-based porous coordination polymer showing single-crystal to single-crystal transformation, selective gas adsorption and catalytic properties. *Polyhedron* **2016,** *105*, 228-237.
123. Zhang, J. P.; Liao, P. Q.; Zhou, H. L.; Lin, R. B.; Chen, X. M., Single-crystal X-ray diffraction studies on structural transformations of porous coordination polymers. *Chem. Soc. Rev.* **2014,** *43* (16), 5789-814.

124. Du, X. S.; Yan, B. J.; Wang, J. Y.; Xi, X. J.; Wang, Z. Y.; Zang, S. Q., Layer-sliding-driven crystal size and photoluminescence change in a novel SCC-MOF. *Chem. Commun.* **2018,** *54* (42), 5361-5364.
125. Zhang, W. X.; Xue, W.; Chen, X. M., Flexible mixed-spin Kagome coordination polymers with reversible magnetism triggered by dehydration and rehydration. *Inorg. Chem.* **2011,** *50* (1), 309-16.
126. Li, P.; Vermeulen, N. A.; Malliakas, C. D.; Howarth, A. J.; Farha, O. K.; Gomez-Gualdron, D. A.; Mehdi, B. L.; Browning, N. D.; Dohnalkova, A.; Browning, N. D.; O'Keeffe, M.; Farha, O. K., Bottom-up construction of a superstructure in a porous uranium-organic crystal. *Science* **2017,** *356* (6338), 624-627.
127. Carter, K. P.; Surbella, R. G., 3rd; Kalaj, M.; Cahill, C. L., Restricted Speciation and Supramolecular Assembly in the 5f Block. *Chem. Eur. J.* **2018,** *24* (49), 12747-12756.
128. Thuery, P.; Harrowfield, J., Recent advances in structural studies of heterometallic uranyl-containing coordination polymers and polynuclear closed species. *Dalton Trans.* **2017,** *46* (40), 13660-13667.
129. Falaise, C.; Volkringer, C.; Loiseau, T., Mixed Formate-Dicarboxylate Coordination Polymers with Tetravalent Uranium: Occurrence of Tetranuclear {U4O4} and Hexanuclear {U6O4(OH)(4)} Motifs. *Cryst. Growth Des.* **2013,** *13* (7), 3225-3231.
130. Thuery, P.; Harrowfield, J., [Ni(cyclam)](2+) and [Ni(R,S-Me(6)cyclam)](2+) as Linkers or Counterions In Uranyl-Organic Species with cis- and trans-1,2-Cyclohexanedicarboxylate Ligands. *Cryst. Growth Des.* **2018,** *18* (9), 5512-5520.
131. Payne, M. K.; Laird, R. C.; Schnell, M. A.; Mackin, S. R.; Forbes, T. Z., Use of Zwitterionic Ligands in Uranyl Hybrid Materials: Explorations on the Structural Features that Control Water Ordering and Mobility. *Cryst. Growth Des.* **2017,** *17* (12), 6498-6509.
132. Zehnder, R. A.; Boncella, J. M.; Cross, J. N.; Kozimor, S. A.; Monreal, M. J.; La Pierre, H. S.; Scott, B. L.; Tondreau, A. M.; Zeller, M., Network Dimensionality of Selected Uranyl(VI) Coordination Polymers and Octopus-like Uranium(IV) Clusters. *Cryst. Growth Des.* **2017,** *17* (10), 5568-5582.
133. Dolgopolova, E. A.; Ejegbavwo, O. A.; Martin, C. R.; Smith, M. D.; Setyawan, W.; Karakalos, S. G.; Henager, C. H.; zur Loye, H.-C.; Shustova, N. B., Multifaceted Modularity: A Key for Stepwise Building of Hierarchical Complexity in Actinide Metal-Organic Frameworks. *J. Am. Chem. Soc.* **2017,** *139* (46), 16852-16861.
134. Wang, Y.; Li, Y.; Bai, Z.; Xiao, C.; Liu, Z.; Liu, W.; Chen, L.; He, W.; Diwu, J.; Chai, Z.; Albrecht-Schmitt, T. E.; Wang, S., Design and synthesis of a chiral uranium-based microporous metal organic framework with high SHG efficiency and sequestration potential for low-valent actinides. *Dalton Trans.* **2015,** *44* (43), 18810-18814.
135. Hu, F.; Di, Z.; Lin, P.; Huang, P.; Wu, M.; Jiang, F.; Hong, M., An Anionic Uranium-Based Metal–Organic Framework with Ultralarge Nanocages for Selective Dye Adsorption. *Cryst. Growth Des.* **2018,** *18* (2), 576-580.
136. Li, H. H.; Zeng, X. H.; Wu, H. Y.; Jie, X.; Zheng, S. T.; Chen, Z. R., Incorporating guest molecules into honeycomb structures constructed from uranium(vi)-polycarboxylates: Structural diversities and photocatalytic activities for the degradation of organic dye. *Cryst. Growth Des.* **2015,** *15* (1), 10-13.
137. Jennifer, S. J.; Jana, A. K., Influence of pyrazine/piperazine based guest molecules in the crystal structures of uranyl thiophene dicarboxylate coordination polymers: Structural diversities

and photocatalytic activities for the degradation of organic dye. *Cryst. Growth Des.* **2017,** *17* (10), 5318-5329.
138. Liao, Z. L.; Li, G. D.; Bi, M. H.; Chen, J. S., Preparation, structures, and photocatalytic properties of three new uranyl-organic assembly compounds. *Inorg. Chem.* **2008,** *47* (11), 4844-53.
139. Spencer, E. C.; Ross, N. L.; Surbella, R. G.; Cahill, C. L., The influence of pressure on the structure of a 2D uranium(VI) carboxyphosphonoate compound. *J. Solid State Chem.* **2014,** *218*, 1-5.
140. Payne, M. K.; Pyrch, M. M.; Jubinsky, M.; Basile, M. C.; Forbes, T. Z., Impacts of oxo interactions within actinyl metal organic materials: highlight on thermal expansion behaviour. *Chem. Commun.* **2018,** *54* (77), 10828-10831.
141. Thuéry, P.; Harrowfield, J., Structural Variations in the Uranyl/4,4′-Biphenyldicarboxylate System. Rare Examples of 2D → 3D Polycatenated Uranyl–Organic Networks. *Inorg. Chem.* **2015,** *54* (16), 8093-8102.
142. Guillerm, V.; Kim, D.; Eubank, J. F.; Luebke, R.; Liu, X.; Adil, K.; Lah, M. S.; Eddaoudi, M., A supermolecular building approach for the design and construction of metal–organic frameworks. *Chem. Soc. Rev.* **2014,** *43* (16), 6141-6172.
143. Ascherl, L.; Sick, T.; Margraf, J. T.; Lapidus, S. H.; Calik, M.; Hettstedt, C.; Karaghiosoff, K.; Doblinger, M.; Clark, T.; Chapman, K. W.; Auras, F.; Bein, T., Molecular docking sites designed for the generation of highly crystalline covalent organic frameworks. *Nat. Chem.* **2016,** *8* (4), 310-316.
144. Fletcher, A. J.; Thomas, K. M.; Rosseinsky, M. J., Flexibility in metal-organic framework materials: Impact on sorption properties. *J. Solid State Chem.* **2005,** *178* (8), 2491-2510.
145. Ramsahye, N. A.; Maurin, G.; Bourrelly, S.; Llewellyn, P. L.; Loiseau, T.; Serre, C.; Férey, G., On the breathing effect of a metal–organic framework upon CO2 adsorption: Monte Carlo compared to microcalorimetry experiments. *Chem. Commun.* **2007,** (31), 3261-3263.
146. Fairen-Jimenez, D.; Moggach, S. A.; Wharmby, M. T.; Wright, P. A.; Parsons, S.; Düren, T., Opening the Gate: Framework Flexibility in ZIF-8 Explored by Experiments and Simulations. *Journal of the American Chemical Society* **2011,** *133* (23), 8900-8902.
147. Furukawa, S.; Sakata, Y.; Kitagawa, S., Control over Flexibility of Entangled Porous Coordination Frameworks by Molecular and Mesoscopic Chemistries. *Chem. Lett.* **2013,** *42* (6), 570-576.
148. Sato, H.; Kosaka, W.; Matsuda, R.; Hori, A.; Hijikata, Y.; Belosludov, R. V.; Sakaki, S.; Takata, M.; Kitagawa, S., Self-Accelerating CO Sorption in a Soft Nanoporous Crystal. *Science* **2014,** *343* (6167), 167-170.
149. Bezuidenhout, C. X.; Smith, V. J.; Esterhuysen, C.; Barbour, L. J., Solvent- and Pressure-Induced Phase Changes in Two 3D Copper Glutarate-Based Metal-Organic Frameworks via Glutarate (+gauche right arrow over left arrow -gauche) Conformational Isomerism. *J. Am. Chem. Soc.* **2017,** *139* (16), 5923-5929.
150. Sheldrick, G., SHELXT - Integrated space-group and crystal-structure determination. *Acta Crystallogr. A* **2015,** *71* (1), 3-8.
151. Sheldrick, G., Crystal structure refinement with SHELXL. *Acta Crystallogr. C* **2015,** *71* (1), 3-8.
152. C. Kabuto, S. A., T. Nemoto, and E. Kwon, Release of Software (Yadokari-XG 2009) for Crystal Structure Analyses. *J. Cryst. Soc. Jpn.* **2009,** *51* (3), 218-224.

153. Dolomanov, O. V.; Bourhis, L. J.; Gildea, R. J.; Howard, J. A. K.; Puschmann, H., OLEX2: a complete structure solution, refinement and analysis program. *J. Appl. Crystallogr.* **2009,** *42* (2), 339-341.
154. Spek, A., Structure validation in chemical crystallography. *Acta Crystallogr. D* **2009,** *65* (2), 148-155.
155. Nelson, A. P.; Farha, O. K.; Mulfort, K. L.; Hupp, J. T., Supercritical processing as a route to high internal surface areas and permanent microporosity in metal−organic framework materials. *J. Am. Chem. Soc.* **2009,** *131* (2), 458-460.
156. Moulton, B.; Zaworotko, M. J., From Molecules to Crystal Engineering: Supramolecular Isomerism and Polymorphism in Network Solids. *Chem. Rev.* **2001,** *101* (6), 1629-1658.
157. Matlin, A. J.; Clark, F.; Smith, C. W. J., Understanding alternative splicing: towards a cellular code. *Nat. Rev. Mol. Cell Biol.* **2005,** *6* (5), 386-398.
158. Yang, X.; Coulombe-Huntington, J.; Kang, S.; Sheynkman, Gloria M.; Hao, T.; Richardson, A.; Sun, S.; Yang, F.; Shen, Yun A.; Murray, Ryan R.; Spirohn, K.; Begg, Bridget E.; Duran-Frigola, M.; MacWilliams, A.; Pevzner, Samuel J.; Zhong, Q.; Trigg, Shelly A.; Tam, S.; Ghamsari, L.; Sahni, N.; Yi, S.; Rodriguez, Maria D.; Balcha, D.; Tan, G.; Costanzo, M.; Andrews, B.; Boone, C.; Zhou, Xianghong J.; Salehi-Ashtiani, K.; Charloteaux, B.; Chen, Alyce A.; Calderwood, Michael A.; Aloy, P.; Roth, Frederick P.; Hill, David E.; Iakoucheva, Lilia M.; Xia, Y.; Vidal, M., Widespread Expansion of Protein Interaction Capabilities by Alternative Splicing. *Cell* **2016,** *164* (4), 805-817.
159. Lee, A. Y.; Erdemir, D.; Myerson, A. S., Crystal Polymorphism in Chemical Process Development. *Annu. Rev. Chem. Biomol. Eng.* **2011,** *2* (1), 259-280.
160. Rodríguez-Spong, B.; Price, C. P.; Jayasankar, A.; Matzger, A. J.; Rodríguez-Hornedo, N. r., General principles of pharmaceutical solid polymorphism: A supramolecular perspective. *Adv. Drug Deliv. Rev.* **2004,** *56* (3), 241-274.
161. Stannard, A.; Russell, J. C.; Blunt, M. O.; Salesiotis, C.; Giménez-López, M. d. C.; Taleb, N.; Schröder, M.; Champness, N. R.; Garrahan, J. P.; Beton, P. H., Broken symmetry and the variation of critical properties in the phase behaviour of supramolecular rhombus tilings. *Nat. Chem.* **2012,** *4* (2), 112-117.
162. Gupta, M.; Vittal, J. J., Control of interpenetration and structural transformations in the interpenetrated MOFs. *Coord. Chem. Rev.* **2021,** *435*, 213789-213804.
163. Bergeron, H.; Lebedev, D.; Hersam, M. C., Polymorphism in Post-Dichalcogenide Two-Dimensional Materials. *Chem. Rev.* **2021,** *121* (4), 2713-2775.
164. Aykol, M.; Dwaraknath Shyam, S.; Sun, W.; Persson Kristin, A., Thermodynamic limit for synthesis of metastable inorganic materials. *Sci. Adv.* **2018,** *4* (4), eaaq0148.
165. Sorrenti, A.; Leira-Iglesias, J.; Markvoort, A. J.; de Greef, T. F. A.; Hermans, T. M., Non-equilibrium supramolecular polymerization. *Chem. Soc. Rev.* **2017,** *46* (18), 5476-5490.
166. van Rossum, S. A. P.; Tena-Solsona, M.; van Esch, J. H.; Eelkema, R.; Boekhoven, J., Dissipative out-of-equilibrium assembly of man-made supramolecular materials. *Chem. Soc. Rev.* **2017,** *46* (18), 5519-5535.
167. Chamorro, J. R.; McQueen, T. M., Progress toward Solid State Synthesis by Design. *Acc. Chem. Res.* **2018,** *51* (11), 2918-2925.
168. Sheckelton, J. P.; Neilson, J. R.; Soltan, D. G.; McQueen, T. M., Possible valence-bond condensation in the frustrated cluster magnet LiZn2Mo3O8. *Nat. Mater.* **2012,** *11* (6), 493-496.
169. Kumar, D. K.; Steed, J. W., Supramolecular gel phase crystallization: orthogonal self-assembly under non-equilibrium conditions. *Chem. Soc. Rev.* **2014,** *43* (7), 2080-2088.

170. Brown, R. D.; Corcelli, S. A.; Kandel, S. A., Structural Polymorphism as the Result of Kinetically Controlled Self-Assembly. *Acc. Chem. Res.* **2018,** *51* (2), 465-474.
171. Mikita, R.; Aharen, T.; Yamamoto, T.; Takeiri, F.; Ya, T.; Yoshimune, W.; Fujita, K.; Yoshida, S.; Tanaka, K.; Batuk, D.; Abakumov, A. M.; Brown, C. M.; Kobayashi, Y.; Kageyama, H., Topochemical Nitridation with Anion Vacancy-Assisted N3–/O2– Exchange. *J. Am. Chem. Soc.* **2016,** *138* (9), 3211-3217.
172. Allendorf, M. D.; Stavila, V.; Witman, M.; Brozek, C. K.; Hendon, C. H., What Lies beneath a Metal–Organic Framework Crystal Structure? New Design Principles from Unexpected Behaviors. *J. Am. Chem. Soc.* **2021,** *143* (18), 6705-6723.
173. Kalmutzki, M. J.; Hanikel, N.; Yaghi, O. M., Secondary building units as the turning point in the development of the reticular chemistry of MOFs. **2018,** *4* (10), eaat9180.
174. O'Keeffe, M.; Peskov, M. A.; Ramsden, S. J.; Yaghi, O. M., The Reticular Chemistry Structure Resource (RCSR) Database of, and Symbols for, Crystal Nets. *Acc. Chem. Res.* **2008,** *41* (12), 1782-1789.
175. Karmakar, A.; Paul, A.; Pombeiro, A. J. L., Recent advances on supramolecular isomerism in metal organic frameworks. *CrystEngComm* **2017,** *19* (32), 4666-4695.
176. Makal, T. A.; Yakovenko, A. A.; Zhou, H.-C., Isomerism in Metal–Organic Frameworks: "Framework Isomers". *J. Phys. Chem. Lett.* **2011,** *2* (14), 1682-1689.
177. Cheetham, A. K.; Kieslich, G.; Yeung, H. H. M., Thermodynamic and Kinetic Effects in the Crystallization of Metal–Organic Frameworks. *Acc. Chem. Res.* **2018,** *51* (3), 659-667.
178. Gong, X.; Noh, H.; Gianneschi, N. C.; Farha, O. K., Interrogating Kinetic versus Thermodynamic Topologies of Metal–Organic Frameworks via Combined Transmission Electron Microscopy and X-ray Diffraction Analysis. *J. Am. Chem. Soc.* **2019,** *141* (15), 6146-6151.
179. Liu, W.-G.; Truhlar, D. G., Computational Linker Design for Highly Crystalline Metal–Organic Framework NU-1000. *Chem. Mater.* **2017,** *29* (19), 8073-8081.
180. Bara, D. J.; Wilson, C.; Mörtel, M.; Khusniyarov, M. M.; Ling, S.; Slater, B.; Sproules, S.; Forgan, R. S., Kinetic control of interpenetration in Fe-biphenyl-4,4′-dicarboxylate metal-organic frameworks by coordination and oxidation modulation. *J. Am. Chem. Soc.* **2019,** *141*, 8346–8357.
181. He, T.; Huang, Z.; Yuan, S.; Lv, X.-L.; Kong, X.-J.; Zou, X.; Zhou, H.-C.; Li, J.-R., Kinetically Controlled Reticular Assembly of a Chemically Stable Mesoporous Ni(II)-Pyrazolate Metal-Organic Framework. *J. Am. Chem. Soc.* **2020,** *142* (31), 13491-13499.
182. Lee, S.-J.; Mancuso, J. L.; Le, K. N.; Malliakas, C. D.; Bae, Y.-S.; Hendon, C. H.; Islamoglu, T.; Farha, O. K., Time-Resolved in Situ Polymorphic Transformation from One 12-Connected Zr-MOF to Another. *ACS Mater. Lett.* **2020,** *2* (5), 499-504.
183. Akimbekov, Z.; Katsenis, A. D.; Nagabhushana, G. P.; Ayoub, G.; Arhangelskis, M.; Morris, A. J.; Friščić, T.; Navrotsky, A., Experimental and Theoretical Evaluation of the Stability of True MOF Polymorphs Explains Their Mechanochemical Interconversions. *J. Am. Chem. Soc.* **2017,** *139* (23), 7952-7957.
184. Karadeniz, B.; Žilić, D.; Huskić, I.; Germann, L. S.; Fidelli, A. M.; Muratović, S.; Lončarić, I.; Etter, M.; Dinnebier, R. E.; Barišić, D.; Cindro, N.; Islamoglu, T.; Farha, O. K.; Friščić, T.; Užarević, K., Controlling the Polymorphism and Topology Transformation in Porphyrinic Zirconium Metal–Organic Frameworks via Mechanochemistry. *J. Am. Chem. Soc.* **2019,** *141* (49), 19214-19220.
185. Lo, S.-H.; Feng, L.; Tan, K.; Huang, Z.; Yuan, S.; Wang, K.-Y.; Li, B.-H.; Liu, W.-L.; Day, G. S.; Tao, S.; Yang, C.-C.; Luo, T.-T.; Lin, C.-H.; Wang, S.-L.; Billinge, S. J. L.;

Lu, K.-L.; Chabal, Y. J.; Zou, X.; Zhou, H.-C., Rapid desolvation-triggered domino lattice rearrangement in a metal–organic framework. *Nat. Chem.* **2020,** *12* (1), 90-97.
186. Liu, J.; Lukose, B.; Shekhah, O.; Arslan, H. K.; Weidler, P.; Gliemann, H.; Bräse, S.; Grosjean, S.; Godt, A.; Feng, X.; Müllen, K.; Magdau, I.-B.; Heine, T.; Wöll, C., A novel series of isoreticular metal organic frameworks: realizing metastable structures by liquid phase epitaxy. *Sci. Rep.* **2012,** *2* (1), 921-925.
187. Li, Z.-J.; Ju, Y.; Zhang, Z.; Lu, H.; Li, Y.; Zhang, N.; Du, X.-L.; Guo, X.; Zhang, Z.-H.; Qian, Y.; He, M.-Y.; Wang, J.-Q.; Lin, J., Unveiling the Unique Roles of Metal Coordination and Modulator in the Polymorphism Control of Metal-Organic Frameworks. *Chem. Eur. J.* **2021,** *27* (70), 17586-17594.
188. Hanna, S. L.; Chheda, S.; Anderson, R.; Ray, D.; Malliakas, C. D.; Knapp, J. G.; Otake, K.-i.; Li, P.; Li, P.; Wang, X.; Wasson, M. C.; Zosel, K.; Evans, A. M.; Robison, L.; Islamoglu, T.; Zhang, X.; Dichtel, W. R.; Stoddart, J. F.; Gomez-Gualdron, D. A.; Gagliardi, L.; Farha, O. K., Discovery of spontaneous de-interpenetration through charged point-point repulsions. *Chem* **2022,** *8* (1), 225-242.
189. Li, P.; Vermeulen, N. A.; Malliakas, C. D.; Gómez-Gualdrón, D. A.; Howarth, A. J.; Mehdi, B. L.; Dohnalkova, A.; Browning, N. D.; O'Keeffe, M.; Farha, O. K., Bottom-up construction of a superstructure in a porous uranium-organic crystal. *Science* **2017,** *356* (6338), 624-627.
190. Biology, N. R. M. C., NU-1305 was first published in reference 38 under the name "**1**". We rename it here to "NU-1305" for the sake of consistency. **NU-1305 was first published in reference 38 under the name "1". We rename it here to "NU-1305" for the sake of consistency.**
191. Forgan, R. S., Modulated self-assembly of metal–organic frameworks. *Chem. Sci.* **2020,** *11* (18), 4546-4562.
192. Marshall, C. R.; Timmel, E. E.; Staudhammer, S. A.; Brozek, C. K., Experimental evidence for a general model of modulated MOF nanoparticle growth. *Chem. Sci.* **2020,** *11* (42), 11539-11547.
193. Wu, H.; Chua, Y. S.; Krungleviciute, V.; Tyagi, M.; Chen, P.; Yildirim, T.; Zhou, W., Unusual and Highly Tunable Missing-Linker Defects in Zirconium Metal–Organic Framework UiO-66 and Their Important Effects on Gas Adsorption. *J. Am. Chem. Soc.* **2013,** *135* (28), 10525-10532.
194. Zhang, X.; Huang, Z.; Ferrandon, M.; Yang, D.; Robison, L.; Li, P.; Wang, T. C.; Delferro, M.; Farha, O. K., Catalytic chemoselective functionalization of methane in a metal−organic framework. *Nat. Catal.* **2018,** *1* (5), 356-362.
195. Perdew, J. P.; Ernzerhof, M.; Burke, K., Rationale for mixing exact exchange with density functional approximations. *J. Chem. Phys.* **1996,** *105* (22), 9982-9985.
196. Wang, Y.; He, J.; Liu, C.; Chong, W. H.; Chen, H., Thermodynamics versus Kinetics in Nanosynthesis. *Angew. Chem. Int. Ed.* **2015,** *54* (7), 2022-2051.
197. Balluffi, R. W.; Allen, S. M.; Carter, W. C., Introduction. In *Kinetics of Materials*, 2005; pp 1-19.
198. Laidler, K. J., The development of the Arrhenius equation. *J. Chem. Educ.* **1984,** *61* (6), 494.
199. Bianchini, M.; Wang, J.; Clément, R. J.; Ouyang, B.; Xiao, P.; Kitchaev, D.; Shi, T.; Zhang, Y.; Wang, Y.; Kim, H.; Zhang, M.; Bai, J.; Wang, F.; Sun, W.; Ceder, G., The interplay

between thermodynamics and kinetics in the solid-state synthesis of layered oxides. *Nat. Mater.* **2020,** *19* (10), 1088-1095.
200. Jana, G.; Pan, S.; Merino, G.; Chattaraj, P. K., MNgCCH (M = Cu, Ag, Au; Ng = Xe, Rn): The First Set of Compounds with M–Ng–C Bonding Motif. *J. Phys. Chem. A* **2017,** *121* (34), 6491-6499.
201. Tamayo, A. B.; Alleyne, B. D.; Djurovich, P. I.; Lamansky, S.; Tsyba, I.; Ho, N. N.; Bau, R.; Thompson, M. E., Synthesis and Characterization of Facial and Meridional Tris-cyclometalated Iridium(III) Complexes. *J. Am. Chem. Soc.* **2003,** *125* (24), 7377-7387.
202. Qin, Z.; Zhang, J.; Wan, C.; Liu, S.; Abroshan, H.; Jin, R.; Li, G., Atomically precise nanoclusters with reversible isomeric transformation for rotary nanomotors. *Nat. Commun.* **2020,** *11* (1), 6019.
203. Hua, X.; Liu, Z.; Fischer, M. G.; Borkiewicz, O.; Chupas, P. J.; Chapman, K. W.; Steiner, U.; Bruce, P. G.; Grey, C. P., Lithiation Thermodynamics and Kinetics of the TiO2 (B) Nanoparticles. *J. Am. Chem. Soc.* **2017,** *139* (38), 13330-13341.
204. Hatcher, L. E.; Skelton, J. M.; Warren, M. R.; Raithby, P. R., Photocrystallographic Studies on Transition Metal Nitrito Metastable Linkage Isomers: Manipulating the Metastable State. *Acc. Chem. Res.* **2019,** *52* (4), 1079-1088.
205. Lynch, M. S.; Cheng, M.; Van Kuiken, B. E.; Khalil, M., Probing the Photoinduced Metal−Nitrosyl Linkage Isomerism of Sodium Nitroprusside in Solution Using Transient Infrared Spectroscopy. *J. Am. Chem. Soc.* **2011,** *133* (14), 5255-5262.
206. Kirschner, M. S.; Diroll, B. T.; Guo, P.; Harvey, S. M.; Helweh, W.; Flanders, N. C.; Brumberg, A.; Watkins, N. E.; Leonard, A. A.; Evans, A. M.; Wasielewski, M. R.; Dichtel, W. R.; Zhang, X.; Chen, L. X.; Schaller, R. D., Photoinduced, reversible phase transitions in all-inorganic perovskite nanocrystals. *Nat. Commun.* **2019,** *10* (1), 504.
207. Bechtel, J. S.; Thomas, J. C.; Van der Ven, A., Finite-temperature simulation of anharmonicity and octahedral tilting transitions in halide perovskites. *Phys. Rev. Mater.* **2019,** *3* (11), 113605.
208. Jiang, Y.-s.; Yu, F.-d.; Que, L.-f.; Deng, L.; Xia, Y.; Ke, W.; Han, Y.; Wang, Z.-b., Revealing the Thermodynamics and Kinetics of In-Plane Disordered Li2MnO3 Structure in Li-Rich Cathodes. *ACS Energy Lett.* **2021,** *6* (11), 3836-3843.
209. Gong, Y.; Zhang, Y.; Qin, C.; Sun, C.; Wang, X.; Su, Z., Bottom-Up Construction and Reversible Structural Transformation of Supramolecular Isomers based on Large Truncated Tetrahedra. *Angew. Chem. Int. Ed.* **2019,** *58* (3), 780-784.
210. Ma, C.; Zheng, L.; Wang, G.; Guo, J.; Li, L.; He, Q.; Chen, Y.; Zhang, H., Phase engineering of metal-organic frameworks. *Aggregate* **2022,** *3* (1), e145.
211. Fan, W.-W.; Cheng, Y.; Zheng, L.-Y.; Cao, Q.-E., Reversible Phase Transition of Porous Coordination Polymers. *Chem. Eur. J.* **2020,** *26* (13), 2766-2779.
212. Halder, A.; Ghoshal, D., Structure and properties of dynamic metal–organic frameworks: a brief accounts of crystalline-to-crystalline and crystalline-to-amorphous transformations. *CrystEngComm* **2018,** *20* (10), 1322-1345.
213. Gonzalez-Nelson, A.; Coudert, F.-X.; van der Veen, M. A. Rotational Dynamics of Linkers in Metal–Organic Frameworks *Nanomaterials* [Online], 2019.
214. Zhao, P.; Tsang, S. C. E.; Fairen-Jimenez, D., Structural heterogeneity and dynamics in flexible metal-organic frameworks. *Cell Rep. Phys. Sci.* **2021,** *2* (9), 100544.
215. Redfern, L. R.; Farha, O. K., Mechanical properties of metal–organic frameworks. *Chem. Sci.* **2019,** *10* (46), 10666-10679.

216. Lapidus, S. H.; Halder, G. J.; Chupas, P. J.; Chapman, K. W., Exploiting high pressures to generate porosity, polymorphism, and lattice expansion in the nonporous molecular framework Zn(CN)2. *J. Am. Chem. Soc.* **2013,** *135* (20), 7621-7628.
217. Taylor, M. K.; Runčevski, T.; Oktawiec, J.; Gonzalez, M. I.; Siegelman, R. L.; Mason, J. A.; Ye, J.; Brown, C. M.; Long, J. R., Tuning the Adsorption-Induced Phase Change in the Flexible Metal–Organic Framework Co(bdp). *J. Am. Chem. Soc.* **2016,** *138* (45), 15019-15026.
218. Wu, H.; Zhou, W.; Yildirim, T., Methane Sorption in Nanoporous Metal−Organic Frameworks and First-Order Phase Transition of Confined Methane. *J. Phys. Chem. C* **2009,** *113* (7), 3029-3035.
219. Zhang, J.; Kosaka, W.; Kitagawa, Y.; Miyasaka, H., A metal–organic framework that exhibits CO2-induced transitions between paramagnetism and ferrimagnetism. *Nat. Chem.* **2021,** *13* (2), 191-199.
220. Ferguson, A.; Liu, L.; Tapperwijn, S. J.; Perl, D.; Coudert, F.-X.; Van Cleuvenbergen, S.; Verbiest, T.; van der Veen, M. A.; Telfer, S. G., Controlled partial interpenetration in metal–organic frameworks. *Nat. Chem.* **2016,** *8* (3), 250-257.
221. Choi, S. B.; Furukawa, H.; Nam, H. J.; Jung, D.-Y.; Jhon, Y. H.; Walton, A.; Book, D.; O'Keeffe, M.; Yaghi, O. M.; Kim, J., Reversible Interpenetration in a Metal–Organic Framework Triggered by Ligand Removal and Addition. *Angew. Chem. Int. Ed.* **2012,** *51* (35), 8791-8795.
222. Jiang, H.-L.; Makal, T. A.; Zhou, H.-C., Interpenetration control in metal–organic frameworks for functional applications. *Coord. Chem. Rev.* **2013,** *257* (15), 2232-2249.
223. Novendra, N.; Marrett, J. M.; Katsenis, A. D.; Titi, H. M.; Arhangelskis, M.; Friščić, T.; Navrotsky, A., Linker Substituents Control the Thermodynamic Stability in Metal–Organic Frameworks. *J. Am. Chem. Soc.* **2020,** *142* (52), 21720-21729.
224. Sun, H.; Wu, D., Recent advances in experimental thermodynamics of metal–organic frameworks. *Powder Diffr.* **2019,** *34* (4), 297-301.
225. Lyu, J.; Gong, X.; Lee, S.-J.; Gnanasekaran, K.; Zhang, X.; Wasson, M. C.; Wang, X.; Bai, P.; Guo, X.; Gianneschi, N. C.; Farha, O. K., Phase Transitions in Metal–Organic Frameworks Directly Monitored through In Situ Variable Temperature Liquid-Cell Transmission Electron Microscopy and In Situ X-ray Diffraction. *J. Am. Chem. Soc.* **2020,** *142* (10), 4609-4615.
226. Widmer, R. N.; Lampronti, G. I.; Chibani, S.; Wilson, C. W.; Anzellini, S.; Farsang, S.; Kleppe, A. K.; Casati, N. P. M.; MacLeod, S. G.; Redfern, S. A. T.; Coudert, F.-X.; Bennett, T. D., Rich Polymorphism of a Metal–Organic Framework in Pressure–Temperature Space. *J. Am. Chem. Soc.* **2019,** *141* (23), 9330-9337.
227. Friščić, T.; Halasz, I.; Beldon, P. J.; Belenguer, A. M.; Adams, F.; Kimber, S. A. J.; Honkimäki, V.; Dinnebier, R. E., Real-time and in situ monitoring of mechanochemical milling reactions. *Nat. Chem.* **2013,** *5* (1), 66-73.
228. Walton, R. I.; Millange, F., In Situ Studies of the Crystallization of Metal–Organic Frameworks. In *The Chemistry of Metal–Organic Frameworks*, 2016; pp 729-764.
229. Feyand, M.; Hübner, A.; Rothkirch, A.; Wragg, D. S.; Stock, N., Copper Phosphonatoethanesulfonates: Temperature Dependent in Situ Energy Dispersive X-ray Diffraction Study and Influence of the pH on the Crystal Structures. *Inorg. Chem.* **2012,** *51* (22), 12540-12547.
230. Ragon, F.; Horcajada, P.; Chevreau, H.; Hwang, Y. K.; Lee, U. H.; Miller, S. R.; Devic, T.; Chang, J.-S.; Serre, C., In Situ Energy-Dispersive X-ray Diffraction for the Synthesis Optimization and Scale-up of the Porous Zirconium Terephthalate UiO-66. *Inorg. Chem.* **2014,** *53* (5), 2491-2500.

231. Yeung, H. H. M.; Wu, Y.; Henke, S.; Cheetham, A. K.; O'Hare, D.; Walton, R. I., In Situ Observation of Successive Crystallizations and Metastable Intermediates in the Formation of Metal–Organic Frameworks. *Angew. Chem. Int. Ed.* **2016,** *55* (6), 2012-2016.
232. Wang, B.; Lv, X. L.; Feng, D.; Xie, L. H.; Zhang, J.; Li, M.; Xie, Y.; Li, J. R.; Zhou, H. C., Highly Stable Zr(IV)-Based Metal-Organic Frameworks for the Detection and Removal of Antibiotics and Organic Explosives in Water. *J. Am. Chem. Soc.* **2016,** *138* (19), 6204-16.
233. Wang, X.; Zhang, X.; Li, P.; Otake, K.-i.; Cui, Y.; Lyu, J.; Krzyaniak, M. D.; Zhang, Y.; Li, Z.; Liu, J.; Buru, C. T.; Islamoglu, T.; Wasielewski, M. R.; Li, Z.; Farha, O. K., Vanadium Catalyst on Isostructural Transition Metal, Lanthanide, and Actinide Based Metal–Organic Frameworks for Alcohol Oxidation. *J. Am. Chem. Soc.* **2019,** *141* (20), 8306-8314.
234. Robison, L.; Gong, X.; Evans, A. M.; Son, F. A.; Wang, X.; Redfern, L. R.; Wasson, M. C.; Syed, Z. H.; Chen, Z.; Idrees, K. B.; Islamoglu, T.; Delferro, M.; Dichtel, W. R.; Coudert, F.-X.; Gianneschi, N. C.; Farha, O. K., Transient Catenation in a Zirconium-Based Metal–Organic Framework and Its Effect on Mechanical Stability and Sorption Properties. *J. Am. Chem. Soc.* **2021,** *143* (3), 1503-1512.
235. Liu, T. F.; Vermeulen, N. A.; Howarth, A. J.; Li, P.; Sarjeant, A. A.; Hupp, J. T.; Farha, O. K., Adding to the Arsenal of Zirconium-Based Metal-Organic Frameworks: the Topology as a Platform for Solvent-Assisted Metal Incorporation. *Eur. J. Inorg. Chem.* **2016,** (27), 4349-4352.
236. Bumstead, A. M.; Cordes, D. B.; Dawson, D. M.; Chakarova, K. K.; Mihaylov, M. Y.; Hobday, C. L.; Duren, T.; Hadjiivanov, K. I.; Slawin, A. M. Z.; Ashbrook, S. E.; Prasad, R. R. R.; Wright, P. A., Modulator-Controlled Synthesis of Microporous STA-26, an Interpenetrated 8,3-Connected Zirconium MOF with the the-i Topology, and its Reversible Lattice Shift. *Chem. Eur. J.* **2018,** *24* (23), 6115-6126.
237. Wu, Y.; Henke, S.; Kieslich, G.; Schwedler, I.; Yang, M.; Fraser, D. A. X.; O'Hare, D., Time-Resolved In Situ X-ray Diffraction Reveals Metal-Dependent Metal–Organic Framework Formation. *Angew. Chem. Int. Ed.* **2016,** *55* (45), 14081-14084.
238. Kirlikovali, K. O.; Chen, Z.; Wang, X.; Mian, M. R.; Alayoglu, S.; Islamoglu, T.; Farha, O. K., Investigating the Influence of Hexanuclear Clusters in Isostructural Metal–Organic Frameworks on Toxic Gas Adsorption. *ACS Appl. Mater. Interfaces* **2022,** *14* (2), 3048-3056.
239. Lyu, J.; Zhang, X.; Li, P.; Wang, X.; Buru, C. T.; Bai, P.; Guo, X.; Farha, O. K., Exploring the Role of Hexanuclear Clusters as Lewis Acidic Sites in Isostructural Metal–Organic Frameworks. *Chem. Mater.* **2019,** *31* (11), 4166-4172.
240. Li, P.; Wang, X.; Otake, K.-i.; Lyu, J.; Hanna, S. L.; Islamoglu, T.; Farha, O. K., Synthetic Control of Thorium Polyoxo-Clusters in Metal–Organic Frameworks toward New Thorium-Based Materials. *ACS Appl. Nano Mater.* **2019,** *2* (4), 2260-2265.
241. Jensen, K. M. Ø.; Tyrsted, C.; Bremholm, M.; Iversen, B. B., In Situ Studies of Solvothermal Synthesis of Energy Materials. *ChemSusChem* **2014,** *7* (6), 1594-1611.
242. Van Vleet, M. J.; Weng, T.; Li, X.; Schmidt, J. R., In Situ, Time-Resolved, and Mechanistic Studies of Metal–Organic Framework Nucleation and Growth. *Chem. Rev.* **2018,** *118* (7), 3681-3721.
243. Avrami, M., Kinetics of Phase Change. I General Theory. *J. Chem. Phys.* **1939,** *7* (12), 1103-1112.
244. Avrami, M., Kinetics of Phase Change. II Transformation-Time Relations for Random Distribution of Nuclei. *J. Chem. Phys.* **1940,** *8* (2), 212-224.
245. Avrami, M., Granulation, Phase Change, and Microstructure Kinetics of Phase Change. III. *J. Chem. Phys.* **1941,** *9* (2), 177-184.

246. Henkelis, S. E.; Mazur, M.; Rice, C. M.; Wheatley, P. S.; Ashbrook, S. E.; Morris, R. E., Kinetics and Mechanism of the Hydrolysis and Rearrangement Processes within the Assembly–Disassembly–Organization–Reassembly Synthesis of Zeolites. *J. Am. Chem. Soc.* **2019,** *141* (10), 4453-4459.
247. Walton, R. I.; Millange, F.; O'Hare, D.; Davies, A. T.; Sankar, G.; Catlow, C. R. A., An in Situ Energy-Dispersive X-ray Diffraction Study of the Hydrothermal Crystallization of Zeolite A. 1. Influence of Reaction Conditions and Transformation into Sodalite. *J. Phys. Chem. B* **2001,** *105* (1), 83-90.
248. Kadja, G. T. M.; Azhari, N. J.; Mukti, R. R.; Khalil, M., A Mechanistic Investigation of Sustainable Solvent-Free, Seed-Directed Synthesis of ZSM-5 Zeolites in the Absence of an Organic Structure-Directing Agent. *ACS Omega* **2021,** *6* (1), 925-933.
249. Martell, J. D.; Milner, P. J.; Siegelman, R. L.; Long, J. R., Kinetics of cooperative CO2 adsorption in diamine-appended variants of the metal–organic framework Mg2(dobpdc). *Chem. Sci.* **2020,** *11* (25), 6457-6471.
250. Widmer, R. N.; Lampronti, G. I.; Casati, N.; Farsang, S.; Bennett, T. D.; Redfern, S. A. T., X-ray radiation-induced amorphization of metal–organic frameworks. *Phys. Chem. Chem. Phys.* **2019,** *21* (23), 12389-12395.
251. Das, C.; Nishiguchi, T.; Fan, Z.; Horike, S., Crystallization Kinetics of a Liquid-Forming 2D Coordination Polymer. *Nano Lett.* **2022,** *22* (23), 9372-9379.
252. Donakowski, A.; Miller, D. W.; Anderson, N. C.; Ruth, A.; Sanehira, E. M.; Berry, J. J.; Irwin, M. D.; Rockett, A.; Steirer, K. X., Improving Photostability of Cesium-Doped Formamidinium Lead Triiodide Perovskite. *ACS Energy Lett.* **2021,** *6* (2), 574-580.
253. Ok, K. M.; Lee, D. W.; Smith, R. I.; O'Hare, D., Time-Resolved in Situ Neutron Diffraction under Supercritical Hydrothermal Conditions: A Study of the Synthesis of KTiOPO4. *J. Am. Chem. Soc.* **2012,** *134* (43), 17889-17891.
254. Brunauer, S.; Emmett, P. H.; Teller, E., Adsorption of gases in multimolecular layers. *J. Am. Chem. Soc.* **1938,** *60* (2), 309-319.
255. Galarneau, A.; Villemot, F.; Rodriguez, J.; Fajula, F.; Coasne, B., Validity of the t-plot Method to Assess Microporosity in Hierarchical Micro/Mesoporous Materials. *Langmuir* **2014,** *30* (44), 13266-13274.
256. Zhao, X.; He, H.; Dai, F.; Sun, D.; Ke, Y., Supramolecular Isomerism in Honeycomb Metal−Organic Frameworks Driven by CH···π Interactions: Homochiral Crystallization from an Achiral Ligand through Chiral Inducement. *Inorg. Chem.* **2010,** *49* (19), 8650-8652.
257. Carlucci, L.; Ciani, G.; Proserpio, D. M., Polycatenation, polythreading and polyknotting in coordination network chemistry. *Coord. Chem. Rev.* **2003,** *246* (1), 247-289.
258. Forgan, R. S.; Sauvage, J.-P.; Stoddart, J. F., Chemical topology: complex molecular knots, links, and entanglements. *Chem. Rev.* **2011,** *111* (9), 5434-5464.
259. Hasell, T.; Cooper, A. I., Porous organic cages: soluble, modular and molecular pores. *Nat. Rev. Mater.* **2016,** *1* (9), 16053-16066.
260. Chen, Z.; Li, P.; Anderson, R.; Wang, X.; Zhang, X.; Robison, L.; Redfern, L. R.; Moribe, S.; Islamoglu, T.; Gómez-Gualdrón, D. A.; Yildirim, T.; Stoddart, J. F.; Farha, O. K., Balancing volumetric and gravimetric uptake in highly porous materials for clean energy. *Science* **2020,** *368* (6488), 297-303.
261. Banerjee, D.; Simon, C. M.; Elsaidi, S. K.; Haranczyk, M.; Thallapally, P. K., Xenon Gas Separation and Storage Using Metal-Organic Frameworks. *Chem* **2018,** *4* (3), 466-494.

262. Dong, J.; Zhang, K.; Li, X.; Qian, Y.; Zhu, H.; Yuan, D.; Xu, Q.-H.; Jiang, J.; Zhao, D., Ultrathin two-dimensional porous organic nanosheets with molecular rotors for chemical sensing. *Nat. Commun.* **2017,** *8* (1), 1142-1155.
263. Koo, W.-T.; Jang, J.-S.; Kim, I.-D., Metal-Organic Frameworks for Chemiresistive Sensors. *Chem* **2019,** *5* (8), 1938-1963.
264. Lian, X.; Fang, Y.; Joseph, E.; Wang, Q.; Li, J.; Banerjee, S.; Lollar, C.; Wang, X.; Zhou, H.-C., Enzyme–MOF (metal–organic framework) composites. *Chem. Soc. Rev.* **2017,** *46* (11), 3386-3401.
265. McKinlay, A. C.; Morris, R. E.; Horcajada, P.; Férey, G.; Gref, R.; Couvreur, P.; Serre, C., BioMOFs: metal–organic frameworks for biological and medical applications. *Angew. Chem. Int. Ed.* **2010,** *49* (36), 6260-6266.
266. Sheberla, D.; Bachman, J. C.; Elias, J. S.; Sun, C.-J.; Shao-Horn, Y.; Dincă, M., Conductive MOF electrodes for stable supercapacitors with high areal capacitance. *Nat. Mater.* **2017,** *16* (2), 220-224.
267. Bavykina, A.; Kolobov, N.; Khan, I. S.; Bau, J. A.; Ramirez, A.; Gascon, J., Metal–organic frameworks in heterogeneous catalysis: recent progress, new trends, and future perspectives. *Chem. Rev.* **2020,** *120* (16), 8468-8535.
268. Cao, J.; Ma, W.; Lyu, K.; Zhuang, L.; Cong, H.; Deng, H., Twist and sliding dynamics between interpenetrated frames in Ti-MOF revealing high proton conductivity. *Chem. Sci.* **2020,** *11* (15), 3978-3985.
269. Furukawa, H.; Cordova, K. E.; O'Keeffe, M.; Yaghi, O. M., The chemistry and applications of metal-organic frameworks. *Science* **2013,** *341* (6149), 974-986.
270. Liang, W.; Bhatt, P. M.; Shkurenko, A.; Adil, K.; Mouchaham, G.; Aggarwal, H.; Mallick, A.; Jamal, A.; Belmabkhout, Y.; Eddaoudi, M., A Tailor-Made Interpenetrated MOF with Exceptional Carbon-Capture Performance from Flue Gas. *Chem* **2019**.
271. Zhang, X.; Chen, Z.; Liu, X.; Hanna, S. L.; Wang, X.; Taheri-Ledari, R.; Maleki, A.; Li, P.; Farha, O. K., A historical overview of the activation and porosity of metal–organic frameworks. *Chem. Soc. Rev.* **2020,** *49* (20), 7406-7427.
272. Eddaoudi, M.; Kim, J.; Rosi, N.; Vodak, D.; Wachter, J.; Keeffe, M.; Yaghi, O. M., Systematic design of pore size and functionality in isoreticular MOFs and their application in methane storage. *Science* **2002,** *295* (5554), 469-472.
273. Shekhah, O.; Wang, H.; Paradinas, M.; Ocal, C.; Schüpbach, B.; Terfort, A.; Zacher, D.; Fischer, R. A.; Wöll, C., Controlling interpenetration in metal–organic frameworks by liquid-phase epitaxy. *Nat. Mater.* **2009,** *8* (6), 481-484.
274. Hyde, S. T.; O'Keeffe, M.; Proserpio, D. M., A short history of an elusive yet ubiquitous structure in chemistry, materials, and mathematics. *Angew. Chem. Int. Ed.* **2008,** *47* (42), 7996-8000.
275. Yuan, S.; Zou, L.; Qin, J.-S.; Li, J.; Huang, L.; Feng, L.; Wang, X.; Bosch, M.; Alsalme, A.; Cagin, T.; Zhou, H.-C., Construction of hierarchically porous metal–organic frameworks through linker labilization. *Nat. Commun.* **2017,** *8* (1), 15356.
276. Hönicke, I. M.; Senkovska, I.; Bon, V.; Baburin, I. A.; Bönisch, N.; Raschke, S.; Evans, J. D.; Kaskel, S., Balancing mechanical stability and ultrahigh porosity in crystalline framework materials. *Angew. Chem. Int. Ed.* **2018,** *57* (42), 13780-13783.
277. Düren, T.; Millange, F.; Férey, G.; Walton, K. S.; Snurr, R. Q., Calculating geometric surface areas as a characterization tool for metal−organic frameworks. *J. Phys. Chem. C* **2007,** *111* (42), 15350-15356.

278. te Velde, G.; Bickelhaupt, F. M.; Baerends, E. J.; Fonseca Guerra, C.; van Gisbergen, S. J. A.; Snijders, J. G.; Ziegler, T., Chemistry with ADF. *J. Comput. Chem.* **2001,** *22* (9), 931-967.
279. Zhao, Y.; Truhlar, D. G., A new local density functional for main-group thermochemistry, transition metal bonding, thermochemical kinetics, and noncovalent interactions. *J. Chem. Phys.* **2006,** *125* (19), 194101-194118.
280. Marenich, A. V.; Cramer, C. J.; Truhlar, D. G., Universal solvation model based on solute electron density and on a continuum model of the solvent defined by the bulk dielectric constant and atomic surface tensions. *J. Phys. Chem. B* **2009,** *113* (18), 6378-6396.
281. Anderson, R.; Gómez-Gualdrón, D. A., Increasing topological diversity during computational "synthesis" of porous crystals: how and why. *CrystEngComm* **2019,** *21* (10), 1653-1665.
282. Colón, Y. J.; Gómez-Gualdrón, D. A.; Snurr, R. Q., Topologically guided, automated construction of metal–organic frameworks and their evaluation for energy-related applications. *Cryst. Growth Des.* **2017,** *17* (11), 5801-5810.
283. Sheldrick, G., Phase annealing in SHELX-90: direct methods for larger structures. *Acta Crystallogr. A* **1990,** *46* (6), 467-473.
284. Krause, L.; Herbst-Irmer, R.; Sheldrick, G. M.; Stalke, D., Comparison of silver and molybdenum microfocus X-ray sources for single-crystal structure determination. *J. Appl. Crystallogr.* **2015,** *48* (1), 3-10.
285. Schneider, T. R.; Sheldrick, G. M., Substructure solution with SHELXD. *Acta Crystallogr. D* **2002,** *58* (10 Part 2), 1772-1779.
286. Frisch, M. J.; Trucks, G. W.; Schlegel, H. B.; Scuseria, G. E.; Robb, M. A.; Cheeseman, J. R.; Scalmani, G.; Barone, V.; Petersson, G. A.; Nakatsuji, H.; Li, X.; Caricato, M.; Marenich, A. V.; Bloino, J.; Janesko, B. G.; Gomperts, R.; Mennucci, B.; Hratchian, H. P.; Ortiz, J. V.; Izmaylov, A. F.; Sonnenberg, J. L.; Williams; Ding, F.; Lipparini, F.; Egidi, F.; Goings, J.; Peng, B.; Petrone, A.; Henderson, T.; Ranasinghe, D.; Zakrzewski, V. G.; Gao, J.; Rega, N.; Zheng, G.; Liang, W.; Hada, M.; Ehara, M.; Toyota, K.; Fukuda, R.; Hasegawa, J.; Ishida, M.; Nakajima, T.; Honda, Y.; Kitao, O.; Nakai, H.; Vreven, T.; Throssell, K.; Montgomery Jr., J. A.; Peralta, J. E.; Ogliaro, F.; Bearpark, M. J.; Heyd, J. J.; Brothers, E. N.; Kudin, K. N.; Staroverov, V. N.; Keith, T. A.; Kobayashi, R.; Normand, J.; Raghavachari, K.; Rendell, A. P.; Burant, J. C.; Iyengar, S. S.; Tomasi, J.; Cossi, M.; Millam, J. M.; Klene, M.; Adamo, C.; Cammi, R.; Ochterski, J. W.; Martin, R. L.; Morokuma, K.; Farkas, O.; Foresman, J. B.; Fox, D. J. *Gaussian 16 Rev. C.01*, Wallingford, CT, 2016.
287. Becke, A. D., Density-functional exchange-energy approximation with correct asymptotic behavior. *Phys. Rev. A* **1988,** *38* (6), 3098-3100.
288. Lee, C.; Yang, W.; Parr, R. G., Development of the Colle-Salvetti correlation-energy formula into a functional of the electron density. *Phys. Rev. B* **1988,** *37* (2), 785-789.
289. Landers, J.; Gor, G. Y.; Neimark, A. V., Density functional theory methods for characterization of porous materials. *Colloids Surf. A: Physicochem. Eng. Asp.* **2013,** *437*, 3-32.
290. Mayo, S. L.; Olafson, B. D.; Goddard, W. A., DREIDING: a generic force field for molecular simulations. *J. Phys. Chem.* **1990,** *94* (26), 8897-8909.
291. Kresse, G.; Furthmüller, J., Efficient iterative schemes for ab initio total-energy calculations using a plane-wave basis set. *Phys. Rev. B* **1996,** *54* (16), 11169-11186.
292. Grunder, S.; Valente, C.; Whalley, A. C.; Sampath, S.; Portmann, J.; Botros, Y. Y.; Stoddart, J. F., Molecular gauge blocks for building on the nanoscale. *Chem. Eur. J.* **2012,** *18* (49), 15632-15649.

293. Chai, Z.; Wan, S.; Zhong, C.; Xu, T.; Fang, M.; Wang, J.; Xie, Y.; Zhang, Y.; Mei, A.; Han, H.; Peng, Q.; Li, Q.; Li, Z., Conjugated or broken: the introduction of isolation spacer ahead of the anchoring moiety and the improved device performance. *ACS Appl. Mater. Interfaces* **2016,** *8* (42), 28652-28662.
294. Yuan, S.; Zou, L.; Li, H.; Chen, Y.-P.; Qin, J.; Zhang, Q.; Lu, W.; Hall, M. B.; Zhou, H.-C., Flexible zirconium metal-organic frameworks as bioinspired switchable catalysts. *Angew. Chem. Int. Ed.* **2016,** *55* (36), 10776-10780.
295. Spek, A., PLATON SQUEEZE: a tool for the calculation of the disordered solvent contribution to the calculated structure factors. *Acta Crystallogr. C* **2015,** *71* (1), 9-18.
296. Coupry, D. E.; Addicoat, M. A.; Heine, T., Extension of the universal force field for metal–organic frameworks. *J. Chem. Theory Comput.* **2016,** *12* (10), 5215-5225.
297. Kinoshita, Y.; Matsubara, I.; Saito, Y., The Crystal Structure of Bis(succinonitrilo)copper(I) Nitrate. *Bull. Chem. Soc. Jpn.* **1959,** *32* (7), 741-747.
298. Kinoshita, Y.; Matsubara, I.; Higuchi, T.; Saito, Y., The Crystal Structure of Bis(adiponitrilo)copper(I) Nitrate. *Bull. Chem. Soc. Jpn.* **1959,** *32* (11), 1221-1226.
299. Kinoshita, Y.; Matsubara, I.; Saito, Y., The Crystal Structure of Bis(glutaronitrilo)copper(I) Nitrate. *Bull. Chem. Soc. Jpn.* **1959,** *32* (11), 1216-1221.
300. Jiao, L.; Seow, J. Y. R.; Skinner, W. S.; Wang, Z. U.; Jiang, H.-L., Metal–organic frameworks: Structures and functional applications. *Mater. Today* **2019,** *27*, 43-68.
301. Chen, Z.; Hanna, S. L.; Redfern, L. R.; Alezi, D.; Islamoglu, T.; Farha, O. K., Reticular chemistry in the rational synthesis of functional zirconium cluster-based MOFs. *Coord. Chem. Rev.* **2019,** *386*, 32-49.
302. Yaghi, O. M., Reticular Chemistry in All Dimensions. *ACS Cent. Sci.* **2019,** *5* (8), 1295-1300.
303. Gilson, S. E.; Li, P.; Szymanowski, J. E. S.; White, J.; Ray, D.; Gagliardi, L.; Farha, O. K.; Burns, P. C., In Situ Formation of Unprecedented Neptunium-Oxide Wheel Clusters Stabilized in a Metal–Organic Framework. *Journal of the American Chemical Society* **2019,** *141* (30), 11842-11846.
304. Farha, O. K.; Eryazici, I.; Jeong, N. C.; Hauser, B. G.; Wilmer, C. E.; Sarjeant, A. A.; Snurr, R. Q.; Nguyen, S. T.; Yazaydın, A. Ö.; Hupp, J. T., Metal–Organic Framework Materials with Ultrahigh Surface Areas: Is the Sky the Limit? *J. Am. Chem. Soc.* **2012,** *134* (36), 15016-15021.
305. Luo, S.; Zeng, Z.; Zeng, G.; Liu, Z.; Xiao, R.; Chen, M.; Tang, L.; Tang, W.; Lai, C.; Cheng, M.; Shao, B.; Liang, Q.; Wang, H.; Jiang, D., Metal Organic Frameworks as Robust Host of Palladium Nanoparticles in Heterogeneous Catalysis: Synthesis, Application, and Prospect. *ACS Appl. Mater. Interfaces* **2019,** *11* (36), 32579-32598.
306. Wasson, M. C.; Buru, C. T.; Chen, Z.; Islamoglu, T.; Farha, O. K., Metal–organic frameworks: A tunable platform to access single-site heterogeneous catalysts. *Appl. Catal., A* **2019,** *586*, 117214.
307. Elkin, T.; Saouma, C. T., Effect of linker and metal on photoreduction and cascade reactions of nitroaromatics by M-UiO-66 metal organic frameworks. *Inorganica Chimica Acta* **2019,** *497*, 119076.
308. Platero-Prats, A. E.; Li, Z.; Gallington, L. C.; Peters, Aaron W.; Hupp, J. T.; Farha, O. K.; Chapman, K. W., Addressing the characterisation challenge to understand catalysis in MOFs: the case of nanoscale Cu supported in NU-1000. *Faraday Discussions* **2017,** *201* (0), 337-350.

309. Li, X.; Wang, B.; Cao, Y.; Zhao, S.; Wang, H.; Feng, X.; Zhou, J.; Ma, X., Water Contaminant Elimination Based on Metal–Organic Frameworks and Perspective on Their Industrial Applications. *ACS Sustain. Chem. Eng.* **2019,** *7* (5), 4548-4563.
310. Yang, W.; Pan, Q.; Song, S.; Zhang, H., Metal–organic framework-based materials for the recovery of uranium from aqueous solutions. *Inorg. Chem. Front.* **2019,** *6* (8), 1924-1937.
311. Shah, M.; McCarthy, M. C.; Sachdeva, S.; Lee, A. K.; Jeong, H.-K., Current Status of Metal–Organic Framework Membranes for Gas Separations: Promises and Challenges. *Ind. Eng. Chem. Res.* **2012,** *51* (5), 2179-2199.
312. Nugent, P.; Belmabkhout, Y.; Burd, S. D.; Cairns, A. J.; Luebke, R.; Forrest, K.; Pham, T.; Ma, S.; Space, B.; Wojtas, L.; Eddaoudi, M.; Zaworotko, M. J., Porous materials with optimal adsorption thermodynamics and kinetics for CO2 separation. *Nature* **2013,** *495*, 80.
313. Li, L.; Lin, R.-B.; Krishna, R.; Wang, X.; Li, B.; Wu, H.; Li, J.; Zhou, W.; Chen, B., Flexible–Robust Metal–Organic Framework for Efficient Removal of Propyne from Propylene. *Journal of the American Chemical Society* **2017,** *139* (23), 7733-7736.
314. Wang, Y.; Hu, Z.; Cheng, Y.; Zhao, D., Silver-Decorated Hafnium Metal–Organic Framework for Ethylene/Ethane Separation. *Ind. Eng. Chem. Res.* **2017,** *56* (15), 4508-4516.
315. Kalmutzki, M. J.; Diercks, C. S.; Yaghi, O. M., Metal–Organic Frameworks for Water Harvesting from Air. *Adv. Mater.* **2018,** *30* (37), 1704304.
316. Peng, Y.-L.; Pham, T.; Li, P.; Wang, T.; Chen, Y.; Chen, K.-J.; Forrest, K. A.; Space, B.; Cheng, P.; Zaworotko, M. J.; Zhang, Z., Robust Ultramicroporous Metal–Organic Frameworks with Benchmark Affinity for Acetylene. *Angew. Chem. Int. Ed.* **2018,** *57* (34), 10971-10975.
317. Wang, C.; Volotskova, O.; Lu, K.; Ahmad, M.; Sun, C.; Xing, L.; Lin, W., Synergistic Assembly of Heavy Metal Clusters and Luminescent Organic Bridging Ligands in Metal–Organic Frameworks for Highly Efficient X-ray Scintillation. *Journal of the American Chemical Society* **2014,** *136* (17), 6171-6174.
318. Perry, J. J.; Feng, P. L.; Meek, S. T.; Leong, K.; Doty, F. P.; Allendorf, M. D., Connecting structure with function in metal-organic frameworks to design novel photo- and radioluminescent materials. *J. Mater. Chem.* **2012,** *22* (20), 10235-10248.
319. Doty, F. P.; Bauer, C. A.; Skulan, A. J.; Grant, P. G.; Allendorf, M. D., Scintillating Metal-Organic Frameworks: A New Class of Radiation Detection Materials. *Adv. Mater.* **2009,** *21* (1), 95-101.
320. Small, L. J.; Hill, R. C.; Krumhansl, J. L.; Schindelholz, M. E.; Chen, Z.; Chapman, K. W.; Zhang, X.; Yang, S.; Schröder, M.; Nenoff, T. M., Reversible MOF-Based Sensors for the Electrical Detection of Iodine Gas. *ACS Appl. Mater. Interfaces* **2019,** *11* (31), 27982-27988.
321. Small, L. J.; Nenoff, T. M., Direct Electrical Detection of Iodine Gas by a Novel Metal–Organic-Framework-Based Sensor. *ACS Appl. Mater. Interfaces* **2017,** *9* (51), 44649-44655.
322. Li, J.; Wang, X.; Zhao, G.; Chen, C.; Chai, Z.; Alsaedi, A.; Hayat, T.; Wang, X., Metal–organic framework-based materials: superior adsorbents for the capture of toxic and radioactive metal ions. *Chem. Soc. Rev.* **2018,** *47* (7), 2322-2356.
323. Xiao, C.; Silver, M. A.; Wang, S., Metal–organic frameworks for radionuclide sequestration from aqueous solution: a brief overview and outlook. *Dalton Trans.* **2017,** *46* (47), 16381-16386.
324. Kang, C.; Peng, Y.; Tang, Y.; Huang, H.; Zhong, C., Sulfate-Rich Metal–Organic Framework for High Efficiency and Selective Removal of Barium from Nuclear Wastewater. *Ind. Eng. Chem. Res.* **2017,** *56* (46), 13866-13873.

325. Zare Karizi, F.; Beheshti, S.; Morsali, A., Modulating iodine adsorption in nanoporous metal-organic framework via cation exchange process. *Inorganica Chimica Acta* **2018,** *482*, 113-117.
326. Al Lafi, A. G.; Assfour, B.; Assaad, T., Metal Organic Framework MIL-101(Cr): Spectroscopic Investigations to Reveal Iodine Capture Mechanism. *J. Inorg. Organomet. Polym.* **2019**.
327. Assaad, T.; Assfour, B., Metal organic framework MIL-101 for radioiodine capture and storage. *Journal of Nuclear Materials* **2017,** *493*, 6-11.
328. Sava, D. F.; Garino, T. J.; Nenoff, T. M., Iodine Confinement into Metal–Organic Frameworks (MOFs): Low-Temperature Sintering Glasses To Form Novel Glass Composite Material (GCM) Alternative Waste Forms. *Ind. Eng. Chem. Res.* **2012,** *51* (2), 614-620.
329. Jones, R. H., Radiation Effects; A Compilation of Special Topic Reports, prepared for the Waste Package Materials Performance Peer Review, submitted to U.S. DOE and Bechtel SAIC Company, 18-1 (2002).
330. Volkringer, C.; Falaise, C.; Devaux, P.; Giovine, R.; Stevenson, V.; Pourpoint, F.; Lafon, O.; Osmond, M.; Jeanjacques, C.; Marcillaud, B.; Sabroux, J. C.; Loiseau, T., Stability of metal–organic frameworks under gamma irradiation. *Chem. Commun.* **2016,** *52* (84), 12502-12505.
331. Xiong, L.-p.; Lv, K.; Gu, M.; Yang, C.-t.; Wu, F.-c.; Han, J.; Hu, S., Efficient capture of actinides from strong acidic solution by hafnium phosphonate frameworks with excellent acid resistance and radiolytic stability. *Chem. Eng. J.* **2019,** *355*, 159-169.
332. Berseneva, A. A.; Martin, C. R.; Galitskiy, V. A.; Ejegbavwo, O. A.; Leith, G. A.; Ly, R. T.; Rice, A. M.; Dolgopolova, E. A.; Smith, M. D.; zur Loye, H.-C.; DiPrete, D. P.; Amoroso, J. W.; Shustova, N. B., "Boarding-Up": Radiation Damage and Radionuclide Leaching Kinetics in Linker-Capped Metal–Organic Frameworks. *Inorg. Chem.* **2020,** *59* (1), 179-183.
333. Zhu, L.; Sheng, D.; Xu, C.; Dai, X.; Silver, M. A.; Li, J.; Li, P.; Wang, Y.; Wang, Y.; Chen, L.; Xiao, C.; Chen, J.; Zhou, R.; Zhang, C.; Farha, O. K.; Chai, Z.; Albrecht-Schmitt, T. E.; Wang, S., Identifying the Recognition Site for Selective Trapping of 99TcO4– in a Hydrolytically Stable and Radiation Resistant Cationic Metal–Organic Framework. *Journal of the American Chemical Society* **2017,** *139* (42), 14873-14876.
334. Lee, S.-J.; Yoon, T.-U.; Kim, A.-R.; Kim, S.-Y.; Cho, K.-H.; Hwang, Y. K.; Yeon, J.-W.; Bae, Y.-S., Adsorptive separation of xenon/krypton mixtures using a zirconium-based metal-organic framework with high hydrothermal and radioactive stabilities. *J. Hazard. Mater.* **2016,** *320*, 513-520.
335. Liu, W.; Dai, X.; Bai, Z.; Wang, Y.; Yang, Z.; Zhang, L.; Xu, L.; Chen, L.; Li, Y.; Gui, D.; Diwu, J.; Wang, J.; Zhou, R.; Chai, Z.; Wang, S., Highly Sensitive and Selective Uranium Detection in Natural Water Systems Using a Luminescent Mesoporous Metal-Organic Framework Equipped with Abundant Lewis Basic Sites: A Combined Batch, X-ray Absorption Spectroscopy, and First Principles Simulation Investigation. *Environ. Sci. Technol.* **2017,** *51* (7), 3911-3921.
336. Drout, R. J.; Otake, K.; Howarth, A. J.; Islamoglu, T.; Zhu, L.; Xiao, C.; Wang, S.; Farha, O. K., Efficient Capture of Perrhenate and Pertechnetate by a Mesoporous Zr Metal–Organic Framework and Examination of Anion Binding Motifs. *Chem. Mater.* **2018,** *30* (4), 1277-1284.

337. Chibani, S.; Badawi, M.; Loiseau, T.; Volkringer, C.; Cantrel, L.; Paul, J.-F., A DFT study of RuO4 interactions with porous materials: metal–organic frameworks (MOFs) and zeolites. *Physical Chemistry Chemical Physics* **2018,** *20* (24), 16770-16776.
338. Wang, T. C.; Vermeulen, N. A.; Kim, I. S.; Martinson, A. B. F.; Stoddart, J. F.; Hupp, J. T.; Farha, O. K., Scalable synthesis and post-modification of a mesoporous metal-organic framework called NU-1000. *Nat. Protoc.* **2015,** *11*, 149.
339. Islamoglu, T.; Otake, K.-i.; Li, P.; Buru, C. T.; Peters, A. W.; Akpinar, I.; Garibay, S. J.; Farha, O. K., Revisiting the structural homogeneity of NU-1000, a Zr-based metal–organic framework. *CrystEngComm* **2018,** *20* (39), 5913-5918.
340. Ayoub, G.; Islamoglu, T.; Goswami, S.; Friščić, T.; Farha, O. K., Torsion Angle Effect on the Activation of UiO Metal–Organic Frameworks. *ACS Appl. Mater. Interfaces* **2019,** *11* (17), 15788-15794.